Multi-wavelength cosmology with clusters of galaxies

Miren Muñoz Echeverria

Université Grenoble Alpes

THÈSE

Pour obtenir le grade de

DOCTEUR DE L'UNIVERSITÉ GRENOBLE ALPES

École doctorale : PHYS - Physique
Spécialité : Physique Subatomique et Astroparticules
Unité de recherche : Laboratoire de Physique Subatomique et Cosmologie

Cosmologie multi-longueur d'onde avec les amas de galaxies

Multi-wavelength cosmology with clusters of galaxies

Présentée par :

Miren MUÑOZ ECHEVERRíA

Direction de thèse :

Juan-Francisco MACíAS PÉREZ CNRS, Université Grenoble Alpes	Directeur de thèse

Rapporteures :

Sophie MAUROGORDATO
Directrice de recherche, CNRS
Anne EALET
Directrice de recherche, CNRS

Thèse soutenue publiquement le **26 octobre 2023**, devant le jury composé de :

Sophie MAUROGORDATO Directrice de recherche, CNRS	Rapporteure
Anne EALET Directrice de recherche, CNRS	Rapporteure
Tony MROCZKOWSKI Astronome adjoint, European Southern Observatory (ESO)	Examinateur
Laurent DEROME Professeur des universités, Laboratoire de Physique Subatomique et Cosmologie	Président
Roser PELLÓ Astronome, Laboratoire d'Astrophysique de Marseille	Examinatrice

“ A (wo)man with a watch knows what time it is.
A (wo)man with two watches is never sure.”

Acknowledgements

This thesis is the result of three years of work at the Laboratoire de Physique Subatomique et Cosmologie (LPSC) in Grenoble. It began in the era of COVID-19 and online meetings and ended after the successful launch of the JWST and Euclid space telescopes and in a world full of injustice and (even more) wars.

I would like to start these acknowledgements by thanking the jury members for agreeing to participate in my thesis defence. Thank you to Sophie Maurogordato and Anne Ealet for the careful reading of my thesis and the inspiring feedback. Thank you also to Tony Mroczkowski for travelling to Grenoble for my defence, it was an honour for me to have you as a jury member. I am also grateful to Roser Pelló for joining the defence from Brazil, and to Laurent Derome for being the director of the Particle Physics and Cosmology master's programme, director of the LPSC and president of my PhD defence jury, always so rigorous and helpful.

Cette thèse a été préparée au sein de l'équipe COSMO-ML et je tiens à remercier l'équipe d'avoir mis à disposition les moyens (économiques, matériels et humains) qui ont rendu mes travaux possibles. Merci à Laurence Perotto et Frédéric Mayet d'avoir dirigé le LPSZ dans un cadre de travail excellent, d'avoir assisté avec autant de patience à tellement de répétitions et réunions, et de votre regard critique et au même temps humain. Je voudrais aussi remercier Nicolas Ponthieu et François-Xavier Désert pour toute la connaissance sur l'analyse de données de NIKA2 transmise et Andrea Catalano d'apporter toujours un point de vue différent aux discussions scientifiques.

Un grand merci également aux membres transitoires du COSMO-ML, à Florian Kéruzoré, Alejandro Jiménez Muñoz et Emmanuel Artis de m'avoir accompagné dans le début de ma thèse et m'avoir donné plein d'astuces sur Python, Mathematica et LaTeX ; à Corentin Hanser et Alice Moyer-Anin pour les bons moments dans notre beau bureau de co-working ; et à Florian Ruppin et Rémi Adam d'avoir été des exemples à suivre et avoir partagé avec moi votre expertise dans l'étude des amas. Je souhaite à Sofia et à Damien des belles thèses dans l'équipe et une bonne continuation dans le service info/Euclid à Gaël ! Je voudrais aussi remercier les stagiaires (en particulier, Renaud, Victor et Abigail), doctorant.e.s et post-docs du LPSC, avec une mention spéciale aux collègues du troisième étage et des repas à H2.

Todo el trabajo presentado en esta tesis no hubiese existido sin la dirección, inteligencia y generosidad de Juan Francisco Macías Pérez. Muchas gracias por estos tres años de preguntas y respuestas, por acompañarme en la búsqueda de respuestas a las nuevas preguntas, y por haberme abierto tantas puertas. Yo, así, puedo seguir siendo estudiante de tesis toda mi vida. Eskerrik asko Juan!

In addition to the people working in Grenoble, I would like to thank the members of the LPSZ, Gabriel Pratt, Jean-Baptiste Melin, Iacopo Bartalucci, and Etienne Pointecouteau for following and contributing to my work with your knowledge on the domain. Special thanks go to the Italian (Indian) and Spanish colleagues: Marco de Petris, Antonio Ferragamo, Aishwarya Paliwal, Daniel de Andres, and Gustavo Yepes. It has been a pleasure to share so many Zoom meetings with you and to meet you in person at the collaboration meetings at La Cristalera and Tenerife. Thank you for your kindness and work on hydrodynamical simulations.

I am also very grateful to the NIKA2 collaboration and to the staff at the IRAM 30-metre telescope. Your work has been essential to make this thesis possible. Moreover, I have had the chance to collaborate with Roberto Neri, from whom I have learnt almost all I know about NOEMA and interferometry. Thanks Roberto, and thanks also to the NOEMA staff. Similarly, I would like to thank the CONCERTO collaboration and the people working at the APEX telescope. Muchas gracias Alessandro por los paseos en San Pedro de Atacama y el pescado en Marsella, la próxima vez en Tenerife o Toulouse!

These three years, I have also had the opportunity to meet very inspiring people at conferences and schools. Thanks to all of them for the scientific and personal conversations and shared moments.

Et puisque, malgré une thèse, la terre continue de tourner et la vie ne s'arrête pas, j'ai été très heureuse de partager ces dernières années avec mes grenoblois.es préféré.e.s.

Merci à María, Florie et Espe d'être arrivées tout au début de ma vie à Grenoble, d'avoir crié fort, cuisiné bon et dansé tard avec moi. Quand je serai grande, je veux être comme vous.

Muchísimas gracias a los pececillos del Isère. Gracias Jorge, María y Gonzalo por los días de monte, por las conversaciones sinceras y por ser casa. Estos años nada hubiese sido lo mismo sin vosotr@s.

Gracias también al club de expatriados, a Ana, Dani, Jesús, Martina, Álvaro, Ángel, Mario... por las tan poco objetivas comparaciones entre Francia y España. Thank you to Saranath, David, Ariel, Xinye, and the italian people for being so nice with me. Merci aussi à Gaétan, Capucine, Damien, Marie Laure, Ion et Martin de m'avoir permis de garder les pieds sur terre, malgré ma vie dans la bulle des physicien.ne.s. Et une mention spéciale à la Bastille, qui me rend toujours de bonne humeur. Tu vas tellement me manquer !

Eta eskerrik beroenak etxekoei. Mila esker Ainize, Irati eta Irati nire aurkezpena ikustera Grenobleraino etorri izanagatik. Horregatik, eta beste guztiagatik.

Eskerrik asko Oñatiko lagunei. Itzultzen naizen aldiro inoiz joan izan ez banintz bezala egiten jarrai dezagun! Mila esker baita ere nafarrei. Zenbat maite ditudan gure bazkari/afari/egun pasa/oporrak! Eta Leioan elkar ezagutu genuenetik hain kuttun bihurtu diren fisikari eta ingeniari elektronikoei ere eskerrak! Ziurrenik Antzokiko gaurik gabe ez nintzateke inoiz doktoretza tesi hau bukatzera iritsi izango.

Y a Gonzalo, gracias con el alma. Gracias por las risas y el amor. Eskerrik asko urte hauetan bizitza nirekin partekatzea aukeratu izanagatik. Zaila izango da ahazten!

Eta bukatzeko, eskerrak bihotzez ama, aita eta Carlosi, eta baita inguruko Etxeberria, Muñoz, Murgiondo eta Sánchez guztiei ere. Gracias por estar siempre, sea cual sea la distancia.

Nere bizitzako emakumeei, y a todas las personas que saben caminar a nuestro lado.

Contents

Introduction

The ultimate goal of cosmological analyses is to model the observed Universe so that we can explain its evolution from the primordial ages to our days. The last decades have brought accurate measurements of the temperature and anisotropies in the Cosmic Microwave Background [1], of the abundances of the primordial elements [2], of the accelerating expansion of the Universe [3] and of the baryon acoustic oscillations [4] that helped to improve our knowledge of the content and expansion rate of the Universe. These observations are fairly well represented by the standard model of cosmology.

Aiming towards a concordance model, the combination of different cosmological probes is thought to be the best way to improve on accuracy and reduce to a minimum the contribution of systematic effects that each observable could be subject to. The high-precision era of cosmology has demonstrated that despite the overall agreement between cosmological models and observations, some fundamental questions remain unanswered and several inconsistencies appear from the comparison of the results obtained from different probes. These days, we still fail to describe both the early- and late-Universe with a unique model.

This could mean that the current prevailing cosmological models are either wrong or incomplete. Although we are able to reproduce at large scales the structure formation in the Universe driven by gravitational forces, at small scales additional forces come into play and these are not yet well understood. We now know that the latter have a non-negligible impact on the formation history of galaxy clusters, galaxies and even smaller astrophysical objects. In addition, the inconsistencies between different observables could originate from an incorrect treatment of systematic effects in the data. Thus, it is essential to dig into the biases and uncertainties of each individual analysis.

In the framework of observational cosmology, the present thesis focuses on different systematic effects that might limit the use of galaxy clusters as cosmological probes. Galaxy clusters are formed at the end of the hierarchical structure formation process in the Universe and their distribution in mass and redshift traces the evolution and matter content of the Universe. Thus, the mass of galaxy clusters is a fundamental property of interest for cosmological analyses with clusters. However, cluster masses are not direct observable quantities and have to be estimated under several assumptions from observations. Mass estimates of clusters and their associated biases and uncertainties constitute the major field of study of this thesis.

In the last years, several galaxy cluster surveys [5–15] have been able to exploit large catalogues of clusters of galaxies and infer the so-called *cosmological parameters*. At millimetre wavelengths, the *Planck* satellite [16], the Atacama Cosmology Telescope (ACT) [17] and the South Pole Telescope (SPT) [18] have observed large fractions of the sky with arcminute resolutions and detected thousands of clusters through the Sunyaev-Zel'dovich (SZ) effect, being able to obtain statistically significant cosmological results. To date, these analyses are limited by the incomplete knowledge of galaxy clusters' physical properties. In particular, the characterisation of high redshift clusters requires high angular resolution observations. The NIKA2 camera, installed at the IRAM 30-metre telescope, is an ideal instrument for observing clusters through the SZ effect at sub-arcminute resolution. Even higher resolution can be attained thanks to the NOrthern Extended Millimeter Array (NOEMA) interferometer.

This thesis offers a multi-wavelength view of galaxy clusters. An important part of the work is devoted to

the analysis of NIKA2 data at millimetre wavelengths. We investigate the impact of different systematic effects related to the raw data analysis on the mass reconstruction of clusters. From the comparison to X-ray and optical data, we assess the error in the mass related to data selection or assumed hypotheses. We also make use of simulated galaxy clusters to evaluate intrinsic effects in the cluster mass estimations that are unquantifiable from observations. The manuscript is divided into eight chapters.

- The first chapter (1) presents the current understanding of the structure formation in the Universe within the standard model of cosmology. We describe also the physical properties and components of galaxy clusters, as well as their observations at different wavelengths. We motivate the use of galaxy clusters as a cosmological probe and explain the importance of their masses for cosmological purposes. The last part of the chapter is consecrated to the different approaches used to estimate cluster masses from observations.

- Chapter 2 is devoted to the NIKA2 camera. We present the main characteristics of the instrument and the observations with NIKA2, together with the steps in the raw data processing pipeline that are needed to get to calibrated data. In the same chapter, we describe the noise subtraction methods for NIKA2 observations and the assessment of the quality of the final maps.

- The NIKA2 SZ Large Programme is presented in chapter 3, where we explain the scientific goals of the programme and the selected targets. The method used to reconstruct the thermal pressure of clusters accounting for the contamination by other astrophysical sources in the data and by instrumental and data processing effects is detailed also in chapter 3. We propose different approaches to estimate the mass of galaxy clusters from the combination of NIKA2 data with X-ray observations under the hydrostatic equilibrium assumption.

- In chapter 4 we study the impact of the systematic effects related to the NIKA2 data analysis presented in the previous chapters on the reconstructed hydrostatic masses. We illustrate with the example of the CL J1226.9+3332 galaxy cluster. We compare the results obtained in our analysis to other works in the literature, taking care of the different assumptions and definitions considered in each case.

  We then seek to quantify and understand the origin of the bias of cluster masses estimated under the hydrostatic equilibrium hypothesis. These masses are compared to the estimates obtained from the lensing effects on background galaxies. Two distinct studies are presented in two chapters.

- In chapter 5 we investigate the bias of hydrostatic masses with respect to lensing mass estimates for four clusters (CL J1226.9+3332, PSZ2 G144.83+25.11, PSZ2 G228.16+75.20 and MACS J1423.8+2404) observed with the NIKA2 camera or with its pathfinder NIKA. For the lensing masses, we make use of the convergence maps reconstructed with the Cluster Lensing And Supernova survey data from the Hubble space telescope. We study the different biases of hydrostatic masses obtained from the combination of SZ and X-ray data or from X-ray data only. We also compute the gas mass fraction in the clusters.

- A larger sample of clusters spanning a redshift range of $0.05 < z < 1.07$ is used in chapter 6 to explore a potential evolution of the hydrostatic mass bias with redshift. In this case, hydrostatic masses are derived from X-ray-only analyses. An important part of the chapter is devoted to the sample selection and to the comparison of masses obtained by different works in the literature. Then, we model the evolution of the bias, both neglecting and accounting for the intrinsic scatter of hydrostatic and lensing masses with respect to the true masses of clusters.

- Chapter 7 is based on simulated clusters from THE THREE HUNDRED project and explores the intrinsic effects that bias the reconstruction of the mass of clusters from projected data, without considering observational and instrumental uncertainties. We use a sample of synthetic clusters selected to be twins to the NIKA2 SZ Large Programme targets. We reconstruct the mass of each object by modelling the projected convergence maps, following the same method as for the lensing mass reconstructions in chapter 5. From

the comparison to the true masses of the clusters known from the simulation, we investigate the origin of the mass bias and its scatter.

– The last chapter (8) of this thesis is devoted to an unprecedented observation of a galaxy cluster with the NOEMA interferometer. We describe the principles of radio interferometry and the observations of the CL J1226.9+3332 galaxy cluster. NOEMA offers a very high angular resolution that, if demonstrated to be adapted to detect the SZ of clusters, can be used to investigate the gas distribution in the core of very high redshift clusters, as well as the background, foreground and member galaxies. In this chapter, we present the analysis of the sources in the field of CL J1226.9+3332 and the first detection of the SZ of a cluster with NOEMA.

CHAPTER 1

Cosmology and clusters of galaxies

The precise reconstruction of the physical properties and, in particular, of the mass of clusters of galaxies is the main topic of this thesis. In this chapter, we present the cosmological framework that explains the formation of structures in the Universe, from the primordial Universe until the formation of galaxy clusters. We describe the general physical properties of clusters and present their observations at different wavelengths. We then motivate the use of galaxy clusters as a cosmological probe and, at the end of the chapter, we detail different approaches to estimate their mass.

1.1 Structure formation in an evolving Universe

In this section, we introduce the standard model of cosmology, which offers a temporal and spatial description of the Universe related to its content. In such evolving Universe, we present how, to our current understanding, halos are formed in a structure formation process that is hierarchical.

1.1.1 The standard model of cosmology

The standard model of cosmology describes in a remarkable manner the evolution of the Universe (see Abdalla et al. (2022) [19] for a review). Following Einstein's theory of General Relativity, it assumes that changes in space-time are related to the energetic content of the Universe through

$$G_{\mu\nu} - \Lambda g_{\mu\nu} = \frac{8\pi G}{c^4} T_{\mu\nu}, \tag{1.1}$$

where $G_{\mu\nu}$ and $g_{\mu\nu}$ are the Einstein tensor and metric, respectively, and describe space-time. $T_{\mu\nu}$ is the stress-energy tensor that describes the content of the Universe. In Eq. 1.1 Λ, G and c are the cosmological constant, the gravitational constant and the speed of light in vacuum. Considering the content of the Universe to be a perfect fluid, the stress-energy tensor can be written as

$$T_{\mu\nu} = (p/c^2 + \rho)u_\mu u_\nu - p g_{\mu\nu}, \tag{1.2}$$

with p, ρ and u_μ the pressure, the energy density and the four-velocity of the fluid, respectively.

If we assume an isotropic and homogeneous Universe, the simplest metric is given by the Friedmann-Lemaître-Robertson-Walker (FLRW) metric, which can be written in spherical coordinates (r, θ, ϕ) as

$$\mathrm{d}s^2 = g_{\mu\nu}\mathrm{d}x^\mu \mathrm{d}x^\nu = c^2\mathrm{d}t^2 - a^2(t)\left[\frac{1}{1-kr^2}\mathrm{d}r^2 + r^2\mathrm{d}\theta^2 + r^2\sin^2\theta\,\mathrm{d}\phi^2\right]. \tag{1.3}$$

In Eq. 1.3 we introduce the scale factor of the Universe $a(t)$ that describes its expansion along cosmic time. It was shown for the first time by Lemaître [20] and Hubble observations [21] that photons of wavelength λ_1 emitted (by a galaxy) at time t_1 are observed at time t_0 with a larger wavelength λ_0. Thus, the Universe is expanding (i.e., a increasing) and photons are *red shifted* due to the expansion of space-time. The scale factor and the *redshift*, z, are related to this dilatation of wavelengths following:

$$1 + z = \frac{\lambda_0}{\lambda_1} = \frac{a(t_0)}{a(t_1)}. \tag{1.4}$$

The curvature of the Universe is represented by the k parameter in Eq. 1.3. From the combination of the above-mentioned equations (Eq. 1.1, 1.2 and 1.3), we get the Friedmann equations that relate the expansion of the Universe to its content:

$$H^2(t) \equiv \left(\frac{\dot{a}}{a}\right)^2 = \frac{8\pi G}{3}\rho + \frac{\Lambda c^2}{3} - \frac{kc^2}{a^2}, \tag{1.5}$$

$$\frac{\ddot{a}}{a} = -\frac{4\pi G}{3}\left(\rho + \frac{3}{c^2}p\right) + \frac{\Lambda c^2}{3}, \tag{1.6}$$

where $\dot{a}$ is the time derivative of the scale factor a and $H(t)$ is the Hubble parameter that quantifies the rate of expansion of the Universe. Considering the Universe to be formed by matter and radiation fluids, we can write the Friedmann equation as the sum of the different component densities,

$$H^2(t) = \frac{8\pi G}{3}\rho_\mathrm{m}(a) + \frac{8\pi G}{3}\rho_\mathrm{r}(a) + \frac{\Lambda c^2}{3} - \frac{kc^2}{a^2}, \tag{1.7}$$

with ρ_m the matter density and ρ_r the radiation density. The matter component comprises the non-relativistic ($p \ll \rho c^2$) elements in the Universe, that is, the baryons (with the cosmological definition of "baryons", including both baryons and leptons) and the cold dark matter (hereafter CDM). The radiation component refers to the photons and any other relativistic element in the Universe, such as neutrinos. We note that ρ_m and ρ_r are both functions of the scale factor, but with a different dependency in each case: $\rho_\mathrm{m} \propto a^{-3}$ and $\rho_\mathrm{r} \propto a^{-4}$.

The density of a Universe with a curvature equal to $k = 0$ and a null cosmological constant, $\Lambda = 0$, defines the critical density of the Universe,

$$\rho_\mathrm{crit} \equiv \frac{3H^2(a)}{8\pi G}. \tag{1.8}$$

It is from the ratio of the different densities with respect to the critical density that we define the widely used *cosmological parameters*: $\Omega_{\rm m}(a) \equiv \rho_{\rm m}(a)/\rho_{\rm crit}$ and $\Omega_{\rm r}(a) \equiv \rho_{\rm r}(a)/\rho_{\rm crit}$. With the cosmological parameters corresponding to the cosmological constant and the curvature defined as $\Omega_\Lambda \equiv \Lambda c^2/3H^2$ and $\Omega_k \equiv -kc^2/(aH)^2$, we rewrite the rate of expansion of the Universe as

$$H^2(a) = H_0^2 \left[\Omega_{\rm m}(a) + \Omega_{\rm r}(a) + \Omega_\Lambda(a) + \Omega_k(a)\right]. \tag{1.9}$$

We introduce here another cosmological parameter, the Hubble constant, H_0, that quantifies the current expansion rate, $H_0 = H(z = 0)$. As we will see in Sect. 1.2.3, the ultimate goal of cosmological analyses [19] is to constrain at the highest precision the values of these cosmological parameters. The standard cosmological model is often separated into the Big Bang theory describing the expansion of the Universe from the Friedmann equations and the ΛCDM describing the energy content of the Universe.

1.1.2 The thermal history of the Universe

According to the Big Bang theory in the standard model of cosmology, the Universe emerged from an extremely hot and dense state. This primordial plasma was composed of ionised particles confined in a very small volume at high pressure. In this compressed state, particles were free and in constant interaction, and the energy density of the universe was dominated by the radiation component, $\rho_{\rm r}$.

The Universe started to expand, decreasing significantly its density and temperature and, therefore, reducing the interactions between particles. Soon afterwards, $\sim$ 3 minutes after the Big Bang ($z \sim 4 \times 10^8$), when the Universe was cool enough ($\sim$ 100 keV $\sim 10^9$ K) the first nuclei were formed from the combination of protons and neutrons. In this Primordial Nucleosynthesis or Big Bang Nucleosynthesis (BBN) hydrogen, helium, and, then, lithium were composed. The success of the theory has been to predict the abundances of the observed amounts of these elements [2].

The Universe kept expanding and with it the density of radiation decreased more rapidly ($\rho_{\rm r} \propto a^{-4}$) than the matter density ($\rho_{\rm m} \propto a^{-3}$). At redshift $z \sim 3400$ ($T \sim 10^4$ K), right after the matter-radiation equality, the Universe reached a matter-dominated era and with it, the expansion rate increased. When the temperature decreased down to $\sim$ 3000 K, the protons and electrons became bound to form the first hydrogen atoms. This is the recombination era of the Universe. The transition of hydrogen atoms from the high energy state to the low energy state emitted photons that could travel freely and decoupled from matter. This light, emitted at redshift $z \sim 1100$, is the first light of the Universe and it is known as the Cosmic Microwave Background (CMB).

Given that the primordial plasma was in thermal equilibrium, the emission of the CMB follows a black-body spectrum, with a temperature that depends on the energetical content of the Universe. In Penzias and Wilson (1965) [1] authors estimated for the first time the temperature of the CMB radiation to be 3.5 ± 1.0 K from the measurement of the unexplained temperature in the Holmdel Horn Antenna. The posterior measurement of the black-body spectrum with the FIRAS instrument in the COBE satellite [22] enabled to constrain the temperature of the CMB black-body to $T_{\rm CMB} = 2.725 \pm 0.002$ K [23]. The great agreement of the model to the observed data was another success for the standard model of cosmology.

Since then, other instruments have again measured the temperature of the CMB [24, 25]. Despite the exceptional homogeneity of the emission, primordial anisotropies of the order of 10^{-4} (few 100 μK) with respect to the average temperature were found[1]. We present in Fig. 1.1 a full-sky map of the CMB temperature anisotropies obtained with the *Planck* satellite. These anisotropies, created by weak fluctuations in the primordial plasma, are the first sign of the structures that were later created in the dense regions of the Universe. The characteristics of the CMB anisotropies are closely related to the properties of the Universe at the time of the emission of this light. For this reason, the analysis of the power spectrum of the CMB temperature anisotropies has been a very powerful tool to constrain cosmological parameters [24]. However, the standard model of cosmology is not able to fully explain the presence of such fluctuations.

[1] In addition to the primordial anisotropies, the temperature map of the CMB contains also a few mK signal from the CMB dipole, introduced mainly by the motion of the solar system with respect to the background [26]

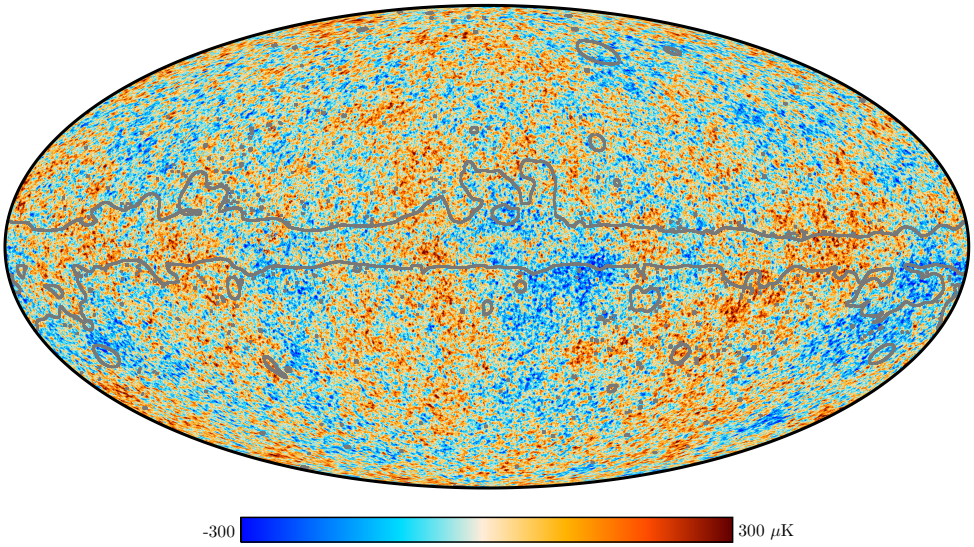

Figure 1.1: CMB temperature anisotropies measured by *Planck*. The grey line indicates the confidence galactic mask. Figure from https://www.cosmos.esa.int/web/planck/picture-gallery, published in Planck Collaboration et al. (2020) [27].

9×10^9 years after the Big Bang, at redshift $z \sim 0.4 - 0.5$, the dark energy (represented in our equations by the cosmological constant Λ) started to dominate the energetical content of the Universe. From this moment on the expansion of the Universe started to accelerate. The observational evidence of the accelerated expansion was obtained from the observation of Type Ia supernovae in Riess et al. (1998) [3].

1.1.3 Origin of large-scale structures explained by the inflation

Even though the standard model of cosmology succeeds in describing many of the observations, it is not able to answer some fundamental questions. We briefly explain here three phenomena that can not be explained by the standard model.

The presence of inhomogeneities. As aforementioned, the measurements of the CMB temperature showed that the Universe, although homogeneous at large scales, it presents inhomogeneities at smaller angular scales. These anisotropies in the density field are the precursors of the astrophysical objects, such as the stars, galaxies or clusters of galaxies, that we observe today (Sect. 1.1.4). Nonetheless, the standard cosmological model can not explain the presence of inhomogeneities in the Universe.

The horizon problem. The prominent homogeneity of the CMB at large scales is also a problem for the standard cosmological model. Observations show that the CMB is (almost) homogeneous in the whole sky map, which contains regions separated by up to 180 degrees. Nevertheless, at the epoch of recombination only regions separated by less than the Hubble horizon of $\sim$ 100 Mpc were causally connected, meaning that in the CMB map regions separated by more than $\sim$ 1 degree should not be causally connected.

The flatness problem. The Friedmann equation has unstable solutions towards $k = 0$, that is, for a flat Universe. However, recent cosmological analyses [27] agree on a Universe with a geometry very close to flatness. According to Planck Collaboration et al. (2020) [28] results, the current curvature of the Universe is of $\Omega_{k,0} \sim 10^{-3}$, which would imply a curvature in the first 10^{-43} seconds of the Universe smaller than 10^{-60}. Such flatness can not be easily understood with the standard model, since it requires the Hubble constant to be fine-tuned to reproduce observations.

In the 1980s the inflationary model was proposed [29, 30] as a possible mechanism to understand some of the issues in the standard cosmological model. According to *inflation*, the primordial Universe goes through an inflationary phase characterised by an extremely fast (of some 10^{-32} seconds) accelerated expansion.

During the inflation phase the Hubble comoving horizon radius decreases with time, before starting to

increase as we observe in the late-Universe. This means that regions that seem causally disconnected in the CMB, in the past had been within the same Hubble sphere, solving in this way the horizon problem. In addition, the inflationary process can also solve the flatness problem, as $\Omega_k = 10^{-60}$ at the end of the inflation.

Also, the presence of inhomogeneities can be explained by inflation. Quantum fluctuations of the inflationary scalar field produced initial perturbations, introducing inhomogeneities in the primordial plasma that evolved to form the structures we observe today.

1.1.4 Evolution of large-scale structures in the linear regime

The quantum fluctuations in the inflationary field lead to tiny density perturbations that evolve first in the linear regime. We can write the density at every (comoving) position $\vec{x}$ and time t as the sum of the mean density of the Universe, $\overline{\rho}(t)$, and the first order perturbation,

$$\rho(\vec{x}, t) = \overline{\rho}(t)\left[1 + \delta(\vec{x}, t)\right], \tag{1.10}$$

with $\delta(\vec{x}, t)$ the density contrast parameter.

Using the Euler, continuity and Poisson equations, we obtain that the contrast parameter evolves as

$$\ddot{\delta} + 2H(t)\dot{\delta} = \left[4\pi G\overline{\rho}(t) + \frac{c_s^2}{a^2}\nabla^2\right]\delta(\vec{x}, t), \tag{1.11}$$

with c_s the speed of sound of the Universe. By defining the Jeans length $\lambda_{\rm J} \equiv c_s/\sqrt{\pi/G\overline{\rho}}$, its associated mode $k_{\rm J} = 2\pi a/\lambda_{\rm J}$ and $\delta_k \sin\left(\vec{k}\cdot\vec{r}\right) = \delta(\vec{x}, t)$, the evolution of the perturbations is written in Fourier space as

$$\ddot{\delta}_k + 2H\dot{\delta}_k = \frac{c_s^2}{a^2}\left(k_{\rm J}^2 - k^2\right)\delta_k. \tag{1.12}$$

We can distinguish two different regimes: $k^2 \ll k_{\rm J}^2$ and $k^2 \gg k_{\rm J}^2$. When the Jeans length is smaller than the scale of perturbations, that is, when $k^2 \ll k_{\rm J}^2$, gravitation dominates this evolution and perturbations grow. If perturbations happen in a smaller scale than the Jeans length, $k^2 \gg k_{\rm J}^2$, pressure is more important than gravitation and the collapse stops.

In the course of the thermal history of the Universe (Sect. 1.1.2), perturbations evolve differently depending on the epoch. In the primordial radiation-dominated era density perturbations oscillate, growing due to gravitational forces and then decreasing when the pressure becomes more important than gravitation. Thus, during this epoch inhomogeneities overall do not evolve. At $z \sim 3400$, when the Universe becomes dominated by matter, gravitation turns out to be stronger than pressure forces and perturbations grow, following $\delta(t) \propto t^{2/3}$ and creating the structures we observe in the Universe. Now, in the dark energy dominated era ($z < 0.5$), the accelerated expansion of the Universe is making the value of the contrast parameter decrease as $\delta(t) \propto \exp(-2Ht)$.

Under the assumption of Gaussian fluctuations in the primordial Universe, the correlation function of the contrast parameter is a valuable function to understand the primordial density distribution. Averaging over all positions $\vec{x}$ in the Universe we obtain

$$\xi(\vec{r}) = \left\langle \delta(\vec{x} + \vec{r})\delta(\vec{r}) \right\rangle. \tag{1.13}$$

The Fourier transform of the correlation function gives the power spectrum,

$$P(k) = \int \xi(\vec{r}) e^{-i\vec{k}\cdot\vec{r}} \mathrm{d}\vec{r}. \tag{1.14}$$

As aforementioned, the primordial fluctuations evolve to form the inhomogeneities in the current Universe. Thus, the power spectrum of the matter distribution observed at $z = 0$ is not the same as the power spectrum of the primordial density distribution. However, both are closely related via the transfer function, $T(z, k)$, which is

used to quantify the evolution of perturbations along cosmic time, and relate the power spectrum in Eq. 1.14 to the spectrum at any redshift z:

$$P(z,k) = P(k)_{\text{primordial}} \times T^2(z,k). \tag{1.15}$$

Observationally constraining and understanding the shape of this power spectrum and its evolution are key elements for the comprehension of the structure formation in the Universe [27]. From the power spectrum we can define the σ_8 cosmological parameter that quantifies the amplitude of the matter fluctuations in a sphere of $8h^{-1}$ Mpc radius at redshift $z = 0$:

$$\sigma_8 = \sqrt{\sigma^2(z=0, r=8h^{-1}\text{ Mpc})}\text{ , with }\sigma^2(z,r) = \frac{1}{(2\pi)^3}\int W(kr)P(z,k)\mathrm{d}^3k. \tag{1.16}$$

Here $W(kr)$ is the window function (see Cui et al. (2008) [31] for details on window functions). We will see in the next sections that the measurement of σ_8 is very important for cosmological studies with galaxy clusters.

1.1.5 Halos in the non-linear regime

When in a given region of the Universe the contrast parameter reaches $\delta(\vec{x}, t) \sim 1$, meaning that the amplitude of the inhomogeneities is of the same order as the average density, the linear regime is no longer valid. In these overdense regions matter is accumulated creating structures by gravitational collapse. The largest gravitationally bound structures in the Universe are the clusters of galaxies and the density in their cores can reach currently $\sim 10^{-22}$ kg/m^3, which corresponds to a contrast of $\sim 10^4$ with respect to the average density of the Universe. Thus, the inhomogeneities in which galaxy clusters lie are very far from the $\delta \ll 1$ required to consider the linear regime.

To date, there is not a rigorous description of the evolution of the density field in the non-linear regime. Nonetheless, observations and large scale structure N-body simulations (see Sect. 7.1) show that structures created in such regime tend to form relatively stable objects in hydrostatic equilibrium [32]. Based on this fact, phenomenological approaches try to explain the dynamics of the density field in the non-linear regime.

A widely accepted approach is the Press-Schechter formalism [33], which predicts the number of objects of a certain mass and within a given volume of the Universe created by gravitational collapse. This formalism assumes that at redshift $z = 0$ all the matter in the Universe is contained in spherical halos that are virialised (Sect. 1.3.3). According to Press-Schechter, the radii of overdense regions first grow, but then collapse gravitationally, reaching finally an equilibrium in which the pressure forces compensate the gravity. The number of halos with masses between M and $M + \mathrm{d}M$ is given by the *halo mass function*: $\mathrm{d}n/\mathrm{d}M$.

Based on the distribution of dark matter halos from numerical simulations, authors in Tinker et al. (2008) [34] gave a formal shape to the halo mass function:

$$\frac{\mathrm{d}n}{\mathrm{d}M} = f(\sigma)\frac{\overline{\rho}}{M}\left|\frac{\mathrm{d}\ln\sigma^{-1}}{\mathrm{d}M}\right|, \tag{1.17}$$

with $\overline{\rho}$ and σ the mean density of the Universe and the amplitude of matter fluctuations (Eq. 1.16). Here $f(\sigma)$ is the halo multiplicity function, that varies from one halo mass function model to another. Regardless of the chosen model, the halo mass function will predict a different amount of halos depending on the matter distribution in the Universe (through the power spectrum in Eq. 1.16) and, therefore, depending on the cosmological parameters. In Fig. 1.2 we show the halo mass function predicted by the model in Tinker et al. (2008) [34] at redshift $z = 0.5$ for different values of the Ω_m and σ_8 parameters. We observe that varying those parameters changes the number of matter halos: higher matter density (Ω_m) and fluctuations in the matter distribution (σ_8) create more halos, and, therefore, more clusters of galaxies. Thus, measuring the distribution of clusters in the Universe with respect to their mass and redshift is a way to constrain the values of Ω_m and σ_8, and the other cosmological parameters. This is the principle of the cosmological analyses with cluster number counts that we will present in Sect. 1.2.3.

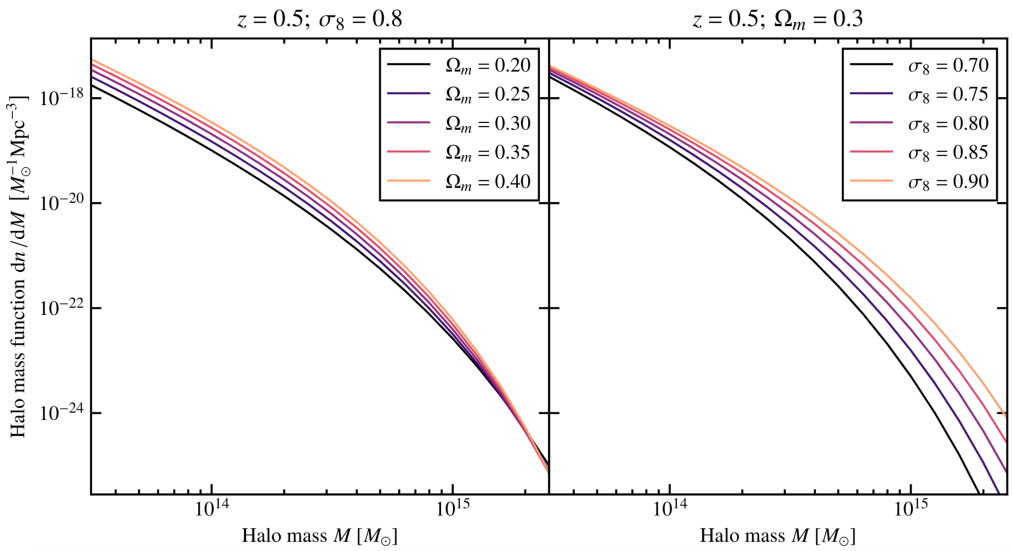

Figure 1.2: Halo abundances at redshift $z = 0.5$ predicted by the halo mass function in Tinker et al. (2008) [34] for different values of the $\Omega_{\rm m}$ (left) and σ_8 (right) cosmological parameters. Figure from Kéruzoré (2021) [35].

From Fig. 1.2 we observe that variations of the matter density have an important influence on the abundance of low mass halos (left panel), while changes in σ_8 modify principally the number of massive halos (right panel). Given the impact that both parameters have on the halo abundances, cosmological analyses with cluster number counts can not constrain both parameters separately, but they are sensitive to a combination of $\Omega_{\rm m}$ and σ_8, usually defined as: $S_8 \equiv \sigma_8 \sqrt{\Omega_{\rm m}/0.3}$ (Sect 1.2.3).

Recent observations from the James Webb Space Telescope (JWST), launched in December 2021, have allowed us to detect the most distant galaxies discovered to date. Some of them appear to be larger and more massive than initially expected [36], at redshifts ($z \sim 10-13$) where such large structures would not be predicted to be bound according to the standard model. Posterior works have shown that the presence of such galaxies could be in reality explained by our current cosmological models [37]. In any case, these observations have opened new questions regarding our understanding of the evolution of the Universe and the impact of baryonic physics on the formation of structures at early times.

1.2 Clusters of galaxies

Since the observations of Charles Messier and William Herschel in the 18th century, it was known that nebulae tend to cluster [32]. Posterior galaxy observations in the 19th and early 20th centuries confirmed the tendency of galaxies to group in very large systems (see Kravtsov and Borgani (2012) [32] and references therein). It was in the 1930s when, from the measurement of the galaxy velocities in clusters, it was shown that under the virial equilibrium assumption the total gravitating mass of clusters had to be enormous [38–40]. These high masses did not match the amount of matter from the observed stars in the clusters and Zwicky postulated the existence of a halo of *dark matter* (DM) that would explain the missing matter. In the 1970s observations of the Coma cluster in X-rays [41–43] showed the existence of an extended emission at very high energies. It was understood to be a thermal bremsstrahlung emission of the hot intracluster medium (ICM) that was filling the intergalactic space in the cluster [44]. In order to explain the presence of bound objects at such high temperatures, it was also necessary to have a very strong gravitational potential. This confirmed the need to have a very prominent dark matter component in galaxy clusters. Since then, thousands of clusters of galaxies have been observed at different wavelengths (see Sect. 1.2.2) and we now know that galaxy clusters are the most massive halos in the Universe.

From our current understanding of a structure formation process that is hierarchical, the perturbations in the primordial density field led to the collapse of small-scale structures that then merged and accreted surrounding

matter to create a filamentary large-scale structure (LSS), also known as the cosmic web [32]. Thus, small structures such as stars and, later galaxies, virialised first and, then, assembled in larger systems in equilibrium. This way, at redshift $z \sim 3$ [45] the first clusters started to form in the nodes of the cosmic web, where the Universe is the densest.

In the past years, great effort was also put into observing high-redshift protoclusters, which are thought to be the progenitors of virialised galaxy clusters [45]. Numerical simulations allow us to trace back clusters in order to define and understand protoclusters [46]. Recent observations of a protocluster at redshift $z \sim 2.16$ [47] show that a protocluster is not only an association of galaxies, since the observed system already contains a halo of hot baryonic gas. This supports the hierarchical structure formation picture. The evolution from sparse protoclusters into virialised clusters requires very energetic events, such as infall and accretion of surrounding matter, mergers of subclusters and feedback from active galactic nuclei (AGN). These effects will certainly impact the thermalisation process, until equilibrium, and the properties of the resulting galaxy cluster. It is hoped that we will be able, in the years to come, to better comprehend these processes and, therefore, have a complete understanding of the cluster formation history.

We will dedicate this section to galaxy clusters. In the first place, we present the properties of clusters as the astrophysical objects they are. In the second place, we describe the observations of galaxy clusters at different wavelengths. And third, we review the different approaches that can be followed to use them as a cosmological probe.

1.2.1 Physical properties

As discovered in the 1930s, galaxy clusters are very massive objects, with masses that span from $\sim 10^{14}$ $M_\odot$ to some few 10^{15} $M_\odot$. We now estimate that $\sim 85\%$ of their total mass is in the form of dark matter, $\sim 12\%$ is hot baryonic matter (again, with the cosmological definition of "baryonic") in the ICM and only the remaining $\sim 3\%$ corresponds to member galaxies. Thus, the matter content in galaxy clusters is fairly representative of that of the Universe [48]. Clusters have typical sizes of the order of some Mpc, but given their extended nature, one can only define their extent based on the drop off of the mass density towards the outskirts or from the radius within which the virial equilibrium is satisfied ($R_{\rm vir}$, see Sect. 1.3.3). Most commonly, we define the mass of the cluster M_Δ enclosed in a radius R_Δ as:

$$M_\Delta = \frac{4\pi}{3}\Delta\rho R_\Delta^3, \tag{1.18}$$

where ρ is either the mean ($\rho_{\rm m}$) or critical ($\rho_{\rm crit}$, Eq. 1.8) matter density of the Universe at the cluster's redshift. The overdensity Δ can take any positive value, but typically masses are given at overdensities of $\Delta = 2500$, 500 or 200. R_{200} is usually close to the virial radius.

Dark matter

Since dark matter is the main component in clusters, at first approximation we can imagine their formation to be driven only by spherical gravitational collapse in an expanding Universe, without any other force playing a role. In that case, the characteristics of the fluctuations in the random Gaussian field that forms the large-scale matter distribution, make the collapsed halos to be self-similar [49]. This means that, since gravitation does not have preferred scales, when normalised with respect to mass and redshift, matter halos are scaled versions of each other.

The self-similarity of DM halos has been observed from cosmological simulations [50]. In Navarro et al. (1996) [51] and Navarro et al. (1997) [52] authors used N-body simulations of a CDM Universe to reproduce the collapse of DM in halos. They obtained that there is a *universal* spherical mass density profile that, when scaled, describes the density profile of every halo. This is the well-known Navarro-Frenk-White (NFW) spherical mass density profile:

$$\rho^{\rm NFW}(r) = \frac{\rho_s}{r/r_s(1+r/r_s)^2} = \frac{\rho_{\rm crit}\delta_{c_\Delta}(c_\Delta)}{r/r_s(1+r/r_s)^2} = \frac{\rho_{\rm crit}\delta_{c_\Delta}(c_\Delta)}{rc_\Delta/R_\Delta(1+rc_\Delta/R_\Delta)^2}, \tag{1.19}$$

where $r_s = R_\Delta / c_\Delta$ is the scale radius, c_Δ the concentration parameter at the Δ overdensity and δ_{c_Δ} is a function that depends only on the concentration and the overdensity,

$$\delta_{c_\Delta} = \frac{\Delta}{3} \frac{c_\Delta^3}{\ln(1 + c_\Delta) - c_\Delta/(1 + c_\Delta)}. \tag{1.20}$$

Navarro et al. (1996) [51] concluded that the concentration of halos is correlated to their mass. In addition, the concentration of halos is related to the cluster's redshift, since it traces the density of the Universe at the epoch of their collapse. Thus, according to Navarro et al. (1996) [51] there is also a relation between the mass of clusters and the redshift at which halos were formed. In summary, if clusters were formed only under gravitational collapse, they could be fully characterised by their redshift and mass.

Intracluster medium

However, clusters also contain $\sim$ 15% of baryonic matter. This implies the interplay of forces other than gravitation, and, therefore, more complex physics. As discussed above, most of the baryonic matter in clusters is in the fully ionised intracluster medium. The ICM is a hot gas ($10^7 - 10^8$ K) of light nuclei and free electrons. It is a sparse plasma, with electron and proton densities of $\sim 10^{-2}$ cm^{-3} in the core of the cluster, decreasing towards the outskirts. Thus, it behaves as an ideal gas that is practically thermalised.

During the structure growth process by the merging of smaller substructures or the accretion of the surrounding material, the co-evolution of gas and DM introduces bulk and turbulent motion in the ICM. As a consequence, ICMs are not fully thermalised and it is estimated that $\sim$ 10% to 30% of their pressure has different natures other than the thermal [53]. In addition, the energetic processes in the formation of clusters can create shocks and adiabatic compression of the gas plasma, as well as turbulence, that as a consequence can heat the ICM [54, 55]. The kinetic energy dissipated in the ICM during the formation process can also contribute to amplifying magnetic fields [56, 57] or to accelerating cosmic rays [58] associated with the intracluster medium.

Shocks are characterised by a discontinuity in the pressure of the ICM. For some time now shocks have been observed in disturbed clusters [59, 60] at X-ray and millimetre wavelengths (Sect. 1.2.2). Recently, they have also been detected in the outskirts of clusters [61]. Such detection is interpreted as the shock produced during the accretion with infalling gas from the outskirts towards the cluster, as we would expect in the hierarchical structure formation context. Even in relaxed clusters, where isobaric perturbations dominate, the ICM turbulence introduces pressure fluctuations. According to simulations [62, 63], these fluctuations are of $\sim$ 10% of the pressure in the core of relaxed systems and of $\sim$ 20% for disturbed clusters, increasing towards the outskirts. In parallel, the subsonic bulk motion of the gas in clusters is identified from high density cold fronts.

The exact origin of magnetic fields within clusters ICM is still unclear and it could derive both from the primordial Universe [64] or from the galaxy formation processes [65]. Along the structure formation, magnetic fields are amplified. The amplitude of the field increases with the electron density in pure adiabatic compression as $|\vec{B}| \propto n_e^{2/3}$. Nonetheless, additional contributions are needed to explain the amplitude of the measured magnetic fields in clusters. Turbulence during merging processes and matter accretion introduces kinetic energy to the ICM, that it is converted through dynamo effects in an amplification of the magnetic fields. Such fields produce synchrotron emission that it is observed in radio frequencies (Sect. 1.2.2) as a diffuse signal coincident with the ICM position.

We also know that cosmic rays (CRs) are present and accelerated within cluster ICMs, due to multiple and possibly entangled processes [58]. Jets of AGNs or the star formation activity could inject these high-energy particles into the ICM. In addition, shocks during cluster formation introduce high energies that can accelerate the particles [59], but it is still difficult to model the relation between the dissipated energy in the ICM shocks and the energy of CRs [66]. Turbulence is also considered an important mechanism that reaccelerates CRs [58].

This dynamical activity goes on for $\sim$ Gyr timescales, which is of the same order as cluster formation processes. As a consequence, observed clusters can be in multiple dynamical states (from disturbed to completely

relaxed) and their physical properties will change depending on their level of relaxation. Overall, baryonic physics will introduce deviations from self-similarity. Comparisons of simulations and observations in Nagai et al. (2007) [67] showed the impact that astrophysical processes have on the thermodynamical quantities of cluster ICMs. Despite the scatter, they demonstrated that the pressure profiles of clusters are also close to self-similarity and that, when scaled, they can be described by an analytical model, the generalised NFW (gNFW):

$$\frac{P(r)}{P_{500}} = \frac{P_0}{x^c(1+x^a)^{(b-c)/a}}, \tag{1.21}$$

with $x \equiv x/r_p$ and $r_p \equiv R_{500}/c_{500}$. b and c are the external and internal slopes, respectively, and a the parameter describing the steepness of the slopes transition. The model is scaled by the pressure P_{500} defined as $P_{500} = 1.45 \times 10^{-11}\text{erg cm}^{-3}\left(\frac{M_{500}}{10^{15}h^{-1}\text{M}_\odot}\right)^{2/3} E(z)^{8/3}$ according to self-similarity [49, 68]. $E(z)$ is the dimensionless Hubble parameter, $E(z) = H(z)/H_0$ and $h = H_0/100\,\text{km s}^{-1}\,\text{Mpc}^{-1}$. In Nagai et al. (2007) [67] the best-fit model parameters on clusters observed with *Chandra* [69] are given by $[P_0, c_{500}, a, b, c] = [3.3, 1.8, 1.3, 4.3, 0.7]$.

Similarly, in Arnaud et al. (2010) [70] (hereafter, A10) XMM-*Newton* satellite [71] observations of the ICM of clusters were used to study the thermodynamical profiles for the REXCESS cluster sample. The REXCESS sample comprises 33 local ($z < 0.2$) clusters spanning a mass range of $10^{14}\ \text{M}_\odot < M_{500} < 10^{15}\ \text{M}_\odot$. In Planck Collaboration et al. (2013) [72] data from *Planck* and XMM-*Newton* satellites were combined to study the ICM of 62 clusters, most of them with redshifts lower than 0.3.

We present in the left panel in Fig. 1.3 the normalised best pressure profiles obtained in A10 in green and in Planck Collaboration et al. (2013) [72] in black. In both works the full sample of clusters was separated, according to their dynamical state, in two: the relaxed cool-core clusters (CC, dashed lines) and the disturbed clusters (non-CC, solid lines). As we observe in Fig. 1.3, on average relaxed clusters have a higher pressure in the core than disturbed ones, showing the impact of the relaxation state on the pressure profile. Nonetheless, both populations of clusters are self-similar at radial ranges between $0.5 < r/R_{500} < 1$, where gravity is driving the physical process. In the right panel in Fig. 1.3 we show in red the pressure profile reconstructed in Pointecouteau et al. (2021) [73] by stacking 31 clusters ($0.16 < z < 0.70$) from the PACT project combining millimetre observations (Sect. 1.2.2) from *Planck* and ACT. The figure shows a comparison to the mean profiles obtained in the aforementioned works.

Just like for the pressure, the whole thermodynamical history of each cluster induces characteristic shapes in the entropy, temperature and electron density profiles [76, 77]. However, the mentioned scatter in the profiles is the smallest for the pressure [70]. The cited works [67, 70, 72, 73] studied the average thermodynamical profiles for low redshift clusters, with most of the objects at $z < 0.5$. Analyses based on higher redshift samples [78, 79] seem to agree on a weak evolution of the ICM physics, at least until $z \sim 1.5$. In particular, in McDonald et al. (2014) [80] *Chandra* observations of 80 SPT-detected clusters (with redshifts $0.3 \lesssim z \lesssim 1.2$) were used to study the potential evolution of the pressure profile along cosmic time. They found that outside the core of clusters the profile does not evolve with redshift.

Galaxies

A small fraction (of the order of a few percent) of the matter in galaxy clusters corresponds to its member galaxies. The distribution and number of galaxies (richness) associated with a cluster are understood to trace the total matter distribution in the cluster (see Sect. 1.3.5). On average, and depending on the cluster's mass, each cluster contains some hundreds or thousands of member galaxies, the galaxy number density decreasing towards the outskirts. Galaxies also interplay with the rest of the matter in the cluster.

Close to the centre of mass of the dark matter halo lies usually the Brightest Cluster Galaxy or BCG. This BCG hosts often an active galactic nucleus (AGN) with a black hole that releases energy in the ICM in the so-called AGN feedback mechanism [81]. In the absence of AGN feedback, the gas in the ICM of relaxed clusters would cool down due to the X-ray radiation. In such a case it would be impossible to understand the high temperatures and entropy in the cluster cores [82] and the evidence that the star formation rate of galaxies

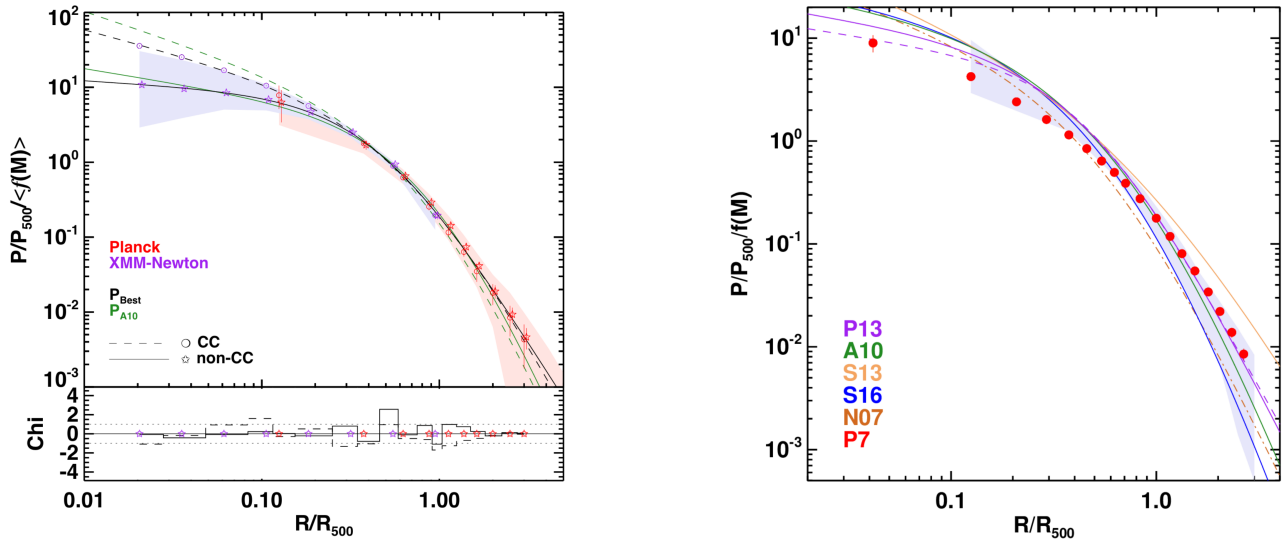

Figure 1.3: Scaled galaxy cluster pressure profiles. Left: profiles derived from *Planck* and XMM-*Newton* observations. Solid and dashed lines show the average profiles for non cool-core and cool-core clusters, respectively. In green the results from Arnaud et al. (2010) [70] and in black from Planck Collaboration et al. (2013) [72]. The figure has been extracted from Planck Collaboration et al. (2013) [72]. Right: a comparison of the profile obtained from *Planck* and ACT data [73] in red, to other results in the literature. The purple, green, yellow, blue and brown lines correspond respectively to the outcomes from Planck Collaboration et al. (2013) [72], Arnaud et al. (2010) [70], Sayers et al. (2013) [74], Sayers et al. (2016) [75], and Nagai et al. (2007) [67]. Figure from Pointecouteau et al. (2021) [73]. The purple shaded area in the right panel and the red in the left panel show the dispersion of the profiles along the sample in Planck Collaboration et al. (2013) [72].

in relaxed clusters is much smaller than expected otherwise [83]. In other words, the energy injected by the powerful jets of AGNs quenches star formation and explains the observed thermodynamical properties of the ICMs of clusters [84].

The metallicity of the ICM is also a consequence of the interplay with galaxies, the latter producing the metals ejected to the intracluster plasma. In addition, the triaxial orientation of the BCG and the cluster have been shown to be correlated [85, 86], proving again the close connection of galaxies within clusters and the surrounding matter in the halo.

In summary, clusters are not perfect spherical systems in hydrostatic equilibrium. In the last years, many efforts have been made to understand and characterise their dynamical state. Simulations have helped to define different indicators that relate observables to morphological and dynamical properties [87, 88] and these indicators have then been applied to observations [89, 90]. For example, a positional offset between the cluster X-ray emission peak and the BCG is a sign of an unrelaxed system. Equally, clusters that are experiencing merging events have their total matter content distributed in various substructures [91]. Discrepancies between masses of clusters estimated from different methods (Sect. 1.3) have also been correlated to systems with complex morphologies [47].

The described astrophysical effects break the ideal self-similarity of halos, but turn clusters into very interesting laboratories to investigate the interactions between dark and baryonic matter. Still, dominated by the dark matter content, we will see in Sect. 1.2.3 that galaxy clusters are great cosmological probes.

1.2.2 Observations of clusters of galaxies

Given the multi-component nature of clusters and the many physical processes that take place in them, galaxy clusters can be observed at different frequency ranges. In this section, we present the observables that allow us to detect and characterise clusters, as well as the physical properties that each probe traces.

Optical and infrared wavelengths

Observations in optical and infrared frequencies trace the galaxies in the field of view of the cluster. On the one hand, we observe the member galaxies, that is, the galaxies that belong to clusters. As we have seen in Sect. 1.2.1, the star formation rate of galaxies in clusters is closely related to the density and temperature of the ICM. Therefore, by studying the nature of these galaxies [92], we can learn about the properties and formation process of the matter halos that they occupy. In addition, the number of galaxies associated with a cluster (richness) and their dynamics (velocity dispersion) are tracers of the cluster mass (Sect. 1.3). The radial distribution of the galaxies in the cluster [93] is also important for cluster detection algorithms at optical and infrared wavelengths [94].

On the other hand, optical and infrared wavelengths also trace indirectly the total matter in the cluster from the observation of the galaxies in the background of clusters. The shapes and positions of these galaxies are distorted by the total matter the light has traversed on its way to the observer. This is the lensing effect (Sect. 1.3 and 5.1) produced by the deep gravitational potential well of halos. Therefore, as we will see in Sect. 1.3 and 5.1, galaxy observations are a very valuable tool to reconstruct the total mass of clusters.

From a technical point of view, optical and infrared observations can be performed in photometry and spectroscopy modes. When in photometry, the sky is mapped to obtain images in different frequency bands. Such images allow observers to identify simultaneously large numbers of galaxies and to estimate their redshifts from the combination of multiple bands [95]. In the last few years, photometry techniques have enabled to build large galaxy catalogues that are then used to detect clusters and study their properties [11, 96]. Spectroscopic observations target sources detected in photometry and extract the spectra of the light from galaxies. From the analyses of these spectra we can identify the emission lines of different elements and, thus, precisely constrain the redshifts of the emitting sources. Spectroscopic techniques, although time-consuming, provide more accurate and reliable redshift estimates than photometry. From the instrumental side, spectroscopy has gone through big improvements in the last years [97–99]. The redshift estimates of member galaxies, from optical and infrared observations are used to estimate the redshift of clusters.

Future large surveys, such as the Legacy Survey of Space and Time (LSST) at the Vera Rubin Observatory [100] and the recently launched *Euclid* mission [101], will provide huge galaxy catalogues and, in this way, contribute to the picture of stellar and total matter distribution in clusters. It is expected that the *Euclid* mission will observe $\sim 10^6$ galaxy clusters [101], while $\sim 10^5$ clusters will be detected by LSST [102].

X-rays

X-ray observations trace the bremsstrahlung emission of the ionised electrons in the hot ICM plasma. The surface brightness of a cluster observed in X-rays, S_X, is given by the integral along the line-of-sight of the electron density in the ICM, n_e, and the cooling function, $\Lambda(T_e, Z)$,

$$S_X = \frac{1}{4\pi(1+z)^4} \int \Lambda(T_e, Z) n_e^2 \mathrm{d}l. \tag{1.22}$$

Note that the electron density is squared in the integral and that the cooling function depends on the temperature in the plasma, T_e, and on the metallicity of the ICM, Z. The surface brightness is affected by cosmological dimming, implying that it decreases with redshift as $(1+z)^{-4}$ (Eq. 1.22). For this reason, it is challenging to observe high redshift clusters in X-rays.

The metallicity, Z, informs us about the amount of heavy elements, that is, elements other than hydrogen or helium, in the medium. Spectroscopic measurements are used to identify emission lines of energy transitions for different elements and estimate their abundance in the clusters. Regarding the temperature, T_e, it can also be measured from spectroscopic X-ray observations, since the shape of the ICM spectrum depends on its temperature [103]. We can clearly see, from figure 6 in Böhringer and Werner (2010) [103], that bremsstrahlung emission becomes more important at higher temperatures, contrary to emission lines of heavy elements, that

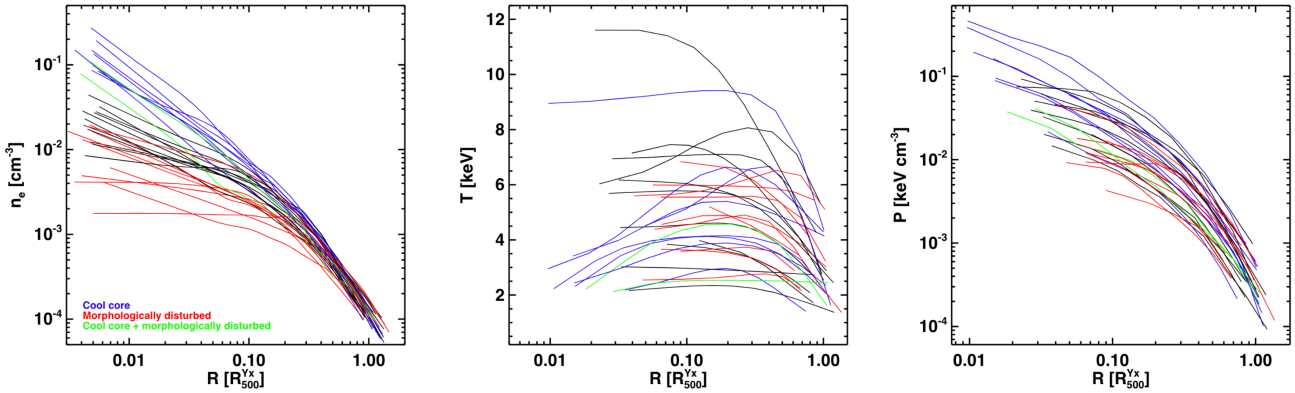

Figure 1.4: Electron density (left), temperature (centre) and pressure (right) profiles of the REXCESS clusters reconstructed from X-ray data. Colours indicate the dynamical state. Figure from Pratt et al. (2009) [106].

are less and less dominant since elements are ionised at high temperatures. However, a reliable and resolved temperature mapping of clusters in X-rays [104] requires deep and, therefore, time-consuming observations.

Following Eq. 1.22, X-ray surface brightness maps of clusters can be used to reconstruct the underlying electron density. The classical procedure follows a geometrical deprojection of concentric annuli from the surface brightness map [77, 105]. Therefore, high quality X-ray observations enable the reconstruction of the electron temperature and density in the ICM. Gas clumps and temperature inhomogeneities in the cluster can bias these estimates and data has to be carefully corrected for them. In addition to the emission from the cluster, other X-ray emitting point sources can also contaminate the signal and they need to be removed (as for example, in Pratt et al. (2007) [76]). Assuming that the ICM behaves as an ideal gas, X-ray measurements are enough to estimate the electron pressure in the medium: $P_e = n_e k_B T_e$, with k_B the Boltzmann constant. In Fig. 1.4 we present the electron density, temperature and pressure profiles reconstructed from XMM-*Newton* observations for the clusters in the REXCESS sample [70, 106].

As shown in Fig. 1.3, relaxed and unrelaxed or, respectively, cool-core and non-cool-core clusters show different pressure profile shapes. As for the pressure, the electron density is higher in the core of relaxed clusters (see also figure 4 in Hudson et al. (2010) [107]). This makes cool-core clusters to be more easily detected in X-rays, introducing the so-called *Cool-core Bias* [108, 109] in X-ray-selected samples.

Since the discovery in the 1970s of the X-ray emission of galaxy clusters with the *Uhuru* satellite [42, 43], several satellites have been launched above the Earth's atmosphere to map the Universe in X-rays. Nowadays, most of the observations are carried out with XMM-*Newton* [71] and *Chandra* [69] instruments, at high angular resolution. Although the extended ROentgen Survey with an Imaging Telescope Array (eROSITA) [110] operations are currently paused, these full-sky observations will provide a large catalogue of X-ray detected clusters. From the already available eROSITA observations, 542 galaxy cluster and group candidates have been detected in an area of $\sim$ 140 square degrees [15]. According to Liu et al. (2022) [15] the clusters span a redshift range between $z = 0.01$ and 1.3 with an average temperature of $\sim$ 2 keV. The *(New)Athena* mission (which is being redesigned) will probably bring competitive X-ray spectroscopic measurements in the future [111].

Millimetre wavelengths

Soon after the discovery of the X-ray emission of clusters, Y. N. Pariysky observed a deficit of brightness in the CMB signal in the direction of the Coma cluster [112]. According to Sunyaev and Zeldovich (1972) [112] that deficit could only be explained by the presence of the recently detected hot gas in the ICM: the light from the CMB is scattered by inverse Thomson (also named as inverse Compton) effect in the presence of the very energetic electrons in the ICM. It was the discovery of the Sunyaev-Zel'dovich (SZ) effect (left panel in Fig. 1.5).

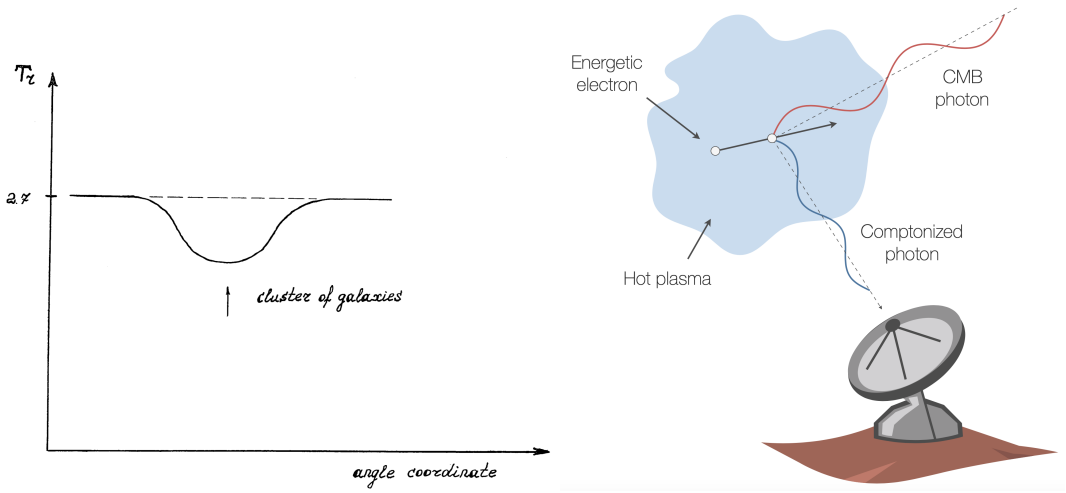

Figure 1.5: The Sunyaev-Zel'dovich effect. Left: illustration of a *decrement* observed in the CMB temperature. Figure from Sunyaev and Zeldovich (1972) [112]. Right: illustration of the SZ effect from Mroczkowski et al. (2019) [113]. A low energy CMB photon gains energy (changing from red to blue wavelengths in the illustration) when traversing the hot ICM plasma.

We define the Sunyaev-Zel'dovich effect as the distortion of the CMB spectrum caused by the interaction of the Cosmic Microwave Background photons with the electrons in the cluster [114, 115]. It is a weak distortion and, just like the CMB emission, we observe it at millimetre wavelengths (in the GHz−THz frequency range). When low energy CMB photons (of some 10^{-6} keV) traverse the ICM of a cluster, part of the kinetic energy of the electrons is transferred to the CMB photons (see the right panel in Fig. 1.5 for an illustration). As a consequence, the CMB black-body spectrum changes its shape. Depending on the origin of the kinetic energy of the electrons we distinguish the thermal and kinematic or kinetic SZ effects. We also need to consider their relativistic corrections, as well as the hardly assessable polarised and non-thermal SZ effects. In this section and all along this thesis we will focus on the thermal SZ effect. More detailed descriptions of the different contributions can be found in Birkinshaw (1999) [115] and Mroczkowski et al. (2019) [113].

I. The thermal SZ effect

The thermal SZ effect (tSZ) corresponds to the SZ effect caused by the thermal energy of the electrons. At temperatures of the order of $10^7 - 10^8$ K in the ICM (Sect. 1.2.1), the thermalised plasma reaches energies of $1 - 10$ keV. At these energies, electrons are non-relativistic ($m_e c^2 \gg k_B T_e$).

The Kompaneets equation (Eq. 12 in Kompaneets (1957) [116]) allows us to relate the spectral distortion of a I_ν intensity light at a frequency ν with the thermal energy of the ICM electrons. If the temperature of the incident photons is negligible with respect to the temperature of the medium, which is true for the SZ effect of clusters, the Kompaneets equation can be written as

$$\frac{\partial n}{\partial y} = \frac{1}{x^2}\frac{\partial}{\partial x}\left(x^4 \frac{\partial n}{\partial x}\right), \tag{1.23}$$

where $n \equiv I_\nu c^2/2h\nu^3$ is the occupation number of photons. Here x is defined as $x \equiv h\nu/k_B T_{CMB}$ with ν the frequency of photons and T_{CMB} the temperature of the CMB. The Compton parameter y is related to the thermal energy of the electrons in the ICM through

$$y \equiv \int \frac{k_B T_e}{m_e c^2}\, \mathrm{d}\tau_e = \frac{\sigma_T}{m_e c^2} \int k_B T_e n_e \, \mathrm{d}l. \tag{1.24}$$

Here τ_e is the Thomson scattering optical depth crossed by the photons in the ICM, given by $\tau_e = \sigma_T n_e l$, with σ_T the Thomson cross section and l the line-of-sight depth. In the integral in Eq. 1.24 we can easily identify

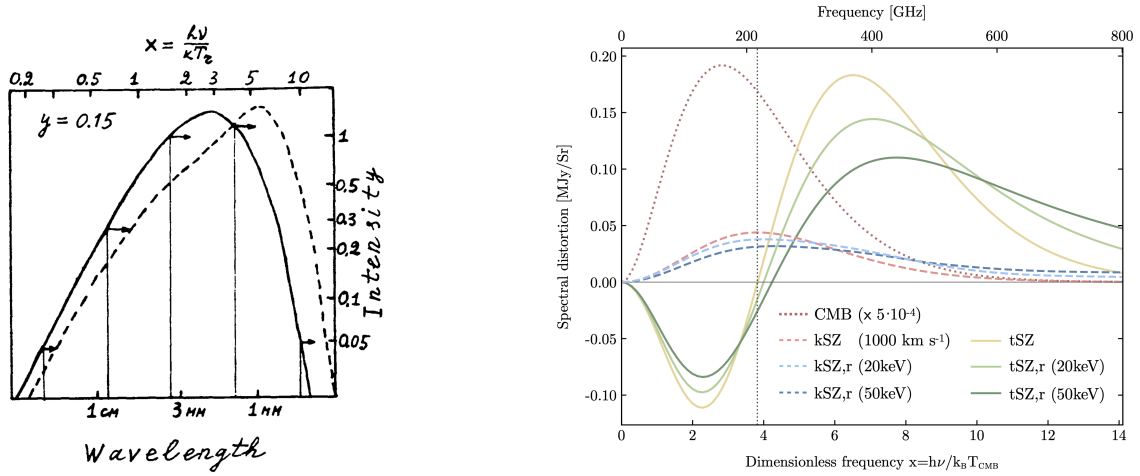

Figure 1.6: Distortion of the CMB spectrum due to the SZ effect. Left: the solid line shows the black-body spectrum of the CMB (I_ν) and the dashed line the same spectrum distorted after multiple Compton scattering ($I_\nu^{\rm tSZ}$). Figure extracted from Sunyaev and Zeldovich (1980) [114]. Right: rescaled CMB spectrum (red dotted line) and the spectral distortions of the thermal (solid) and kinematic (dashed) SZ effects including and not the relativistic corrections. Extracted from Mroczkowski et al. (2019) [113].

the expression of the pressure for an ideal gas, $P_{\rm e} = k_{\rm B} T_{\rm e} n_{\rm e}$. Thus, the Compton parameter can be defined as proportional to the integral of the thermal pressure of the electrons,

$$y = \frac{\sigma_{\rm T}}{m_{\rm e} c^2} \int P_{\rm e}\, {\rm d}l. \tag{1.25}$$

Accounting for the black-body spectrum of the CMB for I_ν and solving the Eq. 1.23 leads to a distortion given by:

$$\Delta I_\nu^{\rm tSZ} = I_\nu^{\rm tSZ} - I_\nu = I_0 \times y \times \frac{x^4 e^x}{(e^x - 1)^2} \left[x {\rm coth}\left(\frac{x}{2}\right) - 4 \right] [1 + \delta_{\rm tSZ}(x, T_{\rm e})]\,, \tag{1.26}$$

with $\delta_{\rm tSZ}$ the relativistic correction (see Mroczkowski et al. (2019) [113] for more detailed explanations) and I_0 the CMB intensity [113],

$$I_0 = \frac{2(k_{\rm B} T_{\rm CMB})^3}{(hc)^2} = 270.33 \left[\frac{T_{\rm CMB}}{2.7255\ {\rm K}} \right]^3\ {\rm MJy/sr}. \tag{1.27}$$

If we ignore the relativistic correction, which will only be relevant for extremely hot clusters, we observe in Eq. 1.26 that the spectral dependence of the distortion is independent of the temperature in the cluster (right side of the equation). The amplitude of the effect is given by the Compton parameter and it changes also with x, that is, with the frequency ν. The left panel in Fig. 1.6 illustrates the distortion in the CMB black-body spectrum due to the tSZ effect. A very large value of the Compton parameter ($y = 0.15$) has been used to amplify the effect. We observe that photons have increased their energy (dashed lines) after the inverse Compton scattering.

The yellow line in the right panel in Fig. 1.6 shows the distortion $\Delta I_\nu^{\rm tSZ}$ of the CMB spectrum for $y = 10^{-4}$. This is the order of magnitude for the tSZ amplitude in cluster centres, which varies with the cluster mass and redshift. As a consequence of the deformation of the spectrum, the intensity of the light at frequencies below 217 GHz decreases with respect to the intensity of the CMB. Thus, the distortion takes negative values. On the contrary, it is positive at higher frequencies. Multi-frequency observations at millimetre wavelengths detect the decrement (for $\nu < 217$ GHz) and increment ($\nu > 217$ GHz) in the surface brightness of the CMB in the direction of galaxy clusters. We present in Fig. 1.7 seven maps of the Abell2319 galaxy cluster observed by the *Planck* satellite in seven bands. At low frequencies the cluster is seen as a negative blue decrement in the centre of the map, and as a red positive signal at high frequencies. As expected, no tSZ signal is detected at 217 GHz.

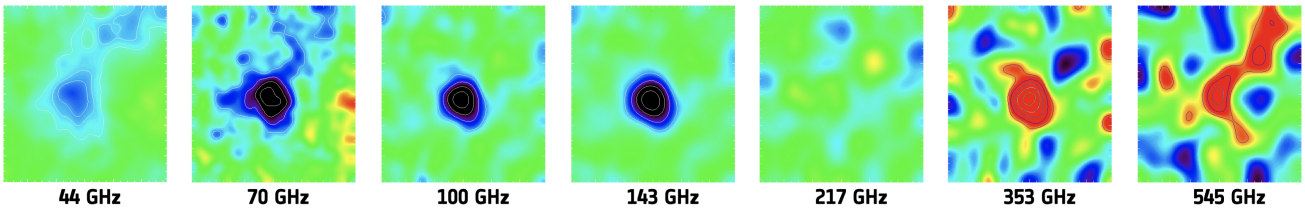

Figure 1.7: The Abell2319 galaxy cluster observed by *Planck*. Blue and red represent negative and positive distortions, respectively. Figure obtained from the *Planck* data base at https://sci.esa.int/s/WvJQxgW.

We have seen in Eq. 1.24 that the Compton parameter traces the integral along the line-of-sight of a combination of the electron density and temperature in the ICM. Consequently, mapping galaxy clusters at millimetre wavelengths and estimating the contribution of the tSZ effect enables the reconstruction of $k_B T_e n_e$ or, equivalently, the pressure, P_e, of an ideal gas. This is how the thermal pressure of galaxy clusters has been reconstructed in a large number of works in the literature (as in Planck Collaboration et al. (2013) [117], Romero et al. (2017) [118], Adam et al. (2015) [119] and Di Mascolo et al. (2023) [47] to cite a few examples). In chapter 3 we will describe the reconstruction of the cluster pressure from NIKA2 observations.

Contrary to the X-ray surface brightness, the tSZ effect is not affected by cosmological dimming. Given that the observable is a distortion of the CMB spectrum instead of a brightness, its amplitude does not depend on the redshift of the cluster. For this reason, the tSZ effect is an excellent tool to detect and characterise the ICM of high redshift clusters (Fig. 1.3). The comparison of the pressure reconstructed from X-rays and from tSZ can shed light on the origin of systematic effects (chapter 4 and 5). In addition, tSZ observations offer the possibility to estimate the temperature in the ICM by combining the pressure from the tSZ and the electron density from X-rays, without the need of X-ray spectroscopy [120].

II. The kinematic SZ effect

The kinetic or kinematic SZ effect (kSZ) is the scatter of the cold CMB photons induced by the bulk motion of the cluster plasma with respect to the CMB rest frame [121],

$$\Delta I_\nu^{\rm kSZ} = I_0 \times y_{\rm kSZ} \times \frac{x^4 e^x}{(e^x - 1)^2} \left[1 + \delta_{\rm kSZ}(x, T_e, v_z)\right]. \tag{1.28}$$

In this case, the relativistic correction $\delta_{\rm kSZ}(x, T_e, v_z)$ depends also on the velocity of the gas along the line-of-sight, v_z. For the kSZ, the equivalent to the Compton parameter is $y_{\rm kSZ}$, that increases with the line-of-sight velocity as

$$y_{\rm kSZ} \equiv -\frac{v_z}{c} \int {\rm d}\tau_e = -\frac{v_z \sigma_T}{c} \int n_e {\rm d}l. \tag{1.29}$$

The stronger the bulk motion of the gas, the more important its kinetic energy is and, in consequence, the larger the amplitude of the kSZ effect. The red dashed line in the right panel in Fig. 1.6 shows the effect on the CMB brightness caused by ICM gas moving at $v_z = 1000$ km/s, with the peak of the spectrum at 217 GHz. The contribution of the kSZ can be both positive or negative, depending on the direction of the bulk motion.

The peculiar motion of clusters is expected to be of the order of a few 100 km/s [113], which corresponds to $y_{\rm kSZ} \sim 10^{-5}$. Therefore, for hot clusters with temperatures of $T_e \sim 10$ keV, the amplitude of the kSZ effect is 10 times weaker than the tSZ. Then, detecting the kSZ and separating its contribution from the tSZ requires very sensitive multi-frequency observations. When detected, it can be used to reconstruct the bulk velocity or density of the electronic plasma as given by Eq. 1.29, if density or velocity is already known, respectively.

In addition, if the angular resolution of the observations is enough to resolve substructures within clusters, the kSZ effect can be used to estimate the relative velocities between different clumps and probe the gas dynamics. Such detection has been possible for the merging system in the MACS J0717.5+3745 galaxy cluster [74,

122, 123]. In Adam et al. (2017) [123] authors mapped the kSZ effect on MACS J0717.5+3745 by using 150 and 260 GHz resolved observations from the NIKA camera [119, 124, 125]. From the combination with X-ray data they obtained that two of the subclusters in MACS J0717.5+3745 are moving along the line-of-sight, one of them away and the other one towards us, with velocities of the order of $\sim$ 1000 km/s. Statistical approaches can also be used to detect the kSZ [126].

III. Non-thermal and polarised SZ and relativistic corrections

The Sunyaev-Zel'dovich effect has additional flavours besides the thermal and kinematic SZ. On the one hand, relaxing the hypothesis of thermalised electrons, we find a more general formalism that describes the scattering of the CMB. This is the non-thermal SZ effect. The shape of the non-thermal SZ spectrum depends on the energy distribution of the electrons and can be intricate to detail [113]. Assuming a relativistic Maxwell-Boltzmann distribution for electron energies, the non-thermal SZ is equivalent to the tSZ effect with temperature corrections.

On the other hand, it is known that the SZ effect is polarised due to multiple mechanisms [113]. However, for all the cases the polarised SZ signal is very weak (two orders of magnitude fainter than the kSZ). On top of that, multiple astrophysical objects contaminate the polarised SZ, so in practice, the detection of polarised SZ is very challenging.

Regarding the relativistic $\delta_{\rm tSZ}$ and $\delta_{\rm kSZ}$ corrections in Eq. 1.26 and 1.28, they have to be accounted for when the thermal energy and bulk motion of electrons induce velocities of the order of the speed of light. At high temperatures the relativistic corrections become important and contribute to the SZ spectra by shifting them in frequency and changing their amplitudes [113]. The right panel in Fig. 1.6 shows the impact of the relativistic corrections on the spectral distortions of the tSZ and kSZ effects.

Detecting such fine effects and disentangling the different contributions is extremely challenging and requires observations at several frequency bands. In the millimetre observations analysed in this thesis (in chapters 3, 4 and 5) we will only be able to detect the tSZ effect. The kSZ will be at the level of the noise and relativistic corrections, as well as the non-thermal and polarised SZ, out of reach. Thus, for simplicity, in the following we will use SZ to refer to the thermal SZ effect.

IV. CMB lensing

Galaxy clusters can also be observed at millimetre wavelengths through the lensing effect they produce on the CMB [127]. CMB lensing is a tracer of the total mass and, therefore, it can be directly used to reconstruct cluster masses [128, 129] (Sect. 1.3).

Other than the clusters in themselves, observations at millimetre wavelengths allow us to detect dusty galaxies in the field. Flux measurements of dusty galaxies will be very useful to estimate their contamination in cluster maps for the characterisation of the SZ effect in chapter 3.

Radio

At radio frequencies ($\sim$ GHz) we can also observe galaxy clusters. The presence of magnetic fields within clusters (Sect. 1.2.1) brings with it synchrotron radiation and, therefore, a diffuse radio emission coincident with the ICM [130]. These radio halos are usually compact ($\sim$ 100 kpc) in cool-core clusters and more extended ($\sim$ Mpc) in mergers.

In addition, in the outskirts of clusters we can observe extended radio emissions, also known as relics. These relics are related to the presence of shocks [131]. Thus, radio observations trace the dynamical history of clusters. Recently, results from the LOFAR instrument have shown that the magnetic field in distant clusters is as strong as in low redshift ones [57].

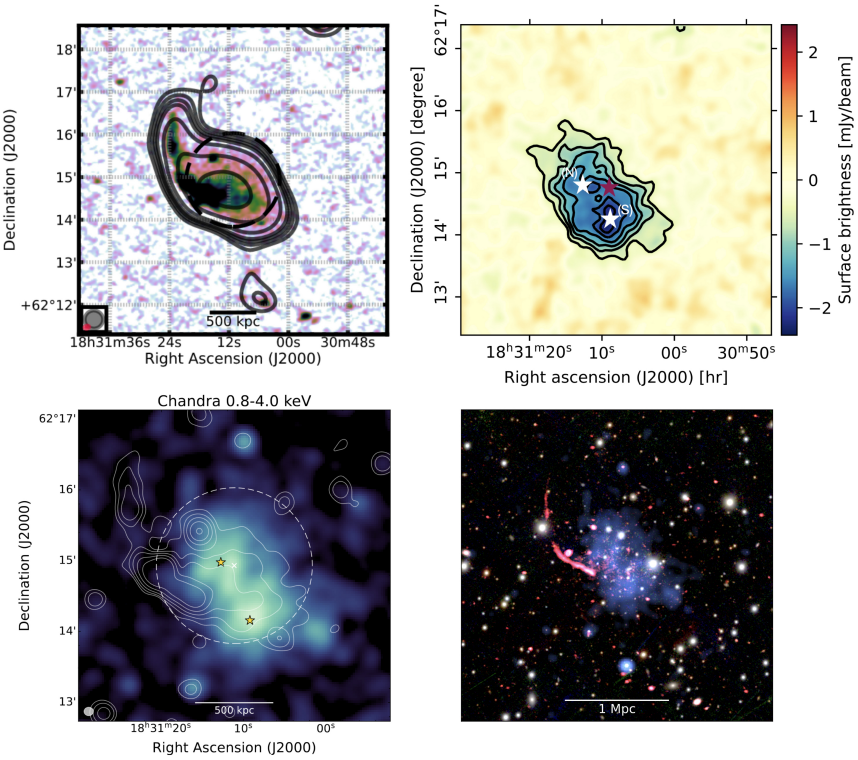

Figure 1.8: Multi-wavelength view of the PSZ2 G091.83+26.11 galaxy cluster. Top left: the diffuse radio emission observed with LOFAR with the black contours indicating the S/N levels. The figure was taken from Di Gennaro et al. (2021) [57]. Top right: the map of PSZ2 G091.83+26.11 at 150 GHz obtained from NIKA2 data in Artis et al. (2022) [132]. The northern (N) and southern (S) white stars indicate the X-ray peaks detected from XMM-*Newton* observations and the purple star corresponds to the X-ray centroid. Bottom left: X-ray *Chandra* data image extracted from Di Gennaro et al. (2023) [133]. Yellow stars show the same X-ray peaks as in the top right panel, the white cross indicates the cluster centre and white contours show the radio emission at 3 GHz from the Very Large Array (VLA). Bottom right: in white the optical observations with PanSTARRS *gri*. Blue and red in the image correspond to *Chandra* X-ray and VLA radio data. Figure taken from Di Gennaro et al. (2023) [133].

Radio observations can also be very useful to measure the emission of member galaxies. Typically cool-core clusters host powerful radio-loud BCGs, which are responsible for injecting energy into the ICM [130]. As for dusty galaxies, flux measurements of radio galaxies in the field of clusters will be used to account for their contribution in SZ analyses (chapter 3).

For illustration, in Fig. 1.8 we present a multi-wavelength view of the PSZ2 G091.83+26.11 galaxy cluster at $z = 0.822$ from X-ray, optical, radio and millimetre observations. We witness the same elongated shape in the four maps, as well as hints of a double interacting system [132].

1.2.3 Clusters of galaxies as a cosmological probe

As we have seen in Sect. 1.1, the distribution of matter halos in the Universe is sensitive to its expansion history and matter content, as well as to the initial conditions in the primordial Universe [134]. Thus, galaxy clusters can be used to probe the underlying cosmology through the estimation of the cosmological parameters. In this section, we present the methods based on cluster number counts, on the analysis of the angular power spectrum of the tSZ effect and on the measurement of the baryon fraction in clusters. Less common approaches related, for example, to the ellipticity of clusters [135], to the measurement of H_0 from the combination of SZ and X-ray observations [136], to the nature of DM from merging clusters [137] or to the evolution of the CMB temperature [138], will not be discussed. At the end of this section we compare the cosmological constraints obtained with clusters to other cosmological probes.

Cluster number counts

Cluster number count analyses consist in comparing the predicted abundance of halos, in a given cosmological scenario, with the observed one. The abundance of halos expected in a given redshift and mass range is provided by the halo mass function $\mathrm{d}n/\mathrm{d}M\mathrm{d}z$ (Eq. 1.17). This function has to be calibrated on simulations in order to relate the cosmological parameters to the number of clusters that are formed. With the drop of statistical errors thanks to large cluster catalogues in the near future (Sect. 1.2.3), the uncertainties related to the knowledge of the halo mass function will become non-negligible. It will, therefore, be necessary to improve its accuracy [139].

From the observational side, large surveys map the sky, detect clusters and provide catalogues of galaxy clusters with their mass and redshift [95, 140–142]. However, multiple things have to be considered before comparing the observed cluster abundances to the halo mass function.

First, a survey will never be able to observe all the clusters in the sky. Owing to the finite speed of light, only a portion of the sky, given by the comoving volume V_c, will be observable. In addition, the surveys might not cover the full sky, but only a solid angle, Ω. Under ideal conditions, the abundance of observed clusters per mass, redshift and solid angle unit is:

$$\frac{\mathrm{d}n}{\mathrm{d}M\mathrm{d}z\mathrm{d}\Omega} = \frac{\mathrm{d}n}{\mathrm{d}M}\frac{\mathrm{d}V_c}{\mathrm{d}z\mathrm{d}\Omega}. \tag{1.30}$$

Secondly, all the clusters within the observable volume of the survey will not be detected. Quantified by the selection function $\hat{\chi}(M, z, l, b)$, the probability of a survey to detect a cluster of mass M and redshift z at a position in the sky (l, b), will depend on the quality of the observations, the algorithm used to detect clusters and on the observable in itself. Thus, the selection function quantifies the capacity of an experiment to identify clusters and it has to be assessed from simulations. The number of expected clusters with redshift and masses between z_i and $z_i + \Delta z_i$ and M_i and $M_i + \Delta M_i$ is,

$$n_i = \int \mathrm{d}\Omega \int_{z_i}^{z_i+\Delta z_i} \mathrm{d}z \int_{M_i}^{M_i+\Delta M_i} \mathrm{d}M \frac{\mathrm{d}n}{\mathrm{d}M}\frac{\mathrm{d}V_c}{\mathrm{d}z\mathrm{d}\Omega}\,\hat{\chi}(M, z, l, b). \tag{1.31}$$

Third, as we will see in Sect. 1.3, the mass of clusters is not an observable quantity and has to be estimated under diverse assumptions that will depend on the type of observation. Therefore, the selection function must encode instrumental selection effects related to the quantity used to estimate the mass. For instance, for surveys at millimetre wavelengths (Sect. 1.2.2) observing the SZ effect, the observable is given by the integrated Compton parameter Y_Δ (Eq. 1.55) and the probability of observing a cluster of amplitude Y_Δ and size θ_Δ for a cluster of mass and redshift M_Δ and z is $P(Y_\Delta, \theta_\Delta|z, M_\Delta)$. Therefore, the selection function is

$$\hat{\chi}(M_\Delta, z, l, b) = \int \mathrm{d}Y_\Delta \int P(Y_\Delta, \theta_\Delta|z, M_\Delta)\,\chi(Y_\Delta, \theta_\Delta, l, b)\,\mathrm{d}\theta_\Delta, \tag{1.32}$$

where $\chi(Y_\Delta, \theta_\Delta, l, b)$ is the probability of the experiment to detect a cluster of amplitude Y_Δ and size θ_Δ at a given sky position (l, b) above a given signal-to-noise (S/N) ratio.

The number of clusters N_i measured by a survey in the mass and redshift bin i can finally be compared to the predicted value n_i (Eq. 1.31). The cosmological parameters in n_i (encoded in the halo mass function and the comoving volume factors) that maximise the likelihood with respect to the N_i distributions are the cosmological result of cluster number count analyses. Potential biases in the raw data, in the selection function or in the observable-mass relation impact directly the inferred cosmological parameters and have to be accounted for [5].

In the last decade the *Planck*, ACT and SPT instruments have observed large fractions of the sky at millimetre wavelengths and, by measuring the SZ effect, they have provided large galaxy cluster catalogues [8, 141, 142] with a few thousand of detected clusters in total. The different instrumental and observational capabilities of those instruments have been complementary to observe clusters in different mass and redshift ranges. In the left panel in Fig. 1.9 we show the detections in the mass-redshift plane for the different surveys.

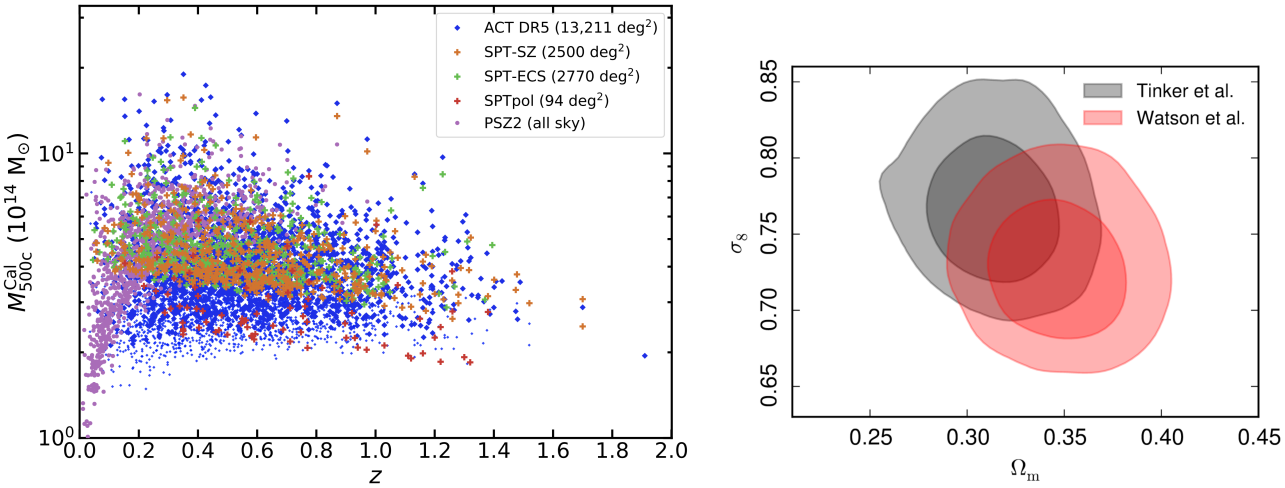

Figure 1.9: Cluster number counts. Left: mass and redshift of clusters detected with *Planck* (purple), ACT (blue) and SPT (plus sign markers, different colours for different sky coverages). Small and big blue markers show the detected clusters for different S/N thresholds. Figure from Hilton et al. (2021) [141]. Right: impact of the halo mass function on the posterior distributions of the σ_8 and Ω_m parameters in the cluster number count analysis in Planck Collaboration et al. (2016) [6]. Grey contours are obtained by assuming the function in Tinker et al. (2008) [34], while the red is the result with Watson et al. (2013) [143].

Cosmological analyses with cluster number counts have been carried out individually [5–9] and from the combination of multiple instrument detections [144]. The analysis in Planck Collaboration et al. (2016) [6] with 439 *Planck* clusters, combined with baryon acoustic oscillations (BAO) and BBN constraints, concluded that the amplitude of the matter fluctuations and the matter density are $\sigma_8 = 0.76 \pm 0.03$ and $\Omega_m = 0.33 \pm 0.03$, the results varying with the priors in the mass calibration. In the right panel in Fig. 1.9 we show the impact of the chosen halo mass function on the resulting cosmological parameters. As mentioned at the end of Sect. 1.1.5, we also observe in Fig. 1.9 that σ_8 and Ω_m are correlated.

The cosmological analysis of 343 SPT clusters spanning the redshift range $0.25 < z < 1.75$ concluded that $\sigma_8 = 0.781 \pm 0.037$ and $\Omega_m = 0.276 \pm 0.047$, assuming a flat Cold Dark Matter cosmological model with dark energy and with the sum of neutrino masses as a free parameter [8]. In Salvati et al. (2022) [144] *Planck* and SPT cluster number counts were jointly reanalysed, showing the impact that the mass calibration, the assumed priors and the sample can have on the cosmological results. Making use of 15 ACT clusters and a fixed scaling relation between the observable and the mass, in addition to BBN and H_0 constraints, authors in Hasselfield et al. (2013) [9] obtained $\Omega_m = 0.252 \pm 0.047$ and $\sigma_8 = 0.872 \pm 0.065$.

Observations at optical wavelengths have also enabled cluster number count analyses. In Costanzi et al. (2019) [10] the Sloan Digital Sky Survey (SDSS) data was used to estimate the abundance of clusters from the observation of member galaxies. For the cosmological study they used a sample of 6964 clusters in the redshift range $0.1 < z < 0.3$ and concluded that $S_8 = 0.79^{+0.05}_{-0.04}$, including some priors on H_0 and BBN and assuming a flat ΛCDM model with massive neutrinos. In Abbott et al. (2020) [96] a very low value of S_8 was obtained from optical observations of clusters from the Dark Energy Survey (DES) Year 1 dataset, $S_8 = 0.65 \pm 0.04$. Authors in Abbott et al. (2020) [96] indicated that modelling issues or systematic errors in the data might be present in their analysis. By exploiting the 3652 galaxy clusters in the redshift range $0.1 < z < 0.6$ of the AMICO Kilo Degree Survey (KiDS) DR3 catalogue, the number count study in Lesci et al. (2022) [11] obtained $\Omega_m = 0.24^{+0.03}_{-0.04}$, $\sigma_8 = 0.86^{+0.07}_{-0.07}$ and $S_8 = 0.78^{+0.04}_{-0.04}$.

Large galaxy cluster catalogues have also been built from observations at X-ray wavelengths [12–14]. In the last years possible biases in cluster catalogues selected from X-ray observations have been largely debated (Sect. 1.2.2). A careful selection was done when building the XXL Survey, with the aim of having a sample suitable for cosmological studies [14]. In Garrel et al. (2022) [145] 128 of the XXL clusters with redshifts up to $z \sim 1$ and observed with the XMM-*Newton* satellite were used for a cosmological analysis. Authors concluded

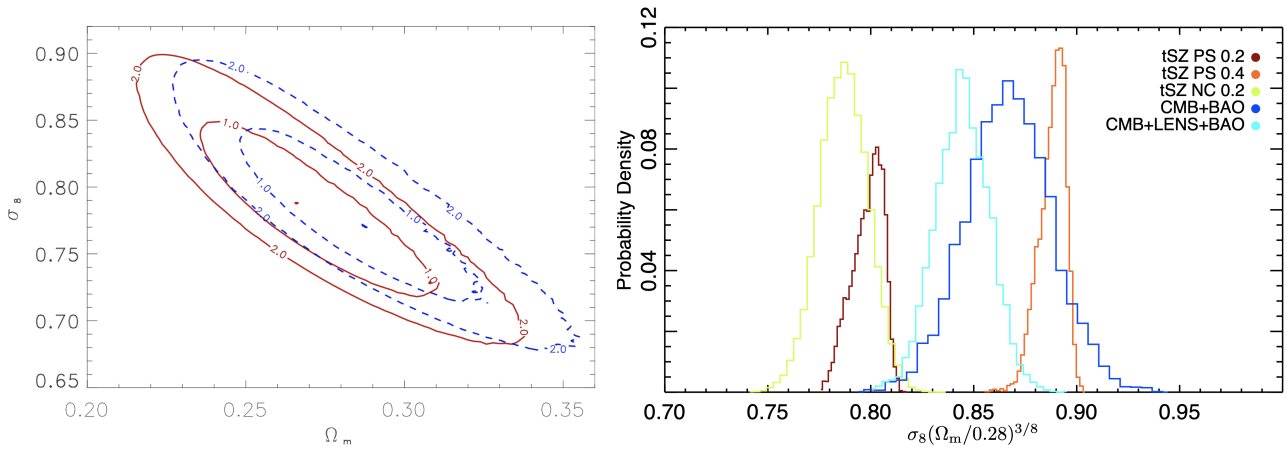

Figure 1.10: Marginalised probability density distributions of σ_8 and Ω_m. Left: constraints obtained from ROSAT cluster catalogues. The solid red contours correspond to the NORAS II cluster sample and the blue dashed lines to REFLEX II. Figure from Böhringer et al. (2017) [146]. Right: a combination of σ_8 and Ω_m posterior distributions from the analysis of the tSZ power spectrum (in brown and orange), from cluster number counts (in green), and from the analysis of the CMB anisotropies with BAO constraints (dark blue), and with additional constraints from CMB lensing (bright blue). Extracted from Planck Collaboration et al. (2016) [148].

that the best parameters describing the observed cluster abundances are: $\sigma_8 = 0.99^{+0.14}_{-0.23}$, $\Omega_m = 0.296 \pm 0.034$ and $S_8 = 0.98^{+0.11}_{-0.21}$. By using 860 clusters with a median redshift of $z = 0.102$ observed with the ROentgen SATellite (ROSAT), authors in Böhringer et al. (2017) [146] obtained the posterior distributions for σ_8 and Ω_m shown with red contours in Fig. 1.10. The blue contours correspond to the analysis in Böhringer et al. (2014) [147] for 910 different galaxy clusters also observed by ROSAT. After ROSAT, eROSITA has imaged the sky in X-rays and, for the moment, a catalogue of 542 candidate clusters and groups of galaxies has been made available [15]. In addition to the mentioned works, multiple X-ray-based studies have used cluster number counts to infer the underlying cosmology (see section 5.1.2 in Pratt et al. (2019) [48]).

Together with eROSITA, which plans to detect $\sim 10^5$ galaxy clusters up to $z > 1$ in X-rays, at optical wavelengths *Euclid* and the Nancy Grace Roman Space Telescope, as well as the LSST camera, will provide very large galaxy cluster catalogues that will reduce the statistical errors in cluster number count analyses. At millimetre wavelengths, the Simons Observatory [149] plans also to detect $\sim 16,000$ galaxy clusters, being able to observe more than 3000 at $z > 1$ and about 50 at $z > 2$. The next generation of CMB experiments, named CMB-S4, is expected to observe at high significance ($> 5\sigma$) 70,000 clusters of galaxies [150].

Angular power spectrum of the tSZ effect

An alternative approach consists in using the angular power spectrum of the full-sky thermal SZ effect (Sect. 1.2.2) to constrain the cosmological parameters. We have seen that the amplitude of the distortion of the CMB spectrum caused by the tSZ at millimetre wavelengths is characterised by the Compton parameter y. By mapping the full sky, one can build a $y(\vec{n})$ map, that can be decomposed in spherical harmonics

$$y(\vec{n}) = \sum_{\ell,m} y_{\ell m} Y_{\ell m}(\vec{n}). \tag{1.33}$$

From this, the power spectrum of the y-map is given by

$$C_\ell^{\rm tSZ} = \frac{1}{2\ell+1} \sum_m y_{\ell m} y^*_{\ell m}, \tag{1.34}$$

with ℓ the multipoles. However, the cluster population does not follow a Gaussian field and it is not well represented by Eq. 1.34. Instead, according to the halo model, the statistical properties of the matter density field can be modelled assuming that all the matter content in the Universe is in the form of virialised halos. In

this framework, the 1-halo contribution to the angular power spectrum of the tSZ effect is

$$C_\ell^{1\mathrm{h}} = \int \frac{\mathrm{d}V_c}{\mathrm{d}z\mathrm{d}\Omega}\mathrm{d}z \int \frac{\mathrm{d}n}{\mathrm{d}M_{500}} |y_\ell(M_{500}, z)|^2 \, \mathrm{d}M_{500}, \tag{1.35}$$

where $y_\ell(M_{500}, z)$ is the two dimensional Fourier transform of the electron pressure profile P_e,

$$y_\ell(M_{500}, z) = \frac{\sigma_\mathrm{T}}{m_\mathrm{e}c^2} \frac{4\pi R_{500}}{\ell_{500}^2} \int x^2 \frac{\sin(\ell x/\ell_{500})}{\ell x/\ell_{500}} P_\mathrm{e}(x|M_{500}, z) \, \mathrm{d}x, \tag{1.36}$$

with $x \equiv r/R_{500}$ the normalised radial distance to the centre of the halo, $\ell_{500} \equiv \mathcal{D}_\mathrm{A}/R_{500}$ and $P_\mathrm{e}(x|M_{500}, z)$ a universal pressure profile model that depends on M_{500} and z. $\mathcal{D}_\mathrm{A}$ is the angular diameter distance.

The observed C_ℓ power spectrum is, in reality, the sum of several components. In practice we use component separation algorithms (like, for example, the Internal Linear Combination technique used in the MILCA algorithm [151]) in multi-frequency sky maps to isolate the tSZ signal. Nevertheless, residuals from other components are expected. For the *Planck* case we measure

$$C_\ell = C_\ell^{1\mathrm{h}} + A_\mathrm{CIB} C_\ell^\mathrm{CIB} + A_\mathrm{IR} C_\ell^\mathrm{IR} + A_\mathrm{rad} C_\ell^\mathrm{rad} + A_\mathrm{CN} C_\ell^\mathrm{CN}, \tag{1.37}$$

where $C_\ell^{1\mathrm{h}}$ is the component that will be used to recover the cluster cosmological information and C_ℓ^CIB, C_ℓ^IR, C_ℓ^rad and C_ℓ^CN are respectively the residual power spectrum of the Cosmic Infrared Background (CIB), the power spectrum of infrared sources, the power spectrum of radio sources and the correlated noise. A_CIB, A_IR, A_rad and A_CN are the corresponding amplitudes, which are generally fitted to the data.

By assuming a universal pressure profile (Sect. 1.2.1) and a relation between the thermal energy in clusters and their mass, as well as the number of expected clusters according to a halo mass function, one can model $C_\ell^{1\mathrm{h}}$ [148]. Thus, the model of the tSZ power spectrum will depend also on Ω_m and σ_8. The parameters that maximise the likelihood between the C_ℓ measurements and the model described by the Eq. 1.37 will be the cosmological results of the tSZ angular power spectrum analysis. In the right panel in Fig. 1.10 we present in brown and orange the posterior distributions of the combined Ω_m and σ_8 parameters obtained from the power spectrum analysis of the tSZ data from *Planck* observations [148]. The difference between the brown and orange results resides in the mass calibration of clusters. The brown histogram can be compared to the result from number counts in green.

In conclusion, the tSZ power spectrum approach is complementary to cosmological studies based on cluster number counts, but it also requires precise knowledge of the pressure profile and mass in clusters. In addition, the presence of contaminants (CIB, IR, rad, CN) has to be carefully considered. The capability of different instruments to probe different multipoles can help disentangle the contribution of each component in Eq. 1.37. For instance, the angular resolution of *Planck* observations limits the power spectrum to multipoles of $\ell \leq 2000$. The higher resolution of ACT and SPT instruments enables probing larger multipoles [152].

Baryon fraction

The baryon fraction in clusters and its evolution with redshift are additional cosmological probes. We define the baryon fraction in clusters as the ratio between their baryonic and total mass,

$$f_\mathrm{b} = \frac{M_\mathrm{b}}{M_\mathrm{tot}} = \frac{M_\mathrm{gas} + M_*}{M_\mathrm{tot}} = f_\mathrm{gas} + f_*, \tag{1.38}$$

with the baryonic mass being the sum of the mass of the ionised gas in the ICM (M_gas) and of the stellar content (M_*).

On the one hand, baryon fraction measurements are used to quantify to which extent the distribution of matter in clusters is representative of the matter content in the Universe [153]. From the comparison of f_b to the ratio of baryonic matter density and total matter density in the Universe, $\Omega_\mathrm{b}/\Omega_\mathrm{m}$, we can measure the departure

from the Universal fraction. How this deviation from Ω_b/Ω_m evolves with redshift and with the size of the clusters, as well as how the baryonic content is separated between the gas and the stellar matter will impact the cluster assembly and the galaxy evolution and star-formation efficiency within clusters [154]. In Sect. 5.3 we will measure the gas fraction f_{gas} for four intermediate to high redshift clusters and explain all the additional physical processes that have to be taken into account to conform to the Universal value.

On the other hand, some works [155, 156] try to directly infer cosmological parameters from the measurement of the gas fraction in individual clusters. The relation between the Universal baryon fraction and the gas fraction can be modelled as

$$f_{gas} = K\frac{\Upsilon(M,z)}{B(M,z)}A(z)\left(\frac{\Omega_b}{\Omega_m}\right)\left(\frac{\mathcal{D}_A^{ref}(z)}{\mathcal{D}_A(z)}\right)^{3/2} - f_*, \tag{1.39}$$

with

$$A(z) \simeq \left(\frac{H(z)\mathcal{D}_A(z)}{[H(z)\mathcal{D}_A(z)]^{ref}}\right)^{0.442}. \tag{1.40}$$

In these equations K is the instrumental calibration factor that accounts for possible biases in the masses estimated with the data from a given instrument with respect to the results from another instrument (see chapter 6). $B(M,z)$ quantifies the potential bias in the total mass estimate related to the assumed hypotheses. All the quantities denoted with "ref" correspond to the reference cosmology used for the analysis and $\Upsilon(M,z)$ is the baryon depletion factor that describes the amount of baryons that are depleted in clusters due to physical processes that occur within them. To reconstruct the gas mass, as we will do in Sect. 5.3, this type of analyses require X-ray observations. For example, authors in Wicker et al. (2023) [156] fit the cosmological parameters in Eq. 1.39 to the measurement of f_{gas} for 120 clusters observed with *Planck* and XMM-*Newton* satellites. The dependence on the cosmological model is encoded in the $A(z)$, Ω_b/Ω_m and $\mathcal{D}_A(z)$ factors.

Comparison to other cosmological probes

Cosmology with clusters of galaxies is limited by systematic effects and, usually, these analyses rely on multiple assumptions. However, they give a complementary picture of the matter distribution in the late-Universe.

The cluster number count analysis in Planck Collaboration et al. (2014) [5] showed a tension on the S_8 parameter with respect to the results obtained from the analysis of the CMB anisotropies also with *Planck* data (as shown in the right panel in Fig. 1.10). The left panel in Fig. 1.11 shows in blue the posterior probability distribution contours obtained from the combination of cluster number counts, BAO and BBN and in red the posterior distributions corresponding to the CMB analysis. Such tension, at the level of $\sim 2.7\sigma$, was confirmed by the analysis in Planck Collaboration et al. (2016) [6], the tension level varying with the assumed scaling relation between the observable (Y_Δ) and the mass of clusters. According to the CMB results, we should observe twice as many massive galaxy clusters in the Universe as we detect [19]. In Fig. 1.12 we present a summary of the constraints on S_8 from different observables and works. The dark blue markers on top show the results for different CMB analyses. Brown markers correspond to cluster count (CC) analyses based on SZ data.

A different calibration of the cluster masses in the SZ analyses, including, for example, a corrective bias that would increase the mass values (Sect. 1.3.4) would move the blue contours in Fig. 1.11 towards CMB results and resolve the tension. Also, adding a non-minimal mass for neutrinos would lower the σ_8 results obtained with the CMB anisotropies [6]. However, the second option would increase the tension on the H_0 parameter between the CMB and other direct H_0 estimates, in particular, the discrepancy with the results from Supernovae calibrated with Cepheids (see figure 2 in Abdalla et al. (2022) [19]).

We observe in Fig. 1.12 that cluster number count analyses based on optical and X-ray observations (shown in red) also tend towards lower values of S_8 than CMB anisotropies. Even if the tension is weak, the situation is not satisfactory. From the clusters side, it is not clear if the discrepancy has its origin in a wrong modelling

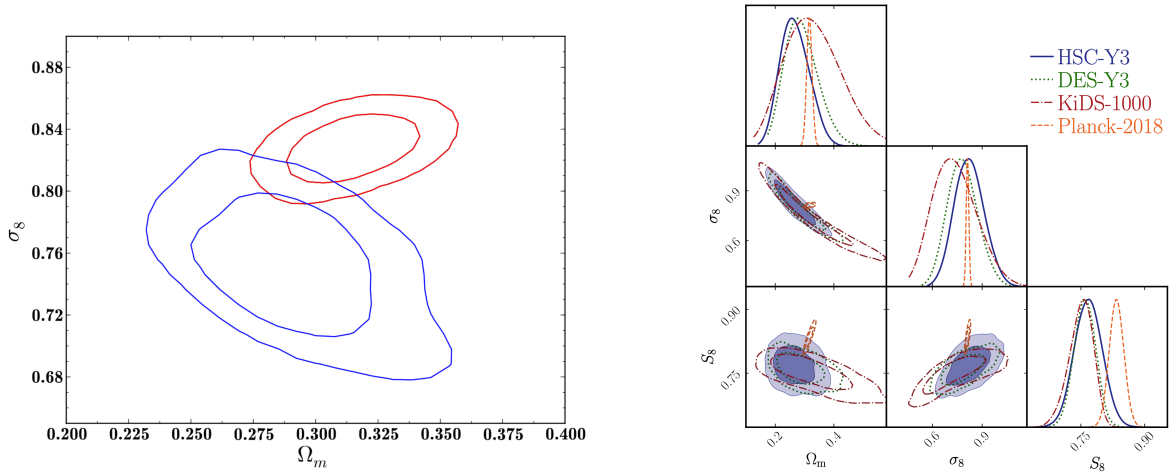

Figure 1.11: Posterior density distributions of cosmological parameters. Left: red contours show the results for the CMB analysis in Planck Collaboration et al. (2014) [157] and the blue correspond to the cluster count analysis with clusters detected in SZ by *Planck*, with additional constraints from BAO and BBN. Figure from Planck Collaboration et al. (2014) [5]. Right: comparison of recent cosmological results obtained from cosmic shear analyses (blue, green and red) and from the Planck Collaboration et al. (2020) [28] CMB anisotropies (orange). Figure from Li et al. (2023) [158].

of the astrophysical processes in clusters or if it corresponds to an incomplete understanding of the structure formation and evolution in the Universe.

There are also cosmological studies based on the weak lensing (WL or cosmic shear) of the light of galaxies by all the matter in the way to the observer. Yellow markers show in Fig. 1.12 the constraints on S_8 from different WL works in the literature. In addition, the distribution of galaxies in the Universe can also be used as a cosmological probe (galaxy clustering, Baryon Acoustic Oscillations and Redshift-space distortions, respectively, GC, BAO and RSD). Orange markers in Fig. 1.12 indicate the results for the S_8 parameter from combined WL and galaxy clustering analyses. Bright blue and green markers show respectively the constraints on S_8 for GC and RSD studies. We observe that, in agreement with cluster number count and tSZ power spectrum results, they tend to low values. The discrepancy between the cosmological parameters inferred from CMB anisotropies and from cluster and galaxy observations is understood to be a tension between early-Universe (the CMB at $z \sim 1100$) and late-Universe (galaxies and clusters mainly at $z < 1-2$) probes. In this regard, the Subaru Hyper Suprime-Cam (HSC) collaboration focused their Year 3 (Y3) data analysis on the inference of a robust and unbiased S_8 estimate. The results, published at the beginning of 2023, confirm that from an analysis of cosmic shear, galaxy-galaxy weak lensing and projected galaxy clustering (with the HSC-Y3 shape catalogue and the SDSS DR11 spectroscopic galaxy catalogue) and assuming a ΛCDM model, S_8 exhibits a $\sim 2.5\sigma$ tension with *Planck* CMB results [159]. From the analysis in Miyatake et al. (2023) [159], they obtain $S_8 = 0.763^{+0.040}_{-0.036}$. By using a different modelling, but also based on HSC-Y3 and SDSS DR11 data, authors in Sugiyama et al. (2023) [160] obtain less tight results, which are compatible with both the Planck Collaboration et al. (2020) [28] and the Miyatake et al. (2023) [159] constraints. Cosmic shear analyses based on HSC-Y3 data [158, 161] show also a $\sim 2\sigma$ tension with Planck Collaboration et al. (2020) [28] (right panel in Fig. 1.11).

Also in the spring of 2023, new cosmological results were published based on the CMB lensing signal measured with ACT [162, 163]. This probe traces the matter distribution in the Universe in the redshift range between $z \simeq 0.5$ to 5 and in linear scales. In the left panel in Fig. 1.13 we present in red the posterior distributions for the σ_8 and Ω_m parameters obtained from the combined CMB lensing data from ACT and *Planck*. The different blue contours correspond to the latest HSC, KiDS and DES constraints and in black the result from the analysis of the CMB anisotropies with *Planck*. In the right panel in Fig. 1.13 the constraints on S_8 are shown in green for CMB anisotropy analyses, in red for CMB lensing results (combined with BAO measurements) and in blue for late-Universe probes in the non-linear regime, as well as for some cross-correlation studies. We

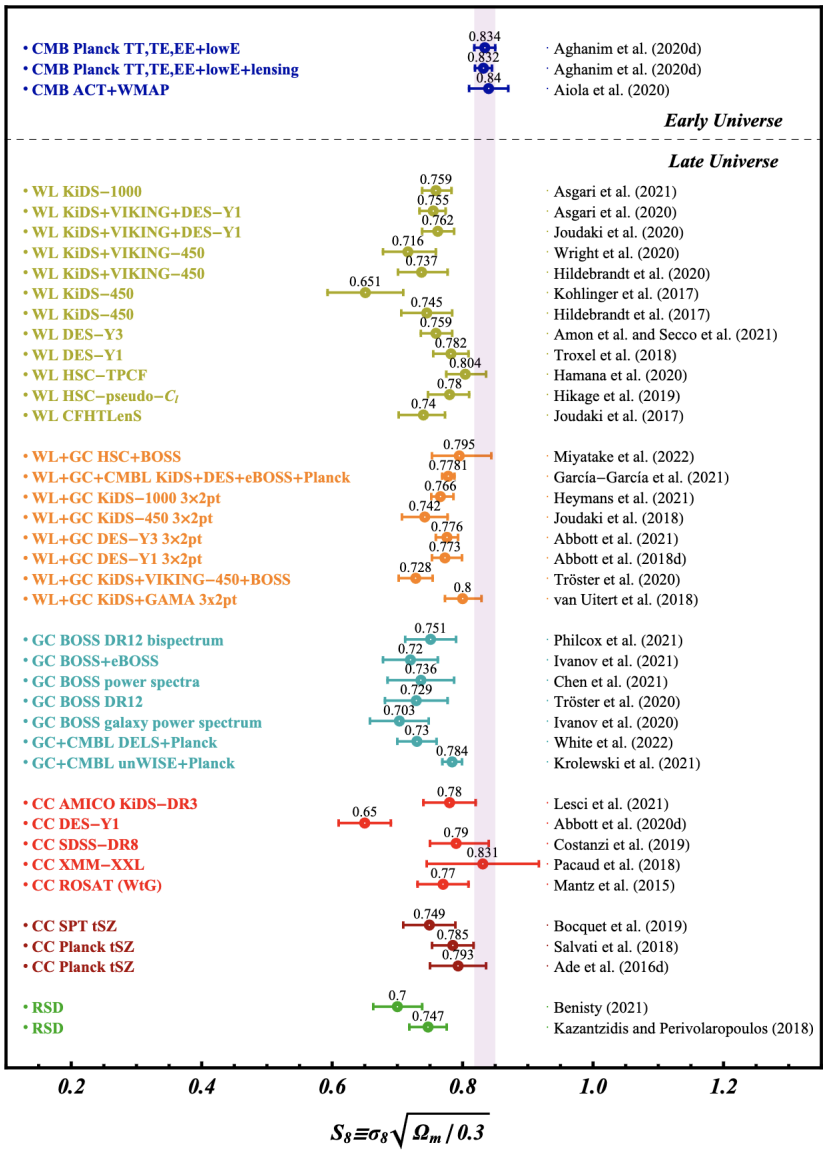

Figure 1.12: A summary of the constraints on S_8 from different probes and works in the literature. The dark blue results on top correspond to early-Universe observations, while the rest were derived from the analysis of the late-Universe large scale structure. The figure has been extracted from the review by Abdalla et al. (2022) [19].

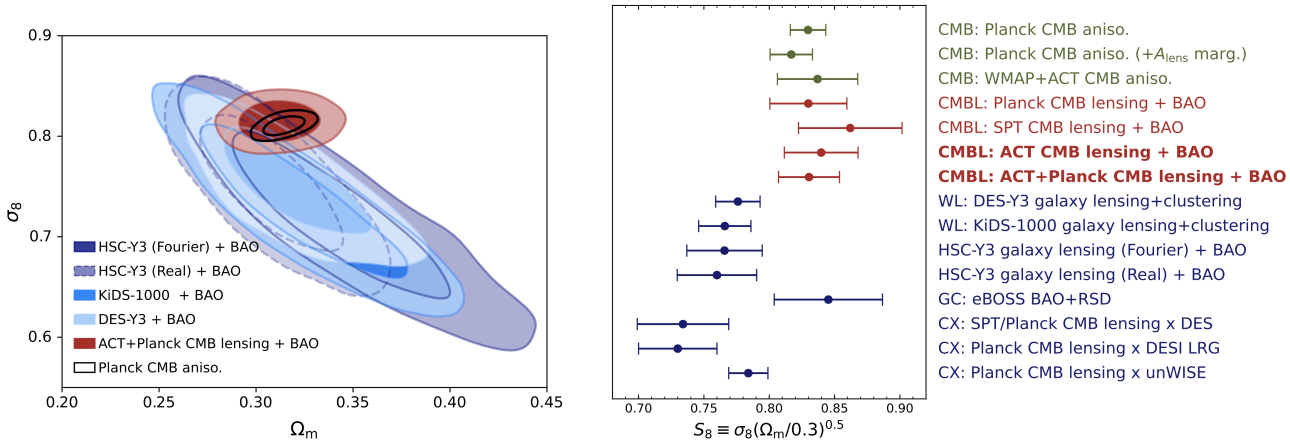

Figure 1.13: Cosmological results from the ACT CMB lensing compared to other works. Left: posterior probability density distribution for σ_8 and Ω_m. Red contours show CMB lensing results from ACT and *Planck* combined with BAO constraints. Blue contours correspond to the latest results from galaxy weak lensing. Right: marginalised posteriors of S_8 for studies with CMB anisotropies, CMB lensing+BAO and galaxy distributions, in green, red and blue, respectively. Both figures are from Madhavacheril et al. (2023) [162].

observe from this figure that CMB lensing results agree with the prediction from the early Universe, while blue markers tend towards lower values. In conclusion, authors in Madhavacheril et al. (2023) [162] suggest that the aforementioned tension of low redshift probes with high redshift observables might be more of a discrepancy between low/intermediate redshifts and non-linear/linear scales: the matter at intermediate-z and linear scales and the matter at low-z and in non-linear scales give different cosmological results.

In conclusion, further investigation is required to clarify whether these tensions originate from systematic effects in the analyses or from unrevealed physical processes. Studies based on galaxy observations are reaching now high precision results. Regarding the cosmology with galaxy clusters, a better knowledge of their masses will be fundamental. Large cluster catalogues will help to downsize the statistical errors in the near future.

1.3 The mass of galaxy clusters

The mass of galaxy clusters is, together with their redshift, the most fundamental property for cosmological analyses with clusters. Nevertheless, the mass is not an observable quantity and has to be estimated under several hypotheses from observations. A large part of this thesis is dedicated to the reconstruction and comparison of cluster masses. In this section, we describe different approaches for their estimation.

We first present the mass reconstruction from the kinematics of member galaxies and from the lensing on background sources. Then, we detail the estimation of the mass under the hydrostatic equilibrium hypothesis, as well as its related bias. The scaling relations between observables and masses are explained at the end of this section.

1.3.1 Kinematics of member galaxies

The first evidence of the large mass of clusters arose from the observation of the cluster galaxy members by Zwicky in the 1930s [39]. Assuming that galaxies are tracers of the total matter in the cluster, the distribution of radial and tangential velocities of the cluster member galaxies is related to the mass of the underlying matter halo. If in dynamical equilibrium and in the absence of bulk motions, following the Jeans equation we can write

$$M^{\rm dyn}(< r) = -\frac{r^2}{nG}\frac{{\rm d}(n\sigma_r^2)}{{\rm d}r} - \frac{2r}{G}\left(\sigma_r^2 - \sigma_t^2\right). \tag{1.41}$$

Here $M^{\rm dyn}(< r)$ is the dynamical mass of the cluster at a radius r from the centre and it can be used as an estimator of the total mass. The number density of galaxies is n and σ_r and σ_t are the radial and tangential

velocity dispersions of the galaxies, respectively. Thus, the estimation of the dynamical mass requires the measurement of individual galaxy velocities. In practice, only the line-of-sight component of the velocities can be observed, via the redshift measurements. The impossibility of having access to the radial and tangential components introduces the so-called *mass-anisotropy degeneracy*, which can only be solved by assuming matter and velocity distribution models (see Pratt et al. (2019) [48] for a more detailed explanation). Beyond the virial equilibrium region, the `Caustic` method is used to relate galaxy velocities to the mass of the cluster they belong to [164].

The kinematics of galaxies have been very useful to trace the matter profile in halos for large radial ranges, from the core to the outskirts of clusters [140, 165]. Nonetheless, these mass estimates are subject to numerous systematic effects. In addition to the mass-anisotropy degeneracy, reliable dynamical mass estimates need a large amount [48] of well measured galaxy redshifts per cluster. If member galaxies are not properly selected, that is, if interlopers contaminate the sample of member galaxies, according to simulations [166] cluster masses are overestimated (underestimated) for low (high) mass halos. Moreover, if the triaxial shape of clusters and their orientation with respect to the line-of-sight are not considered, dynamical masses are biased. Latest dynamical mass studies rely on scaling relations to estimate masses based on velocity dispersion measurements (see Sect. 1.3.5, [167, 168]).

1.3.2 Lensing of background sources

The light rays of sources in the background of galaxy clusters are deflected via the lensing effect on the way to the observer due to the deep gravitational potential well of clusters. These deviations are sensitive to all the gravitating matter the light traverses, therefore, they trace the total mass of clusters, including both the dark and the baryonic content.

At visible and infrared wavelengths (Sect. 1.2.2) the stars in galaxies emit in the background of clusters and the lensing effect distorts the galaxy shapes. This lensing effect can be used to reconstruct the total mass of clusters. The formalism that describes the relation between the light deflection and the traversed cluster mass density is presented in chapter 5. We distinguish the strong and weak lensing effects, that show different features, depending on the density of the matter traversed by the light with respect to the background density (Sect.5.1.1).

We are currently experiencing a rise in galaxy cluster mass reconstructions based on lensing data, which is closely related to the technical improvements in the last decade [48]. The most important asset of lensing masses is that they do not rely on any assumption regarding the physical nature of the matter and neither on the dynamical state of the cluster. However, for the cluster mass reconstruction an estimation of the redshift of every emitting background galaxy is needed. The precision of these redshift estimates, together with the accuracy of the galaxy shape and multiple images measurements, will determine the quality of the lensing masses.

In addition, since the early Universe contains a smaller amount of galaxies, high redshift galaxy clusters have less background sources [169]. As a consequence, their lensing mass reconstructions are intrinsically subject to larger statistical uncertainties. The triaxial nature of dark matter halos is also a source of error for lensing masses. We will present a dedicated study based on simulations in chapter 7. Overall, lensing masses are thought to be (almost) unbiased, but scattered, estimates of the total mass in clusters.

As aforementioned, the light from the CMB that we observe at millimetre wavelengths is also lensed in the presence of matter along the line-of-sight (Sect. 1.2.2). Presented in Melin and Bartlett (2015) [129] as "a promising new technique" to estimate cluster masses, the CMB lensing method is based on the modelling of the characteristic pattern that the potential well of clusters imprints on the CMB anisotropies. One of the advantages of the CMB lensing is that it works for high redshift clusters as well as for low redshift ones and that, contrary to the lensing of galaxies, the redshift of the emitting source, that is, the CMB, is precisely known. Nevertheless, the signal is extremely weak and individual cluster mass reconstructions have still very large uncertainties [129]. Moreover, CMB lensing reconstructions are affected by the contaminants in the

foreground of the CMB; namely, by the SZ effect of clusters. The thermal SZ effect of clusters can be removed by spectral separation methods, but it is not the case of the kSZ, which has the same spectral signature as the CMB.

Planck data has already enabled the statistical measurement of the CMB lensing signal related to individual clusters [6, 170]. Present and future experiments, such as ACT [171, 172], SPT [173] and CMB-S4 [174], will make use of the CMB lensing to reconstruct the gravitational potential of clusters of galaxies.

1.3.3 The hydrostatic mass

Following the assumptions in the Press-Schechter formalism (Sect. 1.1.5), galaxy clusters at redshift $z = 0$ are virialised spherical matter halos. A system is virialised within a volume when the total internal energy in that volume is $-1/2$ times the total gravitational binding energy. The radius at which this condition is satisfied defines the virial radius $R_{\rm vir}$.

If, in addition, we assume that the equilibrium between the internal energy and the gravitational force is assured at all positions in the cluster, with negligible velocity fields, we can write that

$$\frac{1}{\rho_{\rm coll}} \vec{\nabla} P_{\rm coll} = -\vec{\nabla}\Phi, \tag{1.42}$$

which is the hydrostatic equilibrium (HSE) equation. Here $\rho_{\rm coll}$ and $P_{\rm coll}$ are the density and pressure of a collisional gas and Φ the cluster gravitational potential,

$$\Phi(\vec{r}) = -G \int \mathrm{d}^3\vec{r'} \frac{\rho(\vec{r'})}{|\vec{r'} - \vec{r}|}, \tag{1.43}$$

with $\rho(\vec{r})$ the total mass density of the cluster at a position $\vec{r}$ from the centre.

Considering collisionless dark matter, the only collisional gas in clusters is the ICM plasma. After $\sim 10^9$ years of formation process galaxy clusters are expected to reach HSE [32]. At the same time, all the kinetic energy of merger and accretion processes is predicted to thermalise [175]. Thus, most of the gas pressure in evolved and relaxed clusters is considered to have a thermal origin ($P_{\rm coll} \sim P_{\rm thermalised\ gas}$). Under these assumptions and following Eq. 1.42, if the gas distribution traces the potential well, the measurement of ICM gas density and thermal pressure enables the reconstruction of the total gravitational potential of the cluster. For spherical clusters the hydrostatic equilibrium equation is

$$\frac{1}{\rho_{\rm coll}} \frac{\mathrm{d}P_{\rm coll}}{\mathrm{d}r} = -\frac{\mathrm{d}\Phi}{\mathrm{d}r} = -\frac{-GM^{\rm HSE}(< r)}{r^2}, \tag{1.44}$$

with $M^{\rm HSE}(< r)$ the hydrostatic mass of the cluster enclosed within the radius r. As presented in Sect. 1.2.2, the observations of galaxy clusters in X-rays and through the SZ effect allow us to reconstruct their electron density ($n_{\rm e}$), temperature ($T_{\rm e}$) and thermal pressure ($P_{\rm e}$). The gas mass density in clusters is proportional to the electron number density, $\rho_{\rm coll} = \mu m_{\rm p} n_{\rm e}$, with μ and $m_{\rm p}$ the mean molecular weight of the ICM gas and the proton mass, respectively. We can assume $\mu \approx 0.6$ [175, 176] for the gas in clusters. Therefore, the HSE mass is related to the observables with,

$$M^{\rm HSE}(< r) = -\frac{1}{\mu m_{\rm p} G} \frac{r^2}{n_{\rm e}(r)} \frac{\mathrm{d}P_{\rm e}(r)}{\mathrm{d}r}. \tag{1.45}$$

Following this equation and as already demonstrated in the literature [119, 177, 178], the HSE hypothesis offers a way to directly compute the mass profile of clusters from SZ and X-ray observations. An alternative formulation of Eq. 1.45 is

$$M^{\rm HSE}(< r) = -\frac{k_{\rm B} T_{\rm e}(r) r}{\mu m_{\rm p} G} \left(\frac{\mathrm{d}\ln n_{\rm e}}{\mathrm{d}\ln r} + \frac{\mathrm{d}\ln T_{\rm e}}{\mathrm{d}\ln r} \right), \tag{1.46}$$

which is commonly used in X-ray-only analyses, since the derivatives are directly computed on the electron density and temperature observables. It has been shown that how the pressure profile derivative is computed, either using Eq. 1.45 or 1.46, matters [86, 179]. In addition, X-ray and SZ observations are subject to different systematic effects of instrumental (e.g., absolute calibration of the spectroscopic temperatures) and physical (e.g., gas clumping) origin. In chapters 4 and 5 we compute the HSE masses of individual galaxy clusters from the combination of X-ray electron density and SZ-derived electron pressure profiles and compare them to the HSE mass estimates obtained from X-ray-derived electron density and temperature profiles.

The reconstruction of HSE mass profiles requires spatially resolved X-ray and/or SZ observations. The XMM-*Newton* and *Chandra* satellites offer angular resolutions below 10 arcsec, allowing them to resolve clusters up to high redshift and to identify contaminating gas clumps and point sources in the field of view. At millimetre wavelengths, NIKA, MUSTANG [180] and Bolocam [181] have been key instruments to probe the ICM of clusters through the SZ effect. Nowadays, NIKA2 (see chapter 2) and MUSTANG2 [182] cameras offer the best capabilities for mapping galaxy clusters. By using the Atacama Large Millimeter/submillimeter Array (ALMA), recent works have also re-demonstrated the possibility to observe and investigate the ICM gas in the core of halos through interferometry [183], which was already known since the first SZ observations of clusters at the end of the 20th century (Sect. 8.1). In chapter 8 we present the first detection with the NOrthern Extended Millimeter Array (NOEMA) of the thermal SZ in a cluster.

Compared to lensing masses, HSE estimates are less scattered, since the gas in clusters is more spherically distributed than the dark matter. Based on hydrodynamical simulations, we will study this difference in chapter 7. The main drawback of HSE mass estimates is the large number of assumptions they rely on. Deviations from hydrostatic equilibrium, non-spherical symmetry or an incomplete thermalisation of the ICM will bias the reconstructed mass.

1.3.4 The hydrostatic mass bias

It has been widely investigated and proved that masses reconstructed under the hydrostatic equilibrium hypothesis are biased low. This *HSE mass bias*, b or $b_{\rm HSE}$, could be the needed element to reconcile the cosmological tension of cluster number count analyses that rely on HSE masses with the power spectrum of CMB anisotropies [5, 184] presented in Sect. 1.2.3. Nevertheless, as explained in Sect. 1.2.3, this S_8 tension is not unique to cluster count results with HSE masses. However, all along this thesis we will assume hydrostatic equilibrium to compute cluster masses from the combination of SZ and X-ray data and we will investigate the validity of such an assumption. Comprehending the HSE mass bias might be a way to shed light on the still incomplete understanding of the baryonic physics that could be at the origin of the S_8 tension.

The HSE mass bias is defined as the relative difference between the HSE mass estimate and the true mass of the cluster, $M^{\rm true}$,

$$b = (M^{\rm true} - M^{\rm HSE})/M^{\rm true}. \tag{1.47}$$

In the literature, we find different approaches to estimate the hydrostatic mass bias. On the one hand, studies based on simulations compare the HSE masses of clusters to their true masses. HSE masses are computed by combining, under the HSE hypothesis (Eq. 1.42), the thermodynamical quantities (density, temperature and/or pressure) from the intracluster medium in the simulations. A large variety of simulations have been used in different works in the literature [5, 179, 185, 186] and they all tend to a bias of $(1-b) = M^{\rm HSE}/M^{\rm true} > 0.7$. The left panel in Fig. 1.14 shows a compilation of the bias values obtained from various simulations in different studies [179].

On the other hand, combined CMB power spectrum and cluster number count analyses fit the bias value that is required to get consistent results. According to Planck Collaboration et al. (2014) [5] $(1-b) = 0.59 \pm 0.05$ would be needed to reconcile the results from the *Planck* CMB analysis in Planck Collaboration et al. (2014) [187] with the cluster counts cosmology from Planck Collaboration et al. (2014) [5]. The posterior analysis of *Planck* data in Planck Collaboration et al. (2016) [6] obtained $(1-b) = 0.58 \pm 0.04$, together with $(1-b) =$

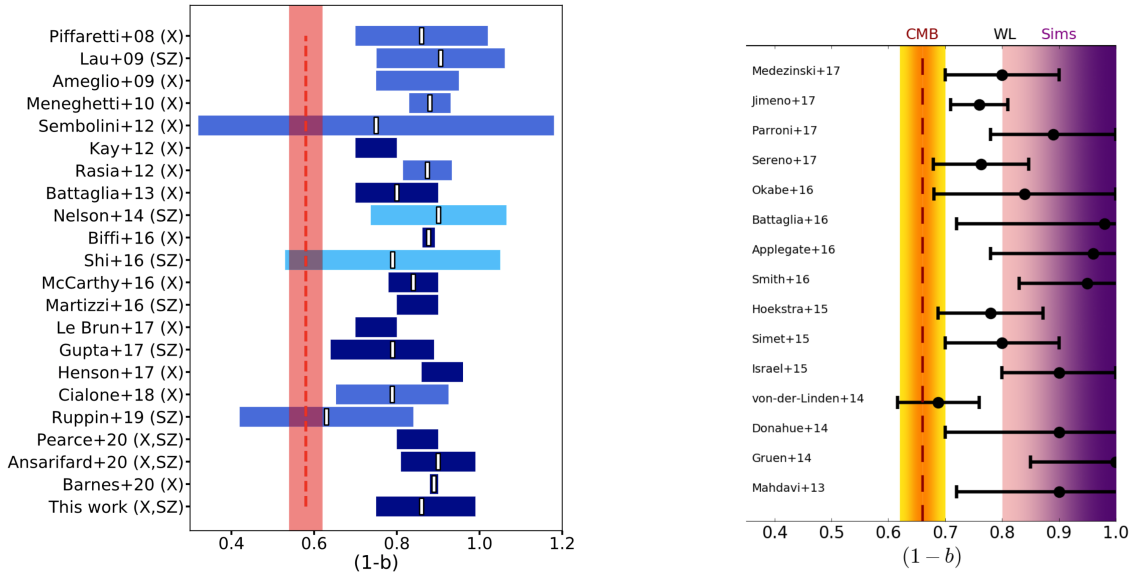

Figure 1.14: Summary of HSE mass bias measurements from different works in the literature with vertical red and orange areas showing the value needed to reconcile the CMB. Left: HSE bias measurements from simulations, shades of blue representing different complexity in the physics included in the simulations. Figure from Gianfagna et al. (2021) [179]. Right: estimates of the HSE bias values obtained from the comparison of hydrostatic mass estimates to weak lensing masses. The purple area represents the bias preferred by simulations. Figure extracted from Salvati et al. (2018) [184].

0.60 ± 0.042, $(1-b) = 0.61 \pm 0.049$ and $(1-b) = 0.66 \pm 0.045$ considering different priors for the bias (based both on X-ray and lensing data). The updated analysis in Planck Collaboration et al. (2020) [28] gave $(1-b) = 0.62 \pm 0.03$, compatible with the $(1-b) = 0.62 \pm 0.07$ from Salvati et al. (2018) [184]. Accounting for the power spectrum of the thermal SZ effect together with the cluster number counts, Salvati et al. (2018) [184] concluded that the bias needed to reconcile the CMB should be $(1-b) = 0.63 \pm 0.04$. Considering also the trispectrum in the covariance matrix of the tSZ power spectrum analysis, Bolliet et al. (2018) [188] estimated $(1-b) = 0.58 \pm 0.06$ (68% C.L.) to be compatible with CMB anisotropies.

In an attempt to have a direct measurement of the bias of observational HSE masses, several works have compared the HSE masses to lensing mass estimates. Under the assumption that lensing masses are unbiased estimates of the true mass of clusters, such HSE-to-lensing mass biases are good estimators of the HSE bias. Most of the studies in the literature are based on lensing masses estimated from the weak lensing signal on background galaxies (chapter 5). The right panel in Fig. 1.14 shows a compilation of hydrostatic-to-lensing mass biases from different works. Despite the heterogeneity of the data and methods used in the various studies, the presented results prefer values of $M^{\rm HSE}/M^{\rm lens}$ above 0.7. The orange area in Fig. 1.14 indicates the value of the HSE mass bias needed for *Planck* masses to reconcile the CMB anisotropy results. We observe that, in general, it is not compatible with the HSE-to-weak lensing mass biases. Lensing mass reconstructions from a combination of weak and strong lensing data have also been used to measure the HSE-to-lensing mass bias on small samples [189–191], obtaining $M^{\rm HSE}/M^{\rm lens}$ values that span from ~ 0.6 to ~ 1.

As above-mentioned, the lensing of the CMB anisotropies due to the presence of clusters can also be used to estimate their mass [129]. A comparison of HSE and CMB lensing masses based on *Planck* data gave $1/(1-b) = 0.99 \pm 0.19$, approximately $(1-b) = 1.01^{+0.24}_{-0.16}$ [6]. The posterior analysis in Zubeldia and Challinor (2019) [170] fitted jointly the cosmological parameters and the HSE mass bias in the scaling relation between the SZ signal from *Planck* and cluster masses, using CMB-lensing. They obtained that the bias is of $(1-b) = 0.71 \pm 0.10$. According to the SPT data analysis by Baxter et al. (2015) [173], the masses inferred from CMB-lensing are consistent with those estimated from the SZ.

Other than lensing, some works in the literature use the dynamical mass estimates of clusters, based on the velocity dispersion of member galaxies, to compute the bias corresponding to HSE masses (see Ferragamo

et al. (2021) [192] and references therein). According to the analysis with SDSS archival data in Ferragamo et al. (2021) [192], for the 207 galaxy clusters studied, the HSE-to-dynamical bias of *Planck* masses is $(1-b) = 0.83 \pm 0.07(\text{stat.}) \pm 0.02(\text{sys.})$. Also from optical observations, authors in Aguado-Barahona et al. (2022) [140] measured the HSE-to-dynamical mass bias for a different sample of 297 *Planck* clusters and obtained $(1-b) = 0.80 \pm 0.04(\text{stat.}) \pm 0.05(\text{sys.})$.

In Wicker et al. (2023) [156] authors investigated the evolution of the HSE bias with mass and redshift by studying the gas mass fraction in galaxy clusters with XMM-*Newton* mass reconstructions from Lovisari et al. (2020) [193]. The main result in Wicker et al. (2023) [156] is that the value of the HSE bias and its dependence on mass and redshift varies significantly with the analysed cluster sample, in agreement with the conclusions in Salvati et al. (2019) [194]. However, according to Wicker et al. (2023) [156] a value of $(1-b) \sim 0.8$ is preferred. A different approach was taken in Hurier and Lacasa (2017) [195], where authors used the *Planck* galaxy cluster number counts, tSZ power spectrum and bispectrum to constrain $(1-b) = 0.71 \pm 0.07$. This was obtained by fitting the normalisation of the SZ-mass scaling relation (SR), interpreting that the bias must appear in the calibration of the scaling relation. They assumed a gNFW pressure profile for the gas in clusters, using the best-fitting parameter values from Arnaud et al. (2010) [70], with the normalisation parameter computed to agree with the scaling relation in Planck Collaboration et al. (2014) [5]. The choice of this particular pressure profile could affect the resulting bias value.

There are, therefore, different issues to be considered. Firstly, as stated in Planck Collaboration et al. (2016) [6], the main limitation of cosmological analyses with cluster number counts from SZ data (and, more generally, from HSE cluster masses) is the large uncertainty on the HSE mass bias. But despite the large uncertainty, the compilation of many studies shows that the bias values estimated with and without considering the need to reconcile CMB results have different tendencies. Such inconsistency is in line with the more general tension between results from early- and late-Universe probes presented in Sect. 1.2.3 (see Abdalla et al. (2022) [19] for a review).

Any deviation from the assumptions needed to estimate HSE masses can introduce a bias on the mass. However, the non-thermal pressure component in clusters seems to be the main source of bias. If the hypothesis that gas in the ICM is thermalised is not satisfied, meaning that the kinetic energy is not completely dissipated, it implies that non-thermal processes, such as turbulence and bulk motions, contribute also to the pressure in the ICM. Thus, the thermal pressure underestimates the total pressure in the cluster, and in turn, does the HSE mass. Simulations [62, 196] predict the non-thermal pressure to be 15 to 30% of the total, varying with the accretion history of each cluster or with the considered radial range [48]. In Eckert et al. (2019) [53] authors estimated the non-thermal pressure fraction from observations. They concluded that, for the 12 clusters in their sample, the median non-thermal pressure fraction is 6% at R_{500} and 10% at R_{200}.

Hence it is essential to have a deeper understanding of the HSE mass bias and its possible evolution with mass and/or redshift. In chapters 5 and 6 we will investigate the deviation from hydrostatic equilibrium of galaxy clusters by comparing HSE masses to lensing estimates.

1.3.5 Mass proxies and scaling relations

The masses of galaxy clusters are essential for cosmological purposes (Sect. 1.2.3). However, most of the large galaxy cluster surveys cannot reconstruct resolved mass profiles of individual clusters using the presented approaches and they need to rely on scaling relations that relate the observed quantities to the masses. Assuming that galaxy clusters are self-similar, they are all expected to follow the same physical processes. If a global physical property in a cluster is closely related to its mass in a given way, the same physical property will be related in the same manner to the mass in every cluster. For this reason, scaling relations $Q \propto E(z)^{\beta} M_{\Delta}^{\alpha}$ [49] should naturally exist between the mass and certain physical quantities, Q. The latter are named *mass proxies*. Any deviation from the self-similar hypothesis implies a different physical behaviour, which is translated into a scatter with respect to the scaling relation.

In practice, large galaxy cluster analyses proceed in the following way. First, a small and well characterised

sample of clusters is selected. For those clusters the masses are estimated using any of the above-mentioned reconstruction methods (or from simulations). Measurements of the *proxy* observable of interest are also available for each of the clusters in the sample, which allows one to build the observable-mass scaling relation. The observable-mass scaling relation calibrated on the small sample is then applied to the observations of the full cosmological catalogues. This method requires an accurate calibration of the SR since it will directly impact the mass estimates and, consequently, the cosmological analyses. For instance, the sample of clusters used to calibrate the SR has to be representative of the full population.

Multiple observables are *proxies* of the mass. Regarding the stellar content, the galaxy richness in clusters is known to be correlated to the total mass of the matter halo [48]. The richness of a cluster is defined as the number of member galaxies in the cluster brighter than a given magnitude limit. If the light traces the underlying mass content, there should be a scaling relation between the number of galaxies and the mass in a cluster. Robust scaling laws between the richness and lensing masses have now been established (see, for example, Rozo et al. (2009) [197], Ford et al. (2015) [198] and Melchior et al. (2017) [199]) and are of crucial importance for the cosmological exploitation of large-area optical surveys (e.g., SDSS, LSST, *Euclid*).

In addition, the velocity dispersion of the member galaxies is used as a mass proxy. For example, in Ferragamo et al. (2021) [192] and Aguado-Barahona et al. (2022) [140] the dynamical masses within R_{200} were computed following

$$\frac{M_{200}^{\rm dyn}}{10^{15}\ {\rm M}_\odot} = \left(\frac{\sigma_{200}}{A}\right)^{1/\alpha}, \tag{1.48}$$

with α and A the parameters of the scaling relation calibrated on simulations [167, 168].

Different observables of the ICM scale also with the mass. For self-similar clusters [48] we distinguish the SR between the gas mass and the total mass,

$$M_\Delta^{\rm gas} \propto M_\Delta, \tag{1.49}$$

the scaling relation between the temperature (as derived from X-ray spectroscopy) and the mass,

$$T_{\rm X} \propto E^{2/3}(z) M_\Delta^{2/3}, \tag{1.50}$$

and the SR with the X-ray luminosity,

$$L_{\rm X} \propto E^{7/3}(z) M_\Delta^{4/3}. \tag{1.51}$$

The integrated SZ signal (and its X-ray equivalent, $Y_{\rm X}$, established by Kravtsov et al. (2006) [200]) is also related to the mass. For an ideal gas and in the case of an isothermal sphere, a solution to the hydrostatic equilibrium equation in Eq. 1.45 is given by,

$$M(<r) = 4\pi \int_0^r r^2 \rho(r) dr = \frac{2 k_{\rm B} T}{G m} r, \tag{1.52}$$

where $m = \mu m_{\rm p}$ and $\rho(r)$ are the mass of the particles that constitute the ICM and the spherical mass density, respectively, so that $\rho(r) = m n_{\rm e}(r) = \mu m_{\rm p} n_{\rm e}(r)$. As explained in Sect. 1.2.1, the size and mass of clusters is usually defined at a given overdensity Δ compared to the critical density of the Universe,

$$R_\Delta = \left[\frac{2 G M_\Delta}{\Delta H^2(z)}\right]^{1/3}, \tag{1.53}$$

which means that the temperature and the mass of a cluster can be related with

$$k_{\rm B} T = \mu m_{\rm p} \Delta^{1/3} \left[\frac{G M_\Delta H(z)}{4}\right]^{2/3}. \tag{1.54}$$

In addition, we can define the integrated Compton parameter Y_Δ, from the spherical integral of the electronic pressure in the ICM

$$Y_\Delta = 4\pi \frac{\sigma_T}{m_e c^2} \int_0^{R_\Delta} P_e(r) r^2 \mathrm{d}r. \tag{1.55}$$

And by using again the ideal gas equation and Eq. 1.54,

$$Y_\Delta = 4\pi \frac{\sigma_T}{m_e c^2} \mu m_p \Delta^{1/3} \left[\frac{G M_\Delta H(z)}{4}\right]^{2/3} \int_0^{R_\Delta} n_e(r) r^2 \mathrm{d}r. \tag{1.56}$$

The integral of the electron density is related to the gas mass density through the mean molecular weight, μ_e, of the electrons, $\rho^{gas} = \mu_e m_p n_e$. Therefore, the gas mass is calculated as

$$M_\Delta^{gas} = 4\pi \mu_e m_p \int_0^{R_\Delta} r^2 n_e(r)\ \mathrm{d}r. \tag{1.57}$$

So, by defining the gas mass fraction in clusters as the ratio of the gas mass with respect to the total mass, $f^{gas} \equiv M^{gas}/M$ (Eq. 1.38), the integrated Compton parameter scales with the cluster mass following,

$$Y_\Delta = \frac{\sigma_T}{m_e c^2} \left(\frac{G}{4}\right)^{2/3} f^{gas} \frac{\mu}{\mu_e} \Delta^{1/3} H^{2/3}(z) M_\Delta^{5/3}. \tag{1.58}$$

Numerical simulations try to understand the potential deviations from the self-similar scaling relations and scatters related to gas physics [201–203]. For example, L_X–M and Y–M relations depend directly on the gas content in clusters and they will be wrongly calibrated if the baryon depletion in clusters is misunderstood. In this sense, calibrating the relations from simulations requires complete hydrodynamical models that consider, in particular, the AGN feedback.

The scatters of the scaling relations change with the chosen observable. Good observables are those whose relation to the total mass depends as little as possible on the gas physics and, therefore, give low scatter scaling laws. The SZ is considered to be a robust mass proxy, given that the behaviour of the pressure in the cluster (besides the core) is mainly driven by the potential well [204, 205]. For this reason, large galaxy cluster surveys in SZ are key for the cosmology with cluster number counts, together with the SZ angular power spectrum.

A widely used SR between the SZ effect and the hydrostatic mass of clusters is the one derived from X-ray data in Arnaud et al. (2010) [70] (see left panel in Fig. 1.15). However, this scaling relation was calibrated on local clusters ($z < 0.2$) and any potential redshift evolution of the relation could not be accounted for. Posterior works in Planck Collaboration et al. (2011) [206] and Planck Collaboration et al. (2014) [5] estimated also the scaling relation between the SZ signal and the mass for 62 and 71 nearby galaxy clusters, respectively. Measuring the scaling relation between the integrated Compton parameter and resolved HSE masses for intermediate to high redshift ($0.5 < z < 0.9$) clusters is one of the goals of the NIKA2 SZ Large Programme (see Sect. 3.1).

To estimate the mass of ACT clusters, authors in Hilton et al. (2021) [141] used also the scaling relation from Arnaud et al. (2010) [70], but compared the results to the masses obtained from scaling laws based on additional scaling relations between richness and weak lensing [208, 209]. They concluded that masses from the SR in Arnaud et al. (2010) [70] are lower than those from relations based on weak lensing measurements. For the SPT analysis in Bocquet et al. (2019) [8] authors used the significance of the cluster detection, given directly by the employed detection algorithm, as a mass proxy. In this work weak lensing masses were used to calibrate the proxy-mass scaling relation. However, for the cosmological analysis in Bocquet et al. (2019) [8], the cosmological parameters and those of the scaling relation were simultaneously fitted. There is now an increasing preference towards cosmological analyses that fit jointly the observable-mass scaling laws and the cosmological parameters. Nonetheless, as stated in Pratt et al. (2019) [48] and studied in Bocquet et al. (2015) [210], both outcomes are degenerated and results have to be interpreted carefully.

Before finishing this section dedicated to the estimation of the mass of galaxy clusters, we would like to remark that comparing different mass estimates and their corresponding uncertainties requires a careful understanding of the underlying hypotheses. An important part of this thesis is dedicated to this subject, especially

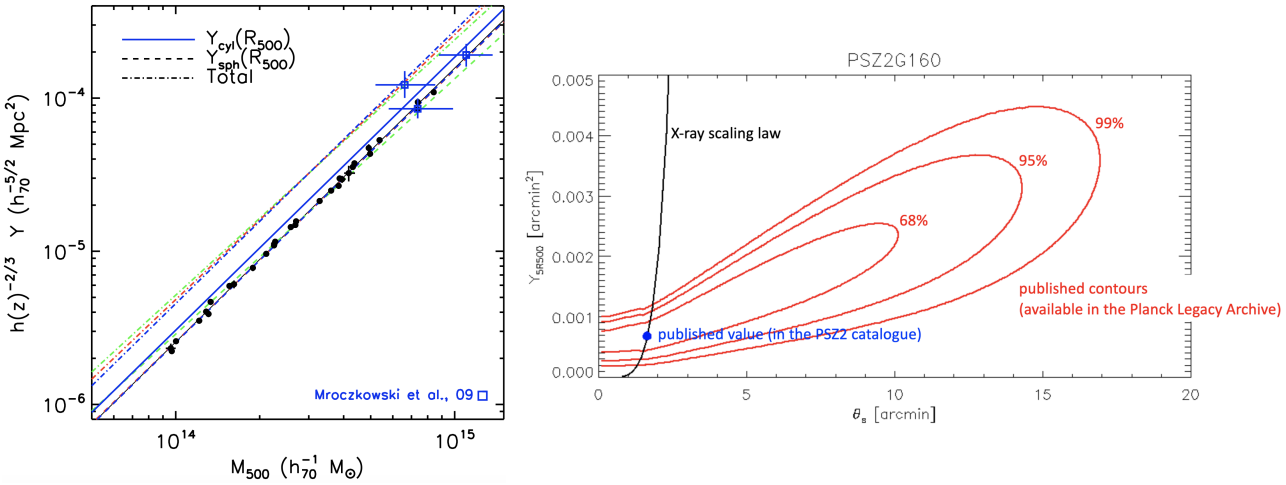

Figure 1.15: Left: scaling relation between the integrated Compton parameter and the mass of clusters within R_{500}. The thin black line shows the best scaling law fitting the black data points. Different colour and linestyles correspond to different departures from self-similarity and to different definitions of the integrated Compton parameter, respectively. Figure from Arnaud et al. (2010) [70]. Right: 2D posterior probability density contours of the $Y_{5R_{500}}$ and θ_s parameters obtained with the `MMF3` Matched Multi-filters on *Planck* data [207]. Results for the PSZ2 G160.83+81.66 (CL J1226.9+3332) galaxy cluster. The black line shows the relation between $Y_{5R_{500}}$ and θ_s given by the pressure profile in Arnaud et al. (2010) [70] and the blue marker corresponds to the SZ flux value published in the PSZ2 catalogue [142]. Figure provided by J.-B. Melin, equivalent to figure 16 in Planck Collaboration et al. (2016) [142].

in chapters 4, 5, and 6. Nonetheless, we will work with individual cluster masses that have been estimated mostly from resolved observations. The comparison to masses provided in large cluster catalogues, such as in the *Planck* Legacy Archive[2], is even more delicate. In addition to all the aforementioned drawbacks and hypotheses of scaling relations, the angular resolution of instruments like *Planck* is not enough to resolve the cluster signal above a certain redshift. In those cases, only integrated quantities can be recovered using cluster detection adapted filters [207]. In the right panel in Fig. 1.15 we show in red the outcome of one *Planck* cluster detection algorithm for the PSZ2 G160.83+81.66 galaxy cluster. *Planck* data allows one to measure the integrated Compton parameter at radii of 5 times R_{500} with respect to the size of the cluster (here given by the θ_s parameter). However, uncertainties are too large and an additional constraint from X-rays (here in black) was used to restrict the size and the SZ flux of the cluster. The value of the integrated Compton parameter in the intersection shown by the blue marker was then used to estimate the cluster mass with an SZ-mass scaling relation. It is therefore evident that the uncertainties of masses obtained with this method (for example, in Planck Collaboration et al. (2016) [142]) and the ones from the M_{500} measurement in resolved mass profiles are not of the same nature.

1.4 Conclusions

The standard model of cosmology offers, in general, a good description of the observed Universe and, combined with inflation, can explain most of its history. However, understanding the nature of dark matter and dark energy is still an open topic in the modern cosmology. All along this chapter we have also insisted on the discrepancy between the measurements of the matter density and the amplitude of the density field fluctuations in the current Universe and the results obtained from the extrapolation of high redshift measurements assuming the evolution described by the standard cosmological model. The inconsistency is even stronger for the Hubble constant, H_0, describing the expansion rate. Such tensions motivate, on the one hand, a thorough investigation of the systematic effects affecting each analysis, and, on the other hand, the research of possible extensions to the standard model.

Clusters of galaxies are unique tracers of the structure formation in the Universe. They are (almost) self-

[2] https://pla.esac.esa.int/#catalogues

similar and multi-component objects that, observed at different wavelengths, probe the baryonic and dark matter distribution. How the matter is accumulated in the overdensity peaks and how gravity interplays with other forces can be understood from the multi-wavelength studies of galaxy clusters. Thus, clusters are both interesting astrophysical laboratories where galaxies coexist with the hot ionised plasma of the intracluster medium and the dark matter, and also, key tools that can contribute to answering the open questions in cosmology.

The constraining power of cluster analyses for cosmological purposes is currently limited by the difficulty in accurately recovering the mass of galaxy clusters. In this chapter we have presented different methods to reconstruct the mass, based on diverse hypotheses and types of data. The comparison of masses estimated under different assumptions will reveal the systematic effects related to each method and, in particular, precise constraints on the HSE mass bias will be very valuable. Moreover, cosmological analyses with clusters observed at millimetre wavelengths need to rely on a profile that describes, on average, the distribution of the pressure in the ICM of every cluster. A well characterised profile from the core to the outskirts of clusters will require the combination of different instruments that probe small to large angular scales. In addition, the evolution of the mentioned HSE mass bias and of the mean pressure profile with redshift have still to be explored in detail.

Only multi-probe, multi-wavelength and multi-instrument studies will be able to answer these questions. In this thesis, we intend to move a step forward in understanding the systematic effects that affect galaxy cluster analyses.

Throughout the thesis we assume a flat ΛCDM cosmology with $H_0 = 70$ km s^{-1} Mpc^{-1} and $\Omega_{\rm m} = 0.3$. The only exception is chapter 7, where we use the cosmology based on Planck Collaboration et al. (2016) [24] results, to agree with the cosmological model assumed in the simulations.

CHAPTER 2

NIKA2: from observations to SZ maps

As described in the previous chapter, from millimetre and X-ray observations we can reconstruct the thermal energy and electron density in the ICM of galaxy clusters and, therefore, the hydrostatic mass of clusters. In this chapter, we present the NIKA2 instrument, that is used to observe the SZ of clusters at millimetre wavelengths. We describe the steps needed to build cluster maps from NIKA2 observations. We will focus on the raw data processing pipeline that aims at subtracting the different noise contaminants from the data. We also present different approaches to quantify and account for the residual noise in the final maps and for the filtering of the cluster signal due to the data processing.

2.1 NIKA2

The *New IRAM KID arrays 2* or NIKA2 camera is a millimetre dual-band camera built by the NIKA2 collaboration in Grenoble [211–213] and installed in the Nasmyth cabin of the 30-metre telescope. It is the instrument that follows its pathfinder NIKA [119, 124, 125].

2.1.1 The 30-metre IRAM telescope

The NIKA2 camera is operated at the Institut de Radioastronomie Millimétrique (IRAM) 30-metre telescope on Pico Veleta (03°23′33.7″W, 37°03′58.3″N, Sierra Nevada, Spain) at 2850 metres above the sea level. A picture of the telescope is shown in the left panel in Fig. 2.1. A 30-metre diameter primary mirror, constituted by aluminium and polyurethane panels forming a paraboloid shape, collects the sky light. The panels have been covered with an infrared reflector that reduces the deformations due to the temperature gradients, especially at

sunrise and sunset. In addition, the primary mirror is actively thermalised. The secondary mirror is located 10.5 metres from the primary, which corresponds to the focal distance of the 30-metre primary mirror. The secondary is a 2-metre diameter hyperboloidal mirror that collects the light from the primary and reflects it into the Nasmyth cabin of the telescope [214].

The large diameter of the primary mirror provides a high angular resolution. In an ideal case, the diffraction of a monochromatic light of wavelength λ, when impinging on a circular aperture of diameter D, forms an Airy disk. The instrumental angular resolution can be defined as the full width at half maximum (FWHM) of the main peak in the Airy disk: $\theta = \arcsin(1.029\lambda/D)$. For 150 and 260 GHz monochromatic light the ideal angular resolution would be of 14.1 and 8.2 arcsec, respectively. Nevertheless, the sky light reaching the 30-metre telescope is always polychromatic and the effective instrumental beam for NIKA2 is characterised as described in Sect. 2.1.2.

The high altitude and low humidity of the Pico Veleta observatory are key elements for good atmospheric transmission. Despite these conditions, the atmosphere is still the main contaminant in the observations at the 30-metre telescope. On the one hand, the opacity of the atmosphere increases with the humidity, making observations very difficult when the precipitable water vapour (PWV) gets to large values. On the other hand, unstable weather conditions can introduce large fluctuations in the signal of the atmosphere, which complicates the subtraction of the atmospheric contribution from raw data. The best period for observations are stable very cold winter nights.

2.1.2 The NIKA2 camera

Main characteristics of the NIKA2 camera

NIKA2 operates simultaneously at 150 and 260 GHz, with three arrays of Kinetic Inductance Detectors (KIDs) [211]. One of the arrays, composed of 616 KIDs of 2.8×2.8 mm^2 each, has a bandpass with maximum sensitivity at 150 GHz and it is referred to as the 2 mm array or A2. The other two arrays (A1 and A3) contain 1140 KIDs of 2×2 mm^2 each, with a maximum sensitivity at 260 GHz and are named the 1 mm arrays. The bandpasses of NIKA2 are adapted to the millimetre wavelength atmospheric transmission windows since they avoid the atmospheric absorption lines of the dioxygen (at $\sim$ 118 GHz) and water (at $\sim$ 185 and 325 GHz). They are also ideal to identify the characteristic spectrum of the thermal SZ effect (Sect. 1.2.2). NIKA2 has an instantaneous field of view (FoV) of 6.5′ in diameter.

In Fig. 2.1 we present the bandpass or relative spectral response for the three NIKA2 arrays. Bright and dark blue lines show the response of the two 260 GHz arrays (A1 and A3), while the red line indicates the transmission of the 150 GHz A2 array (the orange line corresponds to an old 150 GHz array). The black lines in Fig. 2.1 illustrate the transmission related to the atmosphere, according to the ATM model [215], for 1 and 5 mm of precipitable water vapour. We observe the oxygen absorption line at $\sim$ 118 GHz and the two water lines at $\sim$ 185 and $\sim$ 325 GHz.

The light arriving in the Nasmyth cabin is transmitted following an optical path with four mirrors to the cryostat of the NIKA2 instrument (the light enters the cryostat from the left in the illustration shown in Fig. 2.2). Once inside the cryostat, the light is reflected by another optical system (with two additional mirrors and a diaphragm) until it reaches the dichroic filter that splits the light beam in two. The dichroic splits the beam between the light reflected to the 150 GHz array and the rest, which is transmitted and passes through a polariser before reaching the two 260 GHz arrays. Thus NIKA2 has also the capability for observing the polarisation of photons at 260 GHz. Throughout this thesis we combine the data from the two 260 GHz arrays together, without exploiting the polarisation capabilities of NIKA2. Detectors in the focal plane are cooled down to $\sim$150 mK using a closed ^{3}He $-$ ^{4}He dilution circuit. In Fig. 2.2 we show the different cryogenic stages of the NIKA2 camera (see Adam et al. (2018) [211] for more details).

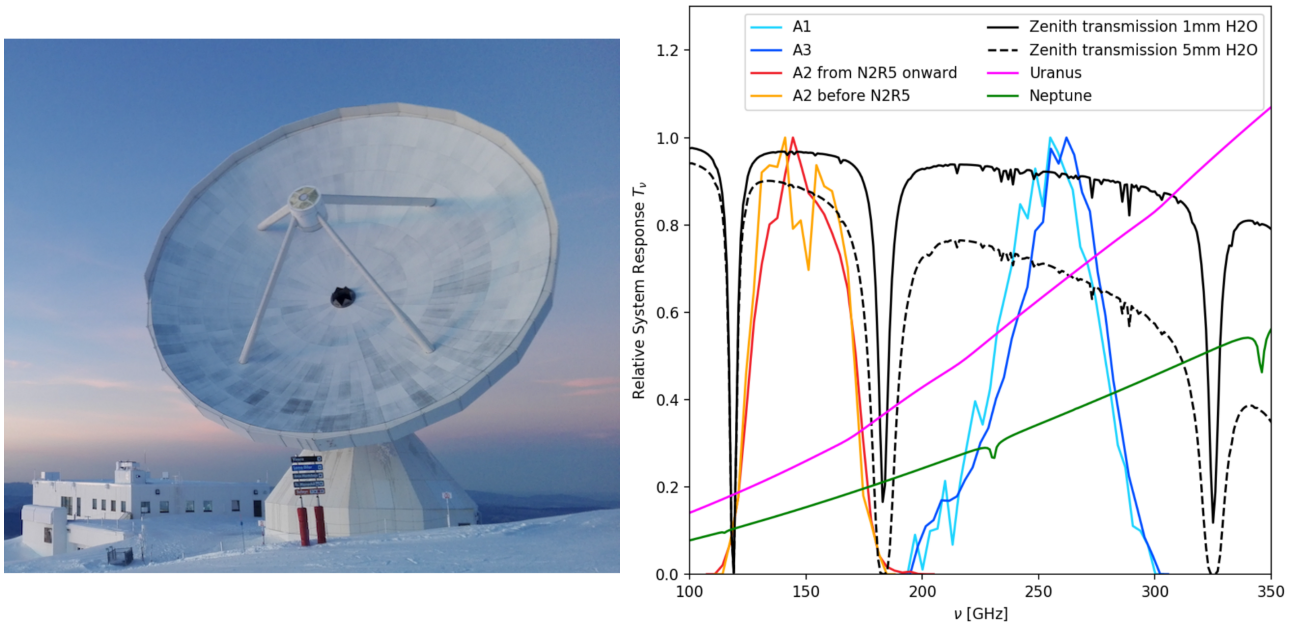

Figure 2.1: Left: The IRAM 30-metre telescope. Figure by K. Zacher (IRAM) taken from https://iram-institute.org/observatories/30-meter-telescope/. Right: Bandpasses of the three NIKA2 arrays. The two 260 GHz arrays are shown in blue and the 150 GHz array in red. Solid and dashed lines represent the atmospheric transmission for 1 and 5 mm PWV, respectively. Figure from Perotto et al. (2020) [216].

Kinetic Inductance Detectors

The KIDs or Kinetic Inductance Detectors are superconducting detectors [217]. Below a critical temperature T_c, the electrons in superconductors are separated into two populations. Some electrons remain free and are called quasiparticles. Others create Cooper pairs, bounded electron pairs that have boson properties and conduct electric current without resistance. Therefore, in the presence of a direct current, this is all conducted by the Cooper pairs. But if the current is alternating, Cooper pairs will show resistance against the changes in the electric field and introduce a kinetic inductance L_k in the material.

At temperatures below T_c the kinetic inductance in a thin film of a superconducting material is inversely proportional to the density of Cooper pairs. This is the most important property used for NIKA2 observations. At a constant $T << T_c$ photons reaching the superconducting material can break the Cooper pairs if their energy is larger than the gap energy of the Cooper pairs ($2\Delta \simeq 3.53 k_B T_c$ [218]), modifying the kinetic inductance δL_k.

In order to measure the variations of the kinetic inductance, each KID is an RLC resonant circuit, whose resonance frequency f is given by:

$$f = \frac{1}{2\pi\sqrt{(L_g + L_k)C}}, \tag{2.1}$$

where L_g is the geometric inductance and C is the capacitance. Therefore, a change in the resonance frequency of the KID will mean a change in the L_k, which at the same time is inversely proportional to a change in the incident optical power $P_{\rm opt}$:

$$\delta f = -2\pi^2 C f^3 \delta L_k \propto -\delta P_{\rm opt}. \tag{2.2}$$

NIKA2 KIDs are made of an $\sim$ 18 nm aluminium film deposited on a silicon substrate of 150 and 260 microns for maximal optical absorption at 150 and 260 GHz, respectively. The critical temperature of the aluminium is $T_c = 1.19$ K and, as discussed above, the detector arrays are placed inside the NIKA2 cryostat, which reaches 150 mK. Thus, the aluminium KIDs are superconductors. With $T_c = 1.19$ K, the gap energy needed to break a Cooper pair in the aluminium is of $2\Delta \simeq 0.36$ meV, which corresponds to the energy of $\sim$ 90 GHz photons. Therefore, photons from the CMB at the characteristic frequency ranges of the thermal SZ

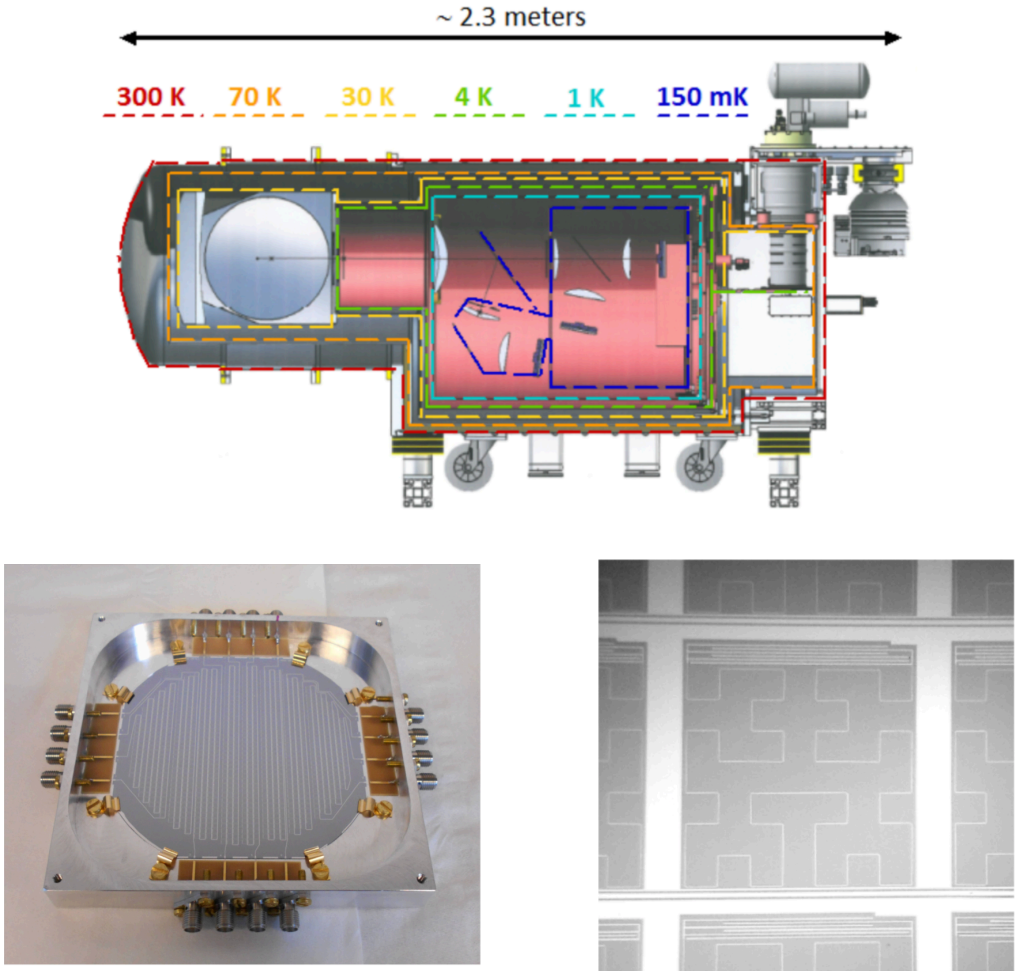

Figure 2.2: Top: the cryostat of NIKA2 and the different cryogenic stages needed to reach 150 mK. NIKA2 arrays are inside the dark blue contours. Left: one of the NIKA2 260 GHz arrays. Right: a KID in the 150 GHz array. Figures from Adam et al. (2018) [211].

effect will be detected with these KIDs. Assuming a Rayleigh-Jeans spectrum, the resonance frequency of a NIKA2 KID changes ~ 2 kHz and ~ 1 kHz per Kelvin for the 260 and 150 GHz arrays, respectively. NIKA2 KIDs are *Lumped Element KID*s (LEKIDs) [219] and so act also as antennae for absorbing directly the photons.

In the left panel in Fig. 2.2 we show a picture of one of the two 260 GHz arrays, composed of 1140 detectors, after packaging. The picture in the right panel in Fig. 2.2 corresponds to a back-illuminated KID used for NIKA2 observations at 150 GHz. The image is resolved enough to distinguish the different components of one detector in the centre of the image: the inductance meander is in the centre, the capacitor on top of it and the transmission line in the bright horizontal line in the bottom. Many KIDs can be simultaneously monitored with the same readout line (multiplexed) if the resonance frequency of each detector is different and spaced enough from others. As indicated in the Eq. 2.1 the resonance frequency can be modulated by varying the capacitance C of the condensator of each RLC circuit. The reading of the NIKA2 KIDs is performed with 4 electronic NIKEL boxes [212] for the 150 GHz array and 8 for each of the 260 GHz arrays (20 boxes in total).

Performance of NIKA2 observations

After the *commissioning* phase and instrument performance measurements carried out between 2015 and 2018, the main characteristics of NIKA2 observations at the 30-metre telescope were described in Perotto et al.

Table 2.1: Main characteristics of the NIKA2 instrument. We give the values measured in Perotto et al. (2020) [216] and in Ruppin et al. (2018) [177].

Characteristic	260 GHz arrays	150 GHz array
Reference Wavelength [mm]	1.15	2
Reference frequency [GHz]	260	150
Number of design detectors	1140×2	616
Fraction of valid detectors [%]	84	90
Main beam FWHM [arcsec]	11.1 ± 0.2	17.6 ± 0.1
Field of view [arcmin]	6.5	6.5
RMS pointing error [arcsec]	< 3	< 3
Absolute calibration uncertainty [%]	5	5
NEFD [mJy·s$^{1/2}$]	30 ± 3	9 ± 1
Conversion factor y-Jy/beam	-11.9 ± 0.9	3.7 ± 0.4

(2020) [216]. Here we present briefly the most important features and summarise them in Table 2.1.

The effective angular resolution or beam of NIKA2 was characterised during the *commissioning* phase from the measurement of the angular response of the instrument to bright point sources. Despite the complex structure of the precise beam (see Fig. 5 in Perotto et al. (2020) [216]), the angular resolution of NIKA2 at the 30-metre telescope can be described by a primary beam of $11.1'' \pm 0.2''$ and $17.6'' \pm 0.1''$ FWHM at 260 and 150 GHz, respectively. These values are slightly larger than the ideal angular resolution for monochromatic light. The efficiency of the primary beam, i.e. the ratio between the solid angle covered by the primary beam with respect to the solid angle covered by the actual beam of the instrument, was quantified to be of $47 \pm 3\%$ at 260 GHz and $64 \pm 3\%$ at 150 GHz.

Another important feature is the noise level or sensitivity in the observations, given by the Noise Equivalent Flux Density (NEFD). The NEFD is defined as the 1σ error, in one second of integration time, on the flux density of a point source for zero atmospheric opacity. For NIKA2 it was measured during the instrument performance observation campaign, from the residual noise in the maps of weak sources (here weak sources mean those with a flux density smaller than 1 Jy) and it is of 9 and 30 mJy·s$^{1/2}$ at 150 and 260 GHz, respectively. The NEFD being three times better at 150 GHz than at 260 GHz, it translates into an easiest detection of weak sources at 150 GHz. Overall, the very good sensitivity of the NIKA2 camera makes of it a competitive instrument for the observation of very weak sources, such as clusters of galaxies, in a reasonable amount of time (from 2 to 20 hours per object for the reconstruction of pressure profiles up to R_{500}). On average, 84% and 90% of the detectors in the 260 GHz and 150 GHz arrays are valid in each observation [216].

2.2 NIKA2 raw data processing pipeline

The frequency shifts measured by the electronic readout lines have to be calibrated and projected into surface brightness maps of the observed sky. In this section, we present first the different operations carried out at the telescope necessary to calibrate the observations for science. Then we describe the different steps followed during the NIKA2 data analysis.

The schematic Fig. 2.3 summarises the NIKA2 raw data processing pipeline. In blue and green we show the technical and science operations performed at the telescope and the data we get from those observations. In orange we present the steps followed in the NIKA2 raw data analysis pipeline to get calibrated data. All the information is combined to obtain the NIKA2 maps in Sect. 2.3 (pink in Fig. 2.3).

Currently, two completely independent pipelines enable going from raw data to NIKA2 maps (that is, following all the steps in Fig. 2.3). On the one hand, we have the Interactive Data Language (IDL) [220] pipeline developed within the NIKA2 collaboration. It corresponds to the pipeline used for the *baseline* method presented in Perotto et al. (2020) [216] and for previous NIKA analyses [221]. This will be the reference pipeline used to analyse the NIKA2 data in this thesis, hereafter named *Iterative Multi Common Modes* (IMCM). On

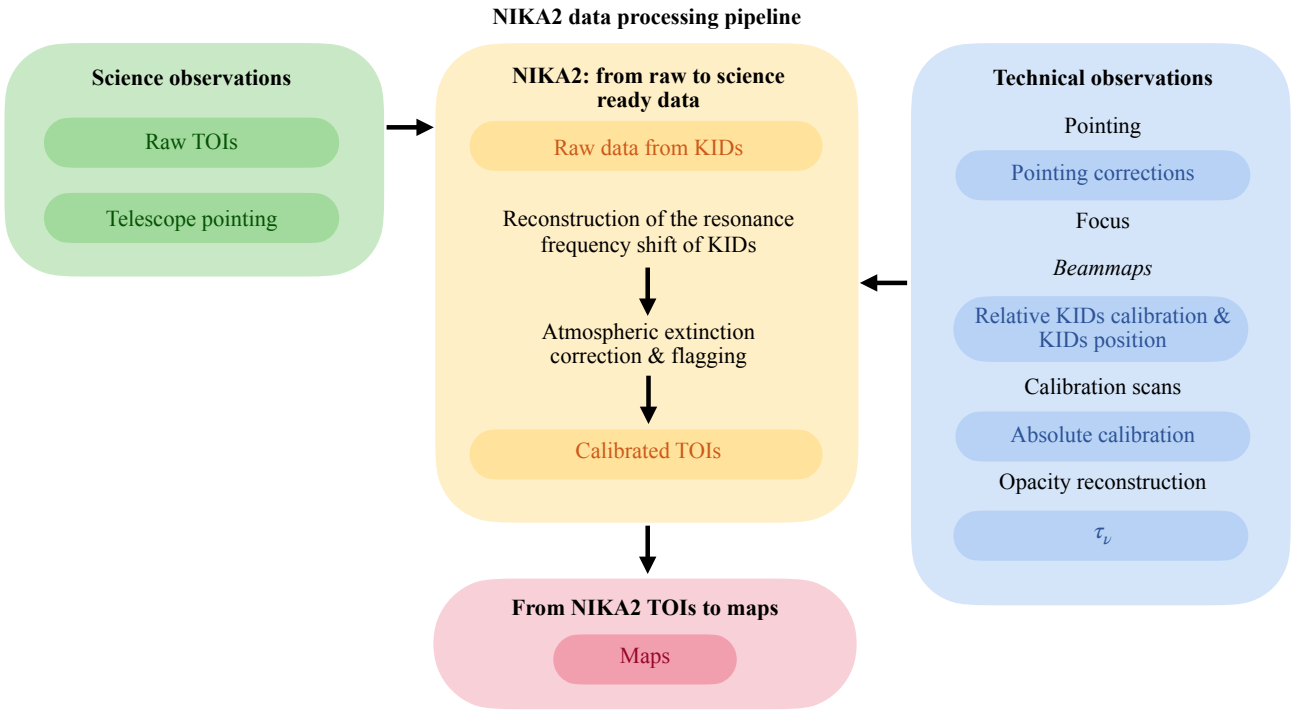

Figure 2.3: Overview of the NIKA2 pipeline. In blue, green, orange and pink we indicate the technical observations at the telescope, the science observations, the NIKA2 raw data analysis, and the map making, respectively.

the other hand, the *Pointing and Imaging In Continuum*[3] (PIIC) software was developed at IRAM. It is now used for calibrations at the telescope and we will make use of it to check the robustness of our results. More details on the differences between both pipelines are given in respect of the noise subtraction and map making in Sect. 2.3. An alternative pipeline, based on the Scanamorphos algorithm originally developed for *Herschel* data, has also been adapted to analyse calibrated NIKA2 data (based on the IDL pipeline calibration) [222]. We will not present this method.

2.2.1 Operations at the telescope

Before observing the scientific targets different types of operations need to be performed at the telescope, to both optimise the quality of the observations and have the necessary information to calibrate the data.

Pointing

The first step consists in verifying the correct alignment of the optics in the telescope and the NIKA2 detectors. For that purpose, during observations, we regularly perform pointing scans on bright and point-like sources. These correspond to cross-shaped scans around the source: we first do a two-way scan in azimuth and then in elevation. We fit a 1D Gaussian function to the signal measured in both ways and directions and compare the position of the peak on the fitted Gaussian functions to the known position of the source in the sky. This gives a correction factor in azimuth and elevation that is applied in order to adjust the pointing of the instrument. In addition, at the beginning of each observation campaign the pointing model of the telescope is updated using a set of continuous observations of point sources.

[3] https://publicwiki.iram.es/PIIC

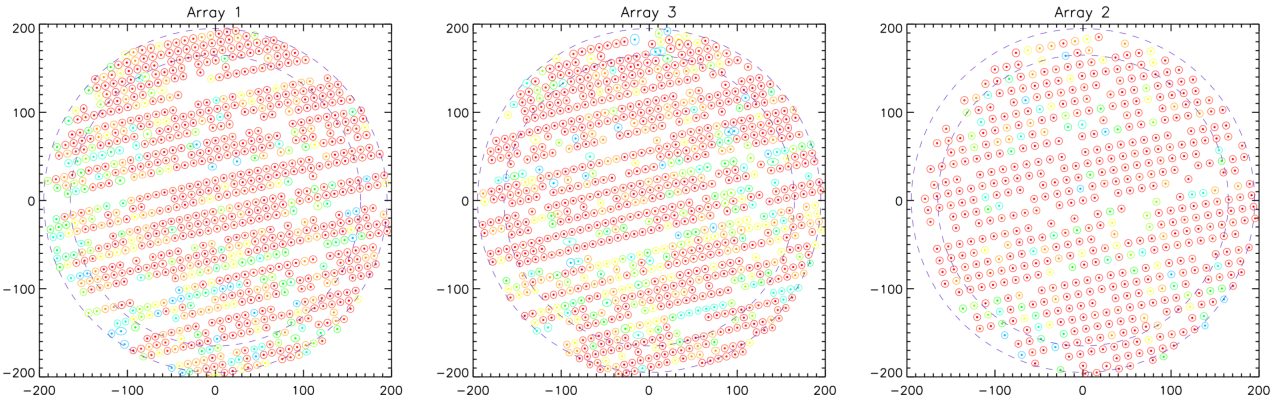

Figure 2.4: Reconstruction of the focal plane for the KIDs in the three NIKA2 arrays during the technical campaign. The circles indicate 5.5 arcmin and 6.5 arcmin diameter regions. Figure from Perotto et al. (2020) [216].

Focus

Moreover, the telescope has to be regularly focused by moving the secondary mirror with respect to the primary one. A wrongly focused telescope introduces a broadening of the beam and, therefore, a degradation of the angular resolution and deformations in the observed objects. Focus scans consist of five raster scan observations of a very bright source (see more on raster scans at the end of this section). Each of the scans is done by varying the distance between the primary and secondary mirror by a given step. We produce one source map for each of the scans and measure the size of the beam and the flux of the source. Either by searching to minimise the size of the beam or to maximise the source flux we obtain the needed correction for the distance between the mirrors.

Beammaps: reconstruction of the focal plane

The readout electronic of NIKA2 gives only the list of resonance frequencies corresponding to the detectors (Sect. 2.2.2) but does not inform directly about the physical KIDs associated with these resonances. For this reason, before science observations it is necessary to reconstruct the geometry of the focal plane to identify the KID corresponding to each resonance frequency, or equivalently, its position in the sky. This is achieved with the so-called *Beammaps*, which consist of deep observations of bright and well-known sources, most often planets, such as Uranus, Neptune or Jupiter. These observations have to be of high quality so that a map of the source can be reconstructed for every single detector [216].

From the position of the bright source in these maps, the resonance frequencies are associated with positions in the sky. In addition, this procedure permits identifying fake resonances that do not correspond to real detectors, out-of-resonance KIDs and detectors in diaphony. The relative calibration of KIDs is obtained from the observed shift in frequency for each detector compared to the known flux of the source. The instrumental beam of each KID is also characterised from the *Beammaps*, being a way to discard those detectors with very large beams. Finally, the absolute calibration of the surface brightness observed by NIKA2 is done from the combination of the *Beammaps* for all the good detectors, by calibrating the amplitude of the flux of the observed planet with its known brightness. The three panels in Fig. 2.4 show the average positions in the focal plane of the detectors in the three NIKA2 arrays, as reconstructed for the commissioning of the camera [216]. Only the detectors that were considered valid for at least two *Beammaps* during the NIKA2 technical campaign are shown [216]: 952, 961 and 553 detectors for A1, A3 and A2, respectively. Red KIDs are those that are considered always valid. Blue detectors were valid only in two out of the ten *Beammaps*. *Beammaps* are done a few times during each observation campaign.

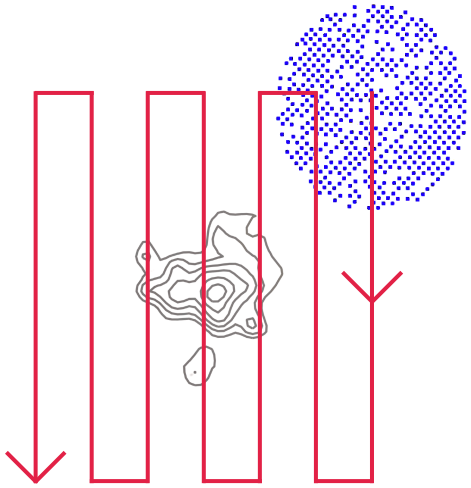

Figure 2.5: Illustration of a raster scan performed by the telescope. In red we show the path of a vertical scan composed of seven subscans, in blue the detectors in the 150 GHz NIKA2 array and in grey the observed source. Contours correspond to the NIKA2 S/N levels for the ACT-CL J0215.4+0030 galaxy cluster at 150 GHz [178].

Calibration scans

Other than *Beammaps*, all along the observation periods we also perform calibration scans to monitor the absolute flux calibration. As described in Perotto et al. (2020) [216], we distinguish two types of calibration sources. The primary calibrators correspond to the well-known sources that we observe to define the absolute calibration. For NIKA2 observations we use planets as primary calibrators, typically Uranus and Neptune. The calibration factors derived from the primary sources are verified on secondary calibrators. We use MWC349 (a stellar binary system), CRL2688 (an Asymptotic Giant Branch star) or NGC7027 (a young, dusty, carbon rich Planetary Nebula with an ionized core) [216].

Science observations: Time ordered information

As explained in Sect. 2.1.2, KIDs are sensitive to the variation of the optical power. In order to detect non-varying sources, such as clusters of galaxies, we take the following observing strategy [211, 223]. Once the focus and pointing of the telescope have been corrected, the telescope performs raster scans around the region of interest (see Fig. 2.5), knowing at all times the position in the sky of the reference KID. Each detector measures the variation of the optical power with a sampling frequency of 23.7 Hz. This is stored in the Time Ordered Information (TOI) or data timelines. A pointing matrix allows one to project the TOI of each KID into a position in the sky. The pointing matrix for every KID is calculated by combining the pointing of the telescope at all times and the relative position of the KID with respect to the reference detector.

All the NIKA2 observations exploited in this work followed the same observation strategy, with raster scans of 4×8 arcmin^2 or 10.33×3 arcmin^2 in a series of four scans with angles of 0, 45, 90, and 135 degrees with respect to the right ascension axis. Each scan is composed of multiple subscans (Fig. 2.5). Changing the observation angle improves the isotropic coverage of the sky. In Fig. 2.6 we illustrate the observation of a mock galaxy cluster seen by different KIDs. In the left panel we see the TOI in units of Jy/beam of different detectors during the observation of the cluster. Given that KIDs are located at different positions in the focal plane, each of them detects the cluster (negative peaks in the figure) at a different time. In the right panel we present the projected surface brightness map of the mock cluster of galaxy.

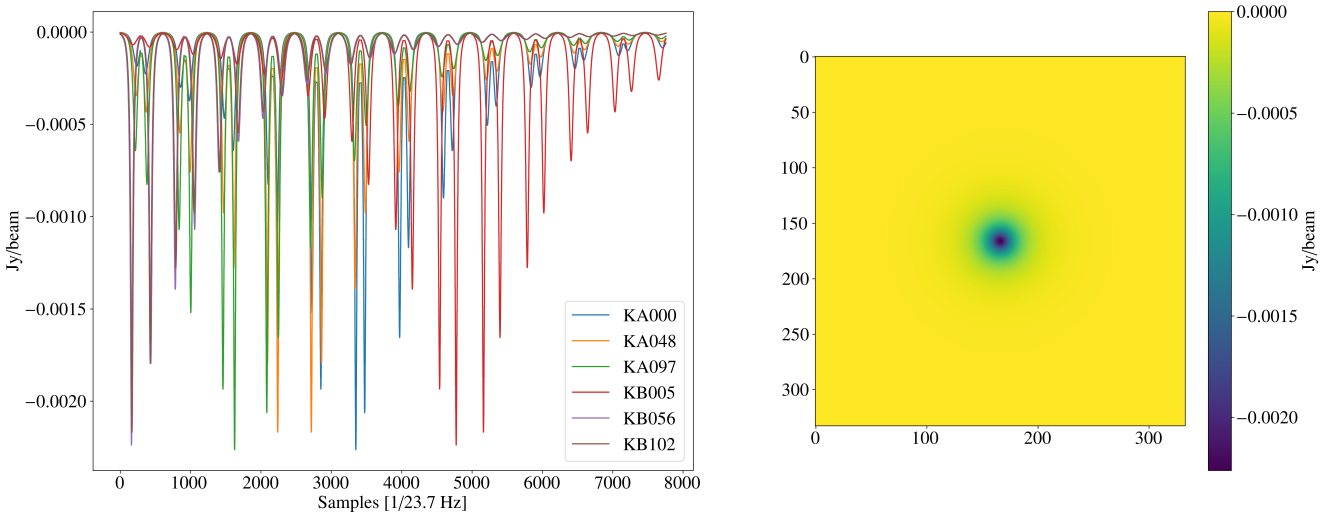

Figure 2.6: Signal of a mock galaxy cluster. Left: the cluster signal seen by different KIDs in the 150 GHz array assuming a raster scan. The negative peaks correspond to the cluster signal as seen by each detector, which are represented with different colours. Right: surface brightness map at 150 GHz.

2.2.2 NIKA2: from raw to science ready data

All the information collected at the telescope is then combined and processed to get science ready NIKA2 data. We present in this section the different steps.

Reconstruction of the resonance frequency shift in KIDs

We have seen that the incident optical power introduces a change in the resonance frequency of the KIDs. Aiming to measure such resonance frequency change, an input electric signal is fed to the detectors through the transmission line. This signal is composed of multiple tones, $f_{\rm LO}$, at the expected resonance frequencies of the detectors for the reference background. The tones are kept fixed during the duration of the science scan, so that we can measure the differences induced by the input signal with the KID transfer function. The KID transfer function is defined as the ratio of the transmitted signal to the input signal and it can be represented by a complex quantity,

$$S(f) = I + iQ, \tag{2.3}$$

with I and Q the real and imaginary parts, respectively.

Ideally, we would like to have a measurement of the transfer function at every time t and at every frequency, so that the shift in frequency of each KID can be monitored precisely. However, this would be very complex and would require large computational resources. Instead, we modulate at 1 kHz each frequency tone by $\pm\delta f_{\rm LO}$ via a synthesiser. This way we can compute four quantities at 23.7 Hz: $I, Q, {\rm d}I$ and ${\rm d}Q$ (mean and differences). From these quantities we can estimate the shifts of the resonance frequency for each KID, as in Calvo et al. (2013) [224].

Calibration

The resonance frequency shift of each KID in Hz is then converted into Jy/beam flux densities during a calibration procedure. As described in Perotto et al. (2020) [216], the procedure is performed in two steps. First, the *Beammaps* are used to measure the beam size of each detector. It is at this stage also that the maps of the observed source per KID are calibrated to the known flux of the source at 150 and 260 GHz. From the

comparison of the calibration per detector we obtain the relative calibration between KIDs. Then, using both the compilation of the *Beammaps* for all the KIDs and the calibration scans, we refine the absolute calibration of the KID resonance frequencies into flux density units.

In addition, we have discussed above that *Beammaps* are used to reconstruct the position of each detector in the focal plane. From the combination of these data with the information of the pointing of the telescope at every time t, we can build the pointing matrix $P_k(t, x, y)$, which gives the position in the sky (x, y) of each detector k at every time t.

Atmospheric extinction correction

As shown in Fig. 2.1, millimetre observations are very sensitive to the PWV in the atmosphere. When the amount of water vapour in the air increases the opacity of the atmosphere increases with it and, therefore, the transmission deteriorates. We can see in Fig. 2.1 that the effect is more important at high frequencies. In general, we say that the transmission of the atmosphere at a frequency ν is

$$T_\nu = \exp(-\tau_\nu / \sin(\delta)), \tag{2.4}$$

with τ_ν the atmospheric opacity at a frequency ν and δ the elevation. The opacity of the sky quantifies the ratio between the observed flux density in a ground-based telescope and the flux density out of the atmosphere. It is constantly monitored at the telescope and it can be extracted either from taumeter measurements[4] or by `skydip` procedures following Catalano et al. (2014) [223] and Perotto et al. (2020) [216]. The air mass $1/\sin(\delta)$ accounts for the variations with elevation of the atmosphere.

We notice in Fig. 2.1 that bad atmospheric conditions reduce the measured absolute brightness (lower transmission) and also filter some of the frequencies in the NIKA2 bandpasses. To account for both, in practice, we quantify the flux that is lost integrated in the NIKA2 bandpasses and apply a corrective factor to the TOIs. A thick atmosphere also increases the noise in detectors.

Flagging

Next, noisy and saturated detectors are discarded (as explained in Catalano et al. (2014) [223]). In addition, for the well-behaving KIDs, noisy regions in the TOIs are also excluded. They correspond mainly to the regions of the scan in between two subscans (see Fig. 2.5) or at the beginning or the end of each subscan. Moreover, parts of scans affected by large accelerations of the telescope are flagged.

All of that leads to science ready TOIs. We will see in Sect. 2.3 how these TOIs are analysed to remove contaminants and build the maps of our astrophysical sources of interest.

2.3 From NIKA2 TOIs to maps

At this stage, TOIs are ready for scientific analyses, but the signal from astrophysical sources needs to be separated from atmospheric and electronic noise. In this section, we describe different approaches to subtract the contaminants from the TOIs and their impact on the cluster signal. We also evaluate the residual noise in the final maps.

The measured surface brightness for each detector k at the frequency ν can be written as:

$$\mathrm{TOI}_k(t, \nu) = P_k(t, x, y) \times S(x, y, \nu) + \alpha_k(t) A_k(t, \nu) + \beta_k(t) E_k(t, \nu) + C_k(t) + N_k(t) \tag{2.5}$$

where $S(x, y, \nu)$ is the signal of astrophysical objects at the position (x, y) in the map and $P_k(t, x, y)$ is the pointing matrix (Sect. 2.2.2) for the calibrated detector k. At millimetre wavelengths the signal of the sky

[4] https://www.iram.es/IRAMES/weather/tauMeter.html

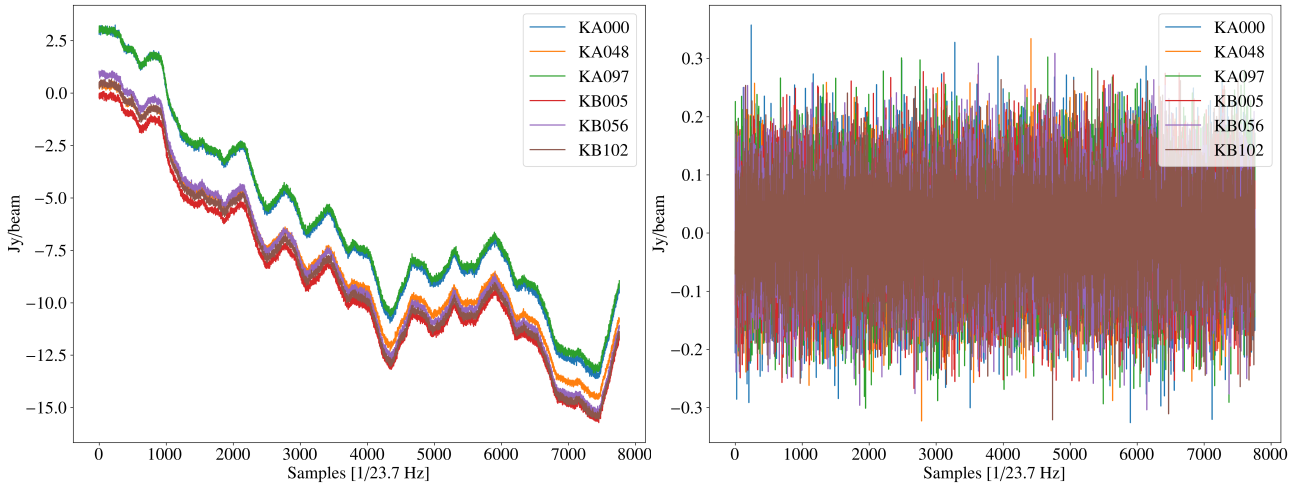

Figure 2.7: Mock NIKA2 observations for different detectors in the 150 GHz array. Left: TOIs including the signal of a mock cluster, a common mode due to the atmospheric emission and white noise. Right: TOIs from the left panel after estimation and subtraction of a common mode.

contains, in addition to the CMB and the SZ due to the presence of galaxy clusters, the emission of galaxies (Sect. 1.2.2). The galaxies in the field of view can be cluster members or foreground sources, as well as background galaxies that can be even lensed by the strong potential well in clusters. The infrared emission of dusty galaxies, quasars accretion disks and intergalactic stars form the Cosmic Infrared Background (CIB) that is also present in the NIKA2 bands. The amplitude of the CMB and CIB signal is in general an order of magnitude smaller than other contaminants (Sect. 2.3.3), so they do not represent a major problem.

In Eq. 2.5 $A_k(t, \nu)$ is the signal of the atmosphere seen by each KID, that for a large telescope such as the 30-metre can be considered, to first order, to be the same for all the detectors, $A_k(t, \nu) = A(t, \nu)\ \forall k$, by a factor α_k. As aforementioned, for the observations at Pico Veleta observatory, the amplitude of the atmospheric signal is several orders of magnitude larger than the signal from clusters. We show in the left panel in Fig. 2.7 the TOIs of several detectors when observing the mock cluster presented in Fig. 2.6 with the $\alpha_k(t)A_k(t, \nu)$ contribution extracted from NIKA2 observations carried out in February 2018. Note the large amplitude of the signal in Fig. 2.7 with respect to the flux of the expected signal of a cluster in Fig. 2.6. These TOIs also contain the $N_k(t)$ intrinsic noise per detector extracted from white noise realisations for each KID. The emission of the atmosphere at millimetre wavelengths fluctuates due to the non-homogeneous thermal emission, mainly created by the changes in the distribution of water vapour (for example, by clouds) in the sky along the raster scans of the telescope. The contribution of the atmosphere to the TOIs is so important that it will have to be carefully subtracted to detect the signal from the cluster. $N_k(t)$ is the ultimate noise of the detectors and it is not correlated amongst the KIDs. Therefore, it can not be removed and constitutes the limiting factor that determines the sensitivity of NIKA2.

The correlated noise introduced by the electronics is given by $\beta_k(t)E_k(t, \nu)$, where β_k represents the response of each detector, and $E_k(t, \nu)$ is common for the KIDs in the same electronic box. Although less important than the atmosphere regarding the amplitude, the electronic noise is correlated for different detectors and its proper subtraction is crucial (Sect. 2.3.1). Finally, $C_k(t)$ corresponds to the cryogenic induced noise, mainly due to the vibrations of the 4 K stage. Such vibrations leave a sinusoidal signal in the data timelines, and so, they can be subtracted after their identification in the Fourier transforms of the TOIs.

2.3.1 Decorrelation: correlated noise subtraction

We have seen that the contamination by cryogenics vibrations can be easily removed from the TOIs. On the contrary, separating the signal coming from astrophysical objects from the contribution of the atmosphere and electronics is very delicate, especially for weak sources such as clusters of galaxies. In the following we

present the general principles of noise subtraction for NIKA2 data. Then, we compare the approaches taken in the IMCM and PIIC pipelines.

General principles

The goal of our data processing pipeline is to maximise the recovered signal of galaxy clusters as well as to minimise the residual noise. We aim to reach the intrinsic white noise of detectors. The main principle of the atmospheric and electronic noise subtraction procedure resides in the fact that the noise for different KIDs is correlated. That is why we call the data processing procedure *decorrelation*.

We assume that at a given time t all the detectors observe the same contribution from the atmosphere. On the contrary, along the raster scan each KID points towards the astrophysical object of interest at different times. We see in Fig. 2.6 that different detectors go across the cluster at a different moment. Thus, we can calculate the common signal (also known as *common mode*) amongst all the KIDs in an array to have an estimate of the atmospheric noise contribution. In the right panel in Fig. 2.7 we show the TOIs of several KIDs once the common mode has been removed from the data timelines in the left panel. Given the presence of the white noise, it is impossible to distinguish the cluster signal in individual TOIs.

By construction, the detectors associated with the same electronic box are subject to electronic noise contributions that are alike. Thus, the electronic noise in KIDs connected to the same readout line are correlated. As for the atmosphere, common modes of TOIs from the same electronic box and readout can be used to estimate the electronic noise [221]. Although weaker than the contribution of the atmosphere, the electronic noise has to be removed from the data timelines if we aim at recovering the SZ of clusters at $\sim$ mJy levels. In addition to the mentioned correlations, some KIDs have sometimes TOIs that are strongly correlated to others, without necessarily being connected by the same electronics. Therefore, another approach consists of calculating the correlation matrix of the TOIs for all the KIDs and identifying for each detector the most correlated detectors.

In either case, once a common mode is estimated, it is removed from the TOIs to obtain a cleaner data set. However, if the estimation of the common mode is not refined enough, in addition to the noise it will contain some signal from the astrophysical source of interest. And when subtracting the common mode from the TOIs the signal of interest will also be removed and lost forever. In such cases, we say that the signal has been filtered.

The filtering of the signal can be reduced using masks. The idea is to mask, when estimating the common mode, the regions on the TOIs that contain the signal from the astrophysical object of interest. As we have seen in Fig. 2.6, each KID detects the source at a different time. Thus, masks for the different detectors are not at the same position in time. Excluding those regions, the common mode will contain a significantly reduced contribution from the source we are interested in. Although the precise area covered by the cluster's signal is not known in advance, it is a good starting point to assume that the cluster will appear as a circular object of a given radius R in the centre of the map. The pointing matrix allows us to relate the positions we want to mask in the map to the positions in the TOI of each KID.

In general, the decorrelation analysis is performed by subscans to limit the contribution of strong variations in the TOIs signal induced by acceleration and deceleration at the beginning and end of each subscan.

Based on these principles, different approaches can be used to build clean NIKA2 maps. The quality of the decorrelation method used to reconstruct NIKA2 maps is evaluated with two criteria. Firstly, we consider that the method is satisfactory if the residual noise in the maps is close to white noise. Secondly, the decorrelation works well if the filtering effects on the astrophysical source of interest are as small as possible. Satisfying both criteria at the same time can be difficult since methods that remove very well the correlated noise tend to filter the signal of the source and those that preserve better the signal give noisier maps. It is, therefore, a matter of finding a compromise. We present in the following the decorrelation methods used in the IMCM and PIIC pipelines.

Iterative Multi Common Modes

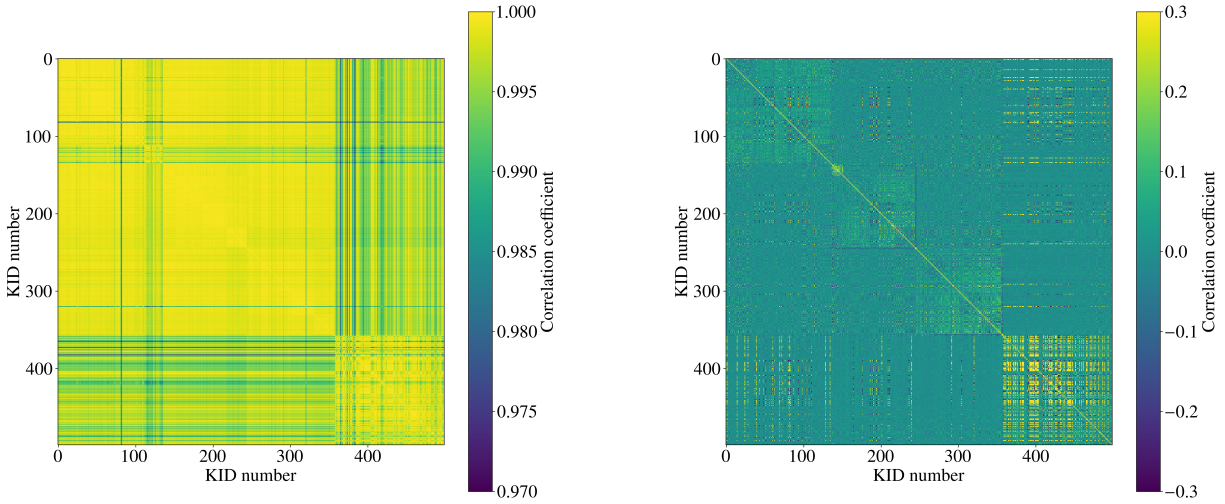

Figure 2.8: Correlation matrices between the TOIs of the KIDs in the 150 GHz array of NIKA2, before (left) and after (right) decorrelation.

The so-called *Iterative Multi Common Modes* (IMCM) is the decorrelation method of reference used to reduce NIKA2 data in this work and within the LPSZ. It corresponds to the *most correlated pixels* method from Adam et al. (2015) [119] and Perotto et al. (2020) [216]. It uses the correlation matrix between the TOIs of all the KIDs within an array to group those KIDs that are the most correlated. However, before computing the correlation matrix the sky region where the source is expected to be is masked, so that the KIDs correlation is due only to noise and systematic contributions. In the left panel in Fig. 2.8 we show the correlation matrix of the KIDs in the 150 GHz NIKA2 array before any noise subtraction in the TOIs. For each *block* of N most correlated KIDs the common mode is estimated with:

$$\mathrm{CM}(t,\nu) = \frac{\sum_{k=1}^{N} \frac{1}{g_k}\mathrm{TOI}_k(t,\nu) \times M_k(t,\nu)}{\sum_{k=1}^{N} M_k(t,\nu)}, \tag{2.6}$$

where the sum runs for the N KIDs in the block. $\mathrm{TOI}_k(t,\nu)$ is the TOI of each KID k and g_k is the intercalibration factor, calculated from the distance to the median of the TOIs of all the KIDs, $\mathrm{TOI}_k(t,\nu) = g_k \times \mathrm{Med}[\mathrm{TOI}_{k'}(t,\nu)]_{k'}$. $M_k(t,\nu)$ is the mask so that $M_k(t,\nu) = 1$ if outside the source and $M_k(t,\nu) = 0$ if inside. This common mode is then removed from the TOIs of the detectors in the corresponding block:

$$\mathrm{TOI}_k^{\mathrm{clean}}(t,\nu) = \mathrm{TOI}_k(t,\nu) - \alpha_k \mathrm{CM}(t,\nu), \tag{2.7}$$

where α_k is computed via linear regression for each subscan. In this procedure we also use other templates like, for example, the elevation variation with time. Furthermore, we can do extra filtering using polynomials or Fourier series to account for gaps in the data. In the right panel in Fig. 2.8 we show the correlation matrix of the clean TOIs for the KIDs in the 150 GHz NIKA2 array. We observe that the largest correlations have been removed. However, there are residual correlations and we almost distinguish by eye four blocks that correspond to the four electronic boxes in the 150 GHz array.

The initial mask is assumed, as abovementioned, a disk centred in the coordinates of the cluster. After the first common mode subtraction the data are projected into maps. The maps of all the available scans of the same source are coadded to get a first clean map (Sect. 2.3.2). The residual noise map is also calculated following the description in Sect. 2.3.3, and so, it is possible to get a signal-to-noise map.

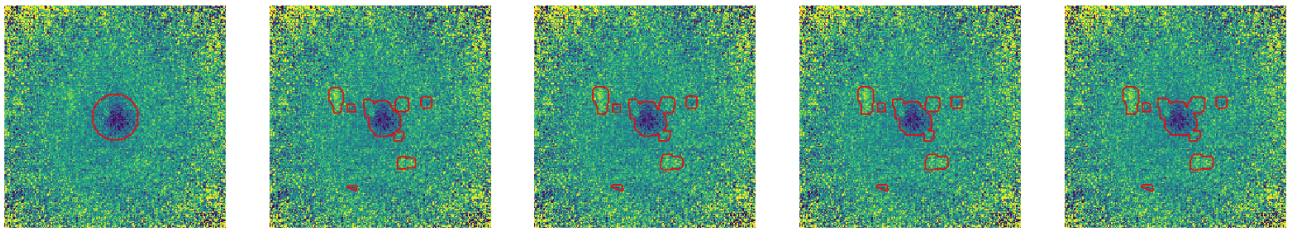

Figure 2.9: Evolution of the mask in the IMCM decorrelation for CL J1226.9+3332. The red contours show the masks used to obtain each of the maps.

In this work we use the IMCM method iteratively. From the signal-to-noise map obtained in the 0th iteration, we have a better knowledge about the extent and shape of the source and we can define a new mask in the area where the signal-to-noise is larger than a given threshold, which is generally fixed to 3. We can then repeat the common mode estimation procedure to get a new clean and noise map. This procedure can be repeated multiple times until convergence, usually after $\sim 4-5$ iterations. The contours in red in Fig. 2.9 are the masks defined at the beginning of each iteration, using the S/N map from the previous one, except for the 0th. In the left panel in Fig. 2.10 we show the NIKA2 150 GHz map of CL J1226.9+3332 (also known as PSZ2 G160.83+81.66) galaxy cluster obtained after 5 iterations. The negative region in the centre of the map is the signal of the thermal SZ effect due to the presence of the cluster. The positive sources in the field are point sources that we will discuss in Sect. 3.2.1.

PIIC

PIIC can also be used in an iterative way to get clean maps of clusters. In the 0th iteration, after discarding the noisy detectors and those that are pointing towards the mask of the source, common modes are estimated for the most correlated KIDs. Therefore, the first step is equivalent to the IMCM method. The obtained common modes are removed from the TOIs and clean timelines are projected into sky maps to obtain signal, noise and signal-to-noise maps.

PIIC also uses the signal-to-noise map to identify the source, but unlike the IMCM approach, it subtracts that first estimation of the source signal from the TOIs. In the next iteration, the correlation matrix of the KIDs is recalculated and common modes are estimated from TOIs that do not contain the source signal, so that in principle they are a better estimation of the noise. The new common modes are removed from the original TOIs and again clean timelines are projected into maps. The procedure can be repeated as many times as desired.

The main difference between both pipelines is that for the estimation of common modes the IMCM method just masks a region, while PIIC removes the signal of the source estimated from the previous iteration. Furthermore, PIIC uses a projection kernel (taken to be a Gaussian of the size of the expected beam), while the IMCM pipeline uses a nearest grid projection algorithm. In the right panel in Fig. 2.10 we present the CL J1226.9+3332 map obtained after 5 iterations with PIIC. The comparison to the map in the left panel shows that the reconstructed structures and their fluxes are slightly different between the two methods. In the following sections we will quantify how these differences propagate to the reconstruction of physical properties of clusters.

It is worth reminding that all the raw data preprocessing described in Sect. 2.2.2 is performed with the PIIC and IMCM methods independently. Hence the agreement between IMCM and PIIC results will prove the robustness of the whole NIKA2 calibration and data analysis pipeline.

2.3.2 Signal maps

These *decorrelation* methods are applied independently on single scans that have to be correctly combined to obtain the final signal maps. Firstly, cleaned TOIs of all k detectors in a scan s are projected, using the

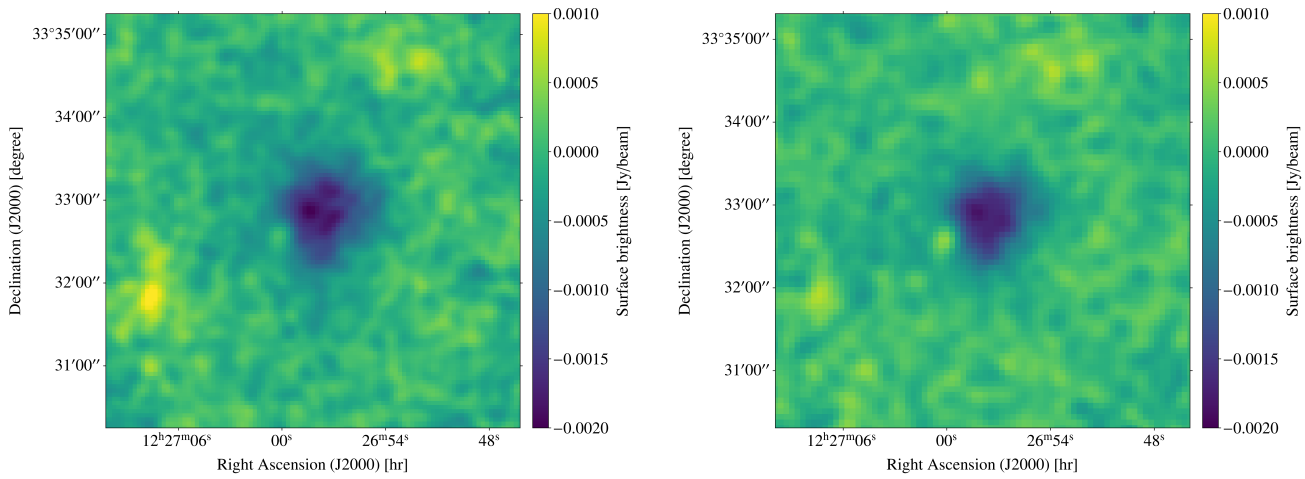

Figure 2.10: NIKA2 maps of CL J1226.9+3332 galaxy cluster at 150 GHz. The map on the left is obtained with the IMCM decorrelation method and the map on the right with PIIC.

$P_k(t, x, y)$ pointing matrix, in sky maps per scan,

$$M_s(x, y) = \frac{\sum_{k,t} P_k(t, x, y) w_k \mathrm{TOI}_k^{\mathrm{clean}}(t)}{\sum_{k,t} P_k(t, x, y) w_k}. \tag{2.8}$$

The weight w_k of each KID k is estimated from the variance of its TOI (considering the values outside the source mask), so that noisier detectors are less relevant:

$$w_k = \frac{1}{\mathrm{Var}[\mathrm{TOI}_k(t)]_t}. \tag{2.9}$$

Second, we estimate the *hits* map per scan. This map quantifies the number of samples from the TOIs that lie in each pixel and is calculated from the sum of the pointing matrices for all the valid KIDs within a scan and along the whole scan:

$$N_{\mathrm{hits},s}(x, y) = \sum_{k,t} P_k(t, x, y). \tag{2.10}$$

The larger the value of N_{hits} in a pixel, the better, since it means that the value of the signal map in that pixel has been obtained from the combination of many samples, reducing the statistical uncertainty. Similarly, the variance map is calculated by summing the variances of the TOIs of the detectors ($\mathrm{Var}[\mathrm{TOI}_k(t)]_t$) that lie in each pixel. The square root of the variance map is the RMS map and it constitutes an estimation of the uncertainty related to the signal measured in each pixel of the map. Finally, from the combination of all scans we get the signal map:

$$M(x, y) = \frac{\sum_s w_s(x, y) M_s(x, y)}{\sum_s w_s(x, y)}, \tag{2.11}$$

where $w_s(x, y)$ is the weight in the (x, y) pixel of the scan s:

$$w_s(x, y) = \frac{N_{\mathrm{hits},s}(x, y)}{\mathrm{Var}\left[M_s \times \sqrt{N_{\mathrm{hits},s}}\right]}. \tag{2.12}$$

The variance is calculated for the pixels outside the mask and with this definition noisy scans have lower weights. As discussed before, all LPSZ cluster observations are performed using raster scans at 0, 45, 90, and 135 degrees with respect to the right ascension axis. The scans observed in different directions are combined

using the coaddition methods presented here. This improves the coverage of the observed region and reduces the directional effects.

The final outputs of the pipeline are the maps of the sky at 150 and 260 GHz, and per array, and the maps of the number of hits and of the standard deviation per pixel.

2.3.3 Residual correlated noise

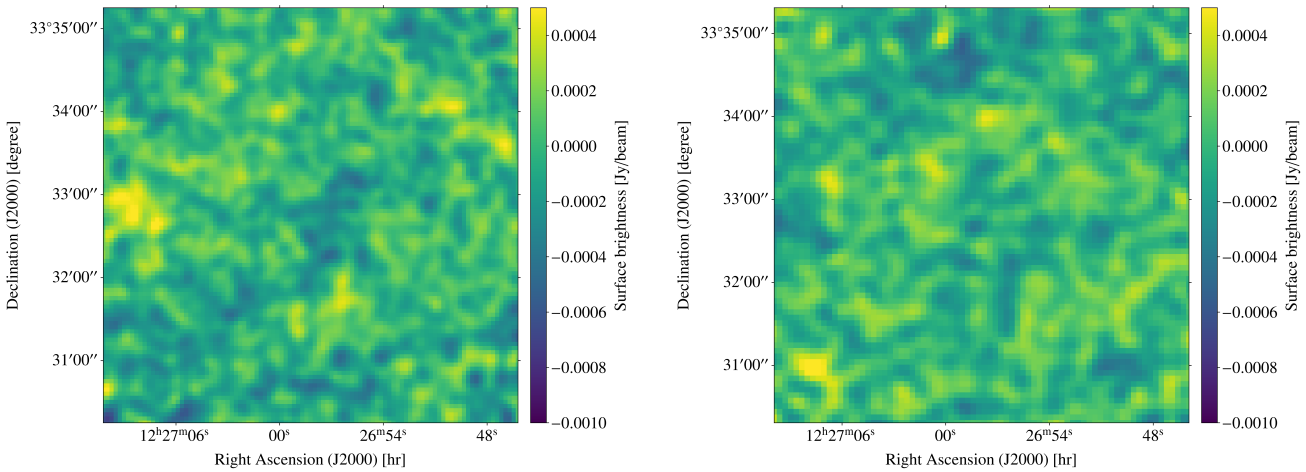

Figure 2.11: Null maps for NIKA2 150 GHz observations of the CL J1226.9+3332 cluster. On the left the JK map that corresponds to data reduced with IMCM and on the right with PIIC. The differences are computed between scans with the same angle with respect to the right ascension axis.

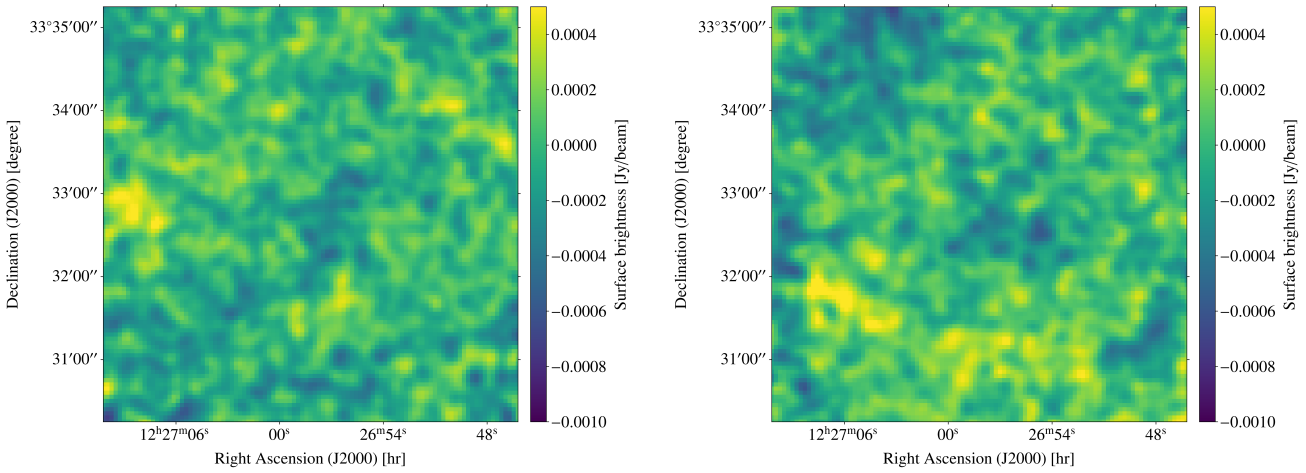

Figure 2.12: Null maps for NIKA2 150 GHz observations of CL J1226.9+3332 cluster using the IMCM method. The differences are computed between scans with the same angle with respect to the right ascension axis (AO, left) and between consecutive scans (TO, right).

The decorrelation methods try to eliminate the correlated noise from the data, but some residual noise, both from the atmospheric emission and the electronics, will always be present in the final NIKA2 maps, independently of the processing method. The significant contribution of correlated noise in the maps can introduce fake structures that might be difficult to distinguish from the signal of interest. The residual noise is usually

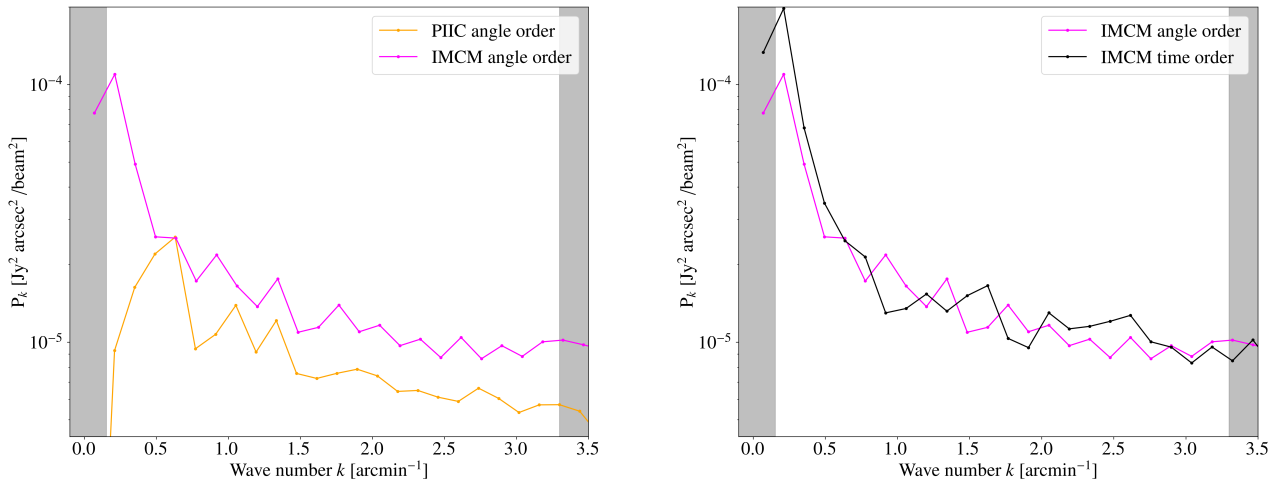

Figure 2.13: Power spectra of JK maps. Left: in magenta and orange the power spectra for the IMCM and PIIC null maps in Fig. 2.11. Right: again in magenta the power spectrum for the AO IMCM noise map and in black the spectrum for TO. Grey-shaded areas correspond to the NIKA2 field of view (for small angular frequencies) and beam FWHM (for large angular frequencies) instrumental limits.

estimated on null maps, also known as jackknives (JKs), by computing half-differences of two statistically equivalent sets of scans to eliminate the astrophysical signal and recover the residuals:

$$\mathrm{JK}(x,y) = \frac{\sum_s w_s(x,y) M_s(x,y) \times (-1)^s}{\sum_s w_s(x,y)}. \tag{2.13}$$

We assume that the astrophysical signal is the same for the maps of all the scans. Therefore, given that even scans are multiplied by (-1), the astrophysical signal is cancelled in the JK map. By contrast, the residual noise will, in first approximation, keep its statistical properties when following Eq. 2.13. Thus, the JK map can be considered as an estimate of the noise in the clean map. In Fig. 2.11 we present the residual noise maps for the IMCM and PIIC pipelines. From their visual comparison we can already guess that the PIIC noise map is smoother.

During this thesis we proposed two different noise estimates to evaluate possible systematic bias and uncertainties. The angle order (AO) noise map is computed from the half-differences of scans observed with the same angle with respect to the right ascension axis. This ensures that signal residuals from differential filtering along the scan direction are minimised in the null maps. Alternatively, the time order (TO) noise map is calculated from the half-differences of consecutive scans. This minimises the time-dependent effects that may be induced by atmospheric residual fluctuations. In Fig 2.11 both JK maps were obtained from angle ordered scans. We present in Fig. 2.12 the noise maps of IMCM estimated with the angle order (left) and time order (right) approach. From the maps we observe that the residual noise structures generally contribute more when estimated with the TO method.

To quantify the presence of residual noise in the clean NIKA2 maps we calculate the power spectrum of null maps, after correcting for the non-homogeneous exposure time (i.e., we divide by the estimated noise per pixel in the maps). A flat power spectrum is indicative of white noise only in the map, while correlated noise at large angular scales appears as a power law function of the form $P(k) \propto k^{-\alpha}$. We define k from the quadratic sum of the k_x and k_y angular frequencies in the two directions, $k^2 = k_x^2 + k_y^2$.

The left panel in Fig. 2.13 shows the power spectra corresponding to the IMCM and PIIC null maps in Fig. 2.11. As we could see from the maps, PIIC noise is smoother than IMCM, the latter containing strongly correlated noise at large scales (small k-s). Similarly, in the right panel in Fig. 2.13 we compare the power spectra of the AO and TO null maps at 150 GHz for CL J1226.9+3332 obtained with the IMCM decorrelation

method (Fig. 2.12). The AO null map has a flatter power spectrum for large angular scales (small wave numbers), meaning that it contains less large-scale correlated noise than the TO null map. This suggests that the TO null map might be affected by signal or atmospheric residuals which are differently filtered for each scanning angle.

The residual noise in the final 150 GHz NIKA2 maps needs to be accounted for in the reconstruction of the pressure profiles of clusters in Sect. 3.2. Following the method developed in Adam et al. (2016) [225], the power spectra shown in Fig. 2.13 are used to estimate the pixel-pixel noise covariance matrices. First, 1000 realisations of white noise maps are generated, with pixel values randomly selected from a $\mathcal{N} \sim (0, 1)$ distribution. Then, each of the white noise maps is convolved with the power spectrum of the noise and multiplied by the RMS map (Sect. 2.3.2). By means of this procedure, we obtain 1000 maps that contain the correlation and noise level of the JK map. With these 1000 maps we can compute the pixel to pixel covariance matrix to account for the correlations of the noise in the final maps. This correlation matrix is used in the likelihood presented in Sect. 3.2.2.

2.3.4 Transfer function

The filtering induced by the observation and the data reduction process on the cluster signal needs also to be evaluated to be accounted for when reconstructing the pressure profile of the cluster (see Sect. 3.2.2). We estimate the filtering from simulations, with a transfer function that measures the ratio in Fourier space between a simulated cluster signal, $S_{\rm in}$, and the outcome of this signal after the decorrelation procedure, $S_{\rm out}$:

$$\mathrm{TF}(k_x, k_y) = \frac{|\mathcal{FT}(S_{\rm out})|^2}{|\mathcal{FT}(S_{\rm in})|^2}. \tag{2.14}$$

The input SZ signal map is a mock map created by integrating the pressure profile of the cluster, assuming the *universal pressure profile* from Arnaud et al. (2010) [70], along the line-of-sight (Eq. 1.25). Considering the $M_{500} = 5.7 \times 10^{14}$ $\mathrm{M}_\odot$ mass from Planck Collaboration et al. (2016) [142] and $z = 0.89$ redshift for the CL J1226.9+3332 galaxy cluster, we obtained the map in the right panel in Fig. 2.6. We add to the simulated cluster a Gaussian signal with flat spectrum in map space (i.e. random white signal following $\mathcal{N} \sim (0, 0.1 \times$ flux of SZ peak)) to explore angular scales at which the cluster signal is negligible. From a technical point of view, this avoids the presence of zeros in the input power spectra and their ratio computation in Eq. 2.14.

The input signal, $S_{\rm in}$, is converted into TOIs of detectors using the pointing matrix and added to the TOIs of real observations. The decorrelation procedure described for NIKA2 data is repeated on these TOIs that contain, in addition to the real data, the signal of the simulated cluster. We use the last mask obtained for the real data decorrelation to compute the common modes. In this case, the output of the data processing pipeline gives a map that contains the NIKA2 clean data together with the $S_{\rm in}$ affected by the filtering of the decorrelation. Subtracting the NIKA2 data clean map we get $S_{\rm out}$. We can apply this procedure both to the IMCM and PIIC based pipelines.

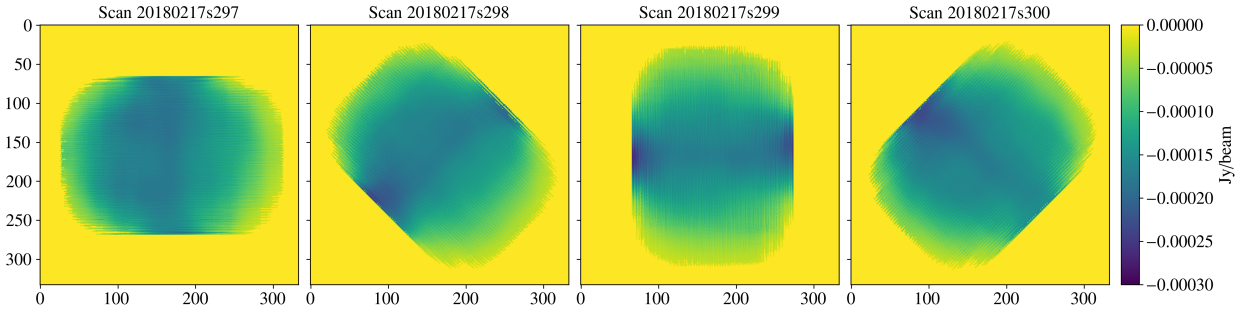

Figure 2.14: The signal filtered per scan in the subtraction of a common mode. From left to right, four scans with angles of 0, 45, 90, and 135 degrees with respect to the right ascension axis. Examples without masking the source.

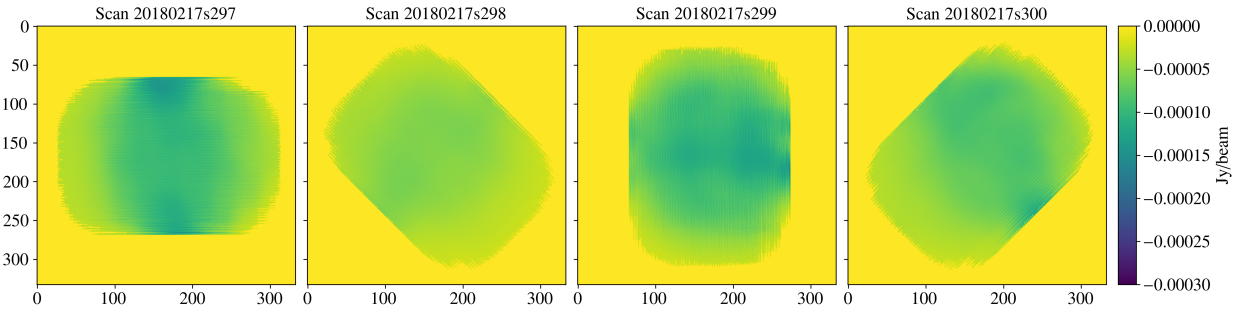

Figure 2.15: Same as Fig. 2.14, but using a 100 arcsec radius mask centred in the source.

Traditionally the NIKA2 SZ Large Programme and NIKA analyses [119, 177, 178] considered one-dimensional transfer functions (1D TF). In these cases, circular symmetry is assumed and the 1D TF is obtained by averaging the power spectra ratio (Eq. 2.14) in Fourier-domain annuli at a fixed angular scale k. Nevertheless, the filtering is not isotropic in the maps. In Fig. 2.14 we show the lost cluster signal in the subtraction of a common mode from the simulated TOIs in Fig. 2.7. We present the example for four scans with angles of 0, 45, 90, and 135 degrees with respect to the right ascension axis. We notice that the filtering is not homogeneous nor isotropic, with a strong dependence on the direction of the scan. Similarly, in Fig. 2.15 we show the signal of the cluster that is lost in the subtraction of a common mode, but this time masking the data points inside a circle of a radius of 100 arcsec. The improvement introduced by the use of the mask is evident, with the signal being less filtered when a mask is used in the estimation of the common mode. However, the directionality of the filtering remains.

The anisotropy of the filtering motivated the development in this thesis of the two-dimensional transfer function (2D TF). In the right panel of Fig. 2.16 we present the 2D TF in the (k_x, k_y) plane describing the filtering of the CL J1226.9+3332 cluster signal in the NIKA2 150 GHz map. It is the transfer function that corresponds to the map in the left panel in Fig. 2.10, obtained with the IMCM decorrelation pipeline. The black line in the left panel of Fig. 2.16 shows the 1D TF, whereas the coloured lines correspond to the one-dimensional cuts of the 2D TF for the different directions represented in the right plot. Grey-shaded areas correspond to the NIKA2 field of view (for small angular frequencies) and beam FWHM (for large angular frequencies) instrumental limits.

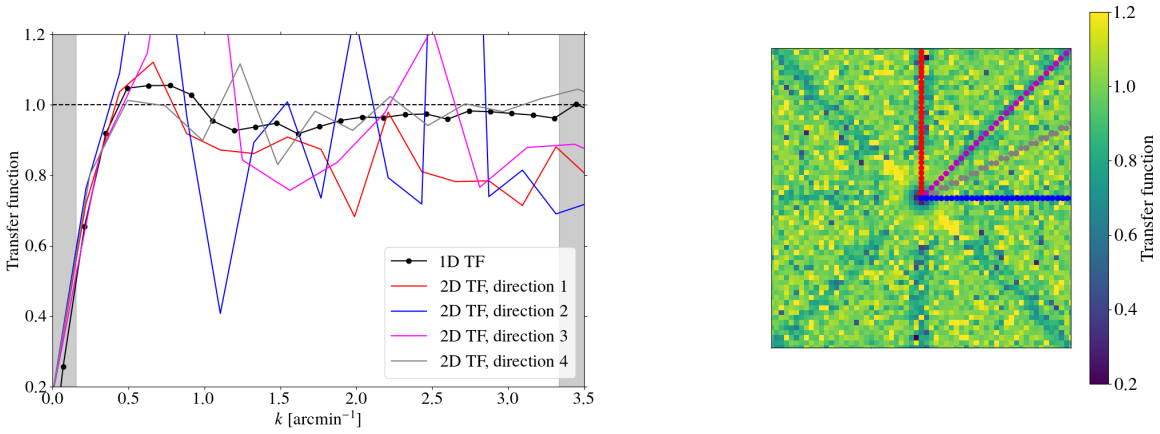

Figure 2.16: Transfer functions, 1D (left) and 2D (right), describing the filtering induced by data processing for the 150 GHz map in the left panel in Fig. 2.10. The coloured lines in the left panel represent the values of the 2D transfer function for the directions shown with the same colours in the right panel.

Except for the scanning directions, the 2D TF is compatible with the 1D TF, and is greater than 0.8 at

large angular scales, meaning that the signal is well preserved. On the contrary, filtering is strong for angular frequencies below ~ 0.5 arcmin^{-1}. At 0.4 arcmin$^{-1} \lesssim k \lesssim 0.8$ arcmin^{-1} the transfer function is larger than unity, meaning that at these scales the signal has been slightly enhanced by the data analysis process.

From the 2D TF shown in Fig. 2.16 the anisotropy of the filtering is undeniable. We can see that angular frequencies perpendicular to the scanning directions are more strongly filtered. A bad knowledge of this filtering could lead to a wrong interpretation of the data in NIKA2 maps. We stress that the goal of the transfer function is to represent, in the most accurate manner, the filtering that the cluster's signal has undergone. In Fig. 2.17 we show a different way to check the precision of the TFs. In the left panel we present the "true filtering", i.e. the difference between the simulated map after and before the decorrelation procedure. In the central panel we show an equivalent figure, but assuming that $S_{\rm out}$ is well represented by the convolution between $S_{\rm in}$ and the two-dimensional transfer function. The right panel presents the same figure using the 1D TF. Although it is not able to represent all the structures of the filtering, the 2D transfer function can cope, as expected, with the anisotropies.

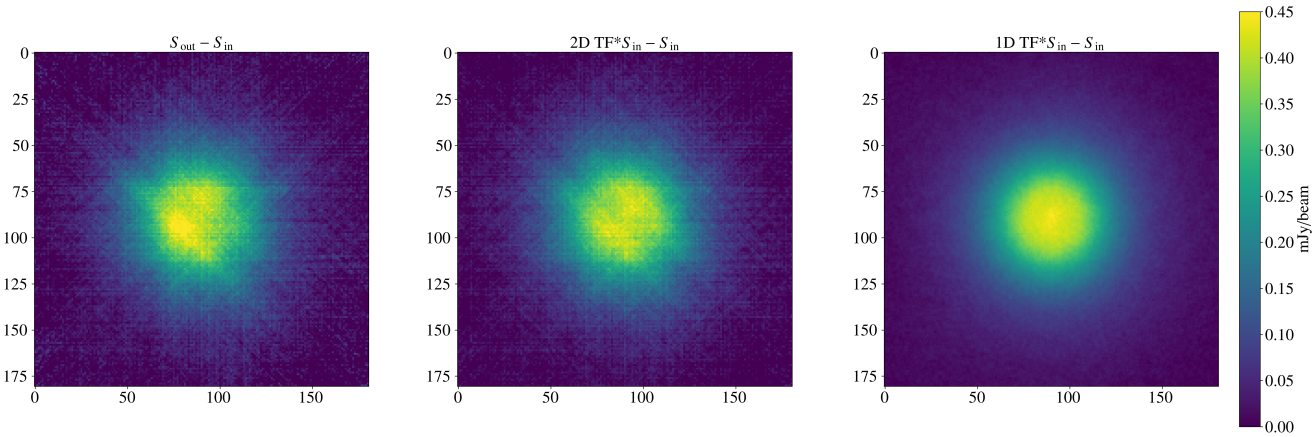

Figure 2.17: Performance of transfer fuctions. Left: the difference between a mock cluster signal after and before going through the decorrelation pipeline. Centre: the difference between the input signal convolved by the 2D transfer function and the input signal. Right: same, but convolved by the 1D transfer function.

In chapter 4 we will evaluate the robustness of the different pipelines and the impact of considering the AO or the TO noise estimator, as well as the anisotropy of the filtering, on the analysis of the CL J1226.9+3332 galaxy cluster.

CHAPTER 3

The NIKA2 SZ Large Programme

In this chapter we present the scientific goals and targets of the NIKA2 Sunyaev-Zel'dovich Large programme (LPSZ), which is an important part of this thesis. In the context of the LPSZ, we describe how the thermal pressure profile of galaxy clusters is reconstructed from NIKA2 SZ maps. From the combination with X-ray data, we detail the estimation of the hydrostatic mass profile for LPSZ clusters. This chapter is devoted to the description of the general procedure, illustrating the developments performed during this thesis with the analysis of the PSZ2 G228.16+75.20 galaxy cluster.

3.1 The NIKA2 SZ Large Programme

The NIKA2 Sunyaev-Zel'dovich Large programme or LPSZ [226–229] is one of the large programmes of the NIKA2 collaboration. As reward for the construction of the NIKA2 camera, 1300 hours of guaranteed time (GT) were allocated to the five large programmes: Galactic Star Formation with NIKA2 (GASTON), The NIKA2 Cosmological Legacy Survey (N2CLS), Interpreting the Millimetre Emission of Galaxies with IRAM and NIKA (IMEGIN), Probing the B-Field in star-forming Filaments Using NIKA2-Pol (B-FUN) and the LPSZ. The latter benefits from 300 hours.

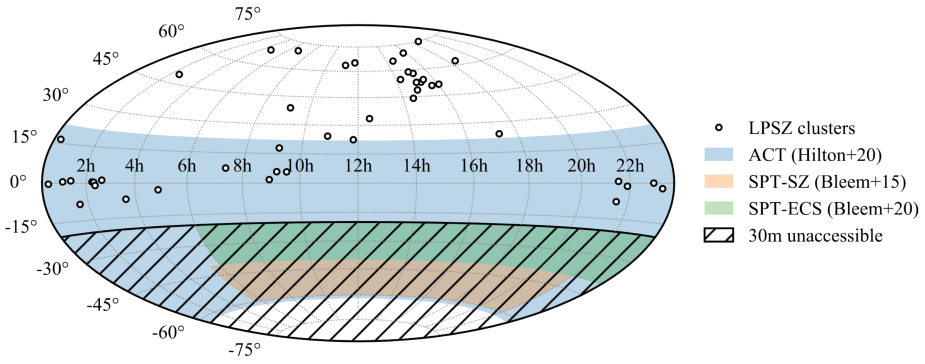

Figure 3.1: Sky coverage of different surveys in equatorial coordinates. The blue area shows the region of the sky observed by ACT [141] and the orange and green are the areas covered by SPT [230, 231]. The dashed area is inaccessible from the 30-metre telescope. Each point represents one of the 45 LPSZ clusters. Figure extracted from Kéruzoré (2021) [35].

3.1.1 The sample of the LPSZ

The NIKA2 Sunyaev-Zel'dovich Large Programme consists of 45 clusters of galaxies observed through the SZ effect with the NIKA2 camera and selected to cover uniformly the redshift and mass ranges $z \in [0.5, 0.9]$ and $M_{500} \in [3, 11] \times 10^{14}$ $M_\odot$. Clusters were chosen from *Planck* and ACT catalogues [9, 142] available at the time of the creation of the Large Programme. Given the location of the 30-metre telescope, LPSZ observations were limited to sky declinations above $-20°$. This limitation prevents from using the clusters detected with the SPT [230, 231] survey for the LPSZ follow-up. In Fig. 3.1 we show the regions of the sky covered by different SZ surveys, the LPSZ sample and the inaccessible sky at the 30-metre. The *Planck* catalogue covers the full sky.

The mass and redshift ranges were divided into five bins in mass and two in redshift and five clusters were randomly chosen from the mentioned catalogues for each mass-redshift bin. For the lowest mass bin the clusters were selected from the ACT catalogue and for the rest of the bins from *Planck* detections. The masses used to classify the clusters in bins were estimated from the SZ signal of each cluster with the SZ-mass scaling relation from Arnaud et al. (2010) [70]. Selecting clusters in these bins was a way to ensure a homogeneous repartition of the sample in mass and redshift. Given that clusters were chosen according to their SZ signal, the sample is not subject to the selection effect biases of X-ray samples (discussed in Sect. 1.2.2). The distribution in mass and redshift of the LPSZ clusters is shown in Fig. 3.2. As indicated in Fig. 3.2, some of the clusters in the LPSZ sample have also been observed in X-rays with the XMM-*Newton* satellite. *Chandra* data is also available for others.

The 300 NIKA2 hours allocated to the LPSZ were distributed amongst the clusters in the sample to ensure a S/N = 3 in the SZ surface brightness radial profiles at θ_{500} for all clusters. These calculations were performed assuming the scaling relation and pressure profile from A10, the outcomes of the *Planck* and ACT catalogues and the expected performances of the NIKA2 instrument, which was not built at the time of the selection of the sample. Therefore, the final quality of the maps can differ from the anticipated data if any of these hypotheses are not satisfied.

At the time of writing this manuscript the 300 hours have already been observed (LPSZ observations finished in February 2023) and the first analyses of the whole sample are being carried out. Some clusters appear to be weaker than expected, which is also confirmed by the X-ray follow-ups. In order to ensure a homogeneous data quality along the sample, some clusters will be dropped and the final LPSZ sample will contain $\sim$ 35 objects.

In addition to SZ and X-ray data, the clusters in the LPSZ sample are also being observed by the Gran Telescopio de Canarias. These observations provide a spectroscopic view of the member galaxies in the clusters, which can be used to have an independent estimate of the mass for each cluster [140, 233]. Some LPSZ clusters have also been observed by the *Hubble Space Telescope* as part of the CLASH sample. This data is used in

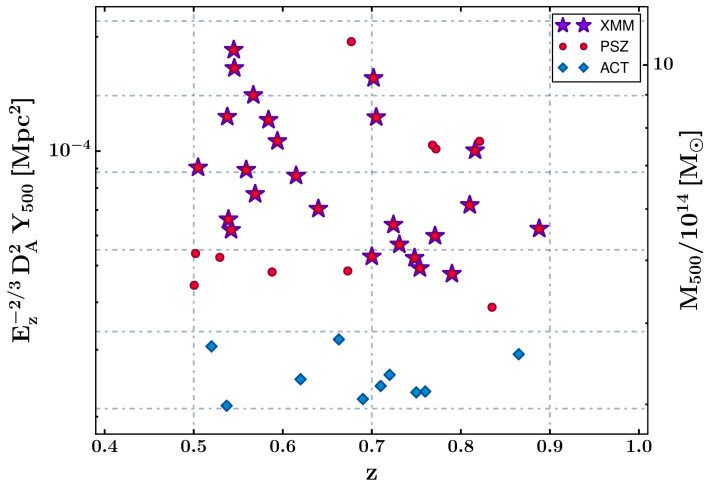

Figure 3.2: Distribution of the LPSZ cluster sample in the five bins in mass and two in redshift. Red circles and blue diamonds indicate the clusters from *Planck* and ACT catalogues, respectively. Purple stars show the objects followed up in X-rays with XMM-*Newton*. Figure from Ruppin (2018) [232].

chapter 5 to get lensing mass estimates and to assess the deviation from the hydrostatic equilibrium hypothesis of the LPSZ clusters. At the same time, simulated clusters from THE THREE HUNDRED Project [234] allow us to investigate intrinsic effects that might also affect LPSZ results and can not be studied from observations (chapter 7).

3.1.2 Scientific goals

The LPSZ seeks to address some of the open questions of the cosmology with clusters of galaxies. As presented in chapter 1 different surveys have obtained large SZ-detected galaxy cluster catalogues [141, 142, 230, 235]. However, they need to rely on a mean pressure profile and an SZ-mass scaling relation to carry out cosmological analyses.

Mean pressure profile. The first objective of the LPSZ is to re-estimate the mean pressure profile of galaxy clusters. The cosmological analyses of *Planck* and ACT collaborations [141, 142] used the so-called *universal* pressure profile from Arnaud et al. (2010) [70] to build their catalogues. But, as mentioned in chapter 1, this profile was obtained from the X-ray observations of the REXCESS sample, a sample with clusters at $z < 0.2$. A posterior work [72] reconstructed the mean pressure profile combining *Planck* and XMM-*Newton* data. The analysis was done for a sample of massive low redshift clusters, all of them at $z < 0.5$ and most of them at $z < 0.3$. Recently the PACT sample was used to build a stacked pressure profile for $0.16 < z < 0.70$ clusters [73].

The goal of the LPSZ is to go beyond $z = 0.5$ and to check the potential evolution of the average pressure profile of galaxy clusters with the sample at $0.5 < z < 0.9$. Pressure profiles could evolve with redshift, meaning that the mean profiles from the abovementioned works are not representative of the clusters at higher redshifts. Some works in the literature use already high-resolution X-ray observations to study such evolution [80, 236], but the pressure profile reconstructed using exclusively SZ data could differ from the profiles with X-ray data, due to different instrumental limitations and to the used sample selection method (see chapter 1). Therefore, a comparison to the results from SZ data is essential. As shown in Ruppin et al. (2019) [237] slight changes in the mean pressure profile have an important impact on the cosmological analyses performed with SZ data, so well resolved profiles and precise observations are key.

SZ-mass scaling relation. Another important goal of the SZ Large Programme is to deliver to the community a revised scaling relation between the SZ effect and the mass of clusters. As for the pressure profile, to date, most of the SZ-mass scaling relations have been determined from low-redshift ($z < 0.5$) cluster samples

with masses obtained from X-ray observations [70, 206]. Other scaling relations, with optical data for example [238] are also used. In any case, it is necessary to study the redshift evolution of these scaling relations as they have an important impact on the final cosmological results [239]. To build such scaling relations the precise reconstruction of the mass of galaxy clusters is crucial. As presented in chapter 1, under several assumptions, namely the hydrostatic equilibrium hypothesis, we can reconstruct the mass profile of single clusters from the combination of SZ and X-ray data. It is for this purpose that the LPSZ counts on X-ray observations from the XMM-*Newton* and *Chandra* satellites, being the LPSZ the only sample of clusters at $z > 0.5$ with equivalent resolution for X-ray and SZ data. We will present in the following sections the detailed HSE mass reconstruction procedure for the LPSZ.

Thermodynamical properties at high angular resolution. Together with the pressure and the HSE mass, the LPSZ will study the temperature and entropy (as defined by Voit et al. (2002) [240]) profiles of galaxy clusters. The shape of the entropy profile of clusters can be an indicator of their dynamical state and thermal history [77], so the resolved LPSZ profiles could be a way to learn about the distribution of relaxed and disturbed cluster populations. As explained in chapter 1 all the mentioned thermodynamical quantities can be inferred from X-ray observations only. Nevertheless, estimating the temperature with X-ray data requires spectroscopic measurements, which are time-consuming and difficult for high redshift objects. Combining SZ data with X-rays we can reconstruct the ICM temperature of clusters without X-ray spectroscopy.

Some analyses of individual clusters have already been performed based on LPSZ data. The first analysis on PSZ2 G144.83+25.11 comprised a science verification study, as well as the proof of the impact of substructures on the reconstruction of the physical cluster properties [177]. The second, the worst-case scenario for the NIKA2 SZ Large Programme, analysed the ACT-CL J0215.4+0030 galaxy cluster, proving the quality of NIKA2 camera in the most challenging case of a high-redshift and low-mass cluster [178]. In the next chapter we will present the third work, a study of the systematic effects related to the data reduction and modelling used within the LPSZ and their impact on the mass of the CL J1226.9+3332 galaxy cluster, published in Muñoz-Echeverría et al. (2023) [191].

3.1.3 The adequacy of NIKA2 for the LPSZ

The NIKA2 camera is an ideal instrument for achieving the aforementioned goals through the observation of the SZ effect of clusters of galaxies. As shown in Fig. 3.3, the two observing frequency bands are adapted to detect the decrement due to the SZ effect at 150 GHz and the positive signal at 260 GHz. In practice, with NIKA2 it is difficult to observe the galaxy clusters at 260 GHz. Firstly, and as indicated in the previous chapter, NIKA2 is three times less sensitive at 260 GHz than at 150 GHz. Therefore, larger integration times are needed to reach the same signal-to-noise level for the same flux density at 260 GHz. Secondly, the amplitude of the SZ signal integrated in the NIKA2 bandpasses is smaller in the 260 GHz band than in the 150 GHz one by a factor of ~ 3 [177] in mJy/beam units. And, in addition, the atmospheric transmission is always worse at 260 GHz (Fig. 2.1). As a result, the clusters are not detected in the 260 GHz NIKA2 maps, but these maps are very useful to characterise the contamination of the cluster signal by millimetre point sources (see Section 3.2.1), mainly dusty or radio galaxies.

The high angular resolution of NIKA2 is one of its most powerful capabilities. Clusters of galaxies are about a couple of megaparsecs large, which translates into angular diameters of ~ 10 and ~ 3 arcmin at $z = 0.2$ and $z = 1$, respectively. The arcminute scale angular resolution of large SZ survey instruments limits their capacity to resolve clusters at high redshift. On the contrary, NIKA2 provides an angular resolution (~ 18 arcsec at 150 GHz) that in addition to resolving the clusters up to $z \sim 2$, it is enough to map in detail the different substructures.

Detecting the SZ effect in a reasonable amount of time requires a very good sensitivity since the signal of clusters is very weak. While the fluctuations of the atmosphere give typically surface brightnesses of $1 - 10$ Jy/beam for NIKA2 observations, the flux density of the thermal SZ effect at 150 GHz is of the order of a few mJy/beam at the peak. At 150 GHz the sensitivity of NIKA2 being able to map a 1400 arcmin^2 region in

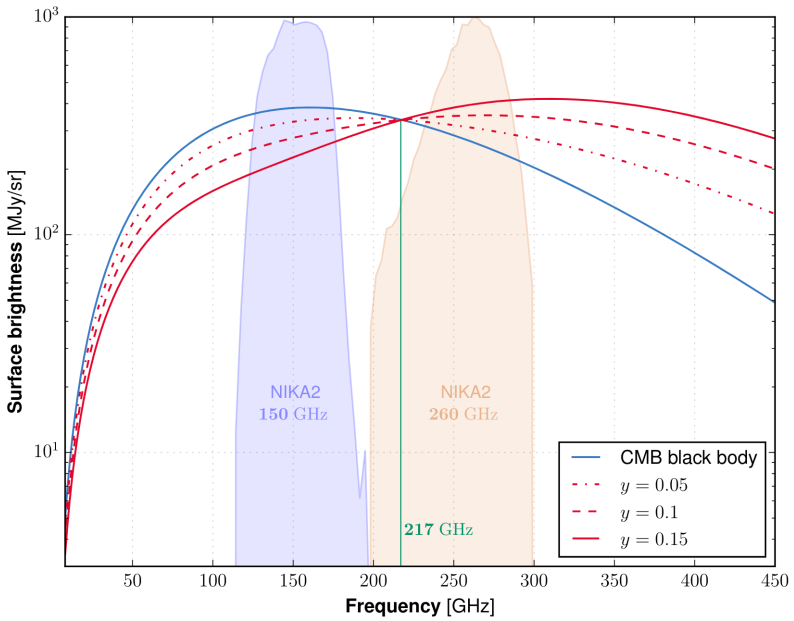

Figure 3.3: NIKA2 bandpasses in purple (150 GHz) and orange (260 GHz), the black body spectrum of the CMB in blue and its spectral distortion due to the tSZ effect in red, for large Compton parameter values. Figure from Ruppin (2018) [232].

one hour with a $1\sigma = 1$ mJy noise level, it is enough to map the SZ of clusters up to θ_{500} in a few hours.

3.2 Pressure profile reconstruction within the LPSZ

Within the SZ Large Programme, the NIKA2 150 GHz maps of clusters of galaxies are used to reconstruct the thermal pressure in the ICM of clusters. In this section, we present the modelling of the SZ effect, but before going into the pressure reconstruction, we will discuss the contamination by point sources and their characterisation. We illustrate the different steps of the analysis for the PSZ2 G228.16+75.20 galaxy cluster and a more detailed study will be presented in chapter 4 for CL J1226.9+3332.

3.2.1 Contamination by point sources

The presence of positive point sources in the 150 GHz maps can affect the modelling of the SZ effect. When those sources lie on the same line-of-sight as the cluster, they can partially or completely compensate the negative signal from the thermal SZ effect, and therefore, bias the pressure reconstruction. Thus, it is essential to consider their contamination. The high angular resolution of NIKA2 is key in this respect since it permits identifying sources that would be unresolved and potentially ignored with lower resolution instruments.

Overall, in a simplified way, we classify the galaxies emitting in the 150 GHz band into two types. On the one hand, the submillimetre galaxies are the dusty galaxies that emit mostly at wavelengths below the millimetre domain, thus they emit more at 260 GHz than at 150 GHz. On the other hand, the so-called radio galaxies emit mainly at frequencies of the order of a few GHz, much lower than the NIKA2 bands, but can contaminate the 150 GHz map and sometimes also contribute to the 260 GHz one. We deal with the two types of sources slightly differently.

Submillimetre sources

For the characterisation of submillimetre sources we make use of the NIKA2 260 GHz maps. We present in Fig. 3.4 the 150 GHz and 260 GHz maps of PSZ2 G228.16+75.20 galaxy cluster obtained with the IMCM decorrelation method on the NIKA2 data from 1.6 hours of observations. Black contours indicate significance

levels starting from 3σ with a 3σ spacing. In the left panel the cluster appears as a decrement in the centre of the 150 GHz map. At the same time, some positive sources are detected above the 3σ noise level. In the right panel we present the map at 260 GHz. As expected, we do not observe any SZ signal in the 260 GHz map, but we detect some positive sources, a few of them being coincident with the detections at 150 GHz. Sources that are weaker at 150 than at 260 GHz are good submillimetre galaxy candidates.

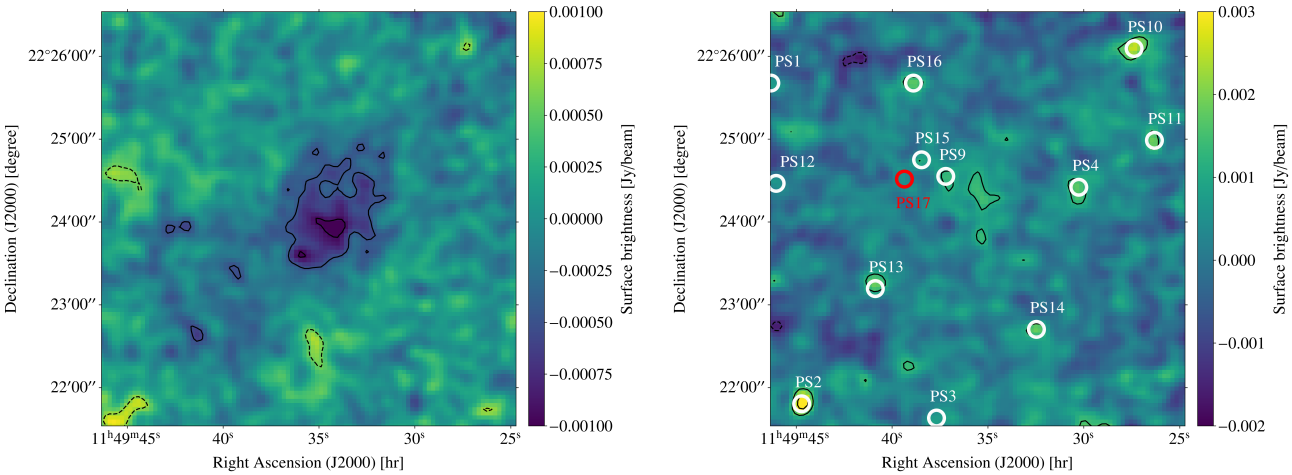

Figure 3.4: NIKA2 maps of PSZ2 G228.16+75.20 at 150 GHz (left) and 260 GHz (right) in Jy/beam units. Contours show S/N levels in multiples of $\pm 3\sigma$. Both maps have been smoothed with a 10″ FWHM Gaussian kernel. White and red circles in the 260 GHz map show the submillimetre and radio point sources, respectively.

We cross-check the detections with S/N greater than 3 with the *Herschel* SPIRE[5] and PACS[6] catalogues. These catalogues contain fluxes and positions of galaxies identified at 600, 860 and 1200 GHz with SPIRE and at 1870 and 3000 GHz with PACS. We present in Table 3.1 the *Herschel* fluxes for the point sources found within the PSZ2 G228.16+75.20 cluster map. Fluxes for sources from PS1 to PS12 were directly extracted from SPIRE and PACS catalogues, while the flux values of PS13 to PS16 were obtained from *Herschel* maps[7].

After sources have been identified, we use the `PSTools` software to estimate their flux at 260 GHz from NIKA2 maps. `PSTools` was originally presented in Kéruzoré (2021) [35] and it is based on Adam et al. (2016) [225] and Ruppin et al. (2017) [241].

This tool fits simultaneously the flux and the position of a point source, as well as a zero level, in a 1 arcminute cropped region of the 260 GHz NIKA2 map. Point sources are modelled as two dimensional Gaussian functions with the size of the 260 GHz beam that was used for the absolute calibration in the NIKA2 commissioning [216]: FWHM = 12.5″. The amplitude of the Gaussian function fitted to each source corresponds to its flux. `PSTools` uses the Python `iminuit` library [242] to minimise the χ^2.

For each of the submillimetre sources, a modified black-body spectrum model is adjusted to the fluxes from *Herschel* data together with the measurements at 260 GHz from the NIKA2 map:

$$F(\nu) = F_0 \left(\frac{\nu}{\nu_0}\right)^{\beta} B_\nu(T). \tag{3.1}$$

Here $F(\nu)$ is the flux of the source at the frequency ν, $B_\nu(T)$ is a T temperature black-body spectrum, F_0 is the

[5]European Space Agency, Herschel SPIRE Point Source Catalogue, Version 1.0, 2007. https://doi.org/10.5270/esa-6gfkpzh

[6]European Space Agency, Herschel PACS Point Source Catalogue, Version 1.0, 2007. https://doi.org/10.5270/esa-rw7rbo7

[7]http://herschel.esac.esa.int/twiki/pub/Public/Level-3Products/SPIRE_Level3_HCSS14.2.1.txt

Table 3.1: Submillimetre point sources identified in the field of PSZ2 G228.16+75.20. We give the coordinates, the name assigned to each source and the fluxes from *Herschel* PACS and SPIRE data.

Coordinates J2000	Source	3000 GHz [mJy]	1800 GHz [mJy]	1200 GHz [mJy]	860 GHz [mJy]	600 GHz [mJy]
11h49m46.33s +22d25m40.58s	PS1	15.527 ± 2.898		47.200 ± 8.100	46.500 ± 9.000	41.700 ± 6.600
11h49m44.72s +22d21m48.31s	PS2	20.165 ± 3.988		18.900 ± 3.800	22.100 ± 6.700	26.100 ± 5.900
11h49m37.68s +22d21m38.02s	PS3			17.300 ± 4.900	21.800 ± 6.600	20.100 ± 5.400
11h49m30.26s +22d24m25.15s	PS4	20.608 ± 1.872	104.356 ± 19.185	53.300 ± 6.700	51.800 ± 8.200	31.000 ± 4.200
11h49m24.84s +22d26m43.85s	PS5			34.100 ± 8.400	46.300 ± 12.000	36.800 ± 8.500
11h49m21.61s +22d26m30.42s	PS6			71.300 ± 9.300	62.200 ± 13.600	40.500 ± 10.000
11h49m16.66s +22d25m14.02s	PS7			30.200 ± 4.100	31.000 ± 7.400	18.700 ± 5.400
11h49m49.33s +22d24m44.60s	PS8					21.200 ± 6.700
11h49m37.20s +22d24m33.02s	PS9			24.300 ± 5.700		
11h49m27.37s +22d26m05.61s	PS10			19.100 ± 5.700	24.400 ± 7.000	
11h49m26.31s +22d24m59.09s	PS11	31.139 ± 6.773		31.400 ± 7.400		
11h49m46.05s +22d24m27.95s	PS12			33.000 ± 5.300	21.700 ± 6.500	
11h49m40.87s +22d23m11.75s	PS13			49.778 ± 5.977	57.749 ± 6.891	54.705 ± 6.829
11h49m32.47s +22d22m42.23s	PS14			56.627 ± 6.613	65.676 ± 7.675	49.966 ± 6.331
11h49m38.46s +22d24m45.02s	PS15			26.021 ± 3.364	54.384 ± 6.514	46.055 ± 5.848
11h49m38.89s +22d25m40.58s	PS16			31.900 ± 4.088	47.729 ± 5.794	51.690 ± 6.438

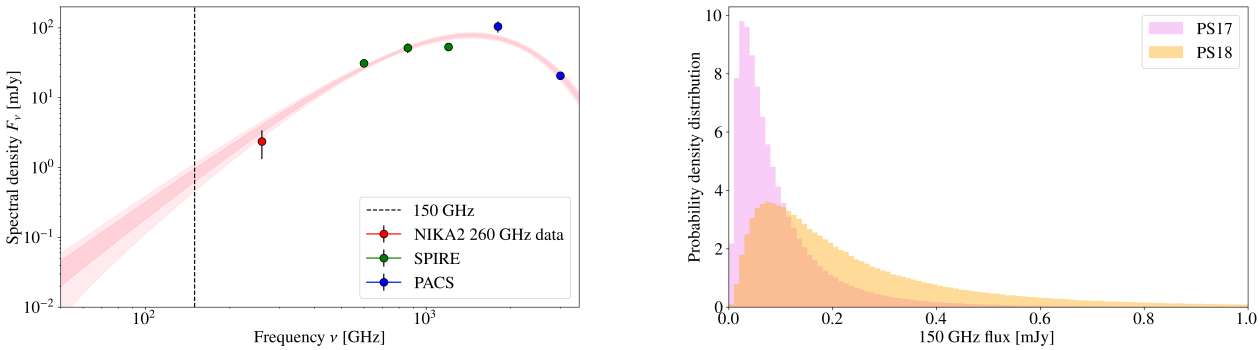

Figure 3.5: Some characteristics of point sources in the field of PSZ2 G228.16+75.20. Left: the fit of a modified black-body SED for PS4. Blue and green data points show the fluxes from PACS and SPIRE, respectively. In red we present the flux at 260 GHz measured from the NIKA2 map. In pink we show the 1σ and 2σ contours of the fit and the black dashed line indicates the 150 GHz frequency at which the SED will be evaluated. Right: PDFs of the flux at 150 GHz for the two radio sources.

amplitude of the spectral energy distribution (SED) at $\nu_0 = 500$ GHz and β describes a possible deviation from a black-body spectrum. The T temperature of the black-body is the effective emitting temperature.

The SED fits are also performed with a modified version of `PSTools` (that I modified to account for PACS data), through a Markov chain Monte Carlo (MCMC) method using the `emcee` Python package [243, 244]. To remove the degeneracy of F_0, β and T free parameters, first F_0 is fitted linearly to data and fixed for the following (as in Désert et al. (2008) [245]). Then β and T are fitted with a normal and flat prior, $\beta \sim \mathcal{N}(2, 0.5)$ and $T \in [0, 50]$ K, based on prior knowledge of the SEDs of dusty galaxies from the literature [246]. The fitted spectra are then extrapolated to 150 GHz to obtain an estimate of the flux of each source at 150 GHz. In the left panel in Fig. 3.5 we show the SED fit for the PS4 source.

Radio sources

Often radio sources close to the centre of LPSZ clusters correspond to the Brightest Cluster Galaxy (BCG), typically AGNs with very strong magnetic fields emitting due to the synchrotron radiation [247]. We know beforehand that their contribution at 150 GHz is small, but given their central position it is important to consider them.

Usually radio sources are not detected at 260 GHz, so we use external radio surveys (as in Adam et al. (2014)

[221]), such as VLA FIRST [248] and NVSS [249], to get an approximative estimation of their contribution at 150 GHz. Assuming a synchrotron spectrum $F(\nu) = F_0(\nu/\nu_0)^\alpha$ with $\alpha = -0.7 \pm 0.2$, which describes the spectral energy distribution for an average radio source [250], we extrapolate the fluxes to 150 GHz. The extrapolation of fluxes from radio to millimetre wavelengths can be dangerous and lead to biasing the electron pressure reconstruction, so extreme care is needed especially with very central sources.

In the VLA FIRST catalogue and within a region of 6′ diameter around PSZ2 G228.16+75.20 galaxy cluster centre we find two radio sources: PS17 in $(\mathrm{RA, DEC})_{\mathrm{J2000}}$ = (11h49m39.357s, +22d24m31.06s) and PS18 in $(\mathrm{RA, DEC})_{\mathrm{J2000}}$ = (11h49m22.315s, +22d23m26.43s). Their fluxes at 1.4 GHz are 1.76 ± 0.15 mJy and 4.86 ± 0.15 mJy, respectively. From the extrapolation, assuming the synchrotron spectrum with a Gaussian distribution for α, we estimate the probability distribution of their fluxes at 150 GHz. We present the distributions in the right panel in Fig. 3.5. Both are weak at NIKA2 frequencies and compatible with a null flux.

In the right panel in Fig. 3.4 we indicate in white and red the dusty and radio galaxies identified around PSZ2 G228.16+75.20. Both from the 150 and 260 GHz maps there seem to be a source in the north-western part of the cluster, compensating the SZ effect. Nevertheless, no counterpart was found in the external catalogues, nor in the *Herschel* maps. For the well characterised submillimetre and radio sources, the probability distributions of the fluxes at 150 GHz are used as priors for the joint fit of the cluster pressure profile and the point sources fluxes described in the following section.

3.2.2 Thermal SZ modelling

As presented in chapter 1, the spectral distortion of the CMB caused by the thermal energy in the cluster (i.e., the tSZ effect) is characterised by its amplitude or Compton parameter, y [112], which is directly proportional to the thermal pressure of the electrons in the ICM (Eq. 1.25). Hence, the SZ surface brightness is proportional to the Compton parameter integrated over the SZ spectrum convolved by the NIKA2 bandpass, and therefore, proportional to the integrated thermal pressure of the ICM in the cluster. In this section we present the pressure profile reconstruction method employed within the NIKA2 Sunyaev-Zel'dovich Large Programme.

To estimate the electron pressure in the ICM for each galaxy cluster we fit a model map of the surface brightness of the cluster, $\mathcal{M}$, to the NIKA2 150 GHz map, $\mathcal{D}$. The model map is obtained from the pressure profile of the galaxy cluster integrated along the line-of-sight in Compton parameter (y) units, following Eq. 1.25. Multiple models can be used to represent the pressure profile in the ICM of clusters. For example, we can describe the pressure of galaxy clusters with a radially binned spherical model (also called *non-parametric* model in Ruppin et al. (2017) [241] and Romero et al. (2018) [251]),

$$P_{\mathrm{e}}(r_i < r < r_{i+1}) = P_i \left(\frac{r}{r_i}\right)^{-\alpha_i}, \tag{3.2}$$

where P_i and α_i are the values of the pressure and the slope at the radial bin r_i. The slope is directly calculated as

$$\alpha_i = -\frac{\log P_{i+1} - \log P_i}{\log r_{i+1} - \log r_i}. \tag{3.3}$$

We initialise the pressure bin values by taking, at each radial bin, random values from a normal distribution centred at the corresponding pressure from the universal profile of A10 [70]. The radial bins are chosen to cover mainly the range between the NIKA2 resolution and field of view capabilities. The derived y-map is convolved with the NIKA2 beam at 150 GHz, which is approximated by a two-dimensional Gaussian with FWHM = 17.6″ [216]. In order to account for the attenuation or filtering effects due to data processing in the NIKA2 150 GHz map, the model map is also convolved with the transfer function calculated as described in Sect. 2.3.4.

Finally, the y-map is converted into surface brightness units with a conversion coefficient, accounting for the SZ spectrum shape convolved by the NIKA2 bandpass. This conversion coefficient was calculated in Ruppin et al. (2018) [177], for the observations of the PSZ2 G144.83+25.11 galaxy cluster, under the observational conditions of April 2017: -11.9 ± 0.9 Jy/beam/y. Given that the coefficient includes the integration in the NIKA2 bandpass, for observations carried out in a different period its value may differ from the one obtained in Ruppin et al. (2018) [177] if the bandpass is not identical, for example, due to different observing conditions. For this reason, the conversion coefficient is also left as a nuisance parameter of the map fit, with a prior value centred on -11.9 Jy/beam/y. In this way, we can also account for uncertainties in the total calibration.

Furthermore, for the comparison with the 150 GHz NIKA2 map, we add the contribution of point sources to the model map $\mathcal{M}$. Point sources are modelled as two-dimensional Gaussian functions, with priors on the fluxes at 150 GHz obtained from the results of the SED fitting procedures presented in Sect. 3.2.1. The last component in the model map is a constant zero-level that we also adjust as a nuisance parameter.

Therefore, the parameters (ϑ) of the fit are the pressure radial bins describing the ICM of the cluster, the conversion factor from Compton to surface brightness units, the fluxes of the contaminant point sources, and the zero-level. The likelihood that we use to compare our model $\mathcal{M}(\vartheta)$ pixel by pixel to the data $\mathcal{D}$ is given by

$$\begin{aligned}\log \mathcal{L}(\vartheta) = &-\frac{1}{2}\sum_{i=1}^{n_{\rm pixels}} \left[(\mathcal{M}(\vartheta)-\mathcal{D})^T\, C^{-1}_{\rm pix-pix}\,(\mathcal{M}(\vartheta)-\mathcal{D})\right]_i \\ &-\frac{1}{2}\left(\frac{Y_{500}(\vartheta)-Y_{500}^{\rm catalogue}}{\Delta Y_{500}^{\rm catalogue}}\right)^2 .\end{aligned} \tag{3.4}$$

Here $C_{\rm pix-pix}$ is the pixel-pixel noise covariance matrix accounting for the residual noise in the NIKA2 150 GHz map (Sect. 2.3.3). For each pressure profile model we also compute the integrated Compton parameter, Y_{500} (Eq. 1.55). We compare in the likelihood in Eq. 3.4 the integrated Compton parameter from the pressure model to the value measured by large SZ surveys and given in the *Planck* and ACT cluster catalogues [9, 142], $Y_{500}^{\rm catalogue}$. This additional condition in the likelihood helps to constrain the external region of the profile, which can be difficult to determine using only NIKA2 data.

For the map fit, we use the `panco2` pipeline [252] and follow the procedure described in Adam et al. (2015) [119], Ruppin et al. (2018) [177], and Kéruzoré et al. (2020) [178]. This pipeline performs an MCMC fit using the `emcee` Python package. The sampling is performed using 40 walkers and 10^5 steps, with a burn-in of 10^3 samples. Convergence is monitored following the $\hat{R}$ test of Gelman and Rubin (1992) [253] and chains autocorrelation as described in Kéruzoré et al. (2023) [252]. The `panco2` code has been successfully tested on simulations.

We present in Fig. 3.6 the NIKA2 150 GHz map of PSZ2 G228.16+75.20 compared to the best-fit model map and the residual. The fit is performed on the IMCM map, using the 2D transfer function (Sect. 2.3.4) and estimating the noise with time ordered scans (Sect. 2.3.3). The SZ emission of PSZ2 G228.16+75.20 is diffuse, with a large number of point sources in the field. The model represents the SZ effect due to the cluster and the flux of sources. The most important residual is the positive emission to the south of the cluster, for which no corresponding point source was found in the catalogues, nor in the NIKA2 260 GHz map (Fig. 3.4).

We show in Fig. 3.7 the electron pressure profile obtained from the fit to the NIKA2 150 GHz map. In the right panel we present the correlation matrix of the pressure bins obtained for PSZ2 G228.16+75.20, where we see that the 4th bin is very anticorrelated with the central ones. First and last bin couples are also remarkably anticorrelated.

3.3 X-ray observations with XMM-*Newton*

For the clusters in the LPSZ with XMM-*Newton* data, the raw X-ray data is analysed following the standard procedure used in previous works in the literature [77, 177, 178, 254]. The electron density and temper-

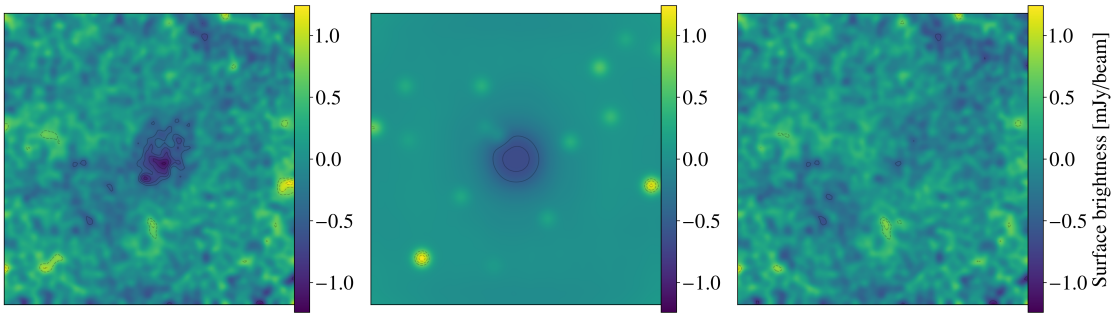

Figure 3.6: Best-fit for the 150 GHz map of PSZ2 G228.16+75.20. From left to right: the NIKA2 surface brightness map, the best-fit model of the SZ signal and point sources, and the difference map between the data and the best-fit model.

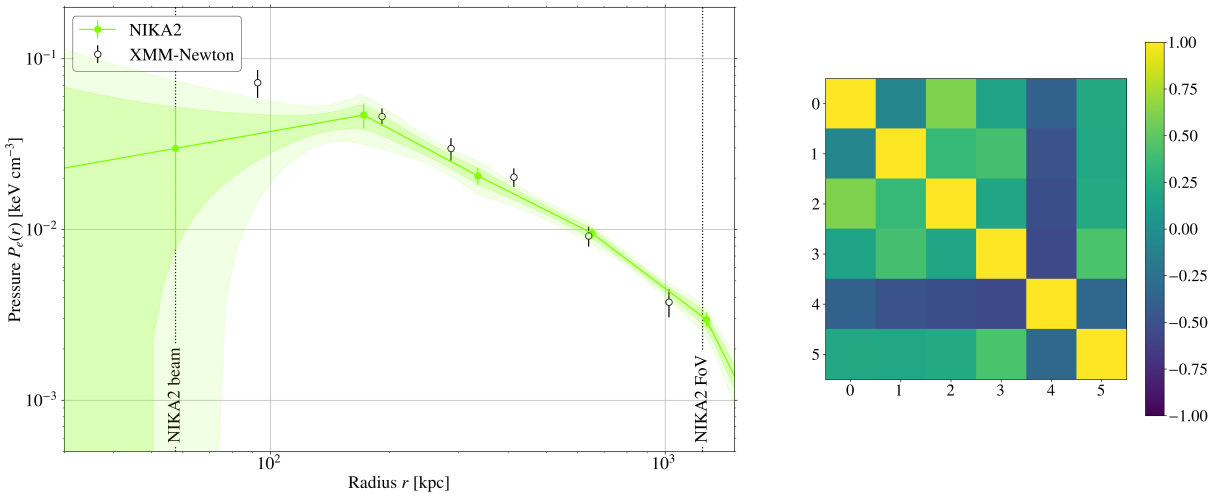

Figure 3.7: Radially binned pressure profile fit to PSZ2 G228.16+75.20 data. Left: in green the mean posterior profile with 1σ and 2σ contours. Empty symbols correspond to the pressure profile obtained from the combination of XMM-*Newton* electron density and temperature profiles. Vertical dotted lines indicate the instrumental limits of NIKA2 as radius of the beam and FoV. Right: correlation matrix for the six fitted pressure bins.

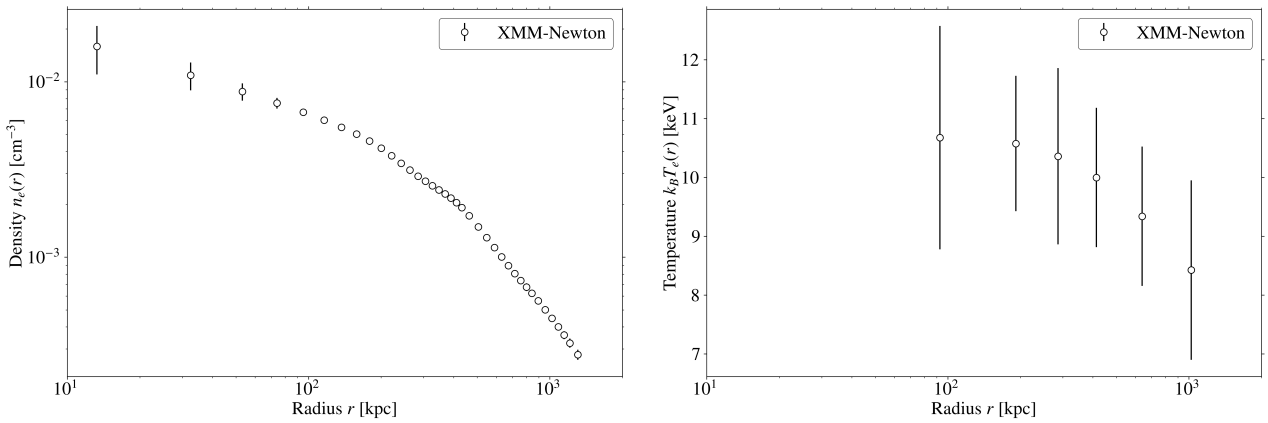

Figure 3.8: Electron density (left) and temperature (right) profiles for the PSZ2 G228.16+75.20 galaxy cluster reconstructed from XMM-*Newton* observations, with 1σ error bars.

ature profiles are extracted following the methodology described by Pratt et al. (2010) [77] and Bartalucci et al. (2017) [254]. Following Eq. 1.22, the electron density profile can be directly inferred from the X-ray surface brightness. The vignetted-corrected and background-subtracted surface brightness profile obtained in concentric annuli from the X-ray peak is deconvolved from the point spread function (PSF) and geometrically deprojected, assuming spherical symmetry, using the regularisation technique described in Croston et al. (2006) [255].

The temperature profile is derived also in concentric annuli from the X-ray map, through a spectral analysis modelling of the ICM emission and accounting for both the instrumental and astrophysical backgrounds. The derived 2D temperature profile is then PSF-corrected and deprojected following the *non-parametric-like* method presented in Bartalucci et al. (2018) [105]. In Fig. 3.8 we present the electron density and temperature profiles for PSZ2 G228.16+75.20.

The gas pressure profile is then derived from the deprojected density, n_e, and temperature, T_e, profiles assuming $P_e \propto n_e \times T_e$. The NIKA2 pressure profile presented in Fig. 3.7 was reconstructed assuming the same centre position as the X-ray profiles, so we can compare the profiles obtained from the NIKA2 SZ data to the pressure reconstructed using X-ray observations from the XMM-*Newton* satellite. Both reconstructions agree at intermediate radii, but there seem to be pressure missing in the SZ data, or overestimated by the X-rays. The fact that we have ignored a lack of SZ in the centre of the 150 GHz map, created maybe by a point source, could explain the lower pressure in the NIKA2 profile. The comparison between SZ and X-ray reconstructions is particularly useful to exhibit this type of effects.

3.4 Hydrostatic mass reconstruction within the LPSZ

Under the hydrostatic equilibrium hypothesis, for a spherical cluster we can compute its total mass enclosed within the radius r (Eq. 1.45). If the electron pressure, P_e, and the density, n_e, have been reconstructed assuming the same centre, we can combine the pressure profile obtained from the thermal SZ or X-ray data with the electron density from the X-rays and estimate the mass of the galaxy cluster, as already demonstrated in the literature [119, 177, 178].

Deriving the mass directly from the radially binned pressure profiles leads to non-physical results (i.e., negative mass contributions) since no constraint was imposed regarding the slope of the profile in the pressure reconstruction. This was done to minimise the imposed assumptions on the model of the pressure profile. To overcome the negative mass issue, we fit here pressure models ensuring physical mass profiles to the radially binned SZ results from Sect. 3.2.2. We propose two different approaches: 1) a direct fit of a gNFW pressure profile to the radially binned pressure, and 2) an indirect fit of an NFW mass density model under the HSE

assumption.

3.4.1 gNFW pressure model

The first approach consists in fitting the widely used gNFW pressure profile model [67] to the SZ data, that we parametrise as

$$P_{\rm e}^{\rm gNFW}(r) = \frac{P_0}{\left(\frac{r}{r_p}\right)^c \left(1+\left(\frac{r}{r_p}\right)^a\right)^{(b-c)/a}}, \tag{3.5}$$

where P_0 is the normalisation constant, b and c are respectively the external and internal slopes, r_p is the characteristic radius of slope change, and a the parameter describing the steepness of the slopes transition.

The fit of the gNFW model to the pressure bins is performed with an MCMC method, using the `emcee` package, with 200 walkers, 15×10^4 steps and a burn-in of 5×10^4. The MCMC searches to maximise the likelihood defined by,

$$\begin{aligned}\log \mathcal{L}(\vartheta) = & \\ & -\frac{1}{2}\left(P_{\rm e}^{\rm gNFW}(\vartheta) - P_{\rm e}^{N2}\right)^T C^{-1} \left(P_{\rm e}^{\rm gNFW}(\vartheta) - P_{\rm e}^{N2}\right) \\ & -\frac{1}{2}\left(\frac{Y_{500}^{\rm gNFW}(\vartheta) - Y_{500}^{\rm catalogue}}{\Delta Y_{500}^{\rm catalogue}}\right)^2,\end{aligned} \tag{3.6}$$

where $P_{\rm e}^{N2}$ and C represent the NIKA2 radially binned pressure profile bins and the associated covariance matrix (Fig. 3.7) and $P_{\rm e}^{\rm gNFW}(\vartheta)$ are the gNFW pressure profile values for a set of parameters $\vartheta = [P_0, r_p, a, b, c]$. We also set a constraint on the integrated Compton parameter of the model $Y_{500}^{\rm gNFW}(\vartheta)$, again using the catalogue results, $Y_{500}^{\rm catalogue}$, and a condition that ensures that HSE mass profiles increase with radius: $\frac{r^2}{n_{\rm e}(r)}\frac{{\rm d}P_{\rm e}(r)}{{\rm d}r} < 0$. In the left panel in Fig. 3.9 we show the fit of the gNFW model using MCMC to the radially binned pressure of PSZ2 G228.16+75.20. Given the small amount of data points a, b and c parameters were fixed to the values of the universal pressure profile from Arnaud et al. (2010) [70]. We observe that the external slope of the pressure profile is not completely well represented by this model.

Following the hydrostatic equilibrium equation, we can combine the posterior parameters of the gNFW model with the electron density profile to get the HSE mass profile. In Fig. 3.9 we present the HSE mass profile for the PSZ2 G228.16+75.20 galaxy cluster. We compare the mass profile obtained from the combination of NIKA2 SZ data and XMM-*Newton* X-ray data to the profile reconstructed using only X-rays (see chapter 4 for a more detailed discussion). Assuming spherical symmetry, the X-ray HSE mass profile was derived, following the Monte Carlo procedure detailed in Démoclès et al. (2010) [256] and Bartalucci et al. (2017) [254] with the XMM-*Newton* electron density and temperature profiles presented in Fig. 3.8.

In parallel, `panco2` offers the possibility of fitting directly a gNFW electron pressure profile to the NIKA2 maps, building the model map in Eq. 3.4 from the integration of the pressure in Eq. 3.5. The derivative of a gNFW profile is analytic and, therefore, at each step of the map fit a mass profile following the HSE equation in Eq. 1.45 can be easily computed. Then, the parameter combinations that do not satisfy an increasing mass profile can be discarded. This alternative pressure and mass reconstruction method has been used in several SZ studies [118, 119, 177, 178] and will be exploited for the analysis of the full LPSZ sample.

The main advantage of fitting gNFW models to maps is that the obtained pressure and mass profiles are smooth and slopes can be supervised during the fit to ensure physical masses. At the same time, this is one of the drawbacks of the method: if the electron density profile derived from X-ray data is employed throughout the NIKA2 map fit to calculate the HSE mass at each step of the MCMC (following Eq. 1.45), the resulting pressure profile will depend on the X-ray data given as an input. Thus, pressure profiles will not be independent SZ estimates. Combining the NIKA2 pressure profile with external data sets is also easier if the pressure

model is radially binned. An example with the CL J1226.9+3332 galaxy cluster is presented in chapter 4. Furthermore, radially binned models are more general, since they are a way of reducing dimensionality with the only requirements of sphericity and a power law relation between the radial bins.

3.4.2 NFW mass density model

The estimation of the pressure derivative (Eq. 1.45) can be very problematic, first because it is very sensitive to local variations in the slope of the pressure profile and because it requires, as discussed above, additional constraints to ensure recovering physical masses. To overcome these issues, in this thesis we also model the pressure profile starting from a mass density model and assuming HSE. An equivalent idea is the *backward process* of fitting X-ray temperatures described in Ettori et al. (2013) [257]. This method was used for mass reconstruction in Ettori et al. (2019) [175] and in Eckert et al. (2022) [258]. From the HSE defined in Eq. 1.45, we can write

$$P_{\rm e}(r_b) - P_{\rm e}(r_a) = \int_{r_a}^{r_b} -\mu m_{\rm p} G n_{\rm e}(r) \frac{M_{\rm HSE}(< r)}{r^2} {\rm d}r. \tag{3.7}$$

Moreover, we can relate a radial mass density profile $\rho(R)$ to the mass by

$$M(< r) = \int_0^r 4\pi R^2 \rho(R)\, {\rm d}R, \tag{3.8}$$

which allows us to relate the pressure directly to a mass density profile. We use here the NFW model (Eq. 1.19), which is a good description of dark matter halos [51] and has been widely used in the literature. Here we switch from an overdensity of 500 to 200 in order to conform to most of previous works. Using this definition, we obtain

$$\begin{aligned} P_{zero} - P_{\rm e}(r_a) = &-\mu m_{\rm p} G 4\pi \rho_c \delta_{c_{200}}(c_{200}) r_s^3 \\ &\int_{r_a}^{r_{zero}} \frac{n_{\rm e}(r)}{r^2} \left[\frac{1}{1 + r/r_s} + \ln(1 + r/r_s) - 1 \right] {\rm d}r, \end{aligned} \tag{3.9}$$

where r_{zero} is the radius at which we are dominated by a zero-level component. Details on the mass integral for the NFW model are given in Eq. 7.5.

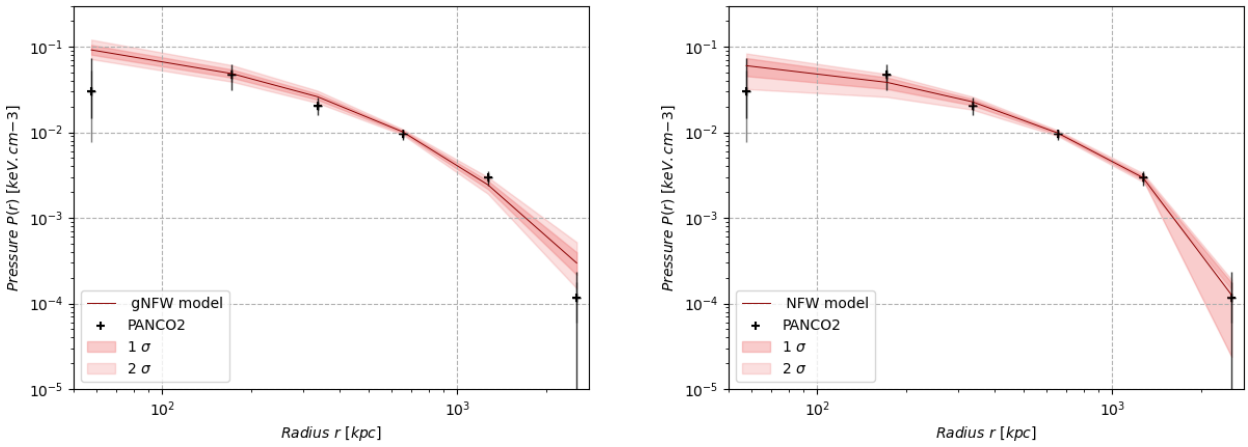

Figure 3.9: Fit to the radially binned pressure profile of PSZ2 G228.16+75.20 with gNFW (left) and NFW (right) models. Results obtained by Renaud Serra during his Master 1 internship under my supervision. For the gNFW model $a = 1.0510$, $b = 5.4905$ and $c = 0.30810$ were fixed.

We can perform an MCMC analysis similar to the one described above for the gNFW pressure profile model. In this case, the free parameters of the model are $\vartheta = [c_{200}, r_s, P_{zero}]$. At each step of the MCMC, we compute

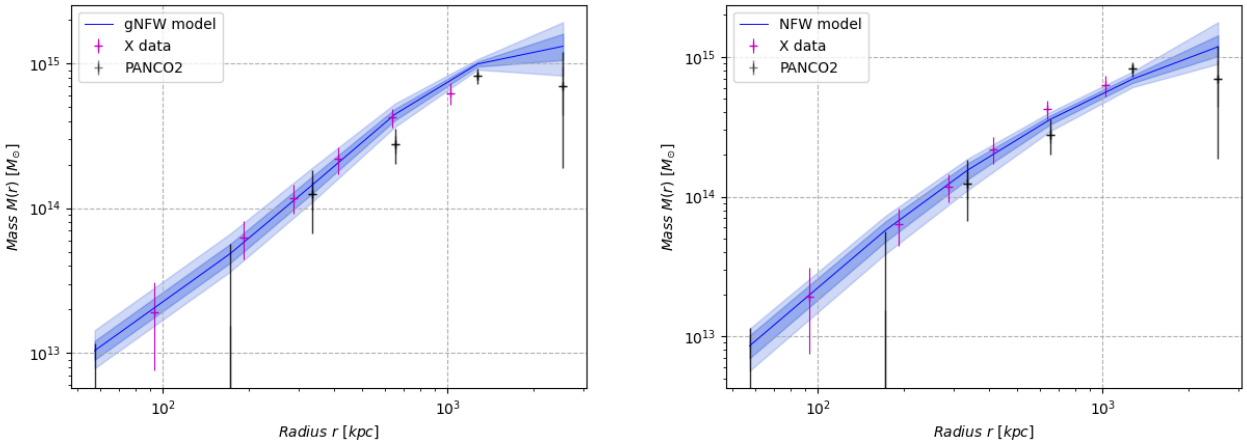

Figure 3.10: The hydrostatic mass profile of PSZ2 G228.16+75.20. In blue the SZ+X-ray profiles obtained from the fit of a gNFW pressure (left) or NFW density (right) model to the pressure bins in Fig. 3.9. Pink markers show the HSE mass profile obtained using only XMM-*Newton* data. Black markers indicate the HSE mass profile obtained from the derivation of the radially binned pressure profile. Results obtained by Renaud Serra during his Master 1 internship under my supervision.

the integral in Eq. 3.9 to evaluate $P_e(\vartheta)$ as needed for the likelihood function in Eq. 3.6. Calculating the integral can be computationally very expensive. As the result of this integral depends only on r_s and r_a, we create a grid of the integrals for a range of r_s values (from 100 to 2000 kpc) and r_a the radial bins of interest. We use this grid to interpolate the values of the integrals at each step. The electron density profile comes also into play in the integral and it is redefined by logarithmic interpolation. In the right panel in Fig. 3.9 we present the pressure profile obtained from the fit of the NFW density model to PSZ2 G228.16+75.20 pressure bins. The model is a good representation of the binned data points. The corresponding mass profile is shown in Fig. 3.10. From the comparison of the gNFW and NFW profiles shown in Fig. 3.10, we observe that masses reconstructed with both models are overall compatible. These profiles also agree with the pink markers that correspond to the X-ray-only mass derived from XMM-*Newton* data. However, we notice that, while the gNFW model is above the black markers at $\sim$ 1000 kpc, NFW is below. This difference comes from the distinct shapes of the models in the pressure profile and it can be crucial when defining M_{500}.

3.4.3 $M_{500} - R_{500}$

As explained in chapter 1, for cosmological analyses with clusters instead of considering mass profiles we use integrated masses. Following Eq. 1.18, the mass at a density contrast of $\Delta = 500$ is defined as

$$M_{500} = 500 \times \rho_{\rm crit}(z) \frac{4}{3} \pi R_{500}^3. \tag{3.10}$$

By definition, M_{500} and R_{500} are correlated quantities and are obtained simultaneously by searching in the mass profile for the mass and radius values that satisfy the condition in Eq. 3.10.

From the profiles in Fig. 3.10 we obtain for PSZ2 G228.16+75.20 the HSE masses $M_{500} = 10.07^{+0.68}_{-0.70} \times 10^{14}$ $M_\odot$ and $M_{500} = 7.87^{+0.59}_{-0.55} \times 10^{14}$ $M_\odot$ for the gNFW and NFW models, respectively. We consider that, given the problems of the gNFW model (with fixed values for a, b and c parameters) to represent the radially binned pressure profile in Fig. 3.9, the corresponding mass is not fully reliable.

Some works in the literature [259, 260] define a fixed R_{500} radius, which may come from a different analysis, and evaluate the mass profile at that radius. In those cases the size of the uncertainties in the mass profile will be directly the error bar on M_{500}. Throughout this thesis we consider M_{500} and R_{500} the values measured simultaneously in the mass profile following Eq. 3.10. It will be explicitly precised if different (chapter 6).

3.5 Conclusions

We have seen in chapters 2 and 3 that the NIKA2 camera is well adapted for mapping the Sunyaev-Zel'dovich effect in clusters at intermediate and high redshifts. Nevertheless, careful and thorough data analysis is required to extract the weak and diffuse SZ signal from raw data.

To characterise the residual noise in the final maps we have proposed two definitions of null maps: 1) time ordered (TO), and 2) angle ordered (AO). The former is well adapted to track time variations, but might be contaminated by signal residuals filtering. These residuals can be minimised with the AO approach. The real noise in the final maps being unknown, we propose computing the jackknives with both TO and AO definitions as a systematic test to be done on every cluster.

Regarding the filtering of the cluster signal due to the data processing, we have demonstrated that for the maps reconstructed with the LPSZ scanning strategy and decorrelation pipeline, it is anisotropic. We propose a two dimensional transfer function that captures the directional effects of the filtering that can not be accounted for with the one dimensional transfer function, which was used by the NIKA2 collaboration before.

In addition, the clean signal maps are contaminated by point sources that can compensate the negative SZ signal at 150 GHz. Ignoring such point sources biases the amplitude of the SZ signal and, consequently, the reconstructed thermal pressure of clusters. We have shown that thanks to the high angular resolution of NIKA2 observations we can detect and characterise these sources. By using external data sets, we are able to have an a priori estimate of the flux of the submillimetre and radio sources at 150 GHz.

These a priori estimates are then used in the joint fit of the cluster pressure and point sources model to the NIKA2 150 GHz map. Making use of the `panco2` pipeline, we have reconstructed the pressure profile of the PSZ2 G228.16+75.20 cluster, which has an extended signal contaminated by many sources in the field. We propose two approaches to estimate the HSE mass from the combination of SZ-obtained pressure and X-ray electron density profiles: either fitting directly a gNFW model to the pressure (traditionally used for this kind of analysis) or instead fitting an integrated NFW mass density model. From the comparison of both approaches, we evidence the importance of having precisely reconstructed pressure profiles to get accurate HSE mass estimates.

CHAPTER 4

The mass of CL J1226.9+3332

In the last two chapters we have presented the procedure needed to go from NIKA2 raw observations to sky maps and, then, to hydrostatic masses of clusters. In this chapter we test the robustness of the NIKA2 data analysis and the impact of the systematic effects related to that data processing on the HSE mass. We then apply the methods described in chapter 3 to, combined with other SZ and X-ray observations, reconstruct the HSE mass of CL J1226.9+3332 galaxy cluster, also known as PSZ2 G160.83+81.66. An important part of the work presented in this chapter has been published in Muñoz-Echeverría et al. (2023) [191].

4.1 The CL J1226.9+3332 galaxy cluster

Discovered by the Wide Angle ROSAT Pointed Survey [261], CL J1226.9+3332 has already been studied at different wavelengths: X-ray [262, 263], visible [264], and millimetre [119, 263, 265, 266] wavelengths. Located at redshift 0.89 [140, 142], it is the highest-redshift cluster of the NIKA2 SZ Large Programme sample, with the X-ray peak at (R.A., Dec.)$_{J2000}$ = (12h26m58.37s, +33d32m47.4s) according to Cavagnolo et al. (2009) [267]. Less than 2 arcseconds away from this peak, its BCG is located at (R.A., Dec.)$_{J2000}$ = (12h26m58.25s, +33d32m48.57s) according to Holden et al. (2009) [268].

4.1.1 Previous observations

Since the first SZ observations with BIMA [269], the projected morphology of CL J1226.9+3332 appeared to have a quite circular symmetry. Nevertheless, the combination of XMM-*Newton* and *Chandra* X-ray data [270] showed a region, at $\sim 40''$ to the south-west of the X-ray peak with a much higher temperature than the average in the ICM. This substructure was also confirmed by posterior SZ analyses with MUSTANG [266] and NIKA [119, 124, 125]. Romero et al. (2018) [251] (hereafter R18) performed a study combining SZ data from the NIKA, MUSTANG, and Bolocam instruments. Their different capabilities allowed them to probe different angular scales in the reconstruction of ICM properties and agreed with a non-relaxed cluster core description for CL J1226.9+3332. For a precise reconstruction of the HSE mass of CL J1226.9+3332, in this chapter we also make use of the pressure profiles obtained from the NIKA, MUSTANG, and Bolocam data summarised in Table 2 in Romero et al. (2018) [251].

Lensing data from the Cluster Lensing And Supernova survey with Hubble (CLASH) [271], as well as the galaxy distribution in the cluster [264], agree on the existence of a main clump centred on the BCG and a secondary clump to the south-west. However, this second region does not appear as a structure in X-ray surface brightness [270]. One hypothesis presented in Jee and Tyson (2009) [264] suggests that the mass of the southwestern galaxy group is not big enough to be observed as an X-ray overdensity. Motivated by the slight elongation of the X-ray peak towards the south-west, Jee and Tyson (2009) [264] also hypothesise that the two-halo system is being observed after the less massive cluster has passed through the central one. A previous study [262] also showed a region of cooler emission on the west side of the BCG, that is, in the north of the mentioned hot region. This was seen using *Chandra* data, and it was explained as a possible infall of some cooler body. Additionally, from the diffuse radio emission analysis with LOFAR data, Di Gennaro et al. (2021) [57] showed that CL J1226.9+3332 hosts the most distant radio halo discovered to date: a radio emission with a size of 0.7 Mpc that follows the thermal gas distribution. In brief, CL J1226.9+3332 shows evidence of disturbance in the core, but a relaxed morphology at large scales.

4.1.2 The mass of CL J1226.9+3332

Regarding the mass of CL J1226.9+3332, which constitutes the main topic in this chapter, we present here the results obtained in previous works (summarised in Table 4.1). These masses have not been homogenised or scaled to the same cosmology, and are the values extracted directly from different analyses.

The first SZ mass analysis of this cluster was done in Joy et al. (2001) [269] and they estimated $M(r < 340\ h_{100}^{-1}\ \mathrm{kpc}) = (3.9 \pm 0.5) \times 10^{14}\,\mathrm{M}_\odot$. Using *Chandra* X-ray data from Cagnoni et al. (2001) [282] and assuming an isothermal β-model, Jee and Tyson (2009) [264] obtained the hydrostatic projected mass $M(r < 1\,\mathrm{Mpc}) = 1.4^{+0.6}_{-0.4} \times 10^{15}\,\mathrm{M}_\odot$. Also assuming an isothermal β-model and hydrostatic equilibrium, Maughan et al. (2004) [262] obtained $M_{1000} = 6.1^{+0.9}_{-0.8} \times 10^{14}\,\mathrm{M}_\odot$ and $M_{200} = (1.4 \pm 0.5) \times 10^{15}\,\mathrm{M}_\odot$ with XMM-*Newton* data. The subsequent analysis of three-dimensional hydrodynamical properties with *Chandra* and XMM-*Newton* by Maughan et al. (2007) [270], again under the assumptions of spherical symmetry and hydrostatic equilibrium, concluded that $M_{500} = 5.2^{+1.0}_{-0.8} \times 10^{14}\,\mathrm{M}_\odot$. According to the X-ray analysis in Mantz et al. (2010) [272], the mass of the cluster is $M_{500} = (7.8 \pm 1.1) \times 10^{14}\,\mathrm{M}_\odot$.

From the combination of the Sunyaev-Zel'dovich Array (SZA) [275] interferometric data and the *Chandra* X-ray observations, under the hydrostatic equilibrium hypothesis, Mroczkowski et al. (2009) [265] obtained $M_{500} = 7.37^{+2.50}_{-1.57} \times 10^{14}\,\mathrm{M}_\odot$ and $M_{2500} = 2.67^{+0.29}_{-0.27} \times 10^{14}\,\mathrm{M}_\odot$. This was compared to the results using only the X-ray data and assuming an isothermal β-model: $M_{500} = 7.30^{+2.10}_{-1.51} \times 10^{14}\,\mathrm{M}_\odot$, $M_{2500} = 2.98^{+0.90}_{-0.63} \times 10^{14}\,\mathrm{M}_\odot$.

Using a new approach, that instead relies on the virial relation, Mroczkowski (2011) [273] and Mroczkowski (2012) [274] estimated the mass for CL J1226.9+3332 using only SZ data from SZA. In this approach, first, a pressure profile model is fitted to the SZ data. The obtained pressure profile is used to calculate the thermal energy profile and the non-vanishing surface pressure in the cluster, which are related, through the virial relation, to the gravitational potential energy of the halo. Finally, the potential energy is related to the total mass in the cluster, modelled in Mroczkowski (2011) [273] using the NFW mass density pro-

Table 4.1: Mass estimates found in the literature for CL J1226.9+3332. We differentiate the masses reconstructed from ICM observables, from the lensing effect on background sources and from the study of the dynamics of member galaxies. Most of the masses were computed from spherical models, and we give the radius at which each mass is evaluated when available. When the mass has been evaluated at a given $R = R_\Delta$ we also present the value of the density contrast Δ.

Observable	R [kpc]	Δ	$M(< R)$ [10^{14} $M_\odot$]	Reference	Comments
ICM					
	$340\ h_{100}^{-1}$	-	3.9 ± 0.5	Joy et al. (2001) [269]	
	1000	-	14^{+6}_{-4}	Jee and Tyson (2009) [264]	Projected
	730 ± 40	1000	$6.1^{+0.9}_{-0.8}$	Maughan et al. (2004) [262]	
	1660 ± 340	200	14 ± 4	Maughan et al. (2004) [262]	
	880 ± 50	500	$5.2^{+1.0}_{-0.8}$	Maughan et al. (2007) [270]	
	1000 ± 50	500	7.8 ± 1.1	Mantz et al. (2010) [272]	
	980^{+100}_{-70}	500	$7.37^{+2.50}_{-1.57}$	Mroczkowski et al. (2009) [265]	
	410^{+10}_{-10}	2500	$2.67^{+0.29}_{-0.27}$	Mroczkowski et al. (2009) [265]	
	980^{+90}_{-70}	500	$7.30^{+2.10}_{-1.51}$	Mroczkowski et al. (2009) [265]	
	420^{+40}_{-30}	2500	$2.98^{+0.90}_{-0.63}$	Mroczkowski et al. (2009) [265]	
	940^{+20}_{-20}	500	$6.49^{+0.34}_{-0.34}$	Mroczkowski (2011) [273], Mroczkowski (2012) [274]	
	390^{+10}_{-10}	2500	$2.35^{+0.15}_{-0.16}$	Mroczkowski (2011) [273], Mroczkowski (2012) [274]	
	940^{+20}_{-20}	500	$6.42^{+0.36}_{-0.36}$	Mroczkowski (2011) [273], Mroczkowski (2012) [274]	
	400^{+10}_{-10}	2500	$2.53^{+0.14}_{-0.15}$	Mroczkowski (2011) [273], Mroczkowski (2012) [274]	
	1140^{+100}_{-80}	200	$7.19^{+1.33}_{-0.92}$	Muchovej et al. (2007) [275]	
	310^{+30}_{-20}	2500	$1.68^{+0.37}_{-0.26}$	Muchovej et al. (2007) [275]	
	812^{+71}_{-81}	500	$4.25^{+1.22}_{-1.14}$	Bulbul et al. (2010) [276]	
	379^{+37}_{-41}	2500	$2.16^{+0.69}_{-0.63}$	Bulbul et al. (2010) [276]	
	-	500	$5.71^{+0.63}_{-0.69}$	Planck Collaboration et al. (2016) [142]	Scaling relation
	930^{+50}_{-43}	500	$5.96^{+1.02}_{-0.79}$	Adam et al. (2015) [119]	
	937^{+72}_{-58}	500	$6.10^{+1.52}_{-1.06}$	Adam et al. (2015) [119]	
	995^{+65}_{-65}	500	$7.30^{+1.52}_{-1.34}$	Adam et al. (2015) [119]	
	910^{+89}_{-72}	500	$5.57^{+1.81}_{-1.23}$	Castagna and Andreon (2020) [277]	
Lensing					
	1640 ± 100	200	13.8 ± 2.0	Jee and Tyson (2009) [264]	
	880 ± 50	-	7.34 ± 0.71	Jee and Tyson (2009) [264]	
	155	-	1.3 ± 0.1	Jee and Tyson (2009) [264]	Projected
	155	-	0.85 ± 0.06	Jee and Tyson (2009) [264]	Projected (SW clump)
	1680^{+100}_{-90}	200	$13.7^{+2.4}_{-2.0}$	Jee et al. (2011) [278]	
	-	200	22.3 ± 1.4	Merten et al. (2015) [279]	
	-	500	15.4 ± 1.2	Merten et al. (2015) [279]	
	-	2500	6.1 ± 1.0	Merten et al. (2015) [279]	
	-	200	10.0 ± 2.4	Sereno and Covone (2013) [280]	
	-	200	11.114 ± 2.442	Sereno and Covone (2013) [280], Sereno (2015) [281][8]	
	-	500	7.96 ± 1.44	Sereno and Covone (2013) [280], Sereno (2015) [281][8]	
	-	2500	3.45 ± 0.37	Sereno and Covone (2013) [280], Sereno (2015) [281][8]	
	500	-	3.947 ± 0.285	Sereno and Covone (2013) [280], Sereno (2015) [281][8]	
	1000	-	7.882 ± 1.013	Sereno and Covone (2013) [280], Sereno (2015) [281][8]	
	1500	-	10.938 ± 1.784	Sereno and Covone (2013) [280], Sereno (2015) [281][8]	
Galaxy dynamics					
	-	500	4.7 ± 1.0	Aguado-Barahona et al. (2022) [140]	52 galaxies
	-	500	4.8 ± 1.0	Aguado-Barahona et al. (2022) [140]	49 galaxies

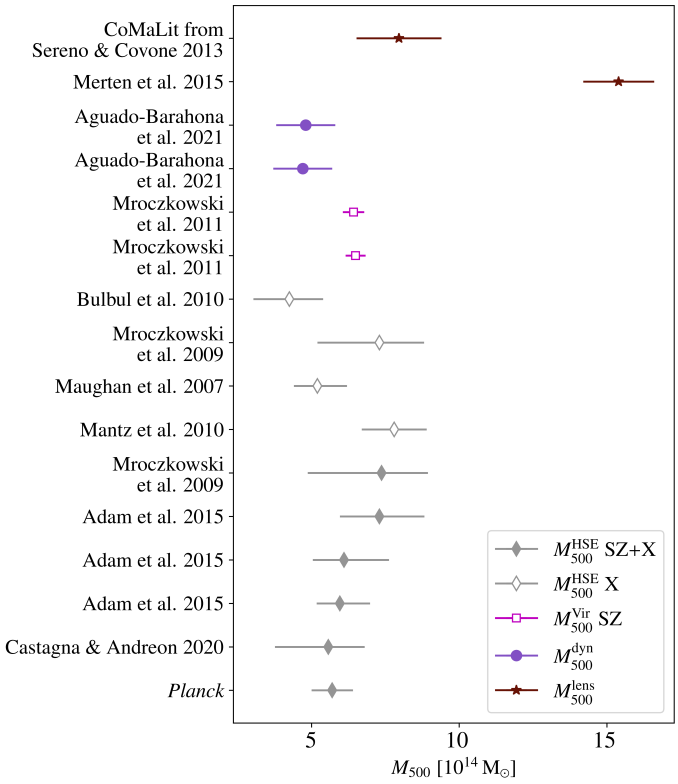

Figure 4.1: M_{500} estimates for CL J1226.9+3332 in the literature. Filled grey diamonds represent HSE masses from the combination of SZ and X-ray data and empty ones correspond to X-ray-only results. Magenta squares show the SZ-only mass assuming virial relation, purple circles are dynamical mass estimates, and brown stars correspond to lensing M_{500}.

file. Following this method, authors in Mroczkowski (2011) [273] and Mroczkowski (2012) [274] estimated: $M_{500} = 6.49^{+0.34}_{-0.34} \times 10^{14}\,M_\odot$ and $M_{2500} = 2.35^{+0.15}_{-0.16} \times 10^{14}\,M_\odot$ assuming a pressure described by a gNFW profile with $(a, b, c) = (0.9, 5.0, 0.4)$ parameters and $M_{500} = 6.42^{+0.36}_{-0.36} \times 10^{14}\,M_\odot$ and $M_{2500} = 2.53^{+0.14}_{-0.15} \times 10^{14}\,M_\odot$ with $(a, b, c) = (1.0510, 5.4905, 0.3081)$ as in A10 [70].

Some years before, Muchovej et al. (2007) [275] fitted the temperature decrement due to the cluster's SZ effect to the SZA data and assuming hydrostatic equilibrium and isothermality estimated $M_{200} = 7.19^{+1.33}_{-0.92} \times 10^{14}\,M_\odot$ and $M_{2500} = 1.68^{+0.37}_{-0.26} \times 10^{14}\,M_\odot$.

Another approach was considered in Bulbul et al. (2010) [276] to compute the hydrostatic mass, with the polytropic equation of state and using only *Chandra* X-ray observations, $M_{500} = 4.25^{+1.22}_{-1.14} \times 10^{14}\,M_\odot$ and $M_{2500} = 2.16^{+0.69}_{-0.63} \times 10^{14}\,M_\odot$. According to the Planck Collaboration et al. (2016) [142] results, the hydrostatic mass of the cluster is $M_{500} = 5.70^{+0.63}_{-0.69} \times 10^{14}\,M_\odot$. This mass was obtained using the SZ−mass scaling relation given in Eq. 7 of Planck Collaboration et al. (2014) [5].

In addition, combining SZ data from NIKA and *Planck* with the X-ray electron density from the *Chandra* ACCEPT data [267], Adam et al. (2015) [119] obtained three hydrostatic mass estimates for different parameters in their gNFW pressure profile modelling: $M_{500} = 5.96^{+1.02}_{-0.79} \times 10^{14}\,M_\odot$ using $(a, b, c) = (1.33, 4.13, 0.014)$, $M_{500} = 6.10^{+1.52}_{-1.06} \times 10^{14}\,M_\odot$ with $(b, c) = (4.13, 0.014)$ and $M_{500} = 7.30^{+1.52}_{-1.34} \times 10^{14}\,M_\odot$ with $(a, b, c) = (0.9, 5.0, 0.4)$. Also combining NIKA and *Chandra* data, Castagna and Andreon (2020) [277] reconstructed $M_{500} = 5.57^{+1.81}_{-1.23} \times 10^{14}\,M_\odot$.

The weak-lensing analysis in Jee and Tyson (2009) [264] found that $M_{200} = (1.38 \pm 0.20) \times 10^{15}\,M_\odot$ by fitting an NFW density profile. Similarly, they computed the weak-lensing mass estimate at the R_{500} from Maughan et al. (2007) [270]: $M(r < (0.88 \pm 0.05)\,\mathrm{Mpc}) = (7.34 \pm 0.71) \times 10^{14}\,M_\odot$, and found a 30% higher mass than the X-ray estimate in Maughan et al. (2007) [270]. This discrepancy was explained in Jee and Tyson (2009) [264] as a sign of an ongoing merger in the cluster that would create an underestimation of the hydrostatic mass with X-rays without altering the lensing estimate. Jee and Tyson (2009) [264] also estimated the projected mass in each of the two big substructures within $r < 20''$. For the most massive and central clump they found $M(r < 20'') = (1.3 \pm 0.1) \times 10^{14}\,M_\odot$, and for the structure at $\sim 40''$ to the south-west of the BCG $M(r < 20'') = (8.5 \pm 0.6) \times 10^{13}\,M_\odot$. Merten et al. (2015) [279] performed a lensing analysis and obtained $M_{200} = (2.23 \pm 0.14) \times 10^{15}\,M_\odot$, $M_{500} = (1.54 \pm 0.12) \times 10^{15}\,M_\odot$, and $M_{2500} = (0.61 \pm 0.10) \times 10^{15}\,M_\odot$ by fitting an NFW density profile to the CLASH data. In addition, based on the weak and strong lensing analysis from Sereno and Covone (2013) [280], Sereno (2015) [281] followed the same procedure as for all clusters in the CoMaLit[8] sample (see chapter 6) and obtained $M_{500} = (7.96 \pm 1.44) \times 10^{14}\,M_\odot$.

Moreover, a recent study based on the velocity dispersion of galaxy members in Aguado-Barahona et al. (2022) [140] obtained two dynamical mass estimates for CL J1226.9+3332: $M_{500} = (4.7 \pm 1.0) \times 10^{14}\,M_\odot$ and $M_{500} = (4.8 \pm 1.0) \times 10^{14}\,M_\odot$ from the velocities of 52 and 49 member galaxies, respectively.

We display in Fig. 4.1 the different M_{500} estimates found in the literature. Grey diamonds with error bars correspond to the HSE mass estimates. We distinguish the HSE masses obtained from the combination of SZ and X-ray data (filled diamonds) and the X-ray-only results (empty diamonds). The mass given by Planck Collaboration et al. (2016) [142] is considered here to be an SZ+X result, but it is important to keep in mind that this mass was obtained by applying a scaling relation (derived from X-ray data) to the *Planck* SZ signal. The empty magenta squares show the M_{500} assuming the virial relation and using only SZ data [273, 274]. The purple circles are the dynamical masses from Aguado-Barahona et al. (2022) [140] and the brown stars the lensing estimates from Merten et al. (2015) [279] and Sereno (2015) [281]. We decided not to present in the same figure the projected masses, as it would be misleading to compare them to the masses integrated in a sphere. The figure shows that both HSE and lensing masses among them vary more than 40% from one analysis to another.

All these mass estimates for CL J1226.9+3332 are hindered by systematic effects, which are difficult to deal

[8] COmparing MAsses in the LITerature. Cluster lensing mass catalogue available at http://pico.oabo.inaf.it/~sereno/CoMaLit/

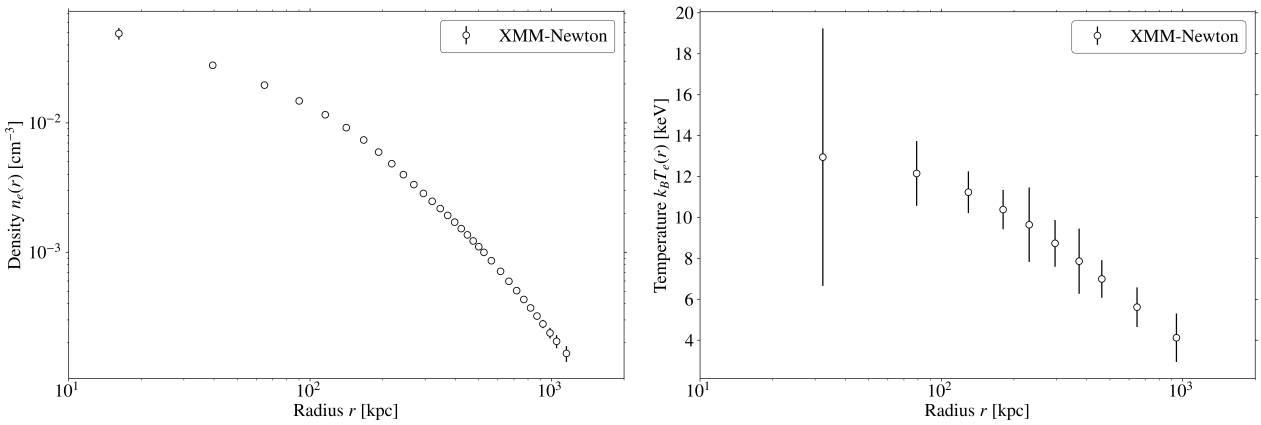

Figure 4.2: Electron density (left) and temperature (right) profiles reconstructed from XMM-*Newton* observations, with 1σ error bars. The profiles are centred at the X-ray peak (R.A., Dec.)$_{J2000}$ = (12h26m58.08s, +33d32m46.6s).

with. Properly comparing masses obtained from different observables, methods, or modelling approaches is crucial, but very challenging. Moreover, as the shape of the mass profile varies depending on the data and the analysis procedure that is considered, the value of R_{500} is not the same for all estimates presented in Fig. 4.1. Comparisons are thus delicate due to the correlation between the mass and the radius at which it is estimated (Eq. 3.10). As mentioned, accurate knowledge of the mass of galaxy clusters is essential for cosmological purposes [48]. This motivates the following study, which continues for the lensing part in chapter 5.

4.2 ICM observations

4.2.1 X-ray observations with XMM-*Newton*

The cluster was observed by XMM-*Newton* for a total observation time of 90/74 ks (MOS/pn), reduced to 63/47 ks after cleaning. Following the XMM-*Newton* data reduction procedure presented in Sect. 3.3, X-ray observations of CL J1226.9+3332 were analysed to obtain the electron and temperature profiles shown in Fig. 4.2.

4.2.2 SZ observations with NIKA2

CL J1226.9+3332 was observed by NIKA2 for 3.6 hours during the 15th science-purpose observation campaign (13-20 February 2018). The data consists of 36 raster scans of 8×4 arcminutes in a series of four scans with angles of 0, 45, 90, and 135 degrees with respect to the right ascension axis. The scans were centred at the XMM-*Newton* X-ray peak, (R.A., Dec.)$_{J2000}$ = (12h26m58.08s, +33d32m46.6s) and the mean elevation of the scans is 58.51°. The raw data were calibrated and reduced as described in Sect. 2.3.

We present in Fig. 4.3 the NIKA2 surface brightness maps at 150 and 260 GHz for CL J1226.9+3332, resulting from the IMCM decorrelation method. These are the maps used for the following analysis. As in Fig. 3.4 black contours indicate significance levels starting from 3σ with a 3σ spacing. Again, the map at 150 GHz (left panel) shows the cluster as a negative decrement with respect to the background, where we also identify positive sources that can compensate the negative SZ signal of the cluster. This is the case for the central south-eastern source. Moreover, in the 150 GHz map, we observe an elongation of the SZ peak towards the south-west. Similar structures were found by Maughan et al. (2007) [270], Korngut et al. (2011) [266], Adam et al. (2015) [119], Zitrin et al. (2015) [271], and Jee and Tyson (2009) [264], as mentioned in Sect. 4.1. The 260 GHz map (right panel) is dominated by the signal of the point sources.

For the 150 GHz map in Fig. 4.3 we computed the 1D and 2D transfer functions (Fig. 2.16) and estimated both the angle order and time order noise estimates (Fig. 2.12), with their associated correlated noise covariance

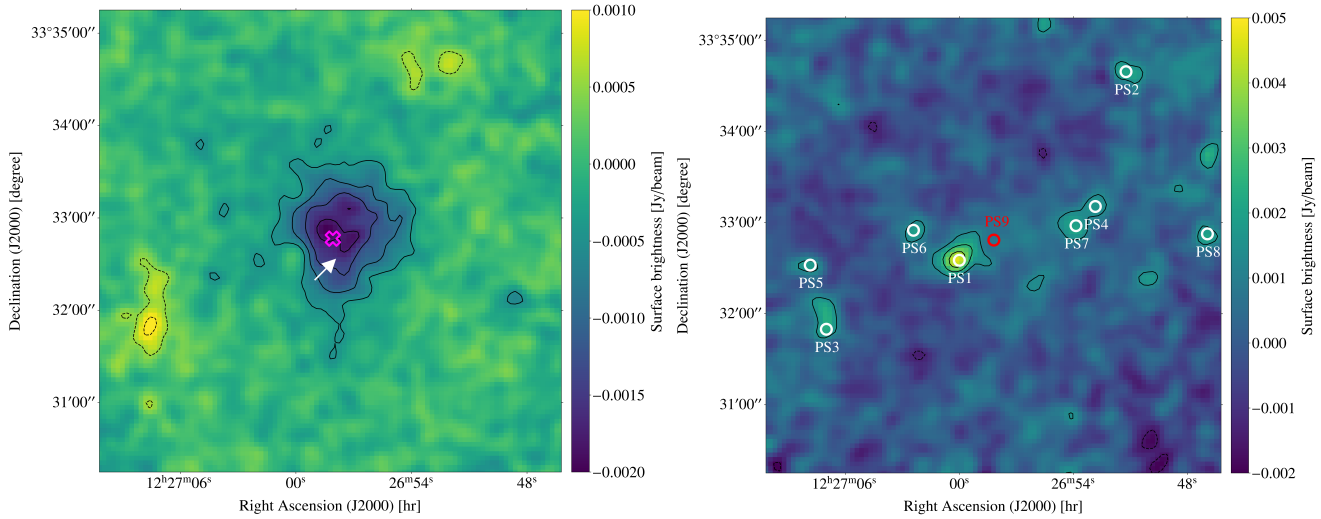

Figure 4.3: NIKA2 maps of CL J1226.9+3332 at 150 GHz (left) and 260 GHz (right). Contours show S/N levels in multiples of $\pm 3\sigma$. Both maps have been smoothed with a 10″ FWHM Gaussian kernel. The position of the X-ray centre is shown as a magenta cross in the 150 GHz map and the elongation of the SZ signal towards the south-west is indicated by the white arrow. White and red circles in the 260 GHz map show the submillimetre and radio point sources, respectively.

Table 4.2: Submillimetre point source coordinates and fluxes identified within a radius of 2′ around the centre of CL J1226.9+3332. Fluxes at 600, 860, and 1200 GHz are obtained from the SPIRE catalogue.[5] Fluxes at 1870 and 3000 GHz are given in the PACS catalogue.[6]

Source	Coordinates J2000	600 GHz [mJy]	860 GHz [mJy]	1200 GHz [mJy]	1870 GHz [mJy]	3000 GHz [mJy]
PS1	12h27m00.01s +33d32m35.29s	100.3 ± 10.0	121.2 ± 10.0	109.8 ± 7.6	55.7 ± 6.0	14.6 ± 2.1
PS2	12h26m51.22s +33d34m39.61s	37.8 ± 9.0	46.4 ± 9.9	29.1 ± 7.5	24.9 ± 7.4	8.0 ± 1.7
PS3	12h27m07.02s +33d31m49.79s	34.8 ± 7.9	32.4 ± 8.7	25.6 ± 7.7	31.1 ± 6.6	25.6 ± 2.5
PS4	12h26m52.84s +33d33m10.74s		33.0 ± 10.3	41.9 ± 9.7	31.5 ± 7.0	17.7 ± 1.8
PS5	12h27m07.87s +33d32m32.08s			30.0 ± 9.4		
PS6	12h27m02.43s +33d32m55.06s					
PS7	12h26m53.86s +33d32m58.10s				21.8 ± 1.5	14.4 ± 3.0
PS8	12h26m46.93s +33d32m52.66s			19.8 ± 5.5		

matrices. We repeated the whole pressure profile reconstruction for the four possible combinations of TF and noise covariance matrices to check for their impact on the final results.

4.2.3 Point source contamination

The contamination of the CL J1226.9+3332 150 GHz map by point sources was characterised as described in Sect. 3.2.1. We started by identifying submillimetre sources by blindly searching for point sources in the NIKA2 260 GHz map. By cross-checking the detections with a S/N greater than 3 with *Herschel* SPIRE and PACS catalogues, seven submillimetre sources were identified in the region covered by the NIKA2 maps. The position and fluxes from the above-mentioned catalogues for each submillimetre point source (PS1 to PS5, PS7, and PS8) are summarised in Table 4.2. Combining these values with the flux measurements in the 260 GHz map, modified black-body spectrum models were adjusted and extrapolated to 150 GHz (as in Fig. 3.5).

The PS6 source does not have a counterpart in the *Herschel* SPIRE and PACS catalogues, but it appears as a weak signal in the *Herschel* maps and as a 3σ detection in the 260 GHz NIKA2 map. Moreover, it compensates the extended SZ signal at 150 GHz (also clearly observed in Adam et al. (2015) [119]). For this source the

Table 4.3: Submillimetre and radio point sources fluxes. Fluxes at 150 GHz obtained from the joint point sources and pressure profile fits.

Source	150 GHz [AO 1D] [mJy]	150 GHz [TO 1D] [mJy]	150 GHz [AO 2D] [mJy]	150 GHz [TO 2D] [mJy]
PS1	$2.0^{+0.1}_{-0.2}$	$1.9^{+0.2}_{-0.2}$	$2.0^{+0.2}_{-0.2}$	$1.9^{+0.2}_{-0.2}$
PS2	$0.9^{+0.5}_{-0.1}$	$0.9^{+0.2}_{-0.1}$	$0.9^{+0.1}_{-0.2}$	$0.9^{+0.2}_{-0.1}$
PS3	$1.3^{+0.2}_{-0.1}$	$1.3^{+0.2}_{-0.1}$	$1.4^{+0.2}_{-0.2}$	$1.3^{+0.2}_{-0.2}$
PS4	$0.4^{+0.1}_{-0.1}$	$0.38^{+0.10}_{-0.07}$	$0.38^{+0.11}_{-0.07}$	$0.39^{+0.09}_{-0.08}$
PS5	$0.6^{+0.1}_{-0.1}$	$0.5^{+0.2}_{-0.1}$	$0.6^{+0.2}_{-0.1}$	$0.5^{+0.2}_{-0.1}$
PS6	$0.3^{+0.2}_{-0.1}$	$0.2^{+0.2}_{-0.1}$	$0.3^{+0.1}_{-0.2}$	$0.2^{+0.2}_{-0.1}$
PS7	$0.03^{+0.08}_{-0.03}$	$0.03^{+0.08}_{-0.03}$	$0.03^{+0.08}_{-0.03}$	$0.04^{+0.08}_{-0.04}$
PS8	$0.5^{+0.1}_{-0.1}$	$0.45^{+0.12}_{-0.09}$	$0.45^{+0.13}_{-0.09}$	$0.44^{+0.14}_{-0.07}$
PS9	$0.06^{+0.11}_{-0.05}$	$0.07^{+0.11}_{-0.06}$	$0.06^{+0.09}_{-0.05}$	$0.06^{+0.10}_{-0.04}$

modified black-body is used to obtain prior knowledge of the flux at 150 GHz from the flux measurement at 260 GHz and the assumed prior distributions of the spectral index and temperature [178] (Sect. 3.2.1). Another tricky point source is PS7. The extrapolated 150 GHz values ($\sim$ 1.2 mJy) clearly overestimate the flux of the source. This is understandable since we do not have enough constraints for the low-frequency slope of the SED. We choose to use the obtained values as upper limits of a flat prior for the flux of PS7 in the estimation of the cluster pressure profile.

In addition to submillimetre sources, according to the VLA FIRST Survey catalogue [248], a radio source of 3.60 ± 0.13 mJy at 1.4 GHz is present in (R.A., Dec.)$_{J2000}$ = (12h26m58.19s, +33d32m48.61s), hereafter PS9 (the source is also detected in NVSS observations [283]). This galaxy corresponds to the BCG identified in Holden et al. (2009) [268] and the compact radio source detected with LOFAR in Di Gennaro et al. (2021) [57]. Assuming a synchrotron spectrum, as explained in Sect. 3.2.1, we obtain a prior estimate of the flux at 150 GHz: 0.1 ± 0.2 mJy.

4.3 Thermal pressure reconstruction

The thermal pressure in the ICM of the cluster and, simultaneously, the flux of point sources were fitted to NIKA2 150 GHz maps assuming a radially binned model and maximising the likelihood in Eq. 3.4. The integrated Compton parameter Y_{500} obtained from the integration of the model was compared to the value measured by Planck Collaboration et al. (2016) [142], $Y_{500}^{Planck} = (3.82 \pm 0.79) \times 10^{-4}$ arcmin^2 within an aperture of θ_{500} = 1.907 arcmin. We decided not to compare the integrated Compton parameter at $5\theta_{500}$, as measured by *Planck*, because it would require extrapolating the pressure profile far beyond the NIKA2 data. We centred the pressure profile at the coordinates of the X-ray peak, as determined from XMM-*Newton* data analysis.

To estimate the robustness of the results, we performed the fit to the NIKA2 data in four different cases with respect to the choice of noise residuals and transfer function estimates. Thus, we considered AO1D (TO1D) and AO2D (TO2D) using the AO (TO) noise residual map and the 1D and 2D transfer functions, respectively. In Fig. 4.4 we compare the NIKA2 150 GHz map of CL J1226.9+3332 to the obtained best-fit models and their residuals for these four analyses. Comparing the power spectra of the residual maps to the power spectra of the noise estimate maps, we see in Fig. 4.5 that for the TO case the fit residuals and the noise estimates power spectra are consistent. For the AO cases there is an excess of power in the fit residuals, which could be interpreted as coming from the signal due to the differential filtering effects that are not captured in the AO noise. Regarding point sources, the reconstructed fluxes are consistent for the four analyses (see Table 4.3).

We present in Fig. 4.6 the radially binned best-fit pressure profiles obtained for the four tested cases. The blue and cyan (dark and light green) dots correspond to the AO (TO) 1D and 2D transfer function estimates, respectively. The plotted uncertainties correspond to 1σ of the posterior distributions derived from the MCMC chains. Overall, the four NIKA2 analyses give consistent results, especially in the radial ranges where we

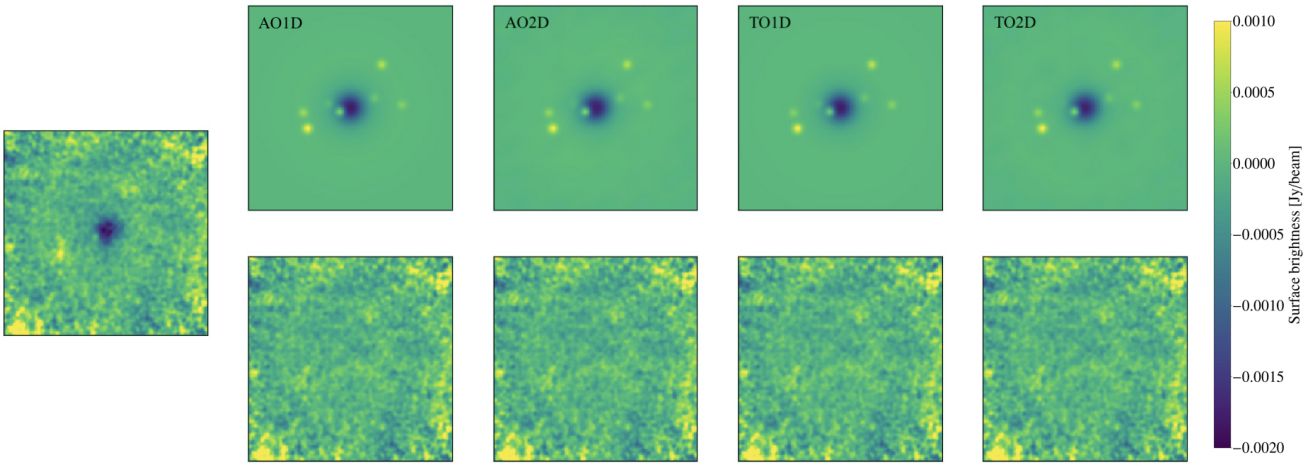

Figure 4.4: 150 GHz maps of CL J1226.9+3332. Left: NIKA2 150 GHz surface brightness map of CL J1226.9+3332. Top: Best-fit models of the SZ signal and point sources. Bottom: Residual maps, the difference between the data map and each best-fit model. Results obtained with different transfer function and noise estimates (from left to right): AO1D, AO2D, TO1D, and TO2D. All maps have been smoothed with a 10″ Gaussian kernel for display purposes and are shown in units of Jy/beam.

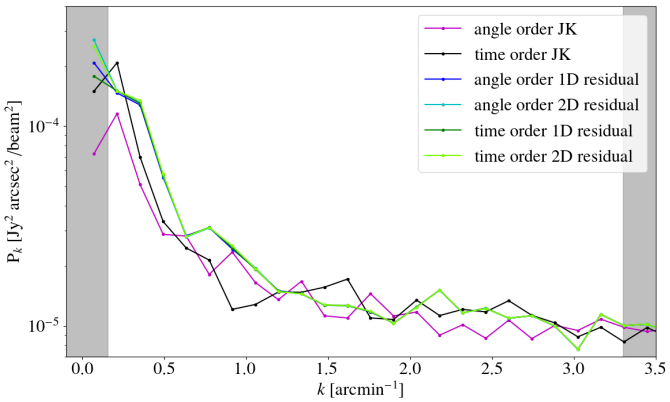

Figure 4.5: Power spectra of noise map estimates for NIKA2 150 GHz data. The spectra for the JK maps estimated with angle ordered and time ordered scans are shown in magenta and black, respectively. The power spectra of the different residual maps for the best-fit models shown in Fig. 4.4 are in blue and green.

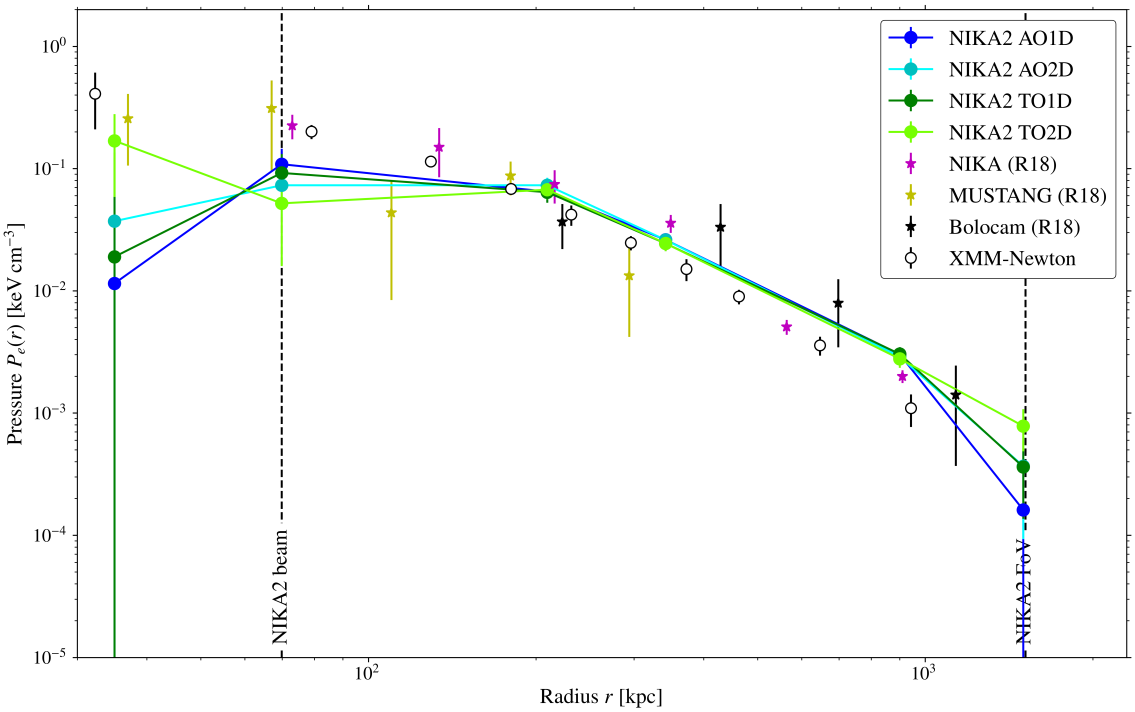

Figure 4.6: Pressure profile of the ICM of CL J1226.9+3332. Blue and green symbols correspond to the results obtained in this work from the NIKA2 150 GHz map. The error bar edges represent the 1σ uncertainties. Magenta, yellow, and black stars show the profiles reconstructed in R18 for NIKA, MUSTANG, and Bolocam data, respectively. Empty symbols correspond to the pressure profile obtained from the combination of XMM-*Newton* electron density and temperature profiles. Vertical dashed lines indicate the instrumental limits of NIKA2 as radius of the beam and FoV.

expect the NIKA2 results to be reliable (i.e. between the beam and the FoV scales, both represented with dashed vertical lines in the figure). We give the FWHM of the NIKA2 beam at 150 GHz (17.6″/2) and half the diameter of the FoV (6.5′/2) in the physical distances corresponding to the redshift of the cluster.

In terms of noise estimates, we observe that the uncertainties on the pressure bin estimates are slightly larger for the time-ordered cases, as expected. However, we note no significant bias between the time and angle ordered results. The effect of the transfer function is hard to evaluate: even if the 2D TF is a more precise description of the filtering in the map, when fitting a spherical cluster model the use of the 1D TF gives consistent results.

4.3.1 Robustness of the NIKA2 analyses

We have seen in Sect. 2.3 that the NIKA2 150 GHz maps reconstructed with different raw data analysis pipelines (IMCM and PIIC) differ both in the filtering of the astrophysical signal and the correlated noise level in the map. However, these effects are considered by using the transfer function and the noise correlation matrix in the fit of the map. To check if the pressure profiles reconstructed from differently reduced maps are compatible, we repeat the pressure profile fit with the CL J1226.9+3332 map obtained from the PIIC analysis. The prior 150 GHz flux estimates of the point sources, given as an input to `panco2`, are also calculated independently for IMCM and PIIC results, using the NIKA2 260 GHz map obtained with each of the pipelines.

In addition, we have repeated the analysis for the 1D and 2D transfer functions. We present in the left panel in Fig. 4.7 the pressure profiles for CL J1226.9+3332 galaxy cluster reconstructed from IMCM and PIIC maps, with angle ordered noise, and using both 1D and 2D TFs. The four profiles are compatible within error bars in the intermediate bins, but they differ beyond $\sim$ 900 kpc.

The explanation for this difference is shown in the right panel in Fig. 4.7. In this figure we present a Compton profile model in black (we used the Compton profile that corresponds to the mock cluster simulation

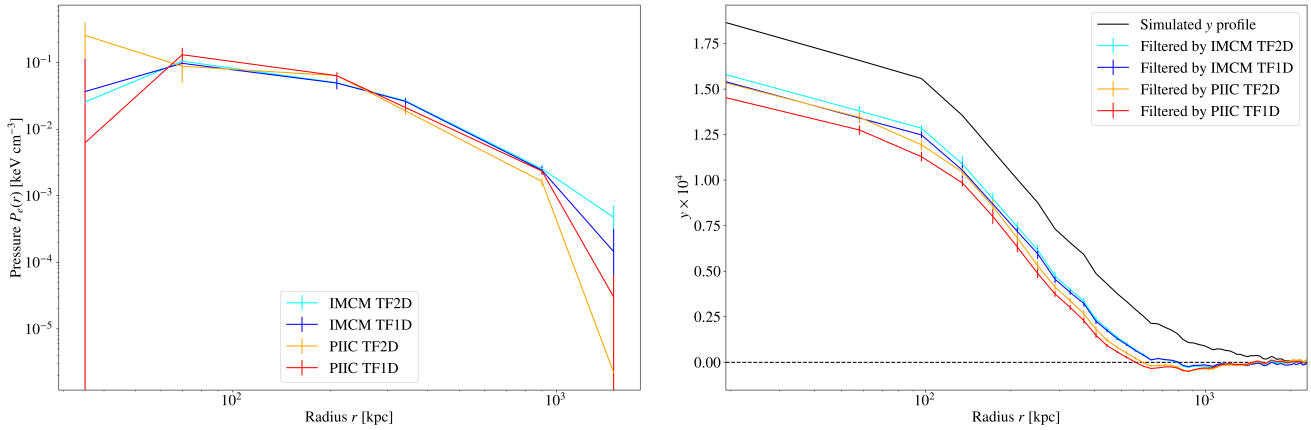

Figure 4.7: Comparison of results with IMCM and PIIC maps in cyan (TF2D) and blue (TF1D) and orange (TF2D) and red (TF1D), respectively. Left: radially binned pressure profiles reconstructed for CL J1226.9+3332 galaxy cluster. Right: a mock Compton profile in black and the same profile filtered by different transfer functions. The black dashed line indicates the zero.

in Fig. 2.6). We also show, in colours, the same profile filtered by different transfer functions. The relative difference to the original Compton profile increases with the radius, meaning that the filtering is more and more strong. At radii between 500 to 1000 kpc, depending on the pipeline, the filtered profiles go below zero. In those cases the signal of the cluster has been fully filtered.

4.3.2 Comparison to previous results

In Fig. 4.6 we compare our results from the IMCM pipeline to the profiles obtained in R18 with SZ data from NIKA (magenta), Bolocam (black), and MUSTANG (yellow). MUSTANG's high angular resolution (9″ FWHM at 90 GHz) enables us to map the core of the cluster, whereas Bolocam's large field of view (8′ at 140 GHz) allows us to recover the large angular scales. NIKA and the improved NIKA2 camera are able to cover all the intermediate radii. The consistency of the different pressure bins in the radial range from the NIKA2 beam to the FoV proves the reliability of the reconstruction with NIKA2 data. In the same figure, we also present the ICM pressure profile reconstructed from X-ray data only (empty black dots), which follows closely the NIKA pressure bins.

Before going any further, we have to consider again the effect of the filtering on the NIKA2 data. As discussed in Sect. 2.3.4 and 4.3.1, the filtering due to the data processing affects mainly small angular frequencies, i.e. small k numbers, which is translated into large angular scales in real space. This means that, in this case, the region at $\sim$ 1000 kpc from the centre of the cluster is strongly filtered. For this reason, we cast doubt on our results for the last NIKA2 bin in pressure. This is confirmed by the spread of the different results for different hypotheses and pipelines.

4.4 Hydrostatic mass

With the two HSE mass estimation approaches presented in Sect. 3.4 we reconstruct the mass of CL J1226.9+3332 starting from the radially binned pressure profiles. Aiming for a precise reconstruction of the HSE mass, which requires having accurately constrained slopes for the pressure profile, in both cases we combine the NIKA2 pressure bins with the results obtained in R18.[9] Thus, we modify the likelihood in Eq. 3.6

[9]The binned profiles in R18 and those in this work are centred at positions separated by 3 arcsec, which is the typical RMS pointing error for NIKA2 [216], so we consider that combining them is a valid approach.

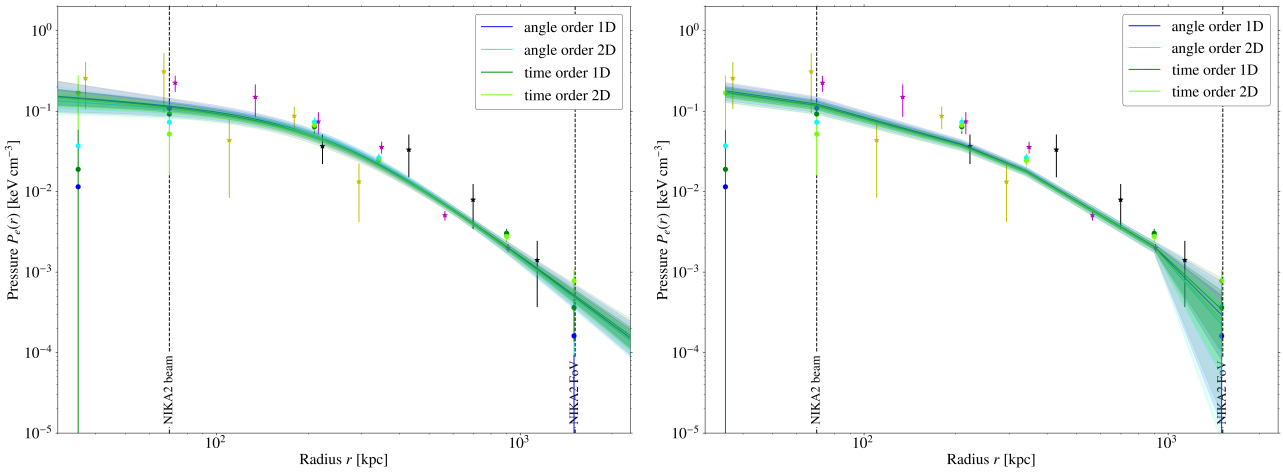

Figure 4.8: Pressure profile and best-fit for the gNFW (left) and NFW (right) models. The data points correspond to the NIKA2 radially binned results for the four data sets discussed above, and to the NIKA, MUSTANG, and Bolocam bins from R18. Blue and green solid lines represent the best-fit values for the four NIKA2 pressure estimates considered. The shaded regions show the 2.5th, 16th, 84th, and 97.5th percentiles.

to fit also to $P_k^{\rm R18}$ and $\Delta P_k^{\rm R18}$, i.e., the pressure bins in R18 and associated error bars:

$$\begin{aligned}\log \mathcal{L}(\vartheta) = & \\ & -\frac{1}{2}\left(P_{\rm e}^{\rm gNFW}(\vartheta) - P_{\rm e}^{N2}\right)^T C^{-1}\left(P_{\rm e}^{\rm gNFW}(\vartheta) - P_{\rm e}^{N2}\right) \\ & -\frac{1}{2}\sum_{k=1}^{n_{\rm R18bins}}\left(\frac{P_{{\rm e},k}^{\rm gNFW}(\vartheta) - P_{{\rm e},k}^{\rm R18}}{\Delta P_{{\rm e},k}^{\rm R18}}\right)^2 \\ & -\frac{1}{2}\left(\frac{Y_{500}^{\rm gNFW}(\vartheta) - Y_{500}^{Planck}}{\Delta Y_{500}^{Planck}}\right)^2,\end{aligned} \tag{4.1}$$

As we do not rely on the value of the last NIKA2 pressure bin, we choose to modify the NIKA2 inverse covariance matrix C^{-1} by setting the last diagonal term to $[C^{-1}]_{5,5} = 0$, so that the correlation of the last bin with the others is taken into account, but not its value.

The best-fit gNFW pressure profiles (solid lines) and uncertainties (shaded area) are presented in the left panel of Fig. 4.8 for the four sets of NIKA2 data. Here the model was fitted using the MCMC method. We observe that the best-fit models are a good representation of the data over the full range in radius, as demonstrated by the corresponding reduced χ^2, which are close to 1 and compatible with the expected χ^2-distribution for all the cases (see solid lines in Fig. 4.10). The posterior distributions of the $\vartheta_{\rm gNFW}$ parameters can be found in Fig. 4.9. We observe there is consistency between the results for the different TF and noise estimates. The degeneracy between the gNFW parameters is very important.

In addition, it is interesting to compare our results to those from *Planck* for which a similar modelling was used. In Fig. 4.11 we present the 2D posterior distributions of the integrated Compton parameter at $5R_{500}$, Y_{5R500}, (with R_{500} calculated independently in each case) with respect to the Θ_s parameter of the gNFW model, at a confidence level (C.L.) of 68%, 95%, and 99%. The parameters Θ_s and r_p are related via the angular diameter distance at the cluster redshift: $\tan(\Theta_s) = r_p/\mathcal{D}_{\rm A}$. We compare the results obtained in Planck Collaboration et al. (2016) [142] (with the `MMF3` matched multi-filter, available in the *Planck* Legacy Archive[2] and also in Fig. 1.15) to the constraints from the gNFW profiles obtained in this work with the NIKA2, R18, *Planck*

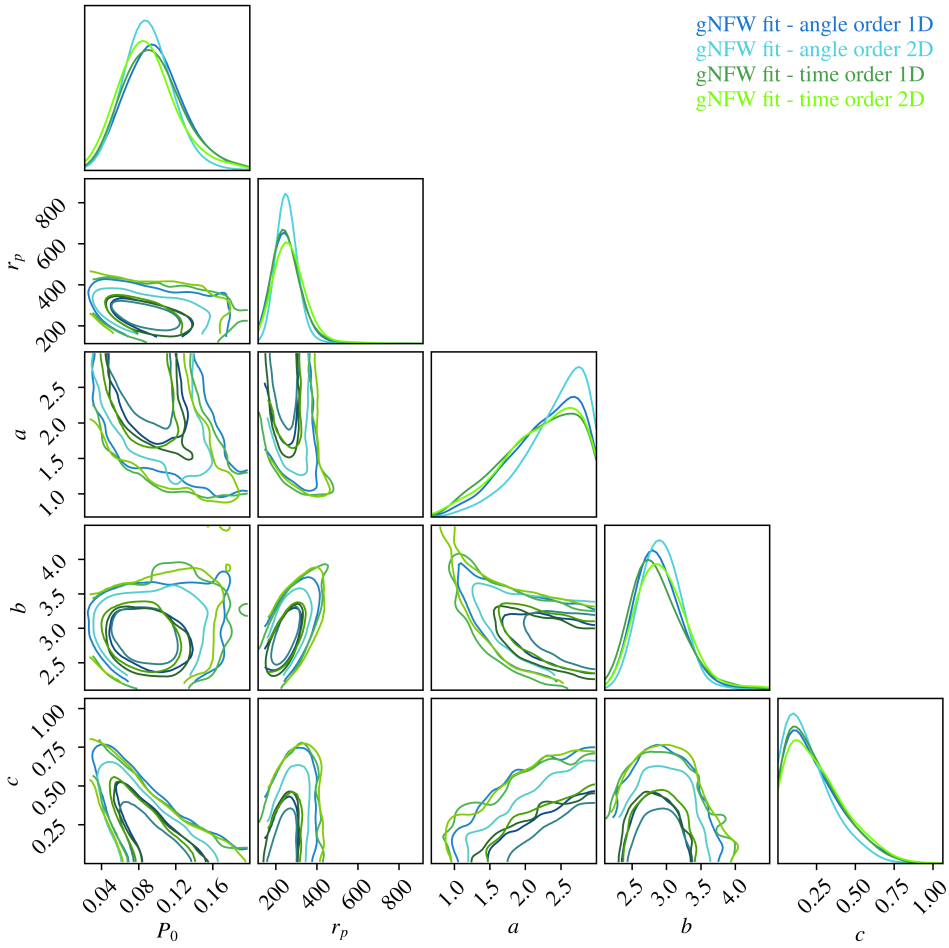

Figure 4.9: Posterior distributions of the parameters obtained in the fit of the NIKA2 and R18 pressure bins for the gNFW pressure model.

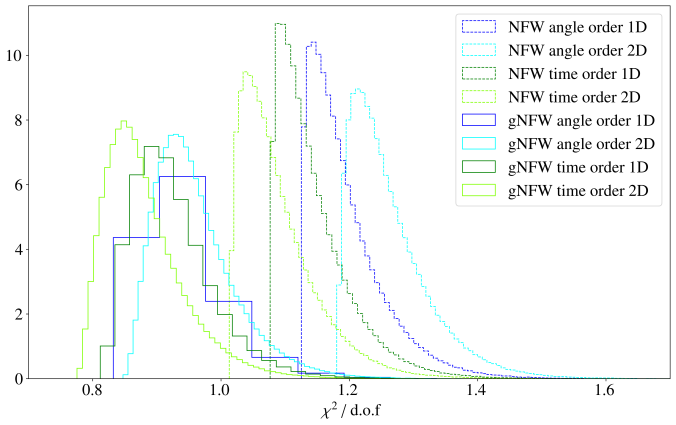

Figure 4.10: Reduced χ^2 of the gNFW (solid) and NFW (dashed) model fits to the NIKA2 and R18 pressure bins. The different blue and green shades show the results for the used NIKA2 bins from different TF and noise estimates.

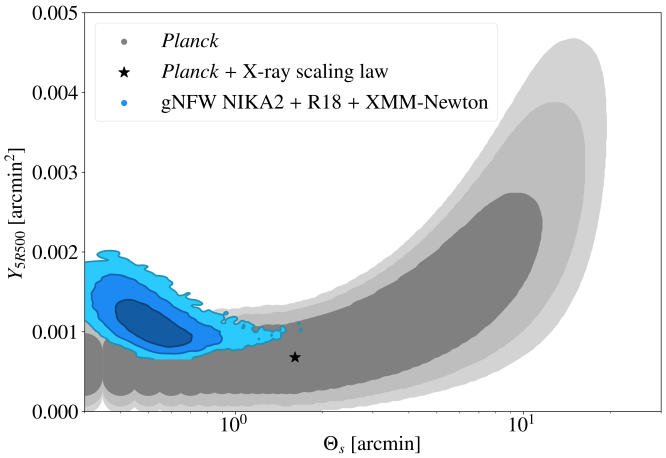

Figure 4.11: Distribution of Y_{5R500} with respect to Θ_s for the gNFW pressure model fits to *Planck* data (grey) in Planck Collaboration et al. (2016) [142] and to the NIKA2 + R18 + XMM-*Newton* data (blue) in this work. Different contours show 68%, 95%, and 99% confidence intervals. The black star corresponds to the intersection between the Planck Collaboration et al. (2016) [142] distribution and the X-ray scaling law shown in Fig. 16 in Planck Collaboration et al. (2016) [142].

and XMM-*Newton* data. Our contours were obtained from the MCMC chains (varying all the parameters in the gNFW model fit) by computing Y_{5R500} and Θ_s, while for *Planck* the a, b, and c parameters were fixed to the A10 values. For simplicity, we only show the contours for the NIKA2 AO1D case. This figure illustrates the important gain in precision due to high-resolution observations: resolving the galaxy cluster allows us to determine, even at such a high redshift, the Θ_s characteristic radius.

The NFW mass density model was also fitted to the pressure bins in Fig. 4.6, in this case taking flat priors for the concentration and the characteristic radius, $0 < c_{200} < 8$ and 100 kpc $< r_s <$ 2000 kpc. The best-fit pressure profiles and uncertainties are presented in the right panel of Fig. 4.8 for the four NIKA2 radially binned data sets discussed above. The posterior probability distributions of the free parameters of the model are shown in Fig. 4.12. The posterior distributions of the c_{200} and r_s parameters can be compared to the results for the analyses of clusters in X-rays [175, 258, 284]. In these studies, c_{200} spans from 1 to 6 and r_s from 200 kpc to 1200 kpc, which is compatible with our results. We find that the NFW model is overall a good fit to the data as shown by the reduced $\chi^2 \sim 1$ (see Fig. 4.10 for the distributions). However, we observe that the uncertainties increase significantly in the outskirts of the cluster with respect to the gNFW model fit. This can probably be explained by the flexibility of the NFW-based approach, which is high enough to show that the last point in the profile is not well constrained by the data. We observe no significant difference between the results for the two TF and noise estimates used for NIKA2.

Once the pressure profiles are fitted, we can directly calculate the corresponding HSE mass profiles for CL J1226.9+3332. We present in Fig. 4.13 the HSE mass profiles inferred from the gNFW best-fit pressure profile, in combination with the XMM-*Newton* electron density, and from the NFW density best-fit model. Uncertainties (shaded areas) are obtained directly from the MCMC chains by computing the HSE mass profile for each sample from the model parameters. For the sake of clarity, we only present the masses obtained with NIKA2 AO1D estimates, but we changed the colour-coding for the gNFW profile so that we can differentiate between the two results.

We observe in Fig. 4.13 that the HSE mass profiles for the gNFW and NFW models are compatible within 2σ. The vertical dashed lines in the figure represent the $R_{500}^{\rm HSE}$ for each mass profile. The capability of the pressure model to describe the shape of the profile slopes is the key element for a good HSE mass reconstruction and we can see that slight differences in the shape of the pressure profile at $\sim R_{500}$ are critical for defining $R_{500}^{\rm HSE}$ and $M_{500}^{\rm HSE}$.

These mass profiles, obtained from the combination of SZ and X-ray data, are also compared to the X-ray-only HSE mass estimate (empty dots) in Fig. 4.13. Assuming spherical symmetry, the X-ray mass profile was

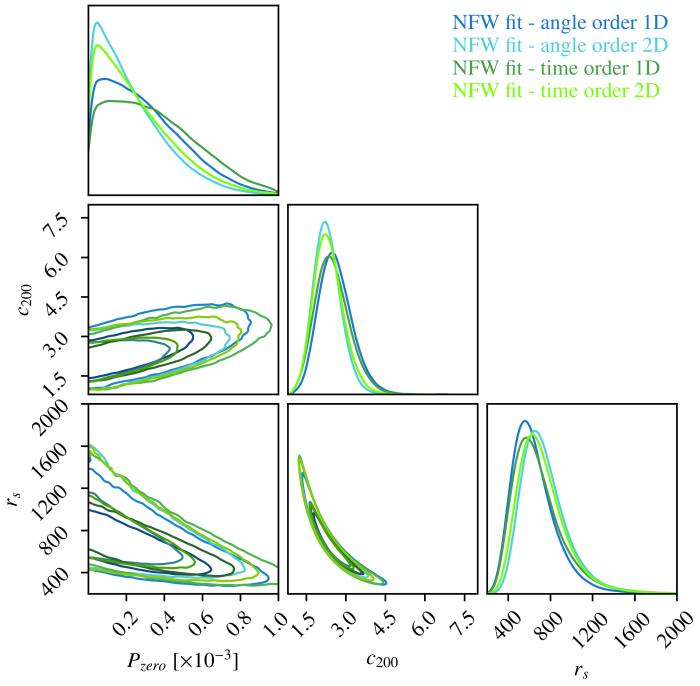

Figure 4.12: Posterior distributions of the parameters obtained in the fit of the NIKA2 and R18 pressure bins, combined with the XMM-*Newton* electron density, for the NFW density model fitted to the pressure.

derived, as in Sect. 3.4, with the XMM-*Newton* electron density and temperature profiles presented in Sect. 4.2.

Despite the different behaviour of the X-ray-only HSE mass profile in the cluster core, it is consistent with the SZ+X estimates at around $R_{500}^{\rm HSE}$. We note that the difference must come from the estimate of the derivative of the pressure, which for X-analyses is computed using the density and spectroscopic temperature profiles. The temperature profile from the X-rays is not used to compute the HSE mass in the SZ+X analyses.

From the reconstructed HSE mass profiles we can obtain the $R_{500}^{\rm HSE} - M_{500}^{\rm HSE}$ probability distributions for each of the considered cases. We present in the left and central panel of Fig. 4.14 the $R_{500}^{\rm HSE} - M_{500}^{\rm HSE}$ distributions for the gNFW and NFW models. They were obtained from the MCMC chains in the same way the uncertainties in Fig. 4.13 were computed. We also account for uncertainties in the electron density profile, which are of the order of 20%. These uncertainties were computed by combining the best-fit NFW and gNFW profiles with random realisations of the electron density profile following a Gaussian distribution centred in the central values of $n_{\rm e}$ and with the error bars as standard deviation. The width of the ellipses in Fig. 4.14 is an artefact from the display procedure, and each value of $M_{500}^{\rm HSE}$ is associated with a single value of $R_{500}^{\rm HSE}$.

In Fig. 4.14 we present the results for the four NIKA2 analyses (AO1D/2D and TO1D/2D). The results are consistent, with little dependence on the chosen TF estimate. From the comparison of the left and central panels in Fig. 4.14 we verify that the largest uncertainty in the HSE mass estimates comes from the modelling of the pressure profile. Despite this effect, the reconstructed HSE mass profiles are compatible within 1σ. The right panel of Fig. 4.14 shows the $R_{500}^{\rm HSE} - M_{500}^{\rm HSE}$ probability distribution obtained with XMM-*Newton*-only data. Even if it is compatible with the gNFW and NFW results, it favours lower HSE masses. A similar effect was observed for the ACT-CL J0215.4+0030 cluster [178], but not for PSZ2 G144.83+25.11 [177]. We summarise in Table 4.4 the marginalised $M_{500}^{\rm HSE}$ masses. We give the mean value and the 84th and 16th percentiles. For gNFW and NFW we combine the probability distributions obtained for the four NIKA2 results so that the results account for systematic effects in the NIKA2 data processing. The error bars also account for the uncertainties related to the electron density.

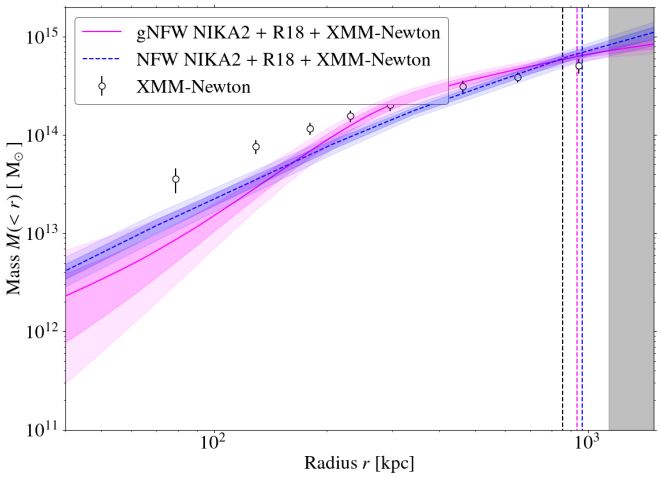

Figure 4.13: HSE mass profile estimates for CL J1226.9+3332 obtained with NIKA2 (angle order 1D) and R18 SZ data combined with the XMM-*Newton* electron density profile. The solid magenta and dashed blue lines correspond to the gNFW and NFW methods, respectively. The shaded areas show the 2.5th, 16th, 84th, and 97.5th percentiles. Empty dots correspond to the HSE mass profile obtained from XMM-*Newton*-only data. Vertical dashed lines show the $R_{500}^{\rm HSE}$ obtained from each mass profile. The grey region represents the radial ranges at which the profiles are extrapolated.

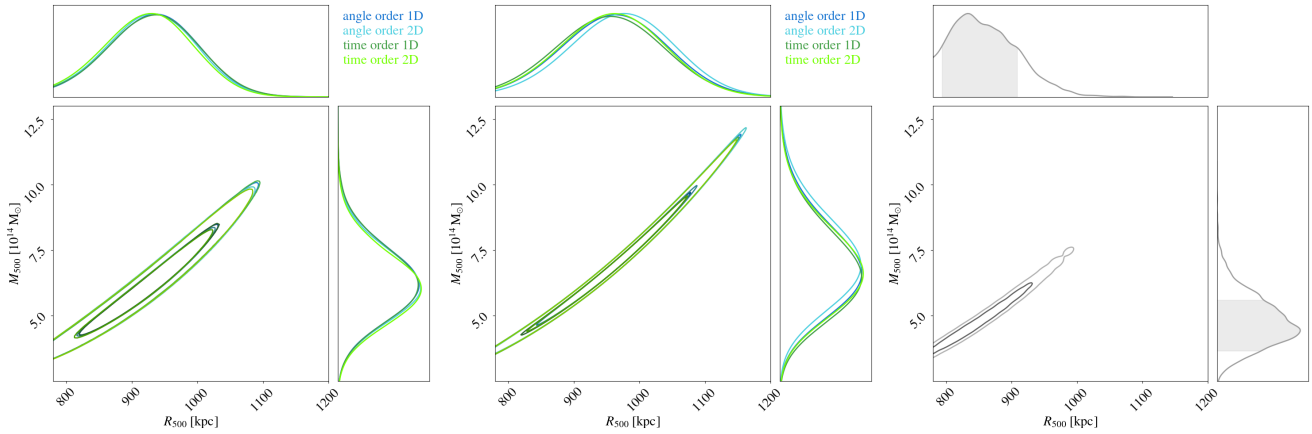

Figure 4.14: Probability distributions (1D and 2D) for $M_{500}^{\rm HSE}$ and $R_{500}^{\rm HSE}$ from the gNFW (left) and NFW (centre) models in the combined XMM-*Newton*, NIKA2 and R18 data, and from the XMM-*Newton* X-ray-only data (right). The different blue and green lines correspond to the results for the four NIKA2 test cases considered. Notice that the width of the contours in the 2D distributions is an artefact of the plotting procedure. Each $R_{500}^{\rm HSE}$ is associated with a single $M_{500}^{\rm HSE}$ value.

Table 4.4: HSE masses for different estimates at $R_{500}^{\rm HSE}$.

HSE mass estimates	$M_{500}^{\rm HSE}$ [10^{14} $M_\odot$]
$(\text{SZ+X-ray})_{\rm gNFW}$	$6.26^{+1.38}_{-1.38}$
$(\text{SZ+X-ray})_{\rm NFW}$	$7.00^{+1.76}_{-1.76}$
X-ray	$4.83^{+0.98}_{-0.96}$

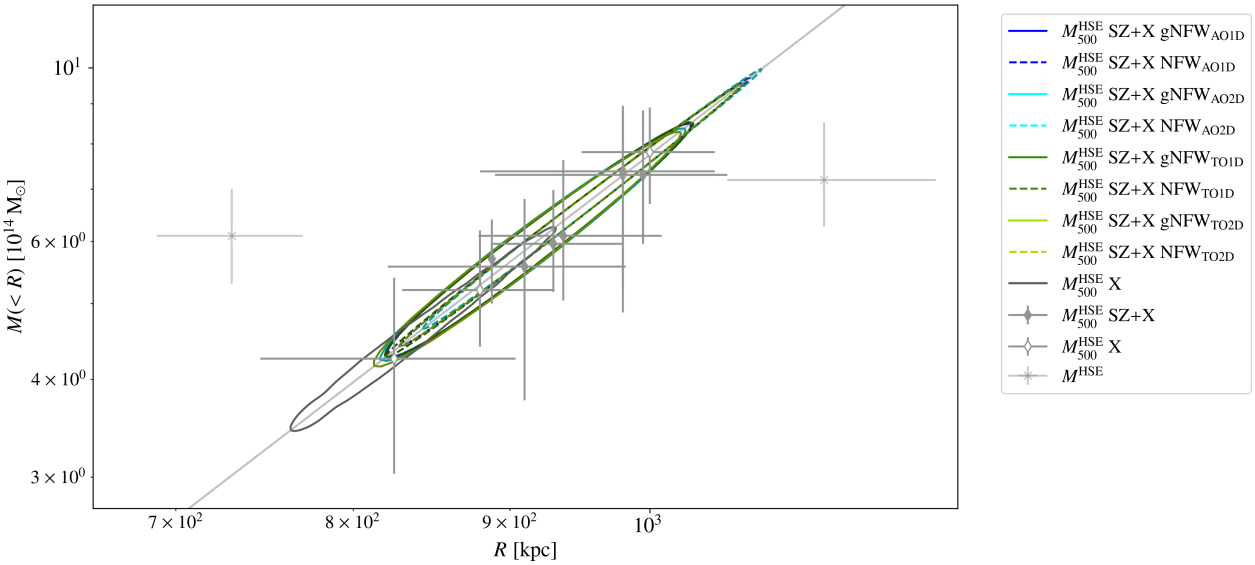

Figure 4.15: $R - M(< R)$ plane summarising the HSE mass results for CL J1226.9+3332. The blue and green 1σ contours show the $M_{500} - R_{500}$ results obtained in this chapter combining SZ and X-ray data for the four NIKA2 analyses. The solid and dashed lines are for the gNFW pressure and the NFW density models, respectively. The grey contour corresponds to the HSE mass estimate for the XMM-*Newton*-only data. In the case of literature data, the filled (empty) grey diamonds represent HSE masses from the combination of SZ and X-ray data (X-ray-only results). Grey crosses show HSE masses from the literature close to M_{500}. The diagonal bright grey line defines the $R_{500} - M_{500}$ relation. Slight deviations from this line are due to differences in the cosmological model used in each work.

4.4.1 Comparison to previous results

The comparison of different mass estimates is difficult and can lead to incorrect physical conclusions. In particular, when comparing integrated masses the radius at which the mass is computed has a significant impact: R_{500} and M_{500} being constrained at the same time, our data are affected by that degeneracy. For this reason, in Fig. 4.15 we show, in the $R - M(< R)$ plane, the results from the literature compared to those obtained in this chapter with NIKA2, XMM-*Newton* and R18 data.

The green and blue contours show again the $R_{500}^{\rm HSE} - M_{500}^{\rm HSE}$ results obtained for the gNFW (solid lines) and NFW (dashed lines) SZ and X-ray data combined analyses. For comparison, the filled grey diamonds correspond to the results from the literature presented in Fig. 4.1, also for combined SZ and X-ray data. We observe that the NIKA2+R18+XMM-*Newton* results are compatible with previous analyses within 1σ, centred around $\sim 7 \times 10^{14}$ M$_\odot$.

Regarding X-ray-only results, the HSE mass estimates obtained with XMM-*Newton* data (grey contours) suggest mass values centred at $\sim 5 \times 10^{14}$ M$_\odot$. This is in agreement with the lowest estimates from the literature (empty grey diamonds) presented in Bulbul et al. (2010) [276] and Maughan et al. (2007) [270]. On the contrary, the results from Mantz et al. (2010) [272] and Mroczkowski et al. (2009) [265] show higher masses. However, the $M_{500}^{\rm HSE}$ in Mantz et al. (2010) [272] is not a direct measurement, but an extrapolation from a gas mass measured at R_{2500} converted into total mass, making this result less reliable. Overall, for CL J1226.9+3332 the HSE masses obtained only from X-ray data tend to lower values than those from the combination of SZ and X-rays.

The result from Planck Collaboration et al. (2016) [142] is also a special case, as it is not a direct mass measurement, but a mass obtained from the X-ray-derived scaling relation (Eq. 7 in Planck Collaboration et al. (2014) [5]) applied to the SZ measurement. This may explain why it lies at the border between the X-ray-only data and the SZ+X combined results. The differences observed between X-ray-only and the combined SZ+X results could have a physical and observational origin. For such a high-redshift cluster X-ray observations become challenging. If the south-western sub-clump in the cluster is really a hot but not dense structure (as

suggested by Jee and Tyson (2009) [264]), the electron density measurements from X-ray observations might be difficult to perform.

4.5 Conclusions

In this chapter we have put together, in a detailed analysis of the hydrostatic mass of CL J1226.9+3332, the methods described in chapters 2 and 3. We have studied the systematic effects related to the NIKA2 raw data analysis and to the HSE mass reconstruction for the highest redshift cluster of the LPSZ.

We have obtained NIKA2 150 and 260 GHz maps, which have allowed us to reconstruct the radially binned pressure profile of the cluster from the SZ data. To characterise the robustness of our results with respect to the data processing, we have repeated the whole analysis for the two pipeline-filtering transfer functions (1D and 2D), and for the two noise estimates (TO and AO) for the 150 GHz map, as well as for the output maps of the two NIKA2 independent data analysis pipelines. We have also accounted for the presence of point sources. The reconstructed pressure profiles are consistent amongst them, and compatible, within the angular scales accessible to NIKA2, with the profiles obtained from three independent instruments in R18. This validates the pressure profile reconstruction procedure that will be used for the analysis of the full sample in the NIKA2 SZ Large Programme. Nevertheless, we have shown that large angular scales are filtered out in these NIKA2 maps.

From the combination of SZ-based pressure and XMM-*Newton* electron density profiles, and by using the two approaches presented in chapter 3, we have reconstructed the HSE mass of CL J1226.9+3332. Modelling the pressure with an NFW mass density profile seems a promising approach to ensure radially increasing HSE mass estimates. Both NFW and gNFW methods give completely compatible HSE mass profiles and integrated $M_{500}^{\rm HSE}$. From the comparison of the different mass estimates, we also conclude that for the moment, when estimating the HSE mass of the CL J1226.9+3332 galaxy cluster in the NIKA2 SZ Large Programme, the error budget is dominated by model dependence rather than by the instrumental and data processing systematic effects that we investigated. We think that the only way to reduce the current uncertainties is to precisely constrain the slope of the mass profile at $\sim R_{500}^{\rm HSE}$ since we have proved that very similar mass profiles overall can result in significant differences at $M_{500}^{\rm HSE}$.

In addition, these results are in agreement with the X-ray-only HSE mass estimate obtained from the XMM-*Newton* electron density and temperature profiles. Nevertheless, the X-ray-only estimate favours lower mass values than the combined SZ+X-ray results. We have also shown that our results are compatible with all the HSE mass estimates found in the literature within uncertainties, which are large.

CHAPTER 5

HSE-to-lensing mass bias for NIKA(2)-CLASH clusters

In the previous chapters we have presented the hydrostatic mass reconstruction of clusters of galaxies within the NIKA2 SZ Large Programme. These estimates, that are robust against NIKA2 data analysis systematic effects and compatible with different results in the literature, are subject to a bias induced by the different assumptions used to compute HSE masses. As introduced in Sect. 1.3.4, if the gas pressure in the ICM is not purely thermal nor spherically distributed, or if the hydrostatic equilibrium hypothesis is not satisfied in the cluster (i.e. if the potential well is not balanced by the gas pressure), HSE masses may suffer from the *HSE mass bias*.

In this chapter we present a different way to estimate the mass of galaxy clusters, using convergence maps obtained from lensing data. We compare the HSE masses of some clusters observed with NIKA and NIKA2 to their lensing mass estimates. We first present the basic concepts of the formalism that describes the lensing of galaxies due to the presence of clusters. We equally introduce the data set from the Cluster Lensing And Supernova survey with Hubble (CLASH) [285] and describe the lensing mass reconstruction method. Then, we present the NIKA(2)-CLASH sample and the comparison of lensing masses to HSE estimates for the clusters in the sample. In addition, we make use of the lensing mass estimates to compute the gas-to-lensing mass fraction.

5.1 Lensing as a tracer of the mass

The lensing masses of the clusters in our sample were reconstructed from the publicly available CLASH convergence maps [271]. However, convergence maps are not observables and need to be estimated from

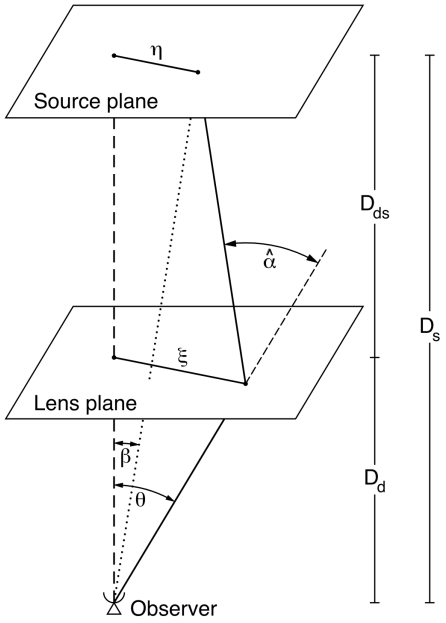

Figure 5.1: Sketch of the gravitational lensing effect in the *thin lens* approximation. Figure from Bartelmann and Schneider (2001) [287].

lensing observations. In this section, we present the basics of the gravitational lens theory needed to understand the reconstruction of convergence maps from observations. Then we briefly describe the CLASH survey and its convergence maps, as well as the lensing mass reconstruction method [190, 191].

5.1.1 Gravitational lensing of background galaxies

Gravitational lensing refers to the deflection of light rays by gravitational fields (see Bartelmann (2010) [286] for a review). As presented in chapter 1 the potential well of different massive objects in the universe can create this deflection on the multiple light sources in the background. In our case we will refer to the bending of the light from galaxies due to the presence of galaxy clusters in the line-of-sight.

In Fig. 5.1 we show a schematic representation of the gravitational lensing effect. The light source (the galaxy) and the deflecting mass (the cluster, the lens) are located at D_s and D_d distances from the observer, respectively. In the absence of the lensing effect, the source would be seen by the observer with an angle $\vec{\beta}$ with respect to the deflecting mass. But the presence of this mass bends the light ray of the source and it is observed at $\vec{\theta}$. The difference between the two angles is the deflection angle: $\hat{\vec{\alpha}}$. The impact parameter is given by $\vec{\xi}$.

In this representation we consider that the width of the deflecting mass along the line-of-sight is much smaller than the distances between the source and the deflecting mass (D_ds) and between the observer and mass (D_d). Under this assumption, we can use the *thin lens* approximation and suppose that the deflection is instantaneous, i.e., that we can represent the path of the light as a straight ray that is deviated in the lens plane. From Fig. 5.1 we can write:

$$\vec{\eta} = \frac{D_\mathrm{s}}{D_\mathrm{d}}\vec{\xi} - D_\mathrm{ds}\hat{\vec{\alpha}}(\vec{\xi}), \tag{5.1}$$

and using $\vec{\eta} = D_\mathrm{s}\vec{\beta}$ and $\vec{\xi} = D_\mathrm{d}\vec{\theta}$ we obtain the lens equation and define the scaled deflection angle, $\vec{\alpha}(\vec{\theta})$:

$$\vec{\beta} = \vec{\theta} - \frac{D_\mathrm{ds}}{D_\mathrm{s}}\hat{\vec{\alpha}}(D_\mathrm{d}\vec{\theta}) \equiv \vec{\theta} - \vec{\alpha}(\vec{\theta}). \tag{5.2}$$

At the same time, General Relativity predicts that the deflection angle created by a point mass M is:

$$\hat{\alpha} = \frac{4GM}{c^2\xi}, \tag{5.3}$$

where G and c are the gravitational constant and the speed of light, respectively. Instead of using a point mass, we can consider a three-dimensional mass distribution with a mass density $\rho(\vec{r}) = \mathrm{d}m/\mathrm{d}V$ that is defined in $\vec{r} = (\xi'_1, \xi'_2, r'_3)$. Assuming that the incoming light from the source propagates along the r'_3 direction, the impact parameter with respect to the three-dimensional mass distribution is $\vec{\xi} - \vec{\xi}'$, with $\vec{\xi}' = (\xi'_1, \xi'_2)$. Then, the deflection angle for the impact parameter $\vec{\xi}$ is given by the integral over the whole mass distribution,

$$\begin{aligned}\hat{\vec{\alpha}}(\vec{\xi}) &= \frac{4G}{c^2}\sum \mathrm{d}m(\xi'_1, \xi'_2, r'_3)\frac{\vec{\xi} - \vec{\xi}'}{|\vec{\xi} - \vec{\xi}'|^2} \\ &= \frac{4G}{c^2}\int \mathrm{d}^2\xi' \int \mathrm{d}r'_3\rho(\xi'_1, \xi'_2, r'_3)\frac{\vec{\xi} - \vec{\xi}'}{|\vec{\xi} - \vec{\xi}'|^2}.\end{aligned} \tag{5.4}$$

The integral or projection along the line-of-sight of the mass density gives the surface mass density:

$$\Sigma(\vec{\xi}') \equiv \int \mathrm{d}r'_3\rho(\xi'_1, \xi'_2, r'_3), \tag{5.5}$$

therefore, the deflection angle is

$$\hat{\vec{\alpha}}(\vec{\xi}) = \frac{4G}{c^2}\int \mathrm{d}^2\xi'\Sigma(\vec{\xi}')\frac{\vec{\xi} - \vec{\xi}'}{|\vec{\xi} - \vec{\xi}'|^2}. \tag{5.6}$$

As mentioned above, for the lensing mass reconstructions in this section we use convergence maps. The convergence, κ, is defined as the surface mass density, Σ, normalised by the critical surface mass density $\Sigma_{\rm crit}$,

$$\kappa(\vec{\theta}) = \Sigma(D_{\rm d}\vec{\theta})/\Sigma_{\rm crit} \text{ , where } \Sigma_{\rm crit} = \frac{c^2}{4\pi G}\frac{D_{\rm s}}{D_{\rm d}D_{\rm ds}}. \tag{5.7}$$

The critical surface mass density delimits, as we will see later on, the difference between *weak* and *strong* lensing regimes. From the previous relations, we can write the scaled deflection angle as

$$\vec{\alpha}(\vec{\theta}) = \frac{1}{\pi}\int \mathrm{d}^2\theta'\kappa(\vec{\theta}')\frac{\vec{\theta} - \vec{\theta}'}{|\vec{\theta} - \vec{\theta}'|^2}, \tag{5.8}$$

and if the scaled deflection angle is the gradient of the deflection potential, $\vec{\alpha} = \nabla\psi$, the deflection potential ψ is

$$\psi(\vec{\theta}) = \frac{1}{\pi}\int \mathrm{d}^2\theta'\kappa(\vec{\theta}')\ln|\vec{\theta} - \vec{\theta}'|. \tag{5.9}$$

Therefore, from the solutions of the lens equation in Eq. 5.2 we would be able to estimate the surface mass density in the lens plane. However, this requires knowing the true $\vec{\beta}$ position of the source, which is actually unknown. Another important characteristic of the lensing effect is that it preserves surface brightness, in other words, the surface brightness $I^s(\vec{\beta})$ of a source will be the same as the lensed one: $I(\vec{\theta}) = I^s[\vec{\beta}(\vec{\theta})]$. If the size of the source is much smaller than the scales on which the distortion changes, we can linearise the lens mapping $\vec{\beta}(\vec{\theta})$:

$$I(\vec{\theta}) = I^s\left[\vec{\beta}_0 + \mathcal{A}(\vec{\theta}_0)(\vec{\theta} - \vec{\theta}_0)\right], \tag{5.10}$$

where $\mathcal{A}(\vec{\theta}_0)$ is the Jacobian matrix of the distortion at $\vec{\theta}_0$,

$$\mathcal{A}(\vec{\theta}) = \frac{\partial\vec{\beta}}{\partial\vec{\theta}} = \left(\delta_{ij} - \frac{\partial^2\psi(\vec{\theta})}{\partial\theta_i\partial\theta_j}\right) = \begin{pmatrix} 1 - \kappa - \gamma_1 & -\gamma_2 \\ -\gamma_2 & 1 - \kappa + \gamma_1 \end{pmatrix}. \tag{5.11}$$

In Eq. 5.11 we have introduced γ_1 and γ_2, the two components of the shear $\gamma \equiv \gamma_1 + i\gamma_2$ that are related to the deflection potential through,

$$\gamma_1 = \frac{1}{2}\left(\frac{\partial^2\psi}{\partial^2\theta_1} - \frac{\partial^2\psi}{\partial^2\theta_2}\right), \ \gamma_2 = \frac{\partial^2\psi}{\partial\theta_1\partial\theta_2}. \tag{5.12}$$

Thus, we can also relate the convergence to the shear with,

$$\gamma(\vec{\theta}) = \frac{1}{\pi}\int \mathrm{d}^2\theta' \mathcal{D}(\vec{\theta} - \vec{\theta}')\kappa(\vec{\theta}'), \text{ where } \mathcal{D}(\vec{\theta}) = \frac{-1}{(\theta_1 - i\theta_2)^2}. \tag{5.13}$$

Weak lensing

When $\kappa, \gamma \ll 1$ we say that we are in the weak lensing regime. This happens when the light ray of the source crosses the lens plane far from the centre of the cluster, where the surface mass density Σ is much smaller than $\Sigma_{\rm crit}$. Due to the deflection of light rays, weak lensing creates small distortions in the shapes of the light sources and the first step of the lensing analyses is to measure those distortions. From Eq. 5.10 we read that circular sources will be observed as elliptical objects.

As mentioned, the lensing effect created by the presence of clusters of galaxies is observed through the distortion of background galaxy shapes. Nevertheless, galaxies are intrinsically elliptical [288] and it is necessary to differentiate the ellipticity introduced by the lensing effect from the intrinsic shape of the source. Fortunately, the intrinsic ellipticities of galaxies are randomly oriented, while the distortion introduced by the presence of a massive object (a cluster) affects in a coherent way all the background galaxy observations. We can write the intrinsic ellipticity of a galaxy as

$$\epsilon^{\rm true} = \epsilon_1^{\rm true} + i\epsilon_2^{\rm true}, \tag{5.14}$$

and with the reduced shear $g = \frac{\gamma}{1-\kappa}$, the observed ellipticity of a galaxy that has been lensed is:

$$\epsilon^{\rm lensed} = \frac{\epsilon^{\rm true} + g}{1 + g^*\epsilon^{\rm true}}. \tag{5.15}$$

Observations of the shape of single galaxies ($\epsilon^{\rm lensed}$) do not allow one to distinguish between g and $\epsilon^{\rm true}$. Assuming that, as mentioned, galaxies are randomly oriented, the average intrinsic ellipticity of all galaxies is zero: $\langle\epsilon^{\rm true}\rangle = 0$. Thus, in a region of the sky where the shear can be considered to be constant and $g \ll 1$ (weak lensing regime), the average over all the galaxy shapes measured in that region is

$$\langle\epsilon^{\rm lensed}\rangle = \langle\frac{\epsilon^{\rm true} + g}{1 + g^*\epsilon^{\rm true}}\rangle \approx \langle\epsilon^{\rm true} + g\rangle \approx g. \tag{5.16}$$

So, in the weak lensing regime where $\kappa \ll 1$, the measurement of the shapes of many galaxies in the field of a cluster permits reconstructing the γ created by the cluster's mass: $\langle\epsilon^{\rm lensed}\rangle \approx g \sim \gamma$. Following Eq. 5.13 it is also possible to recover the corresponding κ.

The measurement of the shapes and sizes of galaxies is a very delicate step in the weak lensing analyses and great efforts are put in the lensing community to obtain precise $\epsilon^{\rm lensed}$ measurements from sky maps [289]. In addition, the distortions introduced by weak lensing are small ($g \sim 10^{-2} - 10^{-1}$) and atmospheric and instrumental effects can produce changes in the galaxy shape that can be stronger than the weak lensing effect itself. As detailed in Bartelmann and Schneider (2001) [287], weak lensing is a very powerful tool, but with numerous sources of uncertainties [290–293].

Strong lensing

If the lens equation in Eq. 5.2 has multiple solutions, that is, if for a source at a position $\vec{\beta}$ different $\vec{\theta}$ are possible, the same source can be observed at different positions in the sky. This can only happen in the *strong lensing* regime, when κ and $\gamma \sim 1$. Therefore, strong lensing happens close to the centres of clusters.

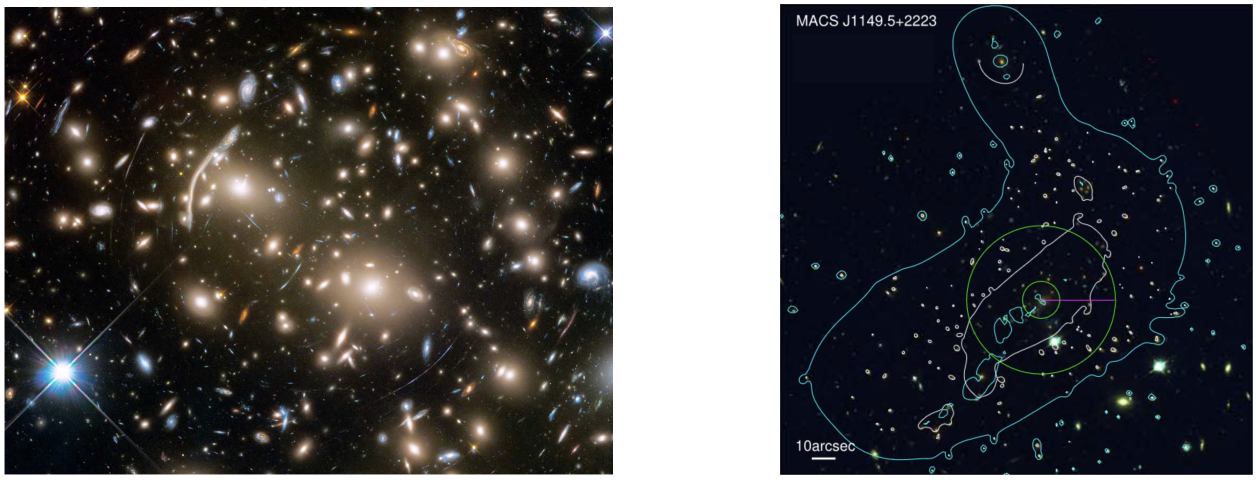

Figure 5.2: Lensing of galaxies. Left: lensing of galaxies around Abell 370. Credit: NASA, ESA, and J. Lotz and the HFF Team (STScI). Right: strong lensing reconstruction for MACS J1149.5+2223. Figure from [295].

Based on their redshift, the objects that correspond to the same galaxy are identified in the observed images, requiring very precise redshift measurements (usually spectroscopic estimates [294]). The repetition and distribution of the galaxies in the images are modelled, as presented in the following, to reconstruct the mass of the lens.

In the left panel in Fig. 5.2 we show an image of the Abell370 galaxy cluster observed with the Hubble Space Telescope (HST). We can see that background galaxies are distorted forming arcs around the cluster. Almost 100 identified galaxies in the field have multiple images due to the strong lens of the cluster. In the right panel in Fig. 5.2 we present a map of MACS J1149.5+2223 galaxy cluster (also known as PSZ2 G228.16+75.20, Sect. 5.2.1 and chapter 3) with different contours reconstructed from the modelling of strongly lensed galaxies: the white contours show the $\kappa = 1$ lines (for $D_{\rm ds}/D_{\rm s} = 1$). The green circles represent the 50 kpc and 200 kpc distances to the BCG.

5.1.2 Cluster Lensing And Supernova survey with Hubble

The Cluster Lensing And Supernova survey with Hubble (CLASH) [285] comprises the study of 25 galaxy clusters. Among them, 20 were X-ray selected and are mostly relaxed and high temperature systems. The remaining 5 were chosen because of their strong lensing power. The main objective of the survey was to use gravitational lensing observations from HST to reconstruct precisely the mass distribution in those clusters and estimate the concentration of dark matter in their cores. In addition, the survey sought to detect high redshift galaxies and Type Ia supernovae, as well as to study the properties of member galaxies of clusters and background galaxies. Observations were carried out between November 2010 and July 2013, being able to reach their main scientific goals.

Estimating the concentration of clusters requires having cluster mass density profiles that are accurately reconstructed from the core to the outskirts, since the concentration is defined from the ratio of an external radius (typically the virial radius) and an internal radius (it can be the radius at which the mass density profile has a slope of -2, that is, $\rho \propto r^{-2}$). Given that strong and weak lensing are good tools to trace the matter in the cluster core and at large scales, respectively, combining both is a clever strategy to map the mass distribution at all radial ranges.

Convergence maps: LTM and PIEMD+eNFW

In Zitrin et al. (2015) [271] authors used the weak and strong lensing measurements from HST to reconstruct the projected mass density distribution for the 25 clusters in the CLASH sample. Convergence maps, together

with shear and magnification maps, were made publicly available[10]. These are the convergence maps used to estimate lensing masses throughout this chapter. In Merten et al. (2015) [279] authors also reconstructed the convergence maps for 19 of the CLASH clusters. Although we will not use their maps, the lensing masses obtained in Merten et al. (2015) [279] will be compared to our results in Sect. 5.2.2.

To account for modelling effects, two different parametrisations were used in Zitrin et al. (2015) [271] to reconstruct the lens model, based on previously used strong lensing modelling methods [296–298] adapted to fit also weak lensing shape distortion measurements. The main principle of the methods is to build mass distribution models and to compare the lensing that those distributions would produce on the background galaxies to the observed strong and weak lensing signal. The minimised $\chi^2_{\rm tot}$ is,

$$\chi^2_{\rm tot} = \chi^2_{\rm SL} + \chi^2_{\rm WL} = \sum_i \frac{(x'_i - x_i)^2 + (y'_i - y_i)^2}{\sigma^2_{pos}} + \sum_j \frac{(g'_{1,j} - g_{1,j})^2 + (g'_{2,j} - g_{2,j})^2}{\sigma^2_{ell}}, \tag{5.17}$$

where (x_i, y_i) and (x'_i, y'_i) are the positions of the observed and modelled multiple images of the i'th galaxy due to strong lensing, and $(g_{1,j}, g_{2,j})$ and $(g'_{1,j}, g'_{2,j})$ are the observed and modelled reduced shear components of the j'th galaxy produced by weak lensing. The uncertainty on the positions is given by σ^2_{pos} (in Zitrin et al. (2015) [271] fixed to $\sigma_{pos} = 0.5''$) and σ^2_{ell} represents the error in the reduced shear (in Zitrin et al. (2015) [271] $\sigma_{ell} = 0.3$, based on the width of the distribution of measured ellipticities, as in the literature).

The first of the parametrisations is called *Light-Traces-Mass*, hereafter LTM, and it is based on the assumption that the observed light in a cluster traces its total matter distribution. LTM models are the sum of multiple components: for every cluster member galaxy a mass distribution is added, depending on the luminosity of the galaxy; the combination of all those galaxy components is smoothed with a 2D Gaussian component to represent the DM and a general normalisation factor is added to the total distribution. Thus, LTM matter models are formed by a sum of matter peaks connected by a smooth DM halo.

The second model is the *Pseudo-Isothermal Elliptical Mass Distribution with an elliptical NFW*, PIEMD+eNFW. As for the LTM, galaxies in the cluster are assumed to trace the matter distribution, but here only for the galaxy component. For every galaxy in the cluster, a Pseudo-Isothermal Elliptical Mass Distribution (from Jullo et al. (2007) [299]) is considered. The mass distribution is scaled by the luminosity of the corresponding galaxy. Then a DM halo centred in the BCG is added following an elliptical NFW (eNFW) model. For some complex clusters, it was required to add a second eNFW dark matter halo.

All the convergence maps reconstructed in Zitrin et al. (2015) [271] are 273×273 arcsec^2 large, which corresponds to different physical sizes depending on the redshift of the cluster.

5.1.3 Lensing mass reconstruction from convergence maps

For the lensing mass profile reconstruction we followed the approach described in Muñoz-Echeverría et al. (2023) [191], similar to the one presented in Ferragamo et al. (2022) [190]. Instead of analysing directly the lensed galaxy measurements, we used the already modelled convergence maps presented in the previous section. The same procedure was also followed in Merten et al. (2015) [279], where they used their own convergence map reconstructions.

As given by Eq. 5.7, the convergence maps describe the projected mass density of the cluster, Σ, in critical density units. The publicly available CLASH κ-maps [271] have been normalised to $D_{\rm s}/D_{\rm ds} = 1$, so by knowing the angular diameter distance $D_{\rm d}$ to the clusters, κ-maps can be converted into projected mass density maps. To estimate the lensing mass profiles of clusters, we fitted a mass density model to each Σ-map. We assumed spherical symmetry and an NFW density profile (see Eq. 1.19). We chose to directly fit the analytical projected NFW density profile to the radially averaged projected profiles of the Σ-maps. Using Eq. 7, 8 and 9

[10] https://archive.stsci.edu/prepds/clash/

in Bartelmann (1996) [300] the projected NFW density profile is,

$$\Sigma_{\rm NFW}(x) = \begin{cases} \frac{2\rho_s r_s}{x^2-1}\left(1 - \frac{2}{\sqrt{x^2-1}}\arctan\sqrt{\frac{x-1}{x+1}}\right) & (x > 1) \\ \frac{2\rho_s r_s}{x^2-1}\left(1 - \frac{2}{\sqrt{1-x^2}}\,\mathrm{arctanh}\sqrt{\frac{1-x}{1+x}}\right) & (x < 1) \\ \frac{2\rho_s r_s}{3} & (x = 1) \end{cases}$$

with $x = R/r_s$ and $\rho_s = \rho_{\rm crit}\delta_{c_{200}}$. R is the projected radius and $\delta_{c_{200}}$ the function of c_{200} presented in Eq. 1.20 for the NFW model. Therefore, the free parameters in the model are the characteristic radius r_s and the concentration c_{200}.

The fits were performed via MCMC analysis using the `emcee` software. We considered flat priors on c_{200} and r_s with $0 < c_{200} < 10$ and $0.01 < r_s/\mathrm{Mpc} < 6$. We checked the convergence following the $\hat{R}$ test of Gelman and Rubin [253]. We centred the Σ-profiles at the same positions as for the HSE mass reconstruction of each cluster (see Sect. 5.2.1) and searched to minimise:

$$\chi^2 = (\Sigma_{\rm NFW} - \Sigma^{\kappa}_{\rm data})^T C^{-1} (\Sigma_{\rm NFW} - \Sigma^{\kappa}_{\rm data}). \tag{5.18}$$

$\Sigma^{\kappa}_{\rm data}$ is the radially averaged projected mass density profile for each κ-map and $\Sigma_{\rm NFW}$ the model. C is the covariance matrix of the $\Sigma^{\kappa}_{\rm data}$ radial bins and it is built accounting for the 100 realisations provided for each κ-map model (also publicly available[10]) and the uncertainties from the dispersion in each radial bin. The 100 realisation maps correspond to random models from the Monte Carlo chains [271]. From the best-fit NFW density profiles we can reconstruct the lensing mass profiles (Eq. 3.8) and subsequently the $M^{\rm lens}_{500}$.

As an example, we show in Fig. 5.3 the CLASH convergence maps for PSZ2 G144.83+25.11 galaxy cluster (also known as MACS J0647.7+7015), the best-fit NFW mass density model converted into a convergence map and their difference. The difference between the LTM (top) and PIEMD+eNFW (bottom) convergence maps is big enough to impact the fitted NFW density models and therefore, the lensing mass estimates. In the following we account for those differences by considering, when available, the lensing masses estimated from both LTM and PIEMD+eNFW maps.

In Fig. 5.4 we present the radial profiles of the projected mass density for CL J1226.9+3332 obtained from the CLASH LTM (left) and PIEMD+eNFW (right) convergence maps. We show for both profiles the projected best-fit NFW density model and percentiles (shaded area). We observe that for the LTM convergence map the best-fit NFW model underestimates the data except for cluster core and that the uncertainties in the model do not fully account for this. By contrast, the fit for the PIEMD+eNFW succeeds in representing the data.

5.2 The HSE-to-lensing mass bias

To assess the deviation from hydrostatic equilibrium in clusters of galaxies, in this section we compare the resolved HSE mass estimates of individual clusters (obtained as described in chapter 3) with their lensing mass estimates (reconstructed from CLASH convergence maps). As presented in chapter 1, some works in the literature have already performed similar analyses for low redshift clusters ($z < 0.5$) [301], and unique studies have compared the resolved HSE masses obtained from X-ray data to lensing estimates at higher redshifts ($z > 0.5$) [105]. Here we compare, for the first time for a $z > 0.5$ sample, the resolved HSE masses obtained from the combination of SZ and X-ray data to lensing estimates. We also compare the results to the X-ray-only analyses.

5.2.1 The NIKA(2)-CLASH sample

By cross-checking the sample of CLASH clusters with the LPSZ clusters, we built a joint sample that contains the CL J1226.9+3332, PSZ2 G144.83+25.11 and PSZ2 G228.16+75.20 clusters. In addition, we added MACS J1423.8+2404 to the sample, a CLASH cluster that was observed with NIKA (as already mentioned,

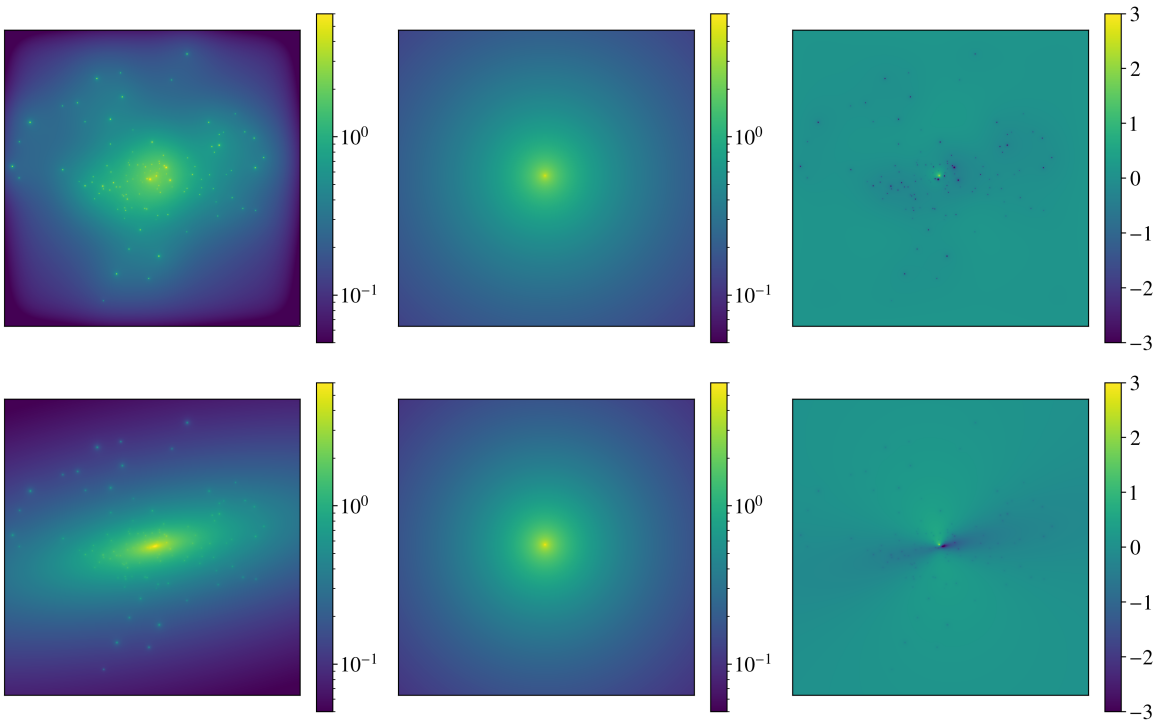

Figure 5.3: CLASH convergence maps, best-fit NFW model and the residual for PSZ2 G144.83+25.11 galaxy cluster. Top: LTM convergence map. Bottom: PIEMD+eNFW.

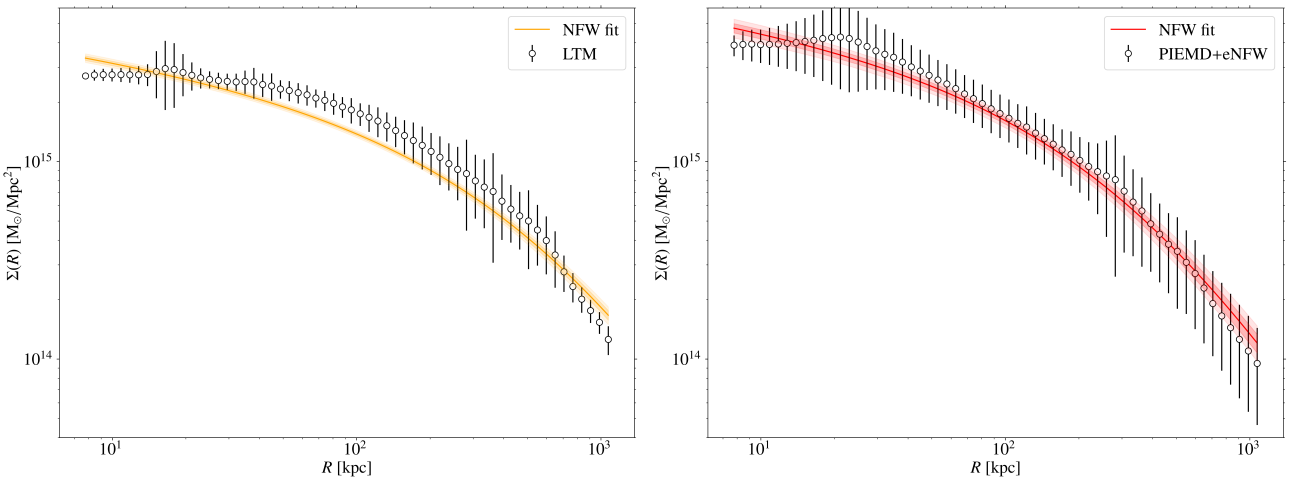

Figure 5.4: Projected mass density profiles obtained from CLASH convergence maps for the LTM (left) and PIEMD+eNFW (right) models for CL J1226.9+3332 galaxy cluster. We also show the best-fit NFW model (orange and red lines) and the 2.5th, 16th, 84th and 97.5th percentiles (shaded areas).

the pathfinder of NIKA2 [223]). We detail in this section the special characteristics of each cluster and show the corresponding mass profiles. The lensing masses for all of them were obtained following the NFW fitting procedure presented in Sect. 5.1.3. Although the general steps to reconstruct the HSE masses are described in chapter 3, we detail the differences from cluster to cluster. Looking for the fairest comparison between the masses of different clusters, in this study we only considered HSE masses obtained from the SZ electron pressure modelled with a gNFW profile (Sect. 3.4).

All the clusters in the NIKA(2)-CLASH sample were also observed by MUSTANG and Bolocam and an SZ analysis that combined data from both instruments allowed to fit a gNFW pressure profile per cluster in Romero et al. (2017) [118]. As shown in chapter 4, the different instrumental capabilities of MUSTANG and Bolocam probe the core and the outskirts of clusters, respectively. The a and b parameters of the gNFW model (Eq. 3.5) were fixed to the values obtained in A10, $a = 1.05$ and $b = 5.49$. We used the gNFW profile parameters given in Table 5 in Romero et al. (2017) [118] to compute the HSE masses per cluster by combining these SZ pressure profiles with the same XMM-*Newton* electron density profiles used to compute NIKA(2) HSE masses. In addition, the archive of *Chandra* data (ACCEPT[11]) [267] contains also the X-ray-only HSE mass profiles for the NIKA(2)-CLASH clusters. Although MUSTANG, Bolocam and *Chandra* profiles were not extracted assuming the exact same centres we considered for NIKA(2), XMM-*Newton* and CLASH, they are very interesting for comparison. On average, the different centres are separated at most by ~ 4 arcsec.

CL J1226.9+3332

The first object in the NIKA(2)-CLASH sample is the already presented CL J1226.9+3332 cluster at $z = 0.89$. The electron density and temperature profiles extracted from XMM-*Newton* data were centred on the XMM-*Newton* X-ray peak, $(\mathrm{RA, Dec})_{\mathrm{J2000}}$ = (12h26m58.08s, +33d32m46.6s). Thus, the electron pressure obtained from SZ data (in chapter 4), as well as the NFW mass density profiles fitted to CLASH convergence maps were centred on the same position.

We present in Fig. 5.5 the different mass profiles for the CL J1226.9+3332 galaxy cluster. The solid blue profile shows the HSE mass from Muñoz-Echeverría et al. (2023) [191] described in chapter 4. It was obtained by combining the gNFW pressure profile from SZ observations and the XMM-*Newton* electron density. We have shown in chapter 4 that the impact of the systematic effects from NIKA2 raw data analysis on the final results is very minor. Thus, here we only consider the "most precise" case, where the pressure profile was reconstructed with the 2D transfer function and the time order noise estimate. Black empty markers show the HSE mass profile from XMM-*Newton* data shown in Fig. 4.13. For comparison, we also present with the dashed blue line and the grey markers the HSE mass estimates obtained by using the pressure reconstruction from Romero et al. (2017) [118] (with 11.8 and 4.9 hours of Bolocam and MUSTANG observations, respectively) and the ACCEPT data (64.4 and 9.8 ks of exposure time for ACIS-I and ACIS-S detectors), respectively. At inner radii the mass profile reconstructed using the pressure from Bolocam and MUSTANG data follows nicely the shape of the XMM-*Newton* mass. In order to avoid any extrapolation we cut the HSE masses from the combination of SZ and X-ray data where the XMM-*Newton* electron density profile ends.

In the same figure, we present the lensing mass profiles obtained from the CLASH LTM (orange) and PIEMD+eNFW (red) convergence maps. The error bars were calculated from the posterior distributions of the model parameters at the end of the fit shown in Fig. 5.4. The envelopes of the lensing mass profiles are very thin compared to the HSE ones. This is due to the small amount of parameters (2 for NFW) that we fit compared to the case of the HSE mass, as well as to the fact that we consider the convergence maps as true. Both profiles end just above 1000 kpc, limited by the size of the convergence maps. The mass at larger radii can only be obtained from the extrapolation of the profiles, where there is no more data.

The vertical lines show the mean R_{500} obtained from each mass profile. The dotted blue and black lines correspond to the HSE mass profiles from NIKA2 and XMM-*Newton* and XMM-*Newton*-only, while the red and orange are the lensing R_{500} from PIEMD+eNFW and LTM convergence maps. The blue dashed line is the

[11] Available at https://web.pa.msu.edu/astro/MC2/accept/

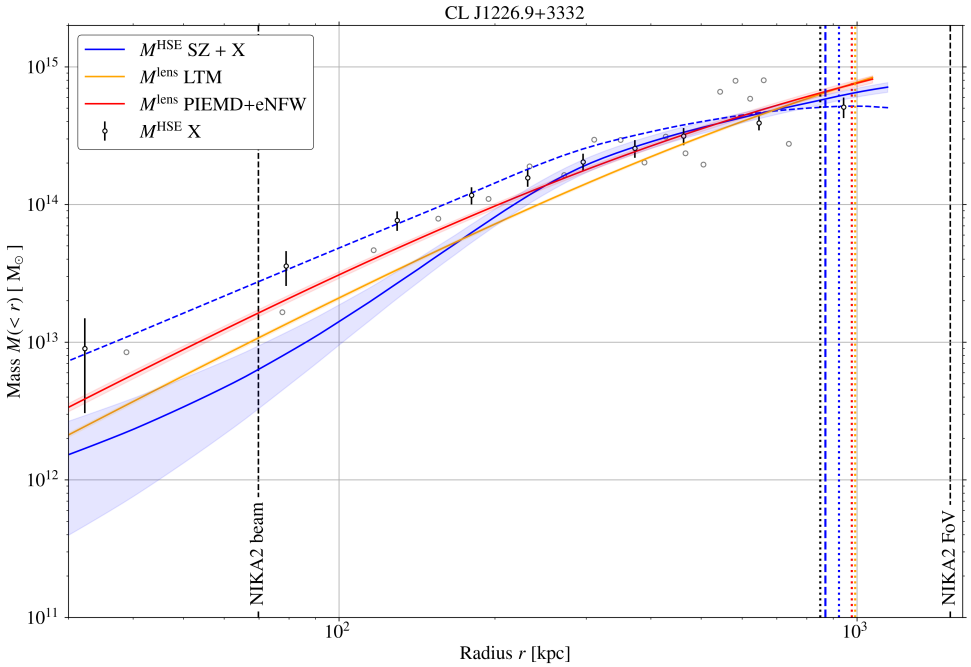

Figure 5.5: Three dimensional mass profiles reconstructed from observations of the CL J1226.9+3332 galaxy cluster. The blue profiles correspond to HSE masses obtained from the combination of SZ pressure and X-ray electron density profiles. The solid blue line was obtained with the gNFW pressure profile from the LPSZ analysis in chapter 4 and the XMM-*Newton* electron density profile. Contours show the 16th to 84th percentiles. The blue dashed line instead was obtained from the gNFW pressure profile reconstructed with Bolocam+MUSTANG data in Romero et al. (2017) [118]. Black and grey empty circles indicate the X-ray-only HSE mass profiles, obtained, respectively, from XMM-*Newton* and *Chandra* data. The error bars in XMM-*Newton* black profiles show the 1σ uncertainties. The lensing mass profiles reconstructed from the CLASH LTM and PIEMD+eNFW convergence maps are shown in orange and red, respectively, with contours indicating 1σ uncertainties. The vertical black dashed lines indicate the instrumental limits of NIKA2 as radius of the beam and FoV. The other vertical lines show the R_{500} for each of the mass profiles with the same colour scheme as the profiles. More details can be found in the text.

R_{500} for the blue dashed profile, i.e. MUSTANG+Bolocam+XMM-*Newton*. ACCEPT data points do not go far enough to define an R_{500}.

PSZ2 G144.83+25.11

The PSZ2 G144.83+25.11 galaxy cluster, at redshift $z = 0.58$, was thoroughly studied with NIKA2, MUSTANG, Bolocam and *Planck* data in Ruppin et al. (2018) [177]. In this work authors performed a complete characterisation of the electron pressure in the ICM of the cluster, accounting for the contamination by point sources in the SZ maps and using the 1D transfer function for NIKA2 data. An overpressure was detected in the south-western region of the cluster and it was shown that such overpressure impacts the pressure profile reconstructed from NIKA2 maps, as well as from X-ray observations. In Fig. 5.6 we show with a solid blue line the HSE mass reconstructed in Ruppin et al. (2018) [177] combining SZ and X-ray observations and with black empty dots the X-ray-only reconstruction, in both cases masking the overpressure region. PSZ2 G144.83+25.11 was observed by NIKA2 and XMM-*Newton* for 11.3 and $\sim$ 18.9 hours ($\sim$ 68 ks), respectively. Limited by the X-ray spectroscopic temperature measurements, the XMM-*Newton* HSE mass profile is here logarithmically extrapolated to reach R_{500} (black dotted line).

In Fig. 5.6 we compare these profiles to other HSE mass reconstructions from the literature (11.7 and 16.4 hours of Bolocam and MUSTANG observations and 39.3 ks with *Chandra*'s ACIS-I): up to $\sim$ 600 kpc there is a very good agreement between all the HSE mass profiles and the dispersion gets more important at larger

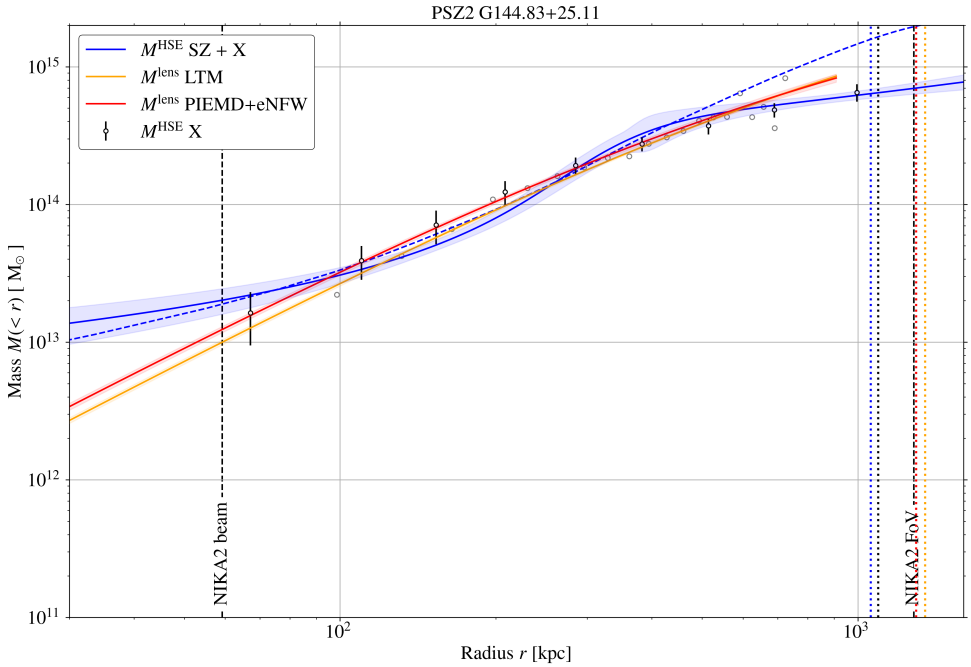

Figure 5.6: Same as Fig. 5.5 for PSZ2 G144.83+25.11 galaxy cluster. The blue contours in this case correspond to the 68% confidence region for the SZ+X HSE mass profile reconstructed in Ruppin et al. (2018) [177].

radii.

The orange and red profiles correspond again to lensing masses from CLASH LTM and PIEMD+eNFW convergence maps (Fig. 5.3). These results were published in Ferragamo et al. (2022) [190], at that time not accounting for the covariance matrix obtained from the 100 convergence maps realisations as described in Sect. 5.1.3. In this thesis we do account for the covariance in the analysis. The angular size of the convergence maps being the same for all clusters, the covered physical area is smaller for PSZ2 G144.83+25.11 as it is at a lower redshift than CL J1226.9+3332. Thus, the lensing mass profiles end before reaching 1000 kpc and have to be extrapolated, following the best-fit NFW model, to reach R_{500}. The profiles in our lensing analyses were centred on (RA, Dec)$_{\rm J2000}$ = (06h47m50.5s, +70d14m53.0s) as in Ruppin et al. (2018) [177].

PSZ2 G228.16+75.20

PSZ2 G228.16+75.20 (z = 0.545), also known as MACS J1149.5+2223, is the third cluster in the NIKA(2)-CLASH sample. As presented in chapter 3, the analysis of the NIKA2 SZ data for this cluster has shown that the thermal emission of the ICM gas is very diffuse and that the thermal SZ is contaminated by many point sources in the field (Fig. 3.4). From multi-wavelength studies in the literature PSZ2 G228.16+75.20 was known to be a massive and impressive lens (see, for example, Smith et al. (2009) [302]) with a complex morphology and radio emission in the ICM [303].

In spite of that, the different HSE mass reconstructions shown in Fig. 5.7 are rather coherent. The solid blue and empty black markers correspond to the mass profiles reconstructed from a gNFW fit to the NIKA2 map combined with the XMM-*Newton* electron density profile and to the XMM-*Newton*-only mass shown in Fig. 3.10, respectively. Extrapolation was needed to reach R_{500}. XMM-*Newton* data was obtained from $\sim$ 7.5 hours of observation, MUSTANG and Bolocam observed PSZ2 G228.16+75.20 for 13.9 and 17.7 hours, respectively, and *Chandra* had 38.5 ks of exposure time with ACIS-I.

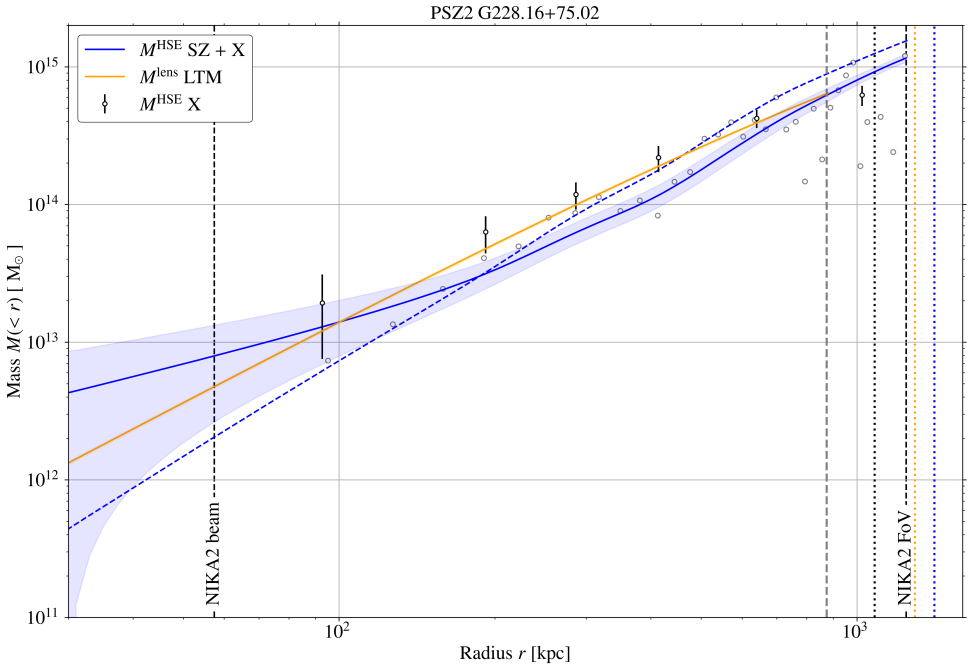

Figure 5.7: Same as Fig. 5.5 for PSZ2 G228.16+75.20 galaxy cluster. The blue contours show the 16th to 84th percentiles for the SZ+X HSE mass profile reconstructed from NIKA2 and XMM-*Newton* data. The vertical grey dashed line shows the R_{500} corresponding to the HSE mass profile from *Chandra* data, which for this cluster reaches R_{500}.

Probably due to the complex matter distribution in this cluster [304], fitting a PIEMD+eNFW model to lensing data was not reasonable and only a LTM convergence map is available for PSZ2 G228.16+75.20. The reconstructed lensing mass, centred at (RA, Dec)$_{\rm J2000}$ = (11h49m35.43s, +22d24m03.89s), is shown in orange in Fig.5.7.

MACS J1423.8+2404

The last cluster in the sample is MACS J1423.8+2404 (z = 0.545). It was observed with the NIKA camera in February 2014 (for 1.47 hours on-target) and its thermodynamical properties were studied in Adam et al. (2016) [225]. The SZ signal of this cluster is strongly contaminated by point sources (Fig. 1 in Adam et al. (2016) [225]), with a radio source that compensates completely the SZ signal in the core of MACS J1423.8+2404. We use here the HSE masses estimated in Adam et al. (2016) [225], considering the M2 method, where point sources were subtracted from the 150 GHz NIKA map before modelling the thermal pressure profile. A gNFW pressure model was directly fit to the NIKA map. In addition, MUSTANG and Bolocam observed MACS J1423.8+2404 for 11.2 and 21.7 hours, respectively. The mass from the combination of NIKA SZ and X-ray data is shown with the solid blue line in Fig. 5.8. We observe that it converges with the MUSTANG+Bolocam+X-ray mass profile (dashed blue) towards the outskirts of the cluster, around R_{500}.

In Adam et al. (2016) [225] two different X-ray data sets were used to reconstruct the X-ray-only thermodynamical quantities, from XMM-*Newton* and *Chandra* instruments. In Fig. 5.8 we present in black the HSE mass obtained from XMM-*Newton* data (from 109 ks ~ 30 hours of observations), which is in agreement with *Chandra* (grey markers) at intermediate radii. *Chandra* data corresponds to 18.5 ks of exposure time with ACIS-I and 115.6 ks with ACIS-S.

The two lensing mass profiles, reconstructed considering the XMM-*Newton* profile extraction centre (RA, Dec)$_{\rm J2000}$ = (14h23m47.9s, +24d04m42.3s), follow closely the HSE masses.

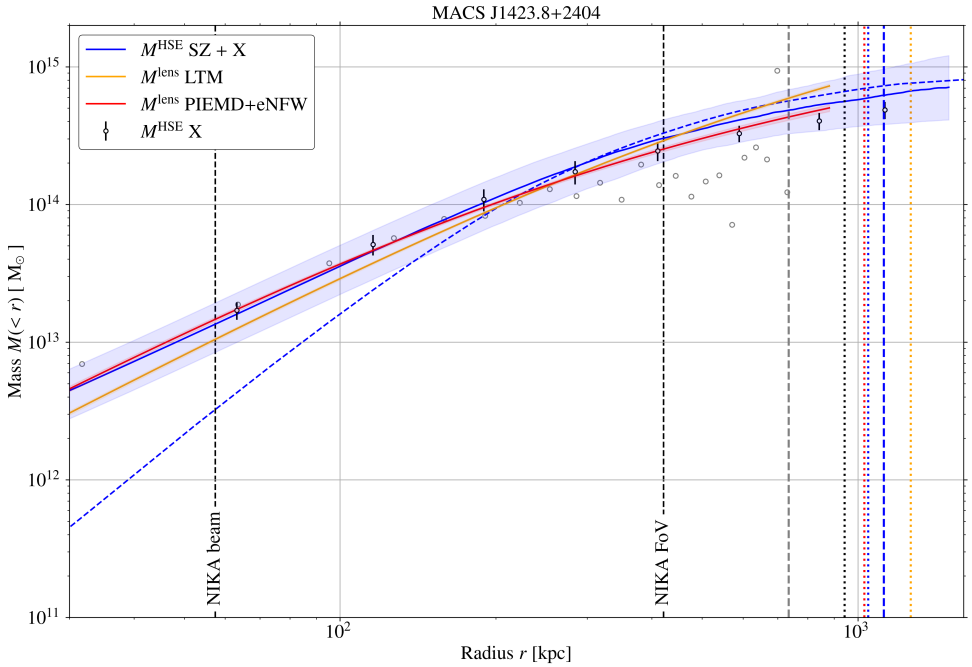

Figure 5.8: Same as Fig. 5.5 for the MACS J1423.8+2404 cluster. The blue shaded area shows the 68% confidence limit from the M2 model in Adam et al. (2016) [225]. Here the vertical black dashed lines indicate the instrumental limits of NIKA as radius of the beam and FoV.

Overall, from the comparison of the mass profiles for these four clusters we do not see any hint that indicates a systematic over or underestimation of the HSE masses reconstructed using NIKA(2) and/or XMM-*Newton* data. For the sake of simplicity, in the following we will only use the HSE mass estimates obtained with NIKA(2) and XMM-*Newton* data.

5.2.2 Comparison of M_{500} estimates

We have seen that galaxy cluster masses are commonly defined as integrated quantities and the consensus in the cluster cosmology analyses during the last years [6, 8] has been to use the masses defined at the $\Delta = 500$ overdensity (Sect. 3.4.3). In this context, from each of the previously presented mass profiles we calculated the corresponding M_{500} and R_{500}. In the following, we compare our results to other mass estimates from the literature. As verified for the HSE masses of the CL J1226.9+3332 galaxy cluster presented in chapter 4, not all the masses in the literature are given homogeneously and comparisons have to be done with care. In addition, we have to keep in mind that although high angular resolution observations enable reconstructing entirely resolved mass profiles, the retained information is reduced to the region where the $R_{500} - M_{500}$ relation crosses the profile (Eq. 3.10). Even so, we present cluster by cluster the comparison of different HSE and lensing results. For the sake of completeness, when available in the literature, we also compare to dynamical masses or to mass estimates reconstructed under the assumption of virial equilibrium (Sect. 4.1.2).

CL J1226.9+3332

The HSE mass of CL J1226.9+3332 galaxy cluster has been thoroughly studied in chapter 4, presenting in Fig. 4.15 a summary of all the HSE estimates around M_{500}. In the same way, we show in Fig. 5.9 all the masses at M_{500} or close to M_{500} found in the literature (summarised in Table 4.1), compared to our results. The lensing

M_{500} estimates reconstructed from the CLASH LTM and PIEMD+eNFW convergence maps are presented as orange and red contours, respectively. The lensing M_{500} from other works are shown as brown stars, while mass estimates evaluated at a radius other than R_{500} are represented with crosses.

We observe that our lensing reconstructions are consistent with the lensing mass from Sereno (2015) [281] and Sereno and Covone (2013) [280] (the brown star just above 1000 kpc) and with some of the HSE mass estimates. On the contrary, they are very different from the Merten et al. (2015) [279] lensing mass (the brown star in the top right corner). In Merten et al. (2015) [279] authors performed an independent analysis of the CLASH data, reconstructing their own convergence map. The projected mass density profile presented in Fig. 16 in Merten et al. (2015) [279] shows a denser cluster than the profiles from the convergence maps that we use (Fig. 5.4). For this reason, Merten et al. (2015) [279] obtained, also with an NFW density fit, 35% higher masses than Jee and Tyson (2009) [264]. The disturbed state of CL J1226.9+3332 could be the reason, according to Merten et al. (2015) [279], for the different lensing mass estimates. Moreover, the high redshift of the cluster makes the precise reconstruction of the convergence map more difficult.

The virial masses estimated in Mroczkowski (2011) [273] and Mroczkowski (2012) [274] are indicated in Fig. 5.9 with magenta squares. As explained in Sect. 4.1.2, they rely on the virial relation and on given pressure and density profile models to relate directly the SZ flux to the mass (Eq. 15 in Mroczkowski (2011) [273]). This kind of analysis seems a good alternative to the HSE mass for clusters without X-ray data. The dynamical mass estimates (purple circles), which we would expect to be larger than the HSE estimates, appear particularly low for CL J1226.9+3332 [140]. According to the $M_{500}^{\rm SZ} - M_{500}^{\rm dyn}$ scaling relation obtained from the analysis of 297 *Planck* galaxy clusters in Aguado-Barahona et al. (2022) [140] (Eq. 8 and Table 2) and considering $M_{500}^{\rm SZ}$ the value in Planck Collaboration et al. (2016) [142], the dynamical mass corresponding to CL J1226.9+3332 should be in the range $6 - 7.5 \times 10^{14}\,{\rm M}_{\odot}$, thus more in agreement with our lensing mass estimates. Similar problems are reported in Ettori et al. (2019) [175] and Logan et al. (2022) [305], the latter showing that a large number of galaxies with spectroscopic redshift measurements (> 200) are needed to get robust results. The orientation of the merger could also be an explanation for the underestimation of the dynamical mass: if the merger is happening in the plane of the sky, the dispersion, and thus the mass, is lower.

PSZ2 G144.83+25.11

In Table 5.1 we present the HSE and lensing mass estimates of PSZ2 G144.83+25.11 galaxy cluster found in the literature and we compare them to our M_{500} estimates (contours) in Fig. 5.10. The blue 1σ contour corresponds to the $M_{500}^{\rm HSE}$ mass obtained from the combination of SZ and X-ray data in Ruppin et al. (2018) [177], while the grey contour is the XMM-*Newton*-only HSE mass. For PSZ2 G144.83+25.11 the HSE masses tend to have lower values than the lensing estimates. Furthermore, we notice some discrepancies between the different lensing mass estimates. The two $M_{500}^{\rm lens}$ masses that we reconstructed from LTM and PIEMD+eNFW convergence maps lie between the different results from the literature.

In this thesis we have only considered the HSE masses from the analysis in Ruppin et al. (2018) [177] for which the overpressure region is masked. It was shown by Ruppin et al. (2018) [177] and Ferragamo et al. (2022) [190] that for this cluster SZ+X hydrostatic mass reconstructions are strongly affected by including or excluding the overpressure: the measured masses vary by $\sim 50\%$ both at a fixed radius close to R_{500} and at the $R_{500}^{\rm HSE}$ estimated from each profile. Only high angular resolution observations allow one to detect such kind of effects on the morphological state of the clusters and evaluate how much they affect the mass reconstructions.

PSZ2 G228.16+75.20

For PSZ2 G228.16+75.20 we present in Fig. 5.11 the masses at and around M_{500} from the literature (summarised in Table 5.2) and our results. X-ray-only HSE masses prefer lower values than the hydrostatic masses from the combination of SZ and X-rays. One could also think that the blue contours, showing the $M_{500}^{\rm HSE}$ from the combination of NIKA2 and XMM-*Newton* data, are overestimating the HSE mass. Nevertheless, the comparison to the MUSTANG+Bolocam+XMM-*Newton* mass profile (dashed blue line) in Fig. 5.7 confirms such

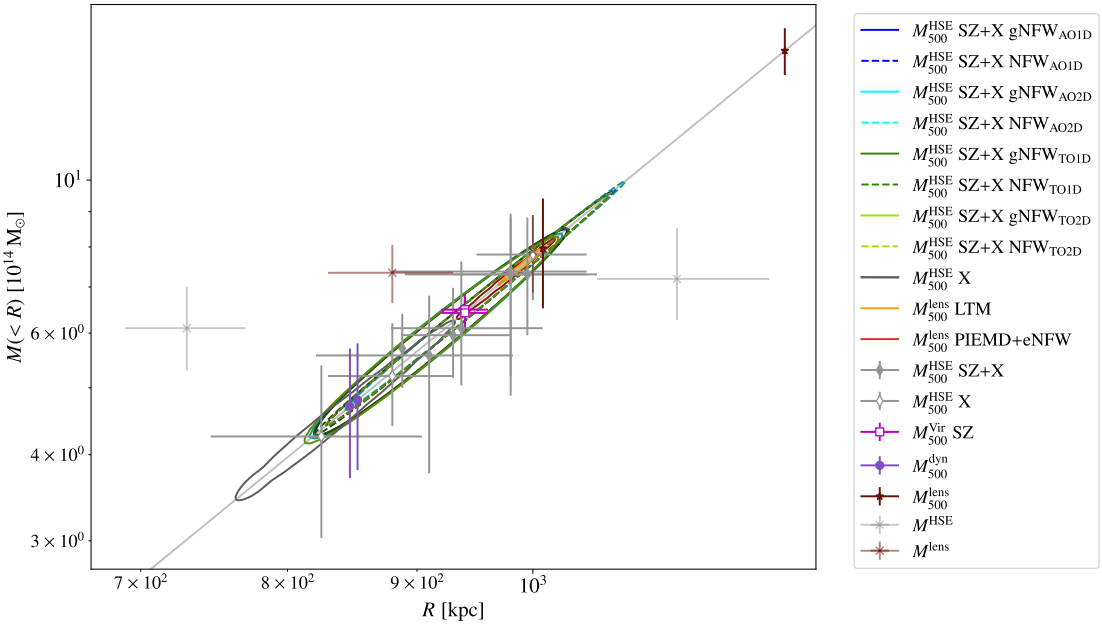

Figure 5.9: Same as Fig. 4.15 but including other mass estimates in addition to HSE masses. The orange and red contours correspond to the lensing mass estimates obtained from the CLASH LTM and PIEMD+eNFW convergence maps in this work, respectively. Magenta squares show the SZ-only mass assuming virial relation, purple circles are dynamical mass estimates, and brown stars the lensing estimates. Brown crosses show lensing masses from the literature close to M_{500}. The diagonal bright grey line defines the $R_{500} - M_{500}$ relation. Slight deviations from this line are again due to differences in the cosmological model used in each work. Figure from Muñoz-Echeverría et al. (2023) [191].

Table 5.1: Mass estimates found in the literature for PSZ2 G144.83+25.11 (equivalent to Table 4.1). We differentiate the masses reconstructed from ICM observables and from the lensing effect on background sources. We give the radius at which each mass is evaluated when available. When the mass has been evaluated at a given $R = R_\Delta$ we also present the value of the overdensity Δ.

Observable	R [kpc]	Δ	$M(< R)$ [10^{14} M$_\odot$]	Reference	Comments
ICM					
	65″	-	$2.6^{+1.5}_{-0.5} h^{-1}$	LaRoque et al. (2003) [306]	
	-	500	$8.22^{+0.71}_{-0.73}$	Planck Collaboration et al. (2016) [142]	Scaling relation
	1180.0	500	8.8556	Piffaretti et al. (2011) [307]	Scaling relation
	-	200	11.69 ± 1.46	Javid et al. (2019) [308]	
	-	500	7.32 ± 0.89	Javid et al. (2019) [308]	
Lensing					
	-	200	13.824 ± 4.177	Umetsu et al. (2016) [309], Sereno (2015) [281][8]	
	-	500	9.427 ± 2.493	Umetsu et al. (2016) [309], Sereno (2015) [281][8]	
	-	2500	3.683 ± 0.97	Umetsu et al. (2016) [309], Sereno (2015) [281][8]	
	500	-	3.668 ± 0.64	Umetsu et al. (2016) [309], Sereno (2015) [281][8]	
	1000	-	7.992 ± 1.413	Umetsu et al. (2016) [309], Sereno (2015) [281][8]	
	1500	-	11.608 ± 2.381	Umetsu et al. (2016) [309], Sereno (2015) [281][8]	
	-	500	7.7 ± 2.7	Umetsu et al. (2014) [310]	
	1500	-	$13.3^{+5.7}_{-5.6}$	Applegate et al. (2014) [311]	
	1500	-	$14.9^{+5.2}_{-5.3}$	Applegate et al. (2014) [311]	

Table 5.2: Equivalent to Table 4.1 for PSZ2 G228.16+75.20 galaxy cluster.

Observable	R [kpc]	Δ	$M(<R)$ [10^{14} $M_\odot$]	Reference	Comments
ICM					
	65″	-	$1.5^{+0.9}_{-0.3}h^{-1}$	LaRoque et al. (2003) [306]	
	-	500	$10.42^{+0.52}_{-0.55}$	Planck Collaboration et al. (2016) [142]	Scaling relation
	1220.0	500	9.3427	Piffaretti et al. (2011) [307]	Scaling relation
	-	200	15.63 ± 1.66	Javid et al. (2019) [308]	
	-	500	9.78 ± 1.01	Javid et al. (2019) [308]	
Lensing					
	-	200	24.855 ± 5.494	Umetsu et al. (2016) [309], Sereno (2015) [281][8]	
	-	500	14.447 ± 3.034	Umetsu et al. (2016) [309], Sereno (2015) [281][8]	
	-	2500	3.68 ± 1.095	Umetsu et al. (2016) [309], Sereno (2015) [281][8]	
	500	-	3.439 ± 0.483	Umetsu et al. (2016) [309], Sereno (2015) [281][8]	
	1000	-	9.41 ± 1.04	Umetsu et al. (2016) [309], Sereno (2015) [281][8]	
	1500	-	15.625 ± 1.852	Umetsu et al. (2016) [309], Sereno (2015) [281][8]	
	-	500	14.2 ± 3.4	Umetsu et al. (2014) [310]	
	500	-	6.7 ± 0.4	Smith et al. (2009) [302]	Projected
	1500	-	$14.4^{+3.3}_{-3.3}$	Applegate et al. (2014) [311]	
	1500	-	$13.6^{+3.1}_{-3.1}$	Applegate et al. (2014) [311]	
	-	500	$7.06 \pm 0.30h^{-1}$	Penna-Lima et al. (2017) [189]	
Galaxy dynamics					
	-	500	14.6 ± 8.9	Aguado-Barahona et al. (2022) [140]	13 galaxies
	-	500	16.0 ± 11.1	Aguado-Barahona et al. (2022) [140]	11 galaxies

a high profile. In any case, PSZ2 G228.16+75.20 is known for its complex morphology, so the hydrostatic equilibrium hypothesis is most probably inappropriate for this cluster.

Purple markers in Fig. 5.11 show the mass estimates from the analysis of the dynamics of the galaxies in the cluster. Given the little amount of galaxies (13 and 11), these estimates are highly uncertain. The projected mass from Smith et al. (2009) [302] provided in Table 5.2 is not presented in Fig. 5.11 to avoid confusion between spherical and projected masses.

MACS J1423.8+2404

The results for MACS J1423.8+2404 are shown and summarised in Fig. 5.12 and Table 5.3. The orange and red contours corresponding to the $M_{500}^{\rm lens}$ reconstructions from the LTM and PIEMD+eNFW convergence maps are not compatible, showing the impact that the modelling of the lens has on the mass estimates. Since the lensing mass profiles in Fig. 5.8 are extrapolated to reach R_{500} (as done for PSZ2 G144.83+25.11 and PSZ2 G228.16+75.20), the estimates could be unreliable. Lensing mass estimates from the literature seem to be more in line with the mass obtained from the PIEMD+eNFW map. The very large uncertainties of the HSE mass reconstructed from NIKA and XMM-*Newton* data (blue contour) make the result compatible with all the other M_{500} estimates.

In conclusion, the estimation of the mass of individual clusters is very complex and subject to different systematic effects. The reconstructed masses vary depending on the used observables, data sets and considered hypotheses and models. Most often uncertainties of mass estimates are not large enough to account for this. However, overall, the HSE and lensing masses that we have reconstructed from NIKA(2), XMM-*Newton* and CLASH data are coherent with the results from previous works. From the comparison of HSE and lensing

Table 5.3: Equivalent to Table 4.1 for MACS J1423.8+2404.

Observable	R [kpc]	Δ	$M(<R)$ [10^{14} $M_\odot$]	Reference	Comments
ICM					
	65″	-	$1.6^{+1.0}_{-0.3}h^{-1}$	LaRoque et al. (2003) [306]	
	990.0	500	4.9804	Piffaretti et al. (2011) [307]	Scaling relation
	-	$178\Omega_m(z)^{0.45}$	$4.52^{+0.79}_{-0.64}h^{-1}$	Schmidt and Allen (2007) [312]	$h = 0.7$
Lensing					
	-	200	8.107 ± 1.422	Merten et al. (2015) [279], Sereno (2015) [281][8]	
	-	500	5.826 ± 0.853	Merten et al. (2015) [279], Sereno (2015) [281][8]	
	-	2500	2.551 ± 1.134	Merten et al. (2015) [279], Sereno (2015) [281][8]	
	500	-	2.768 ± 0.293	Merten et al. (2015) [279], Sereno (2015) [281][8]	
	1000	-	5.588 ± 0.613	Merten et al. (2015) [279], Sereno (2015) [281][8]	
	1500	-	7.799 ± 1.007	Merten et al. (2015) [279], Sereno (2015) [281][8]	
	65″	-	4.35 ± 0.6	Limousin et al. (2010) [313]	Projected
	1500	-	$3.7^{+2.8}_{-2.2}$	Applegate et al. (2014) [311]	
	1500	-	$8.8^{+3.6}_{-3.6}$	Applegate et al. (2014) [311]	

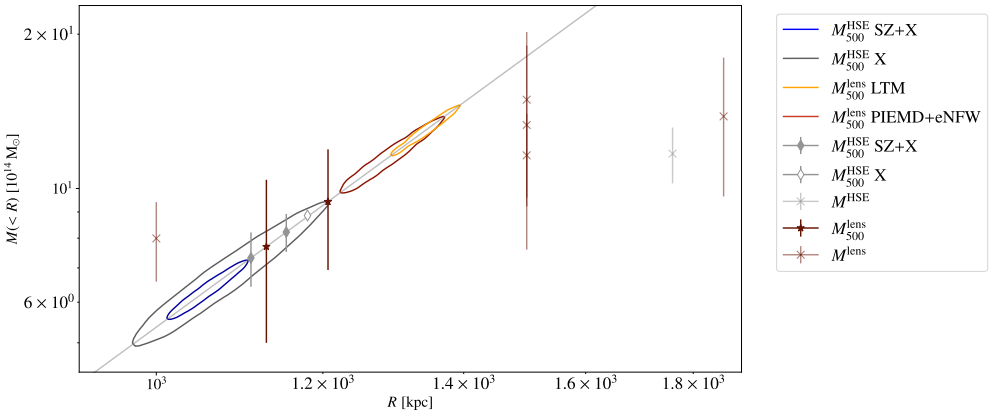

Figure 5.10: Same as Fig. 5.9 but for PSZ2 G144.83+25.11.

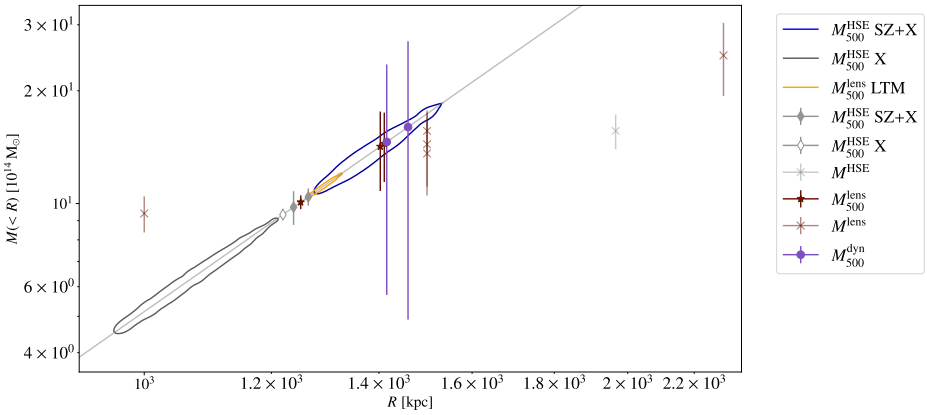

Figure 5.11: Same as Fig. 5.9 but for PSZ2 G228.16+75.20.

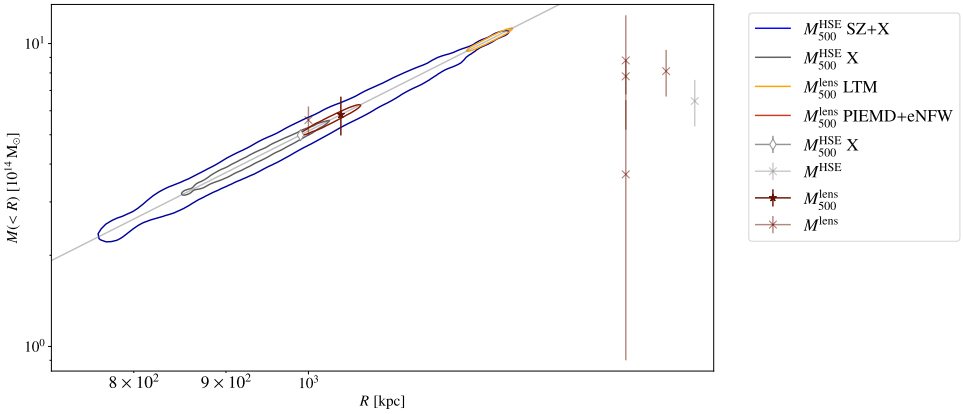

Figure 5.12: Same as Fig. 5.9 but for MACS J1423.8+2404.

estimates, the latter seem to prefer larger mass values. We discuss in the next section the HSE-to-lensing mass bias.

5.2.3 The HSE-to-lensing mass bias

We do not expect the HSE hypothesis to be fulfilled by all galaxy clusters in the Universe and we want to measure how far clusters might be from the hydrostatic equilibrium assumption. As defined in Eq. 1.47, the HSE mass bias is the relative difference between the true mass and the HSE mass of clusters. From the observational point of view, the real HSE bias is unachievable as one cannot determine the true mass of a cluster. However, it can be approximated using mass estimates that do not rely on the HSE hypothesis and trace the total mass of the cluster, for instance, the lensing mass.

In this section we compute the hydrostatic-to-lensing mass bias, $b_{\rm HSE/lens}$, using the results obtained for the clusters in the NIKA(2)-CLASH sample (see Sereno and Ettori (2015) [314] for an analysis of the CoMaLit samples). Assuming that HSE and lensing masses are uncorrelated estimates, we combined their probability distributions and computed the ratio,

$$M_{500}^{\rm HSE}/M_{500}^{\rm lens} = 1 - b_{\rm HSE/lens}. \tag{5.19}$$

We present in Fig. 5.13 the probability density distributions of the HSE-to-lensing mass bias for the four clusters in the NIKA(2)-CLASH sample, with a different colour for each cluster. Solid lines show the bias obtained when considering the LTM convergence maps to estimate the lensing mass. Dashed lines correspond to the bias when using the PIEMD+eNFW lensing estimates. In the left panel, we present the bias for HSE masses obtained from the combination of NIKA(2) pressure profiles and X-ray electron densities, while the distributions in the right panel show the biases with X-ray-only HSE masses from XMM-*Newton* profiles.

For CL J1226.9+3332 both $M_{500}^{\rm lens}$ estimates are in agreement (Fig. 5.9) and the bias of the SZ+X hydrostatic mass is compatible with 0, meaning that lensing masses are consistent with the $M_{500}^{\rm HSE\ SZ+X}$. The complex morphology of PSZ2 G228.16+75.20 makes the spherical modelling results difficult to interpret. Even if our $M_{500}^{\rm HSE\ SZ+X}$ estimate is consistent with Planck Collaboration et al. (2016) [142], uncertainties are large and, as aforementioned, the spherical and equilibrium assumptions doubtful. In the left panel the HSE-to-lensing mass ratio for PSZ2 G228.16+75.20 is larger than 1, meaning a negative HSE mass bias. For PSZ2 G144.83+25.11 the SZ data is of very good quality (see Ruppin et al. (2018) [177]) and the spherical electronic pressure profile, having masked the overpressure region, fits very nicely the data. This gives a very well defined HSE mass estimate (Fig. 5.10) and, consequently, small error bars on the HSE-to-lensing mass bias. The two $M_{500}^{\rm lens}$ estimates for PSZ2 G144.83+25.11 are also in agreement within 1σ uncertainties. On the contrary, the two

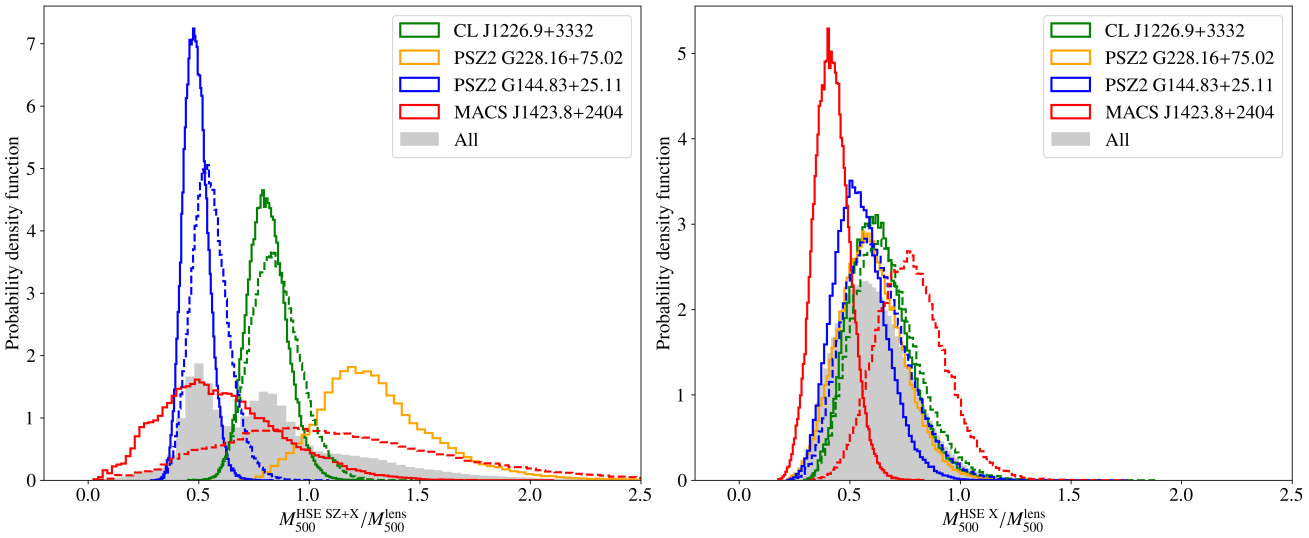

Figure 5.13: The HSE-to-lensing mass ratio at R_{500} for the clusters in the NIKA(2)-CLASH sample, using HSE masses from the combination of NIKA(2) pressure profiles and XMM-*Newton* electron density profiles (left), and, using XMM-*Newton* electron density and spectroscopic temperature profiles (right). In green, orange, blue and red the CL J1226.9+3332, PSZ2 G228.16+75.20, PSZ2 G144.83+25.11 and MACS J1423.8+2404 clusters, respectively. We distinguish with solid and dashed lines the HSE-to-lensing mass ratios obtained with the LTM and PIEMD+eNFW lensing mass estimates. The grey distributions show the HSE-to-lensing mass ratios for the full sample.

incompatible $M_{500}^{\rm lens}$ estimates for MACS J1423.8+2404 (Fig. 5.12) create two distinct HSE-to-lensing mass bias distributions.

The HSE-to-lensing mass ratio distributions presented in the left panel in Fig. 5.13 span from 0 to 2, showing a variety of results for different clusters. In the right panel, where HSE masses correspond to X-ray-only estimates, the biases for different clusters are more alike. Grey histograms show in Fig. 5.13 the HSE-to-lensing mass ratio from the combination of all the NIKA(2)-CLASH clusters, considering both the LTM and PIEMD+eNFW results. We account for the estimates obtained from both convergence map models since there are no clear reasons to favour any of them. The mean values of the distributions with 16th and 84th percentiles are given in Table 5.4. We observe two differences between the SZ+X and X-ray-only biases. First, the distribution of the bias when using SZ+X hydrostatic masses is two times larger than for the masses from X-ray observations. Secondly, the mean HSE-to-lensing mass ratio is smaller for X-ray-only masses, so the bias is larger. This result is in line with the tendency observed for CL J1226.9+3332 in Sect. 4.4.1, where the HSE masses obtained only from X-ray data tend to lower values than those from the combination of SZ and X-rays. Nevertheless, both biases are compatible. Simulations [86] predict that the way in which the derivative of the pressure is computed, in order to estimate the HSE mass profile (Eq. 1.45), has an important impact on the scatter of the profiles at $\sim R_{500}$. According to Ansarifard et al. (2020) [86], if a clump is present in a cluster, it will affect more the derivative of the pressure profile (as done for SZ data, Eq. 1.45) than the sum of the derivatives of the gas density profile and the temperature (as done in the X-ray-only analyses, Eq. 1.46). As a consequence, the scatter of the HSE bias in a sample of clusters is larger for SZ+X-ray masses than for X-ray-only masses [86].

Radial extrapolation of lensing mass profiles was needed to measure the $M_{500}^{\rm lens}$ for PSZ2 G228.16+75.20, PSZ2 G144.83+25.11 and MACS J1423.8+2404 clusters. To avoid extrapolating the profiles we have also compared the HSE-to-lensing mass bias in an inner region of clusters, at an overdensity of $\Delta = 1000$. We show in Fig. 5.14 all the HSE-to-lensing mass ratios. In this case, from the combination of the four clusters we obtain smaller biases (see Table 5.4), but compatible with those at $\Delta = 500$. This result is in agreement with simulations [86, 179], where authors conclude that the HSE mass bias (calculated with respect to the true mass of clusters) increases at large radii, most probably due to an important presence of non-thermal processes

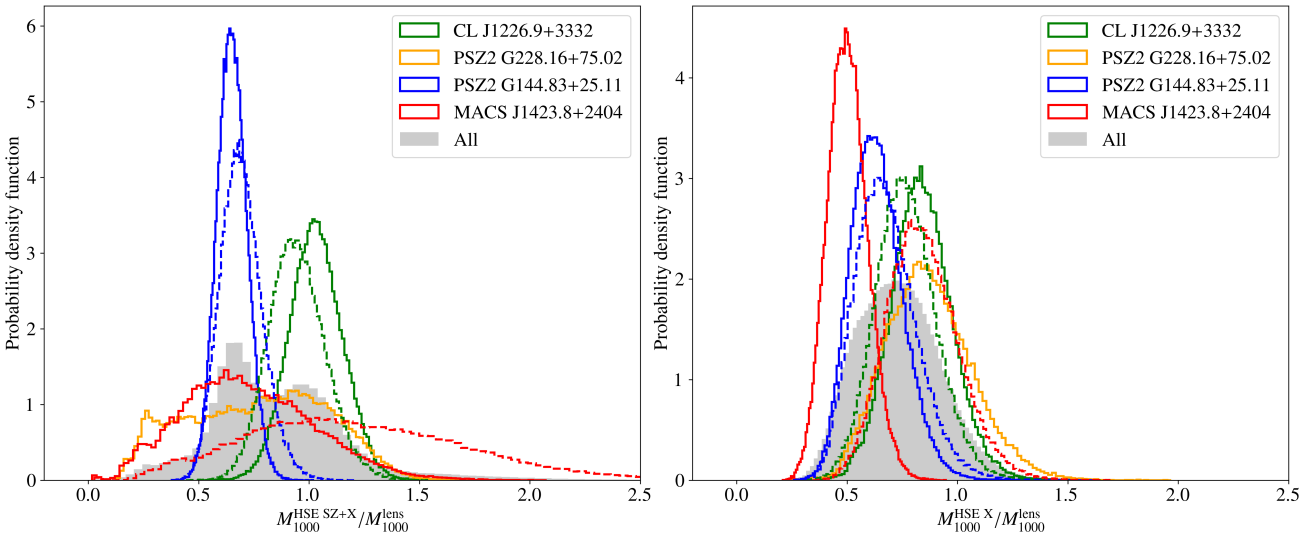

Figure 5.14: The HSE-to-lensing mass ratio at R_{1000} for the clusters in the NIKA(2)-CLASH sample. Equivalent to Fig. 5.13.

Δ	$M_\Delta^{\rm HSE\ SZ+X}/M_\Delta^{\rm lens}$	$M_\Delta^{\rm HSE\ X}/M_\Delta^{\rm lens}$
500	$0.82^{+0.36}_{-0.34}(0.76)$	$0.61^{+0.17}_{-0.17}(0.59)$
1000	$0.86^{+0.26}_{-0.27}(0.82)$	$0.74^{+0.19}_{-0.20}(0.73)$

Table 5.4: HSE-to-lensing mass ratio for the clusters in the NIKA(2)-CLASH sample at overdensities of $\Delta = 500$ and 1000 for HSE masses obtained from the combination of SZ and X-ray data and with X-ray data only. We give the mean value and the 84th and 16th percentiles, and the median value in brackets.

in the outskirts of clusters. Nonetheless, the size of our sample is very small to draw strong conclusions. The tendency of X-ray HSE masses to be more biased than SZ+X masses is also observed at $\Delta = 1000$.

These results highlight the impact that systematic effects can have on our mass estimates and as a consequence on the bias. We see that the data quality, the cluster morphology and dynamical state, as well as the chosen observables and the modelling influence the mass bias. Although the SZ effect and the X-ray observations are both supposed to trace the thermal energy of the gas in the ICM of clusters, we observe that, in practice, for individual clusters, they can drive to different results.

Previous works in the literature have followed similar approaches. In Ettori et al. (2019) [175] authors reconstructed the HSE mass profiles of 13 nearby ($0.04 < z < 0.1$) clusters (12 from the X-COP sample and Abell 780) by using *Planck* and XMM-*Newton* data. They compared the HSE masses to masses obtained from weak lensing, scaling relations, galaxy dynamics and caustics, by evaluating the hydrostatic mass profiles at the radius defined by the other methods at a given overdensity. From the comparison of HSE and weak lensing masses for 6 of the clusters in the X-COP sample they obtained an average ratio of $M_{500}^{\rm lens}/M_{500}^{\rm HSE} \sim 1.14 - 1.18$, that is, $M_{500}^{\rm HSE}/M_{500}^{\rm lens} \sim 0.88 - 0.85$, which is in agreement with our results.

Also in the framework of the X-COP sample, the analysis in Eckert et al. (2019) [53] investigated the contribution of non-thermal pressure to the total pressure in clusters. They used again HSE masses from combined XMM-*Newton* X-ray and *Planck* SZ data and assuming a universal gas fraction, from the measurements of the gas fraction in the galaxy clusters in the sample they obtained that the contribution of non-thermal pressure is very low: $5.9^{+2.9}_{-3.3}\%$ at R_{500}. This corresponds to a median bias for their sample of $M_{500}^{\rm HSE}/M_{500}^{\rm tot} = 0.94 \pm 0.04$. As stated in Eckert et al. (2019) [53], according to simulations the presence of non-thermal pressure is expected to be more important at higher redshift (see for example Fig. 1 in Nelson et al. (2014) [63]), which should imply also a larger bias for HSE masses. Nevertheless, given the small redshift range covered by the clusters in Eckert et al. (2019) [53] and Ettori et al. (2019) [175], all of them being at $z < 0.1$, this evolution could not be proved

in their works.

Other works in the literature [189, 315, 316] compared SZ-derived masses to lensing estimates, but using HSE mass estimates obtained from SZ-mass scaling relations applied to SZ measurements. For high redshift clusters such SZ observations (obtained with *Planck* for the mentioned works) are not resolved enough to reconstruct reliable mass profiles. As we have shown, the identification of substructures, departures from sphericity and contamination by point sources in galaxy clusters impact the HSE mass estimates. To study high redshift clusters and a potential evolution of their characteristics with respect to low redshift clusters high angular resolution observations are necessary. Therefore, the arrival of high-resolution SZ observations is an important step forward and it makes this small NIKA(2)-CLASH sample a unique opportunity to constrain the HSE-to-lensing mass bias at high redshift.

5.3 Gas-to-lensing mass fraction

The baryon content in clusters of galaxies is considered to be representative of the universal baryon fraction [50] and most of the baryonic matter in galaxy clusters is in the form of hot gas in the ICM. Thus, it is interesting to estimate the fraction of gas mass with respect to the total mass of the clusters, since it can be used as a cosmological probe (see Sect. 1.2.3).

The gas mass of a cluster can be calculated with X-ray data following Eq. 1.57 and assuming a mean molecular weight of the electrons, μ_e, so that $\rho^{gas} = \mu m_p(n_e + n_p) = \mu_e m_p n_e$. We fixed $\mu_e = 1.148$ as in Arnaud et al. (2010) [70], but this value varies from work to work in the literature. For example, in Eckert et al. (2019) [53] the ratio of electron and proton number densities is fixed to $n_e = 1.17 n_p$ and $\mu = 0.61$, so that $\mu_e = 1.13$. The difference in the value of μ_e between Arnaud et al. (2010) [70] and Eckert et al. (2019) [53] is propagated to the gas mass estimate.

Assuming that lensing masses are a good proxy of the total mass in clusters, we can approximate (as in Ferragamo et al. (2022) [190]) the gas mass fraction by the gas-to-lensing mass fraction. We present in Fig. 5.15 the ratio of gas mass with respect to lensing mass for all the clusters in the NIKA(2)-CLASH sample. We use the lensing masses reconstructed from CLASH LTM (solid lines) and PIEMD+eNFW (dashed lines) convergence maps and present the radial profiles normalised with respect to the corresponding R_{500}^{lens} for each case. We observe that, in agreement with previous works, the gas fraction within clusters increases with radius, although, as above-mentioned, extrapolation was needed in most of the cases to reach R_{500}^{lens}.

From these results we obtain that the mean gas-to-lensing mass fraction for NIKA(2)-CLASH clusters at R_{500} is: $M^{gas}/M^{lens}(R_{500}^{lens}) = 0.11 \pm 0.02$. Assuming that lensing masses are unbiased estimates of the total mass of clusters, we can compare this value to the universal baryon fraction by using the baryon density, $\Omega_b h^2 = 0.0224 \pm 0.0001$, and the matter density parameter, $\Omega_m = 0.315 \pm 0.007$, from Planck Collaboration et al. (2020) [28]. Considering $h = 0.674$ [28] and no correlation between the parameters, we calculate the universal baryon fraction: $\Omega_b/\Omega_m = 0.157 \pm 0.004$.

Nonetheless, additional considerations are needed to compare the gas mass fraction in clusters to the universal baryon fraction (see Eq. 1.39). First, not all the baryonic content of clusters is in the form of hot gas and the cold gas or stellar content is estimated to hold $\lesssim 6\%$ of the total matter in clusters [317]. From a compilation of works, authors in Eckert et al. (2019) [53] estimated the stellar fraction in clusters to be $1.5 \pm 0.5\%$ of the total matter. Second, the gas in clusters is affected by baryonic physics (such as the heating by AGNs) which can deplete the gas content by driving it out of the potential wells. This gas depletion has been widely studied from hydrodynamical simulations and observations (e.g., Planelles et al. (2013) [318] and references therein) and it is estimated to deplete $\sim 6\%$ [53] to $\sim 15\%$ [318] of the baryons. Including these effects, the baryon fraction for the clusters in our sample is of the order of $M^{baryons}/M^{lens}(R_{500}) \sim 0.14$.

Despite all these uncertainties related to the baryonic physics that interplay in clusters, it is of great interest to study the gas-to-lensing mass fraction from resolved profiles. Multiple works have computed the gas fraction of clusters from the ratio of gas mass and HSE mass estimates [77, 258, 319–321], correcting in some cases

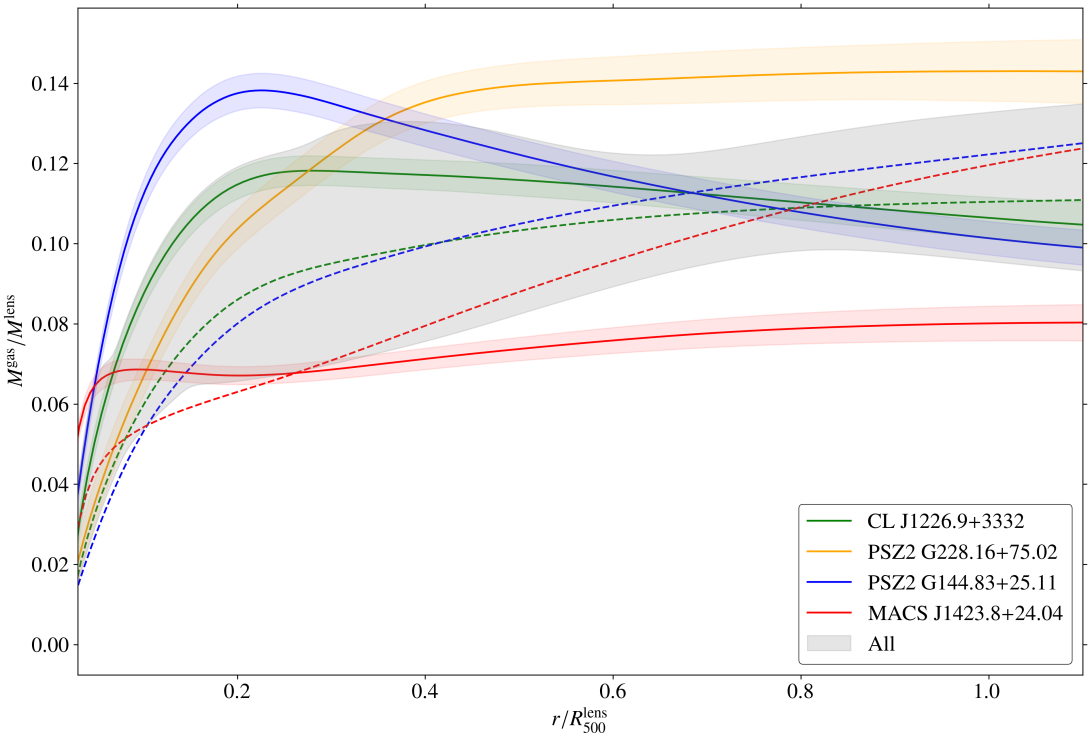

Figure 5.15: Gas-to-lensing mass fraction for the clusters in the NIKA(2)-CLASH sample. Solid lines with envelopes show the fraction of gas mass with respect to the lensing mass obtained from LTM convergence maps. The line gives the mean profile and the envelopes show the 16th to 84th percentiles. Dashed lines show the mean mass fraction when considering lensing masses estimated from PIEMD+eNFW convergence maps. We show in green, orange, blue and red the results for CL J1226.9+3332, PSZ2 G228.16+75.20, PSZ2 G144.83+25.11 and MACS J1423.8+2404 clusters, respectively. The grey area shows the 16th to 84th percentiles for the gas-to-lensing mass from the combination of all the profile distributions.

for the bias of HSE masses. Those analyses obtain gas mass fraction values compatible with our result. The comparison of gas masses to lensing masses (as in Okabe et al. (2014) [322]) has an additional interest since the latter do not rely on ICM observables. By studying the evolution with redshift of the gas fraction we can learn about the evolution along cosmic time of the gas depletion (as in Holanda et al. (2022) [323]) and the disturbance or entropy in galaxy clusters [77].

5.4 Conclusions

The precise measurement of the bias of masses estimated under the hydrostatic equilibrium assumption could be a key element to solve the tension between the cosmology inferred from cluster number counts in SZ and from early-Universe probes. In this chapter we have investigated the bias of resolved HSE masses with respect to lensing estimates for a sample of four clusters at intermediate to high redshift.

We have reconstructed the lensing mass profiles making use of the CLASH convergence maps, considering, when available, two different convergence map models per cluster. We observe that the model used to build the convergence map can have a strong impact on our lensing mass estimates: for CL J1226.9+3332 and PSZ2 G144.83+25.11 lensing masses reconstructed from LTM and PIEMD+eNFW maps are compatible within 1σ, but accounting for both introduces an additional uncertainty on $M_{\Delta}^{\rm lens}$. For MACS J1423.8+2404 the two lensing mass estimates are not consistent. Thus, from the combination of the masses reconstructed from both convergence map models we have been able to estimate, in a certain way, the uncertainties induced by modelling effects. On the contrary, other sources of uncertainties, such as those related to the selection of background galaxies and the estimation of their redshifts, can not be easily quantified with our approach.

Regarding the hydrostatic mass profiles, we have used the profiles reconstructed in chapters 3 and 4, as well as in previous works in the literature. By comparing the mass profiles reconstructed with data from different instruments, we do not observe any clear hint of systematic bias related to a given instrument. Nevertheless, HSE masses from X-ray-only data tend to lower values than the masses estimated from the combination of SZ and X-rays. In addition, we have seen that substructures and the contamination by point sources, as well as the data quality affect directly the HSE mass estimates and their uncertainties. Therefore, we conclude that resolved observations of clusters are mandatory. Given that high angular resolution SZ observations are rare, resolved high redshift cluster observations are unique and the NIKA(2)-CLASH sample is relevant and timely.

From the comparison of our M_{500} estimates to other results from the literature, we demonstrate the complexity of the estimation of the mass of individual clusters. As for the HSE-to-lensing mass bias, we conclude that HSE estimates are overall smaller than lensing masses by $\sim 20\% - 40\%$. Despite the large uncertainties, we have the sensitivity to measure the bias of individual clusters, even for the highest-redshift cluster of the NIKA2 SZ Large Programme. However, a larger sample of clusters would be needed to distinguish between systematic and statistical effects. At this regard, in chapter 6 we extend the analysis to a larger sample, but only for HSE masses reconstructed with X-ray data.

Finally, from the estimation of the gas mass in the ICM, we have computed the gas-to-lensing mass fraction profile for the four clusters in the NIKA(2)-CLASH sample. We find that the fraction of gas mass in the ICM of clusters is smaller than the universal baryon fraction, with the gas-to-lensing mass fraction increasing towards the outskirts of the clusters.

CHAPTER 6

Evolution of the HSE-to-lensing mass bias

Following on with the HSE-to-lensing mass bias analysis in the previous chapter, in this one we aim at extending the study to a larger sample of clusters that covers a wide redshift range. Given the numerous methods and models that can be employed to reconstruct HSE and lensing masses and the potentially different biases that they could be subjected to (see chapter 5), we focus here on a sample of clusters for which X-ray-based HSE and lensing masses have been homogeneously reconstructed from mass profiles.

As indicated by Sereno and Ettori (2015) [314], and shown also in the previous chapters, cluster mass estimates can vary up to $\sim$ 40% from one work to another. Being aware of this, we compile also results from several works that have equally produced M_{500} estimates based on mass profiles. We use those estimates to measure the systematic dispersion with respect to our *homogeneous* sample of masses and propagate such dispersion. This goes a step beyond previous studies [301, 314, 324].

We first present the data describing the *homogeneous* and comparison cluster samples. Then we detail the method used to match clusters from different catalogues and the measurement of the systematic dispersion of

the *homogeneous* masses with respect to other estimates. We build the *reference* sample that is used to estimate the HSE-to-lensing mass bias, the scaling relation and its evolution with redshift. At the end of the chapter, we compare our results to similar works in the literature. This chapter is based on a work accepted for publication in Astronomy and Astrophysics [325].

6.1 Cluster sample construction

6.1.1 *Homogeneous* sample

This study is built aiming for a cluster sample with resolved HSE and lensing masses that are comparable amongst all the objects (*homogeneous* reconstruction procedure) and covers the largest possible redshift range. We present in this section the mass reconstruction and regularisation procedure of the XMM-*Newton* and CoMaLit clusters [281], which constitute our *homogeneous* sample.

CoMaLit sample

The *CoMaLit sample* contains the clusters with lensing masses that we used to build the homogeneous sample. They correspond to the clusters from the Literature Catalogs of weak Lensing Clusters (LC^2) compilation presented in Sereno (2015) [281]. LC^2 contains 806 clusters (in the 3.9 version of the LC^2-*single* catalogue[8]) with weak lensing masses obtained from different works in the literature, including the widely used Canadian Cluster Comparison Project (CCCP) [315, 326] and Weighing the Giants (WtG) [311] cluster samples.

Although the masses were not derived homogeneously amongst the original works, an effort was made in Sereno (2015) [281] to select the most comparable mass estimates. Only masses reconstructed assuming spherical symmetry were considered, clusters without optical, X-ray or SZ counterparts were excluded and when the same authors or collaborations had published several estimates for the same cluster along a refinement process, only the latest result was considered. In addition, all the masses were standardised to the same cosmology (a flat ΛCDM cosmology with $\Omega_m = 0.3$ and $H_0 = 70$ km/s/Mpc) and given at the overdensities of 2500, 500 and 200, as well as at the virial radius. We will consider only the masses at an overdensity of $\Delta = 500$. For some cases, the masses given in the original papers had to be extrapolated following the density profile adopted in the original paper or with an NFW model.

XMM-*Newton* sample with the reference X-ray pipeline

Regarding the HSE masses, we built a sample of clusters with masses reconstructed from XMM-*Newton* data and following the same procedure, hereafter *XMM-Newton* or *reference X-ray pipeline*. This pipeline has already been used in chapters 3, 4 and 5 (as well as in several published works [77, 177, 178, 191, 254]) to reconstruct HSE mass profiles of clusters from XMM-*Newton* data. A brief description of the procedure can be found in Sect. 3.3 and 3.4.

The binned HSE mass profiles (as the ones shown, for example, in Fig. 3.10 and 4.13) were interpolated to define the M_{500} masses used in this analysis. Based on the same XMM-*Newton* data two differently estimated M_{500} are available per cluster: masses derived from an X-ray calibrated scaling relation [70] and masses estimated from a forward NFW profile fit to the density and temperature profiles (same idea as the method in Sect. 3.4.2). We will not use these two types of masses in our main analysis, but they are employed to investigate the consistency of all three estimates in Sect. 6.6. Amongst the clusters with XMM-*Newton* data, we distinguish three different subsamples along the redshift: low-, intermediate- and high-redshift clusters.

I. Low-z clusters: ESZ+LoCuSS

Many of the low redshift ($z < 0.5$) clusters detected by *Planck* were also observed by XMM-*Newton*. It is the case of the 62 *Planck* Early Sunyaev-Zel'dovich (ESZ) clusters [327], whose HSE masses were reconstructed

with X-ray data in Planck Collaboration et al. (2011) [206]. Similarly, based on the Local Cluster Substructure Survey (LoCuSS[12]) sample, Planck Collaboration et al. (2013) [328] reconstructed the HSE mass of 19 clusters.

II. Intermediate-z clusters: LPSZ

As presented in Sect. 3.1, the NIKA2 SZ Large Programme was designed to follow-up clusters with redshifts between $z = 0.5$ and 0.9 by using NIKA2 and XMM-*Newton*. In this chapter we will make use of the HSE masses obtained from XMM-*Newton* data only.

III. High-z clusters: Bartalucci+2018

Bartalucci et al. (2017) [254] and Bartalucci et al. (2018) [105] were able to go beyond $z = 0.9$ and measure the HSE mass of 5 individual clusters from resolved mass profiles. Given the difficulties related to the high redshift of the clusters, XMM-*Newton* data were combined with *Chandra* observations. Although supplementary *Chandra* data was added, we will consider these masses to be homogeneous with respect to the ESZ+LoCuSS and LPSZ samples, since the same reconstruction pipeline was employed. However, special care will be taken when studying the impact of these clusters. Authors in Bartalucci et al. (2018) [105] also indicate that the mass estimate for the SPT-CLJ2106-5844 cluster is not reliable, therefore, we will exclude it from our analyses.

6.1.2 *Comparison* sample

It is undeniable, from the previous chapters of this thesis, that the mass estimate for a cluster often varies from one analysis to another (even up to 50%), because of differences related to the raw data or to the mass reconstruction method. In order to try to account for possible systematic biases in the CoMaLit and the reference X-ray pipeline masses, we gather as many as possible HSE and lensing mass estimates from the literature for the clusters in our *homogeneous* sample. Again, we make sure that the masses in the chosen studies are measured on resolved profiles, excluding masses derived from scaling relations. We only consider HSE masses obtained from X-ray data. Comparing to HSE masses that use SZ data or scaling relations is also of great interest, but it would be an independent analysis in itself (see chapters 4 and 5) and beyond the scope of this chapter. For lensing, in addition to the weak lensing masses, we also compare to masses reconstructed from the combination of strong and weak lensing signals.

We present in the following a brief description of this *comparison* sample, highlighting the distinctive characteristics of each analysis.

Ettori+2010

In Ettori et al. (2010) [329] (and the *Corrigendum* in Ettori et al. (2011) [330]) authors reconstructed the HSE mass of 44 clusters with redshifts $0.092 < z < 0.307$ using XMM-*Newton* observations. They employed two different methods (M1 and M2) and gave the results in units of R_{500}. We converted the R_{500} values into M_{500} masses. The main caveat of these results is that profiles were extrapolated to reach R_{500} assuming an NFW model. As the coordinates of the assumed centre of the clusters are not given in Ettori et al. (2010) [329], we took them from Yuan et al. (2022) [331][13] and when missing, from the 4XMM-DR9 source list[14].

Landry+2013

In Landry et al. (2013) [321] the HSE masses of 35 clusters with redshifts between $0.152 < z < 0.3017$ were obtained using *Chandra* data. Two different mass estimates are given in the paper: either using the Vikhlinin

[12] http://www.sr.bham.ac.uk/locuss/home.php
[13] http://zmtt.bao.ac.cn/galaxy_clusters/dyXimages/newton.html
[14] http://xmmssc.irap.omp.eu/Catalogue/4XMM-DR9/4xmmdr9_obslist.html

model or the polytropic equation of state, and according to authors the profiles of 7 clusters required "slight" extrapolation to reach R_{500}. Again, the coordinates of the assumed centres of the clusters are not given in Landry et al. (2013) [321], so most of the coordinates were taken from Ebeling et al. (1998) [332]. When missing, position coordinates of clusters were found by querying in the Simbad-CDS portal[15] with the cluster name given in Table 1 in Landry et al. (2013) [321].

LoCuSS

The aforementioned LoCuSS sample contains in all 50 clusters, with $0.152 < z < 0.3$ [333]. For our mass comparisons, we used the LoCuSS HSE masses published in Martino et al. (2014) [334] and the lensing masses from Okabe and Smith (2016) [335]. The HSE masses were reconstructed with *Chandra* data for 43 clusters and with XMM-*Newton* observations for 39. For some clusters both estimates are available. Central coordinates of clusters were also taken from Martino et al. (2014) [334]. The analysis in Zhang et al. (2010) [336] studied 12 out the 50 clusters with XMM-*Newton* and Subaru data. The lensing masses published in Zhang et al. (2010) [336] are equivalent to those in Okabe and Smith (2016) [335], but the HSE mass profiles were evaluated at the R_{500} corresponding to the lensing analyses. We, therefore, gave preference to the results in Okabe and Smith (2016) [335] and Martino et al. (2014) [334], and, restricted the LoCuSS masses to the estimates in the latter two studies.

Mahdavi+2008

Uniformly estimated masses of 18 clusters were published in Mahdavi et al. (2008) [337]. Lensing masses were obtained as in Hoekstra (2007) [338], but with the photometric redshift distributions from Ilbert et al. (2006) [339]. The lensing mass reconstruction was done with a method based on aperture mass estimation, that is, obtaining first projected masses, and subsequently deprojecting by assuming an NFW density model and the concentration-mass scaling relation from Bullock et al. (2001) [340]. For the HSE masses, *Chandra* observations were used. As indicated in Table 2 in Mahdavi et al. (2008) [337], for 14 out of the 18 clusters the HSE masses at R_{500} were obtained from extrapolation and all of them were measured at the lensing R_{500}.

Mahdavi+2013

In Mahdavi et al. (2013) [259] authors studied a sample of 50 clusters with redshift $0.152 < z < 0.55$. The clusters correspond to the CCCP sample. The HSE masses were reconstructed from a combined analysis of XMM-*Newton* and *Chandra* data. For the same sample lensing estimates were obtained in Hoekstra et al. (2012) [326], using CFH12k and Megacam data from the Canada-France-Hawaii Telescope. HSE masses were measured at the R_{500} obtained from lensing masses.

Israel+2014

The analysis in Israel et al. (2014) [260] contains 8 clusters with redshift $0.35 < z < 0.80$. The lensing masses were obtained from an NFW fit to the tangential shear profiles of clusters, assuming a mass-concentration relation. To reconstruct the HSE mass authors used the electron density profiles of individual clusters, which were estimated from *Chandra* surface brightness maps. The temperature profile of individual clusters being more challenging to obtain, authors combined the *Chandra* data of all clusters in the sample to reconstruct a single global temperature profile for the whole sample. The HSE masses in Israel et al. (2014) [260] were also evaluated at the R_{500} measured from lensing mass profiles.

[15] http://simbad.u-strasbg.fr/simbad/

LPSZ+CLASH

In chapter 5 we have estimated the lensing mass for three clusters in the sample in common between the LPSZ and CLASH samples (CL J1226.9+3332, PSZ2 G144.83+25.11 and PSZ2 G228.16+75.20). We have reconstructed the masses by fitting a projected NFW mass density profile to the publicly available CLASH convergence maps, having in some cases two estimates per cluster. We use those lensing masses to compare to the CoMaLit estimates, as well as the masses published in Umetsu et al. (2014) [310] and Merten et al. (2015) [279] for the same clusters.

Bartalucci+2018

In Bartalucci et al. (2018) [105] authors studied the HSE-to-lensing mass bias of five SPT clusters. The weak lensing masses were obtained by Schrabback et al. (2018) [341] using Hubble Space Telescope (HST) observations. The profiles were centred in the X-ray peak or the SZ peak (indicated in Table 1 in Schrabback et al. (2018) [341]), giving two different lensing mass estimates per cluster.

6.2 Combination of catalogues

In this section, we present the comparison of the XMM-*Newton* and CoMaLit mass estimates to the results from other works presented in Sect. 6.1.2. We describe the procedure used to match and select clusters from different catalogues, and then quantify the scatter based on the comparison of several mass measurements for each cluster across our sample. With the latter, we intend to estimate overall uncertainties in the mass estimates both for X-ray and lensing.

6.2.1 Matching clusters

We match clusters from different catalogues on the basis of their central coordinates. We consider that two entries in two distinct catalogues correspond to the same cluster for angular separations smaller than 400″. We further verify every match by checking the redshifts given in the different catalogues. We identify suspicious mismatching between A1606 (z = 0.0963) and A2029 (z = 0.078) and exclude it.

At the same time, we discard clusters that appear as one object in some catalogue and as a combination of multiple substructures in another. For example, the cluster A1758 in Landry et al. (2013) [321] has four entries in the LC^2-*single* catalogue: A1758S, A1758NW, A1758N, A1758NE. Similarly, we exclude A222, A223N and A223S. In addition, we identified and discarded A750 (present in CoMaLit, LoCuSS, Mahdavi+2013 and Mahdavi+2008 catalogues), whose mass estimate can not be reliable since it is superimposed along the line-of-sight with MS0906+11 [342].

We summarise in Table 6.1 the overlap between the clusters in the *homogeneous* XMM-*Newton* and CoMaLit samples and those from other works presented in Sect. 6.1.2. For 36 of the XMM-*Newton* and 82 of the CoMaLit clusters we identified other HSE and lensing mass estimates[16].

6.2.2 Estimation of systematic dispersion

We present in the top left panel in Fig. 6.1 the relation between X-ray HSE masses obtained with the reference X-ray pipeline (*homogeneous* masses) with respect to other X-ray HSE masses from the literature (*comparison* sample). In the right panel, we show the relation between lensing masses from different works with respect to the estimates summarised in CoMaLit. Each colour represents one of the samples described in Sect. 6.1.2 and different estimates of the same work are differentiated with markers. The black dashed line shows the one-to-one relation.

[16]Since the LC^2 catalogue is a compilation of masses from many works in the literature, it is not surprising that some CoMaLit masses are directly the estimate published in other works. It is the case for some LoCuSS clusters.

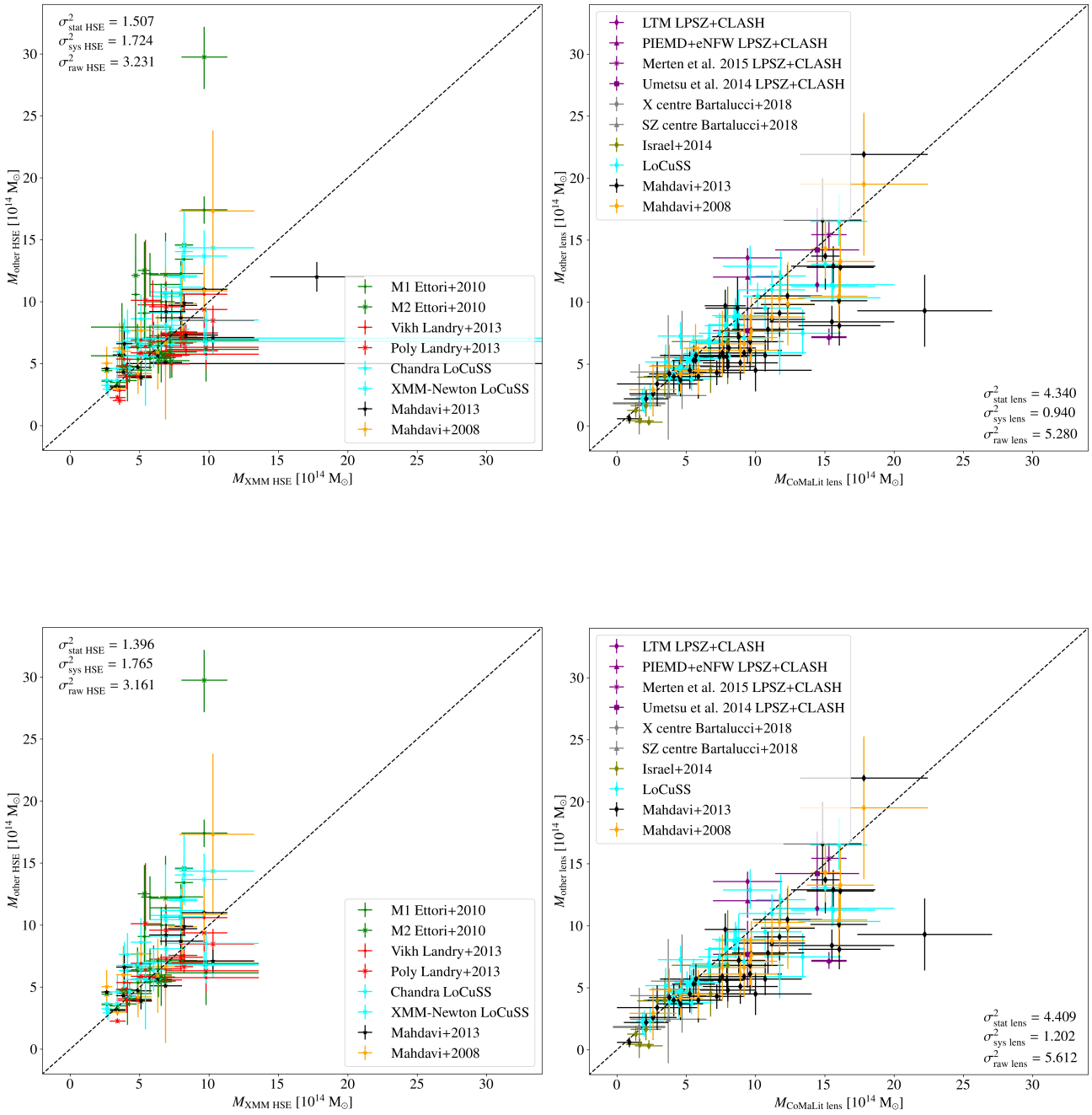

Figure 6.1: The relation between HSE (left) and lensing (right) masses from the *homogeneous* samples in this work (XMM-*Newton* and CoMaLit) with respect to other estimates from the literature (*comparison* sample). Each colour indicates a different analysis and several results for the same work are differentiated by using different markers. The black dashed line shows the one-to-one relation. We give the statistical, systematic and raw variances as defined in the text. All the variances are in units of $(10^{14}\ M_\odot)^2$. In the bottom panels we show the same relations, but not accounting for clusters with very large uncertainties and with very different XMM-*Newton* and CoMaLit centres excluded in Sect. 6.3.1 and 6.3.2.

Sample	Redshift	Type of mass	# of clusters	# of clusters in common with the XMM-*Newton* sample	# of clusters in common with the CoMaLit sample
Ettori+2010	$0.092 < z < 0.307$	HSE	44	24	
Landry+2013	$0.152 < z < 0.3017$	HSE	35	19	
LoCuSS	$0.152 < z < 0.3$	HSE and lensing	50	22	45
Mahdavi+2013	$0.152 < z < 0.55$	HSE and lensing	50	18	44
Mahdavi+2008	$0.170 < z < 0.547$	HSE and lensing	18	11	17
Israel+2014	$0.35 < z < 0.80$	HSE and lensing	8	0	8
LPSZ+CLASH	$0.55 < z < 0.89$	lensing	3		3
Bartalucci+2018	$0.933 < z < 1.066$	lensing	4		3
All				94	120
All without repetition				36	82

Table 6.1: Summary of the number of clusters in each of the *comparison* samples and their overlap with the *homogeneous* XMM-*Newton* and CoMaLit samples. We also report the total amount of matches corresponding to the data points in the top panels in Fig. 6.1 and the number of different objects.

Overall, the agreement between the samples is reasonable, with a significant dispersion around the 1:1 relation. We identify some clusters for which the mass estimates differ significantly. These are Abell521, Abell2390, Abell2163 in X-rays and RXJ1347.5-1145, CL1641, CL1701 in the lensing mass comparisons. The cluster shown with the green marker on top of the top left panel in Fig. 6.1 is Abell2390 and, despite its departure from the 1:1 relation, we do not have strong arguments for excluding it. For lensing masses (in the top right panel in Fig. 6.1) there seem also to be a hint of some bias that we will not propagate hereafter. We verify that the bias does not correlate with a *comparison* sample in particular, but rather with high mass clusters. Further investigation would be needed to understand this trend.

To quantify the systematic dispersion with respect to the 1:1 relation, we follow Eq. 3 and 4 in Pratt et al. (2009) [106]. For the $N_{\rm lens} = 120$ matched entries between the CoMaLit catalogue and the other lensing samples (Table 6.1), we define the raw variance as

$$\sigma^2_{\rm raw\ lens} = \frac{1}{N_{\rm lens} - 2} \sum_{i=1}^{N_{\rm lens}} w_i (M_{\rm other\ lens} - M_{\rm CoMaLit\ lens})^2, \tag{6.1}$$

where, w_i is the weight of each cluster i and $M_{\rm CoMaLit\ lens}$ and $M_{\rm other\ lens}$ are the lensing mass in the CoMaLit catalogue and in a different analysis, respectively. The weight given to each cluster is

$$w_i = \frac{1/\sigma_i^2}{1/N \sum_{j=1}^{N} 1/\sigma_j^2}, \tag{6.2}$$

using $\sigma_i^2 = \delta^2_{M_{\rm other\ lens}} + \delta^2_{M_{\rm CoMaLit\ lens}}$, the sum of the uncertainties related to each cluster. The $\sigma^2_{\rm raw\ HSE}$ is measured in an equivalent way using the HSE masses and uncertainties for each cluster: $M_{\rm XMM\ HSE}$ and $M_{\rm other\ HSE}$ and $\delta^2_{M_{\rm XMM\ HSE}}$ and $\delta^2_{M_{\rm other\ HSE}}$.

The expected statistical error associated with the mass estimates is obtained for both lensing and X-ray masses accounting for the weight, w_i, and uncertainties, σ_i^2, for each cluster:

$$\sigma^2_{\rm stat} = \frac{1}{N-2} \sum_{i=1}^{N} w_i \sigma_i^2 = \frac{1}{N-2} \sum_{i=1}^{N} \frac{N}{\sum_{j=1}^{N} 1/\sigma_j^2}. \tag{6.3}$$

This allows us to define the systematic scatter, that is, the excess of scatter in the raw variance not explained by the statistical uncertainties, as

$$\sigma^2_{\rm sys} = \sigma^2_{\rm raw} - \sigma^2_{\rm stat}. \tag{6.4}$$

Sample	$\sigma^2_{\rm raw\ HSE}$ [10^{28} $M^2_\odot$]	$\sigma^2_{\rm stat\ HSE}$ [10^{28} $M^2_\odot$]	$\sigma^2_{\rm sys\ HSE}$ [10^{28} $M^2_\odot$]	Figure
All	3.231	1.507	1.724	Fig. 6.1
Without $M^{\rm HSE}(< R^{\rm lens}_{500})$	3.393	1.501	1.892	Fig. 6.2
Without clusters discarded in Sect. 6.3	3.161	1.396	1.765	Fig. 6.1
Without $M^{\rm HSE}(< R^{\rm lens}_{500})$ and clusters discarded in Sect. 6.3	3.405	1.388	**2.017**	Fig. 6.2
	$\sigma^2_{\rm raw\ lens}$ [10^{28} $M^2_\odot$]	$\sigma^2_{\rm stat\ lens}$ [10^{28} $M^2_\odot$]	$\sigma^2_{\rm sys\ lens}$ [10^{28} $M^2_\odot$]	Figure
All	5.280	4.340	0.940	Fig. 6.1
Without clusters discarded in Sect. 6.3	5.612	4.409	**1.202**	Fig. 6.1

Table 6.2: Raw, statistical and systematic variances of the HSE and lensing mass estimates from the *homogeneous* samples in this work (XMM-*Newton* and CoMaLit) with respect to other estimates from the literature (*comparison* samples). We report the different values depending on the sample selection criteria, showing in bold the systematic scatters considered for the rest of the chapter.

We report in Fig. 6.1 (and in Table 6.2) the statistical, systematic and raw scatter for the HSE and lensing masses. The raw dispersion of lensing masses is larger than HSE ones and the uncertainties of individual lensing masses being larger, the statistical dispersion is also larger. Nevertheless, the error bars of HSE masses are not large enough to cope with the excess of scatter around the 1:1 relation, making the systematic scatter for HSE masses to be larger than for lensing.

As mentioned in the description of each sample in Sect. 6.1.2, HSE masses in some works were evaluated at the R_{500} obtained from lensing. We check the impact of excluding such estimates from the analysis. In the left panel in Fig. 6.2 we present the relation between the XMM-*Newton* reference pipeline masses and X-ray masses from the *comparison* sample without accounting for $M^{\rm HSE}(< R^{\rm lens}_{500})$ estimates (that is, without Mahdavi et al. (2008) [337] and Mahdavi et al. (2013) [259]). The statistical, raw and systematic variances change by 0.4, 5 and 10%, respectively. Hence, taking the most conservative approach, in the following sections we will consider the largest scatter values obtained.

6.3 Selection and characterisation of the *reference* sample

Following the procedure described in Sect. 6.2.1, we match the clusters in the CoMaLit catalogue (Sect. 6.1.1) with the clusters with HSE masses from the XMM-*Newton* reference pipeline (Sect. 6.1.1) and obtain an *homogeneous* sample composed of 65 clusters. Amongst the 65 clusters, 54 correspond to the ESZ+LoCuSS samples, 8 clusters are from the LPSZ and 3 from Bartalucci+2018. For these clusters, we perform additional checks to verify which of them can be used for the HSE-lensing mass comparison and define the final *reference* sample.

6.3.1 Uncertainties in mass estimates

For the clusters in the *homogeneous* sample, we observe that mass estimates and their associated uncertainties appear correlated: error bars are larger for more massive objects. As already mentioned, lensing mass uncertainties are larger than HSE ones. In addition, the relative uncertainties, when calculated with respect to the value of the measured mass, are also larger for lensing than for HSE estimates. For some clusters the uncertainties on HSE masses are suspiciously large (100%) or abnormal (negative error bars). We decide to exclude for these reasons the clusters Abell119, Abell521 (the LoCuSS and Mahdavi+2013 cluster out of the plot in the left panel in Fig. 6.1) and SPT-CLJ0516-54.

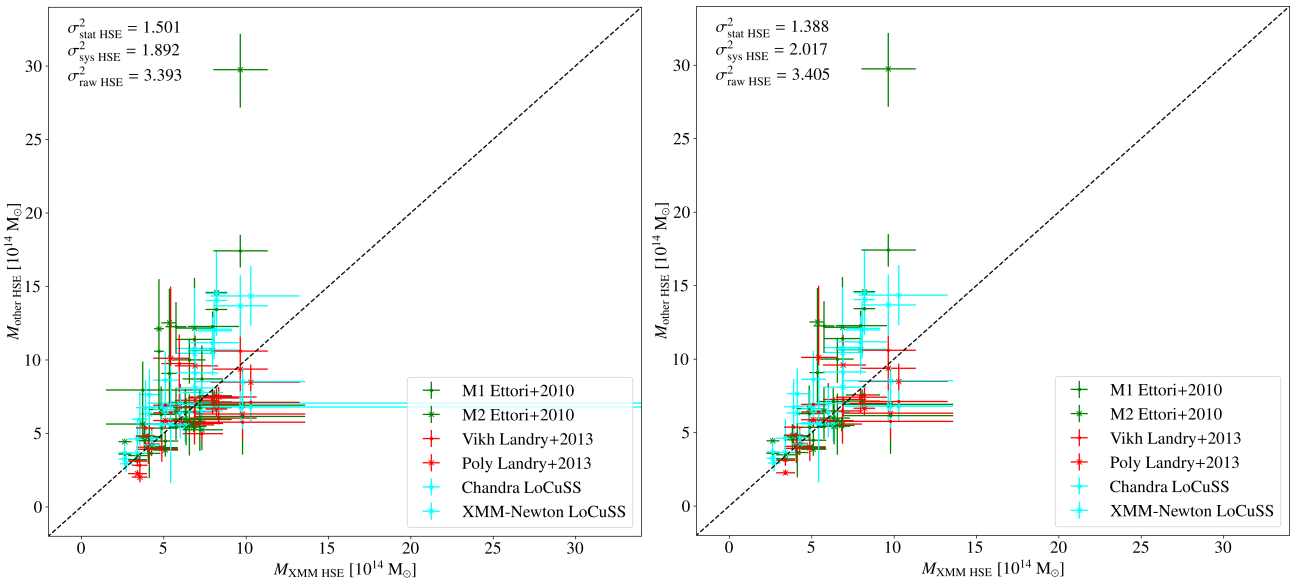

Figure 6.2: Relation between X-ray masses from literature and from the XMM-*Newton* reference pipeline without accounting for $M^{\rm HSE}(< R^{\rm lens}_{500})$. In the left (right) the clusters with very large uncertainties and with very different XMM-*Newton* and CoMaLit centres are considered (not considered).

6.3.2 Difference of centres for HSE and lensing reconstructions

For some of the clusters the HSE and lensing masses have been reconstructed assuming different cluster centre positions. We investigate in the following if this miscentring is correlated to the mass ratio and redshift and how it may affect the mass estimates.

Miscentring

In the left panel in Fig. 6.3 we present the ratios between the HSE and lensing masses with respect to the separations between the centres considered in the X-ray and lensing analyses. Each marker corresponds to one of the 65 clusters, showing with magenta crosses, purple squares and grey circles the clusters from ESZ+LoCuSS, LPSZ and Bartalucci+2018 samples, respectively. Uncertainties have been obtained from the propagation of the individual XMM-*Newton* and CoMaLit uncertainties. The separation between X-ray and lensing centres goes from 1.5 kpc to 700 kpc. However, there is no significant correlation between the miscentring and the HSE-to-lensing mass ratio.

The miscentring could also be related to the redshift of the cluster. In the right panel in Fig. 6.3 we show the redshift with respect to the separation of the centres. There is neither indication of correlation. We do not find any significant correlation between the redshift and the uncertainties of mass ratios either.

The dynamical state of clusters is an important point to better understand the evolution of the HSE bias. In particular, according to simulations, relaxed clusters tend to have smaller HSE bias as compared to disturbed ones Gianfagna et al. (2021) [179]. The offset between the centres used in lensing and X-ray analyses could be an indicator of the departure from sphericity and equilibrium of clusters. However, the absence of correlation between the separation of centres and the HSE-to-lensing mass ratio or the redshift does not enable any clear dynamical classification of the clusters in our sample.

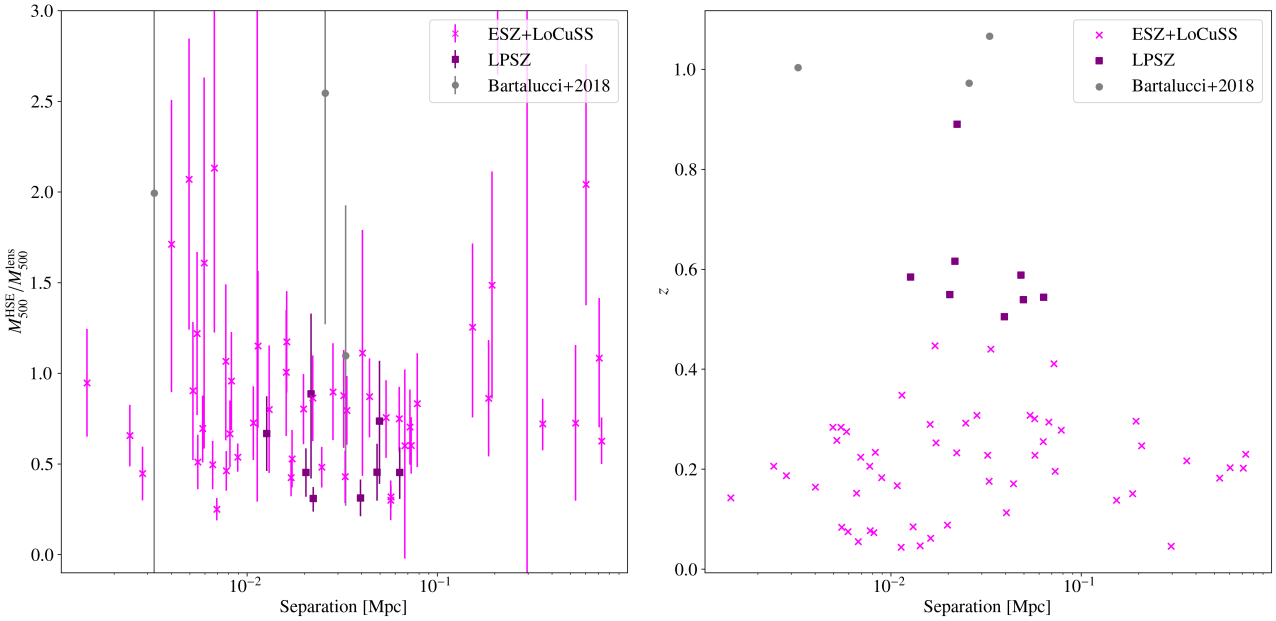

Figure 6.3: Correlation between the HSE-to-lensing mass ratio (left) and redshift (right) of the 65 clusters in the *homogeneous* XMM-*Newton*-CoMaLit sample with respect to the separation between the centres assumed in the X-ray and lensing analyses. Error bars in the left panel do not account for the systematic scatters discussed in Sect. 6.2.2.

Model	c_{500}	α	β	γ	τ	η
NFW	1.0, 2.25, 3.5, 4.75, 6.0					
Hernquist	1.0, 2.25, 3.5, 4.75, 6.0					
gNFW	6.0	0.3, 0.85, 1.4, 1.95, 2.5	2.0, 3.0, 4.0, 5.0, 6.0	0.3, 0.475, 0.65, 0.825, 1.0		
tNFW	6.0				0.2, 1.15, 2.1, 3.05, 4.0	0.5, 1.125, 1.75, 2.375, 3.0

Table 6.3: Different mass density models and their corresponding parameters used to study the miscentring effect in Fig. 6.4.

Simulations to quantify the impact of miscentring

It is evident that two mass estimates computed assuming very different centres are hardly comparable. Moreover, setting a quantitative limit of the acceptable separation is not straightforward. In this section we make use of simulated mock mass density profiles to check the impact of miscentring on the mass profiles and, consequently, on the estimation of M_{500}.

We simulate mass density profiles by using the `profiley`[17] Python package, which contains already tested [172] functions that describe density profiles, as well as the corresponding miscentred density profiles. We test a variety of profile shapes: NFW, gNFW, truncated Navarro-Frenk-White (tNFW) [343] and Hernquist [344] models. To initialise the density profiles we consider different M_{500} (in the range $\sim$ 1 to 9×10^{14} $M_\odot$) and model parameters. The parameters considered for each model are given in Table 6.3.

For each mass density profile we build the corresponding miscentred profiles by displacing the centre by 0.0 to 0.7 Mpc from the original one. We integrate each miscentred density profile to get a mass profile and obtain the miscentred M_{500} estimate at the radius where the overdensity reaches $\Delta = 500$, $M_{500}^{\rm miscent}$. In Fig. 6.4 we show the relative error of the miscentred masses with respect to the separation to the true centre, for all types of profiles considered and for different redshifts, $z = [0.1, 0.45, 0.8, 1.15, 1.5]$. Each marker indicates a different mass density model and the colours show the true M_{500}. For visualisation purposes gNFW, tNFW and

[17] https://profiley.readthedocs.io/en/latest/index.html.

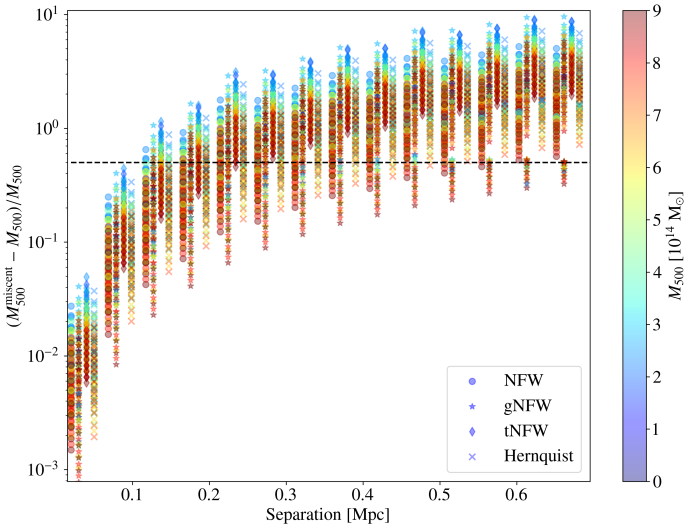

Figure 6.4: Relative error on the estimation of M_{500} as a function of the separation between the true and the considered centre for the mass reconstruction. Colours indicate the true M_{500} and markers the mass density model. Markers have been shifted for visualisation purposes. The black dashed line indicates a 50% error in M_{500}.

Hernquist markers have been shifted by 0.01, 0.02 and 0.03 Mpc. As expected, the figure shows that computing the density profile from a centre that is separated from the true centre gives biased mass reconstructions. This bias increases with the separation, less massive clusters being more sensitive to this effect. The black dashed line in Fig. 6.4 indicates $(M_{500}^{\rm miscent} - M_{500})/M_{500} = 0.5$.

Considering the tested density profiles, and redshift and mass ranges, the error due to miscentring is smaller than 50% only if the distance to the real centre is smaller than 100 kpc. Therefore, we decide to exclude clusters for which X-ray and lensing centres are separated by more than 100 kpc. These clusters are: Abell3856, Abell3888, Abell773, Abell665, Abell267, 1E0657-56, Abell521, Abell3376E, Abell520 and Abell2163.

6.3.3 *Reference* sample

As a result, our *reference* sample contains 53 clusters with homogeneous HSE and lensing masses that can be used for comparisons. We present in Table 6.4 the 53 clusters in the *reference* sample. We give their names (as named in the CoMaLit LC^2 catalogue), redshifts, masses and mass uncertainties from the analyses of reference, i.e., XMM-*Newton* mass reconstruction pipeline masses and CoMaLit estimates.

We present in Fig. 6.5 a summary of the characteristics of the sample. The histograms on the left show the number of clusters with respect to redshift, HSE mass and lensing mass. The right panel in Fig. 6.5 presents the clusters in the mass-redshift plane. While very few works in the literature go above $z = 0.5$ [105, 259, 324, 337], 20% of the clusters in our sample have redshifts higher than 0.5. However, the distribution in redshift of the sample is dominated by low-z clusters.

After excluding in Sect. 6.3.1 and 6.3.2 12 clusters from the XMM-*Newton* and CoMaLit samples, we recalculate the scatter with respect to other HSE and lensing masses in the bottom panels in Fig. 6.1. Compared to top panels, the raw, statistical and systematic dispersions remain of the same order (less than 10% of change as seen in Fig. 6.1 and Table 6.2), but the impact of individual clusters is again noticeable in the resulting values. Therefore, we take the most conservative approach and we will consider that the systematic scatters to be accounted for in the XMM-*Newton* and CoMaLit masses are the largest values we have found: $\sigma^2_{\rm sys\ lens} = 1.202 \times (10^{14}\ {\rm M}_\odot)^2$ and $\sigma^2_{\rm sys\ HSE} = 2.017 \times (10^{14}\ {\rm M}_\odot)^2$. Note that the clusters used for these calculations are not necessarily the 53 in our *reference* sample, but the ones in common between XMM-*Newton* and other X-ray samples and between CoMaLit and other lensing works (summarised in Table 6.1). We compare in

CoMaLit name	z	Centre coordinates [deg]				Masses [10^{14} $M_\odot$]			
		CoMaLit α	CoMaLit δ	XMM α	XMM δ	$M_{500}^{\text{CoMaLit lens}}$	$\delta_{M_{\text{CoMaLit lens}}}$	$M_{500}^{\text{XMM HSE}}$	$\delta_{M_{\text{XMM HSE}}}$
ABELL2744	0.3080	3.57875	-30.38944	3.57752	-30.38633	13.849	2.824	10.472	2.218
CL0016+16	0.5490	4.63933	16.43694	4.63986	16.43622	17.821	4.609	8.062	1.147
ABELL68	0.2550	9.27479	9.16000	9.27792	9.15685	9.171	1.587	6.872	1.181
ABELL85	0.0550	10.46017	-9.30306	10.46132	-9.30438	5.700	2.200	12.150	2.169
ABELL2813	0.2924	10.85167	-20.62139	10.85190	-20.62294	8.557	1.450	4.131	0.665
Abell209	0.2060	22.96892	-13.61122	22.96912	-13.61121	9.614	1.965	6.309	1.010
ABELL291	0.1960	30.43417	-2.20083	30.42942	-2.19678	4.514	0.986	2.718	0.380
RXCJ0232.2-4420	0.2840	38.07750	-44.34667	38.07721	-44.34638	5.380	1.815	6.558	0.986
Abell383	0.1870	42.01417	-3.52914	42.01418	-3.52889	5.871	1.727	2.629	0.409
ABELL478	0.0881	63.35667	10.46694	63.35581	10.46371	8.772	2.078	7.043	0.325
MS0451.6-0305	0.5389	73.54767	-3.01411	73.54705	-3.01620	9.994	4.060	7.352	1.733
RXCJ0528.9-3927	0.2840	82.22083	-39.47161	82.22109	-39.47136	4.480	1.310	9.276	2.541
RXCJ0532.9-3701	0.2750	83.23208	-37.02667	83.23226	-37.02703	6.960	1.430	4.847	0.852
SPT-CLJ0546-5345	1.0660	86.65321	-53.76039	86.65500	-53.76000	3.700	2.760	4.060	0.500
SPT-CLJ0615-5746	0.9720	93.96521	-57.77881	93.96600	-57.77960	4.700	2.252	11.960	1.750
ABELL3404	0.1670	101.37292	-54.22697	101.37122	-54.22732	8.750	2.085	6.360	0.968
MACSJ0647.7+7015	0.5840	101.95946	70.24861	101.95900	70.24810	9.427	2.493	6.296	1.014
MACSJ0911.2+1746	0.5050	137.79529	17.77539	137.79704	17.77603	10.862	3.259	3.392	0.424
ABELL963	0.2060	154.26483	39.04764	154.26530	39.04816	4.583	1.637	4.884	0.968
ABELL1300	0.3080	172.97583	-19.92772	172.97749	-19.92848	5.950	1.695	5.341	0.476
MACSJ1149.5+2223	0.5440	177.39871	22.39850	177.39763	22.40108	14.447	3.034	6.536	1.608
ABELL1413	0.1430	178.82500	23.40503	178.82495	23.40487	7.200	2.100	6.816	0.815
MACSJ1206.2-0847	0.4400	181.55062	-8.80094	181.55208	-8.80017	12.176	2.477	9.681	1.203
ZwCl1215.1+0400	0.0750	184.42137	3.65589	184.42236	3.65650	3.500	2.200	5.629	0.566
CLJ1226.9+3332	0.8900	186.74271	33.54683	186.74203	33.54627	15.298	1.275	4.732	1.042
ABELL1576	0.3010	189.24583	63.19056	189.24408	63.18711	13.543	4.243	4.064	0.782
ABELL1644S	0.0470	194.30000	-17.41306	194.29601	-17.41110	1.309	0.748	13.664	5.775
ABELL1650	0.0840	194.67287	-1.76139	194.67336	-1.76223	7.100	2.000	3.629	0.315
ABELL1651	0.0850	194.84371	-4.19603	194.84380	-4.19831	5.600	2.400	4.486	0.429
ABELL1689	0.1830	197.87300	-1.34100	197.87263	-1.34172	15.033	1.025	8.071	1.078
ABELL1763	0.2279	203.82583	40.99694	203.82979	41.00010	16.014	2.050	5.102	0.779
ABELL1795	0.0620	207.21871	26.59300	207.22115	26.58994	9.300	2.200	10.910	0.291
ABELL1835	0.2530	210.25804	2.87775	210.25916	2.87824	15.510	4.503	8.200	0.660
PSZ2G099.86+58.45	0.6160	213.69662	54.78433	213.69522	54.78396	7.242	3.043	6.421	2.038
ABELL1914	0.1712	216.50667	37.82722	216.51053	37.82434	7.929	1.293	6.909	1.390
ZwCl1454.8+2233	0.2578	224.31292	22.34278	224.31293	22.34242	3.771	1.457	3.407	0.584
Zwicky7215	0.2900	225.34483	42.34750	225.34451	42.34650	5.390	1.504	5.418	1.142
ABELL2034	0.1130	227.54875	33.51472	227.55283	33.51044	5.169	3.100	5.750	0.643
ABELL2029	0.0770	227.73371	5.74481	227.73502	5.74410	12.100	2.500	5.592	0.661
ABELL2065	0.0730	230.62150	27.70769	230.62257	27.70901	8.000	2.100	5.326	0.474
ABELL2204	0.1520	248.19650	5.57583	248.19592	5.57544	16.051	2.963	7.966	1.605
ABELL2218	0.1760	248.95329	66.21417	248.95972	66.21254	8.900	2.700	3.829	0.597
ABELL2219	0.2280	250.08475	46.70833	250.08366	46.71067	11.729	1.852	10.287	2.969
RXJ1720.1+2638	0.1640	260.04167	26.62464	260.04166	26.62503	3.510	1.485	6.006	1.314
Abell2261	0.2240	260.61325	32.13258	260.61267	32.13237	15.613	3.043	3.900	0.590
MACSJ2129.4-0741	0.5880	322.35717	-7.69189	322.35913	-7.69133	13.486	3.890	6.127	1.179
RXJ2129.7+0005	0.2340	322.41650	0.08922	322.41660	0.08861	4.470	1.158	4.277	0.491
ABELL2390	0.2330	328.40446	17.69594	328.40308	17.69493	11.183	2.396	9.652	1.668
RXJ2228.6+2037	0.4110	337.13658	20.62072	337.14047	20.62040	9.728	2.626	6.844	0.819
MACSJ2243.3-0935	0.4470	340.83933	-9.59522	340.83868	-9.59470	20.294	3.865	8.625	1.317
RXJ2248.7-4431	0.3480	342.18317	-44.53092	342.18243	-44.53054	12.400	3.605	14.262	3.762
ABELL2631	0.2780	354.40971	0.27069	354.40634	0.26678	11.748	1.888	9.785	3.807
SPT-CLJ2341-5119	1.0030	355.30092	-51.32850	355.30100	-51.32860	1.600	1.890	3.190	0.750

Table 6.4: The *reference* sample. Column 1: cluster names from the CoMaLit catalogue (entries Comalit_Name and Comalit_Num). Column 2: redshift. Columns 3 to 6: right ascension α and declination δ of the cluster centres according to CoMaLit or X-rays. Columns 7 to 10: cluster masses and uncertainties from the CoMaLit catalogue and from the XMM-*Newton* analysis.

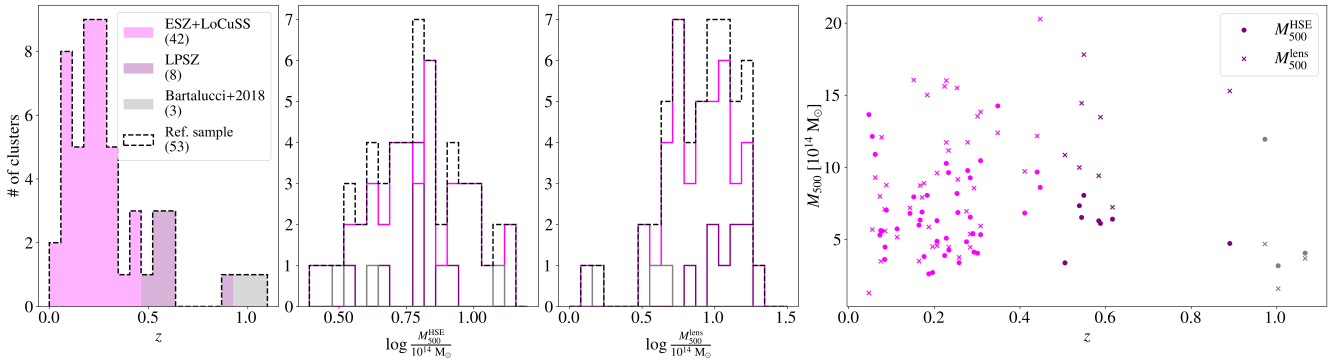

Figure 6.5: Main characteristics of the *reference* sample. Histograms in the left panels show the redshift, HSE mass and lensing mass distributions. We show in magenta, purple and grey the distributions for ESZ+LoCuSS, LPSZ and Bartalucci+2018 clusters, respectively. The black dashed lines represent the distributions for the full *reference* sample. In the right panel we show the HSE and lensing masses as a function of redshift for all the clusters.

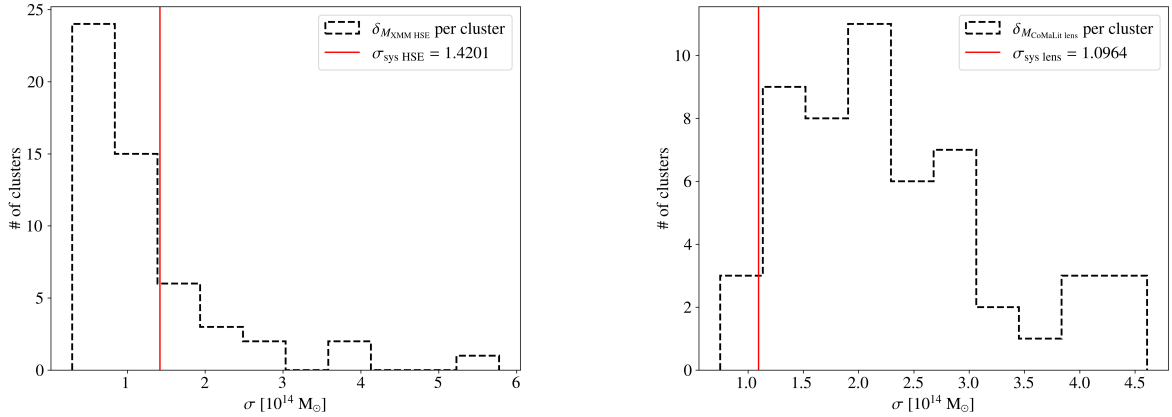

Figure 6.6: Comparison between statistical uncertainties and systematic scatters for the *reference* sample. Dashed line histograms show the statistical uncertainties of all HSE mass estimates from XMM-*Newton* reference analysis (left) and CoMaLit lensing mass estimates (right). Vertical red lines give the systematic scatter estimated with respect to other published results in Sect. 6.3.3.

Fig 6.6 the systematic standard deviation values to the individual statistical uncertainties of the masses from the XMM-*Newton* reference pipeline and the CoMaLit catalogue.

In the following sections we will investigate how the HSE-to-lensing mass bias and scaling relation change when accounting for these systematic scatters. In order to propagate the scatters to the final results, we will consider that the uncertainties in the mass of each cluster are the quadratic sum of the measured statistical uncertainties and the systematic scatters derived in this section. We have

$$\delta^2_{\rm lens} = \delta^2_{M_{\rm CoMaLit\ lens}} + \sigma^2_{\rm sys\ lens} \tag{6.5}$$

for the lensing masses, and

$$\delta^2_{\rm HSE} = \delta^2_{M_{\rm XMM\ HSE}} + \sigma^2_{\rm sys\ HSE} \tag{6.6}$$

for the hydrostatic ones.

This is a very conservative approach that assumes that the mass estimates from the X-ray reference pipeline and the CoMaLit catalogue may have an additional error (due to, for example, the used data set or the mass reconstruction method) that can be quantified from the distance to other estimates. Such supplementary error is usually not considered in the literature. For this reason, we also perform the study without accounting for the systematic uncertainties. An alternative approach was considered in Sereno and Ettori (2015) [314] by separating the analysis in subsamples.

Sample	# of clusters	z_*	No $\sigma^2_{\rm sys}$		With $\sigma^2_{\rm sys}$	
			$(1-\mathcal{B})/(1+z_*)^{\beta_z}$	β_z	$(1-\mathcal{B})/(1+z_*)^{\beta_z}$	β_z
***Reference* sample**	**53**	**0.253**	$0.585^{+0.059}_{-0.050}$	$-0.797^{+0.309}_{-0.373}$	$\mathbf{0.632^{+0.093}_{-0.074}}$	$\mathbf{-0.787^{+0.418}_{-0.529}}$
$z < 0.9$	50	0.234	$0.591^{+0.060}_{-0.050}$	$-0.846^{+0.306}_{-0.381}$	$0.642^{+0.094}_{-0.079}$	$-0.860^{+0.427}_{-0.528}$
$z < 0.5$	42	0.215	$0.578^{+0.095}_{-0.082}$	$-0.744^{+0.724}_{-0.773}$	$0.618^{+0.130}_{-0.112}$	$-0.661^{+0.887}_{-0.948}$
$z < 0.2$	19	0.113	$0.716^{+0.159}_{-0.144}$	$-1.577^{+1.589}_{-1.560}$	$0.802^{+0.216}_{-0.235}$	$-2.226^{+2.515}_{-1.993}$
$z > 0.2$	34	0.305	$0.471^{+0.071}_{-0.057}$	$-0.271^{+0.344}_{-0.424}$	$0.543^{+0.131}_{-0.092}$	$-0.392^{+0.496}_{-0.668}$
$z > 0.5$	11	0.588	$0.665^{+0.620}_{-0.279}$	$-1.043^{+1.020}_{-1.355}$	$0.692^{+1.267}_{-0.356}$	$-0.987^{+1.380}_{-2.249}$
Ref. no CL J1226.9+3332	52	0.244	$0.548^{+0.069}_{-0.060}$	$-0.467^{+0.453}_{-0.505}$	$0.594^{+0.100}_{-0.086}$	$-0.483^{+0.562}_{-0.639}$
$z < 0.9$ no CL J1226.9+3332	49	0.233	$0.560^{+0.071}_{-0.059}$	$-0.578^{+0.443}_{-0.517}$	$0.610^{+0.104}_{-0.085}$	$-0.610^{+0.548}_{-0.648}$
$z > 0.2$ no CL J1226.9+3332	33	0.301	$0.353^{+0.076}_{-0.059}$	$0.855^{+0.552}_{-0.650}$	$0.432^{+0.135}_{-0.096}$	$0.452^{+0.732}_{-0.886}$
$z > 0.5$ no CL J1226.9+3332	10	0.586	$0.060^{+0.154}_{-0.015}$	$4.593^{+0.584}_{-2.867}$	$0.068^{+0.350}_{-0.018}$	$4.398^{+0.592}_{-4.097}$

Table 6.5: Best-fit values and uncertainties for the normalisation and redshift evolution parameters of the mass bias model in Eq. 6.7 for different subsamples of the *reference* sample. Columns 1 to 3 present the considered sample, the number of clusters and the median redshift. Columns 4 to 7 give the best-fit values with 16th and 84th percentiles of the posterior distributions for parameters describing bias evolution, accounting (columns 6 and 7) or not (columns 4 and 5) for the systematic scatters. In bold the values corresponding to the full *reference* sample accounting for the systematic scatters.

6.4 Direct HSE-to-lensing mass bias measurement

The bias of HSE masses with respect to lensing estimates is defined from the ratio of the masses following Eq. 5.19. For simplicity, in the rest of the chapter we will name the HSE-to-lensing mass bias without subscripts, $b = b_{\rm HSE/lens}$.

Following the parametrisation in Salvati et al. (2019) [194] and Wicker et al. (2023) [156], we describe the redshift evolution of the HSE-to-lensing mass bias as

$$M^{\rm HSE}_{500}/M^{\rm lens}_{500}(z) = (1-b)(z) = (1-\mathcal{B})\left(\frac{1+z}{1+z_*}\right)^{\beta_z}, \tag{6.7}$$

where $(1-\mathcal{B})$ is the bias normalised at the pivot redshift, z_*, and β_z describes the evolution with redshift. As in Salvati et al. (2019) [194], we take z_* the median redshift value of the clusters in the analysed sample. In Wicker et al. (2023) [156] the pivot redshift is the mean of the sample.

We perform an MCMC analysis to constrain the model in Eq. 6.7 with the *reference* sample. We use the `emcee` Python package [243, 244] and consider uniform priors for the parameters, $(1-\mathcal{B}) \sim \mathcal{U}(0,2)$ and $\beta_z \sim \mathcal{U}(-8,8)$. We assume a Gaussian likelihood and no correlation between points. We show in Fig. 6.7 the HSE-to-lensing mass ratio with respect to redshift for the 53 clusters in the *reference* sample. Uncertainties include systematic scatter following Eq. 6.5 and 6.6. The grey shaded area in the top panel indicates the 16th to 84th percentile region of the bias evolution model obtained from the posterior distributions of the fitted parameters. For comparison, the horizontal lines show the mean (dash-dotted line), median (dotted line) and error-weighted mean (solid line) HSE-to-lensing mass ratio obtained with the masses for the *reference* sample. Posterior distributions for the fitted parameters are shown with grey contours in Fig. 6.8. The best-fit values and uncertainties are given in the first row of Table 6.5. We give $(1-\mathcal{B})/(1+z_*)^{\beta_z}$, which is the value of the bias at $z = 0$. We also report the results without accounting for the systematic uncertainties on the lensing and HSE masses. As expected, when accounting for $\sigma^2_{\rm sys}$ in the uncertainties, the posterior distributions are enlarged by a factor up to 50%.

Due to the significant differences in the mass uncertainties and the non-uniform distribution of the clusters in redshift, certain subsamples might be driving the fit of the model. To check for these effects and investigate any dependence with redshift, we repeat the fit by considering clusters in different redshift ranges.

Considering only the clusters with $z < 0.9$ (that is, those in ESZ+LoCuSS and LPSZ samples) and only those with $z < 0.5$ (only ESZ+LoCuSS), the results are very close to the ones obtained with the *reference*

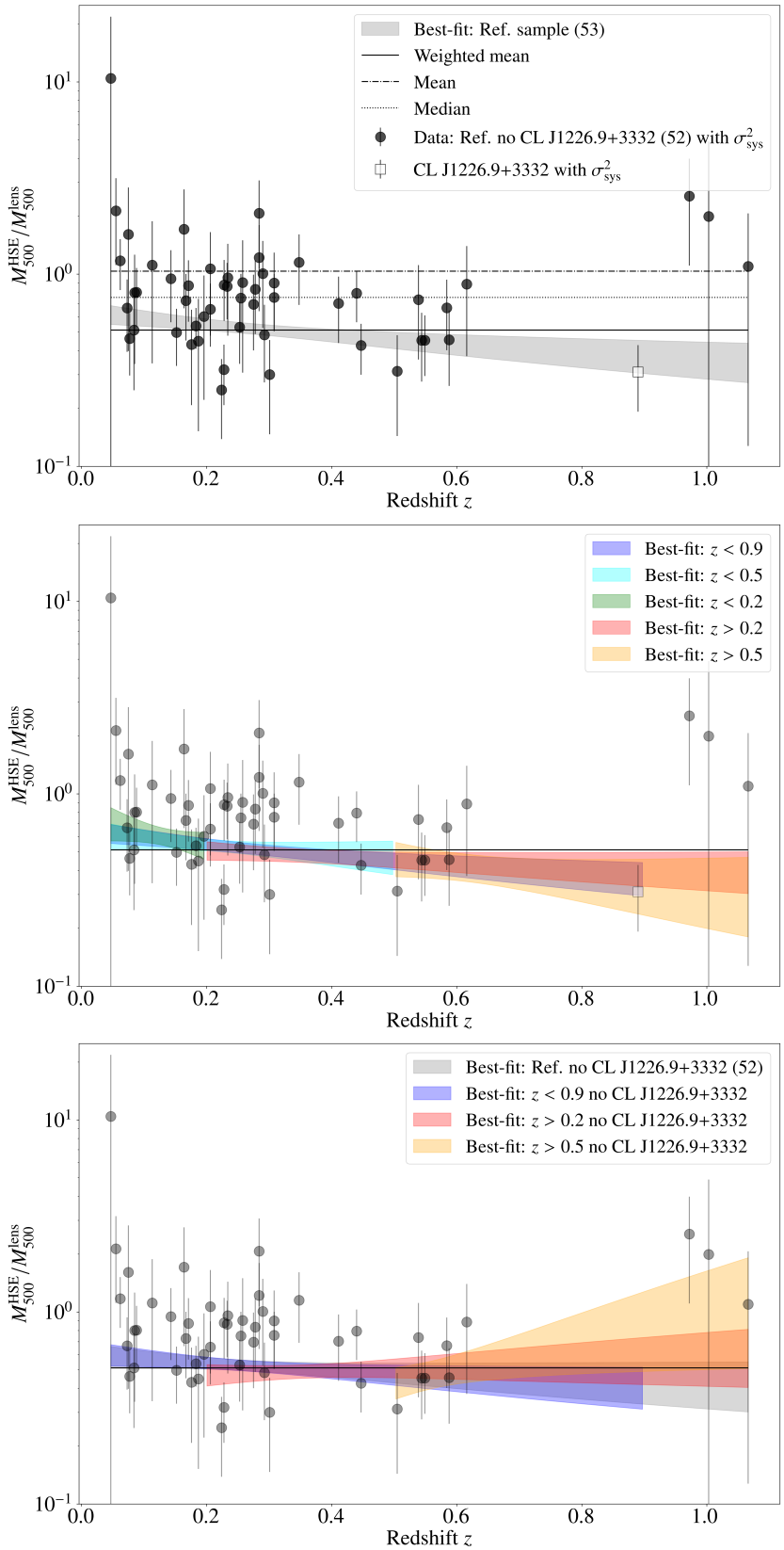

Figure 6.7: HSE-to-lensing mass ratio as a function of the redshift. Markers with error bars show the HSE-to-lensing mass ratio for each cluster in the *reference* sample with error bars accounting for the systematic uncertainties. Horizontal solid, dotted and dash-dotted black lines give the error-weighted mean, median and mean mass ratio for the data points, respectively. Colour shaded areas represent the 16th to 84th percentiles of the bias evolution model obtained by fitting different redshift ranges. Top: the bias evolution model obtained with the *reference* sample. Centre: same as before, but different colours indicate the best-fit models for different redshift ranges. Bottom: as before, but excluding the CL J1226.9+3332 galaxy cluster.

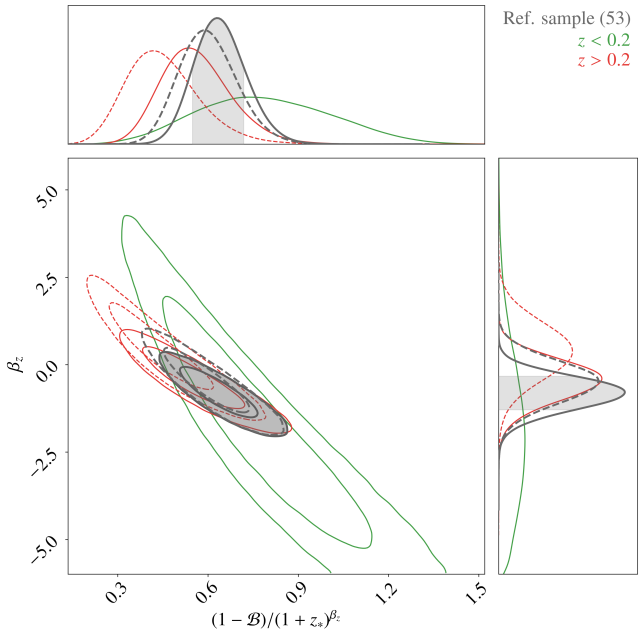

Figure 6.8: 1D and 2D posterior distributions of the parameters for the redshift-dependent mass bias model, accounting for systematic uncertainties. Different colours correspond to the results for the various samples presented in Table 6.5. For the sake of clarity, we only show in grey, green and red the results for the whole sample, the $z < 0.2$, and the $z > 0.2$ subsamples, respectively. Dashed distributions have been obtained excluding CL J1226.9+3332 galaxy cluster.

sample. This means that the grey result in Fig. 6.7 and 6.8 is most probably dominated by ESZ+LoCuSS clusters. Best-fit values and uncertainties for these two cases are given in Table 6.5. The corresponding bias evolution models are shown in blue ($z < 0.9$) and cyan ($z < 0.5$) in the central panel in Fig. 6.7.

We find more significant differences when considering only low redshift clusters ($z < 0.2$, in green), or, when discarding them ($z > 0.2$, in red). For low redshift clusters, the HSE masses at $z = 0$ are less biased with respect to lensing masses ($(1 - \mathcal{B})/(1 + z_*)^{\beta_z}$ closer to 1) than for the *reference* sample, but the dependence on redshift is stronger. Exactly the opposite happens when fitting only $z > 0.2$ masses: the HSE-to-lensing mass bias is larger at $z = 0$ (smaller $(1 - \mathcal{B})/(1 + z_*)^{\beta_z}$), but the redshift evolution is weaker (the absolute value of β_z smaller). These conclusions agree with the results in Wicker et al. (2023) [156], where the same cut in redshift is adopted. In Smith et al. (2016) [333] authors also reported a different tendency for *Planck* cluster masses depending on the redshift, with a larger HSE-to-lensing bias value (smaller $1 - b$) for *Planck* masses at $z > 0.3$, than the bias at $z < 0.3$. However, these masses were inferred from the SZ-mass scaling relation and not measured from profiles. Nonetheless, in our analysis β_z is compatible with no redshift evolution both for $z < 0.2$ and $z > 0.2$ subsamples (see posterior probability density contours in Fig. 6.8).

As shown in Fig. 6.5, the clusters at high redshift are rare in our sample, with a large gap between $z = 0.62$ and $z = 0.89$. Only CL J1226.9+3332, SPT-CLJ0615-5746, SPT-CLJ0546-5345 and SPT-CLJ2341-5119 are above $z = 0.62$. The CL J1226.9+3332 galaxy cluster has bias uncertainties that are more than one order of magnitude smaller than the uncertainties of the three SPT clusters. We suspect that this single cluster may be forcing the bias towards lower values at high redshift. To test the impact that CL J1226.9+3332 has on the fits, we repeat the analyses excluding it. The results without CL J1226.9+3332 are shown, following the same colour scheme as before, in the bottom panel in Fig. 6.7 and with dashed lines in Fig. 6.8. β_z varies significantly when excluding CL J1226.9+3332 and it tends to be more compatible with no redshift evolution. At the same time, the bias at $z = 0$ is slightly shifted towards lower values. All the results are summarised in Table 6.5.

The described HSE-to-lensing mass bias estimation method neglects the intrinsic scatters of the HSE and lensing mass estimates. As explained in Sereno and Ettori (2015) [314], this could influence the resulting bias

that relates HSE and lensing masses. For this reason, in the next section we take a different approach to estimate the HSE-to-lensing mass bias.

6.5 HSE-to-lensing mass scaling relation

Estimating the scaling relation between HSE and lensing masses is an alternative way for measuring the HSE-to-lensing mass bias (Eq. 5.19), together with the intrinsic scatter associated with HSE and lensing masses. We follow the methodology presented in Sereno and Ettori (2015) [314], and, consider that both the HSE and the lensing masses are scattered and biased estimates of the true mass of clusters, such that

$$\ln M^{\rm lens} \pm \delta_{\rm lens} = \alpha^{\rm lens} + \beta^{\rm lens} \ln M^{\rm True} \pm \sigma^{\rm lens}, \tag{6.8}$$

$$\ln M^{\rm HSE} \pm \delta_{\rm HSE} = \alpha^{\rm HSE} + \beta^{\rm HSE} \ln M^{\rm True} \pm \sigma^{\rm HSE}. \tag{6.9}$$

Here $\delta_{\rm lens}$ and $\delta_{\rm HSE}$ are the measurement uncertainties associated with the logarithm of the lensing and HSE mass estimates for each cluster. α and β are the natural logarithm of the bias and the deviation from linearity, respectively. The intrinsic scatters of the lensing and HSE masses with respect to the true mass are given by $\sigma^{\rm lens}$ and $\sigma^{\rm HSE}$. All the masses in the arguments of logarithms are in 10^{14} $M_\odot$ units. Authors in Sereno and Ettori (2015) [314] verified that the scatter and bias results do not vary if $\alpha^{\rm lens} = 0$ or $\alpha^{\rm HSE} = 0$ is considered, so following their work we fix $\alpha^{\rm lens} = 0$.

We use the LInear Regression in Astronomy (LIRA[18]) [345] R package and the `pylira`[19] Python wrapper to perform the fit of the SR. LIRA performs the Gibbs sampling of a posterior distribution constructed from an MCMC fit based on a Bayesian hierarchical modelling. It can account for heteroscedastic measurement errors, intrinsic scatter and time evolution of the SR.

6.5.1 Reference scaling relation

The SR of reference in our analysis is built using the aforementioned 53 clusters in the *reference* sample, assuming that both the lensing and the HSE masses scale linearly with the true mass, $\beta^{\rm lens} = 1$ and $\beta^{\rm HSE} = 1$, and, that there is no evolution of the SR with redshift. The MCMC sampling is performed using 200 chains and 6×10^6 steps, with a burn-in of the first half of the steps. Convergence is checked following the $\hat{R}$ test of Gelman and Rubin (1992) [253]. We take uniform priors for the free parameters: $\alpha^{\rm HSE} \sim \mathcal{U}(-4, 4)$, $\sigma^{\rm HSE} \sim \mathcal{U}(0, 10)$, $\sigma^{\rm lens} \sim \mathcal{U}(0, 10)$.

We present in the left panel in Fig. 6.9 the HSE-to-lensing mass scaling relation obtained with the *reference* sample. Data points correspond to each one of the clusters in the sample, with the ellipses in the figure indicating the error bars in both axes when considering the systematic scatter. We assume no correlation between both mass estimates. The grey and pink lines show respectively the scaling relation accounting and not accounting for the systematic scatter in the error bars of each cluster (Eq. 6.5 and 6.6). Shaded areas indicate the 1σ region. The black dashed line shows the one-to-one relation between HSE and lensing masses.

In the right panel in Fig. 6.9 we show the posterior distributions of the fitted scaling relation parameters. The intrinsic scatter related to HSE masses is remarkably shifted towards zero when accounting for the systematic scatter in the error bars of cluster masses. This is expected since increasing the error bars of clusters reduces the need to have a dispersion around the SR. The median values with the 16th and 84th percentiles of the posterior distributions of $\alpha^{\rm HSE}$, $\sigma^{\rm HSE}$ and $\sigma^{\rm lens}$ are given in the first row of Table 6.6. From $\alpha^{\rm HSE}$ we compute the HSE-to-lensing mass bias at R_{500} (Eq. 5.19), which gives $(1-b) = 0.739^{+0.075}_{-0.070}$ considering the systematic uncertainties as described in Sect. 6.3.3.

[18] https://cran.r-project.org/web/packages/lira/
[19] https://github.com/fkeruzore/pylira

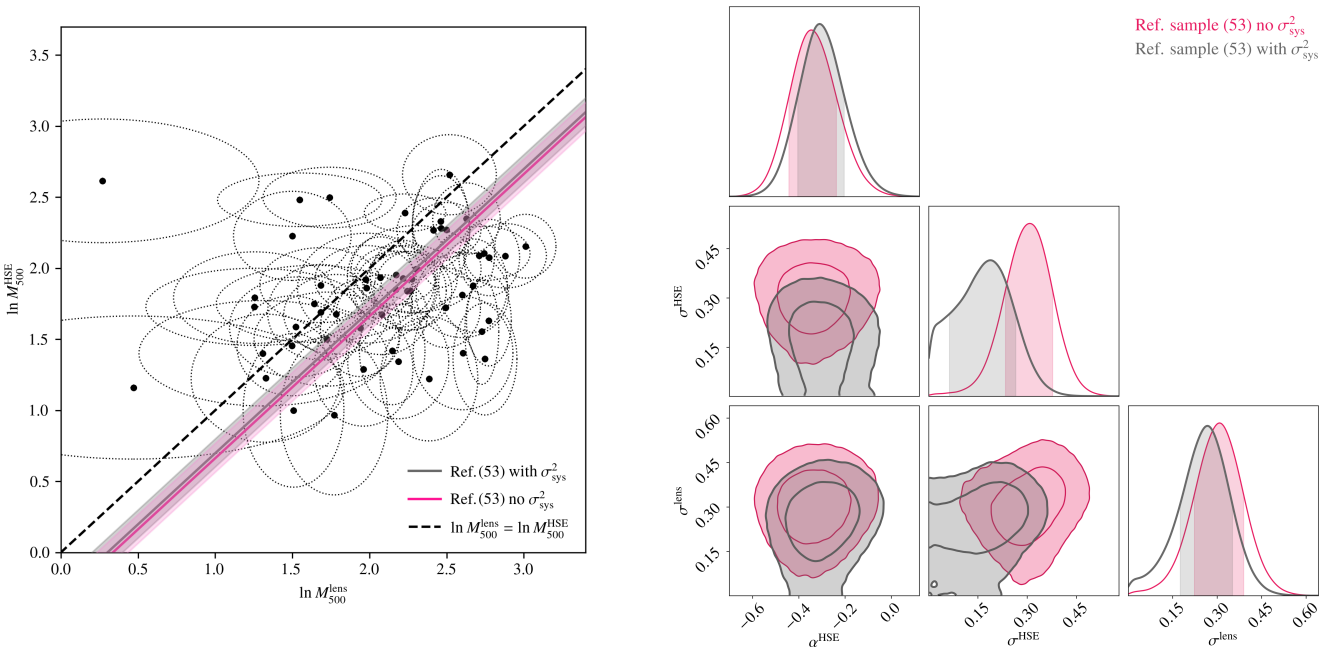

Figure 6.9: Scaling relation between HSE and lensing masses in the *reference* sample. Data points with ellipses represent each cluster masses and the uncertainties in both axes accounting for the systematic scatter. The pink line corresponds to the SR for the median value of parameters obtained without $\sigma_{\rm sys}$ and the solid grey line with $\sigma_{\rm sys}$. The shaded regions show the 16th and 84th percentiles and the black dashed line gives the one-to-one relation. The corner plots in the right panel are the posterior 1D and 2D distributions of the parameters in the SR, including (grey) or not (pink) systematic scatters.

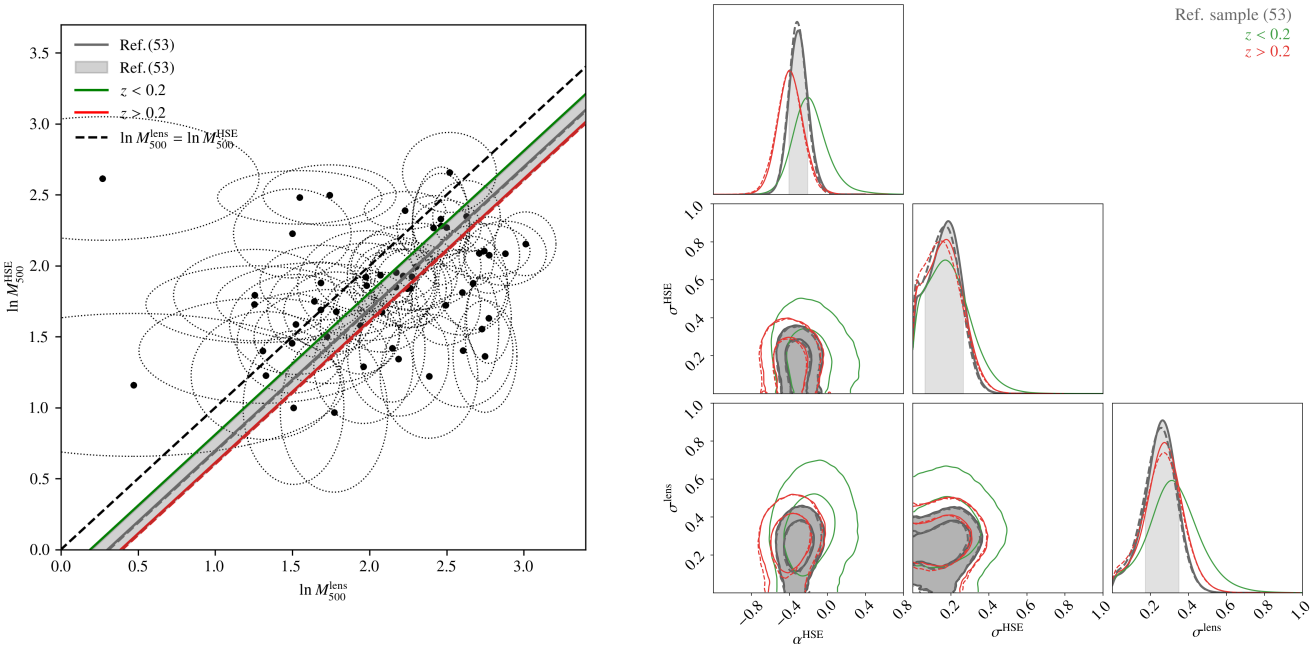

Figure 6.10: Scaling relation between HSE and lensing masses for the *reference* sample in grey and for different subsamples in colours, all accounting for $\sigma_{\rm sys}$. As in Fig. 6.8, we only show the cases for $z > 0.2$ and $z < 0.2$. The corner plots in the right panel are the posterior 1D and 2D distributions of the parameters in the SR.

Cluster sample	# of clusters	No $\sigma^2_{\rm sys}$			
		$\alpha^{\rm HSE}$	$e^{\alpha^{\rm HSE}} = (1-b)$	$\sigma^{\rm HSE}$	$\sigma^{\rm lens}$
Reference sample	53	$-0.338^{+0.105}_{-0.097}$	$0.713^{+0.075}_{-0.069}$	$0.304^{+0.069}_{-0.072}$	$0.305^{+0.080}_{-0.083}$
$z < 0.9$	50	$-0.309^{+0.124}_{-0.110}$	$0.734^{+0.091}_{-0.081}$	$0.275^{+0.071}_{-0.071}$	$0.267^{+0.083}_{-0.086}$
$z < 0.5$	42	$-0.328^{+0.111}_{-0.102}$	$0.720^{+0.080}_{-0.073}$	$0.282^{+0.080}_{-0.086}$	$0.308^{+0.090}_{-0.091}$
$z < 0.2$	19	$-0.215^{+0.223}_{-0.166}$	$0.806^{+0.180}_{-0.133}$	$0.332^{+0.114}_{-0.128}$	$0.368^{+0.155}_{-0.152}$
$z > 0.2$	34	$-0.421^{+0.139}_{-0.129}$	$0.656^{+0.091}_{-0.085}$	$0.298^{+0.076}_{-0.090}$	$0.334^{+0.090}_{-0.086}$
$z > 0.5$	11	$-0.668^{+0.316}_{-0.320}$	$0.513^{+0.162}_{-0.164}$	$0.403^{+0.155}_{-0.116}$	$0.307^{+0.200}_{-0.157}$
Ref. no CL J1226.9+3332	52	$-0.350^{+0.098}_{-0.092}$	$0.705^{+0.070}_{-0.065}$	$0.294^{+0.072}_{-0.075}$	$0.295^{+0.084}_{-0.087}$
$z < 0.9$ no CL J1226.9+3332	49	$-0.338^{+0.114}_{-0.099}$	$0.713^{+0.081}_{-0.070}$	$0.273^{+0.073}_{-0.074}$	$0.274^{+0.083}_{-0.086}$
$z > 0.2$ no CL J1226.9+3332	33	$-0.430^{+0.130}_{-0.126}$	$0.651^{+0.085}_{-0.082}$	$0.289^{+0.082}_{-0.099}$	$0.320^{+0.093}_{-0.093}$
$z > 0.5$ no CL J1226.9+3332	10	$-0.629^{+0.332}_{-0.410}$	$0.533^{+0.177}_{-0.219}$	$0.446^{+0.184}_{-0.133}$	$0.189^{+0.209}_{-0.131}$
		With $\sigma^2_{\rm sys}$			
		$\alpha^{\rm HSE}$	$e^{\alpha^{\rm HSE}} = (1-b)$	$\sigma^{\rm HSE}$	$\sigma^{\rm lens}$
***Reference* sample**	**53**	$\mathbf{-0.303^{+0.101}_{-0.095}}$	$\mathbf{0.739^{+0.075}_{-0.070}}$	$\mathbf{0.166^{+0.086}_{-0.101}}$	$\mathbf{0.257^{+0.080}_{-0.092}}$
$z < 0.9$	50	$-0.260^{+0.124}_{-0.110}$	$0.771^{+0.095}_{-0.084}$	$0.122^{+0.090}_{-0.082}$	$0.220^{+0.084}_{-0.099}$
$z < 0.5$	42	$-0.280^{+0.114}_{-0.104}$	$0.756^{+0.086}_{-0.079}$	$0.136^{+0.098}_{-0.090}$	$0.262^{+0.089}_{-0.100}$
$z < 0.2$	19	$-0.191^{+0.181}_{-0.157}$	$0.827^{+0.150}_{-0.129}$	$0.179^{+0.123}_{-0.111}$	$0.318^{+0.135}_{-0.130}$
$z > 0.2$	34	$-0.388^{+0.136}_{-0.127}$	$0.679^{+0.092}_{-0.086}$	$0.162^{+0.099}_{-0.103}$	$0.271^{+0.095}_{-0.103}$
$z > 0.5$	11	$-0.621^{+0.305}_{-0.308}$	$0.538^{+0.164}_{-0.166}$	$0.293^{+0.175}_{-0.150}$	$0.252^{+0.206}_{-0.156}$
Ref. no CL J1226.9+3332	52	$-0.312^{+0.096}_{-0.091}$	$0.732^{+0.070}_{-0.067}$	$0.154^{+0.089}_{-0.097}$	$0.249^{+0.084}_{-0.096}$
$z < 0.9$ no CL J1226.9+3332	49	$-0.287^{+0.116}_{-0.102}$	$0.750^{+0.087}_{-0.077}$	$0.120^{+0.089}_{-0.080}$	$0.226^{+0.085}_{-0.099}$
$z > 0.2$ no CL J1226.9+3332	33	$-0.397^{+0.131}_{-0.131}$	$0.672^{+0.088}_{-0.088}$	$0.151^{+0.103}_{-0.097}$	$0.264^{+0.100}_{-0.112}$
$z > 0.5$ no CL J1226.9+3332	10	$-0.587^{+0.332}_{-0.427}$	$0.556^{+0.185}_{-0.238}$	$0.339^{+0.207}_{-0.170}$	$0.190^{+0.216}_{-0.132}$

Table 6.6: Table summarising the median values and uncertainties at 16th and 84th percentiles of the parameters for the HSE-to-lensing SR assuming linearity ($\beta^{\rm HSE} = 1$). We present the results for different data subsamples, with and without accounting for the systematic uncertainties in the error bars of the masses. We show in bold the parameters for the scaling relation of reference presented in Sect. 6.5.

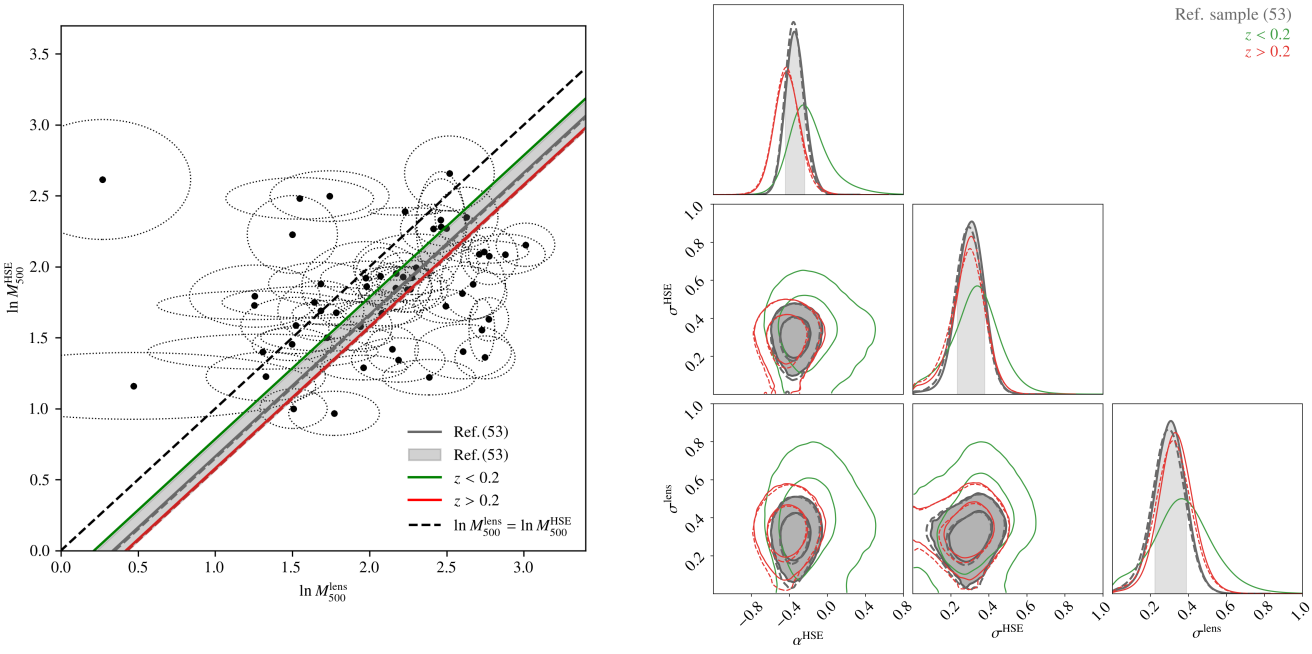

Figure 6.11: Same as Fig. 6.10, but without considering the systematic uncertainties in the data.

As for the bias model in Sect. 6.4, we also want to check how the SR parameters may vary depending on the chosen redshift range. Therefore, we repeat the analysis for the different redshift subsamples considered in Sect. 6.4. We present in Fig. 6.10 and 6.11, and in Table 6.6 the different results, with and without $\sigma^2_{\rm sys}$. Again, we observe that the bias changes for $z < 0.2$ and $z > 0.2$ clusters, in line with a $(1 - b)$ value that decreases with redshift. The SRs for the $z < 0.9$ and $z < 0.5$ samples remain almost unchanged with respect to the SR of reference. Overall, we find that the SRs are compatible for the different subsamples.

The posterior distribution of the SR parameters obtained for the $z < 0.5$ clusters without $\sigma^2_{\rm sys}$ (see Fig. 6.12) can be directly compared to Figure 5 in Sereno and Ettori (2015) [314]. In that work, the 50 CCCP clusters from Mahdavi et al. (2013) [259] were used to measure the HSE-to-lensing mass scaling relation (even though the HSE masses were evaluated at the R_{500} obtained from lensing). The intrinsic scatters seem to be differently correlated in Sereno and Ettori (2015) [314] and in our results. However, in both cases, we observe no strong correlation between $\alpha^{\rm HSE}$ and the intrinsic HSE or lensing scatters. In our case, for the $z < 0.5$ clusters without (with) $\sigma^2_{\rm sys}$ we measure $(1 - b) = 0.720^{+0.080}_{-0.073}$ ($(1 - b) = 0.756^{+0.086}_{-0.079}$). These results (Table 6.6) are in line with the values reported in Table 6 in Sereno and Ettori (2015) [314] and Table 2 in Lovisari et al. (2020) [301].

6.5.2 Investigations of possible model extensions

Beyond the reference scaling relation, for which we have assumed no redshift evolution and a linear scaling between the masses, in this section we test if relaxing some of these assumptions improves the description of the data by the scaling relation model.

Deviation from linearity

The HSE and/or lensing masses could also scale non-linearly with the true mass, meaning that the HSE-to-lensing bias would depend on the mass of the clusters. In Hoekstra et al. (2015) [315] and von der Linden et al. (2014) [316] authors investigated such dependence on the mass comparing *Planck* results to CCCP and WtG lensing masses, respectively. Both works found modest evidence for a mass-dependence: $M_{Planck} \propto M_{\rm CCCP}^{0.64\pm0.17}$

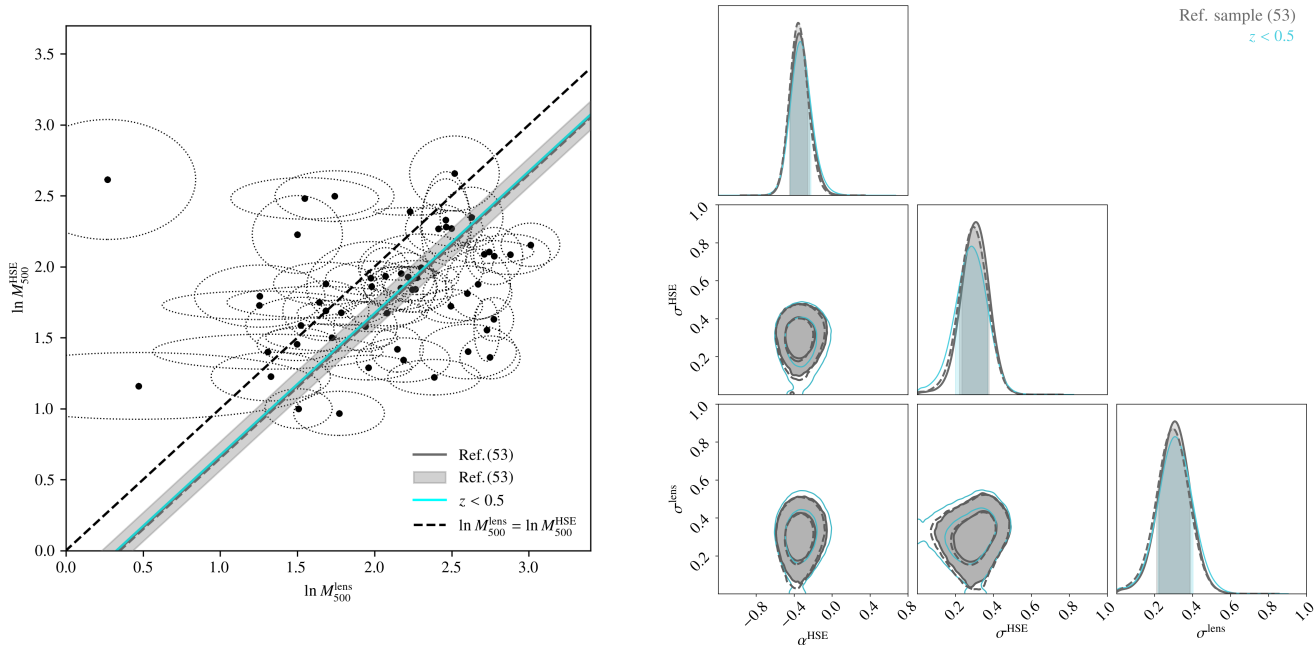

Figure 6.12: As Fig. 6.9, but without considering systematic uncertainties in the data. The grey and cyan lines correspond to the results for the *reference* sample and for the subsample containing only $z < 0.5$ clusters.

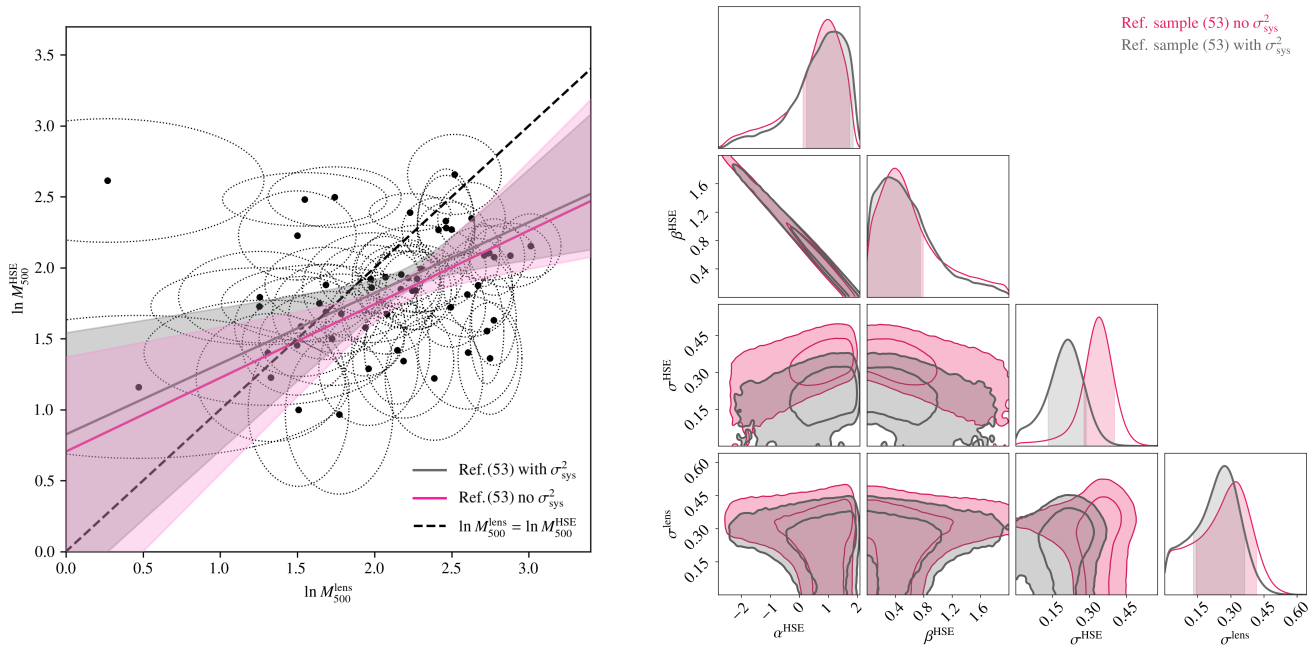

Figure 6.13: Same as Fig. 6.9 considering a deviation from linearity.

Cluster sample	# of clusters	No $\sigma^2_{\rm sys}$				
		$\alpha^{\rm HSE}$	$\beta^{\rm HSE}$	$\sigma^{\rm HSE}$	$\sigma^{\rm lens}$	$\gamma^{\rm HSE}$
Reference sample	53	$0.705^{+0.666}_{-1.249}$	$0.519^{+0.576}_{-0.309}$	$0.335^{+0.057}_{-0.066}$	$0.275^{+0.103}_{-0.163}$	[0]
Reference sample (BCES)	53	0.826 ± 0.886	0.481 ± 0.415	0.326^{*}	-	[0]
Reference sample	53	$-0.219^{+0.137}_{-0.134}$	[1]	$0.303^{+0.069}_{-0.072}$	$0.295^{+0.082}_{-0.085}$	$-1.742^{+1.082}_{-1.083}$
Ref. no CL J1226.9+3332	52	$-0.263^{+0.140}_{-0.136}$	[1]	$0.297^{+0.072}_{-0.073}$	$0.292^{+0.084}_{-0.087}$	$-1.168^{+1.156}_{-1.163}$
		$A^{\rm HSE}$ [10^{14} M$_\odot$]	$B^{\rm HSE}$	$\sigma^{\rm HSE}$ [10^{14} M$_\odot$]	$\sigma^{\rm lens}$ [10^{14} M$_\odot$]	$\gamma^{\rm HSE}$ [10^{14} M$_\odot$]
Reference sample	53	$0.818^{+2.313}_{-3.037}$	$0.614^{+0.351}_{-0.270}$	$1.673^{+0.413}_{-0.640}$	$3.159^{+0.701}_{-0.983}$	[0]
Reference sample (BCES)	53	4.467 ± 1.85	0.246 ± 0.19	2.109^{*}	-	[0]
Reference sample	53	$0.545^{+2.465}_{-2.925}$	$0.675^{+0.334}_{-0.291}$	$1.644^{+0.439}_{-0.700}$	$3.188^{+0.674}_{-0.854}$	$-2.685^{+4.654}_{-4.260}$
		With $\sigma^2_{\rm sys}$				
		$\alpha^{\rm HSE}$	$\beta^{\rm HSE}$	$\sigma^{\rm HSE}$	$\sigma^{\rm lens}$	$\gamma^{\rm HSE}$
Reference sample	53	$0.824^{+0.719}_{-1.087}$	$0.498^{+0.481}_{-0.326}$	$0.204^{+0.068}_{-0.082}$	$0.242^{+0.091}_{-0.135}$	[0]
Reference sample (BCES)	53	1.000 ± 0.692	0.397 ± 0.324	0.191^{*}	-	[0]
Reference sample	53	$-0.193^{+0.135}_{-0.134}$	[1]	$0.168^{+0.086}_{-0.100}$	$0.246^{+0.082}_{-0.095}$	$-1.530^{+1.071}_{-1.085}$
Ref. no CL J1226.9+3332	52	$-0.242^{+0.139}_{-0.137}$	[1]	$0.153^{+0.090}_{-0.096}$	$0.248^{+0.084}_{-0.093}$	$-0.896^{+1.154}_{-1.155}$
		$A^{\rm HSE}$ [10^{14} M$_\odot$]	$B^{\rm HSE}$	$\sigma^{\rm HSE}$ [10^{14} M$_\odot$]	$\sigma^{\rm lens}$ [10^{14} M$_\odot$]	$\gamma^{\rm HSE}$ [10^{14} M$_\odot$]
Reference sample	53	$1.603^{+1.665}_{-2.994}$	$0.522^{+0.349}_{-0.194}$	$0.949^{+0.557}_{-0.602}$	$2.867^{+0.806}_{-1.251}$	[0]
Reference sample (BCES)	53	4.644 ± 1.727	0.226 ± 0.176	1.340^{*}	-	[0]
Reference sample	53	$1.434^{+1.780}_{-3.005}$	$0.570^{+0.346}_{-0.210}$	$0.950^{+0.570}_{-0.612}$	$2.927^{+0.771}_{-1.131}$	$-2.493^{+4.535}_{-4.282}$

Table 6.7: Table summarising the median values and uncertainties at the 16th and 84th percentiles of the parameters in the HSE-to-lensing SR when considering a deviation from linearity, an offset between HSE and lensing masses or an evolution with redshift. We present the results for the *reference* sample, accounting or not for the systematic scatter in the error bars of the masses. For the BCES fit we report the best-fit values and 1σ uncertainties. $^{(*)}$ We also calculate the scatter with respect to the best BCES scaling relations following Eq. 6.4.

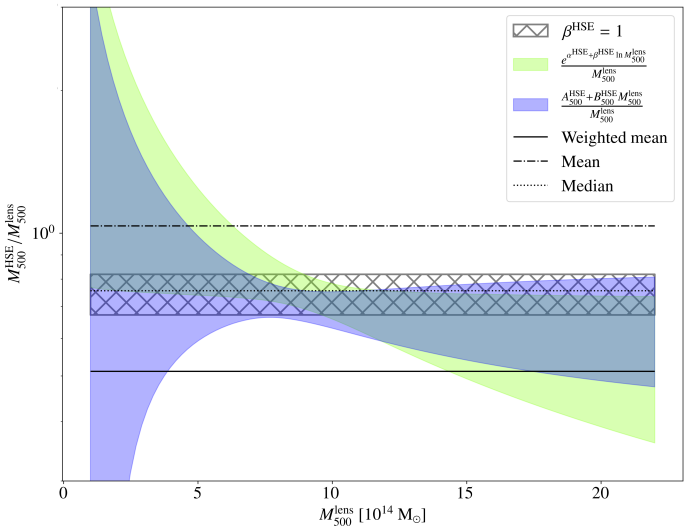

Figure 6.14: HSE-to-lensing mass ratio as a function of the lensing mass. The grey hatched area indicates the 16th to 84th percentiles of the HSE-to-lensing mass bias without mass dependence, accounting for systematic uncertainties on HSE and lensing masses. The green area shows the bias evolution when assuming a deviation from linearity of the HSE and lensing masses. The blue area indicates the bias evolution when considering an offset between HSE and lensing masses. Horizontal solid, dotted and dash-dotted black lines give respectively the error-weighted mean, median and mean mass ratio for the 53 *reference* sample clusters, same as in Fig. 6.7.

with $\alpha^{\rm HSE} \sim 0.55$ in Hoekstra et al. (2015) [315], and $M_{Planck} \propto M_{\rm WtG}^{0.68^{+0.15}_{-0.11}}$ with $\alpha^{\rm HSE} \sim 0.38$ and $M_{Planck} \propto M_{\rm WtG}^{0.76^{+0.39}_{-0.20}}$ with $\alpha^{\rm HSE} \sim 0.19$ in von der Linden et al. (2014) [316] for different cluster samples. Physically, this mass dependence could correspond, for example, to an impact of the baryonic physics that would depend on the strength of the clusters potential wells. In this case, low mass clusters having shallower potential wells, we can imagine that baryonic effects are stronger in them [346]. On the contrary, simulations [347] also indicate that massive objects are the most disturbed ones and have, probably, more complex temperature structures.

We also test this hypothesis by fitting the SR in Eq. 6.8 and 6.9 leaving $\beta^{\rm HSE}$ as a free parameter. We take a uniform prior for $\beta^{\rm HSE} \sim \mathcal{U}(0, 2)$ and consider the same priors for $\alpha^{\rm HSE}$, $\sigma^{\rm HSE}$ and $\sigma^{\rm lens}$. The resulting scaling relations are presented in Fig. 6.13 and the median values are given in Table 6.7. As shown in the corner plot in Fig. 6.13, $\alpha^{\rm HSE}$ and $\beta^{\rm HSE}$ are completely degenerated. Nevertheless, our results are in agreement with Hoekstra et al. (2015) [315] and von der Linden et al. (2014) [316]. Notice however that the HSE masses in those works were *Planck* masses from the SZ-mass scaling relation. We observe again that the HSE intrinsic scatter is shifted towards lower values when the systematic uncertainties are considered in cluster masses.

For comparison to the results obtained with LIRA, we also perform the fit of the SR using the orthogonal *Bivariate Correlated Errors and intrinsic Scatter* (BCES) method [348]. BCES favours a larger deviation from linearity, that is, smaller $\beta^{\rm HSE}$. We also report the results in Table 6.7. Given the large uncertainties on $\alpha^{\rm HSE}$ and $\beta^{\rm HSE}$, the scaling relations obtained with LIRA and BCES are compatible.

In Fig. 6.14 we present the HSE-to-lensing mass ratio as a function of the lensing mass for the $\alpha^{\rm HSE}$ and $\beta^{\rm HSE}$ values obtained from the LIRA scaling relation fit, with the green shaded area showing the 16th to 84th percentiles. The horizontal grey hatched area represents the HSE-to-lensing mass ratio measured in the previous section assuming that HSE and lensing masses scale linearly with the true mass. Given that we obtain $\beta^{\rm HSE} < 1$, on average the difference between HSE and lensing masses is larger for more massive objects. This is in agreement with the mild decreasing tendency for the HSE-to-lensing mass ratio obtained in Hoekstra et al. (2015) [315], von der Linden et al. (2014) [316], and Eckert et al. (2019) [53], but different from the trend observed in Salvati et al. (2019) [194]. Nevertheless, since we obtain $\beta^{\rm HSE} = 0.498^{+0.481}_{-0.326}$ ($\beta^{\rm HSE} = 0.519^{+0.576}_{-0.309}$), our results are consistent with no mass dependence of the ratio within 2σ (1σ) when we (do not) account for systematic uncertainties.

Considering an offset

In addition to the HSE-to-lensing mass bias defined in Eq. 5.19, there could be also an offset between the HSE and lensing mass estimates. Thus, the scaling relation could be defined as,

$$M^{\rm lens} \pm \delta_{\rm lens} = M^{\rm True} \pm \sigma^{\rm lens}, \tag{6.10}$$

$$M^{\rm HSE} \pm \delta_{\rm HSE} = A^{\rm HSE} + B^{\rm HSE} M^{\rm True} \pm \sigma^{\rm HSE}, \tag{6.11}$$

where $A^{\rm HSE}$ and $B^{\rm HSE}$ are the offset and the multiplicative factor, respectively. Here $\sigma^{\rm HSE}$ and $\sigma^{\rm lens}$ are again the scatter of HSE and lensing masses with respect to the SR, but in this case in units of 10^{14} $M_\odot$.

We perform again the fit of the SR using both the LIRA and BCES methods. We present in Fig. 6.15 and Table 6.7 the results. As for the non-linear SR fit, $A^{\rm HSE}$ and $B^{\rm HSE}$ are completely degenerated. The results obtained with LIRA indicate an offset in mass completely compatible with zero. It is reassuring to verify that the data motivates a scaling relation model for which the HSE mass goes to zero in the limit $M^{\rm True} \to 0$. We show in Fig. 6.14 the bias evolution in blue, indicating again that there is no significant trend of the HSE-to-lensing mass ratio with cluster mass.

Evolution with redshift

LIRA enables fitting a scaling relation that evolves with redshift. Looking for such evolution can be particularly interesting with our *reference* sample, given the large redshift range that it covers ($0.05 < z < 1.07$).

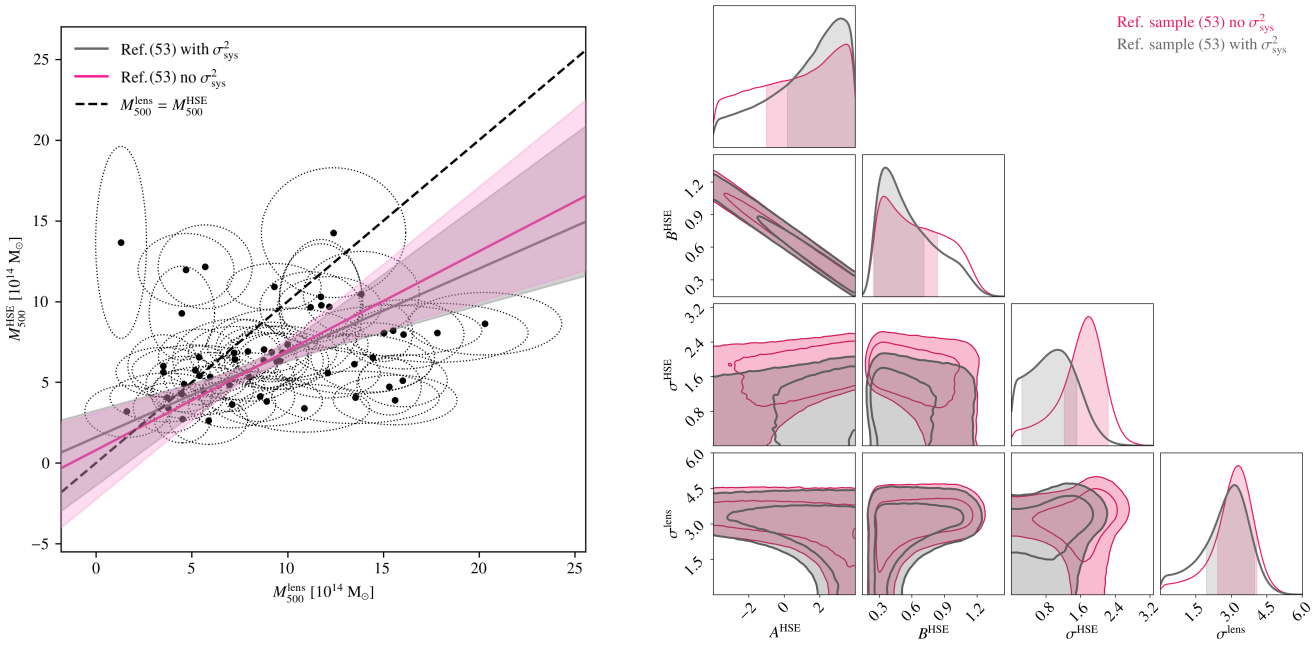

Figure 6.15: Scaling relation between HSE and lensing masses in the *reference* sample considering an offset between both mass estimates. Data points with ellipses represent each cluster's masses and the uncertainties in both axes accounting for the systematic scatter. The pink line corresponds to the SR obtained without σ_{sys} and the solid grey line with σ_{sys}. The black dashed line shows equality. The corner plots in the right panel are the posterior 1D and 2D distributions of the parameters in the SR, including (grey) or not (pink) systematic scatters.

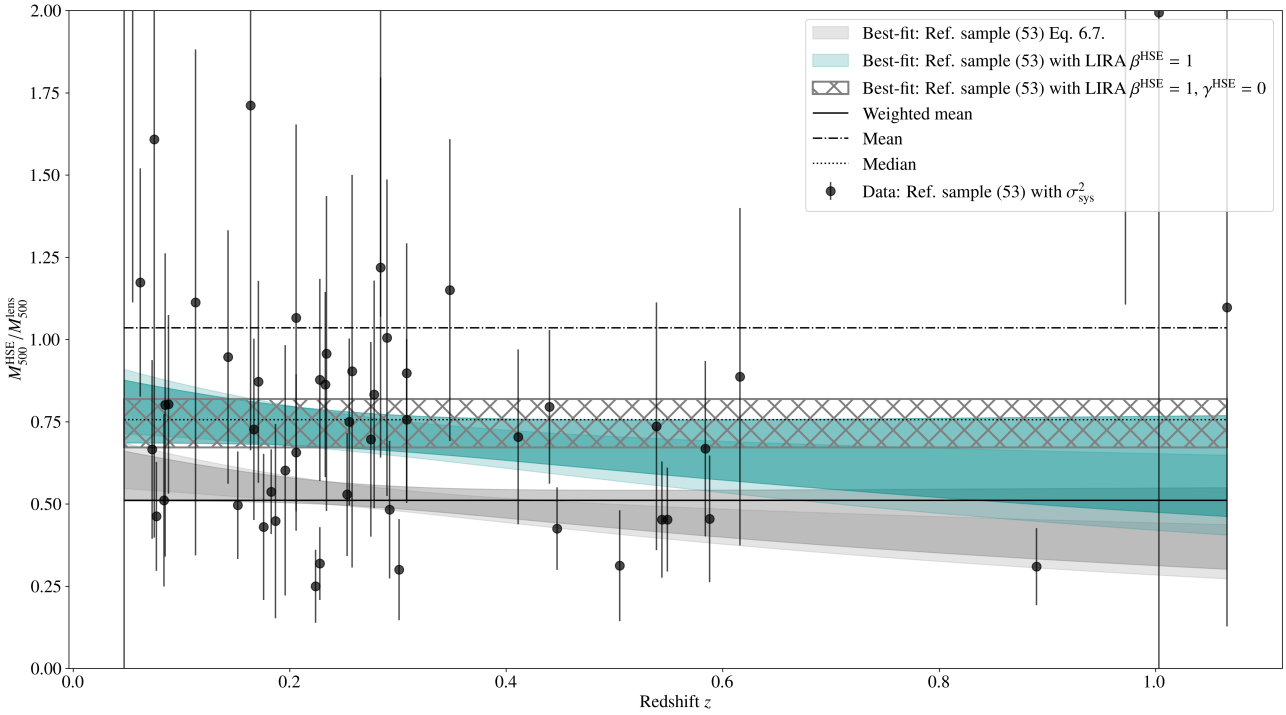

Figure 6.16: HSE-to-lensing mass ratio as a function of redshift. The grey shaded area shows the evolution from Fig. 6.7 for all the clusters in the sample and in darker excluding CL J1226.9+3332. The blue area gives the evolution with redshift obtained from the fit of the SR with the *reference* sample. The grey hatched area corresponds to the results without considering a redshift evolution. The blue dark area is the evolution obtained for the *reference* sample excluding CL J1226.9+3332. As in Fig. 6.7, markers with error bars show the mass ratio per cluster in the *reference* sample and error bars account for the systematic uncertainties. Horizontal solid, dotted and dash-dotted black lines give the error-weighted mean, median and mean mass ratio for the data points, respectively.

Assuming again that HSE and lensing masses scale linearly with the true mass ($\beta^{\rm lens} = \beta^{\rm HSE} = 1$), we write

$$\ln M^{\rm lens} \pm \delta_{\rm lens} = \ln M^{\rm True} \pm \sigma^{\rm lens}, \tag{6.12}$$

and,

$$\ln M^{\rm HSE} \pm \delta_{\rm HSE} = \alpha^{\rm HSE} + \ln M^{\rm True} \pm \sigma^{\rm HSE} + \gamma^{\rm HSE} T. \tag{6.13}$$

T is the time evolution factor, $T = \log\left(\frac{1+z}{1+z_{ref}}\right)$, with $z_{ref} = 0.01$ the normalisation redshift set by default in LIRA. We take flat priors for the parameter describing the evolution with redshift: $\gamma^{\rm HSE} \sim \mathcal{U}(-10, 10)$. Similarly, we consider the evolution with redshift for the SR defined in Eq. 6.10 and 6.11. Given the strong impact on the fits of the CL J1226.9+3332 galaxy cluster at high redshift, we repeat the analysis excluding it. All the results are summarised in Table 6.7.

In Fig. 6.16 we present the redshift evolution of the HSE-to-lensing mass ratio, for the analyses performed with the *reference* sample and accounting for systematic uncertainties for the HSE and lensing masses. We show in grey the results obtained in Sect. 6.4, neglecting the intrinsic scatter of HSE and lensing masses with respect to the true masses. In blue we present the bias evolution model resulting from the scaling relation fit in this section. Darker regions show the evolution with redshift obtained when excluding CL J1226.9+3332 from the analyses.

There seem to be a tendency for a decreasing HSE-to-lensing mass ratio with redshift ($\gamma^{\rm HSE} = -1.530^{+1.071}_{-1.085}$), but it is not statistically significant when removing CL J1226.9+3332 from the sample ($\gamma^{\rm HSE} = -0.896^{+1.154}_{-1.155}$). From the comparison of the grey and blue results we observe directly the impact that has on the bias the fact of accounting for the intrinsic scatters of the SR. Considering the intrinsic scatter reduces the difference between HSE and lensing masses and, therefore, the bias.

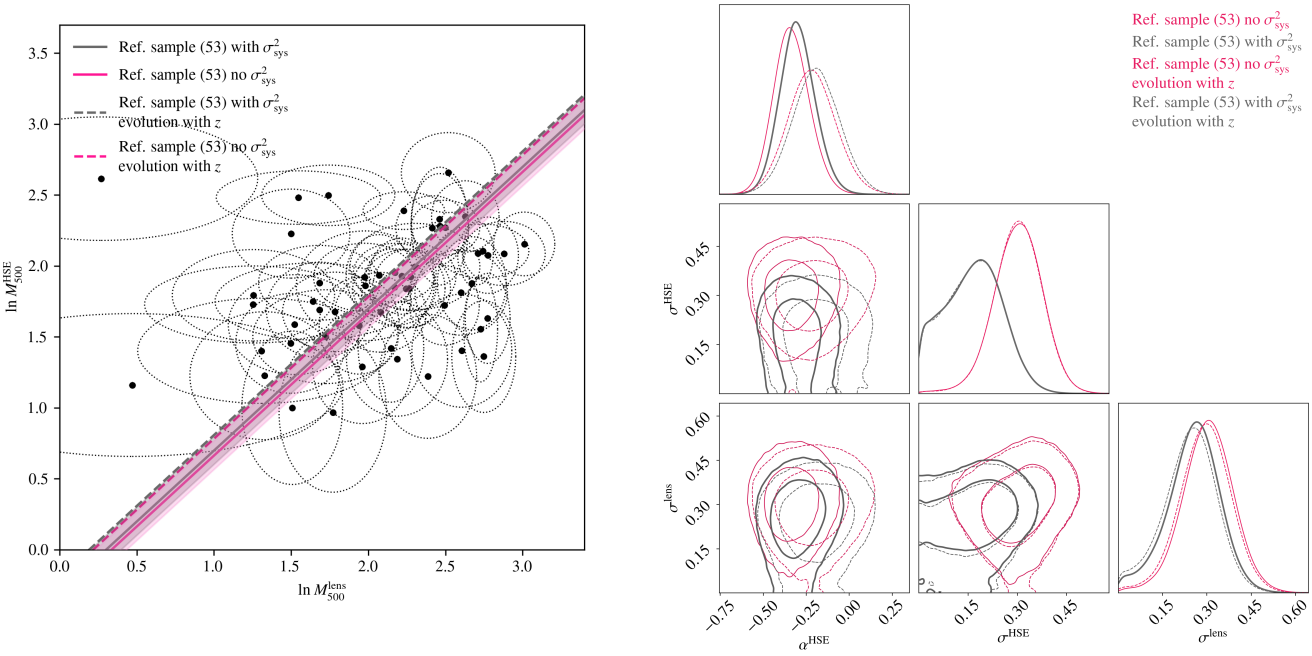

Figure 6.17: Same as Fig. 6.9 with dashed lines showing the results if an evolution with redshift is considered in the scaling relation and solid lines without evolution. The shaded regions show the 16th and 84th percentiles, for visualisation purposes, only for the cases without redshift evolution.

We present in Fig. 6.17 and 6.18 a comparison of the scaling relations and posterior distributions of parameters when accounting for redshift evolution (dashed lines) and not accounting for it (solid lines). The contribution of the redshift evolution factor introduces a change of the order of a few percent (or less) in the intrinsic scatters. Given the correlation of the other parameters with γ^{HSE}, the change is of $\sim 30\%$ for α^{HSE} and of the order of 10% for A^{HSE} and B^{HSE}. However, the results are compatible with the ones obtained without considering redshift evolution, so there is no strong evidence of redshift evolution in the data.

6.5.3 Comparison of SR models

In this section, we compare the tested SR models to assess which is the one preferred by the data. We define the goodness of fit $\hat{\chi}^2$ of the scaling relations following Eq. 3 in Lovisari et al. (2020) [193]:

$$\hat{\chi}^2 = \sum_{i=1}^{N_{clusters}} \frac{\left[\ln M_i^{HSE} - \ln M^{HSE}\left(\ln M_i^{lens}, z_i, \vartheta\right)\right]^2}{\delta^2_{HSE,i} + (\sigma^{HSE})^2 + (\beta^{HSE})^2\left[\delta^2_{lens,i} + (\sigma^{lens})^2\right]}, \tag{6.14}$$

where the sum is done over the $N_{clusters} = 53$ clusters in the *reference* sample. In Eq. 6.14 $\ln M^{HSE}\left(\ln M_i^{lens}, z_i, \vartheta\right)$ is the function described by Eq. 6.9 or 6.13 depending on the SR model, with the parameters $\vartheta = [\alpha^{HSE}, \beta^{HSE}, \gamma^{HSE}]$ defined accordingly. The factors $\ln M_i^{HSE}$, $\ln M_i^{lens}$, $\delta_{HSE,i}$ and $\delta_{lens,i}$ are the HSE and lensing mass of each cluster i and their associated uncertainties, and z_i is the redshift of each cluster. We compare the results obtained considering always the systematic uncertainties in the HSE and lensing masses. We take the posterior distributions of the parameters for α^{HSE}, β^{HSE}, γ^{HSE}, σ^{HSE} and σ^{lens}. For the scaling relations considering an offset in mass (Eq. 6.10 and 6.11), we replace the logarithmic masses and uncertainties by the linear values in the $\hat{\chi}^2$ definition in Eq. 6.14. Similarly, we take A^{HSE} and B^{HSE} instead of α^{HSE} and β^{HSE}.

In Fig. 6.19 we present as solid line histograms the $\hat{\chi}^2$ distributions for each SR model normalised by the

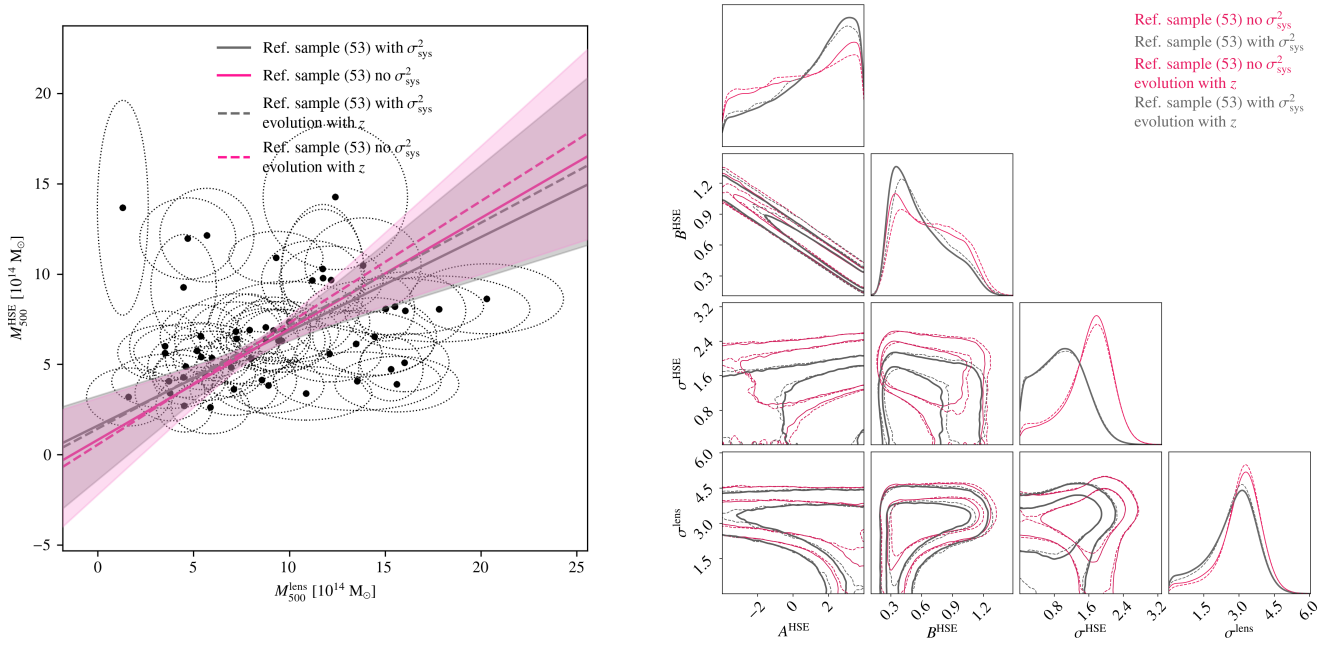

Figure 6.18: Same as Fig. 6.15 with dashed lines showing the results if an evolution with redshift is considered in the scaling relation and solid lines without evolution. The shaded regions show the 16th and 84th percentiles, for visualisation purposes, only for the cases without redshift evolution.

corresponding degrees of freedom (d.o.f.). In the left panel, we present the results for the scaling relations fitted in $\ln M^{\rm HSE} - \ln M^{\rm lens}$ and in the right for $M^{\rm HSE} - M^{\rm lens}$. The blue histogram in the left panel shows the reduced $\hat{\chi}^2$ for the scaling relation of reference in this work and the vertical solid line is the median value of the distribution. For comparison, the dashed lines correspond to the expected χ^2-distributions,

$$f(\chi^2) = \frac{1}{2^{\nu/2}\Gamma(\nu/2)} e^{-\chi^2/2} (\chi^2)^{(\nu/2)-1}, \tag{6.15}$$

where ν is the number of the degrees of freedom (d.o.f.). For the scaling relation of reference we have d.o.f. $= 53 - 3 = 50$. The red and green results show the reduced $\hat{\chi}^2$ for the fits of the scaling relations when considering a deviation from linearity or an evolution with redshift, respectively. In these cases we have 49 degrees of freedom. The histograms follow fairly well the χ^2-distributions with ν degrees of freedom.

We use the Akaike information criterion (AIC) [349] and the Bayesian information criterion (BIC) [350] to compare the improvement in the $\hat{\chi}^2$ when adding parameters to the model. We calculate:

$$\mathrm{AIC} = \hat{\chi}^2_{\rm min} + 2K, \tag{6.16}$$

and

$$\mathrm{BIC} = \hat{\chi}^2_{\rm min} + K \ln N, \tag{6.17}$$

where $\hat{\chi}^2_{\rm min}$ is the minimum of the $\hat{\chi}^2$ values for each model. K and N are the number of free parameters in the model and the total number of data points, i.e. $N = N_{\rm clusters} = 53$, respectively. We report in Table 6.8 the results for the different scaling relation models and the ΔAIC and ΔBIC differences with respect to the simplest scaling law amongst the nested models.

According to the AIC and BIC criteria, the scaling relation of reference and the one considering a deviation from linearity are almost equally probable. On the contrary, there is statistically no gain in adding a parameter

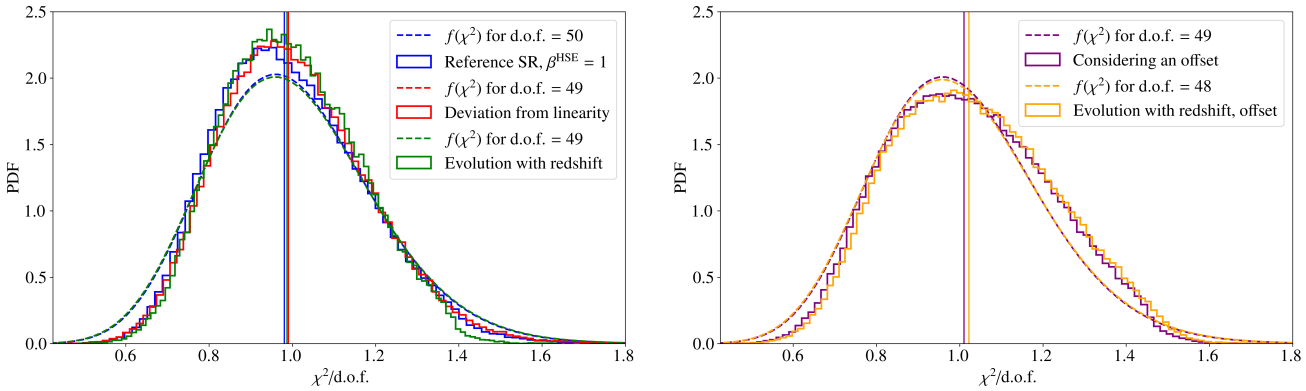

Figure 6.19: Comparison of the reduced $\hat{\chi}^2$ distributions for different scaling relation fits (colour histograms) and the χ^2-distribution (Eq. 6.15) for the degrees of freedom in each fit (dashed colour lines). Vertical lines show the median value of each histogram.

Model	K	N	$\hat{\chi}^2_{\rm min}$	AIC	ΔAIC	BIC	ΔBIC
Reference SR	3	53	18.126	24.126	0.000	21.422	0.000
Deviation from linearity	4	53	16.020	24.020	-0.106	21.565	+0.143
Evolution with redshift	4	53	22.784	30.784	+6.658	28.329	+6.907
Considering an offset	4	53	13.929	21.993	0.000	19.475	0.000
Evolution with redshift and offset	5	53	17.992	27.992	+5.999	26.039	+6.564

Table 6.8: The statistical results for the scaling relation models presented in this analysis. We report the values for the fits accounting for the systematic scatter of HSE and lensing masses.

that describes an evolution with redshift. In other words, redshift evolution does not seem to be favoured by the data.

Anyhow, the intrinsic scatters for the HSE and lensing masses being free parameters in our LIRA fits, we expect all the models to adjust the data points at the expense of increasing these scatters. From the comparison of all the $\sigma^{\rm HSE}$ and $\sigma^{\rm lens}$ (see Tables 6.6 and 6.7), there is not a statistically significant increase, nor decrease in the intrinsic scatters when changing the number of free parameters in the SR model.

In conclusion, our best scaling law between X-ray HSE and lensing masses is given by the scaling relation of reference:

$$\ln M^{\rm lens} = \ln M^{\rm True} \pm 0.257^{+0.080}_{-0.092}, \tag{6.18}$$

$$\ln M^{\rm HSE} = -0.303^{+0.101}_{-0.095} + \ln M^{\rm True} \pm 0.166^{+0.086}_{-0.101}, \tag{6.19}$$

which corresponds to a HSE-to-lensing mass bias of

$$M^{\rm HSE}_{500}/M^{\rm lens}_{500} = (1-b) = 0.739^{+0.075}_{-0.070}\ (\text{stat.}) \pm 0.226\ (\text{intrin. scatter}), \tag{6.20}$$

assuming Gaussian intrinsic scatters for lensing and HSE masses.

6.6 Robustness of XMM-*Newton* masses

As described in Sect. 6.1.1, all the XMM-*Newton* HSE masses used in this work were obtained from mass profiles, by interpolating the binned profile to get M_{500} and R_{500}. For all the clusters in our *reference* sample we also have access to X-ray masses obtained with the $Y_{\rm X} - M^{\rm HSE}_{500}$ scaling relation from Arnaud et al. (2010) [70]. $Y_{\rm X}$ is defined as the product of the gas mass ($M^{\rm gas}_{500}$) and the spectroscopic temperature ($T_{\rm X}$) and it is the X-ray analogue of the integrated Compton parameter [200]. We use these masses as $M^{\rm HSE}$ estimates and fit again the scaling relations in Eq. 6.8, 6.9, 6.10 and 6.11.

Sample	# of clusters	No $\sigma^2_{\rm sys}$				
$Y_{\rm X} - M^{\rm HSE}_{500}$		$\alpha^{\rm HSE}$	$e^{\alpha^{\rm HSE}} = (1-b)$	$\beta^{\rm HSE}$	$\sigma^{\rm HSE}$	$\sigma^{\rm lens}$
Reference sample	53	$-0.237^{+0.095}_{-0.087}$	$0.789^{+0.075}_{-0.069}$	[1]	$0.105^{+0.063}_{-0.067}$	$0.247^{+0.058}_{-0.056}$
Reference sample	53	$-0.131^{+0.542}_{-0.631}$		$0.953^{+0.296}_{-0.263}$	$0.133^{+0.075}_{-0.088}$	$0.231^{+0.068}_{-0.098}$
Reference sample (BCES)	53	0.504 ± 0.262		0.662 ± 0.122	0.250^{*}	-
		$A^{\rm HSE}$ [10^{14} M$_\odot$]	$B^{\rm HSE}$		$\sigma^{\rm HSE}$ [10^{14} M$_\odot$]	$\sigma^{\rm lens}$ [10^{14} M$_\odot$]
Reference sample	53	$0.990^{+1.748}_{-2.050}$	$0.672^{+0.235}_{-0.205}$		$0.930^{+0.508}_{-0.633}$	$2.333^{+0.594}_{-1.032}$
Reference sample (BCES)	53	2.401 ± 0.781	0.487 ± 0.095		1.480^{*}	-
NFW fit		$\alpha^{\rm HSE}$	$e^{\alpha^{\rm HSE}} = (1-b)$	$\beta^{\rm HSE}$	$\sigma^{\rm HSE}$	$\sigma^{\rm lens}$
$z < 0.9$	50	$-0.309^{+0.119}_{-0.107}$	$0.734^{+0.087}_{-0.079}$	[1]	$0.249^{+0.059}_{-0.063}$	$0.212^{+0.077}_{-0.086}$
$z < 0.9$	50	$-0.361^{+0.692}_{-0.955}$		$1.030^{+0.480}_{-0.341}$	$0.246^{+0.073}_{-0.121}$	$0.220^{+0.081}_{-0.119}$
$z < 0.9$ (BCES)	50	0.032 ± 0.485		0.836 ± 0.222	0.329^{*}	-
		$A^{\rm HSE}$ [10^{14} M$_\odot$]	$B^{\rm HSE}$		$\sigma^{\rm HSE}$ [10^{14} M$_\odot$]	$\sigma^{\rm lens}$ [10^{14} M$_\odot$]
$z < 0.9$	50	$1.205^{+1.490}_{-2.463}$	$0.579^{+0.287}_{-0.173}$		$1.576^{+0.408}_{-0.589}$	$1.989^{+0.843}_{-1.164}$
$z < 0.9$ (BCES)	50	0.530 ± 1.343	0.646 ± 0.159		1.944^{*}	-

Table 6.9: Table summarising the median values and uncertainties at the 16th and 84th percentiles of the fitted parameters for the HSE-to-lensing mass SR for HSE masses obtained from the $Y_{\rm X} - M^{\rm HSE}_{500}$ scaling relation and from the fit of an NFW model to the X-ray data. We present the results assuming linearity, a deviation from linearity and an offset between HSE and lensing masses. For the BCES fit we report the best-fit values and 1σ uncertainties. $^{(*)}$ We also calculate the scatter with respect to the best BCES scaling relations following Eq. 6.4.

The median values and uncertainties of the best-fit SR parameters are given in Table 6.9. When using $Y_{\rm X} - M^{\rm HSE}_{500}$ estimates, the intrinsic scatters of HSE and lensing masses with respect to the SR are reduced by $\sim 40\%$ and $\sim 10\%$, respectively. The measured HSE bias is also smaller: $(1-b) = 0.789^{+0.075}_{-0.069}$.

For ESZ+LoCuSS and LPSZ sample clusters we have a third estimate of the HSE mass, obtained by fitting an NFW mass model to the X-ray profiles. Such masses tend to agree with the interpolated ones (the reference XMM-*Newton* masses used in this work, Sect. 6.1.1), with a mean and median ratio for the 50 cluster estimates of $M^{\rm HSE}_{500}/M^{\rm NFW}_{500} \sim 1.11$ and 0.95, indicating that the HSE masses used in the analyses of reference are robust against modelling effects. Masses obtained by fitting an NFW model have in median 30% smaller uncertainties than the interpolated estimates. The scaling relations obtained with NFW fitted masses (Table 6.9) and interpolated ones (the second row in Table 6.6 for the 50 clusters with $z < 0.9$) are almost identical, with $\alpha^{\rm HSE}$ centred in the exact same value, but with $10-20\%$ smaller intrinsic scatters when using NFW masses.

6.7 Caveats

The two main caveats of the analysis presented in this chapter are the representativity of the used sample and the inhomogeneity of lensing masses. The former is hardly quantifiable, given that the selection of the *homogeneous* sample (Sect. 6.1.1) is mainly a combination of the selection criteria used for the ESZ, LoCuSS, LPSZ and Bartalucci et al. (2018) [105] clusters. An equivalent study for a sample that is representative of the clusters in the Universe would refine the presented results. Regarding the lensing masses, we have exploited the compilation of mass estimates from different works standardised in the CoMaLit catalogue. We have treated all the CoMaLit masses equally, but the different quality of the data and/or the methods used in each of the original works make the uncertainties of lensing masses not homogeneous within the CoMaLit sample. By propagating $\sigma_{\rm sys\,lens}$ we account, to first order, for the overall error of CoMaLit masses with respect to other estimates. A possible improvement would be to measure an independent systematic scatter $\sigma_{\rm sys\,lens}$ for each of the works used in the CoMaLit sample. Instead, we quantify a posteriori the goodness of our best scaling relation (estimated with all the 53 clusters in the *reference* sample, Eq. 6.18 and 6.19) for the cluster masses

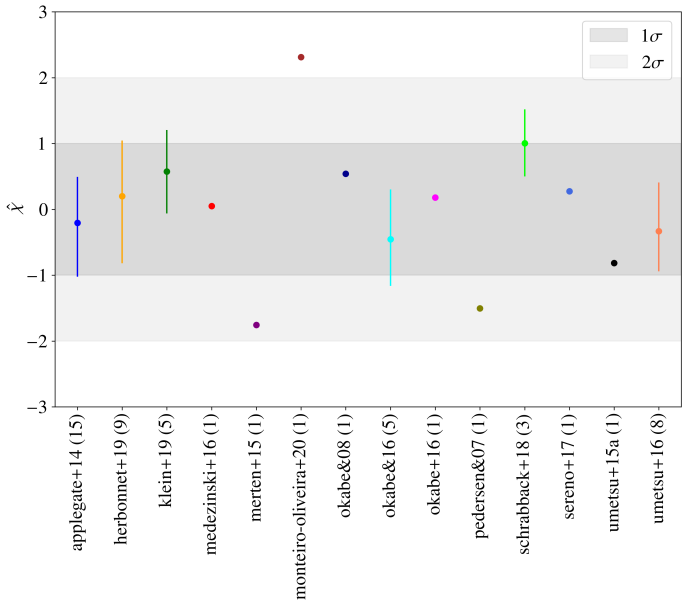

Figure 6.20: $\hat{\chi}$ for the clusters in the *reference* sample with respect to the reference scaling relation. We distinguish the results from the various lensing works used to build the CoMaLit sample with different colour markers. The number of clusters used in the *reference* sample from each of the works is indicated in brackets. For works with multiple clusters, we give the mean $\hat{\chi}$ and the 16th to 84th percentiles over all those clusters. Grey shaded areas indicate 1σ and 2σ regions.

extracted from each of the different works within the CoMaLit catalogue. In Fig. 6.20 we show, for the clusters obtained from each of the lensing works, the corresponding $\hat{\chi}$ defined as

$$\hat{\chi} = \frac{\ln M_i^{\rm HSE} - \ln M^{\rm HSE}\left(\ln M_i^{\rm lens}, z_i, \vartheta\right)}{\sqrt{\delta^2_{{\rm HSE},i} + \left(\sigma^{\rm HSE}\right)^2 + \left(\beta^{\rm HSE}\right)^2\left[\delta^2_{{\rm lens},i} + \left(\sigma^{\rm lens}\right)^2\right]}}. \tag{6.21}$$

For those works with several clusters in our *reference* sample, we give the mean value and the 16th to 84th percentiles over all the used clusters. We observe that only 'merten+15' [279], 'monteiro-oliveira+20' [351] and 'pedersen&07' [352] cluster masses are at more than 1σ. The cluster from 'monteiro-oliveira+20' at more than 2σ from the scaling relation is Abell1644 (on the top left of all our SRs), which is known for being a cluster in a merger scenario. Thus, the scaling relation of reference fits well the large majority of the clusters in the *reference* sample, no matter the work from which the lensing mass has been extracted.

6.8 Comparison to previous results

Similar studies to the one presented in this chapter were previously done in the literature. However, the methods used to estimate the masses and to compute the HSE-to-lensing bias differ from work to work. Thus, comparisons are again very delicate. In Fig. 6.21 we present our best bias estimate together with the HSE-to-lensing M_{500} ratios obtained in the works detailed below. We use Roman numerals (I to IX) to refer to each result from the literature. The different results are also summarised in Table 6.10.

The HSE-to-lensing mass bias was measured in Smith et al. (2016) [333] with the 50 clusters from the LoCuSS sample ($0.15 < z < 0.3$). By using resolved HSE mass estimates, they computed the weighted mean HSE-to-lensing bias: $(1 - b) = 0.95 \pm 0.05$ (I in Fig. 6.21). Uncertainties were calculated from the standard deviation of 1000 bootstrap samples geometric means. Following the equations used to calculate the weighted mean in Smith et al. (2016) [333] (Eq. 1 and 2 in Smith et al. (2016) [333]) we obtain for our *reference* sample a mean bias of: $(1 - b) = 0.763$ and 0.818 not including and including, respectively, the systematic error in the

Reference	Sample	# of clusters	Redshift	$(1-b) = M^{\rm HSE}_{500}/M^{\rm lens}_{500}$	Notes
	This work - Reference SR	53	$0.05 < z < 1.07$	$0.739^{+0.075}_{-0.070}$	Propagating the systematic uncertainties, accounting for intrinsic dispersion
I	Smith et al. (2016) [333]	50	$0.15 < z < 0.3$	0.95 ± 0.05	Weighted mean
II	Mahdavi et al. (2008) [337]	18	$0.170 < z < 0.547$	0.78 ± 0.09	$M^{\rm HSE}(R^{\rm lens}_{500})$
III	Mahdavi et al. (2013) [259]	50	$0.152 < z < 0.55$	$0.8 - 1$	$M^{\rm HSE}(R^{\rm lens}_{500})$
IV	Israel et al. (2014) [260]	8	$0.35 < z < 0.80$	$0.8 - 1$	Global temperature profile for the whole sample, $M^{\rm HSE}(R^{\rm lens}_{500})$
V	Bartalucci et al. (2018) [105]	4	$0.933 < z < 1.066$	$1.39^{+0.51}_{-0.37}$	Weighted mean
VI	This work - Chapter 5	4	$0.55 < z < 0.89$	0.61 ± 0.17	
VII	Eckert et al. (2022) [258]	12	$0.047 < z < 0.09$	$0.85 - 0.9$	
VIII	Lovisari et al. (2020) [301]	62	$z < 0.5$	0.74 ± 0.06	Accounting for intrinsic dispersion
IX	Sereno et al. (2020) [324]	100	$0.054 < z < 1.050$	0.91 ± 0.17	Accounting for intrinsic dispersion, temperature measured within 300 kpc

Table 6.10: HSE-to-lensing mass bias values from resolved mass profiles. We report our reference result and different values from the literature. The last column indicates the singularity of each analysis.

uncertainty of each mass estimate. Considering, as in Smith et al. (2016) [333], only the clusters in the redshift range $0.15 < z < 0.3$, we obtain $(1-b) = 0.769$ and 0.720 with and without the systematic scatter.

In Mahdavi et al. (2008) [337] authors compared the HSE and lensing masses evaluated at the same radius, in particular at the R_{500} measured from the lensing mass profile of each cluster. With a sample of 18 clusters, Mahdavi et al. (2008) [337] concluded that at $R^{\rm lens}_{500}$ the ratio of masses is $M^{\rm HSE}/M^{\rm lens} = 0.78 \pm 0.09$ (II). Extending the analysis, the HSE-to-lensing mass bias obtained in Mahdavi et al. (2013) [259] is consistent with no bias for cool-core clusters, while $(1-b) \sim 0.8$ for non-cool core clusters (III). In the same line, authors in Israel et al. (2014) [260] concluded, from the study of 8 clusters with redshifts $0.35 < z < 0.80$, that HSE and lensing masses differ by 0 to 20% (IV).

By using very high redshift clusters ($0.933 < z < 1.066$), Bartalucci et al. (2018) [105] obtained that HSE masses from X-rays are a factor of $1.39^{+0.51}_{-0.37}$ (V) larger than weak lensing estimates, in contradiction with the rest of the results. The clusters in Bartalucci et al. (2018) [105] are the highest redshift clusters in our *reference* sample (Sect. 6.1.1). Using the same HSE masses as in Bartalucci et al. (2018) [105], but with the CoMaLit lensing estimates, we obtain an error-weighted mean ratio of $M^{\rm HSE}_{500}/M^{\rm lens}_{500} = 1.56(1.58)$ not including (including) the systematic error in the uncertainty of each mass estimate. Instead, the error-weighted mean ratio for our full *reference* sample is $M^{\rm HSE}_{500}/M^{\rm lens}_{500} = 0.47(0.51)$. In chapter 5 we have estimated the mean HSE-to-lensing mass bias from the combination of the results for four $0.55 < z < 0.89$ CLASH clusters and obtained $M^{\rm HSE}_{500}/M^{\rm lens}_{500} = 0.61 \pm 0.17$ (VI). For the clusters in the X-COP sample Eckert et al. (2022) [258] found that HSE masses estimated using XMM-*Newton* data are 10 to 15% lower than the lensing estimates in Herbonnet et al. (2020) [353] (VII). With a different approach and assuming that the gas fraction in clusters is constant, Eckert et al. (2019) [53] obtained that HSE masses are biased (with respect to the true total mass) by 7% at R_{500}.

Regarding the evolution of the bias with redshift, which we have largely discussed in Sect. 6.4 and 6.5, the tendency for a larger bias at higher redshift seems to be in line with the results from Wicker et al. (2023) [156] and Smith et al. (2016) [333].

Particularly interesting are the comparisons to Sereno et al. (2020) [324], Lovisari et al. (2020) [301] and Sereno and Ettori (2015) [314] works, where the used methods are equivalent to the ones employed in this study, making use of the LIRA code and accounting for the intrinsic dispersion of HSE and lensing masses to the SR. The analysis in Lovisari et al. (2020) [301] compares the HSE masses obtained with XMM-*Newton* data (from Lovisari et al. (2020) [193]) to lensing estimates in the CoMaLit LC^2 catalogue, for 62 clusters from the *Planck*-ESZ sample with $z < 0.5$. With this sample, authors obtain $(1-b) = 0.74 \pm 0.06$ (VIII) and no redshift evolution. This is in excellent agreement with our result. In Lovisari et al. (2020) [301] the results

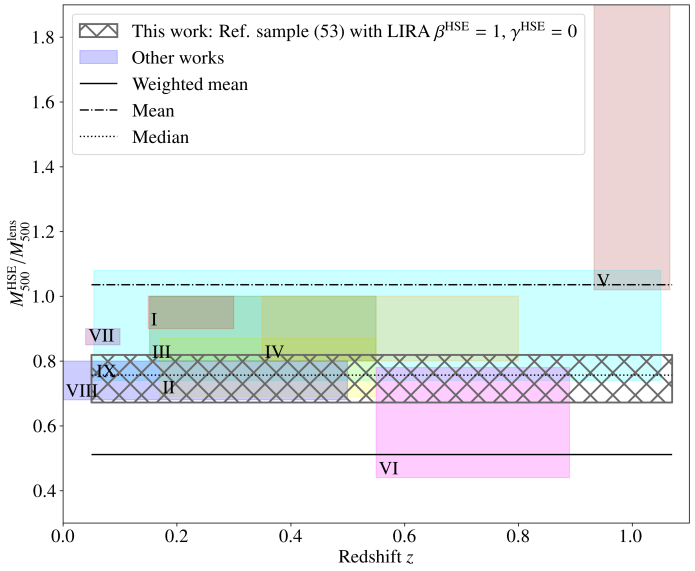

Figure 6.21: HSE-to-lensing mass ratio with respect to redshift. Shaded areas indicate different results from different works in the literature. See text and Table 6.10 to identify Roman numerals with the works. The horizontal grey hatched area represents the HSE-to-lensing mass ratio measured in this chapter assuming that HSE and lensing masses scale linearly with the true mass, accounting for the systematic scatter and considering no evolution with redshift. For comparison, we also indicate the error-weighted mean (solid), mean (dash-dotted) and median (dotted) bias for the clusters in the *reference* sample.

found with CoMaLit lensing masses are also compared to those obtained with other lensing masses from other works in the literature: the HSE-to-lensing mass ratio spans from ~ 0.6 to ~ 1 depending on the used data set.

Conclusions are along the same line in Sereno and Ettori (2015) [314], where different samples with HSE and lensing mass estimates are used to measure the scaling relation and, consequently, the HSE-to-lensing mass bias. The effect that intrinsic scatters have on the determination of scaling relations is also studied in Sereno and Ettori (2015) [314]. They conclude that not taking into account the scatter of masses explicitly makes scaling relations flatter, as we see when using BCES instead of LIRA (also in agreement with Lovisari et al. (2020) [193]). While the intrinsic scatter for lensing masses obtained in Sereno and Ettori (2015) [314] is of the order of the expected values from simulations ($\sim 10 - 15\%$), the intrinsic dispersion for HSE masses is larger than expected ($\sim 20 - 30\%$). An underestimation of the statistical uncertainties in HSE masses could be the reason, according to Sereno and Ettori (2015) [314], for this large intrinsic scatter. Accounting for the systematic scatter in the uncertainty of each cluster mass, as described in this chapter, could help to have more realistic uncertainties of the HSE mass estimates. The HSE-to-lensing mass ratio in Sereno and Ettori (2015) [314] depends again on the used sample and data, and spans from ~ 0.5 to ~ 1.

Also Sereno et al. (2020) [324] used the Bayesian hierarchical modelling from Sereno (2016) [345] to fit a scaling relation between HSE masses from XMM-*Newton* data and weak lensing masses of clusters in the Hyper Suprime-Cam Survey [354]. The median redshift of the 100 clusters in the sample is $z = 0.30$, spanning from $z = 0.054$ to $z = 1.050$. Thus, the analysis in Sereno et al. (2020) [324] is probably the closest study to our work. Nevertheless, to get temperature profiles that reach R_{500} with X-ray data (to compute then the HSE mass), in Sereno et al. (2020) [324] a model was iteratively fitted to the integrated temperature measured per cluster within 300 kpc, well below R_{500}. Assuming $\beta^{HSE} = 1$, $\beta^{lens} = 1$ and $\alpha^{lens} = 0$ they obtained: $\alpha^{HSE} = -0.04 \pm 0.08$, $\sigma^{HSE} = 0.31 \pm 0.05$, and $\sigma^{lens} = 0.37 \pm 0.06$. According to Sereno et al. (2020) [324] the difference between HSE and lensing masses is of $b = 0.09 \pm 0.17$ (IX). The α^{HSE} from Sereno et al. (2020) [324] is at 3σ from our result with the full *reference* sample ($\alpha^{HSE} = -0.338^{+0.105}_{-0.097}$ without accounting for the systematic uncertainties). Their values for σ^{HSE} and σ^{lens} agree with the intrinsic scatter values that we obtain

when we do not account for the systematic uncertainties ($\sigma^{\rm HSE} = 0.304^{+0.069}_{-0.072}$ and $\sigma^{\rm lens} = 0.305^{+0.080}_{-0.083}$).

In addition, the behaviour of the HSE-to-lensing mass bias could vary with the overdensity at which masses are measured (see Table 5.4). By estimating weak lensing masses and HSE masses from X-rays at R_{200}, Jee et al. (2011) [278] concluded that for a sample of 14 very massive and distant clusters ($0.83 < z < 1.46$), the HSE and lensing masses are compatible. However, the HSE masses were obtained from the extrapolation of a singular isothermal sphere profile to reach R_{200}, which likely limits the validity of their HSE mass estimates. Similarly, in Amodeo et al. (2016) [90] authors compared M_{200} masses reconstructed from *Chandra* data (although the radial reach of *Chandra* is way below R_{200}) to their lensing estimates, and concluded that both mass estimates are in agreement. No evolution with redshift was detected in Amodeo et al. (2016) [90]. We prefer to avoid extrapolating the mass profiles to reach R_{200}.

6.9 Conclusions

In this chapter, we have investigated the HSE-to-lensing mass bias with masses inferred at R_{500} from resolved profiles. We carefully selected the clusters and obtained a *reference* sample with 53 objects with redshifts spanning from $z = 0.05$ to 1.07. This is the largest redshift range analysed homogeneously with this type of data, having access to X-ray HSE masses obtained from resolved profiles. HSE masses were estimated with the XMM-*Newton* mass reconstruction reference pipeline and lensing masses were extracted from the LC^2 CoMaLit catalogue.

To account for possible systematic effects in the reference analysis masses, we compared the XMM-*Newton* and CoMaLit masses to other estimates from the literature. The obtained systematic uncertainties were propagated to our analyses, but all the main conclusions do not seem affected by them.

We performed different tests in the measurement of the HSE-to-lensing mass scaling relation and bias, varying the considered redshift range and the scaling relation model. We find that the best scaling relation between HSE and lensing masses is our scaling relation of reference, where we assume that there is no evolution with mass and redshift and that HSE and lensing masses scale linearly. Considering $\sigma^2_{\rm sys\ HSE}$ and $\sigma^2_{\rm sys\ lens}$, we measure for the 53 clusters in the *reference* sample a HSE-to-lensing mass ratio of $M^{\rm HSE}_{500}/M^{\rm lens}_{500} = (1 - b) = 0.739^{+0.075}_{-0.070}$ (stat.) $\pm$ 0.226 (intrin. scatter), which corresponds to a scaling relation given by $\alpha^{\rm HSE} = -0.303^{+0.101}_{-0.095}$, $\sigma^{\rm HSE} = 0.166^{+0.086}_{-0.101}$ and $\sigma^{\rm lens} = 0.257^{+0.080}_{-0.092}$. Ignoring the intrinsic scatter of HSE and lensing masses with respect to the true mass of clusters introduces a bias in the measurement of the HSE-to-lensing mass bias.

When we let the bias evolve with redshift, we observe a trend towards a larger difference between HSE and lensing masses at high redshift, but it is not statistically significant. In conclusion, there is no evidence of evolution with redshift. Furthermore, we find no dependence of the HSE-to-lensing bias on cluster masses.

Given the size of the sample, single clusters can be driving the fits and special care needs to be taken for clusters with very small uncertainties. We have investigated the case of CL J1226.9+3332 galaxy cluster, whose impact is crucial when determining the bias at high redshift.

Additional considerations are needed to compare the HSE-to-lensing mass bias obtained in this study to the bias needed to reconcile cluster number counts and CMB power spectrum results (see chapter 1): 1) the HSE masses used in cluster number count analyses are not direct HSE mass measurements, but masses obtained from an SZ (or X-ray) measurement through an SZ-mass (or X-ray-mass) scaling relation (Sect. 1.3.5), 2) lensing masses can also be biased with respect to the true mass of clusters [290], and 3) this sample is not representative of the cluster population in any given survey. Instead, this study provided a step forward in our understanding of the deviation from hydrostatic equilibrium of galaxy clusters and of the impact of systematic and intrinsic errors on the bias computation.

We have seen in chapter 5 that HSE masses inferred from the SZ+X-ray combination or from X-ray-only data can be differently biased. An equivalent study to the one presented in this chapter, spanning a large range in redshift, but from resolved SZ and X-ray data, will only be possible with high angular resolution SZ

observations. It is in this context that the NIKA(2)-CLASH sample from chapter 5 will be fundamental to cover the intermediate to high redshift ranges.

CHAPTER 7

Mass bias from projected mass maps in THE THREE HUNDRED

As we have seen in the previous chapters, each of the observational galaxy cluster mass reconstruction methods is known to bias differently the results due to instrumental limits or departures from the assumed hypotheses. From comparisons between different observational results, we try to understand those issues (chapters 4, 5 and 6). However, other biases are intrinsic to cluster physics and geometry, and, need to be quantified from simulations. Simulations allow one to compare the three dimensional properties of clusters, needed for cosmological studies, to those inferred from projected maps.

In this chapter we will present a study on the mass bias and its scatter when reconstructed from projected mass maps, leaving aside all observational and instrumental effects. We will make use of THE THREE HUNDRED project simulation[20] in the context of the NIKA2 SZ Large Programme. Given the importance of the sample selection, we will use clusters that are twins to those from the LPSZ, so that the mass and redshift distribution is representative of the real sample. We will describe the mass estimation method and its associated

[20] https://the300-project.org

bias, and we will investigate the different sources of this bias and its scatter. We focus the analysis on total mass observables, but at the end of the chapter we also compare the results of gas observables of clusters. We compare all the masses at an overdensity of $\Delta = 500$ to be consistent with the LPSZ outcomes (chapters 3, 4 and 5). The analysis presented in this chapter is based on a work accepted for publication in Astronomy & Astrophysics [355].

7.1 The Three Hundred project

Since the first cosmological simulations in the 1960s and 1970s based on gravitation-only N-body systems [356, 357], a lot of improvements have been made. Nowadays, a vast variety of cosmological simulations allow us to test models and data analysis pipelines. On the one hand, we distinguish the dark-matter-only N-body simulations, which are able to describe the collapse of matter and the structure formation under the gravitational force. Such simulations can now be performed in $\sim$ Gpc side box volumes at a high resolution [358, 359], with particle mass resolutions going down to $\sim 10^6\ h^{-1}\ \mathrm{M}_\odot$. However, these simulations do not consider the presence and effects of baryonic matter in the Universe. On the contrary, Semi-analytical simulations and hydrodynamical simulations are able to account for baryonic effects. Therefore, they can be used to investigate baryonic observables (galaxies, gas in clusters, etc.) and understand their impact on the surrounding dark matter. Semi-analytical simulations rely on the dark-matter-only simulations that are 'painted' with baryonic models describing physical effects calibrated on observations [360, 361]. Once DM-only Universes are created, Semi-analytical simulations are fast to compute and allow us to cover large sky areas easily. By contrast, hydrodynamical simulations search to solve simultaneously the equations of gravitation and of gas dynamics. As we have seen in chapter 1, the interplay between baryons and dark matter impacts the structure formation at small angular scales, and hydrodynamical simulations can reproduce such effects. Nevertheless, they are computationally very expensive.

The analysis in this chapter is based on The Three Hundred project galaxy cluster simulations. The Three Hundred project consists of zoom-in hydrodynamical re-simulations of the 324 Lagrangian regions centred on the most massive galaxy clusters identified in the *MultiDarkPlanck2* box of side length $1h^{-1}$ Gpc of the *MultiDark*[21] dark-matter-only simulation. The regions, of radius 15 h^{-1} Mpc and identified at $z = 0$, contain clusters with virial masses above $1.2 \times 10^{15}\ \mathrm{M}_\odot$ and dark-matter particles of mass $1.5 \times 10^9 h^{-1}\mathrm{M}_\odot$. The simulation assumes a cosmology based on the Planck Collaboration et al. (2016) [24] results: $h = 0.6777$, $n = 0.96$, $\sigma_8 = 0.8228$, $\Omega_\Lambda = 0.692885$, $\Omega_\mathrm{m} = 0.30711$ and $\Omega_\mathrm{b} = 0.048206$. This is also the cosmological model assumed in the rest of this chapter.

The selected DM-only volumes were mapped back to the initial conditions, dark matter particles were split into dark matter and gas particles and the regions were re-simulated with three hydrodynamical codes: `GADGET-MUSIC` [362], `GIZMO-SIMBA` [363, 364] and `GADGET-X` [365]. We will use the results from the latter, which implements very complete baryonic physics models.

The `GADGET-X` code accounts for dark matter, gas, stellar and black hole particles. Black hole particles in the simulation accrete hot and cold gas [234] and AGN feedback is implemented following the model from Steinborn et al. (2015) [366]. In addition, the cooling of the gas is assumed to be metal dependent [367]. Previous works based on `GADGET-X` have shown agreement between simulations and observations. According to the study in Truong et al. (2018) [203], at R_{500} the gas density and temperature of the clusters in the simulation reproduce the observations. In addition, authors in Rasia et al. (2015) [365] showed that the gas density and entropy profiles of the simulation agree with observed data. Equally, conformity between observed and simulated pressure profiles was demonstrated in Planelles et al. (2017) [368].

[21] Publicly available at the `https://www.cosmosim.org` database.

Twin sample	M_{200} [10^{14} $M_\odot$]	M_{500} [10^{14} $M_\odot$]
TS_{TM}	4.19 - 16.38 (8.43)	2.99 - 11.08 (5.68)
TS_{HEM}	4.40 - 16.95 (8.39)	3.23 - 11.73 (6.03)
TS_Y	5.43 - 17.48 (9.06)	3.94 - 12.64 (6.62)

Table 7.1: Range of masses covered by the clusters in each twin sample and the median value in brackets. We give the masses at overdensities of $\Delta = 200$ and 500.

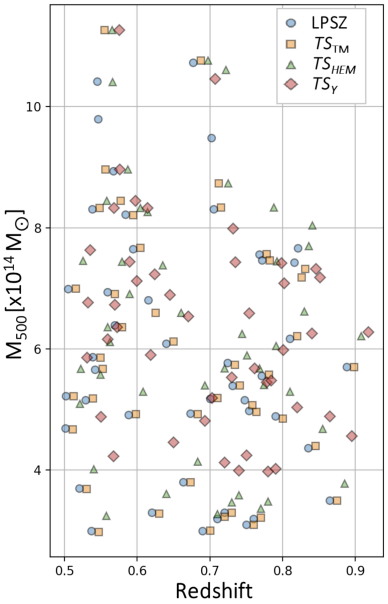

Figure 7.1: Clusters in the NIKA2 LPSZ sample shown in the mass-redshift plane (blue circles). The orange squares, green triangles and red diamonds show respectively the clusters in the twin samples built from The Three Hundred project simulations based on the total M_{500} mass, hydrostatic M_{500} mass and Y_{500} signal of the clusters. Figure from Paliwal et al. (2022) [369].

7.1.1 The Three Hundred-NIKA2 LPSZ samples

For our analysis, we used the clusters from The Three Hundred project simulations selected to constitute twin samples of the LPSZ. As described in Paliwal et al. (2022) [369], the clusters were chosen to cover the same redshift range as the LPSZ, i.e., $0.5 \lesssim z \lesssim 0.9$. Amongst all the clusters in The Three Hundred satisfying this condition, we chose the snapshots 101 at $z = 0.817$, 104 at $z = 0.700$, 107 at $z = 0.592$ and 110 at $z = 0.490$. Three different samples were generated by matching properties of the clusters in the simulation to those known for the clusters in the LPSZ. The three twin samples (TS) are: 1) TS_{TM}, the total mass twin sample, in which the clusters in the simulation are selected so that the total M_{500} from the simulation matches with the M_{500} mass of the LPSZ clusters according to *Planck* or ACT catalogues [141, 142], 2) TS_{HEM}, the hydrostatic mass twin sample, in which the hydrostatic mass of simulated clusters, $M_{500}^{\rm HSE}$, is matched with the *Planck* or ACT masses and 3) TS_Y, the twin sample based on the Y_{500} parameter, the integrated SZ signal within R_{500} (Eq. 1.55).

This selection gives three twin samples with 45 clusters. We present in Table 7.1 the range of masses covered by the clusters in each twin sample. In Fig. 7.1 we show the three twin samples in the mass-redshift plane, together with the clusters from the LPSZ sample. Some of the clusters being repeated, we have altogether 122 different objects. In this analysis we used all the clusters from the three twin samples simultaneously. The results presented in the following do not vary from one twin sample to another and, on the contrary, accounting for the 122 clusters simultaneously improves significantly our statistics.

7.1.2 The synthetic data sets

In this section we present the processed data generated from the simulations and used in our analyses.

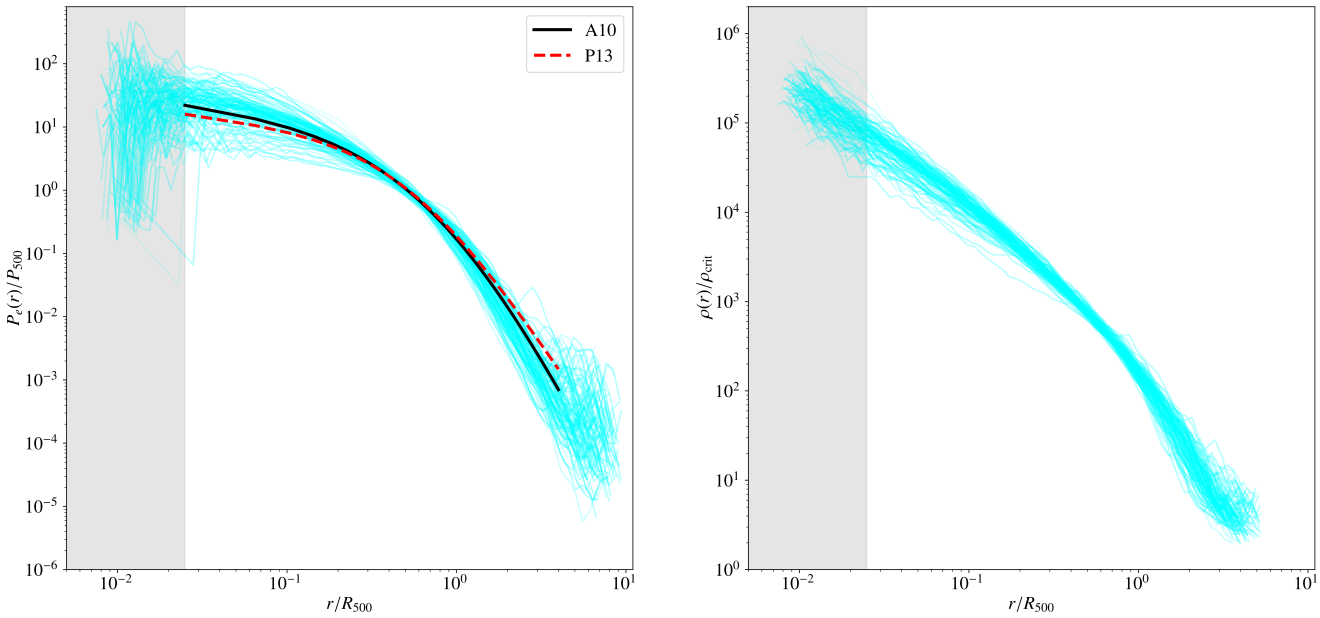

Figure 7.2: Normalised 3D gas pressure (left) and total matter mass density (right) spherical profiles for all the clusters in The Three Hundred-NIKA2 LPSZ twin samples. In the left panel we show the *universal* pressure profile from the X-ray analysis in A10 and the one obtained from the X-ray and SZ analysis in P13. All profiles are drawn with respect to the radii normalised by the R_{500} corresponding to each cluster. The grey shaded areas indicate the regions below $0.025 \times R_{500}$ that are not numerically robust.

Radial profiles

For comparison sake, we made use of the spherical three-dimensional radial profiles of cluster properties extracted from the simulations. In particular, we used the ICM pressure and total mass profiles. The profiles were computed accounting for particles in concentric shells and spheres centred at the maximum density peak, with radial bins starting at 10 kpc from the centre of the cluster and increasing radii by 10% (as in Gianfagna et al. (2023) [91]).

The gas pressure profiles were extracted considering hot gas particles (i.e., only particles with a temperature above 0.3 keV) and following Eq. 1 in Planelles et al. (2017) [368], with the correction for Smoothed-particle hydrodynamics (SPH) simulations proposed in Planelles et al. (2017) [368] and Battaglia et al. (2015) [370]. The total mass profiles account for the mass of all the particles (dark matter, hot and cold gas, stars and black holes) and are used to define the true R_{500} and M_{500} of clusters (Eq. 3.10). Profiles at $r \lesssim 0.025 \times R_{500}$ are not reliable since less than 100 particles are used to measure the thermodynamical quantities at these radial ranges.

In Fig. 7.2 we present the normalised pressure and mass density profiles for all the clusters in our sample. The pressure profiles have been normalised with respect to the P_{500} obtained from Eq. 5 in A10. Following figure 3 in Gianfagna et al. (2021) [179], we plot in the same figure the *universal* pressure profile from A10, as well as the profile obtained from the combination of XMM-*Newton* and *Planck* data in Planck Collaboration et al. (2013) [72], hereafter P13. The density profiles have been obtained by dividing the mass in each spherical shell by the volume of the shell and normalised with the critical density of the Universe at the corresponding redshift of each cluster (Eq. 1.8). The self-similarity of clusters regarding the gas pressure distribution, as well as the total matter density distribution, is clearly visible in Fig. 7.2.

Projected observable maps

I. Projected total mass: κ-maps

To study the projected mass of galaxy clusters, we used the convergence maps or κ-maps produced as described in Herbonnet et al. (2022) [371] and Euclid Collaboration et al. (2023) [169]. These convergence maps were generated together with shear maps to mimic the lensing effect due to the simulated clusters on background sources. As given by the Eq. 5.7, the convergence of a lens at a position $\vec{\theta}$ is defined as the ratio between the projected mass density of the cluster, $\Sigma(\vec{\theta})$, and the critical surface density, $\Sigma_{\rm crit}$.

To create the convergence maps, first the Σ-maps were obtained by adding, within a volume of depth 10 Mpc, the masses of all the particles of the simulated clusters along different projections. Then, these Σ-maps were divided by $\Sigma_{\rm crit}$, assuming all background sources to be at $z = 3$. For each cluster, maps of 6×6 Mpc^2 were produced, centred on the minimums of the gravitational potential wells. To avoid boundary errors, final maps are 5×5 Mpc^2 with 2048×2048 pixels, which gives different angular resolution pixels for different redshift clusters.

Six different maps are available for each cluster, corresponding to different projection axes. Three maps (hereafter 0, 1 and 2) are obtained from the projection along the x, y and z orthogonal axes of the simulation. In principle, they correspond to random directions with respect to the morphology of the clusters. The other three (0_pr_axes, 1_pr_axes and 2_pr_axes) are aligned with the principal axes of the clusters regarding their moments of inertia [372].

II. Sunyaev-Zel'dovich effect: y-maps

The gas in the ICM of galaxy clusters is investigated starting from the y-maps. As described in Cui et al. (2018) [234] (and previously done in Sembolini et al. (2013) [362] and in Le Brun et al. (2015) [373]), in THE THREE HUNDRED project the integration along the line-of-sight needed to obtain the Compton parameter (Eq. 1.24) is converted into a summation[22]. The sum is computed over the gas particles in the line-of-sight and within a $2 \times R_{200}$ depth volume,

$$y = \frac{\sigma_T k_{\rm B}}{m_{\rm e} c^2 {\rm d}A} \sum_{i=0}^{N_{\rm gas\ part.}} T_{{\rm e},i} N_{{\rm e},i} W(r, h_i). \tag{7.1}$$

Here the electron number density $n_{\rm e}$ from Eq. 1.24 is represented as the number of electrons in a given gas particle, $N_{\rm e}$, divided by its spatial volume ${\rm d}V$ (${\rm d}V = {\rm d}l{\rm d}A$): $n_{\rm e} = N_{\rm e}/{\rm d}V = N_{\rm e}/{\rm d}A/{\rm d}l$. $W(r, h_i)$ corresponds to the SPH smoothing kernel used to smear the signal of each particle to the projected pixels, with smoothing length h_i [234].

For each cluster there are 29 y-maps available, projected along the x, y and z main axes of the simulation, plus along other 26 random axes. We analysed only the projections in common with the κ-maps, hence the three main axes projections. Centred on the projected maximum density peak of the clusters, maps have 1920×1920 pixels of $5''$ angular resolution, going up to ~ 14 to $\sim 30 \times R_{200}$.

III. Projected gas mass maps

A different way to characterise the distribution of the gas in the ICM is to use projected gas mass maps. They were generated as the Σ-maps, but accounting only for the gas particles along the line-of-sight. Final maps are also 5×5 Mpc^2 with 2048×2048 pixels and projected along the three main axes of the simulation.

7.2 Sources of the mass bias: state of the art

The orientation of clusters is known to affect the mass reconstruction from observations. As shown in Oguri et al. (2009) [374], Oguri and Blandford (2009) [375], Hennawi et al. (2007) [376], Meneghetti et al. (2010)

[22] Using the publicly available Python package: https://github.com/weiguangcui/pymsz.

[377], Gralla et al. (2011) [378], and Euclid Collaboration et al. (2023) [169] when clusters are observed elongated along the line-of-sight, masses are overestimated. The contrary happens when the major axes of clusters are on the plane of the sky. Thus, the projection through which clusters are observed impacts their mass estimates. In Meneghetti et al. (2014) [379] authors explored the impact of projection effects by using the MUSIC-2 simulations [362, 380], which consist of N-body *MultiDark* simulations to which baryons were added using SPH techniques on the dark matter, in the non-radiative flavour and without accounting for the energy feedback from AGNs. Authors estimated the mass by fitting different density models to the spherical mass density profiles of the clusters as well as to the projected mass maps. Overall, masses reconstructed from projected maps are $\sim 13 - 14\%$ more scattered than those estimated from the fit to three dimensional density profiles. Furthermore, according to this work, masses estimated from projected data are on average underestimated by 5%. They affirm, as in Giocoli et al. (2012) [381], that this bias is due to the orientation of clusters. As explained in chapter 5, lensing observations give an estimate of the projected matter density distribution, therefore, the difficulty resides in recovering precise three dimensional profiles.

According to simulations in the cold dark matter framework [382], clusters are more frequently prolate systems than oblate-shaped. This means that, in general, the ratio of intermediate to minor axes is larger than the ratio of major to intermediate axes in clusters. This prolateness is presented in Giocoli et al. (2012) [381] as another intrinsic source of bias. After halo triaxiality, in Giocoli et al. (2012) [381] the presence of substructures is found to be the second contributor to the mass bias.

The model chosen to reconstruct the three dimensional mass profile can also be a source of bias. In Meneghetti et al. (2014) [379] authors used the NFW, gNFW and Einasto [383] models to fit three dimensional mass density profiles of simulated clusters in ranges between $0.02R_{\rm vir}$ and R_{200}. They concluded that, as expected, models with three parameters (gNFW with $b = \beta = 3$ and $a = \alpha = 1$, and Einasto) fit better the density profile than those with two (NFW). An important projection effect was also found regarding modelling: not all clusters that in three dimensions have density profiles following an NFW shape have an NFW-like density when projected [379]. In Euclid Collaboration et al. (2023) [169] authors created *Euclid*-like weak lensing observables from THE THREE HUNDRED simulation shear maps. By fitting smoothly-truncated NFW density models [343] to this data, they concluded that the truncation radius chosen in the model impacts the bias of reconstructed masses. In addition, they showed that the bias at R_{200} and its relative uncertainty are smaller if the concentration parameter is fixed, namely at $c_{200} = 3$.

Moreover, as presented in Rasia et al. (2012) [347], another reason to explain the bias is the approach used to select the sample. For clusters selected according to their X-ray luminosity, the reconstructed concentration-mass relation has a larger normalisation and steeper slope than the genuine relation [379, 384]. The reason behind is that, for a given mass, the most luminous clusters are the most concentrated ones (Sect. 1.2.2). On the contrary, if clusters are chosen for their strong lensing signal, they are preferentially elongated along the line-of-sight [377, 385] and, as a consequence, the masses obtained from projected maps are overestimated.

Many are the effects at the origin of the bias and the scatter of the weak lensing masses of clusters. As summarised in Lee et al. (2023) [386], assuming an NFW profile and a concentration-mass relation can introduce uncertainties in the mass of 10 to 50% due to the non-sphericity of clusters, structures along the line-of-sight, miscentring and halo concentration. Regarding the concentration-mass relation, from an analysis of mock galaxy cluster lenses created with the MOKA[23] code [387], Giocoli et al. (2012) [381] concluded that the amplitude of the relation is lower when derived from lensing analyses, therefore, from projected mass tracers, than from the three dimensional studies.

In Rasia et al. (2012) [347] they used 20 halos (with 3 projections per cluster) simulated to mimic Subaru observations [388]. By fitting an NFW model to the reduced tangential shear profiles they concluded that the masses at R_{500} are biased low by $\sim 7 - 10\%$ with a scatter of 20%. The lensing analysis based on simulations in Becker and Kravtsov (2011) [290] also concluded that, including shape noise only, these mass estimates are biased by $\sim 5 - 10\%$ with a 20 to 30% scatter. In the same line, the weak lensing analysis in Euclid

[23] https://cgiocoli.wordpress.com/research-interests/moka/

Collaboration et al. (2023) [169] derived an average 5% mass bias at R_{200}, with the bias for a given cluster differing by up to 30% depending on the orientation of the projection of the cluster observation.

Giocoli et al. (2012) [381] investigated also the dependence of the bias with redshift and found very little evolution. Quite the opposite, they showed that the radial range chosen to fit the density or mass profile model has an important impact on the bias. According to Euclid Collaboration et al. (2023) [169], the underestimation of cluster masses in *Euclid*-like weak lensing reconstructions is more important at higher redshift, modulated by the number density of background sources.

Some works compared also the uncertainties of masses reconstructed from total matter observables to those estimated from gas observables. They showed, on the one hand, the small impact of orientation in gas observables with simulated SZ and X-ray data [389] and, on the other hand, the irreducible non-sphericity of halos that affects the intrinsic scatter of the weak lensing masses, tracers of the total matter distribution [290]. In the same line, Meneghetti et al. (2010) [390] suggested that lensing masses are three times more scattered ($\sim 17-23\%$ of scatter) than X-ray estimates. The error budgets given in Pratt et al. (2019) [48] indicate that the assumption of spherical symmetry affects HSE masses at the level of a few percent, while lensing masses are affected by about 10% due to mass modelling. According to Rasia et al. (2012) [347], weak lensing biases are at least twice more scattered than X-ray outcomes.

In the above-mentioned analysis published in Euclid Collaboration et al. (2023) [169], THE THREE HUNDRED simulated data were used also to study the bias of weak lensing mass reconstructions on the prospect of the preparation work for the *Euclid* mission [391]. In this case, the simulated data was converted into a *Euclid*-like weakly lensed galaxy distribution. From shear estimates on these galaxies, they built excess surface mass density profiles. The latter were fitted with the smoothly-truncated NFW model (tNFW) to reconstruct the three dimensional mass density profiles of clusters. In this chapter we do not aim to reproduce such observational effects, but the comparison to the results from Euclid Collaboration et al. (2023) [169] will be valuable to elucidate the origin of some of the observed effects. We also stress that our study differs from the work of Euclid Collaboration et al. (2023) [169] regarding the considered cluster sample and the overdensity of the reconstructed masses. While we restrict, as discussed above, our analysis to a subsample of THE THREE HUNDRED clusters in the redshift and mass range covered by the LPSZ programme and evaluate the masses at R_{500}, in Euclid Collaboration et al. (2023) [169] the bias was studied at R_{200} for all THE THREE HUNDRED clusters at 9 different redshifts between $z = 0.12$ and $z = 0.98$.

7.3 Total mass reconstruction from κ-maps

Just like in Meneghetti et al. (2014) [379], in our analysis we did not consider any systematic effect, such as the accuracy of galaxy shape measurements or photometric redshifts, that may affect lensing analyses (chapters 5 and 6). Those effects can introduce additional uncertainties that require separate investigations [169, 392]. We restricted our work on simulated data to the effects that arise from the reconstruction of three-dimensional quantities from projected data.

7.3.1 Mass reconstruction procedure

To estimate the total mass of the clusters from projected maps we followed the procedure presented in chapter 5 for CLASH convergence maps [190, 191, 393]. As a reminder, in chapter 5 convergence maps from the CLASH data set are used to reconstruct the lensing mass of galaxy clusters: κ-maps are converted into projected mass density maps, Σ, and mass density models are fitted to the radial profile of Σ, which allows one to reconstruct the lensing mass.

Similarly, from the convergence maps described in Sect. 7.1.2, we obtain projected Σ-profiles by radially averaging the values in the map, starting from their central pixel. Uncertainties are computed from the dispersion in each radial bin to account for non-circular features in the map. The size of these uncertainties does not necessarily correspond to what we would expect from observations. For instance, in weak lensing observations

error bars tend to be larger in the centre and smaller in the outskirts of clusters. In a previous work Giocoli et al. (2012) [381] showed that the choice of the radial range for the fit can also impact the results. We decided to take 60 bins in a range between 0.4″ and 500″ with respect to the centre of the map. In this way we account for the central and external regions of the clusters, as in Ferragamo et al. (2022) [190], Muñoz-Echeverría et al. (2023) [191], and Muñoz-Echeverría et al. (2022) [393]. By contrast, to build the excess surface mass density profiles in Euclid Collaboration et al. (2023) [169] authors used 22 logarithmically spaced bins, spanning from 0.02 to $1.7h^{-1}$ Mpc from the cluster centre.

To model the Σ-profile we used the two-parameter NFW mass density model (Eq. 1.19) and the three-parameter Einasto model, as in Meneghetti et al. (2014) [379]. We fitted the Σ-profiles from the convergence maps with the mass density profile models projected following

$$\Sigma_{\rm model}(R) = 2\int_0^{+\infty} \rho_{\rm model}\left(\sqrt{r^2+R^2}\right)\,{\rm d}r. \tag{7.2}$$

Here r is the radius of three-dimensional spherical profiles, while R corresponds to the projected profiles. For this analysis, we parametrised the NFW model as a function of c_Δ and R_Δ (Eq. 1.19).

The Einasto density model is defined as

$$\rho_{\rm Ein}(r) = \rho_s\,\exp\left\{-\frac{2}{\alpha}\left[\left(\frac{r}{r_s}\right)^\alpha - 1\right]\right\}, \tag{7.3}$$

where the free parameters are r_s, ρ_s and α, that correspond to the scale radius, the characteristic density and the shape parameter, respectively.

We made use again of the `profiley` Python package[17], which contains also line-of-sight projected density profiles. As described in Sect. 5.1.3, the fits were performed via MCMC analysis (using the `emcee` software) and we initialised the chains by taking: $1.0 < R_{200}/{\rm Mpc} < 3.5$ and $2.0 < c_{200} < 3.5$ for NFW, and, $10^{14} < \rho_s/{\rm M}_\odot/{\rm Mpc}^3 < 10^{16}$, $0.2 < r_s/{\rm Mpc} < 1.0$ and $0.0 < \alpha < 0.5$ for Einasto. Once the fit is performed, we verify that the modelled Σ-profile is a good representation of the data following the goodness of fit criterion defined as

$$FQ \equiv \text{Fit quality} \;\equiv\; \text{median}(|\Sigma_{\rm data} - \Sigma_{\rm model}|/\sigma_{\Sigma_{\rm data}}), \tag{7.4}$$

where the median is estimated over all the radial bins and posterior distributions of the model. Bad fits are rejected if $FQ > 1$. This means that if the median of the absolute difference between the Σ-profile data bins and the model with respect to the uncertainties is larger than unity, the fit is not satisfactory.

After the fit, mass profiles are obtained by computing for each sample of parameters the corresponding profile. For the NFW model the spherical mass profile is described by,

$$\begin{aligned} M_{\rm NFW}(<r) = 4\pi\rho_s r_s^3\left[\frac{1}{1+r/r_s} + \ln(1+r/r_s) - 1\right] = \\ 4\pi c_{200}^3 200\rho_{\rm crit}/3I(c_{200})(R_{200}/c_{200})^3 \\ \left[\frac{1}{1+rc_{200}/R_{200}} + \ln(1+rc_{200}/R_{200}) - 1\right]. \end{aligned} \tag{7.5}$$

And for Einasto,

$$M_{\rm Ein}(<r) = \frac{4\pi\rho_s r_s^3}{\alpha} e^{2/\alpha}\left(\frac{\alpha}{2}\right)^{3/\alpha}\gamma\left[\frac{3}{\alpha}, \frac{2}{\alpha}\left(\frac{r}{r_s}\right)^\alpha\right], \tag{7.6}$$

where γ is the incomplete lower gamma function:

$$\gamma(a,x) = \int_0^x t^{a-1}e^{-t}{\rm d}t. \tag{7.7}$$

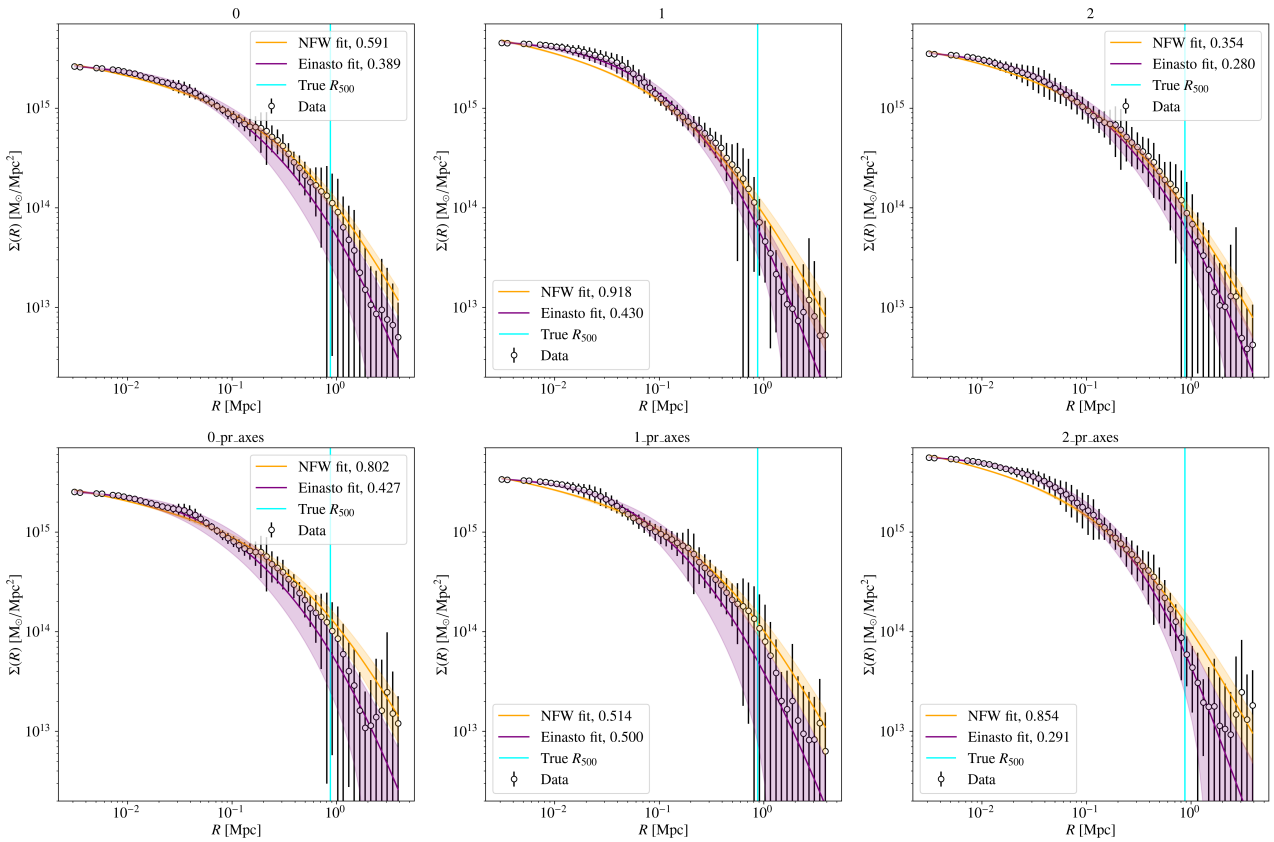

Figure 7.3: The projected mass density profiles (empty markers) for the six available convergence maps for the 0306 cluster in the snapshot 101 ($z = 0.817$). The orange and purple profiles show the best-fit profile for the NFW and Einasto models, respectively. We also show 1σ uncertainties as the shaded areas of the same colours. The numerical values given in the captions correspond to the FQ estimator (Eq. 7.4) for each projection and model. From left to right and top to bottom we present the 0, 1 and 2 random projections and 0_pr_axes, 1_pr_axes and 2_pr_axes principal moment of inertia projections. The vertical cyan line shows the true R_{500} of the cluster.

Finally, from the reconstructed mass profiles we compute the M^{κ}_{500} mass of the cluster at its corresponding radius R^{κ}_{500} (Eq. 3.10). This procedure for both models is applied to all clusters in the twin samples and to all the discussed projections in order to estimate the M^{κ}_{500}. As an example, in Fig. 7.3 we present the Σ-profiles for the six projections of one cluster (number 0306 in THE THREE HUNDRED) at $z = 0.817$. The orange and purple lines show the best-fit profiles (solid lines) and 1σ uncertainties (shaded areas) obtained from the posterior distributions of the NFW and Einasto fits, respectively. This figure shows that the Einasto model is a better fit to the data, being able to describe the multiple slope changes at small and large radii. Nonetheless, at intermediate radii ($0.1 - 1$ Mpc) the NFW fit follows better the data. In the 2_pr_axes projection the cluster is observed along its most elongated axis. For this reason, the centre appears very massive and the density in the outskirts drops fast.

In Fig. 7.4 we show the mass profiles corresponding to the projected mass density best-fits of Fig. 7.3 with the NFW and Einasto models for the 0306 cluster in the snapshot 101. We present again the profiles for the projections along the 3 main axes of the simulation on top, and in the bottom the profiles for the main inertia moment axes of the cluster. The dashed line shows the $R_{500} - M_{500}$ relation and the cyan profile corresponds to the spherical true mass profile (Sect. 7.1.2). The departure of the NFW and Einasto profiles from the true spherical mass profile at $\sim R_{500}$ will determine the difference between the true M_{500} and the NFW and Einasto estimates.

We repeat the analysis for all the clusters in our sample and for the following we take, amongst all the Σ-profile fits, the results that pass the quality criterion in Eq. 7.4 for both the NFW and Einasto fits. Thus, we keep 116 clusters. As we will explain in Sect. 7.4.2, in the following we will only consider the three projections

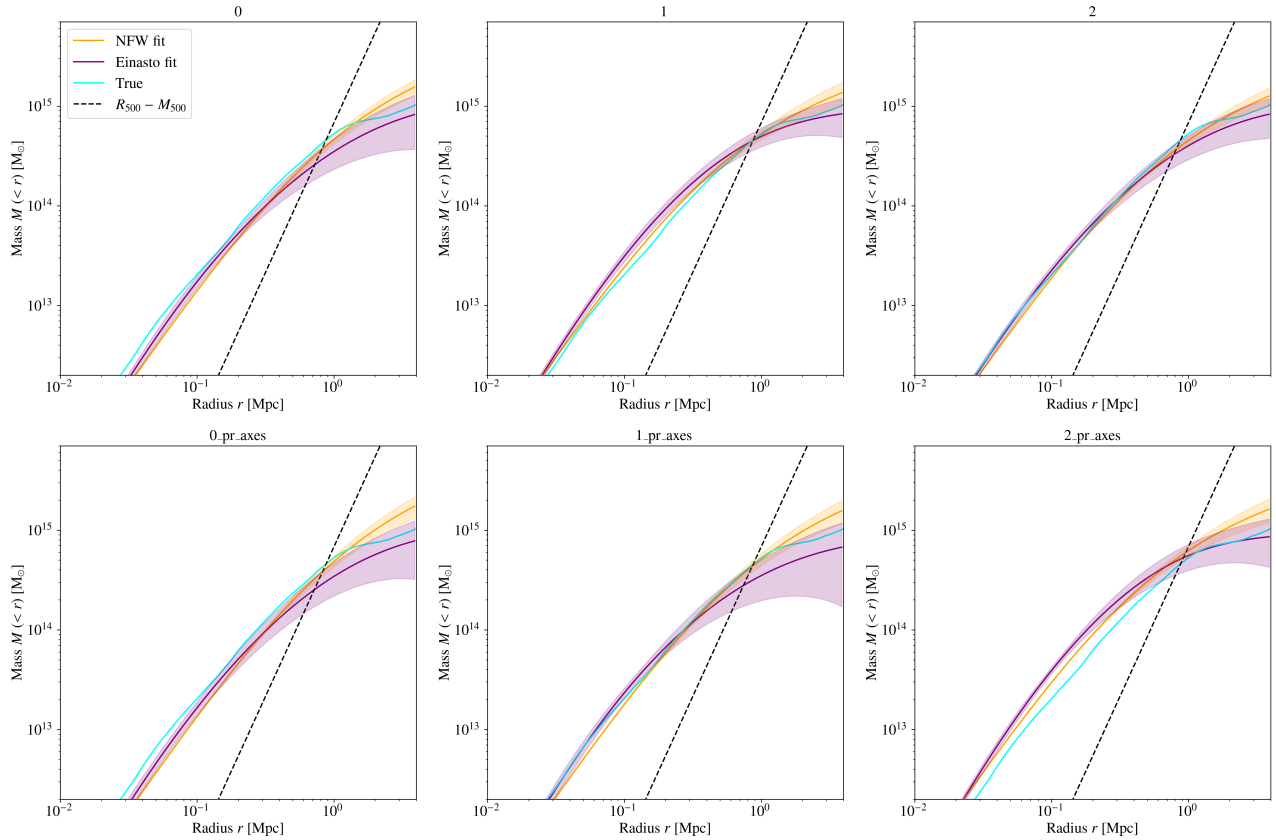

Figure 7.4: Mass profiles reconstructed from the convergence map fits for the 0306 cluster in the snapshot 101 ($z = 0.817$). The orange and purple profiles correspond to NFW and Einasto models, respectively. We give the mean profiles with 1σ contours. The cyan profile is the spherical mass profile computed by adding in concentric spheres the mass of all the particles in the simulation. The black dashed line shows the $R_{500} - M_{500}$ relation.

along the x, y and z orthogonal axes of the simulation, unless stated otherwise.

In Fig. 7.5 we present the relation between the best-fit values of the parameters obtained from all NFW (left) and Einasto (right) fits. We also provide in the figure the Pearson correlation coefficient for each pair of parameters represented. Regarding the Einasto parameters, shown in the right panel of Fig. 7.5, an anticorrelation between ρ_s and r_s parameters is clearly noticeable, with a Pearson correlation coefficient of -0.6. In the left panel we also indicate, with large stars, the mean concentration in bins of M_{200} for NFW, and compare our result to the concentration-mass relations in Cui et al. (2018) [234]. In this paper authors show that the concentration-mass relation of $z = 0$ clusters from THE THREE HUNDRED simulation is flatter for `GADGET-X` clusters than for `GADGET-MUSIC`. The concentration-mass relation obtained in our analysis with the NFW model follows the decreasing tendency of the `GADGET-MUSIC` clusters results from THE THREE HUNDRED in Cui et al. (2018) [234], which is also in agreement with previous studies (such as López-Cano et al. (2022) [394] and references therein). As a reference, we also show the horizontal $c_{200} = 3$ line that corresponds to the concentration value fixed in Euclid Collaboration et al. (2023) [169] to minimise the mass bias when fitting tNFW density models. Some works (e.g., Oguri et al. (2009) [374]) find also a dependence of the concentration parameter with redshift. By contrast, our results do not present any clear evolution along cosmic time (the Pearson correlation coefficient between the redshift and the concentration is r = -0.01). According to Meneghetti et al. (2014) [379] the redshift evolution of the concentration-mass relation is weak for the `MUSIC-2` simulation.

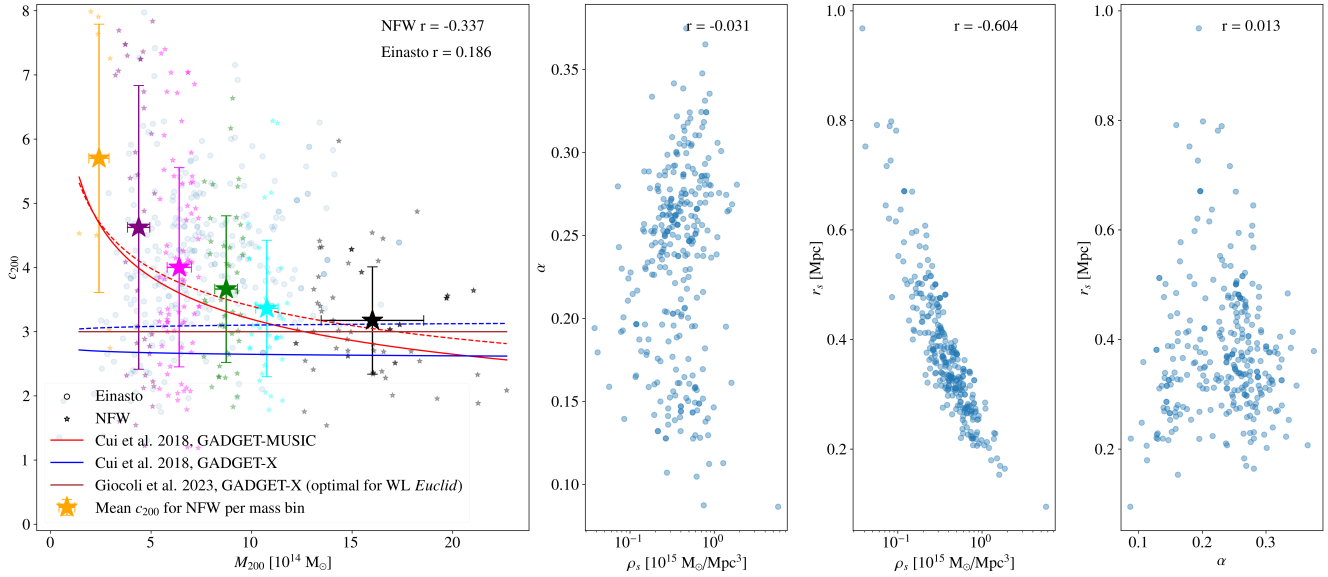

Figure 7.5: The best-fit values of the posterior distributions of NFW (left) and Einasto (right) parameters. Each point corresponds to one projection of one cluster. We give the Pearson correlation coefficients for the parameters presented in each panel. In the left panel the big stars show the mean NFW concentration and the standard deviation in different mass bins. Blue and red lines show the concentration-mass relations for `GADGET-X` and `GADGET-MUSIC` simulations obtained in Cui et al. (2018) [234] accounting for different radial ranges: with solid lines considering data above $0.05 \times R_{200}$ and with dashed lines the results considering data above $34h^{-1}$ kpc. The horizontal brown line at $c_{200} = 3$ in the left panel represents the best concentration value obtained in Euclid Collaboration et al. (2023) [169] to reconstruct unbiased masses. For comparison, in the left panel we also plot the M_{200} and $c_{200} = R_{200}/r_s$ obtained for the Einasto best-fits (blue dots).

7.3.2 Mass bias from convergence maps

The mass bias we refer to in this chapter is the relative difference between each reconstructed mass, M^{κ}_{500} (as above-mentioned, evaluated at the R^{κ}_{500} obtained from the reconstructed mass profile), with respect to the true mass of the cluster, M_{500}:

$$b^{\kappa} = (M_{500} - M^{\kappa}_{500})/M_{500}. \tag{7.8}$$

We present in Fig. 7.6 the bias estimated from all the analysed maps with respect to the true M_{500} for each cluster. Orange and purple markers show the bias and uncertainties measured for the NFW and Einasto mass density models, respectively. Uncertainties are computed from the propagation of the posterior distributions of the parameters in each model. The distributions on the right-hand side plot show also the bias per map fit for each cluster. The horizontal orange line shows the mean bias for NFW, while the purple corresponds to Einasto. The median biases for the NFW and Einasto reconstructions are med(b^{κ}) = 0.036 and 0.179, respectively. Surprisingly, Einasto gives, on average, a more biased estimate of the mass of the clusters.

To address this issue, we come back to the Σ-profiles presented in Sect. 7.3.1. In Fig. 7.7 we show the relative difference between the fit of the Σ-profile for the NFW and Einasto models and the profiles measured from the convergence maps. Although the overall Einasto best-fit models are a better representation of the Σ-profiles, NFW fits the intermediate radial ranges better than Einasto. We see in Fig. 7.7 that Einasto projected mass density fits are systematically biased at $R \sim R_{500}$. Since these are the crucial radii that determine R_{500}, a precise description of the density here, gives proper M_{500} estimates. One could think of improving the fits either by adapting the radial range ad hoc to get a less biased result (given the important role of the outer radii in Einasto fits, we could imagine studying the impact of accounting for the data above 500″, that is, above $\sim 2 - 4 \times R_{500}$) or by choosing a more flexible density model. As discussed above, this type of studies have already been done in the literature [379, 381] and we will not go through those refinements in our analysis. Furthermore, authors in Cui et al. (2018) [234] concluded that the NFW model is a good representation of the

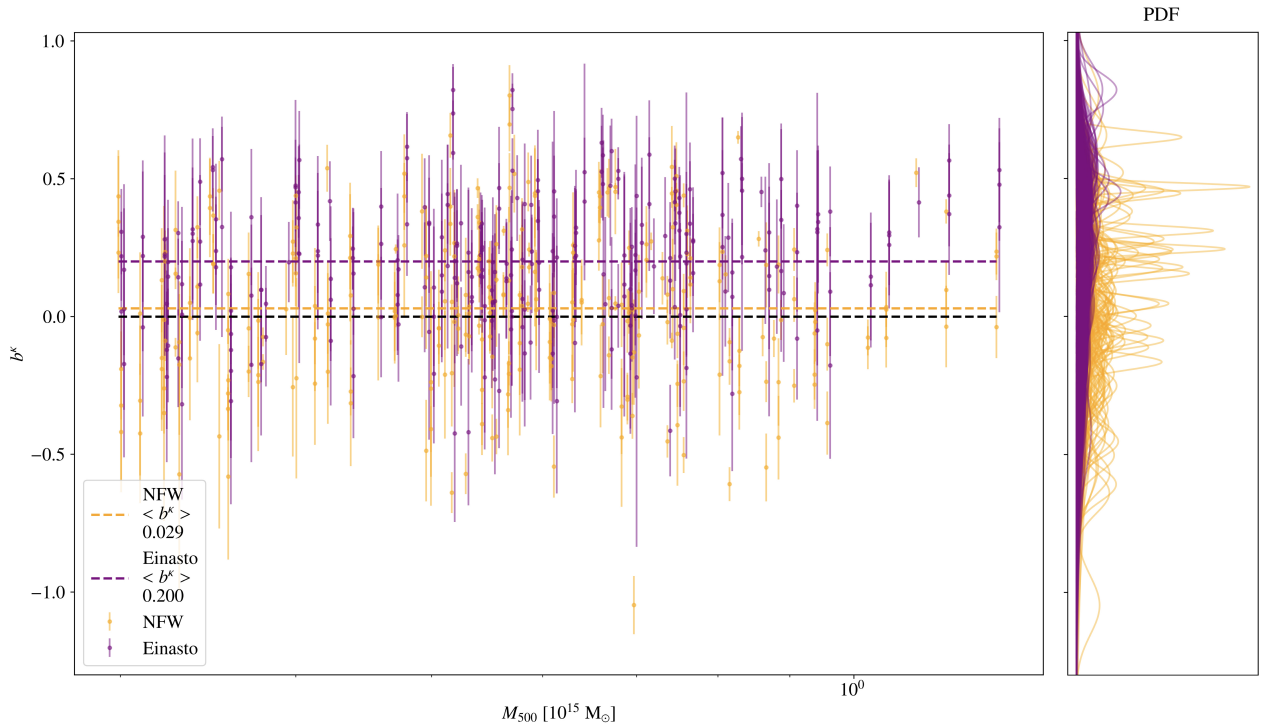

Figure 7.6: Mass bias for masses inferred from fitted κ-maps with respect to M_{500} per cluster. Each data point corresponds to the mean bias of a cluster for a given random projection (0, 1 or 2) with error bars showing the 1σ uncertainty. Results for the Einasto model have been artificially shifted in mass for visualisation purposes. The Gaussian distributions (one per data point) on the right side represent the same results. The horizontal orange and purple dashed lines show the mean for all the results for NFW and Einasto, respectively. The black line indicates the zero.

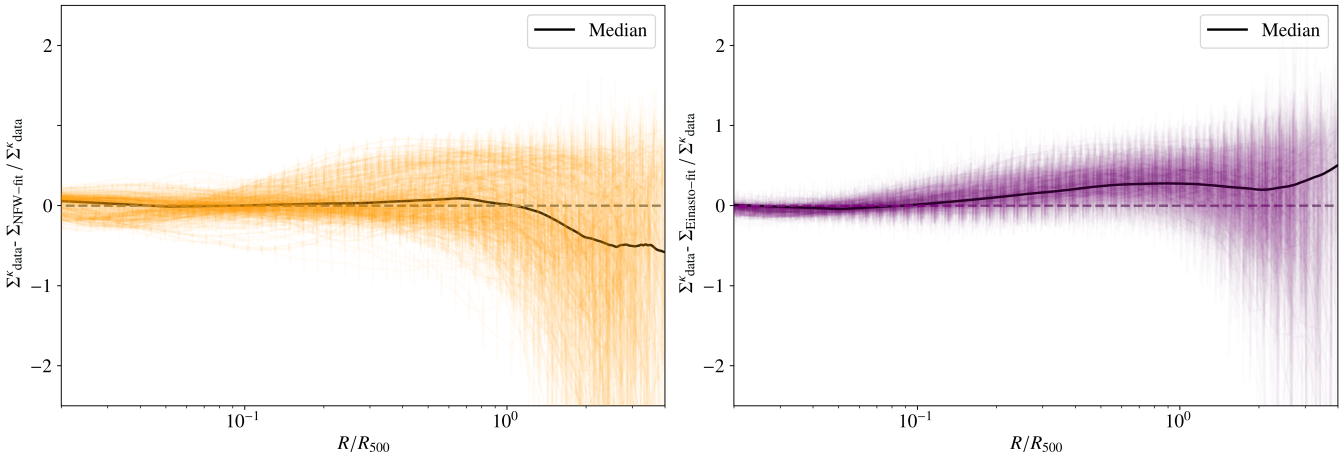

Figure 7.7: Relative difference between the data and best-fit Σ-profiles as a function of the radius for NFW (left) and Einasto (right) models. Solid lines indicate the median of all the profiles in each panel. The horizontal dashed lines show the zero.

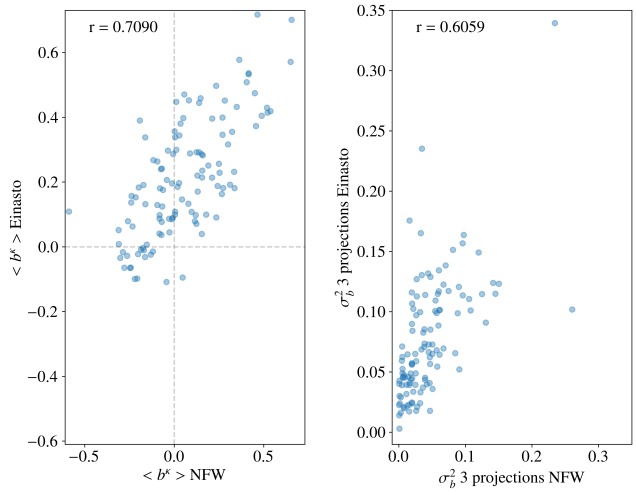

Figure 7.8: Mean bias for the three projections (left) and dispersion, $\sigma^2_{b,3\text{ projections}}$, (right) per cluster for Einasto against NFW reconstructions. Each dot corresponds to one cluster. We give the Pearson correlation coefficient for the values given in each panel and fix the same limits in both axes.

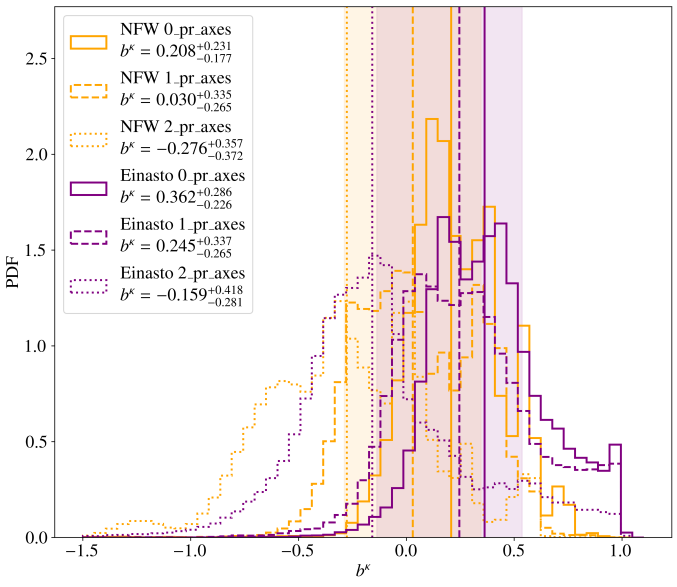

Figure 7.9: Mass bias for NFW (orange) and Einasto (purple) best-fits of the Σ-profiles when aligned with the principal axes of the clusters regarding their moments of inertia. Solid lines correspond to 0_pr_axes, dashed lines to 1_pr_axes and dotted lines to 2_pr_axes. Histograms account for all the results for all the well fitted clusters. We give the value of the median and the 16th and 84th percentiles. The vertical lines show the median value that corresponds to each distribution and the shaded areas represent the 1σ regions of the bias obtained for all the clusters with the three random projections (Fig. 7.6).

spherical mass density profile of the clusters in THE THREE HUNDRED simulation, even considering different inner radii. However, according to the work in Euclid Collaboration et al. (2023) [169], THE THREE HUNDRED clusters are not perfect NFW halos.

In the left panel in Fig. 7.8 we present the mean bias per cluster obtained for the NFW density best-fits with respect to the mean bias for the Einasto ones. There is a direct correlation between the NFW and Einasto biases, with a Pearson correlation coefficient of 0.71. This might mean that, despite the differences in the reconstructed masses due to modelling effects, the impact of the modelling is not enough to blur the information in the convergence maps.

We also verify that the orientation of the cluster affects directly the bias. In Fig. 7.9 we present the bias measured from the maps projected along the three axes of inertia: when the cluster is elongated along the line-of-sight (2_pr_axes) the reconstructed mass is on average overestimated and when the major axes are on the plane of the sky (0_pr_axes), underestimated. In Herbonnet et al. (2022) [371] the authors investigated the relation between the orientation of halos and their brightest cluster galaxy (BCG). They found that the major axes of halos and BCGs are aligned with an average separation of ~ 20 degrees. For this reason, having access to the orientation of the BCG would provide a way to improve the knowledge of the orientation of the cluster, and therefore, of its mass reconstruction.

Given all the mentioned differences between our study and the analysis in Euclid Collaboration et al. (2023) [169], comparisons to the latter have to be done with extraordinary care. By fixing the truncation parameter of the tNFW model to $t = 3$, they find that the weak lensing masses reconstructed for the clusters at redshift $z = 0.22$ are on average biased low by $\sim 7\%$, with a standard deviation of 0.24 (for the reconstructed to true mass ratio) over the full sample (using the full THE THREE HUNDRED sample of clusters). Assuming also a fixed concentration parameter $c_{200} = 3$ and considering the clusters at redshifts below $z = 0.7$, according to Euclid Collaboration et al. (2023) [169], weak lensing M_{200} masses are on average underestimated by less than 5%. We observe in figure 14 in Euclid Collaboration et al. (2023) [169] that, for the redshift range considered in our analysis ($0.5 < z < 0.9$), the mean biases on M_{200} vary from 0% to 20% depending on the chosen value for the c_{200} parameter. Overall, these biases are slightly larger than our NFW results at R_{500} ($\sim 3\%$), but in agreement within uncertainties. It is worth reminding that, unlike in our analysis, the study in Euclid Collaboration et al. (2023) [169] considered the presence of noise in the shear of galaxies. Regarding the impact of the orientation of clusters on the mass bias, in Euclid Collaboration et al. (2023) [169] authors concluded that when clusters are oriented along the major and minor axes, the mass biases are respectively $\sim 25\%$ larger and smaller than the biases for random orientations. Therefore, their results are completely in line with those presented in Fig. 7.9.

7.4 Scatter of the mass bias

In the previous section, we have been looking at the mean biases estimated for each model making use of our full sample. The dispersion from cluster to cluster and for the different projections of the same cluster appear to be very important (Fig. 7.6). In this section we try to identify and quantify the different effects that contribute to the scatter of the biases in the reconstruction. For this, we will use a statistical approach and we will consider the full sample.

We first define the total variance per model from the scatter of the bias values obtained with the same model for all the clusters and all their projections (see Fig. 7.6):

$$\sigma^2_{b,\mathrm{tot}} = \frac{1}{N_{\mathrm{chains}} N_{\mathrm{projections}} N_{\mathrm{clusters}}} \sum_{i,j,k=1,1,1}^{N_{\mathrm{chains}},N_{\mathrm{projections}},N_{\mathrm{clusters}}} (b^{\kappa}_{i,j,k} - < b^{\kappa} >)^2. \tag{7.9}$$

Here N_{chains} is the number of chains kept after each fit, $N_{\mathrm{projections}}$ is the number of different projections per cluster and N_{clusters} the amount of clusters considered. $< b^{\kappa} >$ is the mean bias for all the clusters, accounting for all the projections and chains. Our purpose is to estimate the dispersion expected in a real observed sample.

We separate this total variance into two main contributions: 1) the variance from cluster to cluster, $\sigma^2_{b,\text{cluster-to-cluster}}$, showing how different are the bias values depending on the cluster, and 2) the variance of the results for each cluster, due to the different values depending on the projection, $\sigma^2_{b,3\text{ projections}}$. So we write, as in Bartalucci et al. (2023) [395],

$$\sigma^2_{b,\text{tot}} \sim \sigma^2_{b,\text{cluster-to-cluster}} + \sigma^2_{b,3\text{ projections}}. \tag{7.10}$$

Here $\sigma^2_{b,3\text{ projections}}$ is the dispersion of the results of three projections, that for each cluster c is obtained as,

$$(\sigma^2_{b,3\text{ projections}})_c = \frac{1}{N_{\text{chains}} N_{\text{projections}}} \sum_{i,j=1,1}^{N_{\text{chains}},N_{\text{projections}}} (b^\kappa_{i,j,c} - < b^\kappa >_c)^2, \tag{7.11}$$

where $< b^\kappa >_c$ is the mean bias per cluster c, considering the different projections and all the samples in the MCMC chains of the individual fits.

Furthermore, for each $\sigma^2_{b,3\text{ projections}}$ per cluster there are two sources of dispersion that we name: 1) $\sigma^2_{b,\text{intrinsic proj}}$, which accounts for the fact that the results obtained from three projections differ intrinsically, and, 2) $\sigma^2_{b,\text{fit}}$ that quantifies the uncertainties of the fitting procedure. Therefore, we can write

$$\sigma^2_{b,3\text{ projections}} \sim \sigma^2_{b,\text{intrinsic proj}} + \sigma^2_{b,\text{fit}}. \tag{7.12}$$

In the following subsections we study each contribution to the total scatter.

7.4.1 Fitting procedure uncertainties: $\sigma^2_{b,\text{fit}}$

The most evident source of scatter is the one related to the model fitting uncertainties, i.e., the scatter propagated from the posterior distributions of the parameters of the fitting function at one specific projection for one cluster. We define $(\sigma^2_{b,\text{fit}})_{\text{proj},c}$ as the variance of the bias values of each map fit ('proj') for each cluster (c):

$$(\sigma^2_{b,\text{fit}})_{\text{proj},c} = \frac{1}{N_{\text{chains}}} \sum_{i=1}^{N_{\text{chains}}} (b^\kappa_{i,\text{proj},c} - < b^\kappa >_{\text{proj},c})^2 \tag{7.13}$$

In the left panel in Fig. 7.10 we show the distribution of $\sigma^2_{b,\text{fit}}$ for all the clusters (and all their projections) in our sample. The histograms correspond to the bias variance for the NFW (orange) and Einasto (purple) profiles. We report the mean and median values in Table 7.2. The variance introduced by the fitting procedure or measurement error is larger for Einasto than for NFW. This might be expected since the Einasto model has one degree of freedom more than the NFW one. On average for the NFW and Einasto models 15% ($\sigma^2_{b,\text{fit}} \sim 0.02$) and 25% ($\sigma^2_{b,\text{fit}} \sim 0.06$) of uncertainties in the reconstructed masses come only from the uncertainty in the fit. We also note that the reduced χ^2 for the fits have median values with 84th and 16th percentiles of $\chi^2/\text{d.o.f.} = 1.12^{+1.09}_{-0.53}$ and $\chi^2/\text{d.o.f.} = 0.44^{+0.60}_{-0.26}$ for the NFW and Einasto models, respectively. These are compatible with the expected values for χ^2-distributions of the corresponding degrees of freedom. The small χ^2 values for Einasto fits could be a signature of overfitting with respect to the size of the data point error bars. In some cases, NFW fits have large χ^2, as it is shown by the percentiles of the reduced χ^2 that reach $\chi^2/\text{d.o.f.} \sim 2$.

7.4.2 Projection scatter: $\sigma^2_{b,3\text{ projections}}$

As discussed above, for each cluster three different projections are available and the variance of the results from the three is $\sigma^2_{b,3\text{ projections}}$, as defined in Eq. 7.11. As for the fitting uncertainties, we show the histograms of the variance associated with the projection scatter for each cluster in the right panel in Fig. 7.10. The variance of each cluster accounts for the posterior distributions of the mass biases for the three projections together. We

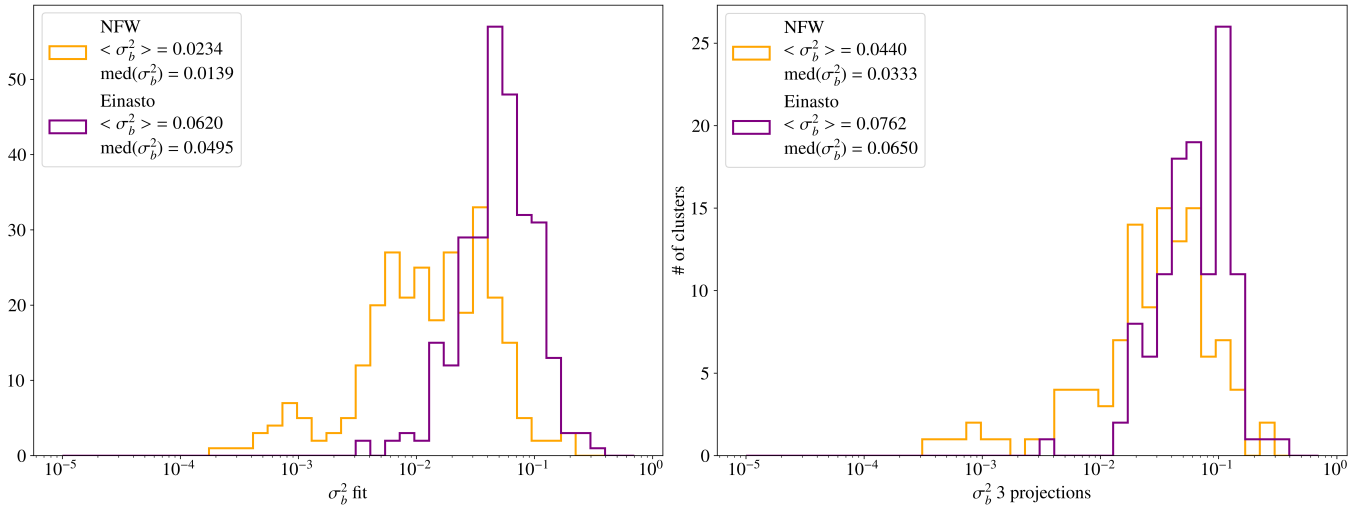

Figure 7.10: Variance of mass bias for all clusters. Left: scatter induced by uncertainties in the fitting procedure, for all the projections for all the clusters in our sample. Right: variance of the bias in the mass reconstruction of each cluster accounting for the results from the different projections.

Name	Definition	NFW	Einasto
$\sigma^2_{b,\mathrm{fit}}$	Eq. 7.13	$\left\langle \sigma^2_{b,\mathrm{fit}} \right\rangle = 0.0234$ $\mathrm{med}(\sigma^2_{b,\mathrm{fit}}) = 0.0139$	$\left\langle \sigma^2_{b,\mathrm{fit}} \right\rangle = 0.0620$ $\mathrm{med}(\sigma^2_{b,\mathrm{fit}}) = 0.0495$
$\sigma^2_{b,3\ \mathrm{projections}}$	Eq. 7.11	$\left\langle \sigma^2_{b,3\ \mathrm{projections}} \right\rangle = 0.0440$ $\mathrm{med}(\sigma^2_{b,3\ \mathrm{projections}}) = 0.0333$	$\left\langle \sigma^2_{b,3\ \mathrm{projections}} \right\rangle = 0.0762$ $\mathrm{med}(\sigma^2_{b,3\ \mathrm{projections}}) = 0.0650$
$\sigma^2_{b,\mathrm{intrinsic\ proj}}$	Eq. 7.12	$\left\langle \sigma^2_{b,3\ \mathrm{projections}} \right\rangle - \left\langle \sigma^2_{b,\mathrm{fit}} \right\rangle = 0.0205$ $\mathrm{med}(\sigma^2_{b,3\ \mathrm{projections}}) - \mathrm{med}(\sigma^2_{b,\mathrm{fit}}) = 0.0194$	$\left\langle \sigma^2_{b,3\ \mathrm{projections}} \right\rangle - \left\langle \sigma^2_{b,\mathrm{fit}} \right\rangle = 0.0142$ $\mathrm{med}(\sigma^2_{b,3\ \mathrm{projections}}) - \mathrm{med}(\sigma^2_{b,\mathrm{fit}}) = 0.0155$
$\sigma^2_{b,\mathrm{tot}}$	Eq. 7.9	0.1005	0.1135
$\sigma^2_{b,\mathrm{cluster-to-cluster}}$	Eq. 7.10	$\sigma^2_{b,\mathrm{tot}} - \left\langle \sigma^2_{b,3\ \mathrm{projections}} \right\rangle = 0.0565$ $\sigma^2_{b,\mathrm{tot}} - \mathrm{med}(\sigma^2_{b,3\ \mathrm{projections}}) = 0.0672$	$\sigma^2_{b,\mathrm{tot}} - \left\langle \sigma^2_{b,3\ \mathrm{projections}} \right\rangle = 0.0373$ $\sigma^2_{b,\mathrm{tot}} - \mathrm{med}(\sigma^2_{b,3\ \mathrm{projections}}) = 0.0485$
$\sigma^2_{b,\mathrm{mean}}$	Eq. 7.22	0.0555	0.0331
$(\sigma^{\kappa-\mathrm{map}}_{b,\mathrm{intrinsic\ proj}})^2$	Eq. 7.14	From maps ~ 0.01	

Table 7.2: Summary of the mass bias scatters studied in this chapter. We present the name given to each scatter term, the reference to the definition in the text and the obtained values for masses reconstructed using NFW and Einasto models. In some cases we give the mean, $\langle ... \rangle$, and median, med(...), values.

Snapshot	z	Cluster	$f_s(R_{200})$	$\Delta_r(R_{200})$	Dynamical state within R_{200}	$f_s(R_{500})$	$\Delta_r(R_{500})$	Dynamical state within R_{500}
101	0.817	0306	0.19	0.11	Disturbed	0.09	0.10	Intermediate
104	0.700	0206	0.18	0.08	Intermediate	0.16	0.16	Disturbed
107	0.592	0046	0.12	0.03	Intermediate	0.07	0.00	Relaxed
110	0.490	0198	0.18	0.14	Disturbed	0.19	0.15	Disturbed

Table 7.3: Dynamical state indicators at R_{200} and R_{500} for the clusters analysed from 100 projections.

Density model	Snapshot	z	Cluster	$< b^\kappa >$ 100 random	$\sigma^2_{b,100\text{ projections}}$ 100 random	$< b^\kappa >$ 3 main	$\sigma^2_{b,3\text{ projections}}$ 3 main	$< b^\kappa >$ 3 inertia	$\sigma^2_{b,3\text{ projections}}$ 3 inertia
NFW									
	101	0.817	0306	0.1401	0.0372	0.1285	0.0377	-0.0443	0.1069
	104	0.700	0206	0.3542	0.0408	0.3091	0.0043	0.1213	0.1408
	107	0.592	0046	-0.1404	0.0466	-0.2298	0.0403	-0.4174	0.2708
	110	0.490	0198	0.0896	0.0407	0.0555	0.0199	-0.1099	0.0569
Einasto									
	101	0.817	0306	0.2079	0.0664	0.2202	0.0709	0.1865	0.1582
	104	0.700	0206	0.3418	0.0357	0.4033	0.0204	0.2680	0.1012
	107	0.592	0046	-0.0905	0.1080	-0.0167	0.1660	0.0539	0.3499
	110	0.490	0198	0.2453	0.0837	0.4707	0.1069	0.3099	0.1650

Table 7.4: Mean bias and variance due to projection effect for the 4 clusters studied with 100 maps. The three main projections are the so-called 0, 1 and 2 or x, y and z projections. The 3 inertia projections are 0_pr_axes, 1_pr_axes and 2_pr_axes.

report the mean and median values of the histograms in Table 7.2. Again, the bias measured for the Einasto model has a larger dispersion than for the NFW one. In the right panel of Fig. 7.8 we present the $\sigma^2_{b,3\text{ projections}}$ obtained with NFW and Einasto models for each cluster in our sample, showing the correlation between the variances measured with the different models.

We study this scatter to quantify the uncertainty that should be accounted for in observational mass reconstructions, when clusters are only observed in one projection. To truly estimate the projection effect, the dispersion of the masses obtained from the infinite projections of each cluster would be needed. To evaluate the uncertainties introduced in our analysis by using only three projections, we compare to the results obtained from 100 projections for a handful of clusters.

Validation of the projection effect

For 4 different clusters in THE THREE HUNDRED simulation we produced 100 κ-maps along random projections. We chose one cluster per snapshot, with diverse dynamical states, mostly unrelaxed. The sample is described in Table 7.3, with the dynamical state indicators defined following the definitions in De Luca et al. (2021) [88].

For each map, we followed the NFW and Einasto mass reconstruction procedure described in Sect. 7.3.1, and estimated the M^κ_{500} and the associated biases. The mean bias and variance for the 100 projections, for the 3 main axes and for the 3 inertia moment axes are summarised in Table 7.4. Although considering the principal axes of the clusters regarding their moments of inertia is a way to account for the whole dispersion due to projection, it gives systematically overestimated scatter values with respect to the dispersion obtained from 100 projections. Instead, for the projections along the 3 main (that is, random) axes the measured dispersion can be both over and underestimated. Hence, for the analysis with the full sample of clusters we decided to remove the 0_pr_axes, 1_pr_axes and 2_pr_axes projections.

7.4.3 Intrinsic projection effect: $\sigma^2_{b,\text{intrinsic proj}}$

For both the NFW and Einasto models, there is a contribution to $\sigma^2_{b,3\text{ projections}}$ that is not explained by the uncertainties on the fitting procedure. We consider that this is due to the real *intrinsic projection effect* presented in Eq. 7.12. From the difference between the mean (and also between the median) values of $\sigma^2_{b,3\text{ projections}}$ and $\sigma^2_{b,\text{fit}}$, the intrinsic projection effect is of the order of $\sim 0.014 - 0.020$. This corresponds to about $12 - 14\%$ error on the mass bias, and then on M_{500}. We stress that this is true for both the NFW and Einasto models, which is comforting since we are looking for an intrinsic effect that should depend only on the clusters themselves. We also note that the values for $\sigma^2_{b,\text{intrinsic proj}}$ obtained from the differences of the mean and the median of $\sigma^2_{b,3\text{ projections}}$ and $\sigma^2_{b,\text{fit}}$ are remarkably close, indicating that the $\sigma^2_{b,\text{intrinsic proj}}$ distribution is well approximated by a Gaussian.

Alternative estimation of the intrinsic projection effect: model independent

We are also interested in quantifying the contribution of $\sigma^2_{b,\text{intrinsic proj}}$ without being affected by modelling effects. For this purpose, we take a different approach and infer masses directly from the projected convergence maps. By integrating the Σ-maps up to the true θ_{500} we compute directly the total mass of clusters from cylindrical integration, $M^{\kappa,\text{cyl}}_{500}$, where $\tan(\theta_{500}) = R_{500}/\mathcal{D}_\text{A}$, with R_{500} the true radius of the cluster and $\mathcal{D}_\text{A}$ the angular diameter distance at the cluster redshift. For each cluster we have three different $M^{\kappa,\text{cyl}}_{500}$ and $b^{\kappa-\text{map}}$, one per projected map. The grey histogram in Fig. 7.11 shows the variance of the mass bias per cluster c for all the clusters in our sample obtained from

$$(\sigma^{\kappa-\text{map}}_{b,\text{intrinsic proj}})^2_c = \frac{1}{N_\text{projections}} \sum_{j=1}^{N_\text{projections}} (b^{\kappa-\text{map}}_{j,c} - < b^{\kappa-\text{map}} >_c)^2. \tag{7.14}$$

On average, the projection effect when integrating the total mass at a fixed aperture is of the order of $(\sigma^{\kappa-\text{map}}_{b,\text{intrinsic proj}})^2 \sim 0.01$. Therefore, uncertainties of about 10% on the mass. The projection effect computed in this way is close, but not enough to fully explain the $12 - 14\%$ uncertainties obtained from the $\sigma^2_{b,3\text{ projections}} - \sigma^2_{b,\text{fit}}$ difference.

An additional term could explain the difference: while the masses used to compute $\sigma^2_{b,3\text{ projections}}$ are estimated at different radii (each M^κ_{500} measured at the corresponding R^κ_{500}), here all the $M^{\kappa,\text{cyl}}_{500}$ for $(\sigma^{\kappa-\text{map}}_{b,\text{intrinsic proj}})^2$ are measured at fixed θ_{500} per cluster. Therefore $(\sigma^{\kappa-\text{map}}_{b,\text{intrinsic proj}})^2$ needs a corrective term to be fully comparable to $\sigma^2_{b,\text{intrinsic proj}}$. We quantified this effect based on mock mass density profiles of galaxy clusters with a large variety of shapes and masses.

Scatter from spherical mass estimates and from projected masses within a fixed aperture

We used simulated profiles following the NFW (parametrised as in Eq. 1.19), gNFW, tNFW and Hernquist models. We define the gNFW mass density profile (equally defined for the pressure in Eq. 3.5) as

$$\rho_\text{gNFW}(r) = \frac{\rho_s}{\left(\frac{r}{r_s}\right)^\gamma \left(1 + \left(\frac{r}{r_s}\right)^\alpha\right)^{\frac{\beta-\gamma}{\alpha}}}, \tag{7.15}$$

with $\alpha = 3$, $r_s = R_\Delta/c_\Delta$ and:

$$\rho_s = \frac{c^3_\Delta \Delta \rho_\text{crit}(-3+\gamma)}{-3(c^3_\Delta)^{1-\gamma/3}\ {}_2F_1((\beta-\gamma)/3, 1-\gamma/3, 2-\gamma/3, -c^3_\Delta)}. \tag{7.16}$$

Here ${}_2F_1$ is a Gaussian hypergeometric function. The tNFW is given by

$$\rho_\text{tNFW}(r) = \frac{\rho_s}{r/r_s(1+r/r_s)^2}\left(\frac{\tau^2}{\tau^2 + (r/r_s)^2}\right)^\eta, \tag{7.17}$$

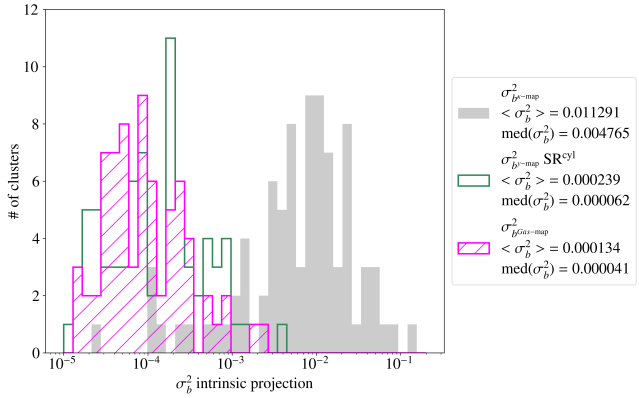

Figure 7.11: Variance of the mass bias estimated from maps. The grey histogram is obtained from the integration of convergence maps, i.e., $M_{500}^{\kappa,\mathrm{cyl}}$. The magenta histogram corresponds to the variance for gas masses ($M_{500}^{\mathrm{Gas,cyl}}$) estimated from gas mass maps. The empty green histogram shows the dispersion of the M_{500}^{cyl} after conversion from the Y_{500}^{cyl} measured from y-maps, using the scaling relation in Fig. 7.17.

with $\eta = 1$, $r_s = R_\Delta/c_\Delta$ and:

$$\rho_s = \frac{c_\Delta^3 \Delta \rho_{\mathrm{crit}}}{3I(c_\Delta)}, \tag{7.18}$$

where,

$$\begin{aligned} I(c_\Delta) = \tau^2 \frac{-1\left[2(1+\tau^2) - (-1+\tau^2)\ln\left(\tau^2\right)\right]}{2(1+\tau^2)^2} + \\ \tau^2 \frac{\frac{2(1+\tau^2)}{(1+c_\Delta)} + 4\tau \arctan(c_\Delta/\tau)}{2(1+\tau^2)^2} + \\ \tau^2 \frac{(-1+\tau^2)\left[2\ln(1+c_\Delta) - \ln\left(c_\Delta^2+\tau^2\right)\right]}{2(1+\tau^2)^2}. \end{aligned} \tag{7.19}$$

The Hernquist mass density profile is defined as

$$\rho_{\mathrm{Hernquist}}(r) = \frac{\rho_s}{\frac{r}{r_s}\left(1+\frac{r}{r_s}\right)^3}, \tag{7.20}$$

with $r_s = R_\Delta/c_\Delta$ and:

$$\rho_s = \frac{c_\Delta \Delta \rho_{\mathrm{crit}} 2(1+c_\Delta)^2}{3}. \tag{7.21}$$

We produced profiles with a wide variety of parameters for 5 different initial M_{500} values between 3×10^{14} $\mathrm{M}_\odot$ and 11×10^{14} $\mathrm{M}_\odot$ and for the four different redshifts in our twin samples ($z = [0.490, 0.592, 0.700, 0.817]$). For NFW and Hernquist models we varied c_{500} from 1 to 6. For gNFW and tNFW we fixed $c_{500} = 4$, and varied $\beta = 3-6$ and $\gamma = 0.4-1$ for gNFW, and $\tau = 0.2-4$ for tNFW. All the considered projected mass density profiles are shown in the left panel in Fig. 7.12 to demonstrate the variety of the analysed density shapes.

To mimic a departure from the true mass, for each profile with M_{500} we estimated a distribution of new profiles with masses that vary by −25% to 25% from the true M_{500}, $M_{500}^{\mathrm{new\ sph}}$ (based on an average $\sigma^2_{b,3\ \mathrm{projections}}$

measured in the mass reconstructions). For each of the new profiles, we integrated the projected density up to the original θ_{500} to obtain $M_{500}^{\text{new cyl}}$. Comparing the new $M_{500}^{\text{new sph}}$ and $M_{500}^{\text{new cyl}}$ to the original M_{500} we got the spherical and cylindrical biases. From the distribution of biased masses, we took randomly trios, to simulate the 3 random projections, and estimated their variance: $\sigma^2_{b^{\text{sph}}}$ is the variance of three biased spherical masses, and with their corresponding cylindrically integrated masses we get $\sigma^2_{b^{\text{cyl}}}$.

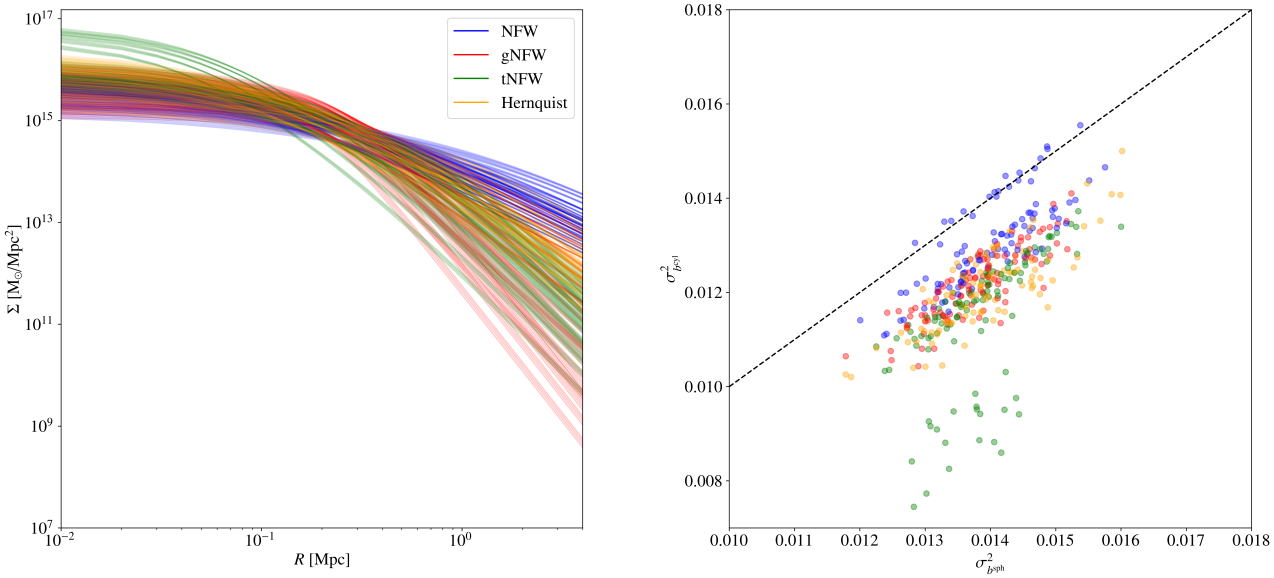

Figure 7.12: Projected mass density profiles used to quantify the difference in scatter for spherically and cylindrically integrated masses (left). The variance of cylindrically integrated masses with respect to spherically integrated masses (right). The black dashed line corresponds to $\sigma^2_{b^{\text{sph}}} = \sigma^2_{b^{\text{cyl}}}$. In blue NFW, in red gNFW, in green tNFW and in orange Hernquist models.

In the right panel in Fig. 7.12 we present the relation between the mean $\sigma^2_{b^{\text{sph}}}$ and $\sigma^2_{b^{\text{cyl}}}$ for each mass, redshift and profile shape considered. Same colours as in Fig. 7.12 are used to refer to each density profile model. The blue points close to the black one-to-one line correspond all to NFW models with a concentration of $c_{500} = 1$.

As expected, the figure shows that the dispersion of cylindrically integrated masses at a given aperture tends to be smaller than spherical integrations up to the corresponding radius in each case. This additional variance is of the order of ~ 0.001 to 0.01, so 1 to 10% of the mass, depending on the mass, redshift and shape of the density profile of the cluster. We note that additional differences could appear when integrating spherically against cylindrically, related, for example, to the presence of substructures.

Therefore, both from a model dependent and a model independent approach we obtain compatible values for $\sigma^2_{b,\text{intrinsic proj}}$. We conclude that when deriving cluster masses from observables tracing the total mass (for instance, the lensing effect), the intrinsic effect of the projection introduces an error in the M_{500} estimates of 10% to 14%. These values could probably vary if the κ-maps are created by integrating the particles in the simulation within a different depth.

7.4.4 Total: $\sigma^2_{b,\text{tot}}$

Finally, we quantify the total variance of the bias along the sample and the scatter from cluster to cluster. We compute, following Eq. 7.9, the total variance of the bias in our sample by accounting for all the clusters, with all the projections and their fit uncertainties. Following Eq. 7.10, we obtain the excess with respect to the projection and fitting effects. All the values are given in Table 7.2.

The total dispersion is significantly larger than the average projection effect. This could be due to some clusters with a very important projection effect (right panel in Fig. 7.8) that might be affecting significantly $\sigma^2_{b,\mathrm{tot}}$. But it could also originate from the scatter of the mean bias values per cluster. We compute first the mean bias per cluster c accounting for the masses reconstructed from all the chains for the three projections convergence maps: $< b^\kappa >_c = < (M_{500} - M^\kappa_{500})/M_{500} >$. Then, we quantify how different the mean biases for all the clusters are in the sample. We define the variance of the mean biases, $\sigma^2_{b,\mathrm{mean}}$, as:

$$\sigma^2_{b,\mathrm{mean}} = \frac{1}{N_{\mathrm{clusters}}} \sum_{j=1}^{N_{\mathrm{clusters}}} (< b^\kappa >_j - \langle < b^\kappa >_c \rangle)^2, \tag{7.22}$$

where $\langle < b^\kappa >_c \rangle$ is the mean over the mean biases of all the clusters. Results are shown in Table 7.2.

The missing dispersion in $\sigma^2_{b,\mathrm{tot}}$ seems to be well explained by the dispersion of the mean bias across clusters, $\sigma^2_{b,\mathrm{cluster-to-cluster}} \sim \sigma^2_{b,\mathrm{mean}}$. We notice that it is a model dependent effect, since results for NFW and Einasto differ significantly, NFW results being more scattered with respect to $\langle < b^\kappa >_c \rangle$. This difference could be due to the fact that the NFW reconstructions fail to describe the mass of some of the clusters and compared to Einasto ones the NFW fitting uncertainties are not large enough to account for it.

7.4.5 Intrinsic scatter: $\sigma^2_{b,\mathrm{cluster-to-cluster}}$

The dispersion of the bias from cluster to cluster can be caused by multiple effects. We investigate here the impact of the limitations of our data set and of the mass, redshift and dynamical state of the clusters.

Limitations of the data set

We only consider 3 projections per cluster and the mean bias obtained from these 3 may not be a good representation of the true mean bias. We test the impact of this effect using the four clusters for which we have 100 projections (Table 7.3). For each cluster we calculate the mean bias accounting for the 100 projections. Values are shown as vertical dashed lines in Fig. 7.13. At the same time, we select randomly three projections out of the 100 and compute the mean for those trios. The histograms in Fig. 7.13 show the results for 100 realisations. They illustrate that the mean bias $< b^\kappa >_c$ estimated from 3 random projections can in some cases be significantly different from the true one. Although histograms are centred in the mean bias of the 100 projections, their variance is of the order of ~ 0.01. The latter also contributes to $\sigma^2_{b,\mathrm{cluster-to-cluster}}$ or $\sigma^2_{b,\mathrm{mean}}$.

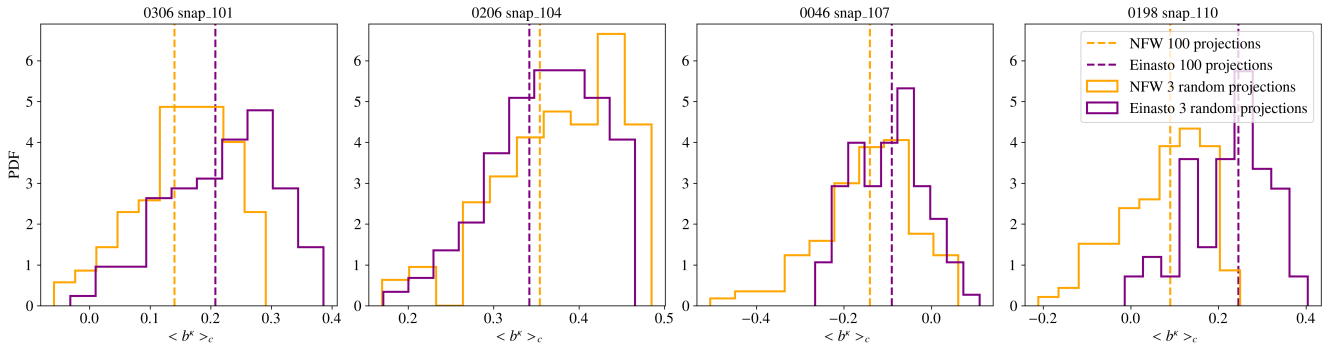

Figure 7.13: Mean bias per cluster. The vertical lines show the mean bias when using 100 projections to reconstruct the mass. The histograms are obtained from the mean bias computed by taking randomly 3 projections out of the 100 available 100 times.

Impact of mass and redshift

There could be also a correlation between the intrinsic properties of clusters (mass, redshift, etc.) and the measured biases. To investigate these effects we separate our sample in subsamples. We choose a binning close

# of clusters	$z = 0.490$	$z = 0.592$	$z = 0.700$	$z = 0.817$
$M_{500}/10^{14}\mathrm{M}_\odot < 4$	3	5	10	2
$4 \leq M_{500}/10^{14}\mathrm{M}_\odot < 6$	13	10	15	8
$6 \leq M_{500}/10^{14}\mathrm{M}_\odot < 8$	14	6	7	6
$8 \leq M_{500}/10^{14}\mathrm{M}_\odot < 10$	12	0	4	1
$10 \leq M_{500}/10^{14}\mathrm{M}_\odot$	3	2	1	0

Table 7.5: Classification of twin samples' clusters in mass and redshift bins. We give the number of clusters per bin.

to the one used for the NIKA2 LPSZ (Sect. 3.1): four bins in redshift (one per snapshot) and five bins in mass (in the NIKA2 LPSZ only two bins in redshift are considered, but with the objective of observing any evolution, we choose to distinguish four). The five bins in mass are defined in Table 7.5, where we also report the number of clusters in each mass and redshift bin.

We show in Fig. 7.14 the evolution of the mean bias with redshift and mass for NFW and Einasto mass reconstructions. A slight evolution of the bias with redshift is observed for NFW results, which is less evident for Einasto. A similar trend is confirmed in Euclid Collaboration et al. (2023) [169] for the bias of M_{200} masses with redshift. In that work, they claim that the evolution is due to the low weak lensing signal-to-noise at high redshift, but this argument does not explain our results, since we have not modified the signal-to-noise ratio depending on the redshift and the available number density of background sources. In the right panel in Fig. 7.14 we observe that in our case and for the Einasto model the bias increases with the true M_{500}, contrary to the evolution with M_{200} obtained in Euclid Collaboration et al. (2023) [169]. We note, in any case, that our results are compatible with no evolution with redshift and mass.

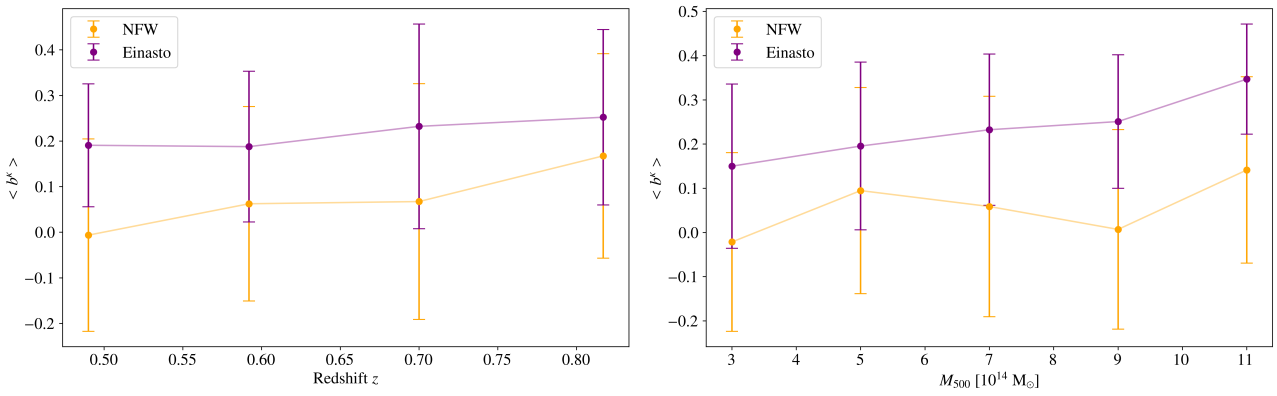

Figure 7.14: Bias for clusters in different redshift (left) and mass (right) bins. We give the mean value and the $\sigma_{b,\mathrm{mean}}$ scatter for the mean bias of clusters in each bin. Results for NFW and Einasto models are shown in orange and purple, respectively, with a line as a guide to the eye.

Impact of the dynamical state

The dynamical state of clusters can also be related to the bias of masses reconstructed from projected maps and to their dispersion. To classify the clusters in our sample according to their dynamical state, we use the f_s and Δ_r indicators at R_{200} (and R_{500}). They correspond, respectively, to the ratio between the sub-halo masses and the cluster mass within R_{200} (R_{500}) aperture, and, to the offset between the centre of mass of the cluster and the maximum density peak position, normalised by R_{200} (R_{500}). Following the definitions in De Luca et al. (2021) [88], clusters are relaxed (disturbed) if $f_s < 0.1$ and $\Delta_r < 0.1$ ($f_s > 0.1$ and $\Delta_r > 0.1$). Otherwise, we consider them in an intermediate dynamical state.

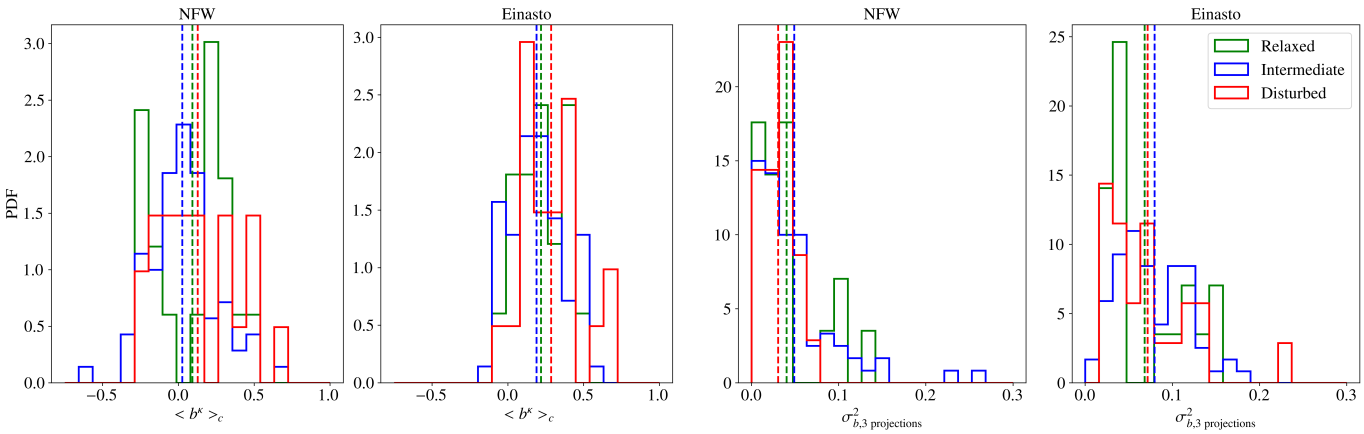

Figure 7.15: Bias dependence on the dynamical state of clusters within R_{200}. Left: distributions of the mean bias per cluster for relaxed (green), intermediate (blue) and disturbed (red) clusters. We show the bias from NFW (left) and Einasto (right) reconstructions. Right: distributions of the variance of the bias per cluster accounting for three projections. Clusters are classified according to their dynamical state and results for NFW (left) and Einasto (right) are shown. The vertical lines show the mean values of the distributions.

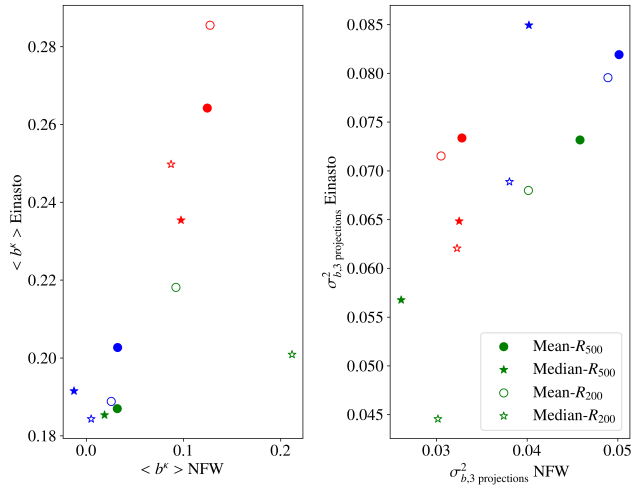

Figure 7.16: Summary of bias properties depending on the dynamical state of clusters within R_{200} (empty) and R_{500} (filled). Left: mean (circle) and median (star) of the mean biases of each type of cluster. Right: mean and median of the $\sigma^2_{b,\ 3\ \mathrm{projections}}$ for all the clusters of each type. We show in green, blue and red the results for relaxed, intermediate and disturbed clusters, respectively.

In the left panels in Fig. 7.15 we present the distribution of the mean bias per cluster independently for relaxed (green), intermediate (blue) and disturbed (red) clusters, classified with the indicators at R_{200}. The variance of these mean biases from cluster to cluster is slightly larger for the disturbed sample ($\sigma^2_{b,\,\mathrm{mean}}$ = 0.0679 and 0.0401 for NFW and Einasto, respectively) than for the relaxed one ($\sigma^2_{b,\,\mathrm{mean}}$ = 0.0592 for NFW and 0.0264 for Einasto). On average, relaxed clusters are less biased than disturbed ones. Clusters that are classified as intermediate have unpredictable behaviour.

In the right panels in Fig. 7.15 we show the variance of the bias per cluster as computed from the three projections. Although we would expect to detect the departure from sphericity in the measurement of $\sigma^2_{b,3\ \mathrm{projections}}$, from these results we observe no difference between relaxed and disturbed clusters, and the three subsamples (relaxed, intermediate and disturbed) give scatter values that are compatible with those of the full sample.

The classification of clusters changes if we use the dynamical state indicators at R_{500}. In Fig. 7.16 we summarise the mean and median values obtained from the distributions in Fig. 7.15 for dynamical states of clusters defined within R_{500} and R_{200}. From this figure, the bias and scatter of masses reconstructed with our method seem weakly correlated to the relaxation status of the galaxy clusters.

In Euclid Collaboration et al. (2023) [169] authors used stronger constraints to classify clusters as relaxed: they considered relaxed systems if $f_s < 0.1$ and $\Delta_r < 0.05$[24] or if $f_s < 0.1$, $\Delta_r < 0.04$ and $0.85 < \eta < 1.15$ (with η the virial ratio, as in Cui et al. (2018) [234]), all within R_{200}, and unrelaxed otherwise. Following this classification, they concluded that for unrelaxed clusters the fitting procedure is less efficient than for relaxed ones, but that the mean bias of both types of clusters is completely consistent with that of the full sample.

7.4.6 Summary

In this section, we have quantified the different contributions to the dispersion of mass estimates of clusters reconstructed from convergence maps. We find that M_{500} cluster masses reconstructed from convergence maps have an uncertainty of the order of 20% that corresponds to uncertainties in the fitting procedure and varies with the chosen model. In addition, a 10 to 14% uncertainty should be added to account for intrinsic projection effects. Regarding the variation of the bias along the cluster sample, which is of the order of 20% ($\sigma^2_{b,\mathrm{cluster-to-cluster}}$ = 0.06 for NFW and 0.04 for Einasto), we conclude that it is probably overestimated due to the limited number of projections per cluster available. When we try to correlate the bias and its dispersion to intrinsic characteristics of clusters, we find that redshift, mass and dynamical state appear weakly correlated to the bias. Additional effects that we have not considered in this analysis, such as the presence of substructures along the line-of-sight, could also be at the origin of the cluster-to-cluster scatter in observations.

7.5 Comparison to gas observables

As investigated in several works (e.g., Meneghetti et al. (2010) [390], Rasia et al. (2012) [347]), the spatial distribution of the gas in the ICM does not follow necessarily the same distribution as the rest of the matter. This implies that the above conclusions may not apply to masses reconstructed from gas observables. In this section we compare the projection effect obtained for total matter observables to the effect for gas observables.

To measure the impact of the projection when estimating masses from gas maps we take two approaches. The most direct option consists in measuring the mass of the gas from the gas mass maps (Sect. 7.1.2). We compute $M^{\mathrm{Gas,cyl}}_{500}$ by integrating the gas mass maps up to θ_{500}. The distribution of dispersions for the three masses calculated from the different projections is shown for all the clusters in the magenta histogram in Fig. 7.11. These results reflect the impact of the orientation as regards the arrangement of the gas in the cluster, but we note that M^{Gas} is not an estimate of the total mass.

A less direct option consists in estimating the mass from the integrated Y_{500} signal in the y-maps by applying a $Y_{500} - M_{500}$ scaling relation. First, the signal in the y-maps is integrated up to the true θ_{500} for each cluster,

[24] Δ_r is named x_{off} in Euclid Collaboration et al. (2023) [169]

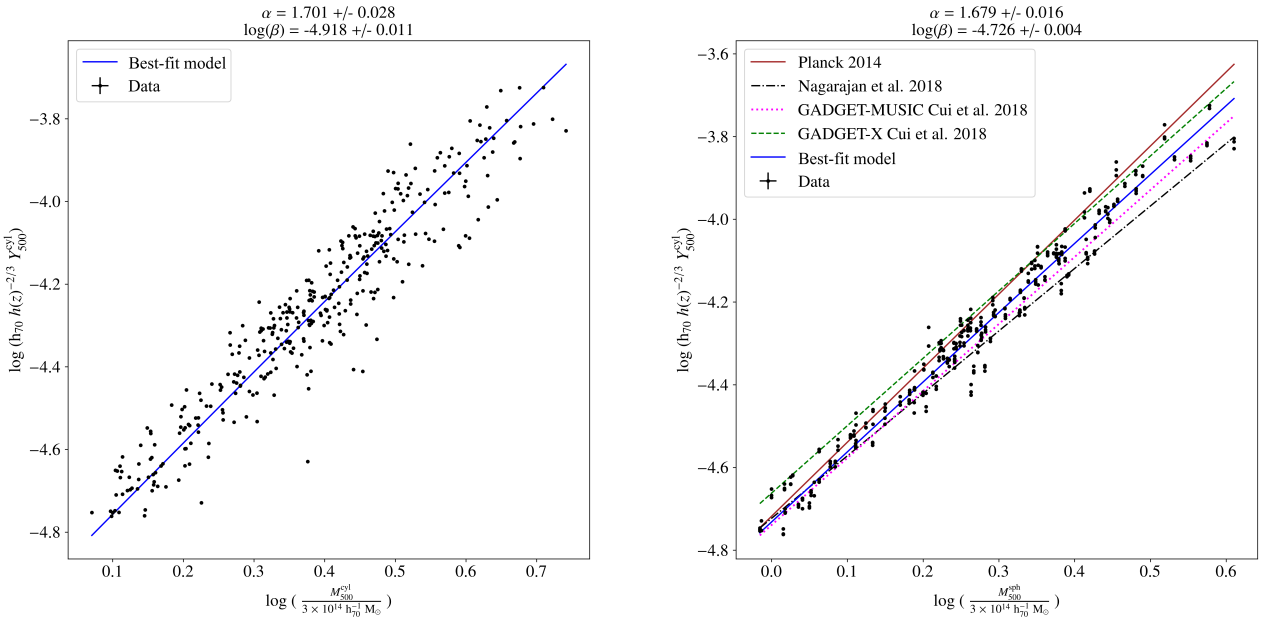

Figure 7.17: $Y_{500} - M_{500}$ scaling relations for cylindrically integrated SZ signal with respect to spherically (right) and cylindrically (left) integrated masses. Black dots correspond to the values per cluster in our sample, while the blue line shows the best-fit relation. In the right panel the solid brown line shows the result from Planck Collaboration et al. (2014) [5], and the black dash-dotted is from Nagarajan et al. (2019) [396]. The pink dotted and green dashed relations are the results of Cui et al. (2018) [234] for the `GADGET-MUSIC` and `GADGET-X` simulations (of all clusters at $z = 0$).

which gives the cylindrically integrated Compton-y parameter $Y_{500}^{\rm cyl}$. We then convert the $Y_{500}^{\rm cyl}$ in M_{500} assuming a given scaling relation.

There are several scaling relations in the literature that relate Y_{500} to M_{500} (e.g., A10 and Cui et al. (2018) [234]). However, most of them look for a relation between the observed $Y_{500}^{\rm cyl}$ and the spherical mass $M_{500}^{\rm sph}$. In our case we build a $Y_{500}^{\rm cyl} - M_{500}^{\kappa,\rm cyl}$ scaling relation for our sample that will allow us to compare cylindrically integrated masses.

Building the $Y_{500} - M_{500}$ scaling relation

We construct our own scaling relation following the parametrisation in Eq. 16 in Arnaud et al. (2010) [70]:

$$h(z)^{-2/3}\ Y_{500} = \beta \left[\frac{M_{500}}{3 \times 10^{14}\ \mathrm{h}_{70}^{-1}\ \mathrm{M}_{\odot}} \right]^{\alpha} \mathrm{h}_{70}^{-1} \tag{7.23}$$

where Y_{500} is in Mpc^2 and M_{500} in $\mathrm{M}_{\odot}$. Here $h(z) = E(z)$ is the ratio of the Hubble constant at redshift z to its present value, and, h_{70} the Hubble constant in units of 70 km/s/Mpc.

We build two scaling relations that relate the cylindrical Y_{500} to the spherical and cylindrical M_{500} mass. The spherical quantities are computed from the ICM profiles: $M_{500}^{\rm sph}$ is obtained by evaluating the mass profile at R_{500}, i.e. the true M_{500} throughout this chapter. The cylindrical quantities $M_{500}^{\rm cyl}$ and $Y_{500}^{\rm cyl}$ are calculated by integrating the signal within θ_{500} in the κ- and y-maps. In each case, we fit the data to the model represented by Eq. 7.23 using the orthogonal BCES method. Uncertainties on the best-fit parameters are estimated from 100000 bootstrap resamples of the data. We show the SRs in Fig. 7.17, as well as the best-fit parameters (top legends in the figure). The slopes of both relations are consistent, but since the cylindrically integrated masses are larger than spherically integrated ones, the intercepts are not compatible.

We compare, as in Fig. 10 in Cui et al. (2018) [234], the $Y_{500}^{\rm cyl} - M_{500}^{\rm sph}$ relation to results in the literature.

In Cui et al. (2018) [234] authors computed the scaling relation using all THE THREE HUNDRED clusters at redshift $z = 0$, for both GADGET-X and GADGET-MUSIC flavours. The SR obtained from our sample has a lower normalisation and slightly steeper slope than the results obtained with GADGET-X simulations in Cui et al. (2018) [234]. The differences may be due to both the considered cluster sample and the redshift range. The GADGET-MUSIC scaling relation from Cui et al. (2018) [234] has an even smaller intercept value, showing the impact of the hydrodynamical model on the simulation. In the same figure, we also compare the results to the SRs obtained from observations in Planck Collaboration et al. (2014) [5] and Nagarajan et al. (2019) [396]. Our SR lies between both observational results, with a flatter slope than Planck Collaboration et al. (2014) [5] and steeper than Nagarajan et al. (2019) [396].

By making use of the SR in the left panel in Fig. 7.17, we compute the $M_{500}^{\rm cyl}$ for each $Y_{500}^{\rm cyl}$. The dispersion of the recovered masses for different projections of a single cluster allows us to quantify, to first order, the intrinsic projection effect. The empty green histogram in Fig. 7.11 shows the distribution of the dispersion of the biases estimated for all clusters from y-maps.

We observe that both approaches (from gas mass and y-maps) suggest an intrinsic projection effect of $\sigma^2_{b,\text{intrinsic proj}} \sim 10^{-4}$ (a few percent scatter on M_{500}) for the gas, meaning that for the considered data and within the same θ_{500} the gas is an order of magnitude less dispersed (i.e., more spherically distributed) than the dark matter. This is in agreement with previous works [48, 290, 347, 389, 390] that also indicate that mass reconstructions from gas observables are less scattered than those from dark matter observables due to the difference in the spatial distribution of the matter.

From the comparison between the bias of cylindrically integrated masses from the κ-maps and the bias of masses obtained from y-maps (with the $Y_{500}^{\rm cyl} - M_{500}^{\kappa,\rm cyl}$ scaling relation) we obtain that their correlation is weak, with a Pearson correlation coefficient of 0.28. The correlation is stronger between the bias dispersions (i.e., σ_b) measured from the three random projections in κ- and y-maps: r = 0.55.

7.6 Conclusions

In this chapter we have studied the bias of galaxy cluster mass estimates reconstructed by fitting three dimensional NFW and Einasto density models to the projected mass density profiles obtained from convergence maps. We have performed the analysis making use of THE THREE HUNDRED GADGET-X hydrodynamical simulated clusters, selected to be representative of the NIKA2 LPSZ sample: THE THREE HUNDRED-NIKA2 LPSZ twin samples. All the results shown here were obtained with the 122 clusters of the three twin samples combined (Sect. 7.1.1). We checked that conclusions do not vary from one twin sample to another.

We decided to fit the mass density profiles accounting for all the radial ranges available. In doing so, we have re-demonstrated the importance of the considered radii and the different behaviour of the models with respect to this. Although the flexibility of the Einasto model permits fitting the projected density profiles by accounting for the different slopes, in our case the fit is driven by the inner and outer bins and it fails to describe the mass at $\sim R_{500}$. The opposite happens with the NFW model. These results are related to the uncertainties of the projected density profiles, that in this analysis were computed from the dispersion in each radial bin. Some works in the literature [379] choose ad hoc the radial range and conclude that, as expected, models with more parameters fit better the density profile and therefore, give lower biases. By contrast, in this study, we have shown that a projected mass density fit that is overall good does not give necessarily a good M_{500} estimate.

But even if NFW and Einasto mass reconstructions are differently biased, we have observed that both the mean bias and the scatter of the recovered masses are correlated for the two models. This could mean that, despite important modelling effects, individual relative cluster properties are preserved in both analyses. Quantitatively, the NFW M_{500} masses are biased by 3%, which is in agreement with the lowest bias estimates from previous works [379, 390]. It is not the case for our Einasto reconstructions, which present a larger bias

(20%) because the procedure is ill-fitting the Σ-profiles at $\sim R_{500}$.

Regarding the uncertainties associated with the mass estimates, we have considered different contributions. With our approach, the uncertainty of the density profile fit to the convergence map introduces a mean uncertainty on the mass of 15% and 25% for the NFW and Einasto profiles, respectively. An additional contribution comes from projection effects and we estimate that about 10 to 14% of dispersion should be considered in lensing mass estimates. Such a result matches the conclusions in the review from Pratt et al. (2019) [48]. Accounting for the projection effect together with the uncertainties on the fitting, the scatter is of the order of $\sim 20 - 25\%$. We, therefore, confirm the values in Becker and Kravtsov (2011) [290] and Rasia et al. (2012) [347], the latter being obtained from the fit of tangential shear profiles of simulated clusters.

When accounting for the full sample of THE THREE HUNDRED-NIKA2 LPSZ clusters, there is an excess of dispersion with respect to what corresponds to projection effects. This depends also on the choice of the model. We investigate the origin of such dispersion and we find, firstly, an uncertainty due to the fact that we use only three projections per cluster. Making use of 100 random projections for four clusters, we verify that considering only 3 projections per cluster the mean bias of the three can be scattered about up to 10%.

We tried to correlate the bias of masses reconstructed from convergence maps to intrinsic properties of clusters and we checked the evolution of the mass bias with the true mass and redshift of clusters. Contrary to Euclid Collaboration et al. (2023) [169], our results show a weak tendency of the bias to increase with the cluster mass, which could be related to the important presence of substructures in massive halos [381]. Despite our narrow range in redshift, we also observe a modest evolution of the bias with redshift, as in Giocoli et al. (2012) [381] and Euclid Collaboration et al. (2023) [169].

In addition, we investigated the relation between the dynamical state and reconstructed masses of clusters, concluding that disturbed clusters are slightly more biased than relaxed ones. Regarding the orientation of clusters, we confirm that with our method and for clusters observed elongated along the line-of-sight, the reconstructed masses are overestimated. On the contrary, masses are underestimated if the major axes of clusters are on the plane of the sky. These conclusions are in agreement with the results in Euclid Collaboration et al. (2023) [169], where THE THREE HUNDRED convergence maps are used to create weak lensing observables for the preparation of the *Euclid* mission.

Finally, we also compared how spherical is the spatial distribution of total matter and gas by measuring the dispersion from projection to projection in total mass and gas maps. Within R_{500} the gas is more spherically distributed than the dark matter, which makes mass reconstructions from projected maps less dependent on the orientation of the cluster. This was already known from previous studies [390] and motivated the observation of clusters in X-rays and at millimetre wavelengths. For observational HSE-to-lensing mass biases estimated as in chapters 5 and 6, this would imply that most of the projection scatter is introduced by the lensing mass estimate.

CHAPTER 8

High-resolution observations of the SZ effect with NOEMA

Current galaxy cluster observations with single-dish telescopes are limited at high angular resolution, which prevents from resolving the structures in the core of clusters. As discussed before, at present, the NIKA2 camera at the 30-metre IRAM telescope and MUSTANG2 on the 100-metre Green Bank Telescope offer the best capabilities. As described in chapter 2, NIKA2 maps the sky at 150 GHz and 260 GHz with 17.6″ and 11.1″ FWHM angular resolutions, respectively. MUSTANG2 has a 9″ FWHM beam at 90 GHz. Increasing the resolution is, at the moment, only possible with radio interferometers like ALMA and the NOrthern Extended Millimeter Array (NOEMA). Recent works have demonstrated the power of ALMA observations to do cluster science [47, 183, 397]. Competitive results in the Northern Hemisphere will only be possible if the SZ of clusters can be detected with NOEMA. In this chapter, we present the basics of radio-interferometry and the NOEMA instrument. We then describe the observations of the CL J1226.9+3332 galaxy cluster with NOEMA, the characterisation of the point sources in the field and the detection of the thermal SZ effect.

8.1 Interferometry with NOEMA

Historically, radio interferometers have had an incomparable importance in the detection of clusters in SZ. To name a few, the Very Large Array [398], the Very Small Array [399], the Ryle telescope [400, 401], the Berkeley-Illinois-Maryland Array [402], the Sunyaev-Zeldovich Array [275] or the Arcminute MicroKelvin Interferometer [403], imaged for the first time the SZ of clusters and performed observations of $\sim$ 60 objects (see Carlstrom et al. (2002) [404] for a review on the status of cluster observations through the SZ effect at the beginning of the century). Recently, the capabilities of the ALMA instrument have led to interferometric SZ observations of clusters able to resolve structures and merger shocks in high redshift objects [47, 183, 397] at arcsecond scales.

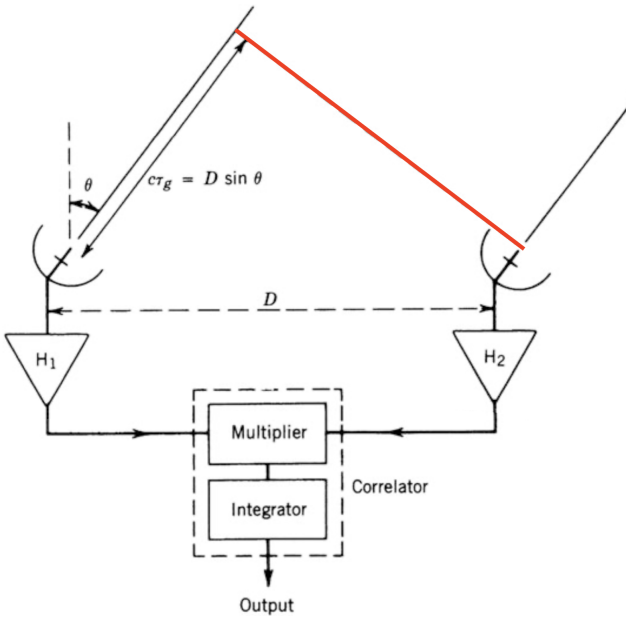

Figure 8.1: A schematic representation of a radio interferometer. The figure shows two antennas, H1 and H2, separated by a physical distance D and the light wavefront arriving from the θ direction. The red line represents the *uv*-plane, parallel to the wavefront and perpendicular to the line-of-sight. The signal received in both telescopes is combined in the correlator. Figure modified from Thompson et al. (2017) [405].

8.1.1 Interferometry

A radio interferometer is composed of a collection of antennas that observe simultaneously the same region of the sky. According to the van Cittert-Zernike theorem, if a source is at large distance from the antennas (compared to the relevant spatial scale of the source distribution), the light emitted by the source has no spatial coherence, and the medium between the source and the antennas is homogeneous, then the spatial correlation of the electric fields measured by two antennas in the plane parallel to the light wavefront is the Fourier transform of the source brightness distribution, $I(\vec{\alpha}, \nu)$, at the sky position $\vec{\alpha}$

$$V(\vec{u}, \nu) =< E(\vec{x_1}, \nu)E(\vec{x_2}, \nu) >= \mathcal{FT}\left[I(\vec{\alpha}, \nu)\right]. \tag{8.1}$$

$E(\vec{x_1}, \nu)$ and $E(\vec{x_2}, \nu)$ are respectively the electric field at the frequency ν measured in the first antenna at the position $\vec{x_1}$ and in the second antenna at the position $\vec{x_2}$, all in the plane parallel to the wavefront. In Eq. 8.1 the average is calculated over time and the correlation will only depend on the spatial frequency $\vec{u} = \vec{x_1} - \vec{x_2} = (u, v)$. $V(\vec{u}, \nu)$ is named *visibility* and it corresponds to the correlation measured by a pair of antennas in the *uv*-plane, that is, in the aforementioned plane parallel to the light wavefront or perpendicular to the line-of-sight. Ideally, if one could measure $V(\vec{u}, \nu)$ for every $\vec{u}$, it would be possible to reconstruct the brightness distribution of the astrophysical object. In Fig. 8.1 we present a schematic representation of the simplest interferometer we can have, with two antennas separated by a distance D and the red line indicating the *uv*-plane. Assuming again that the astrophysical sources we are observing are distant enough to consider that their light reaching the antennas is a planar wavefront, the pair of antennas will measure the signal with a geometrical time delay related to the distance between them: $\tau_g = D \sin\theta / c$, where θ is the direction of the observed source with respect to the zenith. The correlator in Fig. 8.1 will combine the signals from the two antennas, so that the output is directly the visibility $V(\vec{u}, \nu)$.

In practice, the *uv*-plane will never be perfectly and fully covered and, therefore, it will be impossible to recover $I(\vec{\alpha}, \nu)$. Instead, we will recover a *dirty image* of the source, $I_D(\vec{\alpha}, \nu)$, that is defined as the convolution of the image of the source by the *dirty beam*, $B_D(\vec{\alpha}, \nu)$,

$$I_D(\vec{\alpha}, \nu) = I(\vec{\alpha}, \nu) * B_D(\vec{\alpha}, \nu). \tag{8.2}$$

The dirty beam accounts for the incomplete coverage of the *uv*-plane and it can be defined as,

$$B_{\rm D}(\vec{\alpha},\nu) = \int S(\vec{u},\nu) e^{-2\pi i \vec{u}\cdot\vec{x}} {\rm d}\vec{x}, \tag{8.3}$$

with $S(\vec{u},\nu)$ the sampling function tracing the (not-)sampled *uv* positions: $S(\vec{u},\nu) = 1$ at (u,v) points where visibilities are measured, and $S(\vec{u},\nu) = 0$ elsewhere. The better the *uv*-plane is sampled, the better will be the reconstruction of the source brightness (Eq. 8.1).

In addition, the response of each antenna introduces an attenuation of the sky signal, that will depend on the frequency ν. Including the contribution from this *primary beam*, $B_{\rm primary}(\vec{\alpha},\nu)$, we can write each complex visibility as

$$V(\vec{u},\nu) = \int B_{\rm primary}(\vec{\alpha},\nu) I(\vec{\alpha},\nu) e^{2\pi i \vec{u}\cdot\vec{\alpha}} {\rm d}\vec{\alpha}, \tag{8.4}$$

and rewrite Eq. 8.2 as follows

$$I_{\rm D}(\vec{\alpha},\nu) = \left[B_{\rm primary}(\vec{\alpha},\nu) I(\vec{\alpha},\nu)\right] * B_{\rm D}(\vec{\alpha},\nu). \tag{8.5}$$

The angular resolution of an interferometer is related to the distance D between the antennas. For a pair of antennas with a geometric delay of $\tau_{\rm g}$, observing at a frequency ν and pointing towards the θ direction, the phase of the interferometric fringe will be $\phi = 2\pi\nu\tau_{\rm g} = 2\pi\nu D \sin\theta/c$. If, instead, the antennas point towards $\theta + \Delta\theta$ with respect to the zenith, the phase coherence will be $\phi + \Delta\phi = 2\pi\nu D \sin\theta/c + 2\pi\nu D \cos\theta\Delta\theta/c$. The angular resolution at a given frequency ν will be the angular separation of a complete 2π fringe period,

$$\theta_{\rm D} = \frac{\Delta\theta}{2\pi} = \frac{1}{D\cos\theta}\frac{c}{\nu}. \tag{8.6}$$

From this equation, we observe that the resolution improves by increasing the distance between the two antennas. In addition, if we write $\lambda = c/\nu$ we have $\theta_{\rm D} = \lambda/(D\cos\theta)$, which for small θ corresponds to the λ/D used when defining the angular resolution of single-dish telescopes (Sect. 2.1.1). Therefore, in some way, we could think of two antennas separated by a distance D in an interferometer as a single-dish telescope of diameter D. Limited by the size of the dishes, it will be impossible to measure the visibilities at small u and v with an interferometer. Consequently, when performing the Fourier transform of the visibilities (Eq. 8.1) large angular scales will be missing in the image of the source. To overcome this issue some works in the literature combine interferometric data with single-dish observations [406, 407].

8.1.2 NOEMA at Plateau de Bure

The interferometric data used in this chapter were obtained with the NOEMA instrument [408, 409]. NOEMA is located at the Plateau de Bure, in the South of the French Alps at 2560 metres altitude above sea level. Since September 2022, the interferometer comprises 12 antennas that can be moved along a T-shaped track and can reach distances up to 1.7 kilometres. Each antenna is a Cassegrain telescope of 15 metre diameter, limiting the above-mentioned smallest *uv* distance to 15 metres.

Every pair of antennas constitutes a *baseline* and measures a visibility. At a fixed configuration of the interferometer, with N antennas there are simultaneously $N(N-1)/2$ different baselines, and, therefore, the same number of visibilities in different positions of the *uv*-plane. The 12 NOEMA telescopes can be placed in different configurations, depending on the angular resolution and sensitivity required by the scientific case. The noise on each visibility[25] is given by the efficiency, η, the surface of the antenna, A, the system temperature, $T_{\rm sys}$, the integration time per visibility, Δt, and the frequency resolution, $\Delta\nu$,

$$\sigma_V = \frac{\sqrt{2}k_{\rm B}}{\eta A}\frac{T_{\rm sys}}{\sqrt{\Delta t \Delta\nu}}. \tag{8.7}$$

[25] See https://www.iram.fr/IRAMFR/GILDAS/doc/html/noema-intro-html/noema-intro.html for a technical description of NOEMA.

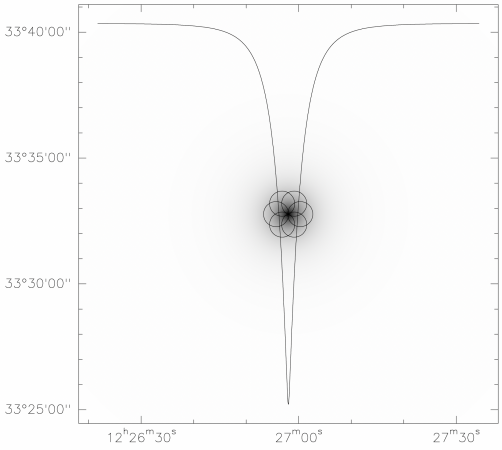

Figure 8.2: Arrangement of the 6 overlapping regions mosaic chosen to observe CL J1226.9+3332 under the D19AB project. We also show the profile and simulated map of the expected SZ emission.

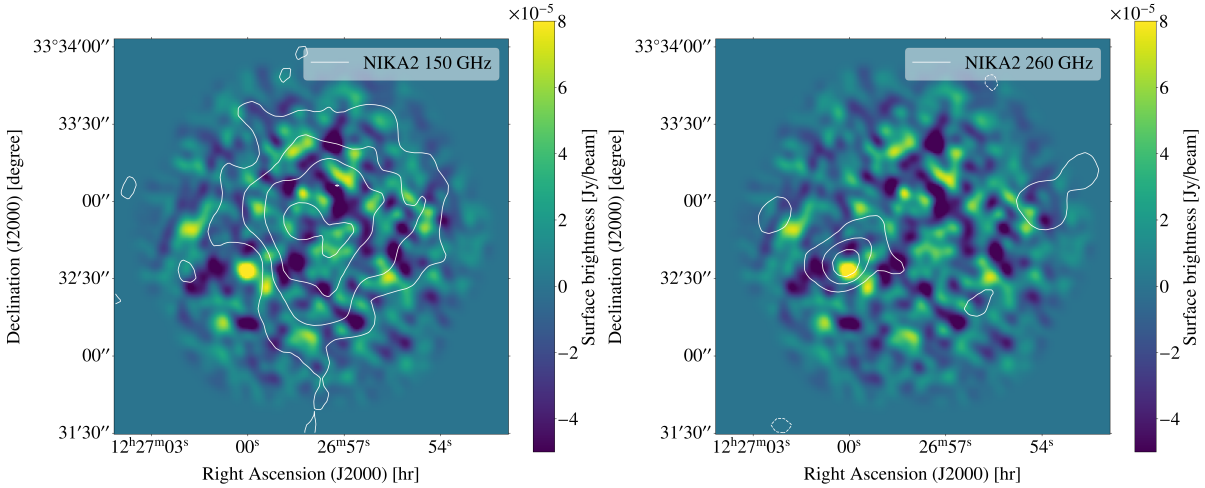

Figure 8.3: Surface brightness map of CL J1226.9+3332 galaxy cluster from the 6-patches mosaic DDT NOEMA observations combined. We also show as white contours the NIKA2 SZ map at 150 GHz in the left panel and at 260 GHz in the right panel.

The signal measured by each antenna is transmitted to the central building, where the PolyFiX correlator processes the data. NOEMA heterodyne receivers can observe from 70 to 380 GHz. Each antenna is equipped with two sideband receivers, the lower (LSB) and the upper sideband (USB) receivers, that cover a $\sim$ 7.7 GHz bandwidth each.

Observations are carried out by the IRAM staff at the Plateau de Bure. Calibrated data containing the visibilities and the related uncertainties in surface brightness units are supplied.

8.2 Observations of the CL J1226.9+3332 galaxy cluster

Aiming for the first SZ detection with NOEMA, the CL J1226.9+3332 galaxy cluster was thought to be a suitable target. As presented in Sect. 4.1, this cluster has been widely observed and studied at different wavelengths. It is the highest redshift cluster of the LPSZ and, therefore, one of the most compact. In addition, it is a hot and massive cluster, which ensures a strong thermal SZ signal. We know from previous observations that the SZ signal of the cluster is contaminated by point sources in the field and that, most probably, the core of the cluster is disturbed. All of that leads to an interesting scientific case to be investigated at high angular resolution.

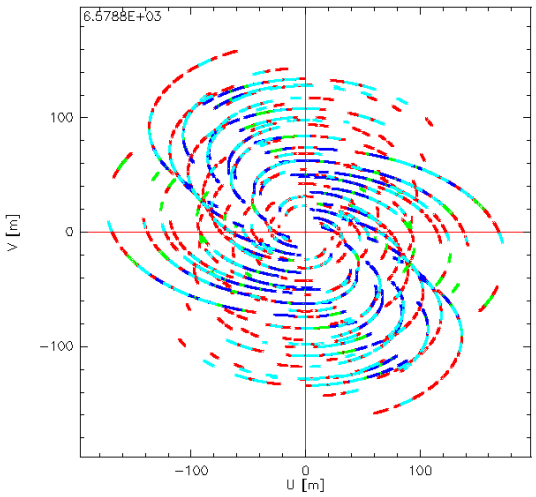

Figure 8.4: Coverage of the *uv*-plane for the lower sideband in the NOEMA single-field observations of CL J1226.9+3332. Different colours correspond to different tracks.

The CL J1226.9+3332 galaxy cluster was first observed with NOEMA on Director's Discretionary Time (DDT) under the proof-of-concept project D19AB (PI: J. F. Macías-Pérez and F. Ruppin). Observations were carried out in a 9-antenna compact configuration in the 72 – 96 GHz frequency range, considering a mosaic of 6 overlapping regions (shown in Fig. 8.2) and a total on-source integration time of 9.5 hours. Although two point sources were identified in the field, sensitivity was not enough to detect the SZ effect of the cluster. We show in Fig. 8.3 the combined NOEMA map from the 6-patches mosaic DDT observations. The white contours indicate the S/N levels from the NIKA2 SZ map (Fig. 4.3) at 150 GHz (left) and 260 GHz (right). The bright source to the south-east of the centre is in agreement with the NIKA2 260 GHz detection, also known as PS1 from Sect. 4.2.2.

In 2022 we requested 27 hours of observation (15.6 hours on source) targeting the core of CL J1226.9+3332 in single-field mapping (proposal S22BU, PI: M. Muñoz-Echeverría). We chose the 10D configuration of the interferometer, which is the compact configuration, best suited for maximising sensitivity at the expense of a lower angular resolution. Given the weak and extended nature of the SZ signal, this is thought to be the most appropriate observing mode for clusters. We requested a 5.2 μJy/beam sensitivity, with the low and upper sidebands covering $\sim$ 70 – 78 GHz and $\sim$ 86 – 94 GHz frequency ranges, respectively. At the time of writing this thesis, the observations are ongoing and we are now at half of the requested sensitivity. The results presented in this chapter have been obtained with the single-field data that we have currently on hand. In Fig. 8.4 we show the positions in u and v of the measurements performed by the NOEMA interferometer during the observations of the CL J1226.9+3332 galaxy cluster for the lower sideband. Each colour corresponds to an observing session. A better coverage is expected when observations will be completed.

By using the `GILDAS`[26] tools, we converted the calibrated *uv* visibilities provided by IRAM into image space maps (by reversing Eq. 8.1). The software gave us a spectral cube of dirty images for the observed region, with a 20 MHz spectral resolution.

8.2.1 Point sources in CL J1226.9+3332

The high angular resolution of NOEMA can be exploited to characterise the point sources in the field of the cluster. As we have seen in chapters 3 and 4, the impact of the sources on the SZ of clusters has to be accounted for, in particular, if the sources lie close to the centre of the cluster [308]. Previous observations presented in chapter 4 have shown that several submillimetre and radio galaxies are present in the field of CL J1226.9+3332.

From the spectral inspection of the NOEMA dirty maps, we identified a source with an emission line centred

[26] `https://www.iram.fr/IRAMFR/GILDAS/`

Table 8.1: Observing frequency (in MHz) of different transitions at different redshifts. The first row indicates the redshift of the galaxy assuming that the emission line at 70.6 GHz corresponds to each of the transitions in the first column. We show in bold the frequencies we could have observed in the NOEMA data.

Redshift	0.633	2.265	3.898	5.530	7.162	8.794	10.426	5.971	10.464
Transition									
CO(1 – 0)	70600								
CO(2 – 1)		70600							
CO(3 – 2)		105897	70600						
CO(4 – 3)			94129	70600					
CO(5 – 4)				**88245**	70600			82665	
CO(6 – 5)				105887	84714	70600		99191	
CO(7 – 6)					98825	82360	70600		**70365**
CI(1 – 0)			100483	**75365**				70600	
CI(2 – 1)					99154	82635	**70835**		70600

at $\sim$ 70.6 GHz and located at (RA, DEC)$_{J2000}$ = (12h27m00s, +33d32m36s). In the left panel in Fig. 8.5 we show the spectrum of the source. The line extends from 70.5 GHz to 71 GHz. In the right panel we show the map obtained by merging the bands in the mentioned frequency range. The emission of the source is clearly visible, coincident with the PS1 source detected also in the mosaic-mode observations, and seems slightly elongated towards the north-west.

Sources close to clusters can be high redshift objects lensed by the power of the deep cluster potential wells. For this reason, the detection of this line can be particularly interesting to determine the redshift of the emitting source. The estimation of a redshift requires as a minimum the identification of two species in the spectrum. We check if the observed line corresponds to any of the usual molecular transitions in galaxies in Table 8.1. The table indicates the possible redshifts of the source if the emission at 70.6 GHz corresponds to any of the considered transitions. In addition, for those redshifts, we give the frequencies at which other transitions should be observed. In bold we indicate the emission lines we could have seen in our data and that exclude the corresponding redshifts. With the data on hand, we can not confirm any nor exclude all of the options, and neither determine the redshift of the galaxy.

A more precise measurement of the frequency of the line will be needed to exclude, with strong arguments, the $z = 3.898$ redshift, which should show a CO(4 – 3) emission line at 94.129 GHz, close to the upper limit of our USB band. In any case, even if we finally conclude that the line is emitting at 70.5 GHz, the CO(4 – 3) line should be observed at 93.995 GHz, which is nearly impossible given the frequency coverage of our bands. A more detailed study and complementary observations searching for CO and other molecular transitions are needed to shed light on the redshift of the source.

To avoid the contamination of the emission line in the measured fluxes, we then filtered out the LSB data between the 70.5 – 71 GHz frequency range. We computed the continuum of the LSB and USB bands using the `MAPPING` software in `GILDAS` and merged both bands to obtain, from the combined *uv* table, the dirty map in Fig. 8.6. The resulting synthesised beam (resolution) in this map is of 5.0 arcsec $\times$ 3.4 arcsec at a position angle of 45° and the Full Width Half Power (FWHP) of the primary beam is of 56.2 arcsec at 90 GHz. The map, with an RMS of 12 μJy/beam, shows some positive detections and an extended negative bowl in the centre, the darkblue region around the central source. The nature of this negative signal will be discussed in the next section. In the right panel in Fig. 8.6 we show the dirty beam corresponding to the map in the left panel.

Regarding the compact sources, we recognise some of the point sources presented in Sect. 4.2. Very close to the centre of the map lies the PS9 radio galaxy (Table 4.3), the BCG of the CL J1226.9+3332 cluster. This source was undetectable in the NIKA2 150 and 260 GHz maps, but, as described in Sect. 4.2, we could account for it from the extrapolation of the flux measured at 1.4 GHz in the VLA FIRST Survey. In addition, its flux

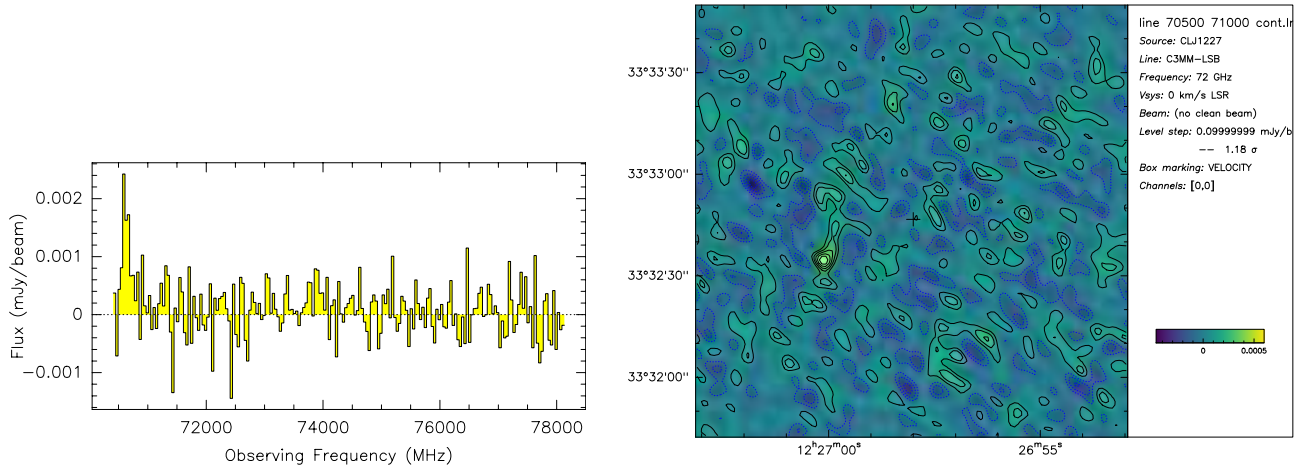

Figure 8.5: Emission line at ∼ 70.6 GHz. Left: detection of the line in the spectrum of the LSB at (RA, DEC)$_{J2000}$ = (12h27m00.0s, +33d32m33s). Figure by R. Neri. Right: dirty map for the combination of the channels between 70.5 GHz and 71 GHz.

at 1.4 GHz is given in the Table 1 in Sayers et al. (2013) [283] from NVSS observations: 4.3 ± 0.5 mJy. The Table 4 in Korngut et al. (2011) [266] summarises also different estimates. According to Korngut et al. (2011) [266] at 1.4 GHz the flux of PS9 is of 3.61 ± 0.22 mJy and 4.34 ± 0.47 mJy from NVSS and FIRST data, respectively. The measurements with OVRO, BIMA and the SZA put an upper limit of < 0.2 mJy at 30 GHz. And, by extrapolating the fluxes with a power law spectral energy distribution, according to Korngut et al. (2011) [266] the source at 90 GHz has a flux of < 0.13 mJy.

Moreover, the previously identified source emitting at 70.6 GHz coincides with the PS1 submillimetre galaxy characterised in Sect. 4.2 from the NIKA and NIKA2 maps, as well as from *Herschel* catalogues. To the south-west of the centre of the map in Fig. 8.6 a ∼ 5σ positive detection indicates the presence of a potentially new source. Although the detection is weak, we will name it PS10 and try to measure its flux. Authors in Korngut et al. (2011) [266] state also that MUSTANG observations at 90 GHz suggest the presence of a point source 10 arcsec north of the cluster's X-ray peak (i.e., cluster centre), which was not detected by Mroczkowski et al. (2009) [265] at 30 GHz. They speculate this source to be a high-redshift lensed galaxy with a rising spectrum that would correspond to a dusty star-forming galaxy. We do not detect such source in the NOEMA single-field data.

For NOEMA observations, we perform the fit of the point sources directly in the space of visibilities. Thanks to the `uv_fit` routine included in `MAPPING` we can simultaneously fit multiple sources, their fluxes, positions and sizes. For point-like sources we used the *point* function, which assumes that they are unresolved for NOEMA. Together with the positive sources we had to account for the negative emission observed in the centre of the map. If this emission, probably due to the SZ effect in the cluster, is not considered, the fluxes of the sources are underestimated. We modelled the negative extended emission with the *circular gaussian* function of `uv_fit`. The resulting values from the fit are summarised in Table 8.2. The left panel in Fig. 8.7 shows the dirty map once the fitted extended emission has been subtracted in the *uv* space. We observe that the large structures in Fig. 8.6 have now significantly disappeared and that the signal of the central radio source is enhanced. In the right panel in Fig. 8.7 we present the dirty map after the subtraction of the sources and the negative extended emission. We have no indication of additional detections in this residual map.

Aiming to quantify the impact of PS10, we repeated the fit in the *uv* space but only for PS1, PS9 and the negative component, in other words, ignoring PS10. The resulting positions, fluxes and FWHP are completely compatible with the results in Table 8.2. Therefore, it is hard to say whether PS10 is a new detection or if we are just fitting some noise that has been boosted by the positive structure that the central negative signal introduces. We hope that increasing the S/N with the observations to come will allow us to conclude on this.

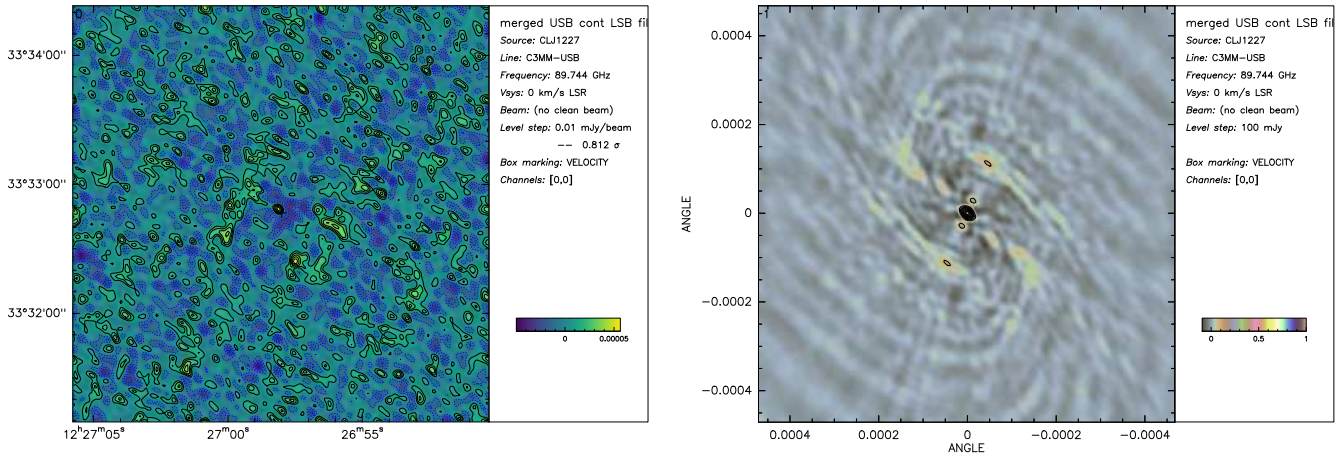

Figure 8.6: Dirty map (left) and dirty beam (right) for the combination of LSB and USB data, once the 70.5 − 71 GHz frequency range is filtered.

Table 8.2: Point sources and negative extended emission identified with NOEMA. We give the best position and flux for each point source fitted to the visibilities. We also provide the position, flux and size of the simultaneously fitted negative emission. None of these values have been corrected for the primary beam attenuation.

Coordinates J2000	Source	Function	Flux [μJy]	FWHP [arcsec]
12h27m00.11s +33d32m36.3s	PS1	*point*	38 ± 10	
12h26m58.11s +33d32m48.5s	PS9	*point*	81 ± 11	
12h26m57.52s +33d32m24.2s	PS10	*point*	60 ± 10	
12h26m57.83s +33d32m49.1s	SZ of the cluster	*circular gaussian*	−2448 ± 662	24.5 ± 2.2

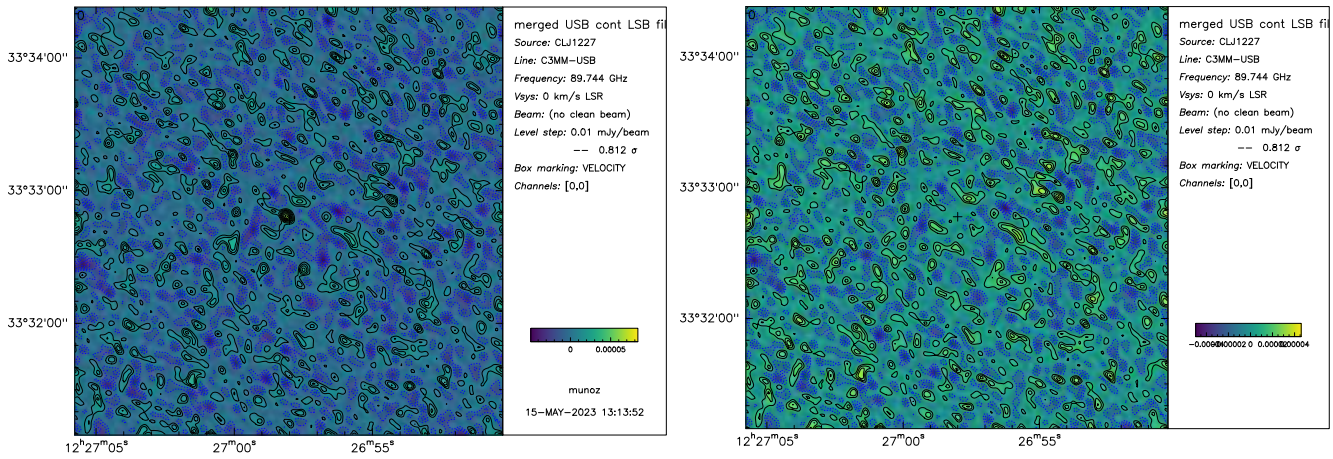

Figure 8.7: NOEMA dirty maps. To obtain the map in the left panel we have subtracted the fitted negative emission from the visibilities. For the right panel, we have subtracted the contribution of the point sources (PS1, PS9 and PS10), in addition to the negative extended emission.

In Fig. 8.8 we show a zoom-up of the NOEMA dirty map from Fig. 8.6 with the NIKA2 and MUSTANG contours for the CL J1226.9+3332 galaxy cluster observations superimposed in black and white, respectively. The red and white circles correspond to the same sources as in Fig. 4.3, while the stars indicate the positions obtained from the analysis of NOEMA data. We observe that the so-called PS10 does not agree with any detection in the NIKA2 260 GHz map, and neither does with missing SZ in the 150 GHz map. MUSTANG contours in the right panel indicate a 1σ positive detection coincident with PS1.

From the flux measurements in Table 8.2, we have a more complete picture of the spectral energy distribution of the galaxies in the field of CL J1226.9+3332. In Fig. 8.9 we put together all the aforementioned flux estimates and correct the NOEMA fluxes for the primary beam attenuation. In the left panel we present the spectral energy distribution for PS9. To have a prior estimate of the flux of this radio source at 150 GHz, in chapter 4 we had to assume a synchrotron spectrum $F(\nu) = F_0(\nu/\nu_0)^\alpha$. We considered a power law with $\alpha = -0.7 \pm 0.2$, but the NOEMA measurement (empty marker in Fig. 8.9) seems to indicate that the spectrum of the source is probably steeper ($\alpha \sim -0.9$), as shown by the dashed line. The posterior flux estimate from the joint fit of the cluster's pressure profile and the flux of sources in the NIKA2 150 GHz map gave a value for PS9 (cyan marker in the left panel of Fig. 8.9) in agreement with the SED preferred by the NOEMA results. Thus, we can confirm that, in the analysis of the pressure profile of CL J1226.9+3332 in chapter 4, we accounted correctly for the contamination by PS9. In the right panel we present the SED for PS1. The pink area shows the modified black-body SED fitted in Sect. 4.2 to the *Herschel* and NIKA2 260 GHz fluxes. The extrapolation of this SED at 150 GHz was used to have a prior estimate to be used in the NIKA2 150 GHz map fit and the resulting flux is the cyan data point with imperceptible error bars. The measurement with NOEMA agrees with the spectrum of a dusty galaxy and it is compatible within 1σ with the best-fit model.

8.2.2 The SZ effect in CL J1226.9+3332

The ultimate goal of this analysis is to prove the capability of NOEMA to observe galaxy clusters through the SZ effect. The dirty image in Fig. 8.6 shows already two signs of such a signal. On the one hand, a negative extended emission is surrounding the central radio source. We observe in Fig. 8.8 that this signal is coincident with the SZ peak in the NIKA2 150 GHz and MUSTANG maps. On the other hand, on both sides of the negative bowl we observe diagonal positive structures, that disappear when subtracting the negative emission from the visibilities (see Fig. 8.7).

In Fig. 8.10 we show for illustration purposes a model of a cluster SZ signal contaminated by two sources. In the left panel we present the model $I(\vec{\alpha}, \nu)$ and in the right panel we show the dirty image obtained following

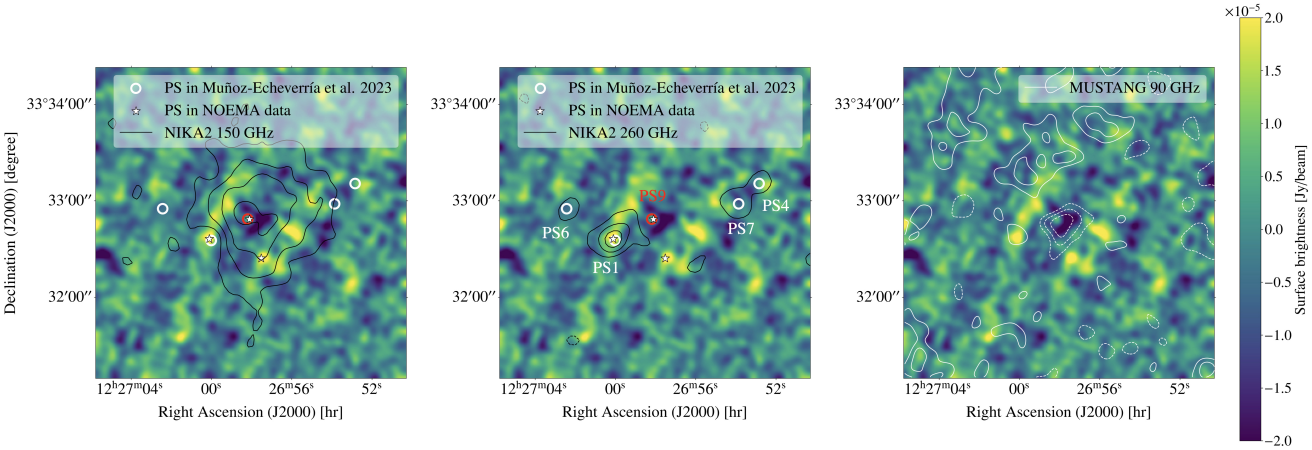

Figure 8.8: Zoom-up of the NOEMA dirty map in Fig. 8.6 with contours from other CL J1226.9+3332 observations. Contours in the left and central panel correspond respectively to NIKA2 150 GHz and 260 GHz S/N levels, starting from 3σ and spaced by 3σ. White and red circles indicate the point sources identified in the NIKA2 analysis, while the white stars show the positions fitted to NOEMA data. White contours in the right panel correspond to MUSTANG S/N levels obtained from https://safe.nrao.edu/wiki/bin/view/GB/Pennarray/MUSTANG_CLASH. We show the [-4, -3, -2, 1, 2] σ levels, with solid and dashed lines for positive and negative values, respectively.

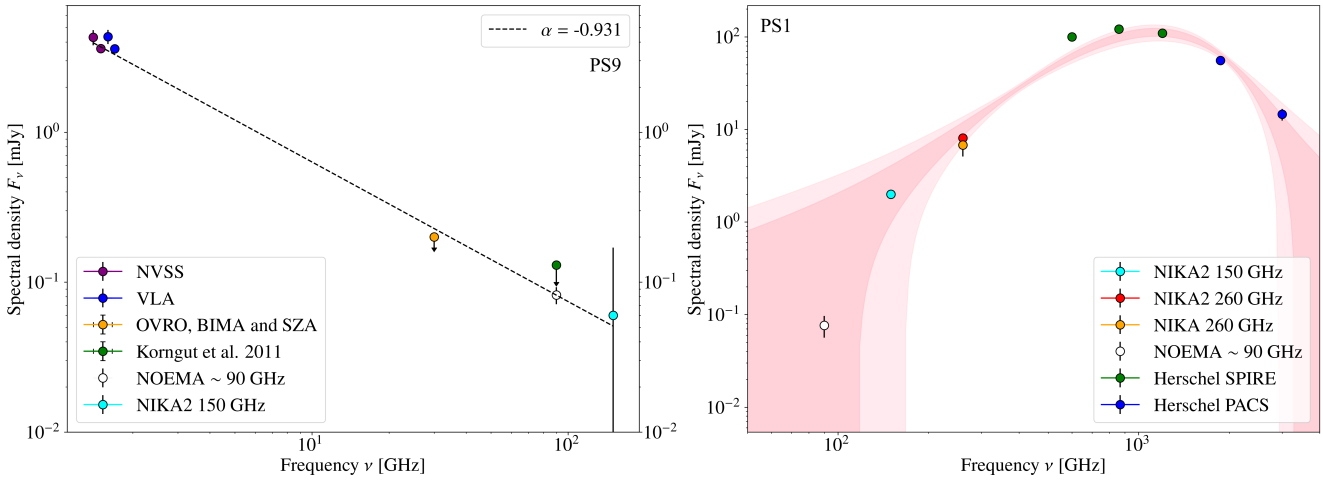

Figure 8.9: Spectral energy distributions of the point sources in the field of CL J1226.9+3332. Left: synchrotron SED of the PS9 radio source. Blue and purple markers show the flux measurements at 1.4 GHz. For visibility purposes, we have shifted in frequency three of the markers. In orange and green we show the upper limits given by Korngut et al. (2011) [266]. The empty circle is the fit to NOEMA data and the cyan marker shows the flux from the joint fit to the NIKA2 150 GHz map. The dashed line represents the best spectrum describing the 1.4 GHz and NOEMA measurements. Right: modified black-body spectrum of PS1. In red and orange the flux at 260 GHz from NIKA2 and NIKA data, respectively, and in green and blue *Herschel* SPIRE and PACS fluxes. In pink we show the 1σ and 2σ contours of the fit to NIKA2 260 GHz, *Herschel* SPIRE and PACS data. Empty and cyan markers correspond again to NOEMA and NIKA2 150 GHz fluxes.

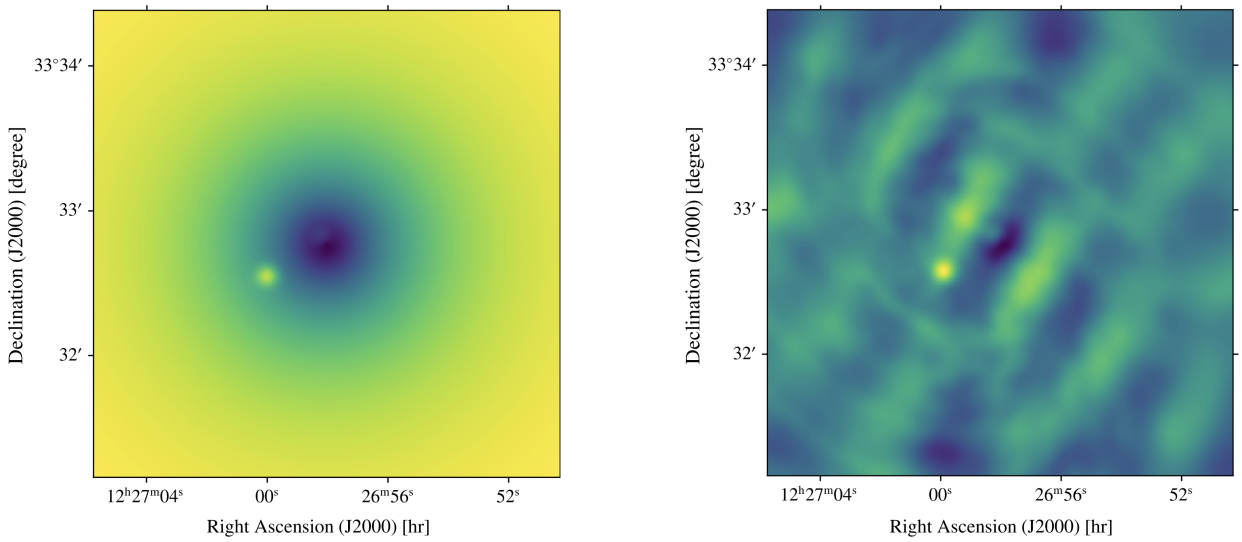

Figure 8.10: Illustration of the impact of the incomplete *uv* coverage on the surface brightness map reconstructed from interferometric observations without noise. Left: surface brightness map of a mock cluster SZ signal and two positive sources. Right: the mock signal in the left panel multiplied by the primary beam and convolved with the dirty beam corresponding to NOEMA observations with the coverage in Fig. 8.4. Maps are shown in arbitrary units.

Eq. 8.5, that is, the model multiplied by the primary beam (of 56.2″ FWHM) and convolved with the dirty beam. We observe that the incomplete coverage of the visibility space encoded in the dirty beam creates complex structures in the dirty image. Note the similarity of the structures in Fig. 8.6 with the simplistic simulation in Fig. 8.10. Thus, from the visual inspection of the dirty map, we see hints of SZ.

We then subtract from the NOEMA visibilities the contribution of the point sources (Table 8.2) and save the data in a new *uv* table. The outcoming dirty map is shown in Fig. 8.11. The negative signal in the centre and the positive structures in the south-east to north-west direction are now more obvious.

However, raw interferometric data and the associated uncertainties being defined in the *uv*-plane, it is preferred to detect and model the signal in the visibility space instead of in the image space [410]. By computing the average visibility values in concentric annuli in the *uv*-plane, we obtain the profiles shown with empty markers in Fig. 8.12. The top panel shows the real part of the visibilities, while the bottom panel corresponds to the imaginary component. We show with black circles the visibilities when subtracting PS1, PS9 and PS10 from the data and with grey stars without any subtraction. Although removing the sources has an impact on the remaining visibilities, in particular at intermediate angular scales, both profiles are compatible. The negative signal in the real component of the visibilities in Fig. 8.12, without such systematic deviation in the imaginary part, is the evidence of the SZ in our data.

In order to check if the amplitude of the detected SZ signal is the expected one, we compare the visibilities measured with NOEMA to the best SZ models estimated from other data sets. We make use of the `galario`[27] [411] library: an SZ model map multiplied by the primary beam is given to `galario`, as well as the table containing the visibilities, the corresponding weights (inverse of the square root of the variance related to each visibility, Eq. 8.7) and their positions in the *uv*-plane for the NOEMA data. As an output `galario` provides the input SZ model in the visibility space. Given that the output model samples the same u and v positions as the NOEMA data, it is affected by the same dirty beam.

We repeat this procedure for different SZ models obtained for CL J1226.9+3332. We show in Fig. 8.12 the best-fit gNFW pressure model reconstructed in Romero et al. (2017) [118] from the combination of MUSTANG and Bolocam data in solid blue and the result from the joint MUSTANG+Bolocam+NIKA fit from Romero et al. (2018) [251] with the dashed blue line. The orange profiles correspond to 100 SZ models obtained by

[27] https://mtazzari.github.io/galario/index.html

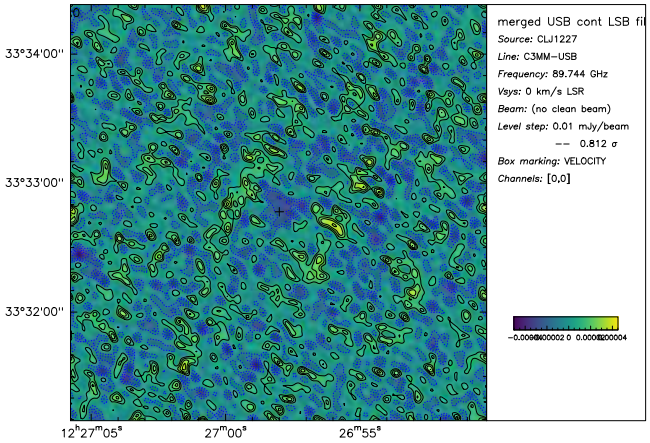

Figure 8.11: Same as Fig. 8.6 once the point sources have been subtracted from the visibilities.

randomly sampling the density distributions of the gNFW parameters in Fig. 4.9. They result from the joint fit to *Planck*, NIKA, NIKA2, MUSTANG and Bolocam data for CL J1226.9+3332. In addition, the solid and dashed red lines correspond to A10 pressure profiles for masses of $M_{500} = 5 \times 10^{14}$ $M_\odot$ and $M_{500} = 6.5 \times 10^{14}$ $M_\odot$, respectively. They represent the $\sim 1\sigma$ limits of the *Planck* constraints[28]. *Planck* measured the integrated SZ emission of the cluster, and assuming the A10 universal pressure profile and scaling relation, estimated that the mass of CL J1226.9+3332 is $M_{500}^{Planck} = 5.7^{+0.63}_{-0.69} \times 10^{14}$ $M_\odot$. We observe in Fig. 8.12 that the NOEMA data points are compatible with the results in this thesis.

The next step will be to fit, as for the arcminute scale SZA analysis in Mroczkowski et al. (2009) [265] and in Muchovej et al. (2007) [275] or the earlier OVRO and BIMA analysis in Joy et al. (2001) [269], the pressure profile of CL J1226.9+3332 to the NOEMA data. Nonetheless, given the filtering of large scales by interferometers, it might be more interesting to solve the *short-spacing problem*, that is, the missing small *uv* distances, with single-dish data (as already done, for example, in Di Mascolo et al. (2019) [406]). This way we will try to probe the maximum number of angular scales as possible and have a complete view of the distribution of the gas in the cluster. However, we anticipate that combining NOEMA and NIKA2 data may be complex given the different observing frequencies and sensitivities of both instruments. A higher signal-to-noise detection of the SZ will be needed to demonstrate also the departure from sphericity of the signal in the core of the cluster and, therefore, the above-mentioned disturbance (Sect. 8.2 and 4.1).

8.3 Conclusions

In this chapter, we have analysed the interferometric data obtained with the NOEMA instrument for the CL J1226.9+3332 galaxy cluster. After the unfruitful attempt to detect the cluster in a mosaic-like observation mode, single-field observations are currently ongoing and we are now at half of the requested sensitivity.

With the data on hand, we have studied the point sources in the field. The angular resolution of NOEMA has enabled the flux measurement of the radio source in the centre of the cluster at 90 GHz, which was not detectable with MUSTANG. With it, we have verified the solidity of the extrapolation of the flux at 150 GHz. NIKA2 and, in particular, LPSZ cluster observations could benefit from a better knowledge of the spectral energy distribution of the (almost) always very central radio loud BCGs with this type of NOEMA data. Characterising these sources can be crucial since they are not detected at higher frequencies, but can bias the SZ signal in the inner part of the cluster. In addition, the spectrum of the PS1 source shows an emission line at $\sim$ 70.6 GHz in

[28] https://heasarc.gsfc.nasa.gov/W3Browse/all/plancksz2.html

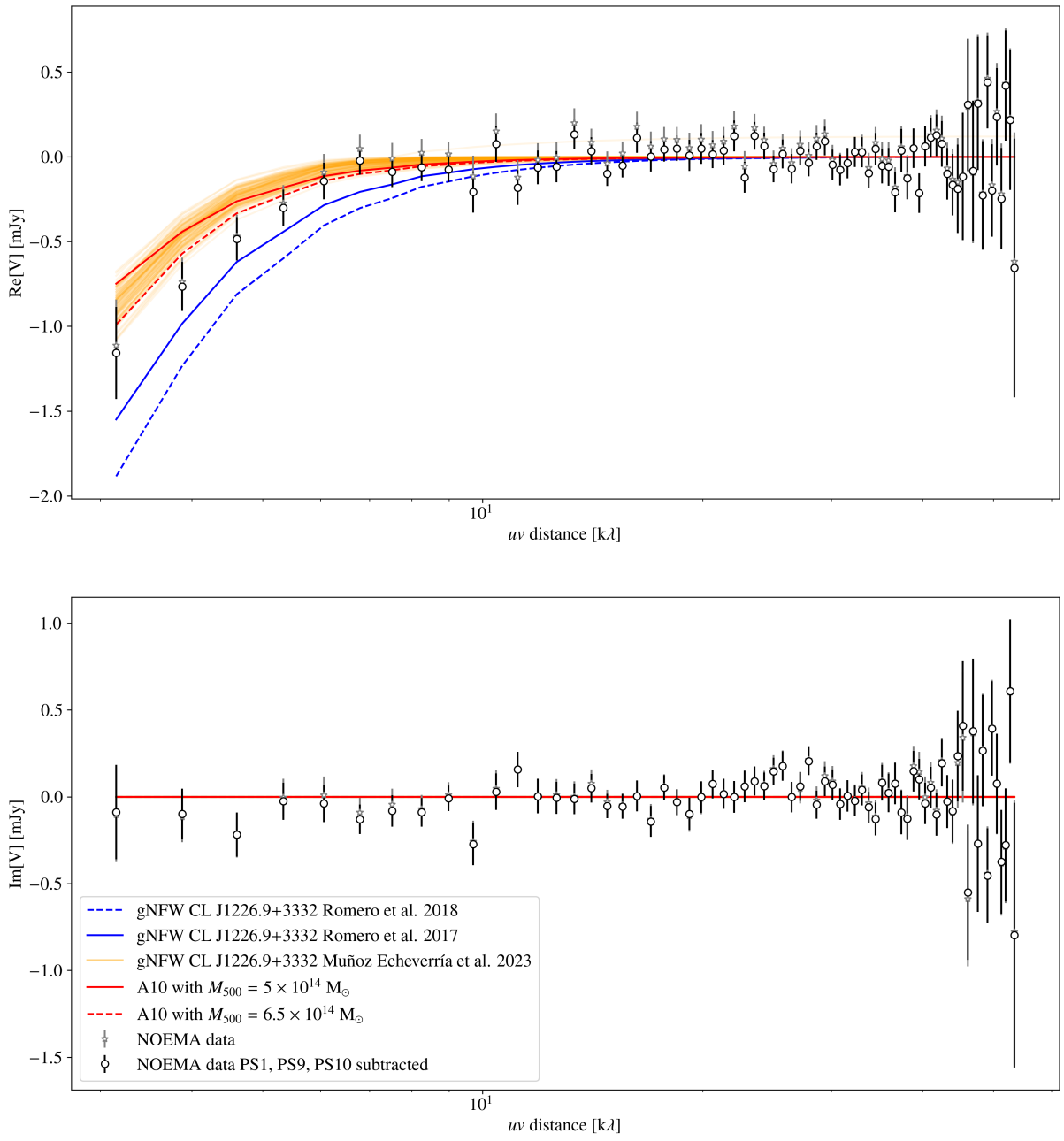

Figure 8.12: Real (top) and imaginary (bottom) components of visibilities as a function of binned *uv* distances. Circles show the profile for the NOEMA data once the contribution of the point sources has been subtracted from the visibilities. Stars correspond to the profile before point source subtraction. Error bars indicate 1σ uncertainties propagated from the error bar associated with each visibility. Dashed and solid blue lines represent the best SZ models from Romero et al. (2018) [251] and Romero et al. (2017) [118]. In orange we show the gNFW models obtained in Fig. 4.9 and the red lines correspond to A10 pressure profiles for masses of $M_{500} = 5 \times 10^{14}$ M$_\odot$ (solid) and $M_{500} = 6.5 \times 10^{14}$ M$_\odot$ (dashed).

NOEMA data, which motivates further spectral observations.

Moreover, we have been able to detect, for the first time with NOEMA, the SZ effect of a cluster. We have verified that the position and amplitude of the SZ signal are in agreement with previous observations and that this result is not sensitive to the subtraction of the point sources in the field. This detection demonstrates the power of NOEMA to do cluster science. Complementary to ALMA in the Northern Hemisphere, the high angular resolution of NOEMA will be very important to resolve high-redshift compact clusters.

Once the observations of CL J1226.9+3332 will be completed, we plan to repeat the analysis presented in this chapter, most probably exploiting the NOEMA capabilities together with the single-dish data from NIKA2 and MUSTANG.

Conclusions and perspectives

The main topic of my PhD thesis has been cluster science from a multi-observation and multi-probe perspective.

An important part of my work has been developed in the framework of the NIKA2 SZ Large Programme. I have become part of the NIKA2 collaboration and participated in observation campaigns at the IRAM 30-metre telescope, both remotely and on-site. Getting involved in data acquisition campaigns has allowed me to understand the origin of different noise contributions in NIKA2 data and the observational challenges that detecting the weak SZ signal requires. My overall implication in the NIKA2 collaboration has granted me the core team status.

The processing of NIKA2 data for SZ observations of clusters of galaxies is a delicate procedure based on the correlation of the signal detected by the different KIDs. The procedure aims at the subtraction of contaminants, including atmospheric fluctuations and electronic noise, with minimal filtering of the SZ signal. In this regard, I have demonstrated that the filtering of the signal at large angular scales is the major problem in NIKA2 cluster SZ analyses. In addition, I have proposed a two-dimensional transfer function that allows us to account for the anisotropic filtering introduced by the scanning strategy and data processing procedures. This option is now implemented in the official LPSZ pipelines. NIKA2 maps reconstructed by using different data reduction pipelines have different characteristics. However, I have shown that if the noise properties and the effect of filtering are well propagated, we reconstruct compatible pressure profiles, all within the limits of the filtering. This was a very reassuring result for the NIKA2 LPSZ. The performance of the NIKA2 camera has demonstrated the power of KIDs technology for future experiments.

For the PSZ2 G228.16+75.20 and CL J1226.9+3332 galaxy clusters in the NIKA2 LPSZ sample, I have performed detailed analyses of their SZ maps. Both studies required a careful treatment of point sources in the field. The modified black-body spectrum used to characterise the spectral energy distribution of submillimetre sources needs a well-constrained slope at high frequencies so that the temperature of the emitting galaxies can be properly estimated. I generalised the existing SED fitting tools to account for flux measurements at high frequencies and, thus, improve on point source subtraction. Moreover, we evidence that the LPSZ is a unique programme allowing us to study galaxies in the vicinity of clusters from intermediate to high redshifts at millimetre wavelengths.

In addition, I reconstructed the thermal pressure profiles of the mentioned clusters and investigated the problems in the hydrostatic mass reconstruction methods. To overcome the filtering issues of the NIKA2 data at large angular scales I proposed modelling the SZ maps with a radially binned pressure model, that can then be easily combined with external data sets. At the same time, to solve the problems in the HSE mass estimation related to the computation of the derivative of the pressure profile, I have implemented an approach based on the modelling of the mass density profile. I conclude that the only way of reducing the current uncertainties on $M_{500}^{\rm HSE}$ masses is to precisely constrain the slope of the mass profiles at $\sim R_{500}^{\rm HSE}$. In that direction, the combination of SZ data from various instruments probing different angular scales appears to be the best way to obtain complete radial coverage of the thermal pressure and mass distribution in clusters.

I have performed a more detailed analysis of the CL J1226.9+3332 galaxy cluster. I have compared the pressure profiles reconstructed from NIKA2 data for different noise estimates and accounting or not for the

anisotropic filtering in the SZ map. In conclusion, the impact of these effects is minor. A thorough investigation in the literature of the mass estimates obtained for this cluster has shown that the HSE masses we reconstructed with SZ and X-ray data are robust. The wide variety of types of analyses and definitions used to estimate and present cluster masses in different works hinders fair comparisons. To overcome this issue, I present the results in the radius-mass plane and explicitly state the underlying assumptions for each estimate. This work has been published in Muñoz-Echeverría et al. (2023) [191].

I have also significantly contributed to the publication of the first combined LPSZ and CLASH analysis for PSZ2 G144.83+25.11 presented in Ferragamo et al. (2022) [190]. I have extended the study to the clusters in common between NIKA, NIKA2 and CLASH samples and reconstructed the lensing mass of CL J1226.9+3332, PSZ2 G144.83+25.11, PSZ2 G228.16+75.20 and MACS J1423.8+2404 clusters based on CLASH convergence maps. We find no hints of systematic bias in our mass reconstructions with respect to other HSE and lensing analyses, but the dispersion of the results amongst different works for the same cluster is very large. We measure the hydrostatic-to-lensing mass bias for the four clusters and confirm that HSE masses are biased low with respect to lensing estimates. In addition, HSE masses appear differently biased if X-ray spectroscopic temperature profiles or, instead, SZ data are employed. This result highlights the importance of SZ analyses to shed light on possible systematic biases in X-ray studies. Multi-wavelength and multi-probe analyses are unavoidable if we aim at identifying and correcting for systematics in the used data sets or in the assumptions of the mass reconstructions. This is the first comparison of lensing and resolved HSE masses obtained from SZ and X-ray data at redshifts $z > 0.5$, and demonstrates the pertinence of NIKA2 observations.

Given the relevant implications the hydrostatic mass bias has on the cluster cosmological analyses calibrated on hydrostatic mass estimates, I performed another study on this subject. Cluster masses used in cosmological analyses are based on scaling relations, that have to be first determined from a sample of clusters with resolved mass estimates. An unbiased scaling relation requires, then, unbiased masses for those individual clusters. In chapter 6, I have presented the study on the bias of X-ray hydrostatic mass estimates with respect to lensing masses, for masses that have been individually obtained for each cluster without considering any scaling relation. As discussed above, the obtained masses can considerably depend on the data set used or on the mass reconstruction method. For this reason, I have built a sample of clusters that is as large as possible, but for which homogeneous methods have been applied consistently to the full sample. From the comparison of these homogeneous mass estimates to other resolved masses we conclude that, in general, the agreement between the works is good, with a non-negligible scatter. I have propagated this scatter and computed the hydrostatic-to-lensing mass bias for the 53 clusters in the sample with redshifts spanning from $z = 0.05$ to 1.07. I have investigated the evolution of the bias with redshift since an evolving hydrostatic mass bias could explain the discrepancies between cosmological analyses from cluster counts calibrated on HSE masses and the CMB power spectrum. In addition, it could be indicative of a deviation from equilibrium of clusters that evolves with cosmic time. Nevertheless, our results do not confirm such evolution. Along this study, I have shown that hydrostatic and lensing masses are scattered estimates of the true mass of clusters and that these uncertainties have to be considered in the computation of the hydrostatic-to-lensing mass bias. A paper describing this analysis was accepted for publication in Astronomy and Astrophysics [325].

During my PhD, I have also become a member of THE THREE HUNDRED collaboration. I have made use of the clusters from THE THREE HUNDRED hydrodynamical simulations to study the bias in cluster mass estimates introduced during the deprojection procedure of mass maps assuming spherical density models. As shown for the mass reconstructions from observational data in chapters 3, 4 and 5, the $M_{500} - R_{500}$ definition used to determine the mass at the overdensity of interest ($\Delta = 500$) is very unstable. Even if density or mass profiles are overall good representations of the distribution of matter in the cluster, the M_{500} estimate will be significantly biased if the model is failing at $\sim R_{500}$. Without considering instrumental nor observational effects, we have seen from simulations that the triaxiality of clusters introduces a 10 to 14% dispersion in the masses reconstructed assuming sphericity from projected data (for total matter tracers). Thus, the orientation of clusters is a very important source of uncertainties and bias, which is hardly quantifiable from observations. On the contrary, we find a very weak correlation between the bias of mass estimates and intrinsic properties

of clusters (mass, redshift and dynamical state). From the comparison of the distribution of the gas and the dark matter in the simulated clusters, we confirm that gas is more spherically distributed, which ensures smaller projection effects for gas tracers and makes gas observables less scattered proxies of the mass of clusters. This conclusion is in line with the observational results in chapter 6 and it was also one of the reasons that motivated SZ and X-ray observations to study cluster masses. I wrote a paper describing this work that was accepted for publication in Astronomy and Astrophysics [355].

The last part of my work has been devoted to the analysis of the NOEMA observations of the CL J1226.9+3332 galaxy cluster. As a follow-up to previous NOEMA observations, I proposed a new open time project that was accepted by the IRAM programme committee. The objective of the observations was to demonstrate that NOEMA is able to detect galaxy clusters through the SZ effect and that it will be a unique tool to investigate the core of clusters and point sources in the field at very high angular resolution. Data acquisition took place during the last months of my thesis and I was able to analyse the first part of the data. From the study of the radio and submillimetre sources in the field, we have now improved the constraints on their spectral energy distributions. We have verified that CL J1226.9+3332 hosts a radio source close to its core that contaminates the SZ signal at 90 GHz. Moreover, the spectral data has revealed an emission line at 70.6 GHz in the submillimetre source close to the cluster, which motivates further investigation. These observations have also shown the presence of a negative and diffuse signal in the centre of the map. We argue in chapter 8 that this can not be an artefact introduced by the noise. Instead, it is coincident in position and flux with the expected thermal SZ signal for CL J1226.9+3332. Extra NOEMA data was available at the time of writing these conclusions, confirming these results. This is the first detection of the SZ effect with NOEMA and paves the way for new observations of galaxy clusters at high angular resolution in the Northern Hemisphere, which is only partially observable with ALMA.

In summary, in this thesis, I have proposed new analysis methods for the LPSZ clusters and assessed the robustness of the final results. This work has been very useful to define a standard LPSZ pipeline. In terms of the determination of the mass of clusters, I have investigated systematic and projection effects using existing data and simulations. I have shown that projection effects are particularly important and that systematics should be considered in scaling relations.

In addition to the work presented in the manuscript, I have also led an open time proposal targeting spectroscopy observations of the MACS J0416.1-2403 galaxy cluster with CONCERTO [412]. The proposed observations aim to disentangle the thermal and kinetic SZ effects and, thus, have a better understanding of the possible merger event. Given the well-known spectral signature of the tSZ and kSZ effects, we will probably take an Internal Linear Combination [413] approach to disentangle the presence of both effects by making use of the multi-frequency maps. We will try to identify possible pressure jumps and to quantify the velocities of the two substructures in the cluster. The proposal, requesting 90 hours of observation, was accepted by the European Southern Observatory (ESO). Data acquisition has now finished and the analysis of the data is ongoing. The CONCERTO data processing pipeline is still under development, so I plan to participate in this task. If successful results are attained, the doors of sub-arcminute and spectral observations will be opened at millimetre wavelengths, which are particularly interesting for investigating the tSZ, kSZ and rSZ effects in clusters. In this context, I have also taken charge of on-site observation campaigns with CONCERTO at the APEX telescope.

In the last chapter of this thesis, we have demonstrated that the NOEMA interferometer is adapted for observing galaxy clusters. After these fruitful proof-of-concept observations, we plan to get the most of the high-resolution data to characterise the gas and galaxies in the core of clusters. From now on SZ observations of clusters with NOEMA will be complementary to ALMA observations in the Southern Hemisphere. Targeting clusters with many point sources in the field and complex internal structures can be particularly interesting. We will certainly propose new observations of high redshift objects (clusters or even protoclusters) that are unresolved by NIKA2 and can be a mine of very high redshift lensed galaxies.

As shown in this thesis, current constraints on individual cluster masses are weak and resolved SZ observa-

tions are essential to identify potential systematic biases in X-ray observations at similar resolutions. No other project but the NIKA2 LPSZ will bring such information, thanks to the angular resolution and sensitivity of the NIKA2 camera. The results from the standard analysis of the NIKA2 LPSZ will be published in the following years. The released mean pressure profile and $Y_{500} - M_{500}$ scaling relation will be unique tools for cluster cosmology in SZ.

The synergy between NIKA2 observations and cosmological simulations will happen in both directions. On the one hand, simulated clusters from THE THREE HUNDRED project will be used to assess the robustness of the LPSZ mass reconstructions, by creating NIKA2-like SZ maps and applying the mass estimation methods employed in the standard LPSZ analyses. However, the use of simulations is currently limited by their accuracy in representing the actual Universe. Therefore, on the other hand, high-resolution observations such as the LPSZ data, will constitute valuable feedback for simulations to improve.

Moreover, the next decades will be rich in large cluster surveys. The recently launched *Euclid* satellite and the very soon commissioning Vera Rubin observatory will build three-dimensional maps of the Universe at visible and infrared wavelengths. By studying the richness of clusters and the lensing effect created on background sources, we will have stronger statistical constraints on the mass of clusters. On the X-rays side, eROSITA has already delivered [414] the first catalogue of galaxy clusters, going deeper than ever in X-rays. The complementary observations at millimetre wavelengths will come by the hands of The Simons Observatory and CMB-S4. Since the SZ effect is not affected by cosmological dimming, it will be the best observable to detect the highest redshift clusters in the Universe. We expect that these large cluster catalogues and the multi-wavelength observations will help to explain the matter content and structure formation along cosmic time. Better modelling of the non-linear regime of the matter power spectrum and the impact of baryonic effects at those scales will have to be tackled if precise cosmological constraints are aimed. From a more general point of view, the future of cosmology will be built on multi-probe analyses able to break the degeneracies between the different cosmological parameters and to identify the subjacent systematic biases each probe is subject to.

Bibliography

[1] A. A. Penzias and R. W. Wilson. "A Measurement of Excess Antenna Temperature at 4080 Mc/s.", *ApJ* 142 (1965), pp. 419–421 (cit. on pp. 9, 15).

[2] A. M. Boesgaard and G. Steigman. "Big Bang nucleosynthesis: theories and observations.", *ARA&A* 23 (1985), pp. 319–378 (cit. on pp. 9, 15).

[3] A. G. Riess et al. "Observational Evidence from Supernovae for an Accelerating Universe and a Cosmological Constant", *AJ* 116.3 (1998), pp. 1009–1038. arXiv: astro-ph/9805201 [astro-ph] (cit. on pp. 9, 16).

[4] D. J. Eisenstein et al. "Detection of the Baryon Acoustic Peak in the Large-Scale Correlation Function of SDSS Luminous Red Galaxies", *ApJ* 633.2 (2005), pp. 560–574. arXiv: astro-ph/0501171 [astro-ph] (cit. on p. 9).

[5] Planck Collaboration et al. "Planck 2013 results. XX. Cosmology from Sunyaev-Zeldovich cluster counts", *A&A* 571 (2014), A20. arXiv: 1303.5080 [astro-ph.CO] (cit. on pp. 9, 31, 32, 35, 36, 41, 43, 45, 89, 101, 185, 186).

[6] Planck Collaboration et al. "Planck 2015 results. XXIV. Cosmology from Sunyaev-Zeldovich cluster counts", *A&A* 594 (2016), A24. arXiv: 1502.01597 [astro-ph.CO] (cit. on pp. 9, 32, 35, 40–43, 115).

[7] T. de Haan et al. "Cosmological Constraints from Galaxy Clusters in the 2500 Square-degree SPT-SZ Survey", *ApJ* 832.1 (2016), p. 95. arXiv: 1603.06522 [astro-ph.CO] (cit. on pp. 9, 32).

[8] S. Bocquet et al. "Cluster Cosmology Constraints from the 2500 deg^2 SPT-SZ Survey: Inclusion of Weak Gravitational Lensing Data from Magellan and the Hubble Space Telescope", *ApJ* 878.1 (2019), p. 55. arXiv: 1812.01679 [astro-ph.CO] (cit. on pp. 9, 31, 32, 45, 115).

[9] M. Hasselfield et al. "The Atacama Cosmology Telescope: Sunyaev-Zel'dovich selected galaxy clusters at 148 GHz from three seasons of data", *Journal of Cosmology and Astroparticle Physics* 2013.7 (2013), p. 008. arXiv: 1301.0816 [astro-ph.CO] (cit. on pp. 9, 32, 70, 77).

[10] M. Costanzi et al. "Methods for cluster cosmology and application to the SDSS in preparation for DES Year 1 release", *MNRAS* 488.4 (2019), pp. 4779–4800. arXiv: 1810.09456 [astro-ph.CO] (cit. on pp. 9, 32).

[11] G. F. Lesci et al. "AMICO galaxy clusters in KiDS-DR3: Cosmological constraints from counts and stacked weak lensing", *A&A* 659 (2022), A88. arXiv: 2012.12273 [astro-ph.CO] (cit. on pp. 9, 24, 32).

[12] H. Böhringer et al. "The Northern ROSAT All-Sky (NORAS) Galaxy Cluster Survey. I. X-Ray Properties of Clusters Detected as Extended X-Ray Sources", *ApJS* 129.2 (2000), pp. 435–474. arXiv: astro-ph/0003219 [astro-ph] (cit. on pp. 9, 32).

[13] H. Böhringer et al. "The ROSAT-ESO Flux Limited X-ray (REFLEX) Galaxy cluster survey. V. The cluster catalogue", *A&A* 425 (2004), pp. 367–383. arXiv: astro-ph/0405546 [astro-ph] (cit. on pp. 9, 32).

[14] C. Adami et al. "The XXL Survey. XX. The 365 cluster catalogue", *A&A* 620 (2018), A5. arXiv: 1810.03849 [astro-ph.CO] (cit. on pp. 9, 32).

[15] A. Liu et al. "The eROSITA Final Equatorial-Depth Survey (eFEDS). Catalog of galaxy clusters and groups", *A&A* 661 (2022), A2. arXiv: 2106.14518 [astro-ph.CO] (cit. on pp. 9, 25, 33).

[16] J. A. Tauber et al. "Planck pre-launch status: The Planck mission", *A&A* 520 (2010), A1 (cit. on p. 9).

[17] D. S. Swetz et al. "Overview of the Atacama Cosmology Telescope: Receiver, Instrumentation, and Telescope Systems", *ApJS* 194.2 (2011), p. 41. arXiv: 1007.0290 [astro-ph.IM] (cit. on p. 9).

[18] J. E. Carlstrom et al. "The 10 Meter South Pole Telescope", *PASP* 123.903 (2011), p. 568. arXiv: 0907.4445 [astro-ph.IM] (cit. on p. 9).

[19] E. Abdalla et al. "Cosmology intertwined: A review of the particle physics, astrophysics, and cosmology associated with the cosmological tensions and anomalies", *Journal of High Energy Astrophysics* 34 (2022), pp. 49–211. arXiv: 2203.06142 [astro-ph.CO] (cit. on pp. 14, 15, 35, 37, 43).

[20] G. Lemaître. "Un Univers homogène de masse constante et de rayon croissant rendant compte de la vitesse radiale des nébuleuses extra-galactiques", *Annales de la Societe Scientifique de Bruxelles* 47 (1927), pp. 49–59 (cit. on p. 14).

[21] E. Hubble. "A Relation between Distance and Radial Velocity among Extra-Galactic Nebulae", *Proceedings of the National Academy of Science* 15.3 (1929), pp. 168–173 (cit. on p. 14).

[22] D. J. Fixsen et al. "The Cosmic Microwave Background Spectrum from the Full COBE FIRAS Data Set", *ApJ* 473 (1996), p. 576. arXiv: astro-ph/9605054 [astro-ph] (cit. on p. 15).

[23] J. C. Mather et al. "Calibrator Design for the COBE Far-Infrared Absolute Spectrophotometer (FIRAS)", *ApJ* 512.2 (1999), pp. 511–520. arXiv: astro-ph/9810373 [astro-ph] (cit. on p. 15).

[24] Planck Collaboration et al. "Planck 2015 results. XIII. Cosmological parameters", *A&A* 594 (2016), A13. arXiv: 1502.01589 [astro-ph.CO] (cit. on pp. 15, 47, 162).

[25] C. L. Bennett et al. "Nine-year Wilkinson Microwave Anisotropy Probe (WMAP) Observations: Final Maps and Results", *ApJS* 208.2 (2013), p. 20. arXiv: 1212.5225 [astro-ph.CO] (cit. on p. 15).

[26] N. Jarosik et al. "Seven-year Wilkinson Microwave Anisotropy Probe (WMAP) Observations: Sky Maps, Systematic Errors, and Basic Results", *ApJS* 192.2 (2011), p. 14. arXiv: 1001 . 4744 [astro-ph.CO] (cit. on p. 15).

[27] Planck Collaboration et al. "Planck 2018 results. I. Overview and the cosmological legacy of Planck", *A&A* 641 (2020), A1. arXiv: 1807.06205 [astro-ph.CO] (cit. on pp. 16, 18).

[28] Planck Collaboration et al. "Planck 2018 results. VI. Cosmological parameters", *A&A* 641 (2020), A6. arXiv: 1807.06209 [astro-ph.CO] (cit. on pp. 16, 36, 42, 123).

[29] A. H. Guth. "Inflationary universe: A possible solution to the horizon and flatness problems", *Phys. Rev. D* 23.2 (1981), pp. 347–356 (cit. on p. 16).

[30] A. D. Linde. "A new inflationary universe scenario: A possible solution of the horizon, flatness, homogeneity, isotropy and primordial monopole problems", *Physics Letters B* 108.6 (1982), pp. 389–393 (cit. on p. 16).

[31] W. Cui et al. "An Ideal Mass Assignment Scheme for Measuring the Power Spectrum with Fast Fourier Transforms", *ApJ* 687.2 (2008), pp. 738–744. arXiv: 0804.0070 [astro-ph] (cit. on p. 18).

[32] A. V. Kravtsov and S. Borgani. "Formation of Galaxy Clusters", *ARA&A* 50 (2012), pp. 353–409. arXiv: 1205.5556 [astro-ph.CO] (cit. on pp. 18–20, 40).

[33] W. H. Press and P. Schechter. "Formation of Galaxies and Clusters of Galaxies by Self-Similar Gravitational Condensation", *ApJ* 187 (1974), pp. 425–438 (cit. on p. 18).

[34] J. Tinker et al. "Toward a Halo Mass Function for Precision Cosmology: The Limits of Universality", *ApJ* 688.2 (2008), pp. 709–728. arXiv: 0803.2706 [astro-ph] (cit. on pp. 18, 19, 32).

[35] F. Kéruzoré. "Cosmologie à partir des observations Sunyaev-Zeldovich d'amas de galaxies avec NIKA2". PhD thesis. Université Grenoble Alpes, 2021. Link (cit. on pp. 19, 70, 74).

[36] B. E. Robertson et al. "Identification and properties of intense star-forming galaxies at redshifts $z > 10$", *Nature Astronomy* (2023). arXiv: 2212.04480 [astro-ph.GA] (cit. on p. 19).

[37] B. W. Keller et al. "Can Cosmological Simulations Reproduce the Spectroscopically Confirmed Galaxies Seen at $z \geq 10$?", *ApJL* 943.2 (2023), p. L28. arXiv: 2212.12804 [astro-ph.GA] (cit. on p. 19).

[38] E. Hubble and M. L. Humason. "The Velocity-Distance Relation among Extra-Galactic Nebulae", *ApJ* 74 (1931), p. 43 (cit. on p. 19).

[39] F. Zwicky. "Die Rotverschiebung von extragalaktischen Nebeln", *Helvetica Physica Acta* 6 (1933), pp. 110–127 (cit. on pp. 19, 38).

[40] S. Smith. "The Mass of the Virgo Cluster", *ApJ* 83 (1936), p. 23 (cit. on p. 19).

[41] J. F. Meekins et al. "Physical Sciences: X-rays from the Coma Cluster of Galaxies", *Nature* 231.5298 (1971), pp. 107–108 (cit. on p. 19).

[42] E. Kellogg et al. "The Extended X-Ray Source at M87", *ApJL* 174 (1972), p. L65 (cit. on pp. 19, 25).

[43] W. Forman et al. "Observations of the Extended X-Ray Sources in the Perseus and Coma Clusters from UHURU", *ApJ* 178 (1972), pp. 309–316 (cit. on pp. 19, 25).

[44] G. B. Rybicki and A. P. Lightman. *Radiative Processes in Astrophysics*. 1986 (cit. on p. 19).

[45] R. A. Overzier. "The realm of the galaxy protoclusters. A review", *A&AR* 24.1 (2016), p. 14. arXiv: 1610.05201 [astro-ph.GA] (cit. on p. 20).

[46] M. Ata et al. "Predicted future fate of COSMOS galaxy protoclusters over 11 Gyr with constrained simulations", *Nature Astronomy* 6 (2022), pp. 857–865. arXiv: 2206.01115 [astro-ph.CO] (cit. on p. 20).

[47] L. Di Mascolo et al. "Forming intracluster gas in a galaxy protocluster at a redshift of 2.16", *Nature* 615.7954 (2023), pp. 809–812. arXiv: 2303.16226 [astro-ph.CO] (cit. on pp. 20, 23, 28, 189).

[48] G. W. Pratt et al. "The Galaxy Cluster Mass Scale and Its Impact on Cosmological Constraints from the Cluster Population", *Space Science Reviews* 215.2 (2019), p. 25. arXiv: 1902.10837 [astro-ph.CO] (cit. on pp. 20, 33, 39, 43–45, 90, 167, 186, 187).

[49] N. Kaiser. "Evolution and clustering of rich clusters.", *MNRAS* 222 (1986), pp. 323–345 (cit. on pp. 20, 22, 43).

[50] S. Borgani and A. Kravtsov. "Cosmological Simulations of Galaxy Clusters", *Advanced Science Letters* 4.2 (2011), pp. 204–227. arXiv: 0906.4370 [astro-ph.CO] (cit. on pp. 20, 123).

[51] J. F. Navarro, C. S. Frenk, and S. D. M. White. "The Structure of Cold Dark Matter Halos", *ApJ* 462 (1996), p. 563. arXiv: astro-ph/9508025 [astro-ph] (cit. on pp. 20, 21, 81).

[52] J. F. Navarro, C. S. Frenk, and S. D. M. White. "A Universal Density Profile from Hierarchical Clustering", *ApJ* 490.2 (1997), pp. 493–508. arXiv: astro-ph/9611107 [astro-ph] (cit. on p. 20).

[53] D. Eckert et al. "Non-thermal pressure support in X-COP galaxy clusters", *A&A* 621 (2019), A40. arXiv: 1805.00034 [astro-ph.CO] (cit. on pp. 21, 43, 122, 123, 149, 157).

[54] J. ZuHone and Y. Su. "The Merger Dynamics of the X-Ray-Emitting Plasma in Clusters of Galaxies", *Handbook of X-ray and Gamma-ray Astrophysics. Edited by Cosimo Bambi and Andrea Santangelo*. 2022, p. 93 (cit. on p. 21).

[55] J. A. ZuHone, M. Markevitch, and R. E. Johnson. "Stirring Up the Pot: Can Cooling Flows in Galaxy Clusters be Quenched by Gas Sloshing?", *ApJ* 717.2 (2010), pp. 908–928. arXiv: 0912.0237 [astro-ph.CO] (cit. on p. 21).

[56] J. Donnert et al. "Magnetic Field Amplification in Galaxy Clusters and Its Simulation", *Space Sci. Rev.* 214.8 (2018), p. 122. arXiv: 1810.09783 [astro-ph.CO] (cit. on p. 21).

[57] G. Di Gennaro et al. "Fast magnetic field amplification in distant galaxy clusters", *Nature Astronomy* 5 (2021), pp. 268–275. arXiv: 2011.01628 [astro-ph.CO] (cit. on pp. 21, 29, 30, 86, 92).

[58] G. Brunetti and T. W. Jones. "Cosmic Rays in Galaxy Clusters and Their Nonthermal Emission", *International Journal of Modern Physics D* 23.4 (2014), pp. 1430007–98. arXiv: 1401.7519 [astro-ph.CO] (cit. on p. 21).

[59] C. L. Sarazin. "The Physics of Cluster Mergers", *Merging Processes in Galaxy Clusters*. Ed. by L. Feretti, I. M. Gioia, and G. Giovannini. Vol. 272. 2002, pp. 1–38. arXiv: astro-ph/0105418 [astro-ph] (cit. on p. 21).

[60] R. Adam et al. "Substructure and merger detection in resolved NIKA Sunyaev-Zel'dovich images of distant clusters", *A&A* 614 (2018), A118. arXiv: 1712.01836 [astro-ph.CO] (cit. on p. 21).

[61] G. Hurier, R. Adam, and U. Keshet. "First detection of a virial shock with SZ data: implication for the mass accretion rate of Abell 2319", *A&A* 622 (2019), A136. arXiv: 1712.05762 [astro-ph.CO] (cit. on p. 21).

[62] E. T. Lau, A. V. Kravtsov, and D. Nagai. "Residual Gas Motions in the Intracluster Medium and Bias in Hydrostatic Measurements of Mass Profiles of Clusters", *ApJ* 705.2 (2009), pp. 1129–1138. arXiv: 0903.4895 [astro-ph.CO] (cit. on pp. 21, 43).

[63] K. Nelson, E. T. Lau, and D. Nagai. "Hydrodynamic Simulation of Non-thermal Pressure Profiles of Galaxy Clusters", *ApJ* 792.1 (2014), p. 25. arXiv: 1404.4636 [astro-ph.CO] (cit. on pp. 21, 122).

[64] K. Subramanian. "The origin, evolution and signatures of primordial magnetic fields", *Reports on Progress in Physics* 79.7 (2016), p. 076901. arXiv: 1504.02311 [astro-ph.CO] (cit. on p. 21).

[65] P. P. Kronberg, H. Lesch, and U. Hopp. "Magnetization of the Intergalactic Medium by Primeval Galaxies", *ApJ* 511.1 (1999), pp. 56–64 (cit. on p. 21).

[66] A. Pinzke and C. Pfrommer. "Simulating the γ-ray emission from galaxy clusters: a universal cosmic ray spectrum and spatial distribution", *MNRAS* 409.2 (2010), pp. 449–480. arXiv: 1001.5023 [astro-ph.CO] (cit. on p. 21).

[67] D. Nagai, A. V. Kravtsov, and A. Vikhlinin. "Effects of Galaxy Formation on Thermodynamics of the Intracluster Medium", *ApJ* 668.1 (2007), pp. 1–14. arXiv: astro-ph/0703661 [astro-ph] (cit. on pp. 22, 23, 80).

[68] G. M. Voit. "Tracing cosmic evolution with clusters of galaxies", *Reviews of Modern Physics* 77.1 (2005), pp. 207–258. arXiv: astro-ph/0410173 [astro-ph] (cit. on p. 22).

[69] M. C. Weisskopf et al. "An Overview of the Performance and Scientific Results from the Chandra X-Ray Observatory", *PASP* 114.791 (2002), pp. 1–24. arXiv: astro-ph/0110308 [astro-ph] (cit. on pp. 22, 25).

[70] M. Arnaud et al. "The universal galaxy cluster pressure profile from a representative sample of nearby systems (REXCESS) and the $Y_{SZ} - M_{500}$ relation", *A&A* 517 (2010), A92. arXiv: 0910.1234 [astro-ph.CO] (cit. on pp. 22, 23, 25, 43, 45, 46, 66, 70–72, 76, 80, 89, 123, 128, 154, 185).

[71] F. Jansen et al. "XMM-Newton observatory. I. The spacecraft and operations", *A&A* 365 (2001), pp. L1–L6 (cit. on pp. 22, 25).

[72] Planck Collaboration et al. "Planck intermediate results. V. Pressure profiles of galaxy clusters from the Sunyaev-Zeldovich effect", *A&A* 550 (2013), A131. arXiv: 1207.4061 [astro-ph.CO] (cit. on pp. 22, 23, 71, 164).

[73] E. Pointecouteau et al. "PACT. II. Pressure profiles of galaxy clusters using Planck and ACT", *A&A* 651 (2021), A73. arXiv: 2105.05607 [astro-ph.CO] (cit. on pp. 22, 23, 71).

[74] J. Sayers et al. “A Measurement of the Kinetic Sunyaev-Zel’dovich Signal Toward MACS J0717.5+3745”, *ApJ* 778.1 (2013), p. 52. arXiv: 1312.3680 [astro-ph.CO] (cit. on pp. 23, 28).

[75] J. Sayers et al. “A Comparison and Joint Analysis of Sunyaev-Zel’dovich Effect Measurements from Planck and Bolocam for a Set of 47 Massive Galaxy Clusters”, *ApJ* 832.1 (2016), p. 26. arXiv: 1605.03541 [astro-ph.CO] (cit. on p. 23).

[76] G. W. Pratt et al. “Temperature profiles of a representative sample of nearby X-ray galaxy clusters”, *A&A* 461.1 (2007), pp. 71–80. arXiv: astro-ph/0609480 [astro-ph] (cit. on pp. 22, 25).

[77] G. W. Pratt et al. “Gas entropy in a representative sample of nearby X-ray galaxy clusters (REXCESS): relationship to gas mass fraction”, *A&A* 511 (2010), A85. arXiv: 0909.3776 [astro-ph.CO] (cit. on pp. 22, 25, 72, 77, 79, 123, 125, 128).

[78] J. S. Sanders et al. “Hydrostatic Chandra X-ray analysis of SPT-selected galaxy clusters - I. Evolution of profiles and core properties”, *MNRAS* 474.1 (2018), pp. 1065–1098. arXiv: 1705.09299 [astro-ph.CO] (cit. on p. 22).

[79] F. Ruppin et al. “Stability of Cool Cores during Galaxy Cluster Growth: A Joint Chandra/SPT Analysis of 67 Galaxy Clusters along a Common Evolutionary Track Spanning 9 Gyr”, *ApJ* 918.2 (2021), p. 43. arXiv: 2012.14669 [astro-ph.CO] (cit. on p. 22).

[80] M. McDonald et al. “The Redshift Evolution of the Mean Temperature, Pressure, and Entropy Profiles in 80 SPT-Selected Galaxy Clusters”, *ApJ* 794.1 (2014), p. 67. arXiv: 1404.6250 [astro-ph.HE] (cit. on pp. 22, 71).

[81] T. Somboonpanyakul et al. “The Evolution of AGN Activity in Brightest Cluster Galaxies”, *AJ* 163.4 (2022), p. 146. arXiv: 2201.08398 [astro-ph.GA] (cit. on p. 22).

[82] M. Donahue et al. “Entropy Profiles in the Cores of Cooling Flow Clusters of Galaxies”, *ApJ* 643.2 (2006), pp. 730–750. arXiv: astro-ph/0511401 [astro-ph] (cit. on p. 22).

[83] M. McDonald et al. “Revisiting the Cooling Flow Problem in Galaxies, Groups, and Clusters of Galaxies”, *ApJ* 858.1 (2018), p. 45. arXiv: 1803.04972 [astro-ph.HE] (cit. on p. 23).

[84] B. R. McNamara and P. E. J. Nulsen. “Heating Hot Atmospheres with Active Galactic Nuclei”, *ARA&A* 45.1 (2007), pp. 117–175. arXiv: 0709.2152 [astro-ph] (cit. on p. 23).

[85] M. J. West et al. “Ten billion years of brightest cluster galaxy alignments”, *Nature Astronomy* 1 (2017), p. 0157. arXiv: 1706.03798 [astro-ph.GA] (cit. on p. 23).

[86] S. Ansarifard et al. “The Three Hundred Project: Correcting for the hydrostatic-equilibrium mass bias in X-ray and SZ surveys”, *A&A* 634 (2020), A113. arXiv: 1911.07878 [astro-ph.CO] (cit. on pp. 23, 41, 121).

[87] W. Cui et al. “On the dynamical state of galaxy clusters: insights from cosmological simulations - II.”, *MNRAS* 464.2 (2017), pp. 2502–2510. arXiv: 1605.07617 [astro-ph.GA] (cit. on p. 23).

[88] F. De Luca et al. “The Three Hundred project: dynamical state of galaxy clusters and morphology from multiwavelength synthetic maps”, *MNRAS* 504.4 (2021), pp. 5383–5400. arXiv: 2011.09002 [astro-ph.CO] (cit. on pp. 23, 177, 182).

[89] M. Rossetti et al. “Measuring the dynamical state of Planck SZ-selected clusters: X-ray peak - BCG offset”, *MNRAS* 457.4 (2016), pp. 4515–4524. arXiv: 1512.00410 [astro-ph.CO] (cit. on p. 23).

[90] S. Amodeo et al. “The relation between mass and concentration in X-ray galaxy clusters at high redshift”, *A&A* 590 (2016), A126. arXiv: 1604.02163 [astro-ph.CO] (cit. on pp. 23, 159).

[91] G. Gianfagna et al. “A study of the hydrostatic mass bias dependence and evolution within The Three Hundred clusters”, *MNRAS* 518.3 (2023), pp. 4238–4248. arXiv: 2211.08372 [astro-ph.CO] (cit. on pp. 23, 164).

[92] R. Wicker et al. "A VLT/VIMOS view of two *Planck* multiple-cluster systems: structure and galaxy properties", *arXiv e-prints* (2023). arXiv: 2304.03058 [astro-ph.CO] (cit. on p. 24).

[93] A. Jiménez Muñoz et al. "THE THREE HUNDRED project: Contrasting clusters galaxy density in hydrodynamical and dark matter only simulations", *mm Universe @ NIKA2 - Observing the mm Universe with the NIKA2 Camera*. Vol. 257. 2022, p. 00022 (cit. on p. 24).

[94] Euclid Collaboration et al. "Euclid preparation. III. Galaxy cluster detection in the wide photometric survey, performance and algorithm selection", *A&A* 627 (2019), A23. arXiv: 1906.04707 [astro-ph.CO] (cit. on p. 24).

[95] E. S. Rykoff et al. "The RedMaPPer Galaxy Cluster Catalog From DES Science Verification Data", *ApJS* 224.1 (2016), p. 1. arXiv: 1601.00621 [astro-ph.CO] (cit. on pp. 24, 31).

[96] T. M. C. Abbott et al. "Dark Energy Survey Year 1 Results: Cosmological constraints from cluster abundances and weak lensing", *Phys. Rev. D* 102.2 (2020), p. 023509. arXiv: 2002.11124 [astro-ph.CO] (cit. on pp. 24, 32).

[97] S. A. Smee et al. "The Multi-object, Fiber-fed Spectrographs for the Sloan Digital Sky Survey and the Baryon Oscillation Spectroscopic Survey", *AJ* 146.2 (2013), p. 32. arXiv: 1208.2233 [astro-ph.IM] (cit. on p. 24).

[98] M. Levi et al. "The DESI Experiment, a whitepaper for Snowmass 2013", *arXiv e-prints* (2013). arXiv: 1308.0847 [astro-ph.CO] (cit. on p. 24).

[99] D. Bina et al. "MUSE observations of the lensing cluster Abell 1689", *A&A* 590 (2016), A14. arXiv: 1603.05833 [astro-ph.GA] (cit. on p. 24).

[100] LSST Dark Energy Science Collaboration. "Large Synoptic Survey Telescope: Dark Energy Science Collaboration", *arXiv e-prints* (2012). arXiv: 1211.0310 [astro-ph.CO] (cit. on p. 24).

[101] B. Sartoris et al. "Next generation cosmology: constraints from the Euclid galaxy cluster survey", *MNRAS* 459.2 (2016), pp. 1764–1780. arXiv: 1505.02165 [astro-ph.CO] (cit. on p. 24).

[102] LSST Science Collaboration et al. "LSST Science Book, Version 2.0", *arXiv e-prints* (2009). arXiv: 0912.0201 [astro-ph.IM] (cit. on p. 24).

[103] H. Böhringer and N. Werner. "X-ray spectroscopy of galaxy clusters: studying astrophysical processes in the largest celestial laboratories", *A&AR* 18.1-2 (2010), pp. 127–196 (cit. on p. 24).

[104] S. Maurogordato et al. "Merging history of three bimodal clusters", *A&A* 525 (2011), A79. arXiv: 1009.1967 [astro-ph.CO] (cit. on p. 25).

[105] I. Bartalucci et al. "Resolving the hydrostatic mass profiles of galaxy clusters at $z \sim 1$ with XMM-Newton and Chandra", *A&A* 617 (2018), A64. arXiv: 1803.07556 [astro-ph.CO] (cit. on pp. 25, 79, 109, 129, 131, 137, 155, 157).

[106] G. W. Pratt et al. "Galaxy cluster X-ray luminosity scaling relations from a representative local sample (REXCESS)", *A&A* 498.2 (2009), pp. 361–378. arXiv: 0809.3784 [astro-ph] (cit. on pp. 25, 133).

[107] D. S. Hudson et al. "What is a cool-core cluster? a detailed analysis of the cores of the X-ray flux-limited HIFLUGCS cluster sample", *A&A* 513 (2010), A37. arXiv: 0911.0409 [astro-ph.CO] (cit. on p. 25).

[108] D. Eckert, S. Molendi, and S. Paltani. "The cool-core bias in X-ray galaxy cluster samples. I. Method and application to HIFLUGCS", *A&A* 526 (2011), A79. arXiv: 1011.3302 [astro-ph.CO] (cit. on p. 25).

[109] M. Rossetti et al. "The cool-core state of Planck SZ-selected clusters versus X-ray-selected samples: evidence for cool-core bias", *MNRAS* 468.2 (2017), pp. 1917–1930. arXiv: 1702.06961 [astro-ph.CO] (cit. on p. 25).

[110] A. Merloni et al. “eROSITA Science Book: Mapping the Structure of the Energetic Universe”, *arXiv e-prints* (2012). arXiv: 1209.3114 [astro-ph.HE] (cit. on p. 25).

[111] K. Nandra et al. “The Hot and Energetic Universe: A White Paper presenting the science theme motivating the Athena+ mission”, *arXiv e-prints* (2013). arXiv: 1306.2307 [astro-ph.HE] (cit. on p. 25).

[112] R. A. Sunyaev and Y. B. Zeldovich. “The Observations of Relic Radiation as a Test of the Nature of X-Ray Radiation from the Clusters of Galaxies”, *Comments on Astro. and Space Physics* 4 (1972), p. 173 (cit. on pp. 25, 26, 76).

[113] T. Mroczkowski et al. “Astrophysics with the Spatially and Spectrally Resolved Sunyaev-Zeldovich Effects. A Millimetre/Submillimetre Probe of the Warm and Hot Universe”, *Space Sci. Rev.* 215.1 (2019), p. 17. arXiv: 1811.02310 [astro-ph.CO] (cit. on pp. 26–29).

[114] R. A. Sunyaev and Y. B. Zeldovich. “Microwave background radiation as a probe of the contemporary structure and history of the universe”, *ARA&A* 18 (1980), pp. 537–560 (cit. on pp. 26, 27).

[115] M. Birkinshaw. “The Sunyaev-Zel’dovich effect”, *Phys. Rep.* 310.2-3 (1999), pp. 97–195. arXiv: astro-ph/9808050 [astro-ph] (cit. on p. 26).

[116] A. S. Kompaneets. “The Establishment of Thermal Equilibrium between Quanta and Electrons”, *Soviet Journal of Experimental and Theoretical Physics* 4.5 (1957), pp. 730–737 (cit. on p. 26).

[117] Planck Collaboration et al. “Planck intermediate results. V. Pressure profiles of galaxy clusters from the Sunyaev-Zeldovich effect”, *A&A* 550 (2013), A131. arXiv: 1207.4061 [astro-ph.CO] (cit. on p. 28).

[118] C. E. Romero et al. “Galaxy Cluster Pressure Profiles as Determined by Sunyaev Zel’dovich Effect Observations with MUSTANG and Bolocam. II. Joint Analysis of 14 Clusters”, *ApJ* 838.2 (2017), p. 86. arXiv: 1608.03980 [astro-ph.CO] (cit. on pp. 28, 80, 111, 112, 199, 201).

[119] R. Adam et al. “Pressure distribution of the high-redshift cluster of galaxies CL J1226.9+3332 with NIKA”, *A&A* 576 (2015), A12. arXiv: 1410.2808 [astro-ph.CO] (cit. on pp. 28, 29, 40, 49, 61, 67, 77, 79, 80, 85–87, 89–91).

[120] R. Adam et al. “Mapping the hot gas temperature in galaxy clusters using X-ray and Sunyaev-Zel’dovich imaging”, *A&A* 606 (2017), A64. arXiv: 1706.10230 [astro-ph.CO] (cit. on p. 28).

[121] R. A. Sunyaev and Y. B. Zeldovich. “The velocity of clusters of galaxies relative to the microwave background - The possibility of its measurement.”, *MNRAS* 190 (1980), pp. 413–420 (cit. on p. 28).

[122] T. Mroczkowski et al. “A Multi-wavelength Study of the Sunyaev-Zel’dovich Effect in the Triple-merger Cluster MACS J0717.5+3745 with MUSTANG and Bolocam”, *ApJ* 761.1 (2012), p. 47. arXiv: 1205.0052 [astro-ph.CO] (cit. on p. 28).

[123] R. Adam et al. “Mapping the kinetic Sunyaev-Zel’dovich effect toward MACS J0717.5+3745 with NIKA”, *A&A* 598 (2017), A115. arXiv: 1606.07721 [astro-ph.CO] (cit. on p. 29).

[124] A. Monfardini et al. “A Dual-band Millimeter-wave Kinetic Inductance Camera for the IRAM 30 m Telescope”, *ApJS* 194.2 (2011), p. 24. arXiv: 1102.0870 [astro-ph.IM] (cit. on pp. 29, 49, 86).

[125] R. Adam et al. “Substructure and merger detection in resolved NIKA Sunyaev-Zel’dovich images of distant clusters”, *A&A* 614 (2018), A118. arXiv: 1712.01836 [astro-ph.CO] (cit. on pp. 29, 49, 86).

[126] H. Tanimura, S. Zaroubi, and N. Aghanim. “Direct detection of the kinetic Sunyaev-Zel’dovich effect in galaxy clusters”, *A&A* 645 (2021), A112. arXiv: 2007.02952 [astro-ph.CO] (cit. on p. 29).

[127] A. Lewis and A. Challinor. “Weak gravitational lensing of the CMB”, *Phys. Rep.* 429.1 (2006), pp. 1–65. arXiv: astro-ph/0601594 [astro-ph] (cit. on p. 29).

[128] M. Zaldarriaga and U. Seljak. “Reconstructing projected matter density power spectrum from cosmic microwave background”, *Phys. Rev. D* 59.12 (1999), p. 123507. arXiv: astro-ph/9810257 [astro-ph] (cit. on p. 29).

[129] J.-B. Melin and J. G. Bartlett. "Measuring cluster masses with CMB lensing: a statistical approach", *A&A* 578 (2015), A21. arXiv: 1408.5633 [astro-ph.CO] (cit. on pp. 29, 39, 42).

[130] R. J. van Weeren et al. "Diffuse Radio Emission from Galaxy Clusters", *Space Sci. Rev.* 215.1 (2019), p. 16. arXiv: 1901.04496 [astro-ph.HE] (cit. on pp. 29, 30).

[131] M. Brüggen et al. "Magnetic Fields, Relativistic Particles, and Shock Waves in Cluster Outskirts", *Space Sci. Rev.* 166.1-4 (2012), pp. 187–213. arXiv: 1107.5223 [astro-ph.HE] (cit. on p. 29).

[132] E. Artis et al. "Massive merging cluster PSZ2G091 as seen by the NIKA2 camera", *arXiv e-prints* (2022). arXiv: 2204.14052 [astro-ph.CO] (cit. on p. 30).

[133] G. Di Gennaro et al. "The diffuse radio emission in the high-redshift cluster PSZ2 G091.83+26.11: total intensity and polarisation analysis with Very Large Array 1-4 GHz observations", *arXiv e-prints* (2023). arXiv: 2304.05893 [astro-ph.GA] (cit. on p. 30).

[134] D. Huterer et al. "Growth of cosmic structure: Probing dark energy beyond expansion", *Astroparticle Physics* 63 (2015), pp. 23–41. arXiv: 1309.5385 [astro-ph.CO] (cit. on p. 30).

[135] S. Ho, N. Bahcall, and P. Bode. "Cluster Ellipticities as a Cosmological Probe", *ApJ* 647.1 (2006), pp. 8–12. arXiv: astro-ph/0511776 [astro-ph] (cit. on p. 30).

[136] J. T. Wan et al. "Measuring H_0 using X-ray and SZ effect observations of dynamically relaxed galaxy clusters", *MNRAS* 504.1 (2021), pp. 1062–1076. arXiv: 2101.09389 [astro-ph.CO] (cit. on p. 30).

[137] D. Clowe et al. "A Direct Empirical Proof of the Existence of Dark Matter", *ApJL* 648.2 (2006), pp. L109–L113. arXiv: astro-ph/0608407 [astro-ph] (cit. on p. 30).

[138] G. Hurier et al. "Measurement of the $T_{\rm CMB}$ evolution from the Sunyaev-Zel'dovich effect", *A&A* 561 (2014), A143. arXiv: 1311.4694 [astro-ph.CO] (cit. on p. 30).

[139] E. Artis et al. "Impact of the calibration of the halo mass function on galaxy cluster number count cosmology", *A&A* 649 (2021), A47. arXiv: 2101.02501 [astro-ph.CO] (cit. on p. 31).

[140] A. Aguado-Barahona et al. "Velocity dispersion and dynamical masses for 388 galaxy clusters and groups. Calibrating the $M_{\rm SZ} - M_{\rm dyn}$ scaling relation for the PSZ2 sample", *A&A* 659 (2022), A126. arXiv: 2111.13071 [astro-ph.CO] (cit. on pp. 31, 39, 43, 44, 70, 85, 87, 89, 116, 118).

[141] M. Hilton et al. "The Atacama Cosmology Telescope: A Catalog of > 4000 Sunyaev-Zel'dovich Galaxy Clusters", *ApJS* 253.1 (2021), p. 3. arXiv: 2009.11043 [astro-ph.CO] (cit. on pp. 31, 32, 45, 70, 71, 163).

[142] Planck Collaboration et al. "Planck 2015 results. XXVII. The second Planck catalogue of Sunyaev-Zeldovich sources", *A&A* 594 (2016), A27. arXiv: 1502.01598 [astro-ph.CO] (cit. on pp. 31, 46, 66, 70, 71, 77, 85, 87, 89, 92, 96, 98, 101, 116–118, 120, 163).

[143] W. A. Watson et al. "The halo mass function through the cosmic ages", *MNRAS* 433.2 (2013), pp. 1230–1245. arXiv: 1212.0095 [astro-ph.CO] (cit. on p. 32).

[144] L. Salvati et al. "Combining Planck and SPT Cluster Catalogs: Cosmological Analysis and Impact on the Planck Scaling Relation Calibration", *ApJ* 934.2 (2022), p. 129. arXiv: 2112.03606 [astro-ph.CO] (cit. on p. 32).

[145] C. Garrel et al. "The XXL survey. XLVI. Forward cosmological analysis of the C1 cluster sample", *A&A* 663 (2022), A3. arXiv: 2109.13171 [astro-ph.CO] (cit. on p. 32).

[146] H. Böhringer et al. "The Extended Northern ROSAT Galaxy Cluster Survey (NORAS II). I. Survey Construction and First Results", *AJ* 153.5 (2017), p. 220. arXiv: 1704.06489 [astro-ph.CO] (cit. on p. 33).

[147] H. Böhringer, G. Chon, and C. A. Collins. "The extended ROSAT-ESO Flux Limited X-ray Galaxy Cluster Survey (REFLEX II). IV. X-ray luminosity function and first constraints on cosmological parameters", *A&A* 570 (2014), A31. arXiv: 1403.2927 [astro-ph.CO] (cit. on p. 33).

[148] Planck Collaboration et al. "Planck 2015 results. XXII. A map of the thermal Sunyaev-Zeldovich effect", *A&A* 594 (2016), A22. arXiv: 1502.01596 [astro-ph.CO] (cit. on pp. 33, 34).

[149] P. Ade et al. "The Simons Observatory: science goals and forecasts", *JCAP* 2019.2 (2019), p. 056. arXiv: 1808.07445 [astro-ph.CO] (cit. on p. 33).

[150] K. N. Abazajian et al. "CMB-S4 Science Book, First Edition", *arXiv e-prints* (2016). arXiv: 1610.02743 [astro-ph.CO] (cit. on p. 33).

[151] G. Hurier, J. F. Macías-Pérez, and S. Hildebrandt. "MILCA, a modified internal linear combination algorithm to extract astrophysical emissions from multifrequency sky maps", *A&A* 558 (2013), A118. arXiv: 1007.1149 [astro-ph.IM] (cit. on p. 34).

[152] M. Douspis et al. "Retrieving cosmological information from small-scale CMB foregrounds. I. The thermal Sunyaev Zel'dovich effect", *A&A* 659 (2022), A99. arXiv: 2109.03272 [astro-ph.CO] (cit. on p. 34).

[153] S. D. M. White and C. S. Frenk. "Galaxy Formation through Hierarchical Clustering", *ApJ* 379 (1991), p. 52 (cit. on p. 34).

[154] A. H. Gonzalez et al. "Galaxy Cluster Baryon Fractions Revisited", *ApJ* 778.1 (2013), p. 14. arXiv: 1309.3565 [astro-ph.CO] (cit. on p. 35).

[155] S. W. Allen et al. "Improved constraints on dark energy from Chandra X-ray observations of the largest relaxed galaxy clusters", *MNRAS* 383.3 (2008), pp. 879–896. arXiv: 0706.0033 [astro-ph] (cit. on p. 35).

[156] R. Wicker et al. "Constraining the mass and redshift evolution of the hydrostatic mass bias using the gas mass fraction in galaxy clusters", *A&A* 674 (2023), A48. arXiv: 2204.12823 [astro-ph.CO] (cit. on pp. 35, 43, 140, 142, 157).

[157] Planck Collaboration et al. "Planck 2013 results. XVI. Cosmological parameters", *A&A* 571 (2014), A16. arXiv: 1303.5076 [astro-ph.CO] (cit. on p. 36).

[158] X. Li et al. "Hyper Suprime-Cam Year 3 Results: Cosmology from Cosmic Shear Two-point Correlation Functions", *arXiv e-prints* (2023). arXiv: 2304.00702 [astro-ph.CO] (cit. on p. 36).

[159] H. Miyatake et al. "Hyper Suprime-Cam Year 3 Results: Cosmology from Galaxy Clustering and Weak Lensing with HSC and SDSS using the Emulator Based Halo Model", *arXiv e-prints* (2023). arXiv: 2304.00704 [astro-ph.CO] (cit. on p. 36).

[160] S. Sugiyama et al. "Hyper Suprime-Cam Year 3 Results: Cosmology from Galaxy Clustering and Weak Lensing with HSC and SDSS using the Minimal Bias Model", *arXiv e-prints* (2023). arXiv: 2304.00705 [astro-ph.CO] (cit. on p. 36).

[161] R. Dalal et al. "Hyper Suprime-Cam Year 3 Results: Cosmology from Cosmic Shear Power Spectra", *arXiv e-prints* (2023). arXiv: 2304.00701 [astro-ph.CO] (cit. on p. 36).

[162] M. S. Madhavacheril et al. "The Atacama Cosmology Telescope: DR6 Gravitational Lensing Map and Cosmological Parameters", *arXiv e-prints* (2023). arXiv: 2304.05203 [astro-ph.CO] (cit. on pp. 36, 38).

[163] F. J. Qu et al. "The Atacama Cosmology Telescope: A Measurement of the DR6 CMB Lensing Power Spectrum and its Implications for Structure Growth", *arXiv e-prints* (2023). arXiv: 2304.05202 [astro-ph.CO] (cit. on p. 36).

[164] A. Diaferio and M. J. Geller. "Infall Regions of Galaxy Clusters", *ApJ* 481.2 (1997), pp. 633–643. arXiv: astro-ph/9701034 [astro-ph] (cit. on p. 39).

[165] A. Biviano and M. Girardi. "The Mass Profile of Galaxy Clusters out to $\sim 2R_{200}$", *ApJ* 585.1 (2003), pp. 205–214. arXiv: astro-ph/0301439 [astro-ph] (cit. on p. 39).

[166] R. Wojtak et al. “Galaxy Cluster Mass Reconstruction Project - IV. Understanding the effects of imperfect membership on cluster mass estimation”, *MNRAS* 481.1 (2018), pp. 324–340. arXiv: 1806.03199 [astro-ph.CO] (cit. on p. 39).

[167] E. Munari et al. “The relation between velocity dispersion and mass in simulated clusters of galaxies: dependence on the tracer and the baryonic physics”, *MNRAS* 430.4 (2013), pp. 2638–2649. arXiv: 1301.1682 [astro-ph.CO] (cit. on pp. 39, 44).

[168] A. Ferragamo et al. “Velocity dispersion vs cluster mass: A new scaling law with THE THREE HUNDRED clusters”, *mm Universe @ NIKA2 - Observing the mm Universe with the NIKA2 Camera*. Vol. 257. 2022, p. 00018. arXiv: 2111.01724 [astro-ph.CO] (cit. on pp. 39, 44).

[169] Euclid Collaboration et al. “Euclid preparation. XXX. Evaluating the weak lensing cluster mass biases using the Three Hundred Project hydrodynamical simulations”, *arXiv e-prints* (2023). arXiv: 2302.00687 [astro-ph.CO] (cit. on pp. 39, 165–168, 170, 171, 174, 182, 184, 187).

[170] I. Zubeldia and A. Challinor. “Cosmological constraints from Planck galaxy clusters with CMB lensing mass bias calibration”, *MNRAS* 489.1 (2019), pp. 401–419. arXiv: 1904.07887 [astro-ph.CO] (cit. on pp. 40, 42).

[171] M. Madhavacheril et al. “Evidence of Lensing of the Cosmic Microwave Background by Dark Matter Halos”, *Phys. Rev. Lett.* 114.15 (2015), p. 151302. arXiv: 1411.7999 [astro-ph.CO] (cit. on p. 40).

[172] M. S. Madhavacheril et al. “The Atacama Cosmology Telescope: Weighing Distant Clusters with the Most Ancient Light”, *ApJL* 903.1 (2020), p. L13. arXiv: 2009.07772 [astro-ph.CO] (cit. on pp. 40, 136).

[173] E. J. Baxter et al. “A Measurement of Gravitational Lensing of the Cosmic Microwave Background by Galaxy Clusters Using Data from the South Pole Telescope”, *ApJ* 806.2 (2015), p. 247. arXiv: 1412.7521 [astro-ph.CO] (cit. on pp. 40, 42).

[174] T. Louis and D. Alonso. “Calibrating cluster number counts with CMB lensing”, *Phys. Rev. D* 95.4 (2017), p. 043517. arXiv: 1609.03997 [astro-ph.CO] (cit. on p. 40).

[175] S. Ettori et al. “Hydrostatic mass profiles in X-COP galaxy clusters”, *A&A* 621 (2019), A39. arXiv: 1805.00035 [astro-ph.CO] (cit. on pp. 40, 81, 98, 116, 122).

[176] M. E. Pessah and S. Chakraborty. “The Stability of Weakly Collisional Plasmas with Thermal and Composition Gradients”, *ApJ* 764.1 (2013), p. 13. arXiv: 1302.3351 [astro-ph.HE] (cit. on p. 40).

[177] F. Ruppin et al. “First Sunyaev-Zel’dovich mapping with the NIKA2 camera: Implication of cluster substructures for the pressure profile and mass estimate”, *A&A* 615 (2018), A112. arXiv: 1712.09587 [astro-ph.CO] (cit. on pp. 40, 53, 67, 72, 77, 79, 80, 99, 112, 113, 116, 120, 128).

[178] F. Kéruzoré et al. “Exploiting NIKA2/XMM-Newton imaging synergy for intermediate-mass high-z galaxy clusters within the NIKA2 SZ large program. Observations of ACT-CL J0215.4+0030 at $z \sim 0.9$”, *A&A* 644 (2020), A93. arXiv: 2009.02563 [astro-ph.CO] (cit. on pp. 40, 56, 67, 72, 77, 79, 80, 92, 99, 128).

[179] G. Gianfagna et al. “Exploring the hydrostatic mass bias in MUSIC clusters: application to the NIKA2 mock sample”, *MNRAS* 502.4 (2021), pp. 5115–5133. arXiv: 2010.03634 [astro-ph.CO] (cit. on pp. 41, 42, 121, 135, 164).

[180] S. R. Dicker et al. “MUSTANG: 90 GHz science with the Green Bank Telescope”, *Millimeter and Submillimeter Detectors and Instrumentation for Astronomy IV*. Ed. by W. D. Duncan et al. Vol. 7020. 2008, p. 702005. arXiv: 0907.1306 [astro-ph.IM] (cit. on p. 41).

[181] J. Glenn et al. “Bolocam: a millimeter-wave bolometric camera”, *Advanced Technology MMW, Radio, and Terahertz Telescopes*. Ed. by T. G. Phillips. Vol. 3357. 1998, pp. 326–334 (cit. on p. 41).

[182] S. R. Dicker et al. "MUSTANG2: a large focal plan array for the 100 meter Green Bank Telescope", *Millimeter, Submillimeter, and Far-Infrared Detectors and Instrumentation for Astronomy VII*. Ed. by W. S. Holland and J. Zmuidzinas. Vol. 9153. 2014, 91530J (cit. on p. 41).

[183] T. Kitayama et al. "The Sunyaev-Zel'dovich effect at 5": RX J1347.5-1145 imaged by ALMA", *PASJ* 68.5 (2016), p. 88. arXiv: 1607.08833 [astro-ph.CO] (cit. on pp. 41, 189).

[184] L. Salvati, M. Douspis, and N. Aghanim. "Constraints from thermal Sunyaev-Zel'dovich cluster counts and power spectrum combined with CMB", *A&A* 614 (2018), A13. arXiv: 1708.00697 [astro-ph.CO] (cit. on pp. 41, 42).

[185] E. T. Lau, D. Nagai, and K. Nelson. "Weighing Galaxy Clusters with Gas. I. On the Methods of Computing Hydrostatic Mass Bias", *ApJ* 777.2 (2013), p. 151. arXiv: 1306.3993 [astro-ph.CO] (cit. on p. 41).

[186] V. Biffi et al. "On the Nature of Hydrostatic Equilibrium in Galaxy Clusters", *ApJ* 827.2 (2016), p. 112. arXiv: 1606.02293 [astro-ph.CO] (cit. on p. 41).

[187] Planck Collaboration et al. "Planck 2013 results. XV. CMB power spectra and likelihood", *A&A* 571 (2014), A15. arXiv: 1303.5075 [astro-ph.CO] (cit. on p. 41).

[188] B. Bolliet et al. "Dark energy constraints from the thermal Sunyaev-Zeldovich power spectrum", *MNRAS* 477.4 (2018), pp. 4957–4967. arXiv: 1712.00788 [astro-ph.CO] (cit. on p. 42).

[189] M. Penna-Lima et al. "Calibrating the Planck cluster mass scale with CLASH", *A&A* 604 (2017), A89. arXiv: 1608.05356 [astro-ph.CO] (cit. on pp. 42, 118, 123).

[190] A. Ferragamo et al. "Comparison of hydrostatic and lensing cluster mass estimates: A pilot study in MACS J0647.7+7015", *A&A* 661 (2022), A65. arXiv: 2112.08298 [astro-ph.CO] (cit. on pp. 42, 104, 108, 113, 116, 123, 167, 168, 204).

[191] M. Muñoz-Echeverría et al. "Multi-probe analysis of the galaxy cluster CL J1226.9+3332. Hydrostatic mass and hydrostatic-to-lensing bias", *A&A* 671 (2023), A28. arXiv: 2209.07460 [astro-ph.CO] (cit. on pp. 42, 72, 85, 104, 108, 111, 117, 128, 167, 168, 204).

[192] A. Ferragamo et al. "Velocity dispersion and dynamical mass for 270 galaxy clusters in the Planck PSZ1 catalogue", *A&A* 655 (2021), A115. arXiv: 2109.04967 [astro-ph.CO] (cit. on pp. 42–44).

[193] L. Lovisari et al. "X-Ray Scaling Relations for a Representative Sample of Planck-selected Clusters Observed with XMM-Newton", *ApJ* 892.2 (2020), p. 102. arXiv: 2002.11740 [astro-ph.CO] (cit. on pp. 43, 152, 157, 158).

[194] L. Salvati et al. "Mass bias evolution in tSZ cluster cosmology", *A&A* 626 (2019), A27. arXiv: 1901.03096 [astro-ph.CO] (cit. on pp. 43, 140, 149).

[195] G. Hurier and F. Lacasa. "Combined analysis of galaxy cluster number count, thermal Sunyaev-Zel'dovich power spectrum, and bispectrum", *A&A* 604 (2017), A71. arXiv: 1701.09067 [astro-ph.CO] (cit. on p. 43).

[196] V. Biffi et al. "On the Nature of Hydrostatic Equilibrium in Galaxy Clusters", *ApJ* 827.2 (2016), p. 112. arXiv: 1606.02293 [astro-ph.CO] (cit. on p. 43).

[197] E. Rozo et al. "Constraining the Scatter in the Mass-richness Relation of maxBCG Clusters with Weak Lensing and X-ray Data", *ApJ* 699.1 (2009), pp. 768–781. arXiv: 0809.2794 [astro-ph] (cit. on p. 44).

[198] J. Ford et al. "CFHTLenS: a weak lensing shear analysis of the 3D-Matched-Filter galaxy clusters", *MNRAS* 447.2 (2015), pp. 1304–1318. arXiv: 1409.3571 [astro-ph.CO] (cit. on p. 44).

[199] P. Melchior et al. "Weak-lensing mass calibration of redMaPPer galaxy clusters in Dark Energy Survey Science Verification data", *MNRAS* 469.4 (2017), pp. 4899–4920. arXiv: 1610.06890 [astro-ph.CO] (cit. on p. 44).

[200] A. V. Kravtsov, A. Vikhlinin, and D. Nagai. "A New Robust Low-Scatter X-Ray Mass Indicator for Clusters of Galaxies", *ApJ* 650.1 (2006), pp. 128–136. arXiv: astro-ph/0603205 [astro-ph] (cit. on pp. 44, 154).

[201] S. R. Pike et al. "Cosmological simulations of galaxy clusters with feedback from active galactic nuclei: profiles and scaling relations", *MNRAS* 445.2 (2014), pp. 1774–1796. arXiv: 1409.0723 [astro-ph.CO] (cit. on p. 45).

[202] A. M. C. Le Brun et al. "Towards a realistic population of simulated galaxy groups and clusters", *MNRAS* 441.2 (2014), pp. 1270–1290. arXiv: 1312.5462 [astro-ph.CO] (cit. on p. 45).

[203] N. Truong et al. "Cosmological hydrodynamical simulations of galaxy clusters: X-ray scaling relations and their evolution", *MNRAS* 474.3 (2018), pp. 4089–4111. arXiv: 1607.00019 [astro-ph.CO] (cit. on pp. 45, 162).

[204] P. M. Motl et al. "The Integrated Sunyaev-Zeldovich Effect as a Superior Method for Measuring the Mass of Clusters of Galaxies", *ApJL* 623.2 (2005), pp. L63–L66. arXiv: astro-ph/0502226 [astro-ph] (cit. on p. 45).

[205] A. C. da Silva et al. "Hydrodynamical simulations of the Sunyaev-Zel'dovich effect: cluster scaling relations and X-ray properties", *MNRAS* 348.4 (2004), pp. 1401–1408. arXiv: astro-ph/0308074 [astro-ph] (cit. on p. 45).

[206] Planck Collaboration et al. "Planck early results. XI. Calibration of the local galaxy cluster Sunyaev-Zeldovich scaling relations", *A&A* 536 (2011), A11. arXiv: 1101.2026 [astro-ph.CO] (cit. on pp. 45, 72, 129).

[207] J.-B. Melin, J. G. Bartlett, and J. Delabrouille. "Catalog extraction in SZ cluster surveys: a matched filter approach", *A&A* 459.2 (2006), pp. 341–352. arXiv: astro-ph/0602424 [astro-ph] (cit. on p. 46).

[208] M. Simet et al. "Weak lensing measurement of the mass-richness relation of SDSS redMaPPer clusters", *MNRAS* 466.3 (2017), pp. 3103–3118. arXiv: 1603.06953 [astro-ph.CO] (cit. on p. 45).

[209] T. McClintock et al. "Dark Energy Survey Year 1 results: weak lensing mass calibration of redMaPPer galaxy clusters", *MNRAS* 482.1 (2019), pp. 1352–1378. arXiv: 1805.00039 [astro-ph.CO] (cit. on p. 45).

[210] S. Bocquet et al. "Mass Calibration and Cosmological Analysis of the SPT-SZ Galaxy Cluster Sample Using Velocity Dispersion σ_v and X-Ray Y_X Measurements", *ApJ* 799.2 (2015), p. 214. arXiv: 1407.2942 [astro-ph.CO] (cit. on p. 45).

[211] R. Adam et al. "The NIKA2 large-field-of-view millimetre continuum camera for the 30 m IRAM telescope", *A&A* 609 (2018), A115. arXiv: 1707.00908 [astro-ph.IM] (cit. on pp. 49, 50, 52, 56).

[212] O. Bourrion et al. "NIKEL_AMC: readout electronics for the NIKA2 experiment", *Journal of Instrumentation* 11.11 (2016), P11001. arXiv: 1602.01288 [astro-ph.IM] (cit. on pp. 49, 52).

[213] M. Calvo et al. "The NIKA2 Instrument, A Dual-Band Kilopixel KID Array for Millimetric Astronomy", *Journal of Low Temperature Physics* 184.3-4 (2016), pp. 816–823. arXiv: 1601.02774 [astro-ph.IM] (cit. on p. 49).

[214] J. W. M. Baars et al. "The IRAM 30-m millimeter radio telescope on Pico Veleta, Spain", *A&A* 175.1-2 (1987), pp. 319–326 (cit. on p. 50).

[215] J. R. Pardo, J. Cernicharo, and E. Serabyn. "Atmospheric transmission at microwaves (ATM): an improved model for millimeter/submillimeter applications", *IEEE Transactions on Antennas and Propagation* 49.12 (2001), pp. 1683–1694 (cit. on p. 50).

[216] L. Perotto et al. "Calibration and performance of the NIKA2 camera at the IRAM 30-m Telescope", *A&A* 637 (2020), A71. arXiv: 1910.02038 [astro-ph.IM] (cit. on pp. 51–53, 55–58, 61, 74, 76, 95).

[217] P. K. Day et al. “A broadband superconducting detector suitable for use in large arrays”, *Nature* 425.6960 (2003), pp. 817–821 (cit. on p. 51).

[218] J. Bardeen, L. N. Cooper, and J. R. Schrieffer. “Theory of Superconductivity”, *Physical Review* 108.5 (1957), pp. 1175–1204 (cit. on p. 51).

[219] M. Roesch et al. “Development of Lumped Element Kinetic Inductance Detectors for NIKA”, *arXiv e-prints* (2012). arXiv: 1212.4585 [astro-ph.IM] (cit. on p. 52).

[220] W. B. Landsman. “The IDL Astronomy User’s Library”, *Astronomical Data Analysis Software and Systems II*. Ed. by R. J. Hanisch, R. J. V. Brissenden, and J. Barnes. Vol. 52. 1993, p. 246 (cit. on p. 53).

[221] R. Adam et al. “First observation of the thermal Sunyaev-Zel’dovich effect with kinetic inductance detectors”, *A&A* 569 (2014), A66. arXiv: 1310.6237 [astro-ph.CO] (cit. on pp. 53, 60, 75, 76).

[222] H. Roussel et al. “NIKA2 mapping and cross-instrument SED extraction of extended sources with Scanamorphos”, *mm Universe @ NIKA2 - Observing the mm Universe with the NIKA2 Camera*. Vol. 228. 2020, p. 00024. arXiv: 1911.03192 [astro-ph.IM] (cit. on p. 54).

[223] A. Catalano et al. “Performance and calibration of the NIKA camera at the IRAM 30 m telescope”, *A&A* 569 (2014), A9. arXiv: 1402.0260 [astro-ph.IM] (cit. on pp. 56, 58, 111).

[224] M. Calvo et al. “Improved mm-wave photometry for kinetic inductance detectors”, *A&A* 551 (2013), p. L12 (cit. on p. 57).

[225] R. Adam et al. “High angular resolution Sunyaev-Zel’dovich observations of MACS J1423.8+2404 with NIKA: Multiwavelength analysis”, *A&A* 586 (2016), A122. arXiv: 1510.06674 [astro-ph.CO] (cit. on pp. 66, 74, 114, 115).

[226] B. Comis et al. “High angular resolution SZ observations with NIKA and NIKA2”, *arXiv e-prints* (2016). arXiv: 1605.09549 [astro-ph.CO] (cit. on p. 69).

[227] J. F. Macias-Pérez et al. “NIKA2: a mm camera for cluster cosmology”, *Proceedings of the European Physical Society Conference on High Energy Physics. 5-12 July*. 2017, p. 42. arXiv: 1711.07088 [astro-ph.CO] (cit. on p. 69).

[228] F. Mayet et al. “Cluster cosmology with the NIKA2 SZ Large Program”, *mm Universe @ NIKA2 - Observing the mm Universe with the NIKA2 Camera*. Vol. 228. 2020, p. 00017. arXiv: 1911.03145 [astro-ph.CO] (cit. on p. 69).

[229] L. Perotto et al. “The NIKA2 Sunyaev-Zeldovich Large Program: Precise galaxy cluster physics for an accurate cluster-based cosmology”, *mm Universe @ NIKA2 - Observing the mm Universe with the NIKA2 Camera*. Vol. 257. 2022, p. 00038. arXiv: 2111.01729 [astro-ph.CO] (cit. on p. 69).

[230] L. E. Bleem et al. “The SPTpol Extended Cluster Survey”, *ApJS* 247.1 (2020), p. 25. arXiv: 1910.04121 [astro-ph.CO] (cit. on pp. 70, 71).

[231] L. E. Bleem et al. “Galaxy Clusters Discovered via the Sunyaev-Zel’dovich Effect in the 2500-Square-Degree SPT-SZ Survey”, *ApJS* 216.2 (2015), p. 27. arXiv: 1409.0850 [astro-ph.CO] (cit. on p. 70).

[232] F. Ruppin. “Cosmologie via les observations d’amas de galaxies par effet Sunyaev-Zel’dovich avec NIKA2”. PhD thesis. Université Grenoble Alpes, 2018. Link (cit. on pp. 71, 73).

[233] R. Barrena et al. “Optical validation and characterisation of Planck PSZ1 sources at the Canary Islands observatories. II. Second year of ITP13 observations”, *A&A* 638 (2020), A146. arXiv: 2004.07913 [astro-ph.CO] (cit. on p. 70).

[234] W. Cui et al. “The Three Hundred project: a large catalogue of theoretically modelled galaxy clusters for cosmological and astrophysical applications”, *MNRAS* 480.3 (2018), pp. 2898–2915. arXiv: 1809.04622 [astro-ph.GA] (cit. on pp. 71, 162, 165, 170, 171, 184–186).

[235] M. Hilton et al. “The Atacama Cosmology Telescope: The Two-season ACTPol Sunyaev-Zel’dovich Effect Selected Cluster Catalog”, *ApJS* 235.1 (2018), p. 20. arXiv: 1709.05600 [astro-ph.CO] (cit. on p. 71).

[236] V. Ghirardini et al. "Evolution of the Thermodynamic Properties of Clusters of Galaxies out to Redshift of 1.8", *ApJ* 910.1 (2021), p. 14. arXiv: 2004.04747 [astro-ph.CO] (cit. on p. 71).

[237] F. Ruppin et al. "Impact of the mean pressure profile of galaxy clusters on the cosmological constraints from the Planck tSZ power spectrum", *MNRAS* 490.1 (2019), pp. 784–796. arXiv: 1905.05129 [astro-ph.CO] (cit. on p. 71).

[238] A. Saro et al. "Optical-SZE scaling relations for DES optically selected clusters within the SPT-SZ Survey", *MNRAS* 468.3 (2017), pp. 3347–3360. arXiv: 1605.08770 [astro-ph.CO] (cit. on p. 72).

[239] L. Salvati, M. Douspis, and N. Aghanim. "Impact of systematics on cosmological parameters from future galaxy cluster surveys", *A&A* 643 (2020), A20. arXiv: 2005.10204 [astro-ph.CO] (cit. on p. 72).

[240] G. M. Voit et al. "Modified Entropy Models for the Intracluster Medium", *ApJ* 576.2 (2002), pp. 601–624. arXiv: astro-ph/0205240 [astro-ph] (cit. on p. 72).

[241] F. Ruppin et al. "Non-parametric deprojection of NIKA SZ observations: Pressure distribution in the Planck-discovered cluster PSZ1 G045.85+57.71", *A&A* 597 (2017), A110. arXiv: 1607.07679 [astro-ph.CO] (cit. on pp. 74, 76).

[242] H. Dembinski et al. *scikit-hep/iminuit: v1.4.9*. 2020. Link (cit. on p. 74).

[243] D. Foreman-Mackey et al. "emcee v3: A Python ensemble sampling toolkit for affine-invariant MCMC", *The Journal of Open Source Software* 4.43 (2019), p. 1864. arXiv: 1911.07688 [astro-ph.IM] (cit. on pp. 75, 140).

[244] J. Goodman and J. Weare. "Ensemble samplers with affine invariance", *Communications in Applied Mathematics and Computational Science* 5.1 (2010), pp. 65–80 (cit. on pp. 75, 140).

[245] F.-X. Désert et al. "Submillimetre point sources from the Archeops experiment: very cold clumps in the Galactic plane", *A&A* 481.2 (2008), pp. 411–421. arXiv: 0801.4502 [astro-ph] (cit. on p. 75).

[246] B. Magnelli et al. "A Herschel view of the far-infrared properties of submillimetre galaxies", *A&A* 539 (2012), A155. arXiv: 1202.0761 [astro-ph.CO] (cit. on p. 75).

[247] M. T. Hogan et al. "A comprehensive study of the radio properties of brightest cluster galaxies", *MNRAS* 453.2 (2015), pp. 1201–1222. arXiv: 1507.03019 [astro-ph.GA] (cit. on p. 75).

[248] R. L. White et al. "A Catalog of 1.4 GHz Radio Sources from the FIRST Survey", *ApJ* 475.2 (1997), pp. 479–493 (cit. on pp. 76, 92).

[249] J. J. Condon et al. "The NRAO VLA Sky Survey", *AJ* 115.5 (1998), pp. 1693–1716 (cit. on p. 76).

[250] J. J. Condon. "Cosmological evolution of radio sources.", *ApJ* 287 (1984), pp. 461–474 (cit. on p. 76).

[251] C. Romero et al. "A multi-instrument non-parametric reconstruction of the electron pressure profile in the galaxy cluster CLJ1226.9+3332", *A&A* 612 (2018), A39. arXiv: 1707.06113 [astro-ph.CO] (cit. on pp. 76, 86, 199, 201).

[252] F. Kéruzoré et al. "panco2: a Python library to measure intracluster medium pressure profiles from Sunyaev-Zeldovich observations", *The Open Journal of Astrophysics* 6 (2023), p. 9. arXiv: 2212.01439 [astro-ph.IM] (cit. on p. 77).

[253] A. Gelman and D. B. Rubin. "Inference from Iterative Simulation Using Multiple Sequences", *Statistical Science* 7 (1992), pp. 457–472 (cit. on pp. 77, 109, 143).

[254] I. Bartalucci et al. "Resolving galaxy cluster gas properties at $z \sim 1$ with XMM-Newton and Chandra", *A&A* 598 (2017), A61. arXiv: 1610.01899 [astro-ph.CO] (cit. on pp. 77, 79, 80, 128, 129).

[255] J. H. Croston et al. "An improved deprojection and PSF-deconvolution technique for galaxy-cluster X-ray surface-brightness profiles", *A&A* 459.3 (2006), pp. 1007–1019. arXiv: astro-ph/0608700 [astro-ph] (cit. on p. 79).

[256] J. Démoclès et al. "Testing adiabatic contraction of dark matter in fossil group candidates", *A&A* 517 (2010), A52. arXiv: 1005.0320 [astro-ph.CO] (cit. on p. 80).

[257] S. Ettori et al. "Mass Profiles of Galaxy Clusters from X-ray Analysis", *Space Science Reviews* 177.1-4 (2013), pp. 119–154. arXiv: 1303.3530 [astro-ph.CO] (cit. on p. 81).

[258] D. Eckert et al. "The gravitational field of X-COP galaxy clusters", *A&A* 662 (2022), A123. arXiv: 2205.01110 [astro-ph.CO] (cit. on pp. 81, 98, 123, 157).

[259] A. Mahdavi et al. "Joint Analysis of Cluster Observations. II. Chandra/XMM-Newton X-Ray and Weak Lensing Scaling Relations for a Sample of 50 Rich Clusters of Galaxies", *ApJ* 767.2 (2013), p. 116. arXiv: 1210.3689 [astro-ph.CO] (cit. on pp. 82, 130, 134, 137, 146, 157).

[260] H. Israel et al. "The 400d Galaxy Cluster Survey weak lensing programme. III. Evidence for consistent WL and X-ray masses at $z \approx 0.5$", *A&A* 564 (2014), A129. arXiv: 1402.3267 [astro-ph.CO] (cit. on pp. 82, 130, 157).

[261] H. Ebeling et al. "Discovery of a Very X-Ray Luminous Galaxy Cluster at Z=0.89 in the Wide Angle ROSAT Pointed Survey", *ApJL* 548.1 (2001), pp. L23–L27. arXiv: astro-ph/0012175 [astro-ph] (cit. on p. 85).

[262] B. J. Maughan et al. "An XMM-Newton observation of the massive, relaxed galaxy cluster CL J1226.9+3332 at $z = 0.89$", *MNRAS* 351.4 (2004), pp. 1193–1203. arXiv: astro-ph/0403521 [astro-ph] (cit. on pp. 85–87).

[263] M. Bonamente et al. "Determination of the Cosmic Distance Scale from Sunyaev-Zel'dovich Effect and Chandra X-Ray Measurements of High-Redshift Galaxy Clusters", *ApJ* 647.1 (2006), pp. 25–54. arXiv: astro-ph/0512349 [astro-ph] (cit. on p. 85).

[264] M. J. Jee and J. A. Tyson. "Dark Matter in the Galaxy Cluster CL J1226+3332 at $z = 0.89$", *ApJ* 691.2 (2009), pp. 1337–1347. arXiv: 0810.0709 [astro-ph] (cit. on pp. 85–87, 89, 90, 102, 116).

[265] T. Mroczkowski et al. "Application of a Self-Similar Pressure Profile to Sunyaev-Zel'dovich Effect Data from Galaxy Clusters", *ApJ* 694.2 (2009), pp. 1034–1044. arXiv: 0809.5077 [astro-ph] (cit. on pp. 85–87, 101, 195, 200).

[266] P. M. Korngut et al. "MUSTANG High Angular Resolution Sunyaev-Zel'dovich Effect Imaging of Substructure in Four Galaxy Clusters", *ApJ* 734.1 (2011), p. 10. arXiv: 1010.5494 [astro-ph.CO] (cit. on pp. 85, 86, 90, 195, 198).

[267] K. W. Cavagnolo et al. "Intracluster Medium Entropy Profiles for a Chandra Archival Sample of Galaxy Clusters", *ApJS* 182.1 (2009), pp. 12–32. arXiv: 0902.1802 [astro-ph.CO] (cit. on pp. 85, 89, 111).

[268] B. P. Holden et al. "The Ellipticities of Cluster Early-type Galaxies from $z \sim 1$ to $z \sim 0$: No Evolution in the Overall Distribution of Bulge-to-Disk Ratios", *ApJ* 693.1 (2009), pp. 617–633. arXiv: 0811.1986 [astro-ph] (cit. on pp. 85, 92).

[269] M. Joy et al. "Sunyaev-Zeldovich Effect Imaging of Massive Clusters of Galaxies at Redshift $z > 0.8$", *ApJL* 551.1 (2001), pp. L1–L4. arXiv: astro-ph/0012052 [astro-ph] (cit. on pp. 86, 87, 200).

[270] B. J. Maughan et al. "Deep XMM-Newton and Chandra Observations of Cl J1226.9+3332: A Detailed X-Ray Mass Analysis of a $z = 0.89$ Galaxy Cluster", *ApJ* 659.2 (2007), pp. 1125–1137. arXiv: astro-ph/0609690 [astro-ph] (cit. on pp. 86, 87, 89, 90, 101).

[271] A. Zitrin et al. "Hubble Space Telescope Combined Strong and Weak Lensing Analysis of the CLASH Sample: Mass and Magnification Models and Systematic Uncertainties", *ApJ* 801.1 (2015), p. 44. arXiv: 1411.1414 [astro-ph.CO] (cit. on pp. 86, 90, 103, 107–109).

[272] A. Mantz et al. "The observed growth of massive galaxy clusters - II. X-ray scaling relations", *MNRAS* 406.3 (2010), pp. 1773–1795. arXiv: 0909.3099 [astro-ph.CO] (cit. on pp. 86, 87, 101).

[273] T. Mroczkowski. "A New Approach to Obtaining Cluster Mass from Sunyaev-Zel'dovich Effect Observations", *ApJL* 728.2 (2011), p. L35. arXiv: 1101.2176 [astro-ph.CO] (cit. on pp. 86, 87, 89, 116).

[274] T. Mroczkowski. "Erratum: "A New Approach to Obtaining Cluster Mass from Sunyaev-Zel'dovich Effect Observations"", *ApJL* 746.2 (2012), p. L29 (cit. on pp. 86, 87, 89, 116).

[275] S. Muchovej et al. "Observations of High-Redshift X-Ray Selected Clusters with the Sunyaev-Zel'dovich Array", *ApJ* 663.2 (2007), pp. 708–716. arXiv: astro-ph/0610115 [astro-ph] (cit. on pp. 86, 87, 89, 189, 200).

[276] G. E. Bulbul et al. "An Analytic Model of the Physical Properties of Galaxy Clusters", *ApJ* 720.2 (2010), pp. 1038–1044. arXiv: 0911.2827 [astro-ph.CO] (cit. on pp. 87, 89, 101).

[277] F. Castagna and S. Andreon. "JoXSZ: Joint X-SZ fitting code for galaxy clusters", *A&A* 639 (2020), A73. arXiv: 2005.12315 [astro-ph.IM] (cit. on pp. 87, 89).

[278] M. J. Jee et al. "Scaling Relations and Overabundance of Massive Clusters at $z > 1$ from Weak-lensing Studies with the Hubble Space Telescope", *ApJ* 737.2 (2011), p. 59. arXiv: 1105.3186 [astro-ph.CO] (cit. on pp. 87, 159).

[279] J. Merten et al. "CLASH: The Concentration-Mass Relation of Galaxy Clusters", *ApJ* 806.1 (2015), p. 4. arXiv: 1404.1376 [astro-ph.CO] (cit. on pp. 87, 89, 108, 116, 119, 131, 156).

[280] M. Sereno and G. Covone. "The mass-concentration relation in massive galaxy clusters at redshift ~1", *MNRAS* 434.1 (2013), pp. 878–887. arXiv: 1306.6096 [astro-ph.CO] (cit. on pp. 87, 89, 116).

[281] M. Sereno. "CoMaLit - III. Literature catalogues of weak lensing clusters of galaxies (LC^2)", *MNRAS* 450.4 (2015), pp. 3665–3674. arXiv: 1409.5435 [astro-ph.CO] (cit. on pp. 87, 89, 116–119, 128).

[282] I. Cagnoni et al. "1WGA J1226.9+3332: A High-Redshift Cluster Discovered by Chandra", *ApJ* 560.1 (2001), pp. 86–91. arXiv: astro-ph/0106066 [astro-ph] (cit. on p. 86).

[283] J. Sayers et al. "The Contribution of Radio Galaxy Contamination to Measurements of the Sunyaev-Zel'dovich Decrement in Massive Galaxy Clusters at 140 GHz with Bolocam", *ApJ* 764.2 (2013), p. 152. arXiv: 1209.5129 [astro-ph.CO] (cit. on pp. 92, 195).

[284] E. Pointecouteau, M. Arnaud, and G. W. Pratt. "The structural and scaling properties of nearby galaxy clusters. I. The universal mass profile", *A&A* 435.1 (2005), pp. 1–7. arXiv: astro-ph/0501635 [astro-ph] (cit. on p. 98).

[285] M. Postman et al. "The Cluster Lensing and Supernova Survey with Hubble: An Overview", *ApJS* 199.2 (2012), p. 25. arXiv: 1106.3328 [astro-ph.CO] (cit. on pp. 103, 107).

[286] M. Bartelmann. "TOPICAL REVIEW Gravitational lensing", *Classical and Quantum Gravity* 27.23 (2010), p. 233001. arXiv: 1010.3829 [astro-ph.CO] (cit. on p. 104).

[287] M. Bartelmann and P. Schneider. "Weak gravitational lensing", *Phys. Rep.* 340.4-5 (2001), pp. 291–472. arXiv: astro-ph/9912508 [astro-ph] (cit. on pp. 104, 106).

[288] C.-Y. Chen, C.-Y. Hwang, and C.-M. Ko. "Ellipticities of Elliptical Galaxies in Different Environments", *ApJ* 830.2 (2016), p. 123 (cit. on p. 106).

[289] Euclid Collaboration et al. "Euclid preparation. XXVI. The Euclid Morphology Challenge: Towards structural parameters for billions of galaxies", *A&A* 671 (2023), A102. arXiv: 2209.12907 [astro-ph.GA] (cit. on p. 106).

[290] M. R. Becker and A. V. Kravtsov. "On the Accuracy of Weak-lensing Cluster Mass Reconstructions", *ApJ* 740.1 (2011), p. 25. arXiv: 1011.1681 [astro-ph.CO] (cit. on pp. 106, 159, 166, 167, 186, 187).

[291] R. Mandelbaum. "Instrumental systematics and weak gravitational lensing", *Journal of Instrumentation* 10.5 (2015), p. C05017. arXiv: 1503.08680 [astro-ph.IM] (cit. on p. 106).

[292] S. Grandis et al. “Calibration of bias and scatter involved in cluster mass measurements using optical weak gravitational lensing”, *MNRAS* 507.4 (2021), pp. 5671–5689. arXiv: 2103.16212 [astro-ph.CO] (cit. on p. 106).

[293] M. W. Sommer et al. “Weak lensing mass modeling bias and the impact of miscentring”, *MNRAS* 509.1 (2022), pp. 1127–1146. arXiv: 2105.08027 [astro-ph.CO] (cit. on p. 106).

[294] G. B. Caminha et al. “Strong lensing models of eight CLASH clusters from extensive spectroscopy: Accurate total mass reconstructions in the cores”, *A&A* 632 (2019), A36. arXiv: 1903.05103 [astro-ph.GA] (cit. on p. 107).

[295] C. Fox et al. “The Strongest Cluster Lenses: An Analysis of the Relation between Strong Gravitational Lensing Strength and the Physical Properties of Galaxy Clusters”, *ApJ* 928.1 (2022), p. 87. arXiv: 2104.05585 [astro-ph.CO] (cit. on p. 107).

[296] A. Zitrin et al. “New multiply-lensed galaxies identified in ACS/NIC3 observations of CL0024+1654 using an improved mass model”, *MNRAS* 396.4 (2009), pp. 1985–2002. arXiv: 0902.3971 [astro-ph.CO] (cit. on p. 108).

[297] A. Zitrin et al. “A Highly Elongated Prominent Lens at $z = 0.87$: First Strong-lensing Analysis of El Gordo”, *ApJL* 770.1 (2013), p. L15. arXiv: 1304.0455 [astro-ph.CO] (cit. on p. 108).

[298] A. Zitrin et al. “CLASH: The Enhanced Lensing Efficiency of the Highly Elongated Merging Cluster MACS J0416.1-2403”, *ApJL* 762.2 (2013), p. L30. arXiv: 1211.2797 [astro-ph.CO] (cit. on p. 108).

[299] E. Jullo et al. “A Bayesian approach to strong lensing modelling of galaxy clusters”, *New Journal of Physics* 9.12 (2007), p. 447. arXiv: 0706.0048 [astro-ph] (cit. on p. 108).

[300] M. Bartelmann. “Arcs from a universal dark-matter halo profile.”, *A&A* 313 (1996), pp. 697–702. arXiv: astro-ph/9602053 [astro-ph] (cit. on p. 109).

[301] L. Lovisari et al. “Comparing different mass estimators for a large subsample of the Planck-ESZ clusters”, *A&A* 644 (2020), A78. arXiv: 2010.03582 [astro-ph.CO] (cit. on pp. 109, 127, 146, 157).

[302] G. P. Smith et al. “Hubble Space Telescope Observations of a Spectacular New Strong-Lensing Galaxy Cluster: MACS J1149.5+2223 at $z = 0.544$”, *ApJL* 707.2 (2009), pp. L163–L168. arXiv: 0911.2003 [astro-ph.CO] (cit. on pp. 113, 118).

[303] A. Bonafede et al. “Discovery of radio haloes and double relics in distant MACS galaxy clusters: clues to the efficiency of particle acceleration”, *MNRAS* 426.1 (2012), pp. 40–56. arXiv: 1206.6102 [astro-ph.CO] (cit. on p. 113).

[304] E. Q. Finney et al. “Mass Modeling of Frontier Fields Cluster MACS J1149.5+2223 Using Strong and Weak Lensing”, *ApJ* 859.1 (2018), p. 58 (cit. on p. 114).

[305] C. H. A. Logan et al. “Chandra follow-up of the Hectospec Cluster Survey: Comparison of caustic and hydrostatic masses and constraints on the hydrostatic bias”, *A&A* 665 (2022), A124. arXiv: 2202.08569 [astro-ph.CO] (cit. on p. 116).

[306] S. J. LaRoque et al. “Sunyaev-Zeldovich Effect Imaging of MACS Galaxy Clusters at $z > 0.5$”, *ApJ* 583.2 (2003), pp. 559–565 (cit. on pp. 117–119).

[307] R. Piffaretti et al. “The MCXC: a meta-catalogue of x-ray detected clusters of galaxies”, *A&A* 534 (2011), A109. arXiv: 1007.1916 [astro-ph.CO] (cit. on pp. 117–119).

[308] K. Javid et al. “Physical modelling of galaxy clusters detected by the Planck satellite”, *MNRAS* 483.3 (2019), pp. 3529–3544. arXiv: 1805.01991 [astro-ph.CO] (cit. on pp. 117, 118, 193).

[309] K. Umetsu et al. “CLASH: Joint Analysis of Strong-lensing, Weak-lensing Shear, and Magnification Data for 20 Galaxy Clusters”, *ApJ* 821.2 (2016), p. 116. arXiv: 1507.04385 [astro-ph.CO] (cit. on pp. 117, 118).

[310] K. Umetsu et al. "CLASH: Weak-lensing Shear-and-magnification Analysis of 20 Galaxy Clusters", *ApJ* 795.2 (2014), p. 163. arXiv: 1404.1375 [astro-ph.CO] (cit. on pp. 117, 118, 131).

[311] D. E. Applegate et al. "Weighing the Giants - III. Methods and measurements of accurate galaxy cluster weak-lensing masses", *MNRAS* 439.1 (2014), pp. 48–72. arXiv: 1208.0605 [astro-ph.CO] (cit. on pp. 117–119, 128).

[312] R. W. Schmidt and S. W. Allen. "The dark matter haloes of massive, relaxed galaxy clusters observed with Chandra", *MNRAS* 379.1 (2007), pp. 209–221. arXiv: astro-ph/0610038 [astro-ph] (cit. on p. 119).

[313] M. Limousin et al. "MACS J1423.8+2404: gravitational lensing by a massive, relaxed cluster of galaxies at $z = 0.54$", *MNRAS* 405.2 (2010), pp. 777–782. arXiv: 0911.4125 [astro-ph.CO] (cit. on p. 119).

[314] M. Sereno and S. Ettori. "Comparing masses in literature (CoMaLit) - I. Bias and scatter in weak lensing and X-ray mass estimates of clusters", *MNRAS* 450.4 (2015), pp. 3633–3648. arXiv: 1407.7868 [astro-ph.CO] (cit. on pp. 120, 127, 139, 142, 143, 146, 157, 158).

[315] H. Hoekstra et al. "The Canadian Cluster Comparison Project: detailed study of systematics and updated weak lensing masses", *MNRAS* 449.1 (2015), pp. 685–714. arXiv: 1502.01883 [astro-ph.CO] (cit. on pp. 123, 128, 146, 149).

[316] A. von der Linden et al. "Robust weak-lensing mass calibration of Planck galaxy clusters", *MNRAS* 443.3 (2014), pp. 1973–1978. arXiv: 1402.2670 [astro-ph.CO] (cit. on pp. 123, 146, 149).

[317] I. Chiu et al. "Baryon content in a sample of 91 galaxy clusters selected by the South Pole Telescope at $0.2 < z < 1.25$", *MNRAS* 478.3 (2018), pp. 3072–3099. arXiv: 1711.00917 [astro-ph.CO] (cit. on p. 123).

[318] S. Planelles et al. "Baryon census in hydrodynamical simulations of galaxy clusters", *MNRAS* 431.2 (2013), pp. 1487–1502. arXiv: 1209.5058 [astro-ph.CO] (cit. on p. 123).

[319] S. Ettori et al. "The cluster gas mass fraction as a cosmological probe: a revised study", *A&A* 501.1 (2009), pp. 61–73. arXiv: 0904.2740 [astro-ph.CO] (cit. on p. 123).

[320] L. P. David, C. Jones, and W. Forman. "The Universal Gas Mass Fraction in Clusters of Galaxies", *ApJ* 748.2 (2012), p. 120. arXiv: 1109.5067 [astro-ph.CO] (cit. on p. 123).

[321] D. Landry et al. "Chandra measurements of a complete sample of X-ray luminous galaxy clusters: the gas mass fraction", *MNRAS* 433.4 (2013), pp. 2790–2811. arXiv: 1211.4626 [astro-ph.CO] (cit. on pp. 123, 129–131).

[322] N. Okabe et al. "Universal profiles of the intracluster medium from Suzaku X-ray and Subaru weak-lensing observations", *PASJ* 66.5 (2014), p. 99. arXiv: 1406.3451 [astro-ph.CO] (cit. on p. 125).

[323] R. F. L. Holanda, K. Bora, and S. Desai. "A test of the evolution of gas depletion factor in galaxy clusters using strong gravitational lensing systems", *European Physical Journal C* 82.6 (2022), p. 526. arXiv: 2105.10988 [astro-ph.CO] (cit. on p. 125).

[324] M. Sereno et al. "XXL Survey groups and clusters in the Hyper Suprime-Cam Survey. Scaling relations between X-ray properties and weak lensing mass", *MNRAS* 492.3 (2020), pp. 4528–4545. arXiv: 1912.02827 [astro-ph.CO] (cit. on pp. 127, 137, 157, 158).

[325] M. Muñoz-Echeverría et al. "The hydrostatic-to-lensing mass bias from resolved X-ray and optical-IR data", *arXiv e-prints* (2023). arXiv: 2312.01154 [astro-ph.CO] (cit. on pp. 128, 204).

[326] H. Hoekstra et al. "The Canadian Cluster Comparison Project: weak lensing masses and SZ scaling relations", *MNRAS* 427.2 (2012), pp. 1298–1311. arXiv: 1208.0606 [astro-ph.CO] (cit. on pp. 128, 130).

[327] Planck Collaboration et al. "Planck early results. VIII. The all-sky early Sunyaev-Zeldovich cluster sample", *A&A* 536 (2011), A8. arXiv: 1101.2024 [astro-ph.CO] (cit. on p. 128).

[328] Planck Collaboration et al. "Planck intermediate results. III. The relation between galaxy cluster mass and Sunyaev-Zeldovich signal", *A&A* 550 (2013), A129. arXiv: 1204.2743 [astro-ph.CO] (cit. on p. 129).

[329] S. Ettori et al. "Mass profiles and $c-M_{\rm DM}$ relation in X-ray luminous galaxy clusters", *A&A* 524 (2010), A68 (cit. on p. 129).

[330] S. Ettori et al. *Mass profiles and c - M_{DM} relation in X-ray luminous galaxy clusters (Corrigendum)*. A&A, Volume 526, id.C1, 1 pp. 2011. arXiv: 1009.3266 [astro-ph.CO] (cit. on p. 129).

[331] Z. S. Yuan, J. L. Han, and Z. L. Wen. "Dynamical state of galaxy clusters evaluated from X-ray images", *MNRAS* 513.2 (2022), pp. 3013–3021. arXiv: 2204.02699 [astro-ph.GA] (cit. on p. 129).

[332] H. Ebeling et al. "The ROSAT Brightest Cluster Sample - I. The compilation of the sample and the cluster log N-log S distribution", *MNRAS* 301.4 (1998), pp. 881–914. arXiv: astro-ph/9812394 [astro-ph] (cit. on p. 130).

[333] G. P. Smith et al. "LoCuSS: Testing hydrostatic equilibrium in galaxy clusters", *MNRAS* 456.1 (2016), pp. L74–L78. arXiv: 1511.01919 [astro-ph.CO] (cit. on pp. 130, 142, 156, 157).

[334] R. Martino et al. "LoCuSS: hydrostatic mass measurements of the high-L_X cluster sample - cross-calibration of Chandra and XMM-Newton", *MNRAS* 443.3 (2014), pp. 2342–2360. arXiv: 1406.6831 [astro-ph.CO] (cit. on p. 130).

[335] N. Okabe and G. P. Smith. "LoCuSS: weak-lensing mass calibration of galaxy clusters", *MNRAS* 461.4 (2016), pp. 3794–3821. arXiv: 1507.04493 [astro-ph.CO] (cit. on p. 130).

[336] Y.-Y. Zhang et al. "LoCuSS: A Comparison of Cluster Mass Measurements from XMM-Newton and Subaru—Testing Deviation from Hydrostatic Equilibrium and Non-thermal Pressure Support", *ApJ* 711.2 (2010), pp. 1033–1043. arXiv: 1001.0780 [astro-ph.CO] (cit. on p. 130).

[337] A. Mahdavi et al. "Evidence for non-hydrostatic gas from the cluster X-ray to lensing mass ratio", *MNRAS* 384.4 (2008), pp. 1567–1574. arXiv: 0710.4132 [astro-ph] (cit. on pp. 130, 134, 137, 157).

[338] H. Hoekstra. "A comparison of weak-lensing masses and X-ray properties of galaxy clusters", *MNRAS* 379.1 (2007), pp. 317–330. arXiv: 0705.0358 [astro-ph] (cit. on p. 130).

[339] O. Ilbert et al. "Accurate photometric redshifts for the CFHT legacy survey calibrated using the VIMOS VLT deep survey", *A&A* 457.3 (2006), pp. 841–856. arXiv: astro-ph/0603217 [astro-ph] (cit. on p. 130).

[340] J. S. Bullock et al. "Profiles of dark haloes: evolution, scatter and environment", *MNRAS* 321.3 (2001), pp. 559–575. arXiv: astro-ph/9908159 [astro-ph] (cit. on p. 130).

[341] T. Schrabback et al. "Cluster mass calibration at high redshift: HST weak lensing analysis of 13 distant galaxy clusters from the South Pole Telescope Sunyaev-Zel'dovich Survey", *MNRAS* 474.2 (2018), pp. 2635–2678. arXiv: 1611.03866 [astro-ph.CO] (cit. on p. 131).

[342] M. J. Geller et al. "A Redshift Survey of the Strong-lensing Cluster Abell 383", *ApJ* 783.1 (2014), p. 52. arXiv: 1401.1440 [astro-ph.CO] (cit. on p. 131).

[343] E. A. Baltz, P. Marshall, and M. Oguri. "Analytic models of plausible gravitational lens potentials", *Journal of Cosmology and Astroparticle Physics* 2009.1 (2009), p. 015. arXiv: 0705.0682 [astro-ph] (cit. on pp. 136, 166).

[344] L. Hernquist. "An Analytical Model for Spherical Galaxies and Bulges", *ApJ* 356 (1990), p. 359 (cit. on p. 136).

[345] M. Sereno. "A Bayesian approach to linear regression in astronomy", *MNRAS* 455.2 (2016), pp. 2149–2162. arXiv: 1509.05778 [astro-ph.IM] (cit. on pp. 143, 158).

[346] I. G. McCarthy et al. "Gas expulsion by quasar-driven winds as a solution to the overcooling problem in galaxy groups and clusters", *MNRAS* 412.3 (2011), pp. 1965–1984. arXiv: 1008.4799 [astro-ph.CO] (cit. on p. 149).

[347] E. Rasia et al. "Lensing and x-ray mass estimates of clusters (simulations)", *New Journal of Physics* 14.5 (2012), p. 055018. arXiv: 1201.1569 [astro-ph.CO] (cit. on pp. 149, 166, 167, 184, 186, 187).

[348] M. G. Akritas and M. A. Bershady. "Linear Regression for Astronomical Data with Measurement Errors and Intrinsic Scatter", *ApJ* 470 (1996), p. 706. arXiv: astro-ph/9605002 [astro-ph] (cit. on p. 149).

[349] H. Akaike. "A New Look at the Statistical Model Identification", *IEEE Transactions on Automatic Control* 19 (1974), pp. 716–723 (cit. on p. 153).

[350] G. Schwarz. "Estimating the Dimension of a Model", *Annals of Statistics* 6.2 (1978), pp. 461–464 (cit. on p. 153).

[351] R. Monteiro-Oliveira et al. "Revising the merger scenario of the galaxy cluster Abell 1644: a new gas poor structure discovered by weak gravitational lensing", *MNRAS* 495.2 (2020), pp. 2007–2021. arXiv: 2004.13662 [astro-ph.GA] (cit. on p. 156).

[352] K. Pedersen and H. Dahle. "Calibration of the Mass-Temperature Relation for Clusters of Galaxies Using Weak Gravitational Lensing", *ApJ* 667.1 (2007), pp. 26–34. arXiv: astro-ph/0603260 [astro-ph] (cit. on p. 156).

[353] R. Herbonnet et al. "CCCP and MENeaCS: (updated) weak-lensing masses for 100 galaxy clusters", *MNRAS* 497.4 (2020), pp. 4684–4703. arXiv: 1912.04414 [astro-ph.CO] (cit. on p. 157).

[354] F. Pacaud et al. "The XXL Survey. II. The bright cluster sample: catalogue and luminosity function", *A&A* 592 (2016), A2. arXiv: 1512.04264 [astro-ph.CO] (cit. on p. 158).

[355] M. Muñoz-Echeverría et al. "Galaxy cluster mass bias from projected mass maps: The Three Hundred-NIKA2 LPSZ twin samples", *arXiv e-prints* (2023). arXiv: 2305.14862 [astro-ph.CO] (cit. on pp. 162, 205).

[356] S. J. Aarseth. "Dynamical evolution of clusters of galaxies, I", *MNRAS* 126 (1963), p. 223 (cit. on p. 162).

[357] S. D. M. White. "The dynamics of rich clusters of galaxies.", *MNRAS* 177 (1976), pp. 717–733 (cit. on p. 162).

[358] A. Klypin et al. "MultiDark simulations: the story of dark matter halo concentrations and density profiles", *MNRAS* 457.4 (2016), pp. 4340–4359. arXiv: 1411.4001 [astro-ph.CO] (cit. on p. 162).

[359] V. Springel et al. "Simulations of the formation, evolution and clustering of galaxies and quasars", *Nature* 435.7042 (2005), pp. 629–636. arXiv: astro-ph/0504097 [astro-ph] (cit. on p. 162).

[360] S. Cole et al. "A recipe for galaxy formation.", *MNRAS* 271 (1994), pp. 781–806. arXiv: astro-ph/9402001 [astro-ph] (cit. on p. 162).

[361] R. S. Somerville and J. R. Primack. "Semi-analytic modelling of galaxy formation: the local Universe", *MNRAS* 310.4 (1999), pp. 1087–1110. arXiv: astro-ph/9802268 [astro-ph] (cit. on p. 162).

[362] F. Sembolini et al. "The MUSIC of galaxy clusters - I. Baryon properties and scaling relations of the thermal Sunyaev-Zel'dovich effect", *MNRAS* 429.1 (2013), pp. 323–343. arXiv: 1207.4438 [astro-ph.CO] (cit. on pp. 162, 165, 166).

[363] R. Davé et al. "SIMBA: Cosmological simulations with black hole growth and feedback", *MNRAS* 486.2 (2019), pp. 2827–2849. arXiv: 1901.10203 [astro-ph.GA] (cit. on p. 162).

[364] W. Cui et al. "THE THREE HUNDRED project: The GIZMO-SIMBA run", *MNRAS* 514.1 (2022), pp. 977–996. arXiv: 2202.14038 [astro-ph.GA] (cit. on p. 162).

[365] E. Rasia et al. “Cool Core Clusters from Cosmological Simulations”, *ApJL* 813.1 (2015), p. L17. arXiv: 1509.04247 [astro-ph.CO] (cit. on p. 162).

[366] L. K. Steinborn et al. “A refined sub-grid model for black hole accretion and AGN feedback in large cosmological simulations”, *MNRAS* 448.2 (2015), pp. 1504–1525. arXiv: 1409.3221 [astro-ph.GA] (cit. on p. 162).

[367] R. P. C. Wiersma, J. Schaye, and B. D. Smith. “The effect of photoionization on the cooling rates of enriched, astrophysical plasmas”, *MNRAS* 393.1 (2009), pp. 99–107. arXiv: 0807.3748 [astro-ph] (cit. on p. 162).

[368] S. Planelles et al. “Pressure of the hot gas in simulations of galaxy clusters”, *MNRAS* 467.4 (2017), pp. 3827–3847. arXiv: 1612.07260 [astro-ph.CO] (cit. on pp. 162, 164).

[369] A. Paliwal et al. “The Three Hundred-NIKA2 Sunyaev-Zeldovich Large Program twin samples: Synthetic clusters to support real observations”, *mm Universe @ NIKA2 - Observing the mm Universe with the NIKA2 Camera*. Vol. 257. 2022, p. 00036. arXiv: 2111.01920 [astro-ph.CO] (cit. on p. 163).

[370] N. Battaglia et al. “On the Cluster Physics of Sunyaev-Zel’dovich and X-Ray Surveys. IV. Characterizing Density and Pressure Clumping due to Infalling Substructures”, *ApJ* 806.1 (2015), p. 43. arXiv: 1405.3346 [astro-ph.CO] (cit. on p. 164).

[371] R. Herbonnet et al. “Brightest cluster galaxies trace weak lensing mass bias and halo triaxiality in the three hundred project”, *MNRAS* 513.2 (2022), pp. 2178–2193. arXiv: 2109.01673 [astro-ph.CO] (cit. on pp. 165, 174).

[372] A. Knebe et al. “The Three Hundred project: shapes and radial alignment of satellite, infalling, and backsplash galaxies”, *MNRAS* 495.3 (2020), pp. 3002–3013. arXiv: 2005.09896 [astro-ph.GA] (cit. on p. 165).

[373] A. M. C. Le Brun, I. G. McCarthy, and J.-B. Melin. “Testing Sunyaev-Zel’dovich measurements of the hot gas content of dark matter haloes using synthetic skies”, *MNRAS* 451.4 (2015), pp. 3868–3881. arXiv: 1501.05666 [astro-ph.CO] (cit. on p. 165).

[374] M. Oguri et al. “Subaru Weak Lensing Measurements of Four Strong Lensing Clusters: Are Lensing Clusters Overconcentrated?”, *ApJ* 699.2 (2009), pp. 1038–1052. arXiv: 0901.4372 [astro-ph.CO] (cit. on pp. 165, 170).

[375] M. Oguri and R. D. Blandford. “What is the largest Einstein radius in the universe?”, *MNRAS* 392.2 (2009), pp. 930–944. arXiv: 0808.0192 [astro-ph] (cit. on p. 165).

[376] J. F. Hennawi et al. “Characterizing the Cluster Lens Population”, *ApJ* 654.2 (2007), pp. 714–730. arXiv: astro-ph/0506171 [astro-ph] (cit. on p. 165).

[377] M. Meneghetti et al. “Strong lensing in the MARENOSTRUM UNIVERSE. I. Biases in the cluster lens population”, *A&A* 519 (2010), A90. arXiv: 1003.4544 [astro-ph.CO] (cit. on pp. 165, 166).

[378] M. B. Gralla et al. “Sunyaev-Zel’dovich Effect Observations of Strong Lensing Galaxy Clusters: Probing the Overconcentration Problem”, *ApJ* 737.2 (2011), p. 74. arXiv: 1011.6341 [astro-ph.CO] (cit. on p. 166).

[379] M. Meneghetti et al. “The MUSIC of CLASH: Predictions on the Concentration-Mass Relation”, *ApJ* 797.1 (2014), p. 34. arXiv: 1404.1384 [astro-ph.CO] (cit. on pp. 166–168, 170, 171, 186).

[380] V. Biffi et al. “The MUSIC of galaxy clusters - II. X-ray global properties and scaling relations”, *MNRAS* 439.1 (2014), pp. 588–603. arXiv: 1401.2992 [astro-ph.CO] (cit. on p. 166).

[381] C. Giocoli et al. “Cosmology in two dimensions: the concentration-mass relation for galaxy clusters”, *MNRAS* 426.2 (2012), pp. 1558–1573. arXiv: 1205.2375 [astro-ph.CO] (cit. on pp. 166–168, 171, 187).

[382] L. D. Shaw et al. “Statistics of Physical Properties of Dark Matter Clusters”, *ApJ* 646.2 (2006), pp. 815–833. arXiv: astro-ph/0509856 [astro-ph] (cit. on p. 166).

[383] J. Einasto. "On the Construction of a Composite Model for the Galaxy and on the Determination of the System of Galactic Parameters", *Trudy Astrofizicheskogo Instituta Alma-Ata* 5 (1965), pp. 87–100 (cit. on p. 166).

[384] E. Rasia et al. "On the Discrepancy between Theoretical and X-Ray Concentration-Mass Relations for Galaxy Clusters", *ApJ* 776.1 (2013), p. 39. arXiv: 1301.7476 [astro-ph.CO] (cit. on p. 166).

[385] C. Giocoli et al. "Mass and concentration estimates from weak and strong gravitational lensing: a systematic study", *MNRAS* 440.2 (2014), pp. 1899–1915. arXiv: 1311.1205 [astro-ph.CO] (cit. on p. 166).

[386] W. Lee et al. "Weak-lensing Mass Bias in Merging Galaxy Clusters", *ApJ* 945.1 (2023), p. 71. arXiv: 2211.03892 [astro-ph.CO] (cit. on p. 166).

[387] C. Giocoli et al. "MOKA: a new tool for strong lensing studies", *MNRAS* 421.4 (2012), pp. 3343–3355. arXiv: 1109.0285 [astro-ph.CO] (cit. on p. 166).

[388] D. Fabjan et al. "X-ray mass proxies from hydrodynamic simulations of galaxy clusters - I", *MNRAS* 416.2 (2011), pp. 801–816. arXiv: 1102.2903 [astro-ph.CO] (cit. on p. 166).

[389] D. A. Buote and P. J. Humphrey. "Spherically averaging ellipsoidal galaxy clusters in X-ray and Sunyaev-Zel'dovich studies - II. Biases", *MNRAS* 421.2 (2012), pp. 1399–1420. arXiv: 1109.6656 [astro-ph.CO] (cit. on pp. 167, 186).

[390] M. Meneghetti et al. "Weighing simulated galaxy clusters using lensing and X-ray", *A&A* 514 (2010), A93. arXiv: 0912.1343 [astro-ph.CO] (cit. on pp. 167, 184, 186, 187).

[391] R. Laureijs et al. "Euclid Definition Study Report", *arXiv e-prints* (2011). arXiv: 1110.3193 [astro-ph.CO] (cit. on p. 167).

[392] Y. M. Bahé, I. G. McCarthy, and L. J. King. "Mock weak lensing analysis of simulated galaxy clusters: bias and scatter in mass and concentration", *MNRAS* 421.2 (2012), pp. 1073–1088. arXiv: 1106.2046 [astro-ph.CO] (cit. on p. 167).

[393] M. Muñoz-Echeverría et al. "The LPSZ-CLASH galaxy cluster sample: Combining lensing and hydrostatic mass estimates", *mm Universe @ NIKA2 - Observing the mm Universe with the NIKA2 Camera*. Vol. 257. 2022, p. 00033. arXiv: 2111.01691 [astro-ph.CO] (cit. on pp. 167, 168).

[394] D. López-Cano et al. "The cosmology dependence of the concentration-mass-redshift relation", *MNRAS* 517.2 (2022), pp. 2000–2011. arXiv: 2207.13718 [astro-ph.CO] (cit. on p. 170).

[395] I. Bartalucci et al. "CHEX-MATE: Constraining the origin of the scatter in galaxy cluster radial X-ray surface brightness profiles", *arXiv e-prints* (2023). arXiv: 2305.03082 [astro-ph.CO] (cit. on p. 175).

[396] A. Nagarajan et al. "Weak-lensing mass calibration of the Sunyaev-Zel'dovich effect using APEX-SZ galaxy clusters", *MNRAS* 488.2 (2019), pp. 1728–1759. arXiv: 1804.03671 [astro-ph.CO] (cit. on pp. 185, 186).

[397] K. Basu et al. "ALMA-SZ Detection of a Galaxy Cluster Merger Shock at Half the Age of the Universe", *ApJL* 829.2 (2016), p. L23. arXiv: 1608.05413 [astro-ph.CO] (cit. on p. 189).

[398] A. T. Moffet and M. Birkinshaw. "A VLA Survey of the Three Clusters of Galaxies 0016+16, Abell 665, and Abell 2218", *AJ* 98 (1989), p. 1148 (cit. on p. 189).

[399] R. A. Watson et al. "First results from the Very Small Array - I. Observational methods", *MNRAS* 341.4 (2003), pp. 1057–1065. arXiv: astro-ph/0205378 [astro-ph] (cit. on p. 189).

[400] M. Jones et al. "An image of the Sunyaev-Zel'dovich effect", *Nature* 365.6444 (1993), pp. 320–323 (cit. on p. 189).

[401] K. Grainge et al. "Detection of the Sunyaev-Zel'dovich effect in Abell 773.", *MNRAS* 265 (1993), pp. L57–L58 (cit. on p. 189).

[402] J. E. Carlstrom, M. Joy, and L. Grego. "Interferometric Imaging of the Sunyaev-Zeldovich Effect at 30 GHz", *ApJL* 456 (1996), p. L75 (cit. on p. 189).

[403] J. T. L. Zwart et al. "The Arcminute Microkelvin Imager", *MNRAS* 391.4 (2008), pp. 1545–1558. arXiv: 0807.2469 [astro-ph] (cit. on p. 189).

[404] J. E. Carlstrom, G. P. Holder, and E. D. Reese. "Cosmology with the Sunyaev-Zel'dovich Effect", *ARA&A* 40 (2002), pp. 643–680. arXiv: astro-ph/0208192 [astro-ph] (cit. on p. 189).

[405] A. R. Thompson, J. M. Moran, and G. W. Swenson. *Interferometry and Synthesis in Radio Astronomy, 3rd Edition*. 2017 (cit. on p. 190).

[406] L. Di Mascolo, E. Churazov, and T. Mroczkowski. "A joint ALMA-Bolocam-Planck SZ study of the pressure distribution in RX J1347.5-1145", *MNRAS* 487.3 (2019), pp. 4037–4056. arXiv: 1812.01034 [astro-ph.CO] (cit. on pp. 191, 200).

[407] A. Plunkett et al. "Data Combination: Interferometry and Single-dish Imaging in Radio Astronomy", *PASP* 135.1045 (2023), p. 034501. arXiv: 2303.02177 [astro-ph.IM] (cit. on p. 191).

[408] S. Guilloteau. "The IRAM Interferometer on Plateau de Bure", *International Astronomical Union Colloquium* 140 (1994), pp. 27–34 (cit. on p. 191).

[409] M. Krips et al. "NOEMA: How One Million Lines of Code Make the Optically Dark Universe Visible", *Astronomical Society of the Pacific Conference Series*. Ed. by J. E. Ruiz, F. Pierfedereci, and P. Teuben. Vol. 532. 2022, p. 313 (cit. on p. 191).

[410] T. J. Pearson. "Non-Imaging Data Analysis", *Synthesis Imaging in Radio Astronomy II*. Ed. by G. B. Taylor, C. L. Carilli, and R. A. Perley. Vol. 180. 1999, p. 335 (cit. on p. 199).

[411] M. Tazzari, F. Beaujean, and L. Testi. "GALARIO: a GPU accelerated library for analysing radio interferometer observations", *MNRAS* 476.4 (2018), pp. 4527–4542. arXiv: 1709.06999 [astro-ph.IM] (cit. on p. 199).

[412] CONCERTO Collaboration et al. "A wide field-of-view low-resolution spectrometer at APEX: Instrument design and scientific forecast", *A&A* 642 (2020), A60. arXiv: 2007.14246 [astro-ph.IM] (cit. on p. 205).

[413] C. L. Bennett et al. "First-Year Wilkinson Microwave Anisotropy Probe (WMAP) Observations: Foreground Emission", *ApJS* 148.1 (2003), pp. 97–117. arXiv: astro-ph/0302208 [astro-ph] (cit. on p. 205).

[414] H. Brunner et al. "The eROSITA Final Equatorial Depth Survey (eFEDS). X-ray catalogue", *A& A* 661 (2022), A1. arXiv: 2106.14517 [astro-ph.HE] (cit. on p. 206).

Abstract

In this thesis, we present a multi-wavelength study of galaxy clusters. The work is focused on the precise reconstruction and comparison of cluster masses, which are an elemental quantity to use galaxy clusters as a cosmological probe. In the context of the NIKA2 guaranteed time Sunyaev Zel'dovich Large Programme, we present the characterisation of the systematic effects affecting the NIKA2 millimetre cluster maps and how they impact the estimation of the hydrostatic mass. The filtering at large angular scales is the main limiting factor to constrain precisely the mass. From the comparison of hydrostatic masses to lensing estimates, we conclude that the former are biased low by about 20 to 40% with respect to lensing and that hydrostatic masses obtained from the combination of Sunyaev Zel'dovich and X-ray data tend to be less biased than X-ray-only estimates. The bias is confirmed in the study of a larger cluster sample with XMM-*Newton* data, while a potential evolution of the hydrostatic-to-lensing mass ratio with redshift is not statistically significant. Regarding the intrinsic effects that affect the reconstruction of cluster masses from observations, we present an analysis based on THE THREE HUNDRED hydrodynamical simulations. We show that, under the assumption of sphericity, the projection along which the cluster is observed is a major source of scatter in the mass estimation for dark matter observables. The effect is an order of magnitude smaller for the tracers of the gas in the intracluster medium, demonstrating the power of X-ray and Sunyaev Zel'dovich observations. However, our knowledge about the distribution of the gas in the core of clusters remains subject to the angular resolution of the instruments in X-ray and millimetre wavelengths. We present in this thesis the first detection of the Sunyaev Zel'dovich effect of a cluster with the Northern Extended Millimeter Array interferometer.

Résumé

Nous présentons une étude multi-longueur d'onde des amas de galaxies. Le travail se concentre sur la reconstruction précise et la comparaison des masses d'amas, qui sont une quantité élémentaire pour utiliser les amas de galaxies comme sonde cosmologique. Dans le cadre du Grand Programme Sunyaev Zel'dovich de temps garanti de NIKA2, nous présentons la caractérisation des effets systématiques affectant les données millimétriques NIKA2 et leur impact sur l'estimation de la masse hydrostatique. Le filtrage aux grandes échelles angulaires est le principal facteur limitant les contraintes précises sur la masse. De la comparaison des masses hydrostatiques aux estimations basées sur l'effet de lentille gravitationnelle, nous concluons que les premières sont biaisées d'environ 20 à 40% par rapport aux deuxièmes et que les masses hydrostatiques obtenues à partir de la combinaison des données millimétriques et des rayons X ont tendance à être moins biaisées que les estimations basées uniquement sur des rayons X. Le biais est confirmé sur l'étude d'un plus grand échantillon d'amas avec des données XMM-*Newton*, alors qu'une potentielle évolution du rapport de masse hydrostatique sur masse de lentille gravitationnelle avec le décalage vers le rouge n'est pas statistiquement significative. En ce qui concerne les effets intrinsèques qui affectent la reconstruction des masses d'amas à partir des observations, nous présentons une analyse basée sur les simulations hydrodynamiques THE THREE HUNDRED. Nous montrons que, sous l'hypothèse de sphéricité, la projection sur laquelle l'amas est observé est une source majeure de dispersion dans l'estimation de masse pour les observables de matière noire. L'effet est un ordre de grandeur inférieur pour les traceurs du gaz dans le milieu intra-amas, démontrant la puissance des observations en millimétrique et en X. Cependant, notre connaissance sur la distribution du gaz au cœur des amas est limitée par la résolution angulaire des instruments. Nous présentons dans cette thèse la première détection de l'effet Sunyaev Zel'dovich d'un amas avec l'interféromètre Northern Extended Millimeter Array.